SLAC-R-315

SLAC 315
CONF-870298
UC-34D
(T/E)

PROCEEDINGS OF THE THIRD MARK II WORKSHOP ON SLC PHYSICS

February 25-28, 1987
Pajaro Dunes Conference Center
Watsonville, CA 95076

July 1987

Prepared for the Department of Energy
under contract number DE-AC03-76SF00515

Printed in the United States of America. Available from the National Technical Information Service, U.S. Department of Commerce, 5285 Port Royal Road, Springfield, Virginia 22161. Price: Printed Copy A25, Microfiche A01.

Preface

In its initial call for SLC experimental proposals, SLAC specified that the first SLC detector would have to be tested at PEP. The reason for this requirement is that SLAC wanted physics production to begin immediately upon achieving usable SLC luminosity. The implication of this requirement is that both the detector hardware and the analysis programs need to be ready and understood at SLC start-up. To achieve the latter goal, the Mark II Collaboration established a series of SLC-physics working groups in August 1985.

The groups and their chairmen are as follows:

Number	Topic	Chairman
1	Z Mass and Width	Patricia Rankin, SLAC
2	Weak Parameters	John Matthews, Johns Hopkins
3	Heavy Particles	Martin Perl, SLAC
4	Toponium	Hartmut Sadrozinski, Santa Cruz
5	New Neutral Particles	Gerry Abrams, LBL
6	Long-lived Particles	Ryszard Stroynowski, Cal Tech
7	Single Higgs Search	Walt Innes, SLAC
8	QCD	Alfred Petersen, SLAC
9	c and b Quark Studies	Bill Ford, Colorado
10	Neutrino Counting	Rudy Thun, Michigan
11	Commissioning	Rudy Larsen, SLAC

In addition, Group 3 developed two distinct subgroups: Open Top, chaired by Gail Hanson, SLAC; and Supersymmetry, chaired by Tim Barklow, SLAC.

Each group was charged with five tasks:

1. identifying the physics goals within its topic,

2. developing the strategy for pursuing those goals,

3. identifying and implementing necessary interfaces with the collider (e.g. beam parameter measurement and control) and/or minor improvements to the detector hardware,
4. developing analysis and Monte Carlo programs and testing these programs, to the extent possible, on PEP data, and,
5. educating the Collaboration on the physics to be done and the required techniques.

To monitor progress of the working groups and to educate the Collaboration, workshops were scheduled at six-month intervals. These were to be intensive three-day meetings, held away from the distractions of the laboratory, at which the whole Collaboration would gather to concentrate on SLC physics.

The first workshop was held at Asilomar Conference Center in Pacific Grove, California on March 16-19, 1986. No proceedings of that meeting were issued, but copies of the almost 1000 pages of transparencies were distributed as Mark II/SLC-Physics Working Group Note #0-2.

The second workshop was held at Granlibakken Conference Center in Tahoe City, California on September 14-17, 1986. The transparencies from that meeting were distributed as Mark II/SLC-Physics Working Group Note #0-4, and a formal proceedings was published as SLAC report number SLAC-306.

The third and final workshop in this series was held at Pajaro Dunes, California on February 25-28, 1987. The meeting followed the format established at the first two workshops: morning and evening sessions each day, an afternoon session on the first day, and the following two afternoons left free for small group meetings and recreation. A total of 114 people attended the workshop, including observers from the Polarization Group, the SLD collaboration, and all four LEP collaborations. In addition to these proceedings, copies of the transparencies are available as Mark II/SLC-Physics Working Group Note #0-8.

The papers in these proceedings have all been given Mark II/SLC Working

Group Note numbers for indexing purposes. The numbering scheme for these notes is "n-m," where n is the working group number and m is a sequential number. Papers that are general in nature or that cover the work of more than one working group are assigned n=0. A list of all Mark II/SLC Working Group Notes is found in the Appendix. Individual notes are available from June Hu at SLAC.

A number of reports presented at Pajaro Dunes are not included in these proceedings. In two cases those reports dealt with material that would be obsolete by the time these proceedings were printed. Witold Kozanecki gave a "Status Report on the Final Focus Commissioning" and Burton Richter reported on "SLAC Schedules, Budgets, and Plans." Jim Smith reported on "Prospects for Heavy Quark Asymmetry Measurements." This report was not written up because it heavily duplicated a report which had previously been published in the proceedings of the Granlibakken workshop. Finally, Dieter Cords's talk on "Detecting Extra Z Bosons" and Paul Grosse-Wiesmann's talk on "Physics with Polarized Beams" were received too late for inclusion in these proceedings. They will be available as separate Mark II/SLC Working Group Notes.

The Pajaro Dunes workshop marked the end of the formal study. However, at the workshop, as a final exercise, Alfred Petersen and I gave the collaboration a "Mock Data Challenge." We prepared some Monte Carlo tapes containing about 10,000 Z decays. These tapes contained all the expected Z decays and possibly some new physics. The Collaboration was to treat them as if they were real data — analyse them and agree on some conclusions. Some of the goals we had in preparing this exercise were as follows:

1. To encourage people to face detector issues such as lepton identification and vertex reconstruction. Much of the initial work has been done with identified 4-vectors taken directly from the Monte Carlo rather than from reconstructed quantities.
2. To encourage people to determine the combination of signatures that will

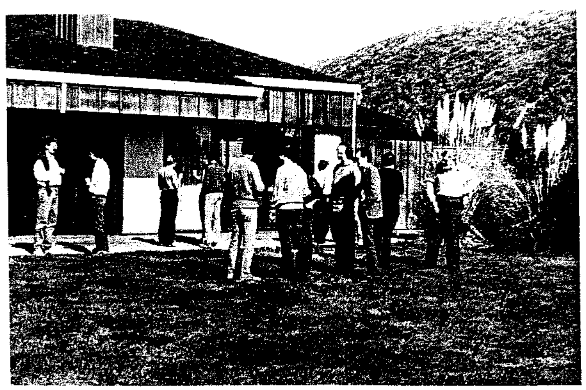

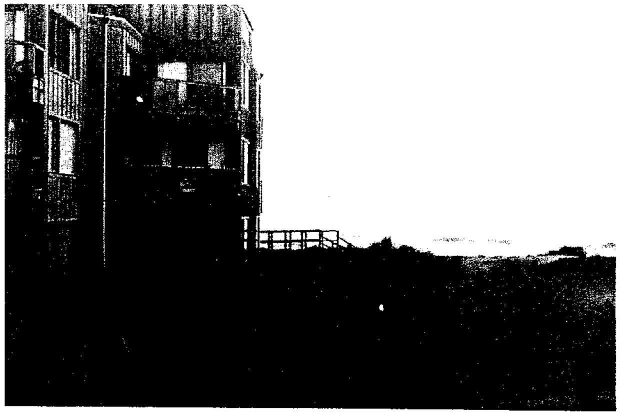

uniquely identify a particular new particle. Many signatures, such as high aplanarity or isolated leptons, are common to many different types of new particles.

3. To encourage data-driven searches. There are two different ways to go about searching for new particles: one can start with a hypothesis and search for evidence for or against it, or one can look at the data and search for ways in which it differs from expectations. Since the number of different new particle scenarios is very large, data-driven searches may prove more efficient in uncovering signals.

4. To understand the limitations of analysis which can be done with a data sample of about 10,000 events.

As of the writing of this preface, the analysis of the mock data is still in progress, but it is already clear that all of the goals listed above have been met to some extent.

Finally, I want to extend the thanks of the Collaboration to Nina Adelman for handling all of the administrative tasks for all three workshops, and to June Hu for helping with the administration of the Pajaro Dunes workshop and for editing these proceedings.

Gary Feldman

TABLE OF CONTENTS

Mark II/SLC-Physics Working Group Note # 0–9

AUTHOR: Chris Hawkes

DATE: April 9, 1987

TITLE: Status Report on Lepton Identification*

ABSTRACT

Electron identification using the dE/dx, time of flight and barrel and endcap calorimeter systems of the Mark II / SLC detector is described. Muon identification is also discussed.

* Talk given at the Third Mark II Workshop on SLC Physics, Pajaro Dunes, February 25-28, 1987

1. INTRODUCTION

This is a review of work done by members of the Particle Identification Group.* It is intended to be a "how to" document which can be used by members of the Mark II / SLC Collaboration to help them to search for leptons in the Mark II data. This is required in order to study a number of different physics topics, which are discussed in other talks at this workshop.

Work on particle identification is still in progress and so much of the information given here is preliminary and should be used with caution.

It is necessary to go into the details of the Mark II analysis programs, and some previous familiarity will be assumed. All FORTRAN code which is mentioned can be found on the ECPUB 192 disk on SLACVM (usually referred to as the G disk), and all data words are part of the standard Mark II track lists (array TRK in COMMON/TRKLST/) which are documented in file EVLST M2DOC on the G disk.

Lepton identification in the following detector components will be reported (see Fig. 1): dE/dx in the main drift chamber, time of flight (TOF), liquid argon barrel calorimeter (LA), endcap electromagnetic calorimeter (ECC or EEC) and the existing muon system. Pair finding from charged tracking has been described in a recent Mark II note by Pat Burchat [1] and will not be repeated here.

Further details exist in the references cited and in minutes of Particle ID Group meetings which are available on request.

* This group consists of representatives working on particle identification algorithms for the various components of the Mark II / SLC detector. Those who have attended meetings or contributed in other ways include: John Bartelt, Pat Burchat, Dave Coupal, Jonathan Dorfan, Gary Feldman, Paul Grosse-Wiesmann, Chris Hawkes, Dave Herrup, Michel Jaffre, Mark Nelson, Art Snyder, Eric Soderstrom, Rick Van Kooten, Eric Wicklund, Andrew Weir and Dolly Wu.

2. dE/dx

Lepton identification using dE/dx measurements is being worked on by Dave Coupal and Rick Van Kooten. A description of the Mark II dE/dx system can be found in the Mark II / SLC Proposal [2].

Charged particles travelling at different speeds through the drift chamber gas lose energy by ionisation at different rates, as shown in Fig. 2. Hence, two particles of the same momentum but different masses can be distinguished using dE/dx provided their momentum is low enough.

Fig. 3 shows the layout of wires in the main drift chamber. Pulse height measurements are available from each of the sense wires, giving a maximum of 72 dE/dx samples of size 8.33 mm at normal incidence.* At lower polar angles the sample length is larger, giving a better dE/dx resolution, until the number of samples begins to decrease beyond $|\cos\theta| = 0.63$. Fig. 4 is a plot of dE/dx (in units of keV/8.33 mm) against $\log_{10} p$, where p is momentum in GeV/c. Included are all charged tracks recorded during the PEP/Upgrade running which have good dE/dx data. Superimposed are the predicted dE/dx curves for electrons, muons, pions, kaons and protons. The separation between different particle types for certain momentum ranges is clear. A dE/dx resolution of 7.8% has been determined from Bhabha scattering events. For pion tracks it is 9.7%, while inside jets the resolution becomes 11.4%.

For a given track, dE/dx information is stored in the track list, subtype 11 (see Table 1). Cuts should be applied to NSAMPL (word 1) and IQQUAL (word 10) to

* For the PEP/Upgrade running, only the lower $\frac{1}{3}$ of the dE/dx system was instrumented, and the data only from run 15121 onwards should be used. This means, for example, that low momentum tracks are unlikely to have the full 72 dE/dx samples, since they will probably bend out of the active region.

ensure good quality data – NSAMPL $\geq$ 50 and IQQUAL $<$ 10 are suitable. The measured dE/dx is QTRK (word 8) and the dE/dx resolution, which depends on the particle type, can be obtained by multiplying DXSIG (word 9) by the expected dE/dx for the relevant particle (words 14-17). For example, for an electron:

$$\sigma_e = \mathrm{DXSIG} * \mathrm{DDXE}$$

For particles not given in the track list (e.g. μ), the expected dE/dx can be calculated by using the subroutine FDCDXP.

CALL FDCDXP (BG, CH, DDXMU)

where:

BG = relativistic $\beta\gamma$ factor for assumed particle ($\beta\gamma = p/m_\mu$ for μ)

and CH = charge (= 1 for μ)

The routine returns:

DDXMU = expected dE/dx in keV/8.33 mm

From the measured and expected dE/dx, and the resolution, the probability of a track being a particular particle type can be determined, e.g. for an electron:

$$P_e = \frac{1}{\sqrt{2\pi}\sigma_e} \exp\left\{ -\frac{1}{2}\left(\frac{\mathrm{QTRK} - \mathrm{DDXE}}{\sigma_e}\right)^2 \right\}$$

Hence, the weight for being an electron is

$$W_e = \frac{P_e}{\sum_i P_i}$$

Note that the denominator, $\sum_i P_i$, is not equal to 1.

For separating two different particle types, e.g. e/π, the important quantity is $\Delta E/\sigma$, where ΔE is the difference between the expected values of dE/dx for the particle types, and σ is the resolution. This is shown for e/π separation as a function of track momentum by the solid curve in Fig. 5. The dE/dx resolution for pions, 9.7%, was used. An e/π separation of about two standard deviations or more is possible in the range $200\,\mathrm{MeV}/c < p < 7\,\mathrm{GeV}/c$.

To understand what this statement means in terms of the number of pion tracks which would be misidentified as electrons, consider Fig. 6(a). This shows the predicted distribution of dE/dx measured from true pions and true electrons for the case of a 3σ separation. The variation of resolution with dE/dx has been neglected, and the curves are normalised to have equal areas. A 1σ cut for electron identification could be applied, as shown. Simple statistics then give the electron identification efficiency as 84% and the pion misidentification probability to be 2.3%. These are the fractions of the areas under the electron and pion curves respectively, to the right of the cut in Fig. 6(a). At first sight this looks quite good, but then the relative normalisations of the two curves must be taken into account. In a typical hadronic event, without any previous track cuts, there are likely to be about 100 times as many true pions as there are true electrons (see Fig. 6(b)). So, with the 1σ cut, the selected "electron sample" will contain 230 pions for every 84 electrons, which does not look so good. The purpose of going through this trivial arithmetic exercise was to illustrate the importance of keeping the pion misidentification probability at the 1% level or lower, while maintaining a reasonable electron identification efficiency. The electrons form a small signal in the tail of a large pion background, for the dE/dx and for the other identification systems.

The solid line in Fig. 7 shows the $\Delta E/\sigma$ curve for separation of electrons from any other stable charged particles. Below $1\,\mathrm{GeV}/c$ there are numerous regions of

confusion, corresponding to the points in Fig. 4 where the predicted dE/dx curve for electrons crosses that for the other particles. Time of flight measurements (see section 3) can be used to resolve this ambiguity, as is shown by the dotted line in Fig. 7. At higher momenta, electron identification in the calorimeters (see section 4) becomes more useful.

For electron identification within hadronic events it is common to study tracks as a function of p, the track momentum, and p_t, the track momentum perpendicular to the thrust axis of the event. Table 2(a) shows the pion misidentification probability for bins of p and p_t as calculated from Monte Carlo events using the theoretical dE/dx resolution, and requiring an electron identification efficiency of 90%. Table 2(b) shows the same quantities, but after an additional 10% smearing of the dE/dx measurements, which is thought to correspond more closely to the real data.*

It is worth pointing out that the numbers in these tables come from a particular set of Monte Carlo events, and might not be correct for any other set of events, selected with cuts appropriate to another analysis, for example.

* These tables are discussed in more detail in reference 3, from which they were taken.

3. TIME OF FLIGHT

Particle identification using TOF is being worked on by Eric Soderstrom and Eric Wicklund [4].

The time of flight counters consist of 48 scintillator counters around the drift chamber (see Fig. 1). The resolution has been determined from tracks in Bhabha scattering events from the PEP/Upgrade running to be 234 ps (Fig. 8) and is estimated to be 250 ps for tracks in hadronic events.

Time of flight information is stored in subtype 3 of the track list (see Table 3). For the moment, a quality cut of TQUAL = 1.0 (word 7) should be applied. The measured time of flight is TOF (word 3) and the flight path length is PATH (word 13). From these, and the momentum as measured in the drift chamber,* the mass-squared of the particle can be calculated. This is AMASS2 (word 12):

$$\mathrm{AMASS2} = p^2 \left\{ \left(\frac{c \times \mathrm{TOF}}{\mathrm{PATH}} \right)^2 - 1 \right\}$$

Fig. 9 is a plot of AMASS2 against momentum for all tracks in the PEP/Upgrade data with good time of flight information. The separation of protons and kaons is clear, but e/π separation is possible only below about 300 MeV/c. The quantity $\Delta M^2/\sigma_{M^2}$ from time of flight is the equivalent of $\Delta E/\sigma$ from dE/dx. Adding these two in quadrature gives the combined dE/dx & TOF separation which is shown by the dotted lines in Fig. 5 and Fig. 7.

Also in subtype 3 are the expected times of flight for various particle types (words 14-17) and the TOF resolution, TOFSIG (word 18), which does not depend

* Here and elsewhere the momentum as determined from a vertex constrained track fit (subtype 6) is used, if it is available. Otherwise the one track fit (subtype 2) is used. Note that, if no secondary vertex finding has been done, then all subtype 6 tracks will be constrained to the beam point and that this can give substantial errors on the momenta of tracks coming from decays.

on particle type.* From these, and the measured TOF, the probability of a track being a particular particle type can be determined. For example, for a pion:

$$P_\pi = \frac{1}{\sqrt{2\pi} \times \mathrm{TOFSIG}} \exp\left\{ -\frac{1}{2} \left(\frac{\mathrm{TOF} - \mathrm{TOFPI}}{\mathrm{TOFSIG}} \right)^2 \right\}$$

4. CALORIMETRY

In the Mark II / SLC detector the electromagnetic calorimetry consists of the liquid argon barrel calorimeter down to about $|\cos\theta| = 0.7$, and then the endcap electromagnetic calorimeter down to about $|\cos\theta| = 0.96$. There are gaps of $3\frac{1}{2}^\circ$ in ϕ between the eight LA modules, and an overlap region in θ between the LA and the ECC, in which neither system is fully efficient. The overlap region has been investigated to some extent by Gerson Goldhaber [5]. The solid angle coverage of the LA alone is 65% of 4π, while LA and ECC combined cover about 90%. Electron identification only within the efficient fiducial volume of either the LA or the ECC will be described in this report.

(A) Liquid Argon Barrel Calorimeter

Mark Nelson and Pat Burchat developed electron identification routines for the LA based on old PEP5 data [6-8]. Dolly Wu is presently working on modifications necessary for the SLC data.

The liquid argon barrel calorimeter consists of eight modules around the coil (Fig. 1), each containing 37 2 mm thick lead plates separated by 3 mm of liquid

* Words 14-18 have only recently been added to subtype 3. They do not exist for the old PEP5 data, and may not be filled for PEP/Upgrade data which was processed some time ago. To ensure that the TOF information is up-to-date, CALL TOFID in your EVANAL before accessing subtype 3.

argon (Fig. 10). The total thickness is 14.5 radiation lengths at normal incidence. Electrons and photons undergo electromagnetic showers and deposit energy by ionisation in the argon. Alternate lead plates are grounded, or kept at high voltage and segmented into strips for readout of the charge collected. Layers are ganged together in depth to give six readout layers, as shown in Fig. 10. The layers F1, F2 and F3 have their strips oriented such that they measure ϕ; T1 and T2 layers measure θ and the U layer is at 45° to F and T, to resolve ambiguities.

A search is made around any charged track from the drift chamber which projects inside the LA, and hence a shower is associated with the track. Information from the calorimeter (LA or ECC) is stored in subtype 4 of the track list (see Table 4). For the LA, LASHQ (word 21) is a measure of the quality of the shower:

$$\text{LASHQ} = A + 100B$$

where A is the percentage of the energy of the shower which has been shared with other clusters nearby, and $B = 0$ if the track lies well within the LA acceptance. For reliable data, a cut of LASHQ < 100 should be applied. If the energy resolution is critical, then a smaller value of LASHQ should be required.

The position of the shower is stored in words 1-3 of subtype 4, and the total energy associated with the track, after all corrections, is ELATOT (word 20). For rejection of electrons, a good cut is:

$$\frac{E}{p} < 0.5$$

where E = ELATOT and p is the momentum of the track measured by the drift chamber. However, for selection of electrons from a large hadronic background

$$\frac{E}{p} > \text{cutoff}$$

is not the best cut to apply. This is because in hadronic jets the track density

is so great that overlap of showers in the LA is substantial. A sharing algorithm tries to assign the best value of ELATOT to each track, but this is difficult to do accurately. Many true pions will be misidentified as electrons due to overlap with photon showers.

Instead, the routine LAELEC has been developed from studies of PEP5 data which does not use the information in subtype 4. LAELEC is described in detail in reference 6, which the serious user should consult. Only a brief explanation will be given here.

CALL LAELEC (ITRACK, TEST1, ICLASS)

where:

ITRACK = the track number

The routine returns:

ICLASS which is 0 if the track is well within the LA acceptance

and TEST1 which is a useful quantity for e/π separation.

The routine makes a search in the LA within a narrow region about the drift chamber track extrapolation, without making any attempt to recover the total shower energy. Each of four readout layers, or groups of layers, is searched separately, and the quantity TEST1 is the minimum of the four values $\frac{E_i}{p\alpha_i}$ where

E_i is the energy found within the search region in layer i

p is the track momentum from the drift chamber

and α_i is the minimum expected value of E_i/p if the track is an electron

The index i runs over the layers F1+F2, T1, U and FRONT = F1+F2+T1+U.

Fig. 11 shows the distribution of TEST1 for a sample of isolated electrons and pions selected from the old PEP5 data. A cut of TEST1 > 1.1 was found to give a good separation between electrons and pions in hadronic jets, when track overlap problems were taken into account.

Table 5(a) shows the hadron misidentification probability from LAELEC for various p and p_t bins, with an electron identification efficiency of 90%.* The contamination is much larger in the middle of jets (low p_t) where overlap problems are more acute. Table 5(b) shows the results of combining dE/dx (Table 2(b)) and LA electron identification together. There is now about 1% or less hadron misidentification probability for the whole p and p_t range. These results are preliminary.

In the upgraded Mark II detector there is more material in front of the LA than there was for PEP5 (1.9 radiation lengths compared to 1.4 before), due to the new coil. The effect of this is shown in Fig. 12 which shows the energy deposited in the most energetic strip in each readout layer, for tracks in Bhabha scattering events in the old and new data. In the PEP/Upgrade data the longitudinal shower distribution has been shifted forwards, as expected. This will require retuning of the parameters α_i inside LAELEC. Work is in progress, using both the data and EGS Monte Carlo studies.

(B) Endcap Electromagnetic Calorimeter

Dave Herrup is developing an electron identification program using the ECC. A description of the calorimeter can be found in the Mark II / SLC Proposal [2].

Each endcap consists of 36 layers of proportional tubes sandwiched between lead sheets. At normal incidence, each layer amounts to half a radiation length, and there are 0.7 radiation lengths in front of the first layer. The tubes are made from aluminium and contain HRS gas. Different layers are oriented along the x-

* These numbers are based largely on studies using low momentum PEP5 data. Work using PEP/Upgrade data and hadronic shower Monte Carlo tracks is in progress to determine more reliable values for use at SLC. In the meantime these tables should be used with caution.

and y-axes, or at 45° along u- and v-axes (see Fig. 13). They are ganged in depth to produce 10 readout layers for each endcap (see Fig. 14).

An e/π separation algorithm, similar to LAELEC, has been investigated using electron and pion test beam data. The search uses roads of ± 1 channel (± 1.5 cm) and only the first 4 radiation lengths of the calorimeter (Section 1 in Fig. 14). The cuts are momentum dependent. The results are shown in Tables 6(a) and 6(b). These are very preliminary and represent the best possible e/π separation available from the ECC. There is likely to be some degradation in a jet environment due to track overlap.

Studies of PEP/Upgrade data and Monte Carlo events are in progress.

5. MUON IDENTIFICATION

Muon identification using the existing muon system has been developed by Mark Nelson and Pat Burchat for PEP5 data [6-8]. Andrew Weir is working on modifications and extensions needed for SLC data.

The existing muon system consists of four walls of alternating layers of iron hadron absorber and proportional tubes, located above, below and on either side of the central detector (see Fig. 1). It covers about 45% of the solid angle.* At normal incidence, a muon of momentum 1.8 GeV/c or more should leave hits in all four layers. The first layer is oriented to measure θ, while the back 3 layers measure ϕ.

Tracks are extrapolated to the muon tubes and a search is made for hits within a region determined by the tracking errors from the drift chamber and the multiple

* The proposed muon upgrade [9] would cover about 80% of the solid angle.

scattering expected for a muon in the material in front of the tubes. A recent modification to the muon code uses the true error matrix generated by the drift chamber tracking program.* Fig. 15 shows the distributions of the deviation between the position of a muon hit and the corresponding track extrapolation. The deviation is in units of σ, where σ is the standard deviation after combining tracking and multiple scattering errors in quadrature. Each layer is shown separately, but avaraged over the four walls. Cosmic ray data from the PEP/Upgrade running were used. The solid lines show the Gaussian distributions to be expected if the errors are treated correctly. There is now good agreement.

Muon information corresponding to a 3σ search region is stored in subtype 5 of the track list (see Table 7). For muon identification, MUSTAT (word 3) and MULEVE (word 5) can be used.

MUSTAT is a 4-bit number, whose bit pattern corresponds to the hit pattern found in the 4 muon layers. For example, MUSTAT $= 7 = 0111_2$ means hits in the first 3 muon layers; whereas MUSTAT $= 8 = 1000_2$ is a hit in only the fourth layer. Hits in all four layers gives MUSTAT $= 15 = 1111_2$.

MULEVE is the number of muon layers in which a hit would be expected if the track were a true muon. It depends on the track's direction and momentum.

To separate <u>isolated</u> muons and pions, requiring MULEVE $= 4$ and MUSTAT $=$ 15 is sufficient, i.e. hits in all four layers expected and found.

In hadronic jets, track overlap is again a problem. This can be limited by reducing the size of the search region used. A FORTRAN function, NUSTAT, has been written for this purpose.

```
FUNCTION NUSTAT(ITRACK,DELCUT)
```

* This code has not yet been put on to the G disk.

where ITRACK is the track number, returns NUSTAT equal to the MUSTAT value obtained by using a search region of DELCUT$\times\sigma$. DELCUT must be a real number.

In PEP5 studies, cuts of NUSTAT(ITRACK, 2.0) $= 15$ and MULEVE $= 4$ were found to give good μ/π separation in hadronic events. This is described in more detail in reference 6.

Backgrounds come from two sources: "hadron punchthrough", which includes the effects of passage of hadrons through the absorber without interaction, secondaries from interactions in the absorber, muon system noise and track overlap; and decays of pions and kaons to muons in flight. These are given for various p and p_t bins in Tables 9(a) and 9(b) respectively, as calculated from PEP5 data (from reference 6). Monte Carlo studies are in progress to determine more reliable values for SLC data. It is possible that the background from decays might be reduced by tagging the decays in the drift chamber.

REFERENCES

1. P. Burchat: Mark II / SLC Physics Working Group Note #0-7 (1987)
2. Proposal for the Mark II at the SLC: SLAC-PUB-3561 or CALT-68-1015 (1983)
3. D.P. Coupal: talk at this workshop
   See also, M. Nelson: Mark II / SLC Physics Working Group Note #0-3 (1986)
4. E. Soderstrom & E.Wicklund: Mark II / SLC Note #130 (1986)
5. G. Goldhaber: Mark II / SLC Notes #139 & #144 (1986)
6. P. Burchat & M. Nelson: Mark II / SLC Note #114 (1985)
7. M. Nelson: Ph.D. Thesis, LBL-16724 (1983)
8. P. Burchat: Ph.D. Thesis, SLAC-292 (1986)
9. Muon Upgrade Proposal (unpublished)

TABLES

FIGURES

9. Track momentum vs. mass-squared, as derived from TOF and drift chamber measurements, for all tracks in the PEP/Upgrade data which have good TOF information.

10. The layers and ganging scheme of the liquid argon barrel calorimeter.

11. Distribution of TEST1 (see text) for isolated electrons and pions of momenta between 5 and 10 GeV/c selected from PEP5 data.

12. Energy deposited in each liquid argon readout layer in the strip with the most energy in that layer for tracks in Bhabha scattering events. The order of the layers in this plot is F1, T1, U, F2, T2, F3. Solid curve: Bhabhas selected from PEP5 data. Dashed curve: Bhabhas selected from PEP/Upgrade data.

13. The endcap electromagnetic calorimeter showing the orientations of the various layers along x-, y-, u- and v-axes.

14. The ganging scheme of the ECC.

15. Distributions of the deviation between the position of a hit in the muon tubes and the associated drift chamber track extrapolation. The units are σ, the standard deviation after combining tracking and multiple scattering errors in quadrature. The four muon layers are shown separately, but averaged over all four walls. Cosmic ray data from PEP/Upgrade running were used. The curves show the predictions for normal distributions of standard deviation σ.

DE/DX information

Subtype	J	Name	Contents
11	1	NSAMPL	total samples before truncation
	2	NTRUNC	Num of samples used in trunc mean (TM)
	3	IQHIT	bit map of samples and TM samples, where
			bit pair = 00, no hit
			" 01, wire hit not used in TM
			" 11, wire hit used in TM.
			for wire layers 01-16
	4		" " " 17-32
	5		" " " 33-48
	6		" " " 49-64
	7		" " " 65-72, bits 16-31 unused
	8	QTRK	Final DE/DX for track, (Kev/8.33 mm)
	9	DXSIG	Resolution of dE/dx (sigma / E)
	10	IQQUAL	quality of QTRK
	11	IQCOR	A Bit map of the corrections used on data
	12	IQCAL	A Bit map of the methods used to find pulses
	13	IQFIT	method of finding QTRK, 0=TM70
	14	DDXE	expected dE/dx for an electron
	15	DDXPI	expected dE/dx for a pion
	16	DDXK	expected dE/dx for a kaon
	17	DDXP	expected dE/dx for a proton

TABLE 1

Hadron misidentification probabilities from dE/dx

$p\backslash p_t$	0.0-0.5	0.5-1.0	1.0-1.5	1.5-2.0	> 2.0
1-3	.002 ± .001	.002 ± .001	.001 ± .001	.002 ± .003	.001
3-5	.020 ± .003	.015 ± .004	.014 ± .005	.014 ± .008	.014
5-7	.061 ± .009	.061 ± .010	.062 ± .015	.050 ± .019	.06
7-9	.095 ± .016	.097 ± .016	.108 ± .024	.084 ± .023	.08
9-11	.157 ± .027	.153 ± .025	.129 ± .033	.142 ± .044	.14
11-13	.186 ± .038	.158 ± .030	.215 ± .045	.189 ± .063	.18
13-15	.192 ± .048	.203 ± .041	.149 ± .050	.212 ± .081	.20
15-17	.222 ± .058	.230 ± .058	.219 ± .067	.217 ± .089	.22

TABLE 2(a)

Hadron misidentification probabilities from dE/dx
with 10% additional smearing

$p\backslash p_t$	0.0-0.5	0.5-1.0	1.0-1.5	1.5-2.0	> 2.0
1-3	.003 ± .001	.003 ± .001	.003 ± .001	.003 ± .004	.003
3-5	.032 ± .004	.028 ± .005	.021 ± .006	.017 ± .008	.02
5-7	.088 ± .011	.095 ± .012	.090 ± .017	.085 ± .024	.08
7-9	.129 ± .018	.128 ± .018	.137 ± .026	.121 ± .035	.12
9-11	.195 ± .029	.202 ± .027	.169 ± .037	.178 ± .048	.18
11-13	.242 ± .041	.214 ± .034	.284 ± .050	.210 ± .066	.24
13-15	.216 ± .050	.236 ± .043	.190 ± .055	.253 ± .086	.24
15-17	.253 ± .060	.255 ± .060	.253 ± .071	.265 ± .095	.25

TABLE 2(b)


```
                Time-of-Flight Counter Items

Subtype   J     Name                Contents
-------   -     ----                --------
   3      1     AIT          azmuthal counter number from projected
                             track fit  ( 1.0 < AIT < 49.0 )

          2     IT           counter number   1-48  : for counters
                                            101-108 : for drift chamber fins
                                              0     : no hit
          3     TOF          time of flight (nsec)
          4     BETA         beta of track
          5     ZTOF         z (m) computed using both phototubes
          6     TOFPH        corrected pulse height
          7     TQUAL        TOF quality (1.0=good trk; .LE.2.0=usable)
                               0.0 if ZT-ZTDC didnt match
                               2.0 if double hit in counter
                               2.1 good trk in one-ended cntr(33-35)
                               2.2 double hit in one-ended cntr
                               3.0 if no hit in counter
                               4.0 all wts are zero;otherwise TQUAL=1.0
                               5.0 all wts are zero;otherw.TQUAL=0,2
                               6.0 if neutral track with good hit
                               7.0 if more than 2 hits per counter
                               8.0 missed one tdc (early cosmic)
          8     WTPI         weight for PI
          9     WTK            "     "  K
         10     WTP            "     "  P
         11     WTEPI          "     "  e for e-pi hypothesis
         12     AMASS2       square of mass (gev)**2 from TOF and P
         13     PATH         flight path length (m)
            Words 14-18 only available for UPGRADE/SLC data
         14     TOFE         expected time for an electron  (nsec)
         15     TOFPI        expected time for a pion       (nsec)
         16     TOFK         expected time for a kaon       (nsec)
         17     TOFP         expected time for a proton     (nsec)
         18     TOFSIG       time resolution for this track (nsec)
```

TABLE 3

Liquid Argon track

Subtype	J	Name	Contents
4	1	XSH	shower coords at trigger plane of LA as
	2	YSH	found by LA reconstruction.
	3	ZSH	..
	4	THETSH	..
	5	PHISH	..
	6-12	ELA(7)	LA energy (GEV) deposited per layer
		ELA(1),(2)	for SAT energy in front, back of sh.cnt.
	13-19	SIGLA(7)	spatial width (m) in each layer
	20	ELATOT	total energy observed in LA (gev)
	21	LASHQ	quality of LA fit
	22	CH2LA	chi sq of geometric fit for charged tracks
			photon type for photons
	23	LAMOD	module number for this track
			for SAT: 16-19 indicate SAT module 1-4

TABLE 4

Hadron misidentification probabilities from calorimeter

$p\backslash p_t$	0.0-0.5	0.5-1.0	1.0-1.5	1.5-2.0	> 2.0
1-3	.060	.010	.010	.010	.010
3-5	.080	.015	.010	.010	.010
5-7	.100	.015	.010	.010	.010
7-9	.090	.020	.010	.010	.010
9-11	.080	.015	.010	.010	.010
11-13	.060	.010	.010	.010	.010
13-15	.050	.010	.010	.010	.010
15-17	.040	.010	.010	.010	.010

TABLE 5(a)

Total hadron misidentification probabilities combining calorimeter with smeared dE/dx

$p\backslash p_t$	0.0-0.5	0.5-1.0	1.0-1.5	1.5-2.0	> 2.0
1-3	.0002	.0000	.0000	.0000	.0000
3-5	.0026	.0004	.0002	.0002	.0002
5-7	.0088	.0014	.0009	.0009	.0008
7-9	.0116	.0026	.0014	.0012	.0012
9-11	.0156	.0030	.0017	.0018	.0018
11-13	.0145	.0021	.0028	.0021	.0024
13-15	.0108	.0024	.0019	.0025	.0024
15-17	.0101	.0026	.0025	.0027	.0025

TABLE 5(b)

Electron identification efficiencies from ECC

Momentum	Efficiency
3 GeV/c	85%
5 GeV/c	84%
10 GeV/c	84%

TABLE 6(a)

Pion misidentification probabilities from ECC

Momentum	Probability
2 GeV/c	0.2%
4 GeV/c	0.4%
8 GeV/c	0.5%

TABLE 6(b)

Muon Chamber items (this list is filled only for charged particles with momenta greater than 600 MeV/c and for incoming cosmic rays)

Subtype	J	Name	Contents
5	1	MUID	muon identifier: 0 = not a mu 1 = mu 2 = cant tell
	2	MUWRDS	number of words in this track list = 6 + 14*MULEVP
	3	MUSTAT	orre. bit code of levels which had a signal within 3 s.d. of the projected coordinate
	4	MULEVR	number of levels "required" for a muon i.e the number of levels in which a muon would have to scatter by more than 3 s.d. in position or momentum to avoid being detected
	5	MULEVE	number of levels "expected" for a muon i.e. the number of levels in which a muon is expected but could avoid being detected by any amount of scattering MULEVE > or = MULEVR
	6	MULEVP	number of levels "possible" for a muon i.e. the number of levels a muon could reach by scattering not more than 3 s.d. MULEVP > or = MULEVE

TABLE 7

$p \setminus pt$	0.0 – 1.0	1.0 – 2.5
2.0 – 3.0	0.3%	0.2%
3.0 – 4.0	0.3%	0.2%
4.0 – 5.0	0.3%	0.3%
5.0 – 6.0	0.4%	0.3%
> 6.0	0.5%	0.4%

TABLE 8(a)

$p \setminus pt$	0.0 – 1.0	1.0 – 2.5
2.0 – 3.0	0.4%	0.7%
3.0 – 4.0	0.5%	0.8%
4.0 – 5.0	0.5%	0.9%
5.0 – 6.0	0.5%	0.6%
> 6.0	0.3%	0.3%

TABLE 8(b)

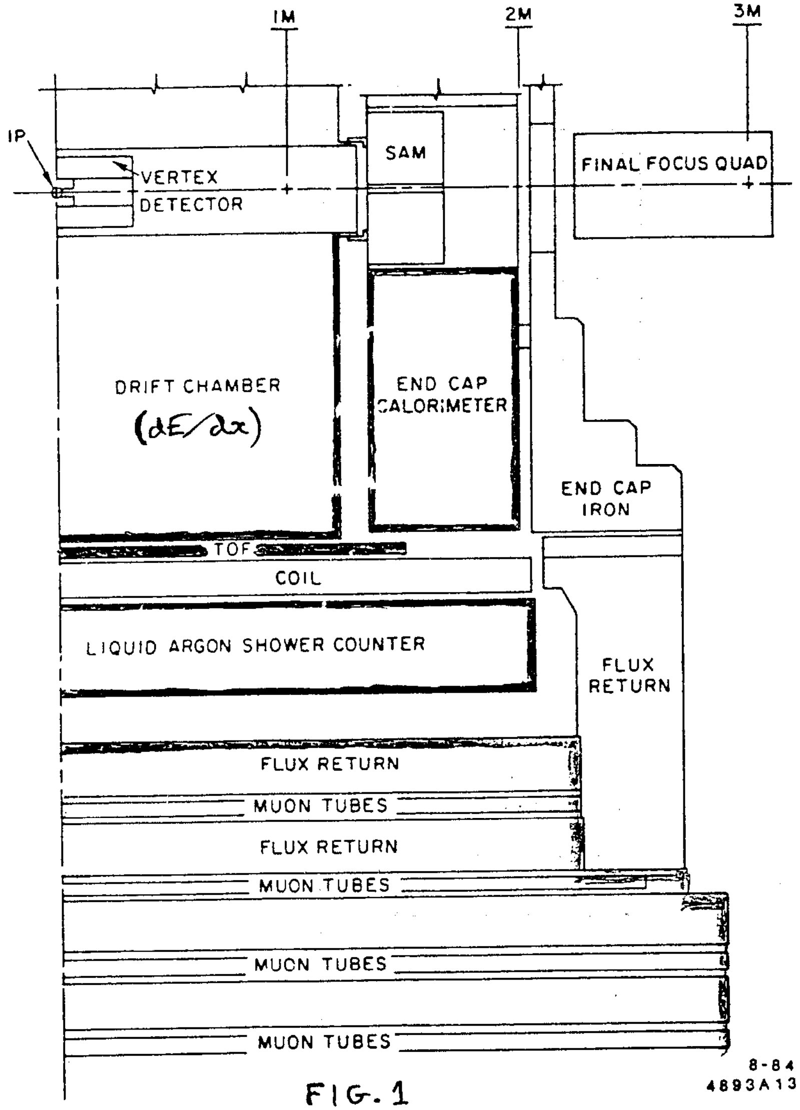

FIG. 1

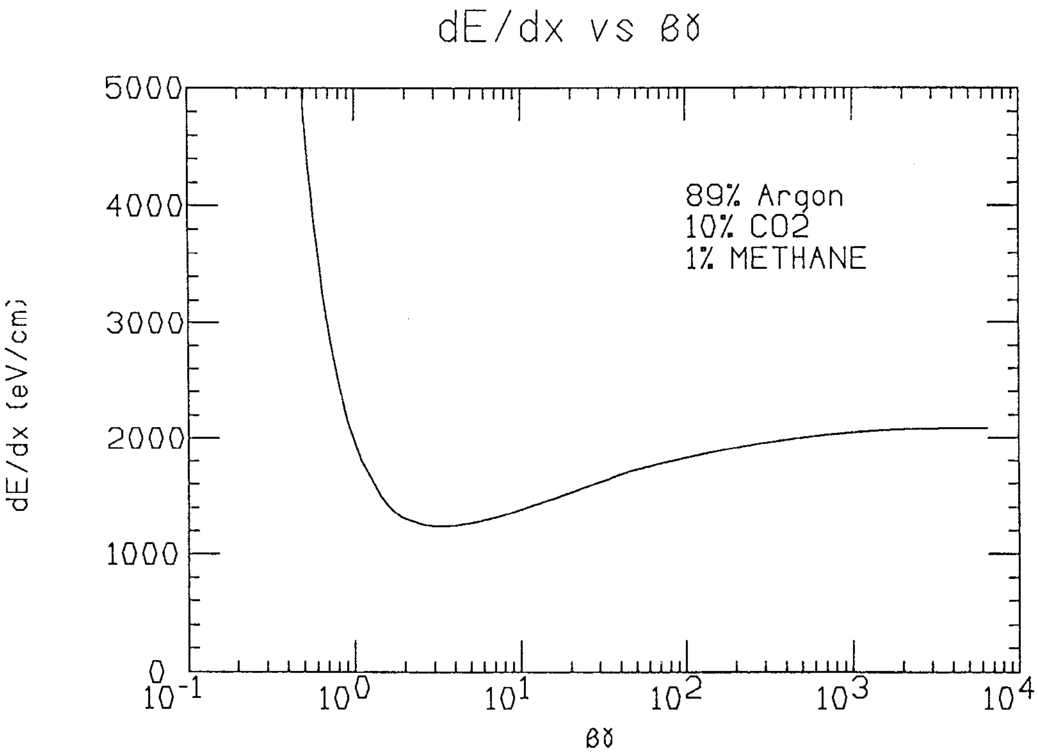
dE/dx vs βγ
5000
4000
3000
2000
1000
0
dE/dx (eV/cm)
89% Argon
10% CO2
1% METHANE
10^{-1}
10^{0}
10^{1}
10^{2}
10^{3}
10^{4}
βγ

FIG. 2

FIG. 3

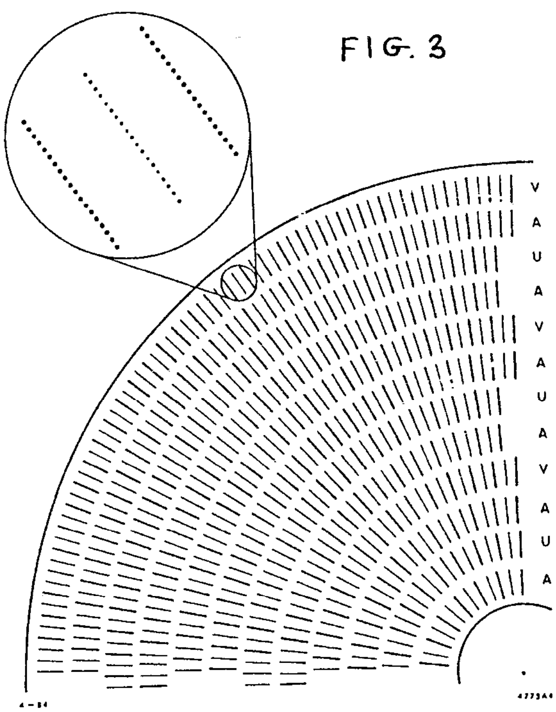
V
A
U
A
V
A
U
A
V
A
U
A

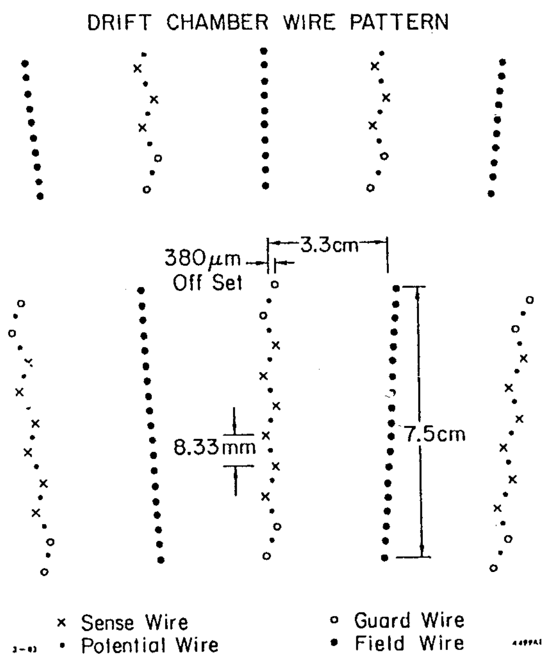
DRIFT CHAMBER WIRE PATTERN
380μm
Off Set
3.3cm
8.33mm
7.5cm
× Sense Wire
• Potential Wire
○ Guard Wire
• Field Wire

ID= 100

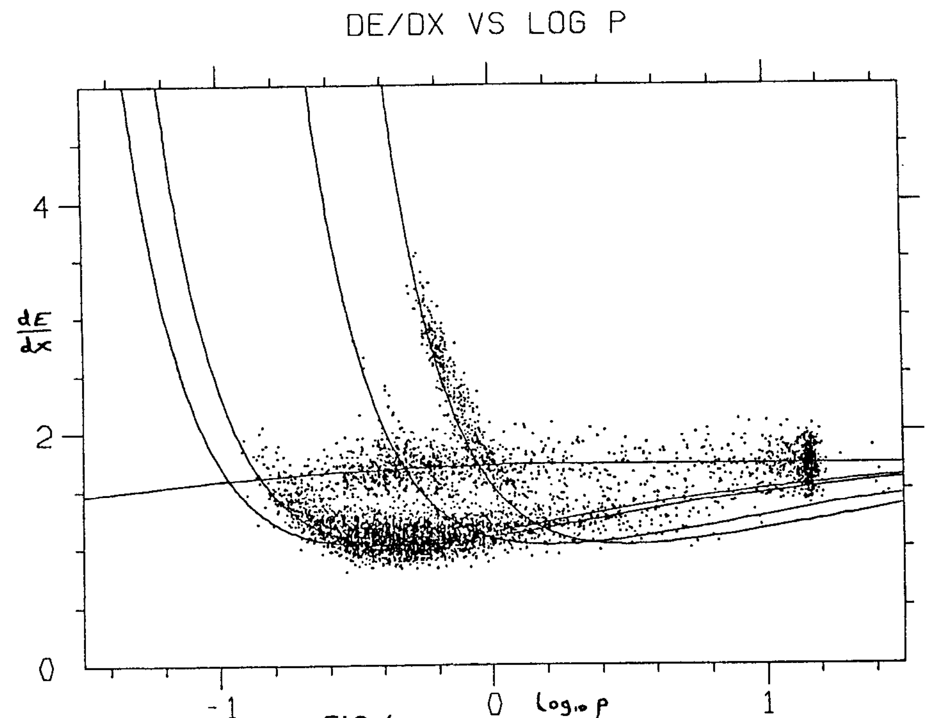

FIG. 4

HANDYPAK DPC271 20JAN87

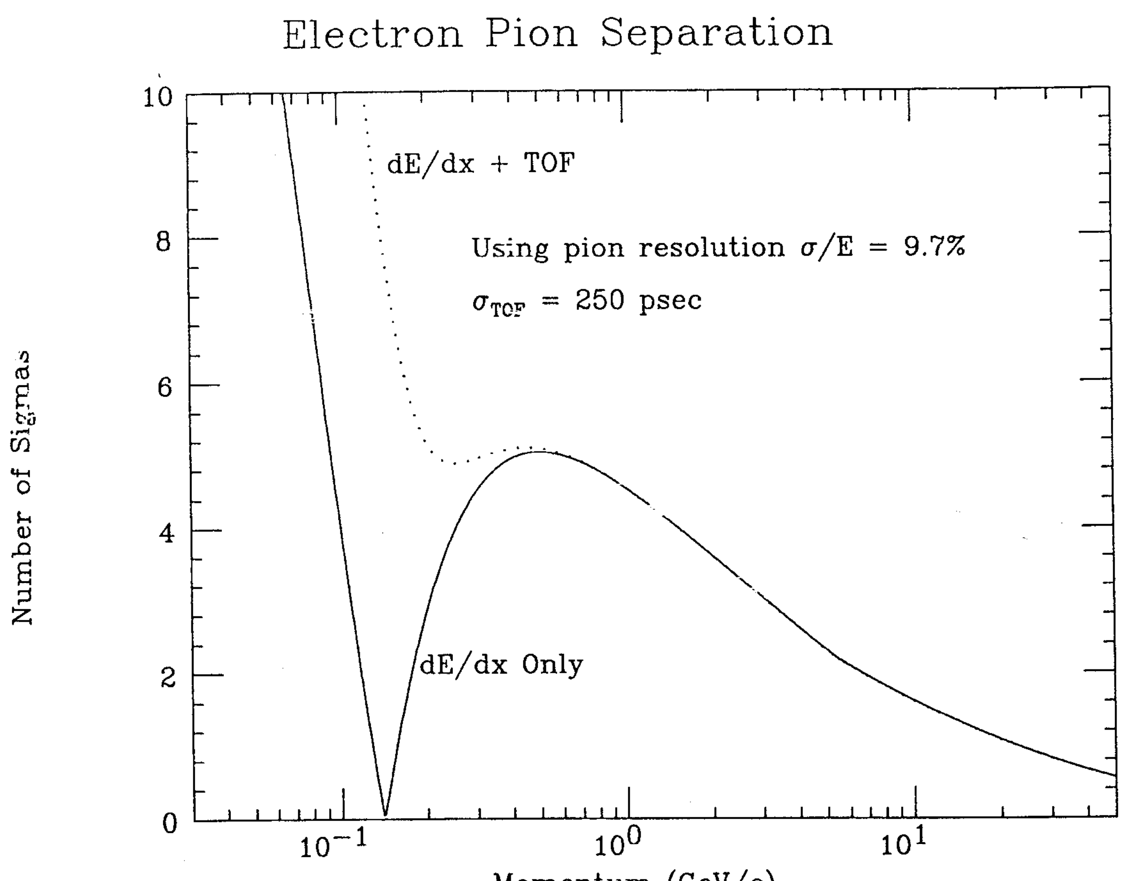

FIG.5

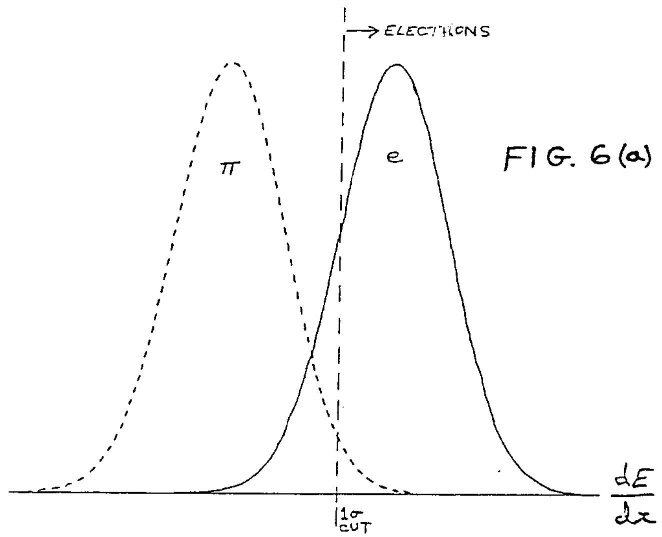

FIG. 6(a)

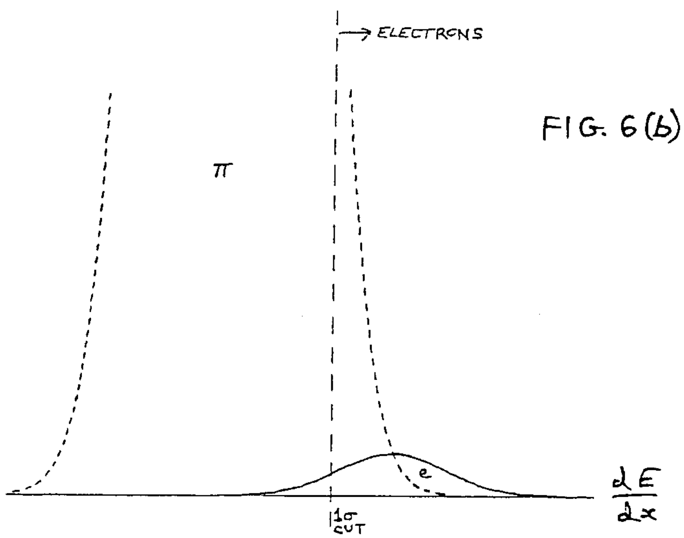

FIG. 6(b)

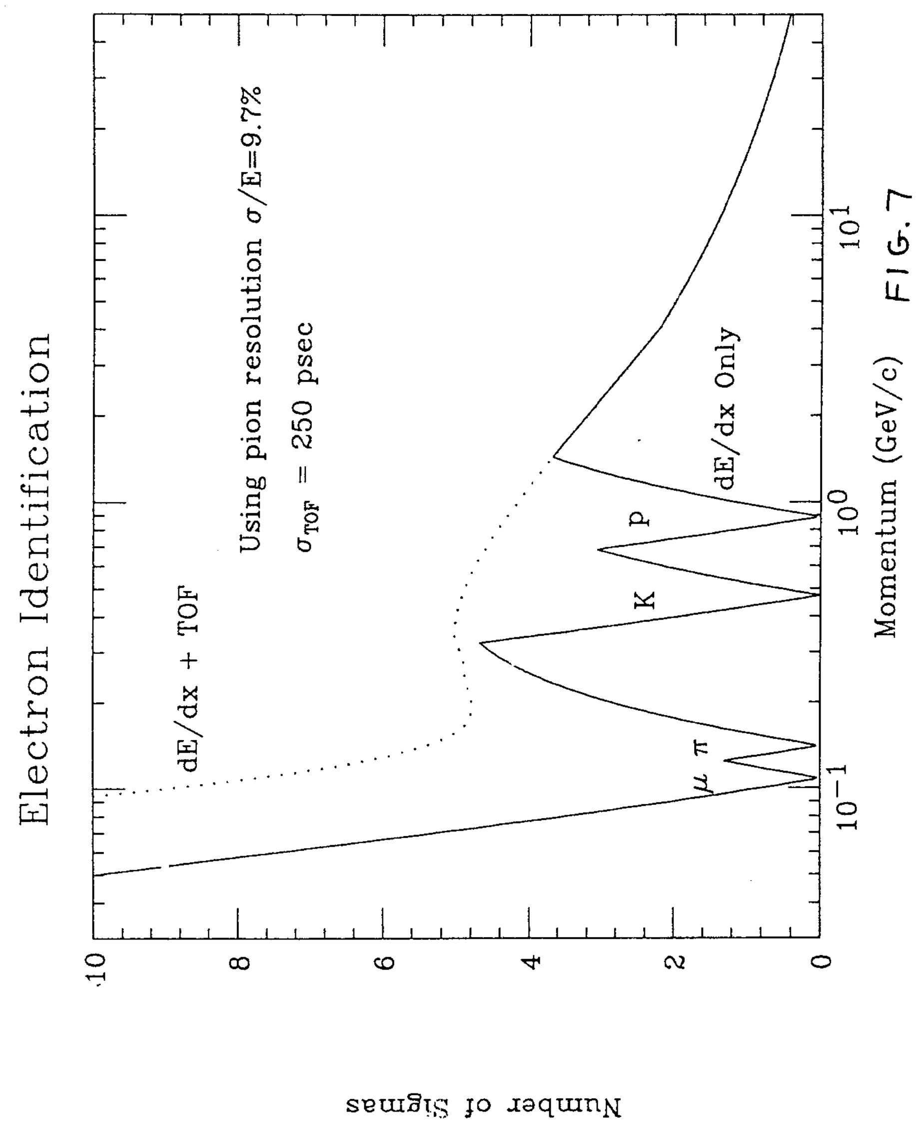

FIG. 7

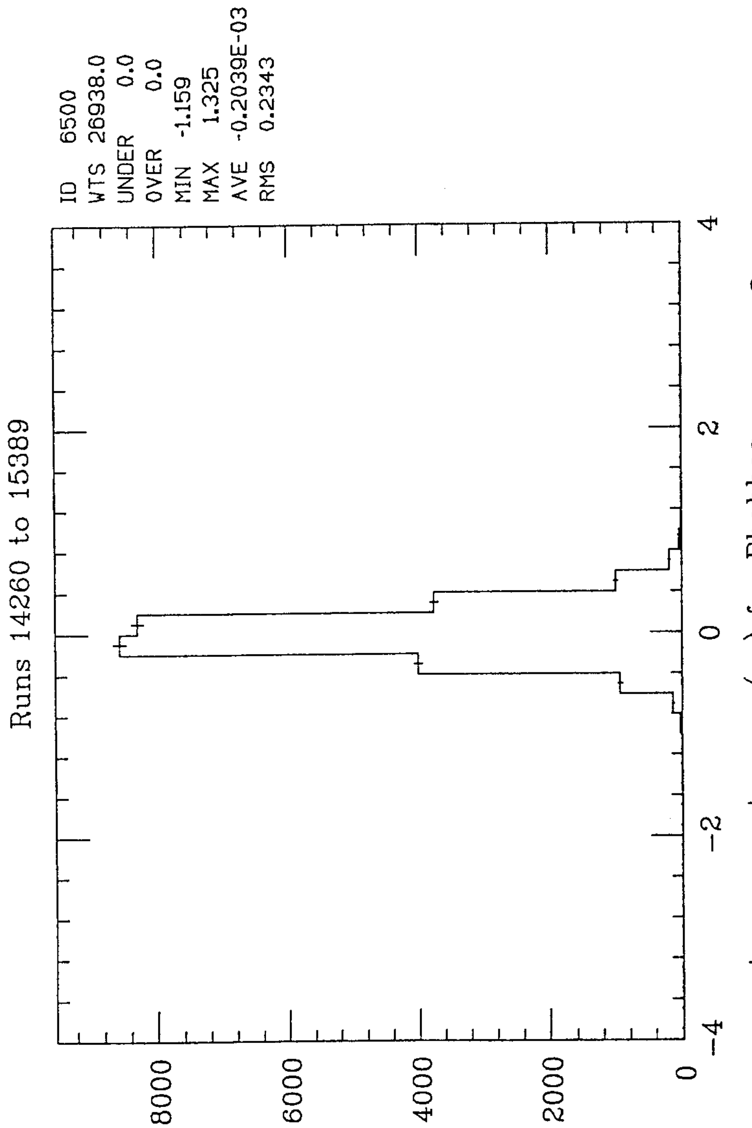
Runs 14260 to 15389
ID 6500
WTS 26938.0
UNDER 0.0
OVER 0.0
MIN -1.159
MAX 1.325
AVE -0.2039E-03
RMS 0.2343
0
2000
4000
6000
8000
−4
−2
0
2
4
$t_{measured} - t_{predicted}$ (ns) for Bhabhas

FIG. 8

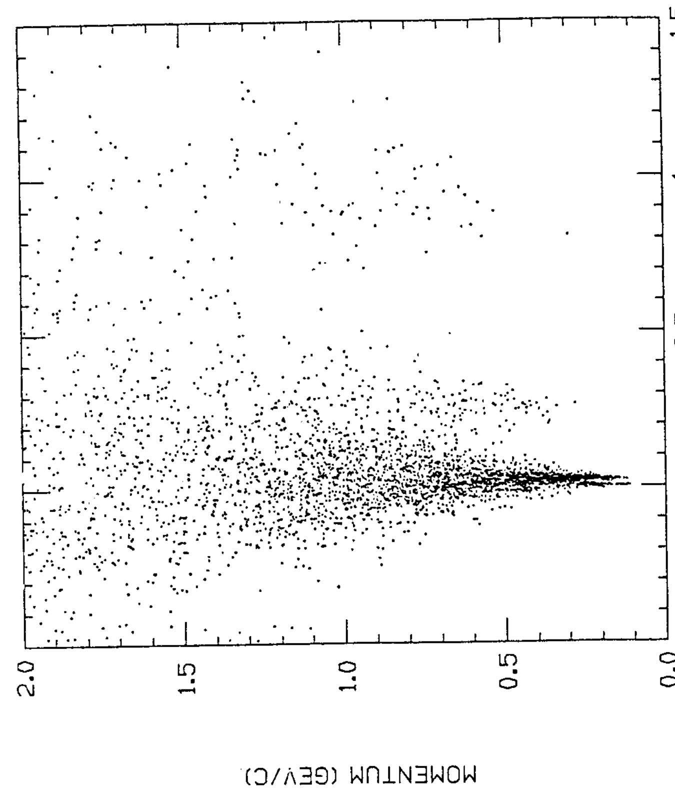
2.0
1.5
1.0
0.5
0.0
MOMENTUM (GEV/C)
-0.5
0
0.5
1
1.5
MASS SQUARED (GEV**2)

FIG. 9

FIG. 10

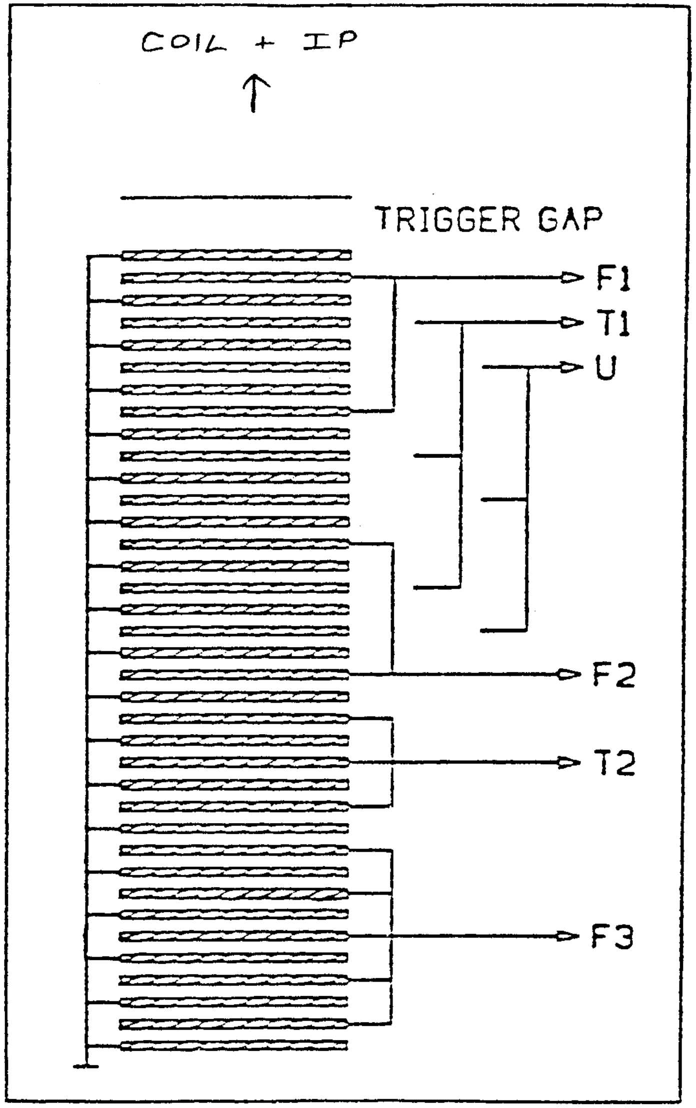

COIL + IP
TRIGGER GAP
F1
T1
U
F2
T2
F3

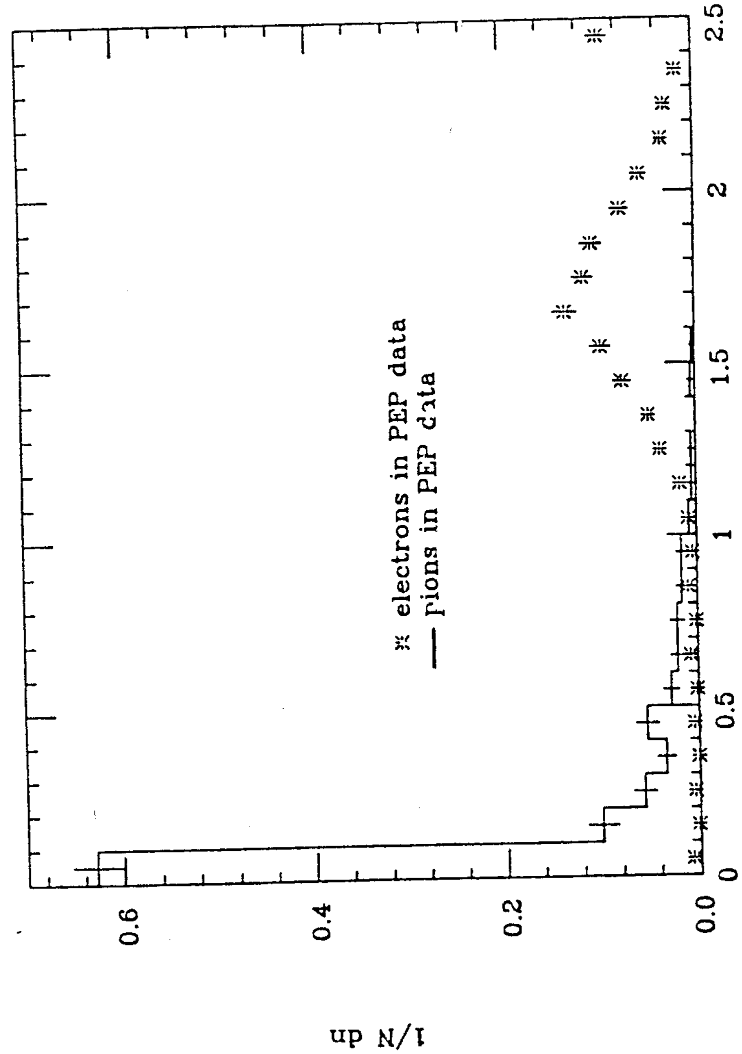

electrons in PEP data
pions in PEP data
0.0
0.2
0.4
0.6
0
0.5
1
1.5
2
2.5
TEST1
1/N dn

FIG. 11

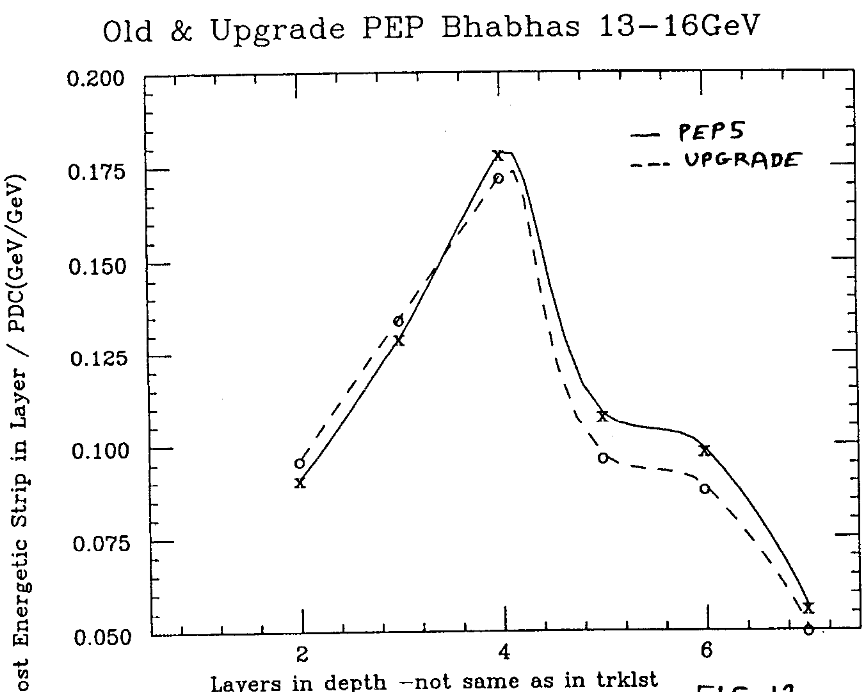

Old & Upgrade PEP Bhabhas 13−16GeV
0.200
0.175
0.150
0.125
0.100
0.075
0.050
Most Energetic Strip in Layer / PDC(GeV/GeV)
2
4
6
Layers in depth −not same as in trklst
— PEP5
--- UPGRADE

FIG. 12

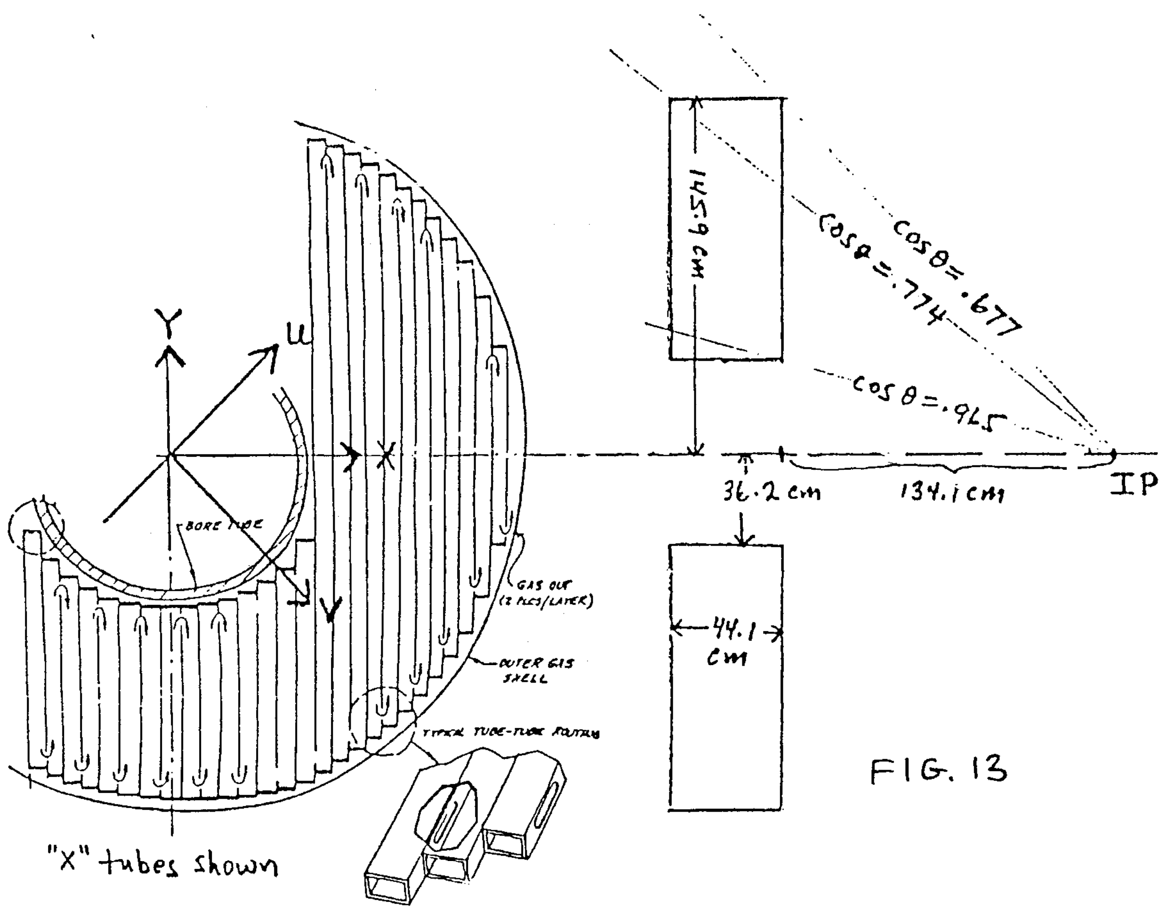

cos θ = .677
cos θ = .774
cos θ = .965
145.9 cm
36.2 cm
134.1 cm
IP
44.1 cm
Y
U
V
BORE TUBE
GAS OUT (2 PLCS/LAYER)
OUTER GAS SHELL
TYPICAL TUBE-TUBE ROUTING
"X" tubes shown

FIG. 13

MarkII End Cap Calorimeter

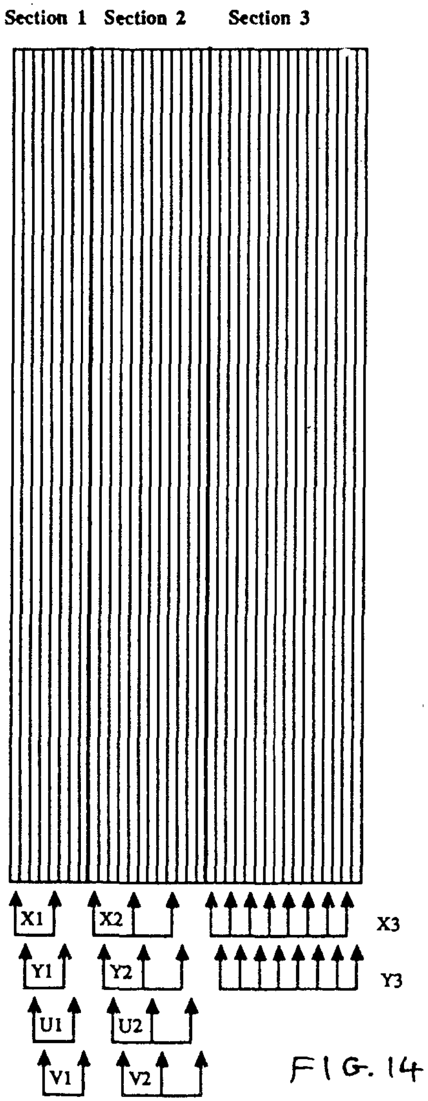

FIG. 14

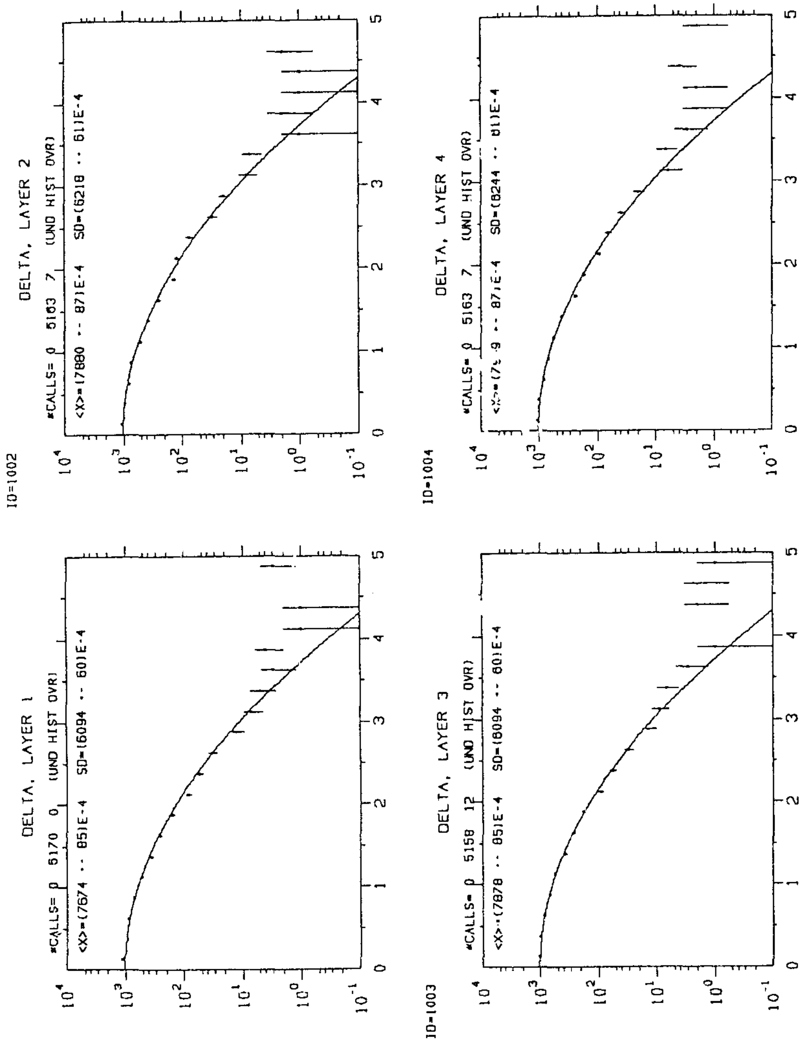

FIG. 15

Mark II/SLC-Physics Working Group Note # 0-10

AUTHOR: G. Goldhaber

DATE: February 25-28, 1987

TITLE: Review of $p\overline{p}$ Collider Physics Relevant to the Mark II

---

1. PRODUCTION AND DECAY OF THE W AND Z PARTICLES

1.1. W and Z Mass

This talk is based on an experimental summary talk I gave at the 6th Topical Workshop on Proton-Antiproton Collider Physics (Aachen, 30 June - 4 July 1986) as well as on additional data I learned about during my 6 month stay at CERN. In particular, where appropriate the numbers I quote have been updated as of December 6, 1986. Unless stated otherwise references to authors refer to talks presented at the Aachen Conference.[1)]

Survey of $W^{\pm}$ and Z^0 luminosity and numbers of events:

$$\int Ldt = 729\ (\mathbf{UA1}) + 880\ (\mathrm{UA2})\ \mathrm{nb}^{-1}$$

$$W \to e\nu \sim 500\ \mathrm{UA1{+}UA2}$$
$$W \to \mu\nu \sim\ 65\ \mathrm{UA1}$$
$$W \to \tau\nu \sim\ 30\ \mathrm{UA1}$$

$$Z^0 \to e^+e^-\ 69\ \mathrm{UA1} + \mathrm{UA2}$$
$$\to \mu^+\mu^-\ 19\ \mathrm{UA1}$$

Figures 1a and b give the UA1 and UA2 $Z \to e^+e^-$ mass distributions. Figure 2 shows the $m_Z - m_W$ mass difference as a function of m_Z. Tables 1 to 4 give a summary of the W and Z masses taken from a report by E. Locci.[2)] These data have been updated to December 6, 1986.

1.2. Z Width and Number of Neutrino Flavors

The kinematical effects of m_{TOP} on the Γ_Z^{TOT} and Γ_W^{TOT} values (assuming 3 ν species) are given in Fig. 3. Both the UA1 and UA2 experiments give an indirect

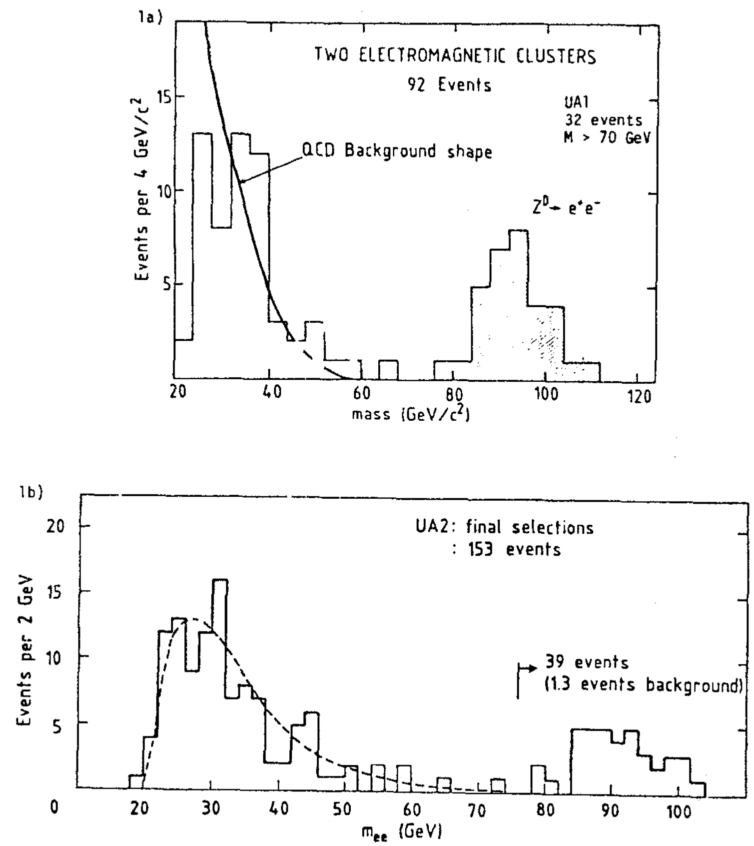

Figure 1. Experimental Mass distribution for $Z \to e^+e^-$.

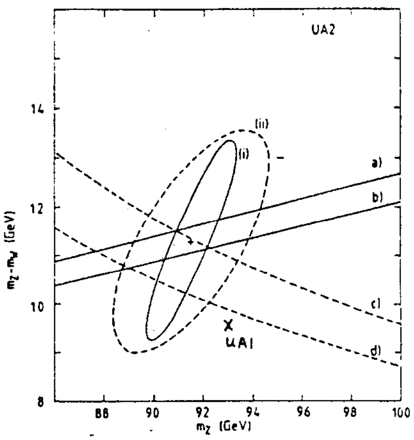

Figure 2. The $m_Z - m_W$ mass difference as a function of m_Z. Data compiled by the UA2 group. The results from ν experiments are also shown (solid curves a and b) as well as the standard model expectations with and without radiative corrections (dashed curves c and d). Also shown is the central value for the UA1 results. Curve i gives the UA2 statistical error (1 std. dev.). Curve ii gives the UA2 systematic error folded in.

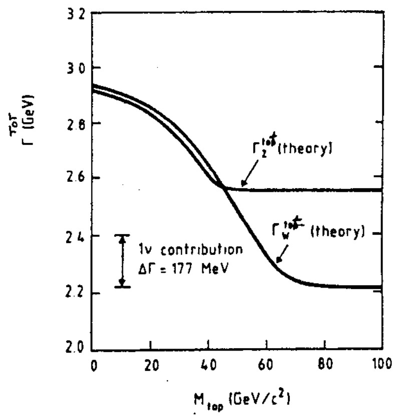

Figure 3. The kinematical effect of M_{TOP} on Γ_Z^{TOT} and Γ_W^{TOT} assuming 3 neutrino species.

Table 1

Z^0 event samples

	UA1		UA2	
$\sqrt{s}$ (GeV)	546	630	546	630
$Z^0 \to e^+e^-$				
Event sample	4	28	9	28
Backgrounds	< 0.1	< 0.7	0.2 ± 0.1	0.8 ± 0.2
Signal			8.8 ± 3.0	27.2 ± 5.4
$Z^0 \to \mu^+\mu^-$				
Event sample	4	15	-	-
Backgrounds	< 0.1	< 1		

Table 2

W event samples

	UA1		UA2	
$\sqrt{s}$ (GeV)	546	630	546	630
$W \to e\nu_e$				
Event sample	59	207	41	214
Backgrounds				
QCD	3.5 ± 1.8	6.1 ± 1.4	1.9 ± 0.4	9.7 ± 2.6
$W \to \tau\nu_\tau$ ($\tau \to e$)	3.3 ± 0.2	13.1 ± 0.9	0.8 ± 0.2	4.4 ± 0.4
$W \to \tau\nu_\tau$ ($\tau \to$ had)		1.3 ± 0.2	-	-
$Z^0 \to e^+e^-$	-	-	1.5 ± 0.4	8.1 ± 1.6
Signal	53 ± 8	186.5 ± 14.5	36.7 ± 6.3	191.8 ± 14.5
$W \to \mu\nu_\mu$				
Event sample	11	57	-	-
Backgrounds	0.6 ± 0.1	3 ± 2		
Signal	10.4 ± 3.3	54 ± 8		
$W \to \tau\nu_\tau$				
Event sample	32		-	-
Backgrounds	2.3 ± 0.3			
Signal	29.7 ± 5.7			

Table 3

Summary of the measurements of the W and Z mass and width in UA1 and UA2

Parameter	UA1	UA2
Electron decay*)		
m_W (GeV/c^2)	$83.5^{+1.0}_{-1.1}$ stat. ± 2.7 syst.	80.2 ± 0.6 stat. ± 0.5 syst. ± 1.3 syst.
Γ_W (GeV/c^2) (90% CL)	< 6.5	< 7.0
m_Z (GeV/c^2)	93.0 ± 1.4 stat. ± 3.0 syst.	91.5 ± 1.2 stat. ± 1.7 syst.
Γ_Z (GeV/c^2) (90% CL)	< 8.3	< 5.8
Muon decay		
m_W (GeV/c^2)	$80.7^{+4.5}_{-4.1}$ stat. $^{+9.0}_{-8.1}$ syst.	-
m_Z (GeV/c^2)	$96.8^{+3.3}_{-3.1}$ stat. $^{+4.3}_{-4.0}$ syst.	-
Tau decay		
m_W (GeV/c^2)	89 ± 3 stat. ± 6 syst.	-

*) For the UA1 electron channel, the results quoted in this table exclude the 1985 data.

Table 4

Measurements of the Standard Model parameters in UA1 and UA2

Parameter	UA1*)		UA2
	Electron	Muon	
$\sin^2\theta_w^a$	0.194 ± 0.031	0.31 ± 0.18	0.232 ± 0.023 ± 0.009
$\sin^2\theta_w^b$	$0.214^{+0.005}_{-0.006}$ ± 0.015	$0.228^{+0.051}_{-0.037}$	0.232 ± 0.004 ± 0.008
ϱ	1.026 ± 0.037 ± 0.019		0.988 ± 0.027 ± 0.006
Δr^a			0.105 ± 0.077 ± 0.029
Δr^b			0.069 ± 0.026 ± 0.030

*) The quoted results exclude data collected in 1985.

measurement of the Z width and hence a limit on the number of extra neutrino flavors ΔN_ν.

The procedure is based on the measurement of

$$R_{exp} = \sigma_W B(W \to l\nu)/\sigma_Z B(Z \to ll).$$

Figure 4 shows the two cross section measurements at 540 and 630 GeV as of the time of the Aachen Conference. In the ratio R_{exp} some systematic errors cancel. This ratio can be expressed as:

$$\sigma_W B(W \to l\nu)/\sigma_Z B(Z \to ll) = (\sigma_W/\sigma_Z)(\Gamma_W^{l\nu}/\Gamma_W^{TOT})/(\Gamma_Z^{ll}/\Gamma_Z^{TOT}).$$

One then uses theoretical values for

σ_W/σ_Z (QCD, but dependent on structure functions and Λ_{QCD} as well as on $\sin^2\theta_W$), take $\equiv 3.25 \pm 0.15$

$\Gamma_W^{l\nu}/\Gamma_Z^{ll}$ (Standard Model), and

Γ_W^{TOT} (Standard Model, dependent on the top mass, i.e., whether $W \to t\bar{b}$ occurs or not, including phase-space effects.)

Here, each additional ν flavor adds 0.177 GeV to Γ_Z^{TOT}. The experiments find (with updated UA2 data)

$$R_{exp} = \begin{array}{llll} 8.7^{+1.6}_{-1.3} & \text{(stat.) or} & < 10.9 \text{ at } 90\% \text{ CL} & \text{(UA1)} \\ 7.2^{+1.7}_{-1.2} & \text{(stat.) or} & \begin{array}{l} < 10.2 \text{ at } 90\% \text{ CL} \\ < 10.4 \text{ at } 95\% \text{ CL} \end{array} & \text{(UA2)} \end{array}$$

The 90% CL upper limit on N_ν, as a function of m_t, is given in Fig. 5a for the UA1 data. This depends on σ_W/σ_Z (Denegri chose an intermediate value of 3.25) as well as on the measured value of R_{exp}. Figure 5b shows the UA2 result for $(\Gamma_Z/\Gamma_W)^{tot}$ versus m_t. they show their measured value and 95% CL value as horizontal bands. The theoretical values for three, four, and seven neutrino species are then superimposed as curves.

If I make a naïve average for the 90% CL values of R_{exp} between UA1 and UA2 data, this implies that the curve in Fig. 5a is translated downward by 7% or lies roughly somewhat below the curve marked $\sigma_W/\sigma_Z = 3.4$.

Similarly, in Fig. 5b I find that the combined UA1 and UA2 90% CL upper limit lies at $\Gamma_Z^{tot}/\Gamma_W^{tot} \simeq 1.16$.

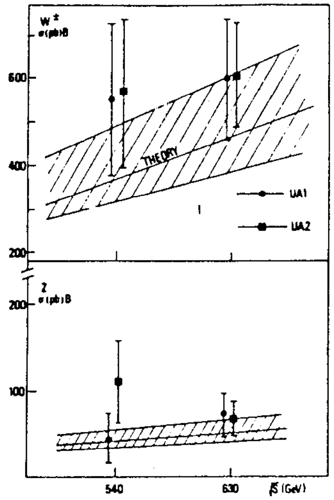

Figure 4. $\sigma_W B(W \to l\nu)$ and $\sigma_Z B(Z \to ll)$ at 540 and 630 GeV.

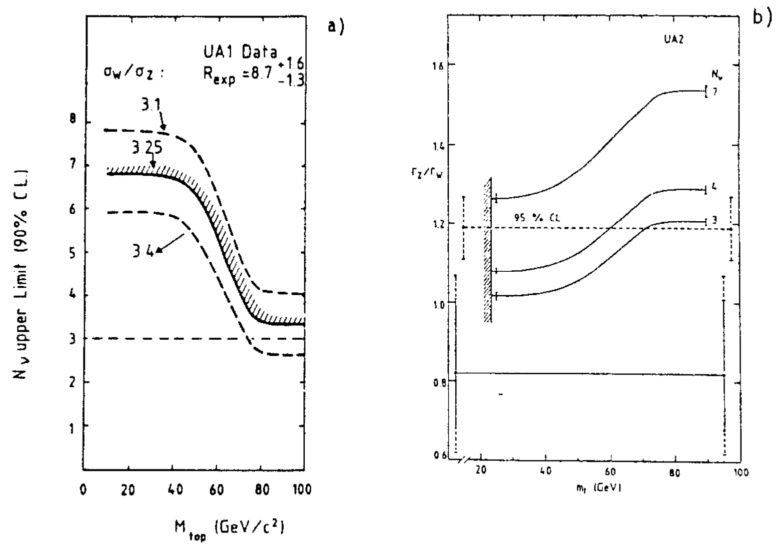

Figure 5a. Limit (90% CL) on total number of neutrino species as a function of the top mass (UA1 data).

Figure 5b. Experimental value and 95% CL limit for $\Gamma_Z^{TOT}/\Gamma_W^{TOT}$ from UA2 data. The curves show the expected values for three, four, and seven neutrino species as a function of m_t. The bars on these curves give the uncertainty due to the spread in $\sin^2\theta_W$. The hatched region represents the PETRA limit on m_t.

Thus in the present data and assumptions, for $m_t \geq 60$ GeV, there is very little room for any extra neutrinos at the 90% CL.

As more information becomes available, these relations impose interesting constraints on m_t and N_ν, which depend on $\sin^2\theta_W$, and the appropriate set of structure functions.

1.3. Mass Limits on Additional Gauge Bosons W', Z'

No evidence for events from additional heavier gauge bosons W' and Z' has been observed in either the UA1 and UA2 experiments.

If one assumes identical couplings to fermions, as for W and Z, for these hypothetical gauge bosons, one can get limits on $\sigma_{W'}B_{W'}$ and $\sigma_{Z'}B_{Z'}$. These limits then give lower bounds for $m_{W'}$ and $m_{Z'}$:

$$m_{W'} \gtrsim 250 \text{ GeV}, \quad m_{Z'} \gtrsim 190 \text{ GeV},$$

for the combined UA1 and UA2 data.

2. RESULTS ON MISSING-ENERGY EVENTS

The UA1 data on events with missing energy: There are 56 such events: 53 are 'monojet' and 3 are 'multijets'. The UA1 Collaboration has evolved criteria for τ identification. They developed a τ log-likelihood function L_τ based on three measurements:

i) the narrowness of the jet;

ii) angle matching between calorimeter and charged-track energy;

iii) charged-particle multiplicity.

Thus for $L_\tau > 0$ they select 32 candidates for $W \to \tau\nu$, leaving 24 events with $L_\tau < 0$ to be accounted for. Essentially all of these ($\sim$ 21 events) can be accounted for by 'old physics' and various forms of background. Figure 6 shows the transverse mass distribution for the 32 $W \to \tau$ candidates.

This analysis leads to several very interesting results:

1) The τ decays indicate $e - \mu - \tau$ universality in W decay,

with $g_\tau/g_e = 1.01 \pm 0.09$ (stat.) ± 0.05 (syst.),
whilst $g_\mu/g_e = 1.05 \pm 0.07$ (stat.) ± 0.08 (syst.) was determined earlier.

2) A limit on the mass of charged heavy leptons. If a heavy lepton (fourth generation) existed it should have contributed to the above sample via $W^{\pm} \to L_4^{\pm} \nu_4$. From Monte Carlo calculations, including phase-space factors and polarization effects, and the fact that there are no excess missing-energy events that are not accounted for, they obtain the mass limit

$$m_{L_4} > 41 \text{ GeV} \quad (90\% \text{ CL}).$$

This is a considerable improvement on the previously available PETRA limit of $m_{L_4} > 22.7$ GeV.

3) From the reaction $p\bar{p} \to Z$ + jet and $Z \to \nu\nu$ they can place a limit of

$$\Delta N_\nu < 7 \quad (90\%\ CL)$$

on the number of extra neutrinos, i.e., $N_\nu < 10$. This is independent of the other limits on ΔN_ν.

4) From the assumed process

$$gq \to \tilde{g}\tilde{q},$$

which under certain assumptions would lead to multijets + missing energy, they can place mass limits on the supersymmetric (SUSY) particles: the gluino and the squark. The fact that only three multijet events with missing energy were observed gives a relation between the limits on $m_{\tilde{g}}$ and $m_{\tilde{q}}$. Extreme values are

$$m_{\tilde{g}} > 60 \text{ GeV},$$

$$m_{\tilde{q}} > 70 \text{ GeV}.$$

3. MUON AND DIMUON PRODUCTION

The UA1 Collaboration has developed criteria for defining ISOLATED and NON-ISOLATED muons.' These are based on how much additional transverse hadronic energy ΣE_T^{had} is contained in a cone or solid-angle interval $\Delta R \leq 0.7$ around the muon. Isolated dimuons are those for which the sum of the squares of the two ΣE_T is < 9 GeV^2.

3.1. Isolated Dimuon Systems

Some very nice data were presented on J/ψ and Υ production observed for isolated unlike-sign dimuon pairs. Figure 7 shows the $m(\mu^+\mu^-)$ mass spectrum on which a Drell-Yan signal as well as a Z^0 signal is also seen. Figure 8 shows the J/ψ mass peak (with more relaxed acceptance criteria) in greater detail on a linear

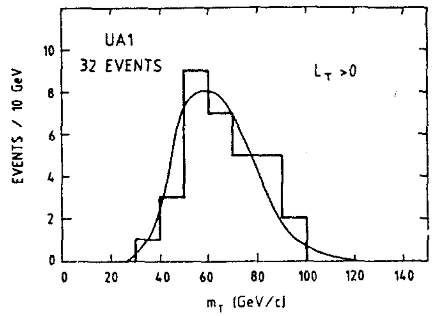

Figure 6. Transverse mass distribution for the $W \to \tau\nu$ candidates (UA1 data). The curve shows the expectation from the Monte Carlo for a W mass of 83.5 GeV/c^2.

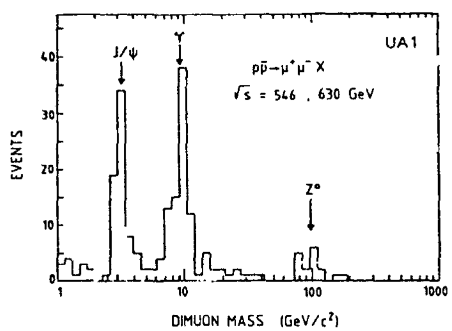

Figure 7. Isolated dimuon mass spectrum (UA1 data). Note the logarithmic mass scale.

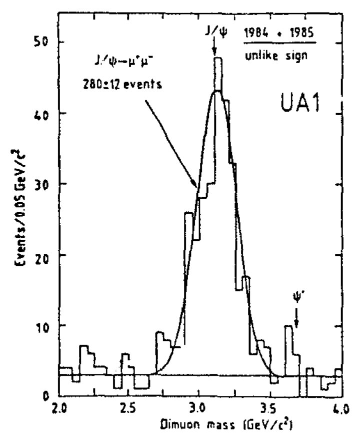

Figure 8. Details of the dimuon mass spectrum in the J/ψ region.

scale. A Gaussian fit gives $m = 3.116 \pm 0.006$ GeV/c^2, with a width consistent with the central detector resolution.

3.2. Non-Isolated Dimuon Systems

From Monte Carlo studies, the authors conclude that for $p_T(\mu) > 3$ GeV/c the non-isolated muons come primarily from direct b decay rather than from c decay, or from the $b \to c \to \mu$ cascade decay. When the above p_T cut together with a $m(\mu\mu) > 6$ GeV cut was applied to the non-isolated μ pairs, the UA1 Collaboration observed 257 unlike-sign dimuons together with 142 like-sign events. The background to the total dimuon sample of 512 events have equal probability of mimicking either like-sign or unlike-sign dimuons. The ratio R of like-sign to unlike-sign dimuon events is thus very sensitive to the precise value of the background estimate, which is known to $\pm 25\%$.

The evidence that these muon pairs come from b decays is based on three points.

i) The observation of the large like-sign sample—which cannot come from $c\bar{c}$ decays.

ii) The p_T distribution of the muons relative to the axis of the accompanying jets. As was shown for e^+e^- data, $p_T(\mu,\text{jet} > 1$ GeV/c comes primarily from b decay.

iii) The high-p_T part of the J/ψ production rate can accommodate the $Br(B \to J/\psi \simeq 1\%$, as observed by CLEO at Cornell and ARGUS at DORIS.

Interpretation of the like-sign dimuon events in terms of $B_s^0\overline{B}_s^0$ mixing. The UA1 Collaboration point out that within the framework of the Standard Model the most plausible interpretation of a like-sign dimuon signal for their kinematic cuts is $B_s^0\overline{B}_s^0$ mixing.

They find $R = N$ (like)/N (unlike) to be $R_{exp} = 0.46 \pm 0.07$ (stat.) $\pm$ 0.03 (syst.). Various Monte Carlo calculations including residual secondary charm decays $b \to c \to \mu$ gives $R_{MC} = 0.24 \pm 0.03$. Thus the observed effect is of order 3σ. Here the 'error' in R_{MC} represents the range corresponding to different Monte Carlo estimates. This result implies a sizeable B_s^0 production rate as well as large mixing. Interpretations of $B_s^0\overline{B}_s^0$ mixing are given by A. Ali and G. Altarelli in their talks at the Aachen Conference.

Earlier results from CLEO and ARGUS placed limits on $B_d^0\overline{B}_d^0$ mixing since the available energy was presumably insufficient to produce B_s^0. Very recently, the

ARGUS group has reported a surprisingly large value of $r_d \simeq 0.2$ (unpublished). If this result holds up, the UA1 measurement would correspond to both B_s^0 and B_d^0 mixing. This would not require such a high r_s value. A result from MARK II at PEP, $\sqrt{s} = 29$ GeV, where B_s^0 can presumably be produced, could only place a limit on B_s^0 mixing if a very large fraction of s-quark production f_s is assumed.

Figure 9 shows the limits for $f_s = 0.2$ in the r_d, r_s plane, where r_s is the fraction B_s^0 (wrong-sign μ)/B_s^0 (right-sign μ) and r_d the same fraction for B_d^0.

We must remember, however, that in all these experiments the results depend critically on the accuracy of the muon background calculation.

4. QCD TESTS

4.1. Evidence for the Decay of W and Z to Jets

P. Bagnaia reported UA2 results on evidence for the observation of

$$W, Z \to j_1 + j_2$$

at a rate compatible with QCD predictions. These are

$$\Gamma(W \to q\bar{q}/\Gamma(W \to e\nu) \simeq 6,$$

and

$$\Gamma(Z \to q\bar{q}/\Gamma(Z \to ee) \simeq 20,$$

excluding possible top-quark decays (which, if they occur, would have a different topology from the one selected).

The method used in this study was to trigger on two jets, each with transverse energy $E_T > 20$ GeV (although for later runs this was reduced to > 12.5 GeV). Only the central detector, $|\eta| < 1$, and two jets which were 'back-to-back' in ϕ were selected. This trigger selection favors W and Z decays over general two-jet events from parton-parton interactions.

Figure 10 shows the observed $m(j_1j_2)$ distribution. When the low- and high-mass regions are fitted to an empirical mass distribution (curve a), a clear 3.3 st. dev. signal can be noted in the W and Z mass regions. After allowing for mass resolution and mass shifts, the observed excess signal is in qualitative agreement with QCD expectations.

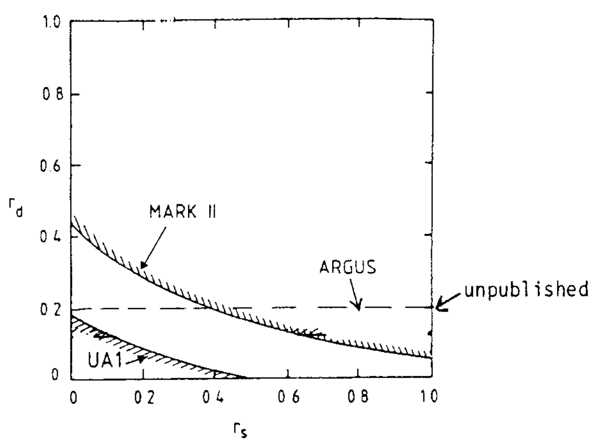

Figure 9. Limits on $B^0\overline{B}^0$ mixing. The new ARGUS value is indicated by the dashed line.

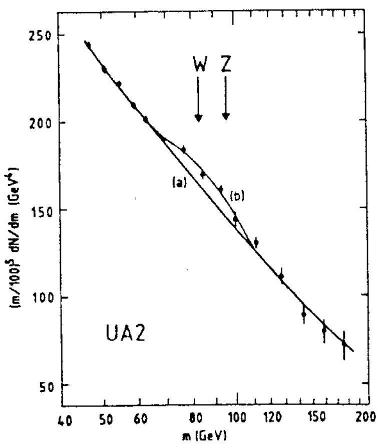

Figure 10. The two-jet mass distribution (UA2 data).

ACKNOWLEDGEMENTS

This work was supported in part by the U.S. Department of Energy under contract DE-AC03-76SF00098.

REFERENCES

1) Proceedings of the 6th Topical Workshop on Proton-Antiproton Collider Physics, Aachen, 30 June-4 July 1986, Karsten Eggert, Editor (in press).

2) E. Locci, preprint CERN-EP/86-159 (1986), to appear in the Proc. 8th European Symposium on Nucleon-Antinucleon Interactions, Thessaloniki, 1986.

Mark II/SLC-Physics Working Group Note # 0–11

AUTHOR: Gary Feldman

DATE: June 29, 1987

TITLE: Pajaro Dunes Workshop Summary

Introduction

The philosophy of the Mark II at the SLC is that by having a detector ready to do physics when the first luminosity is available, we will gain the typical nine or more months that it normally takes for a new detector to come up to speed. For this philosophy to work, both the detector and the physics analysis have to be ready. We have made the detector work by taking data with it at PEP. That we have succeeded is demonstrated by the two physics papers that we have written so far based on the PEP data.[1,2] In the former of these papers we have shown that we understand our experimental efficiencies and that the corrected new data are essentially identical to the pre-upgrade data. In the latter paper we have demonstrated the power of the increased resolution of the new tracking system — we obtained comparable results on the D^0 lifetime to those we had obtained with the old data, but with only one-seventh the integrated luminosity.

In order to be prepared to do physics analysis, we embarked 18 months ago on a study of SLC physics. We established ten physics working groups and gave them the following charge:

1. Identify the physics goals within your topic.
2. Develop the strategy for pursuing these goals.
3. Identify and implementing necessary interfaces with the collider and/or minor improvements to the detector hardware.
4. Develop analysis and Monte Carlo programs and test these programs, to the extent possible, on PEP data.
5. Educate the Collaboration on the physics to be done and the required techniques.

This program has worked extremely well as witnessed by the high caliber of work exhibited in this workshop and the two previous workshops.[3,4] Item 3 of the charge asked for "minor" improvements to the hardware. The working groups responded with the following improvements, which we are in the process of implementing:

1. The energy measurement spectrometer.
2. The muon system upgrade in the forward direction.
3. The SSP-based trigger.
4. The interaction region beam position monitor.
5. The forward veto counter.
6. The liquid argon calorimeter hole fillers.
7. The instrumented mask.

These "minor" improvements will markedly improve our ability to study SLC physics. However, they are costing over one million dollars. I can only say that it is probably fortunate for the laboratory's budget that we did not request "major" improvements.

Exceptional Accomplishments

I would now like to list some of the accomplishments of this study that I have found especially impressive. I have placed items in this list either because of the extensiveness of the work or because the result was somewhat surprising. This is a personal list and omission of an item or name from it should not be taken as an indication that the omitted work was not of high quality. Almost all of the work that has been reported in these workshops has been of very high quality.

1. **Radiative Corrections.** When we began this study, the radiative corrections were quite uncertain and there were discrepancies of 10 to 20% between different calculations. Under the leadership of Patricia Rankin, the radiative corrections group has reduced the uncertainties to about the 1% level. The work of the Gang of Four, Jim Alexander, Giovanni Bonvicini, Persis Drell, and Ray Frey, has been particularly impressive.[5] We are appreciative of the help we have received from the theoretical community, locally particularly from Bob Cahn and Bryan Lynn.
2. **The Physics of Polarization.** The Polarization Group, under the leadership of Ken Moffeit and Herb Steiner, has raised our collective consciousness as to the potential power of having longitudinally polarized beams. Paul Grosse-Wiesmann gave a fine talk at this workshop on this subject. In terms of determining $\sin^2\theta_W$, one event with polarized beams is worth about 100 events with unpolarized beams.
3. **Neutrino Counting on the Z.** The traditional method of directly counting neutrino species is to set the beam energies above the Z and look for a high-p_t radiative transition to the Z. This technique will probably be impractical for the Mark II just from the standpoint of running time. However, the working

group on neutrino counting, under the leadership of Rudy Thun, has shown that it will be possible to do the experiment while sitting on the peak of the Z, albeit with somewhat lower statistical accuracy.[6] To this end, Dave Burke has proposed and is building an instrumented mask to allow electron vetoes down to 15 mrad.

4. **B Tagging.** Early in the workshop process, Ken Hayes showed that we can tag $b\bar{b}$ events with relatively high efficiency.[7] This ability will be extremely useful both for studying B meson physics and for exploring the properties of new particles.

5. **Hadronic Monte Carlo.** Alfred Petersen has done a marvelous job of fitting our PEP data to the world's collection of Monte Carlo models and using the results to predict the hadronic event parameters that we expect for Z decay.[8] From this work we have a reasonable idea of the range that a given observable can take for normal hadronic events. Since these events are the major background to most new particle searches, this work is indispensable in building our confidence in valid new particle signatures.

6. **New Particle Searches.**

   (a) **Top Quark.** I remember that when we were first thinking about SLC physics, it was commonly assumed that finding the top quark would be very easy — one would only have to look for spherical (or with a little more sophistication, aplanar) events. The top working subgroup, under the leadership of Gail Hanson, has shown that, given our present understanding of hadronic fragmentation, these techniques are not as decisive as had been thought.[9] Techniques involving the detection of leptons are much more reliable. Tim Barklow has borrowed a trick from new particle searches in hadron colliders and shown that the detection of isolated leptons is an almost perfectly background free signal for new particle production.

   (b) **Supersymmetry.** Tim Barklow has done a remarkable job of cataloging the myriad of decay signatures that could be expected for supersymmetry.[10] This has given us a framework in which searches for these particles can be carried out.

   (c) **Non-Minimal Higgs.** In most models which try to go beyond the standard model, the Higgs sector is non-minimal. If this occurs in nature, then it is possibly fortunate for SLC physics since the non-minimal Higgs can be copiously pair produced and will thus be more easily detected than minimal Higgs particles, particularly when only a modest numbers of Z's have been produced. Sachio Komamiya has given an extremely lucid discussion of the possibilities for detecting these particles.[11]

   (d) **Long-Lived Neutral Leptons.** The coupling of the Z to neutral fermions gives us the opportunity to search for new neutrinos. If these neutrinos are sufficiently massive, they will decay by mixing with the light neutrinos. These decays can be quite long-lived if the mixing angles are small. Thus, one can even imagine a signature which would be a single vertex originating a meter from the interaction point. Alan Weinstein has shown that we can find these vertices[12] and Spencer Klein has looked into the triggering requirements.[13]

Physics Prospects

We can realistically think about three sets of data which are characterized in the following table:

Character	Number of Z's	$\int \mathcal{L} dt$	Time frame
First look	1-2 k	30-60 nb^{-1} or $3\text{-}6 \times 10^{27}$ for 10^7 sec	Fall 1987
Exploration	10-20 k	300-600 nb^{-1} or $3\text{-}6 \times 10^{28}$ for 10^7 sec	Spring 1988
Measurement	100-200 k	3-6 pb^{-1} or $3\text{-}6 \times 10^{29}$ for 10^7 sec	1989-1990

In order to reach the goals listed under "Time frame," it is clear that the average luminosity of the SLC will have to increase an order of magnitude every year. This is obviously quite a challenge, but conceivable. For example, an 73% increase in the electron and positron currents coupled with a 42% decrease in the linear spot size is worth a factor of 10 in luminosity. I believe that the horizon of the Mark II is the 100-200 thousand event region. After we accumulate that number of events, the SLD should be ready to start its physics program. It is also appropriate to have a detector with the features of the SLD to explore the physics of million event data samples.

Let's now review the physics that can be done with each of these sets of data. The following table discusses the prospects for physics that requires or benefits from scanning in energy:

Topic	Quantity	1-2 k events	10-20 k events	100-200 k events	Ref.
Z mass	δm	70 MeV	50 MeV		14,15
Z width	$\delta\Gamma$	190 MeV	70 MeV	50 MeV	14,15
ν counting (or Γ_{invis}): 1) $\Gamma_{tot} - \Gamma_{invis}$	$\delta\Gamma_{invis}$	95 MeV	50 MeV		16
2) $\gamma\nu\nu$ on peak	$\delta\Gamma_{invis}$		150 MeV	50 MeV	6
3) $\gamma\nu\nu$ at m_Z + 4 GeV	$\delta\Gamma_{invis}$			40 MeV	6
Toponium scan				Possible if $m_\theta < 85$ GeV	17

Notes on the above table: Running the direct neutrino counting experiment above the Z (method 3 under ν counting) looks rather unlikely as a Mark II activity. I can foresee it happening only if three conditions are met:

1. The answer given by the first two methods is not clear.
2. It is the most pressing physics question at the time.
3. The SLD is delayed.

For similar reasons, it is hard to imagine that a toponium scan can be contemplated during the Mark II lifetime.

This table raises the question of what our strategy should be regarding the amount of time we spend scanning versus the amount of time we spend sitting on the peak. There is much to be said in favor of scanning. We need it to determine the Z mass and width; it is beneficial for the direct neutrino scanning experiment on the Z peak since it both allows backgrounds to be studied and yields a higher data rate; and it slightly extends the mass range for the top quark search. Furthermore, there is a general question which can be raised: Shouldn't we spend some time running where part of the amplitude is real? If we spend almost all of our time exactly on the peak, where the amplitude is purely imaginary, we will be insensitive to interference effects from other physics such as another Z at higher energy.

My personal suggestion is that we plan to scan in large steps until we hit the systematic limit on the Z width determination, and then reevaluate the strategy based on the physics outlook at that time. There are broad minima in the optimum scanning strategies,[14] so the scan can be designed to maximize, to some extent, the number of Z's collected.

The final table discusses the prospects for physics that does not require scanning:

Topic	Quantity	1-2 k events	10-20 k events	100-200 k events	Ref.
Electroweak parameters: A^μ_{FB}	$\delta\sin^2\theta_W$	0.06	0.02	0.006	18
A^b_{FB}	$\delta\sin^2\theta_W$	0.08	0.025	0.008	19
A^τ_{pol}	$\delta\sin^2\theta_W$	0.12	0.04	0.012	20
A_{LR}	$\delta\sin^2\theta_W$		0.003	0.001	21
QCD		Some topics	Interesting range		22
B lifetime	τ_b		13%	<10%	23
Top quark		See an indication	Determine mass	Determine couplings	9
Super-symmetry		Indication of easy signals	Measurement of easy signals, indication of harder signals	Detailed measurements	10
Minimal Higgs			m < 4 GeV $H \rightarrow \mu^+\mu^-$	m < 10 GeV $Z \rightarrow H\ell^+\ell^-$	24
Non-minimal Higgs			H^+H^- $H^0_iH^0_j$ (some cases)		11

It is clear from this and the previous table that real physics measurements begin at the 10-20 thousand event level. This is why we are giving very high priority to the goal of reaching this level by the spring of 1988. Notice also the power of having longitudinally polarized beams. The measurement of A_{LR} with 10-20 thousand events using polarized beams gives a considerably better measurement of $\sin^2\theta_W$ than any of the techniques with unpolarized beams and an order of magnitude more luminosity.

Conclusion

The first meeting to plan for the Mark II at the SLC was in December 1980, $6\frac{1}{4}$ years ago. Our proposal was approved in November 1982, $4\frac{1}{3}$ years ago. It has been a long time, but due to your hard work we are now on the verge of starting what could be the most exciting high energy experiment of this decade. The workshop process has created organic groups which will continue to function as needed. It is not an exaggeration to say that through our preparation at PEP and through these physics workshops, we are better prepared than any large collaboration has ever been before.

Let's go do it.

References

1. A. Petersen *el al.*, "Multihadronic Events at $E_{cm} = 29$ GeV and Predictions of QCD Models From $E_{cm} = 29$ GeV to $E_{cm} = 93$ GeV," SLAC report number SLAC-PUB-4290 (1987), submitted to Physical Review D
2. S. R. Wagner *el al.*, "Measurement of the D^0 Lifetime from the Upgraded Mark II Detector at PEP," SLAC report number SLAC-PUB-4304 (1987), submitted to Physical Review D.
3. "Transparencies from the Mark II SLC-Physics Workshop at Asilomar, March 16-19, 1986," Mark II/SLC-Physics Working Group Note # 0-2 (1987)
4. "Proceedings of the Second Mark II Workshop on SLC Physics, Granlibakken, September 14-17, 1986," SLAC report number SLAC-306 (1986).
5. J. Alexander, G. Bonvicini, P.S. Drell, and R. Frey, Mark II/SLC-Physics Working Group Note # 1-12, these proceedings.
6. Neutrino Counting Study Group, Mark II/SLC-Physics Working Group Note # 10-3, these proceedings.
7. K. Hayes, Mark II SLC Note #73 (1984) and in Ref. 3.
8. A. Petersen, Mark II/SLC-Physics Working Group Note # 8-3, these proceedings, and Ref. 1.
9. G. Hanson, Mark II/SLC-Physics Working Group Note # 3-18, these proceedings.
10. T. Barklow, Mark II/SLC-Physics Working Group Note # 3-21, these proceedings.
11. S. Komamiya, Mark II/SLC-Physics Working Group Note # 3-20, these proceedings.
12. A. Weinstein, Mark II/SLC-Physics Working Group Note # 5-1 in Ref. 4.

13. S. Klein, Mark II/SLC-Physics Working Group Note # 5-2, these proceedings.
14. G. J. Feldman, Mark II/SLC-Physics Working Group Note # 1-1 (1986).
15. P. Rankin, Mark II/SLC-Physics Working Group Note # 1-9, these proceedings.
16. G. J. Feldman, Mark II/SLC-Physics Working Group Note # 1-12, these proceedings.
17. H. F. W. Sadrozinski, Mark II/SLC-Physics Working Group Note # 4-6, these proceedings.
18. J. Matthews, Mark II/SLC-Physics Working Group Note # 2-17 in Ref. 4.
19. S. R. Wagner, J. G. Smith, and S. L. White, Mark II/SLC-Physics Working Group Note # 2-8 in Ref. 4.
20. D. Cords, Mark II/SLC-Physics Working Group Note # 2-25, these proceedings.
21. K. Moffeit, Mark II/SLC-Physics Working Group Note # 2-19 in Ref. 4.
22. A. Petersen, Mark II/SLC-Physics Working Group Note # 8-3, these proceedings.
23. W. T. Petersen, Mark II/SLC-Physics Working Group Note # 9-17, these proceedings.
24. W. Innes, Mark II/SLC-Physics Working Group Note # 7-5 in Ref. 4.

Mark II/SLC Physics Working Group Note #1-9

Title: Z^0 Measurements; The Theory and The Practice.

Author: Patricia Rankin

Date: June 6th, 1987.

I. Introduction

This report is based on the efforts of the members of Working Group 1.[1] The group has worked hard for the last eighteen months not only to ensure that the Mark II experiment is ready to measure as accurately as possible the mass,width and total cross section of the Z^0 resonance , but also to make clear the theoretical importance of these measurements. This report is intended to serve both as a summary of what has been learnt and as an introduction to the work to follow. The next section consists of a brief description of the Standard Model and of the basic relationships between the coupling strengths, the Z^0 mass, width and cross section, and the particle content of the model. The third section discusses the experimental measurement of the mass, width and total cross section of the Z^0 and how the accuracy of these measurements will be constrained by experimental limitations. This is followed by an introduction to the theoretical complexities involved in extracting parameters from the Z^0 line shape to use in tests of the Standard Model. The report concludes with a summary of the dominant errors and uncertainties.

II. The Standard Model.

Since the discovery of neutral currents in the seventies[2] the Standard Model ($SU(2)\times U(1)$) of electroweak interactions has become increasingly accepted as the framework within which to interpret a large body of experimental data. The discovery of the W and Z^0 bosons[3] at the CERN collider is widely regarded as being the observation which confirmed that the features of the model were basically correct. Within the next few years studies based on large numbers of Z^0 events will begin to allow detailed checks of these features.

The basic idea behind the Standard Model is that electromagnetic and weak interactions are not two distinct phenomena. Instead the gauge bosons which couple to the weak isospin and hypercharge acquire mass via a Higgs mechanism

so that their interactions appear weaker until the associated momentum transfers become large in relation to their masses. Interactions are therefore mediated by photons, and by the W and Z^0 vector bosons, and interference effects can be observed between the photon and the Z^0.[4]

The simplest variant of the standard model (single Higgs doublet) is defined by fixing three parameters; the SU(2) and the U(1) coupling strengths, and the vacuum expectation value associated with the Higgs field. A more general formulation allows for the existence of more than one Higgs doublet and introduces a fourth parameter (usually termed ρ) which changes value (from one in the simplest case) to reflect the complexity of the Higgs structure. The model defines how a particle with given electroweak quantum numbers will interact, it does not specify exactly which particles exist. However predictions of (for example) the width of the Z^0 do depend on the types and number of generations of particles (and their masses). This means that ultimately what one tests is the consistency of predictions with an assumed particle content.

The three 'bare' parameters of the model must be related to three measurable physical quantities in order to remove infinities from the theory. The subtraction procedure which eliminates divergences leads to a 'renormalization' of the input parameters. The results of Thompson scattering experiments which essentially measure the electric charge at $q^2 = 0$ can be used to renormalize the 'bare' electric charge. However, the effective electric charge seen by a photon coupling to an electron-positron pair in e^+e^- annihilation increases with the center-of-mass energy, and we are free to use any measurement of the charge of an electron to renormalize the bare charge. This means that there are an infinite number of possible renormalization schemes to choose from, all of which relate the bare quantities to measurements at a particular q^2.

The value the theory predicts that an experimentally measurable quantity will take should not depend on the choice of renormalization scheme. Calculations made at lowest order (Born level) however, do not automatically include q^2 dependent correction terms. The values derived for the couplings exactly match the true couplings only at the specific q^2 the bare parameters were renormalized at. The correction terms are needed to adjust the effective strengths of the couplings. Neglecting them means that the choice of which three physical measurements to use in renormalizing the bare parameters of the Standard Model, determines how close a lowest order estimate will come to the final answer. Alternatively, results calculated using different physical measurements as input parameters will give different lowest order predictions.

The calculations can be made to agree by the inclusion of a subset of the higher order diagrams. The subset of interest consists of those diagrams ('oblique' or 'loop') which modify a propagator by introducing an internal loop or loops. They correspond to the vacuum polarization of the photon and to the self energies of the Z^0 and W's. These diagrams effectively scale the coupling constants with q^2. The remaining diagrams involve either initial state photon radiation or final state photon and/or gluon radiation and correspond to the addition of external lines to the lowest order diagrams. A discussion of how the resonance shape is distorted by these higher order effects is postponed to section IV.b.

Since the oblique diagrams can be considered as modifiers of the couplings, an alternative way of including them in calculations is to allow the couplings to run with q^2.[5] Since the changes in all of the renormalized couplings can be calculated precisely to all orders, they can all be replaced by their exact strengths at the q^2 of the process under consideration. Experimental measurements are still needed but these are now used to constrain the theoretical curves which give the dependence of the couplings on q^2. This 'running coupling constant' approach is familiar from QCD. It leads to renormalization scheme independent results, which makes it much easier to compare calculations and Monte Carlos based on different renormalization schemes. It also has the considerable advantage of allowing the lowest order expressions given in this paper to be carried over to higher orders (by hiding the corrections from the casual calculator). The minor disadvantage of this scheme is that not all terms in a given calculation will necessarily be calculated to the same order, and some terms (which have insignificant effects) may be ignored (Box diagrams for example).

An earlier alternative to the running coupling constants scheme which is frequently found in the literature is a modification of the 'on-shell' scheme.[6] One of the best measured of all physical constants is $\alpha_{em}(0)$ and this is included in the set of defining parameters. However, the effective charge of the electron increases by about 7% between $q^2 = 0$ and $q^2 = M_z^2$. The effects of this change are significant enough for it to have become usual to allow for it by including a $(1 - \Delta r)$ term even at 'lowest' order. Strictly speaking, the Δr term also includes the effects of the small q^2 dependent corrections to the remaining parameters. The other two measurements which are used are the muon lifetime (this fixes G_F and can be considered as a substitute for an accurate measurement of M_W) and the mass of the Z^0 which is defined to be the physical position of the pole of the Z^0 resonance.

In the past people have been used to thinking of the weak couplings in terms of $\sin^2\theta_W$, and there is some resistance to eliminating this entirely. However, many of the early definitions of $\sin^2\theta_W$ are more appropriate to low energy measurements. It is most convenient at SLC/LEP energies to define $\sin^2\theta_W$ at $q^2 \approx M_z^2$, and in a way which is valid to all orders in perturbation theory (the approximate

relationship to the three parameters of the modified on-shell scheme is also given because M_W is not yet well measured);

$$\begin{aligned}\sin^2\theta_W &= 1 - \left(\frac{M_W^2}{M_z^2}\right) \qquad (1)\\ &\approx \frac{1}{2}\left[1 - \sqrt{1 - \frac{4\pi\alpha}{\sqrt{2}M_z^2 G_F(1-\Delta r)}}\right]\\ &\approx \frac{1}{2}\left[1 - \sqrt{1 - \frac{5576C}{M_z^2(1-\Delta r)}}\right]\\ \sin^2\theta_W &\approx 0.222\end{aligned}$$

for $M_z = 93$GeV and $\Delta r = 0.07$. An accurate value for M_z will be obtained from SLC data. The current best estimate[7] of $M_z = 92.5$GeV yields a value of about 0.226 ± 0.007 for $\sin^2\theta_W$. This definition of $\sin^2\theta_W$ gives a value very close to that of $\sin^2\theta_W^*(q^2 = M_z^2)$ the equivalent if the running coupling constant technique is being used.

The exact value of Δr is specific to the choice of the modified on-shell renormalization scheme, and depends, among other things, on the Higgs mass and the top quark mass (chosen to be 100 GeV and 45 GeV respectively). The uncertainties are related to the difficulties in exactly evaluating the 'oblique' corrections and are discussed in section IV.c. We assume here that the standard model is valid and nothing is conspiring to hide the true theory from view.

Since the mass of the Z^0 is to be used either as a defining parameter of the model (modified on-shell scheme), or to fix the value of the weak coupling at SLC energies (running coupling constant approach), it should be clear that it is essential to measure this quantity as accurately as possible. The other measurements used are so accurate that the uncertainties due to the error on the Z^0 mass determination dominate the error when deriving a value for $\sin^2\theta_W$. We will aim for an accuracy of better than 50 MeV in measuring M_z which reduces the error on $\sin^2\theta_W$ to ≤ 0.0004.

The coupling (C) of any fermion state to the Z^0 can be written in terms of the 3rd component of its weak isospin (I_3), its charge (Q), and $\sin^2\theta_W$:

$$C = \frac{-ie}{\sin\theta_W\cos\theta_W}\left[(I_{3l} - Q\sin^2\theta_W)\frac{(1-\gamma_5)}{2} + (I_{3r} - Q\sin^2\theta_W)\frac{(1+\gamma_5)}{2}\right] \qquad (2)$$

where the first term in the brackets relates to the left-handed coupling, and the second to the right handed coupling. Since I_{3r} is zero for fermions, right-handed massless neutrinos should not be observed. It is convenient to define an axial vector (a) term which does not depend on $\sin^2\theta_w$ and couples via γ_5, and a vector (v) coupling which is sensitive to $\sin^2\theta_w$:

$$a = 2I_3 \tag{3}$$
$$v = 2(I_3 - 2Q\sin^2\theta_w) \tag{4}$$

so that the total width of the Z^0 can then be written,

$$\Gamma = \frac{G_F M_z^3}{24\sqrt{2}\pi}\sum_i C_i(v_i^2 + a_i^2) \tag{5}$$

where $\quad C_i = 1 + \frac{3\alpha_{em}Q_i^2}{4\pi} \quad$ for leptons

and $\quad C_i = 3 \times \left(1 + \frac{3\alpha_{em}Q_i^2}{4\pi} + \frac{\alpha_s}{\pi}\right) \quad$ for quarks

The terms dependent on α_{em} and α_s allow for the effects of final state photon and gluon radiation respectively. The widths for common types of particles are given in Table 1, assuming a Z^0 mass of 93 GeV, $\sin^2\theta_w = 0.222$, and $\alpha_s = 0.13$.[8] 'All' refers to all known fermions (thus excluding top). A measurement of the width of the Z^0 is necessary in order to define the particle content of the standard model. All particles to which the Z^0 can decay contribute to it. Measurements of the total width and of the partial widths to charged leptons and hadrons allow the contribution from particles not seen in the detector (such as neutrinos) to be isolated.

Table 1

Partial Widths for $M_z = 93.0\text{GeV}, \sin^2\theta_w = 0.222$

STATE	$a^2 + v^2$	$\Gamma(MeV)$
ν	$1 + 1 = 2$	176
e	$(-1)^2 + (-1 + 4\sin^2\theta_w)^2 = 1.01$	89
u	$(1)^2 + (1 - (8/3)\sin^2\theta_w)^2 = 1.17$	$103 \times 3 \times 1.04$
d	$(-1)^2 + (-1 + (4/3)\sin^2\theta_w)^2 = 1.50$	$132 \times 3 \times 1.04$
all		2673

Close to the Z^0 pole (so photon exchange can be neglected), the cross section at a center of mass energy S, is given by;

$$\sigma_f = \frac{G_F^2}{96\pi}\left(\frac{SM_z^4}{(S - M_z^2)^2 + \Gamma^2 M_z^2}\right)(v_e^2 + a_e^2)(v_f^2 + a_f^2) \tag{6}$$

$$= \left(\frac{G_F^2 M_z^4}{96\pi\Gamma^2}\right)(v_e^2 + a_e^2)(v_f^2 + a_f^2) \quad \text{on the pole} \tag{7}$$

$$\Rightarrow \sigma_{tot} = \left(\frac{G_F\sqrt{2}(v_e^2 + a_e^2)}{4}\right)\left(\frac{M_z}{\Gamma}\right) \tag{8}$$

$$\approx 1.6\,\frac{M_z}{\Gamma}\text{ nb}$$
$$\approx 60\text{ nb}$$

The muon cross section is about 1.88 nb for the values assumed in calculating Table 1. These calculations exclude the effects of initial state photon radiation which will decrease the peak cross section (by about 25%). This radiation also significantly changes the shape of the resonance, in particular above the Z^0 pole. This subject is dealt with in detail later (section IV.b).

Measuring cross sections allows an indirect measurement of the Z^0 width to be made which can be compared with direct ones. In order to use this method the partial width to the final state(s) selected must be calculated. Since the muon final state is the least sensitive to the value of the vector coupling and since it can also be isolated cleanly from other events it is probably the best to use for this measurement. The relationship between cross section and width which this method exploits is given below.

$$\Gamma_{tot}^2 = \frac{12\pi\Gamma_{ee}\Gamma_{\mu\mu}}{M_z^2\sigma_\mu} \tag{9}$$

The error on the total width which results from using this method is given by

$$\frac{\Delta\sigma_\mu}{\sigma_\mu} = \frac{2\Delta\Gamma}{\Gamma} \tag{10}$$

This means that the muon cross section must be measured to better than 4% if the error on the width is to be less than 50 MeV (slightly less than 1/3rd of the contribution from an extra light neutrino generation). If no allowance is made for the detector acceptance this implies that about 2×10^4 Z^0's will be necessary for this measurement. If stringent requirements are imposed on the identification of the muons the number required may double. A study of the detectors acceptance of taus however shows that these could be used to reduce the number of Z^0's needed back down to 2×10^4.

An observed discrepancy between the predicted width and that extracted from measurements of the line shape is a signal that other particles are being produced. Exactly what these new particles are however cannot be unambiguously determined without making other measurements. An increase in width with a corresponding decrease in the visible cross section will probably imply the existence of more than three neutrino generations. If the increase in width is instead associated with events seen by the detector then possibly SUSY particles or new quark flavors have been found.

The details of the experimental signatures for various types of particles will be discussed in the reports of the working groups interested in the production of specific particles. I would like to mention here only one quantity which can be used to help distinguish between the possibilities. This is the forward backward asymmetry (A_{fb});

$$A^x_{fb} = \frac{\sigma^x_f - \sigma^x_b}{\sigma^x_f + \sigma^x_b} = \frac{3v_e a_e v_x a_x}{(v_e^2 + a_e^2)(v_x^2 + a_x^2)} \tag{11}$$

which is sensitive to the vector coupling of the particle (and which can distinguish clearly between a top quark or a b'). In addition, a measurement of A_{fb} for a known particle has some sensitivity to physics above the Z^0 since one is testing the predicted coupling (derived from the Z^0 mass) against the measured one. An even more sensitive probe of physics above the Z^0 is however the left-right polarization asymmetry A_{lr};

$$A_{lr} = \frac{\sigma_l - \sigma_r}{\sigma_l + \sigma_r} = \frac{2v_e a_e P}{(v_e^2 + a_e^2)} \quad \text{where P = fractional polarization} \tag{12}$$

which measures the electron couplings regardless of which final states are being studied. This means that the results for all final states can be combined in making this measurement. The value of polarized beams is discussed in detail in the polarization groups contribution to these proceedings. The subject of sensitivity to new physics will be returned to in the section on oblique corrections.

III. Experimental Details.

III.a Scanning Strategy.

The early running at the SLC will be done at low luminosities. The turn on luminosity may be as low as $5 \times 10^{27} \mathrm{cm}^{-2}\mathrm{s}^{-1}$. At this luminosity it will take about two days to accumulate an inverse nanobarn of data. Since only about 80% of the cross section consists of visible decays, and allowing for the decrease in the peak cross section due to initial state photon bremsstrahlung, this corresponds to about 16 events a day in the detector when we run at the peak (assuming 100% running efficiency).

A preliminary scan around the expected peak position (90−95 GeV)[9] of about $10 \mathrm{nb}^{-1}$ can be expected to take about 6 weeks and yield around 250 events. A program[10] has been set up to estimate the statistical errors on the mass, width, and peak cross section. This indicates that even with such a small data set the peak position can be measured to a statistical accuracy of about 200 MeV, the width to within 550 MeV, and the peak cross section to about 14%.

Another purpose of this program is to help evaluate the strategies which may be adopted in scanning across the resonance in order to make the best measurement of the mass, width, and cross section for a given amount of data taken. This work refines an earlier evaluation[11] which was based on a Breit-Wigner resonance shape, by incorporating the most significant of the effects of photon bremsstrahlung on the resonance shape.

The earlier work showed that it was reasonable to space the scan points about a 1/2 GeV apart and to scan between 2-3 GeV below and above the peak. It also established clearly that there was no advantage in equalizing the statistical accuracy of each scan point (same number of events). Instead, strategies based on equalizing the integrated luminosity at each scan point were close to the optimum. The effect of increasing the number of events taken during the scan by taking more data at the higher cross sectional points was studied. To do this, the integrated luminosity taken at each point was weighted by a factor proportional to a power of the fractional cross section at that point. This study showed that although the peak cross sectional measurement was always improved, the mass measurement started to deteriorate gradually with very strong weighting and the width measurement rapidly deteriorated if the weighting became very much stronger than σ_{frac}.

The more detailed study confirmed the broad features of the earlier work while enabling a more exact estimate of the statistical errors to be made. Figure 1 compares a 'blind' strategy (one that does not use information from an early scan to center itself close to the peak) to a strategy where a lower statistics scan is used to decide where to place the scan points for a high statistics scan. It shows how the error on the width decreases as a function of integrated luminosity for the two strategies. The error on the mass is typically about 40% of the error on the width for strategies such as those above which take equal integrated luminosities at all points.

III.b Energy Measurements.

Even running significantly below SLC design luminosity there should be no problem obtaining enough Z^0 events to reduce the statistical error on the Z^0 mass to below 50MeV. It is therefore essential to measure as accurately as possible the center of mass energy at the interaction point since this will be the limiting systematic error in the determination of the position of the resonance peak.

The SLC is a unique machine and as may be expected, many of the problems involved in making an accurate pulse to pulse energy calibration are very different from the difficulties encountered when making such a measurement at a colliding ring like LEP. The SLC arcs which may seem to be the logical place to make a measurement were not built with this purpose in mind. Instead, they were designed to keep the dispersion (η), to a minimum and to prevent the phase space occupied by the beam from growing too large (particles which radiate undergo betatron oscillations). It is possible to measure the energy of the beams at the beam switchyard (at the end of the Linac, before the beams enter the arcs) but even assuming that the synchrotron losses in the arcs can be calculated accurately and allowed for (about 1.5 GeV is lost by each beam when traversing the arcs) the estimated accuracy of this measurement is only 0.35% (about 300 MeV error in the measurement of M_Z).[12]

The decision was made to build energy spectrometers in the beam dumps, partly to ensure as accurate as possible an absolute measurement was made, but also because this removed worries about the accuracy of measurements relative to each other, and about the reproducibility and stability of measurements made at different times. Figure 2 shows the conceptual design of the spectrometers. The basic idea is to bend the beams about 18mrad using a 30 kG-meter magnet and to measure this change in direction as accurately as possible. Two small bend magnets (one before, one after the main bend magnet) produce two horizontal bands of synchrotron radiation, the displacement between these two bands provides a measurement of the amount the beam is bent. The synchrotron x-ray radiation will be detected by a phosphor screen scanned by a video camera and also by a wire array detector (sensitive to secondary emission).

The errors affecting this measurement fall into two groups (significant contributions are summarized in Table 2), those contributing to an inaccurate

Table 2
Single Pulse Systematic Errors in Energy Measurements
Using The North and South Extraction Line Spectrometers
Absolute (Relative) Errors Quoted in MeV for 46.5 GeV beams

Magnetic Field Mapping in Laboratory (0.01% per beam)	5 MeV (-)
Monitoring Magnetic Field (0.01% per beam)	5 MeV (5 MeV)
Detector Localization of Imaged Light Centroid to Centroid error of 80μm/27cm (0.03% per beam)	15 MeV (15 MeV)
Spurious Rotation of Horizontal Bend Magnets for 1 mrad rotation (0.01% per beam)	5 MeV (-)
Summed Systematic Errors For Single Beams (Accuracy of measurement at dump)	30 MeV (20 MeV)
Residual Dispersion in conjunction with a betatron crossing error at the IP (0.03% per interaction)	15 MeV (15 MeV)
Total quadrature error on the CM energy	**45MeV (35 MeV)**
The error in the determination of M_Z is around 0.05%	
The error in the determination of the Γ_Z is around 1%	
(note that 0.05% on CM energy = $\sqrt{2}$ x 0.05% per beam)	

measurement at the dump and those which make the energy measured at the dump different from the energy of the beams at the interaction point (IP). Magnet alignment, field mapping, and field monitoring all contribute to the error in the dump energy measurement but the largest source of error (especially for the width measurement) is in localizing the image of the synchrotron radiation at the detector.

Several small effects change the energy of the beams between the IP and the dumps. For example, some energy will be lost in the collision itself, the amount depends on the size of the beams and the luminosity but even at fairly high luminosities (10^{29} cm^{-2}s^{-1}) only averages about 5 MeV/electron. The synchrotron energy lost as the beams travel from the IP to the septum magnet will be about 50 MeV so it will be necessary to correct for this. The most significant potential source of error which has been considered is the possibility that there may be a residual dispersion at the IP which could combine with a small offset between the two beams to give a difference between the luminosity weighted center of mass energy at the interaction point and the energy measured at the dumps. This error will fluctuate from pulse to pulse and so it is expected that any error in the determination of the energy of a single pulse will be cancelled stochastically when several pulses are averaged. In addition, as Figure 3 shows, the luminosity decreases rapidly as the error in the energy measurement increases. The error estimate given is based on a dispersion of three mm, but it is planned ultimately to reduce the dispersion to less than one mm. If there are slow, coherent drifts in steering which cause a systematic bias in the energy measurement these should be detectable by repeat scanning at given energy points and by cross checking the energy spectrometers results using the lepton acollinearity distributions measured in the Mark II. This error can also be controlled to some extent by studying the change in the position of the interaction point as a function of beam energy. This will allow a measurement of the dispersion to be made (to an estimated accuracy of one beam sigma).

The statistical errors associated with sampling the beams' energy on a fraction of the beam pulses have been studied and have been shown to be small (provided the pulse to pulse energy fluctuations are smaller than the Z^0 width !).[13] The relevant estimate of the energy is a luminosity weighted average and it is planned to measure the energy whenever there is a luminosity trigger. Some redundancy will be supplied by also measuring the energy on an event to event basis and on random (minimum bias) triggers. The energy estimate based on random triggers will tend to give the wrong energy if there is a correlation between luminosity and beam energy. The estimate based on the beam energy for Z^0 events will also be biased since it will be a cross-sectionally weighted average. This bias can be calculated if the pulse to pulse energy variance is known.

Table 3 summarizes for a number of interesting measurements the number of events needed before the statistical error in those measurements is reduced to the level of the systematic error due to the energy measurement. It was assumed that

the smart scanning strategy of section II.a was used to make the measurements.

Table 3
Number of Events Needed To Reach Systematic Limit

QUANTITY	SYSTEMATIC ERROR	SYSTEMATIC LIMIT REACHED AFTER	$\int$ L dt
Mass	δM_Z = 45 MeV/c^2	4.2 x 10^3 events	140 nb^{-1}
$\sin^2\theta_w$	$\delta\sin^2\theta_w = \pm.0003$	4.2 x 10^3 events	140 nb^{-1}
σ_{total}	$\delta\sigma_{tot}/\sigma_{tot} = \pm.03$	7.3 x 10^3 events	180 nb^{-1}
Width	$\delta\Gamma_Z = \pm35$ MeV/c^2	3.7 x 10^4 events	1.1 pb^{-1}

Another couple of points should be made before leaving this section. It is possible that the beam energy may jitter by up to 5% from pulse to pulse due to klystrons misfiring. The frequency of such occurrences is debatable until some prolonged experience has been accumulated, misfires may occur every few minutes, failures every few hours. It is also unlikely that the positron and electron beams will have the same energy. This is part of the reason for measuring the energy of both beams. Independent energy measurements of each beam also allow a check on systematics to be made using the acollinearity distribution of muon pairs in the detector. The inclination angle of a particle with respect to the beam axis can be measured to a resolution of about 6.2 mrad in the central region of the Mark II detector. Allowing for a pessimistic beam spread of 0.5%, it is estimated that about 10,000 Z^0 events will be required to check the absolute calibration of one extraction line spectrometer with respect to the other at a scan point.

III.c Luminosity Measurements.

There are two devices which will be used to provide luminosity measurements for the Mark II at the SLC, both looking at small angle (t-channel) electron scattering.[14] The first of these (the small angle monitor or SAM) has an estimated energy resolution of about 5% for 50 GeV electrons and covers the angular range 50mrad $\leq \theta \leq$ 140mrad. Over this angular range the contribution to the cross section from s-channel Z^0 interactions compared to that coming from t-channel photon interactions is around 1%, the overall counting rate in the detector being slightly higher than the peak Z^0 rate (about 38 nb cross section). The SAM has an estimated angular resolution of 0.2 mrad if the interaction point is known, decreasing to 3 mrad if it is not. The second device (mini-SAM), has a similar energy resolution but works at smaller angles (about 15 - 25 mrad), so the Z^0 contribution is less than 0.1% and the count rate is significantly higher than that in the SAM (around 220 nb). The mini-SAM is divided into four quadrants.

Since the count rates are substantially higher in the mini-SAM the statistical error on luminosity measurements is smaller than for the SAM. The mini-SAM will be used for rapid feedback during running and probably for initial analyses of the line shape. However this detector is more sensitive to variations in the machine performance, and the luminosity measurements may have a higher systematic error than those made by the SAM. A 1% systematic error in a measurement made by the mini-SAM results from a 100μ uncertainty in its inner aperture radius or a 420μ uncertainty in the outer radius. It is also harder to compensate mini-SAM measurements for the effects of unequal beam energies (which mimic an acollinearity in the electron positron pair due to photon radiation and which will give of order .75mrad contribution to the acollinearity angle in the worst case) and to allow for misalignments of the beam axis (again around a .7mrad angular contribution at worst). Precision measurements at reasonable integrated luminosities will therefore depend on luminosity measurements made using the SAM.

Errors in the experimental measurements may be compounded by inaccuracies in the conversion of the count-rates to luminosities. This conversion depends on using bhabha pair Monte-Carlos which may contain errors[15] or may not be precise enough (that is they may neglect significant higher order terms). It is hoped however that systematic errors in both detectors can be kept at the level of a few percent.

Luminosity errors must be controlled at this level if the physics program of the SLC is to be achieved (at least with respect to tests of the Standard Model). Measurements of the cross section depend on the absolute accuracy of the luminosity measurements, for example the indirect width measurement discussed earlier requires that this absolute error be below 4% if the width is to be measured to better than 50 MeV. The width and mass measurements are more sensitive to relative errors in the integrated luminosity values obtained at different scan points, linear biases change the mass (about 10 MeV for 2% change over 10 GeV.), and quadratic biases alter the width (about 10 MeV for 1% change over $\pm$ 5 GeV).

IV. Theoretical Considerations.

IV.a Introduction.

This section deals firstly with how the mass (or pole position) of the Z^0 is extracted from experimental measurements of the line shape, and secondly with how the mass can then be used as an input parameter in order to make predictions based on the theory. The situation is complicated by the existence of 'radiative corrections'. These fall into many classes and Figure 4 is intended to act as a beginners guide to the subject. Perhaps the two most important points to remember are that the initial state QED corrections are large and determine our ability to extract the Z^0 mass from the line shape, and that the oblique corrections are probably small (unless we are very fortunate !) but determine our ability to make precise predictions.

IV.b QED Effects.

When a cross section measurement is made at a particular beam energy, the electron and/or positron which actually interacts may well have reduced its energy before collision by radiating photons. Measurements made at a given center of mass energy therefore represent integrals over a spectrum of collision energies. In the absence of a resonance the spectrum of radiated photon energies is dominated by low frequency radiation since the bremsstrahlung cross section is proportional to 1/k where k is the energy of the radiated photon.

The presence of a resonance (and the Z^0 is an impressive resonance, the cross-section at its peak is about 3000 times background) complicates the picture. Although low energy radiation remains important, there are additional effects which reflect the presence of the resonance, and which in turn significantly alter its observed shape. The first of these is due to the strong tendency for beam particles of too high an energy to radiate onto the resonance pole (and benefit from the larger cross section), the subsequent enhancement of the observed cross section gives the resonance a radiative tail. This tail can however be reduced by applying cuts to the energy of the final state and (if it can be defined) to its acollinearity (since the true center of mass is moving relative to the assumed one). This restores the overall shape of the resonance at the expense of significantly decreasing the cross-section. At energies close to but below the Z^0 pole the Z^0 cross section is rapidly decreasing; the loss by radiation of about a GeV of energy is sufficient to reduce the interaction probability of an electron positron pair which was originally on pole by about 25%. The result is to decrease the observed peak cross-section below what is predicted in the absence of photon radiation. The combination of the effects of increasing the observed cross section above the pole and decreasing it below leads to the resonance peak appearing to lie above the true Z^0 pole.

Figure 5 shows the effects of initial state photon radiation on the line shape and demonstrates how much the emission of a single photon (first order correction) changes the line shape. Figure 5 also shows that multiple photon emission (higher order terms) must also be considered when correcting the line shape to allow for the effects of QED radiation. Many calculations of these effects have been and are being made, they will be discussed in detail in a later report in these proceedings.[16] This report will restrict itself to the basic concepts involved.

Firstly, lets assume that we are making inclusive cross section measurements, with a perfect detector. Since the measurement is inclusive we can ignore all the effects of final state radiation (except the width correction), and because we are not restricting ourselves to a particular region of phase space it is relatively straightforward to calculate effects analytically. The scale of the effects of initial state photon radiation is set by a parameter, t, sometimes known as the 'equivalent radiator', which measures the energy radiated per unit frequency interval, at low frequencies, when electrons and positrons annihilate.

$$\begin{aligned} t &= \frac{2\alpha}{\pi}\left(\ln\frac{S}{m_e^2} - 1\right) \\ &= 0.108 \qquad \text{for } S \approx (93\text{Gev})^2 \end{aligned} \tag{13}$$

A recent calculation[17] incorporating the most important higher order effects evaluates the change in cross section at the peak to be:

$$\begin{aligned} \sigma(M_z) &= \left(1 + \frac{3t}{4}\right)\left(\frac{\Gamma}{M_z}\right)^t \frac{\pi t/2}{\sin \pi t/2}\sigma_0 \\ &\approx 0.74\sigma_0 \quad \text{for } M_z = 93\text{GeV}, \Gamma = 2.8\text{GeV} \end{aligned} \tag{14}$$

where σ_0 is given by equation 9. This is about 5% higher than the result given by a first order calculation (remember we wanted to measure the muon cross section to better than 4% to measure the Z^0 width). It also estimates the pole to peak separation to be given by;

$$S(\text{peak}) - S(M_z) = \left(\frac{\Gamma}{2}\right)\frac{\tan \pi t/2}{(2-t)} \tag{15}$$

This means that the peak is about 120 MeV above the pole. Again, a first order calculation implies that the peak is about 220 MeV higher. The difference between the two estimates is about twice the error on the mass determination expected from the absolute measurements of the beam energy.

As soon as we begin to consider actually observing events in a real detector of limited acceptance we (may) need to replace analytic calculations by a Monte Carlo. It then becomes useful to divide initial state photon radiation into two

classes depending on whether the photon(s) are 'hard' or 'soft'. Hard photons have an energy greater than some cut-off energy (k_0) and soft photons have less than this energy. It should be stressed that the use of k_0 is a convenience to reduce the amount of computer time spent in generating events. Monte Carlo programs can be written which do not make this somewhat arbitrary division of events. Most programs currently in use do divide up events however. The value of the cross section or of any physical observable calculated should not depend on k_0, and will not if sufficient care is taken in calculating each classes contributions. K_0 should be chosen to be below the photon energy detection threshold of the detector since if the energy of the photon is high enough to be detected then this must be allowed for in generating the final state. Even if the photon is not directly detectable, it may still result in the final state fermion pair being measurably acollinear and the choice of k_0 should also allow for this possibility.

It is the 'simpler' pseudo two body final state associated with the soft radiation which presents the most theoretical challenges. This is the contribution most affected by the higher order corrections discussed above. The soft photon contribution to the cross section is naturally included with the other two body contributions with which it is degenerate (corresponding to the emission and re-absorption of virtual photons and shown diagrammatically in figure 6) when the cross section is calculated. A theorem due originally to Kinoshita, Lee, and Nauenberg states that the advantage of this is the automatic cancellation of the singularity associated with the emission of extremely low energy real photons (which can be artificially controlled by giving the photon a fictitious mass) by the infra-red divergences associated with the virtual photons. The possible disadvantage of this technique is that the contribution from a pseudo-two body final state is balancing a genuinely two body contribution, and so care must be taken to calculate to sufficient accuracy for the balancing to work.

Insufficiently accurate calculations coupled with the choice of too small a value of k_0, are in fact a common source of difficulties with Monte Carlos. The problem can be illustrated by considering the cross-section for emission of photons with an energy less than the cut-off energy (k_0),

$$\frac{d\sigma}{d(k < k_0)} \approx \left(1 + \frac{2\alpha}{\pi}\left(\ln\frac{s}{m_e^2} - 1\right)\ln\frac{k_0}{E}\right)\frac{d\sigma^0}{d(k < k_0)} \tag{16}$$

where the smaller (higher order) terms have been dropped, and σ^0 refers to the lowest order calculation. The cross section should tend to zero with k_0, instead, at Z^0 energies the expression above gives an unphysical result for k_0's of less than 10 MeV. This is because this calculation assumes that only a single photon is emitted and, as the Block-Nordsieck theorem tells us, the emission of a finite number of photons has zero probability. Higher order effects are incorporated by allowing for the infinite numbers of quanta actually emitted.

Fortunately the cross section for emission of two photons is simply related to the cross section for single photon emission (the cross sections 'factorize', and a $1/n!$ term allows for the permutations as the number, n, of photons increases) and hence the cross-section for emission of an infinite number of photons can be worked out by summing an infinite series. The result is that the ln(k/E) term is modified and the correct expression for the cross section is given by,

$$\frac{d\sigma}{d(k < k_0)} \approx \left(\frac{k_0}{E}\right)^{\frac{2\alpha}{\pi}\left(\ln\frac{S}{M_e^2}-1\right)} \times \frac{d\sigma^0}{d(k < k_0)} \tag{17}$$

that is, the cross section becomes exponentiated and tends to zero with decreasing k_0.

A rigorous proof of the validity of exponentiation was given about twenty-five years ago by Yennie, Frautschi, and Suura,[18] and their work was extensively applied when the J/ψ peak was being studied. The J/ψ peak however is substantially narrower than the energy spread of the beams used to make it; the situation at the Z^0 is just the opposite. The result of this is that many approximations valid at the J/ψ need to be improved upon at the Z^0. In addition, as well as infra-red divergences, ultra-violet divergences must also be handled correctly (the cancellation of these is related to the Ward identity, a feature of renormalizable QED arising from the fact that the electron and the proton carry charges of equal magnitude). Exponentiation corrects the terms found in the first order calculation to all orders (but does not introduce a complete set of higher order diagrams so some small effects may be lost). Much theoretical effort is now going into renormalization group improved exponentiation to ensure that the calculations are done consistently and any necessary extra terms (all UV related) are added in.[19]

A related approach is based on the evolution of the electron structure functions. This technique is a development of the Alterelli-Parisi formalism of QCD (or originally the equivalent photon method of QED), the gluons being replaced by photons. When the evolution equations are solved perturbatively the most important corrections apply to the leading log term. Advantages of this approach include the fact that once the structure functions have been calculated they can be used by any process, and the fact that beam-spread effects can be included easily.

First order calculations (or Monte Carlos) are inadequate for our purposes.[20] However, it will be difficult, if not impossible, to distinguish experimentally between the line shape predicted by an explicit second order calculation and the

prediction of a calculation including even higher order corrections (see figure 5, or consider that t^3 is around 0.1%). Alternatively, even a first order calculation may be sufficiently improved by the inclusion of the larger corrections to all orders. A Monte Carlo suitable for SLC and LEP use can therefore take any approach (apart from not including the effects at all) and still allow a measurement of the Z^0 mass (resonance pole position) to well within the experimental errors. The lack of a single 'right' way to make corrections, and the options of making only a partial set of corrections may lead to problems in the future in comparing the results of different experiments. **We strongly favor the suggestion that results are presented in a standard fashion in addition to whatever method an experiment ultimately prefers.** The use of a set of canonical cuts which allows the use of calculations rather than Monte Carlos will in addition minimize the chance of accidental discrepancies.

This section has discussed the effects which cause a discrepancy between the Z^0 pole position (which is wanted as a defining parameter of the Standard Model) and the apparent resonance peak. These effects also affect the width and cross section measurements. One of the results is that the cross section changes very slowly around the peak (less than 1% difference between the cross section at the pole and at the peak) which makes it harder to extract the pole position from the data. It also becomes difficult to directly relate the Z^0 width to the line shape. The width is defined by application of the optical theorem to be the imaginary part of the Z^0 self energy. This means the width is energy dependent. It is customary to specify that what is quoted to be the Z^0 width, is the width as measured at the actual Z^0 pole. (Allowance should also be made for the energy dependence of the width itself when studying how width dependent effects modify the Z^0 line shape).[21]

Although only particles to which the Z^0 can actually decay contribute directly to the imaginary part of the Z^0 self energy, the effective strength of the couplings of these particles depends also on the real part of the Z^0 self energy. The couplings can therefore be influenced by particles heavier than the Z^0 to which it can couple virtually. The visible cross section and the width can be extracted from the line shape only after **all** corrections are made (or the theoretical prediction can be directly compared with observation). This brings us to the subject of 'Oblique' radiative corrections.

IV.c Oblique Corrections.

Oblique corrections were introduced in section II, when it was explained that they can be considered as the cause of couplings running with q^2. These corrections are important because measuring the Z^0 mass does not directly test the Standard Model. Only if predictions are made of the Z^0 mass, or the Z^0 mass is used as a parameter in making predictions, does it become involved in verifying the model. The Z^0 mass will be used to help renormalize the bare parameters of the Standard Model as soon as it has been accurately measured. A test of the model requires that a predicted quantity be measured experimentally; sufficiently accurate measurements will require the inclusion of the oblique corrections to match the theory with observation. If all the oblique corrections are included accurately (the models particle content must be defined) and the theory does not agree with experiment then the theory is wrong.

The oblique corrections contribute to the self energies of vector particles and take the form of internal loops (oblique corrections may be termed loop corrections) in Feynman diagrams with no connection to external particle lines. Since the particles circulating in these loops are virtual any and all particles to which the vector boson couples change the correction. This makes the size of the oblique corrections a particularly important probe of the physics which may lie above Z^0 energies. Usually, the effects of very high mass particles are expected to decouple and have no effect on measurements made at low energies. Certainly, the existence of heavy degenerate quark pairs will not be detectable by measuring the size of the oblique corrections needed to match the data to predictions. However, some modifications of the Standard Model predict the existence of particles which do not decouple.[22] Also, if the particles in a doublet are not degenerate in mass, the mass difference (if large enough, a few hundred GeV is the typical requirement) will cause observable effects (as the gauge structure of the theory begins to break down).

The influence of the oblique corrections is illustrated by Figure 7 which shows how the Z^0 width changes as a function of the top quarks mass. If the mass of the top is less than $M_z/2$ then the Z^0 width decreases with increasing top quark mass, since the phase space for producing $t\bar{t}$ is decreasing. Above $M_z/2$ the Z^0 width starts to increase again as the mass of the virtual t quark begins to significantly influence the effective couplings. This influence increases quadratically and if the t-quark becomes too massive (much above 250-300 GeV) then the currently good agreement between low and higher energy measurements of $\sin^2\theta_W$ after correction for loop (oblique) effects will be destroyed. This argument is frequently used to limit the top quark mass to being below a few hundred GeV. This constraint only applies however in the absence of any other particle which could compensate for the effects of a heavy top quark.

One particle, for example, which also influences the couplings via the oblique corrections is the Higgs. In this case, the width of the Z^0 will decrease with

increasing Higgs mass (although the dependence is weaker, the change being logarithmic with Higgs mass). It is worth stressing I think, that any particle with a coupling to a virtual Z^0 will change the oblique corrections. The problem with using the oblique corrections to probe higher energy physics lies in sorting out exactly what is contributing to any discrepancy between what is seen and what is expected (that is, what is calculated, using the defining parameters of the model, and assuming a given particle content). The more quantities measured the easier it will be to limit the possibilities. Forward-backward asymmetries depend on final state couplings unlike the polarization asymmetry which is only sensitive (on the Z^0 pole) to the electron couplings. Until a precise measurement is made which is not needed to define the model, the Standard Model has not been stringently tested since the size of the oblique corrections has not been accurately measured.

The use of a polarized electron beam increases the visibility of the effects of the oblique corrections. The effects of the corrections are difficult to see if the line shape is measured using unpolarized beams. However, the peak cross section is increased about 30% if right-handed polarized beams are used, and decreases slightly more than 30% if left handed beams are used.[23] The polarization asymmetry is a particularly sensitive probe of the oblique corrections at the Z^0 and one which is not significantly affected by initial state bremsstrahlung. There is also a significant statistical advantage in not being restricted to using a particular final state.[24]

Monte Carlo programs may include the effects of the oblique (or loop) corrections either by modifying the couplings they use, or by explicitly adding the loop diagrams to some specific order (one loop, two loop et cetera). Since the corrections can be summed to all orders and the exact couplings defined we prefer the former approach.

A further complication is that the contribution to the oblique corrections due to known physics must be calculated before any discrepancy with measurements can be studied. At SLC/LEP energies the most significant corrections are to the value of the vacuum polarization of the photon (since the photon is massless this is not called a self energy). These corrections correspond to a change in the value of α_{em} with q^2.[26] The contribution to the vacuum polarization due to the known leptons can be calculated exactly. The uncertainty in the contribution due to the known quarks will be what limits our chance of detecting the influence of new physics. The difficulty is due to the fact that the contribution of the lighter quarks cannot be calculated using perturbative QCD. The light quark contribution must instead be estimated from experimental data on e^+e^- interactions at low energies via the use of dispersion relations. The experimental data must be analysed carefully and the use of the data must be balanced against the use of calculations for higher mass quarks to minimize the overall error. Two recent calculations[26] give a value of about 0.028±0.001 for the total contribution from the known quarks, compared to a contribution from all particles of 0.071. In other words the uncertainty due to light quarks is about 1% of the photon vacuum polarization.

Calculations of luminosity at the Z^0 also require an allowance to be made for the effects of the oblique corrections. Once more, corrections may be made either to the couplings or by the explicit inclusion of the oblique diagrams into a Monte Carlo. If the former approach is taken, care must be used to check that the routines used to calculate the coupling corrections have the correct q^2 dependence. Routines setup to calculate the couplings of muons at SLC energies are not applicable to t-channel processes or even to lower energy s-channel reactions.[27]

IV.d Final State Corrections.

The Z^0 line shape can be measured at low integrated luminosities. The integrated luminosity required is not so low however that we can afford to use only muon pairs. We would need to accumulate about twenty times as much data as we need if hadronic events are also used. However, since we are aiming at a very precise measurement we need to consider even small effects which depend on the final state to which the Z^0 decays. The large corrections due to initial state radiation are common to all final states. The oblique corrections change the couplings of particles to the Z^0 and will affect different final states in a slightly different way. More importantly, the exact shape of the resonance around the pole depends on the coupling dependent interference between the Z^0 and the photon. In principle, because the fitting procedure to extract the mass is sensitive to the shape this could complicate the fitting. Estimates of this effect imply that it results in the peak shifting less than 10 MeV if muon data is compared with $d\bar{d}$ data (less for $u\bar{u}$). This change can be corrected for if necessary.

The final state can radiate gluons (if hadronic) or photons and (as shown by Equation 5) this radiation must be allowed for in calculating the Z^0 width. The effect of gluon radiation is about twenty times more significant than the effect of final state photon radiation. If α_s is increased from 0.09 to 0.17 then the Z^0 becomes about 60 MeV wider. One interesting effect of increasing the hadronic width is that this decreases the peak cross section. The Z^0 line-shape is also affected in more subtle ways. Although the pole position of the Z^0 resonance is unchanged, the separation between the peak and pole is not. This is determined by photon bremsstrahlung effects which are altered when the line shape is modified by changing the Z^0 width. However, Equation (16) implies

that a 60 MeV change in the width changes the peak to pole separation by only 2.5 MeV. If we make inclusive measurements we do not need to worry about the effects of final state radiation on the Z^0 mass determination.

However, if (when) we start to use experimental cuts on the data then the effects of final state photon radiation need to be considered more carefully. Light final states radiate more energy than heavy ones and may be more affected by cuts on the visible energy of the final state. The need to make an allowance for this effect can be seen by comparing the muon and tau cross-sections. If the comparison is made after cuts have been applied to the muon and tau final energies, but before corrections are made for final state radiation then it will appear as if muon/tau universality is violated. The expression[28] for their cross-sections, if the amount of energy carried by photons is to be less than an amount ΔE, is given by;

$$\sigma^{x}_{\mathrm{meas}} = \sigma^{x}_{0} \times \exp\left[-\frac{c}{\pi}\left(4\ln\left(\frac{M_z}{\Delta E}\right) - 3\right)\ln\left(\frac{M_z}{m_x}\right) + \frac{\alpha\pi}{2}\right] \tag{18}$$

If the 'missing' energy is required to be less than a GeV, then the apparent ratio of the muon and tau cross sections is 0.90. This ratio rises to 0.98 if as much as 20 GeV of energy could have been radiated.

The effects of final state photon radiation can be corrected for if the Z^0 decays to leptons. There is a problem with also correcting hadronic final states for these losses. If the Z^0 decays to a quark-antiquark pair then the mass of the radiating final state particle is not known so the size of the effects cannot be estimated. One can argue, perhaps convincingly, that the timescales for electromagnetic interactions are very much longer than those governing strong interactions. This implies that the radiating final state will have a mass greater than or equal to that of a pion (and thus final state radiation which is inversely related to the mass will be small). Conversely, quarks may be radiating directly and current quark masses set the scale for the radiative effects in this case. An added complication is that interference effects may occur during hadronization which may enhance photon radiation. Theorists may never be able to remove all of the uncertainties involved. Minimizing the cuts applied to the final state will limit the chance of introducing biases.

An estimate of how severe cuts must be before final state effects cause difficulties (which does not include any possible enhancements due to interference) can be made. The observed Z^0 line shape is generated by varying the assumed mass of the final state fermions, and applying a visible energy cut to the simulated data. We are most concerned (initially) by effects which bias the Z^0 mass extraction. A study was made of how big the cuts on the visible charged energy needed to be before a fit to the generated line shapes gave significantly different results if 2 MeV (a low current quark mass) was used instead of 100 MeV for the final states mass (higher mass choices give almost identical results to those for 100 MeV). This test used the Monte Carlo BREM5.[29] It showed that even when more than 50 GeV of energy is required to be visible in the detector, the peak is shifted less than 10 MeV.[30]

V. Conclusions.

The Z^0 mass is a fundamental quantity which is worthy of the efforts which will be made to measure it as accurately as possible at the SLC. The Z^0 peak position measurement will be limited to an accuracy of about 50 MeV by experimental constraints on how well the beam energy can be measured. The accuracy of the extraction of the Z^0 pole position from the line shape will depend on the calculations of the higher order QED corrections. These corrections need to be incorporated into the Monte Carlos which are used for Z^0 physics. The effects of initial state bremsstrahlung should be calculated accurately enough to keep the theoretical error in extracting the Z^0 mass below 10 MeV. A precise measurement which is not needed to define the Standard Model will then be required to test the model by checking the size of the oblique corrections. The best candidate for such a measurement at the SLC is the polarization asymmetry. This measurement may allow us our first glimpse of the physics beyond the Standard Model.

FIGURE CAPTIONS

1.) Two scanning strategies are compared. The error on the direct Z^0 width measurement is shown as a function of the total integrated luminosity accumulated during Z^0 peak scanning.

2.) The south dump extraction-line spectrometer is shown schematically. The view of the north dump is similar. Electrons exiting the septum magnet enter a quadrupole doublet, Q31 and Q32, followed in turn by horizontal, vertical, and horizontal bend magnets (BH_A, BY, BH_B). Two beams of synchrotron light are emitted by the horizontal bends, which are then detected by x-ray monitors.

3.) The difference between the luminosity weighted center of mass energy determination and the mean center of mass energy for a single pulse is shown as a function of the residual dispersion at the crossing point. Figure 3.a shows the error for a residual dispersion of 3mm (early data) and Figure 3.b for a residual dispersion of 1mm (ultimate aim). The plots both assume that the momentum spread of the bunch is $\pm 0.2\%$ and that the non-dispersed width of the bunches is 2 microns. The decrease in the luminosity is shown normalized to the ideally achievable value. It is stressed that the errors in the beam energy measurements due to this source should cancel when several pulses are averaged.

4.) A beginners guide to radiative corrections.

5.) The effects of initial state radiation (taken from G.Altarelli et al, contribution to the CERN-LEP report 86-02).

6.) 2-body final state diagrams .

7.) The Z^0 width is shown as a function of the assumed mass of the top quark.

REFERENCES

1. The members of Group 1 are : J. Alexander, B. Barish, G. Bonvincini, F. Bulos, R. Cahn, D. Coupal, P. Drell, G. Feldman, C. Field, R. Frey, C. Jung, J. Kadyk, D. Kennedy, J. Kent, W. Kozanecki, M. Levi, B. Lynn, B. Milliken, J. Nash, M. Petradza, J. Smith, P. Voruganti, B. Ward, S. Watson, G. Wormser, and C. Von Zanthier. In addition, F. Berends, W. Hollik, S. Jadach, and R. Stuart made valuable contributions during their visits to SLAC.
2. The GIM mechanism was proposed in 1970 (S.Glashow, J.Iliopoulos, and L.Maiani; Phys Rev D2 (1970) 1285) to explain the absence of $K \to \mu\mu$ decays. Preliminary results from the Gargamelle experiment indicating the existence of neutral currents were reported in 1973 (F.J.Hasert et al, Phys.Lett.46B(1973)121,138).
3. Arnison et al, PL 122B (1983)103; Banner et al, PL 122B (1983)476; Arnison et al, PL 126B (1983)398; Bagnaia et al, PL 129B (1983)130.
4. This interference causes an asymmetry in the distribution of positive muons as a function of θ which is sensitive to the muons axial vector coupling and which has been measured at PEP/PETRA energies. This should be distinguished from the asymmetry of interest at the SLC which is related to the vector coupling and hence is sensitive to $\sin^2\theta_W$. The photon-Z^0 interference reaches a maximum around 80 GeV.
5. This scheme is based around four quantities ($\sin^2\theta^*_w$,α^*, G^*_F, and ρ^*) that can be measured at any q^2. These quantities are then allowed to run with q^2 , as appropriate, in the way that the standard model predicts. If the theoretical curve relating measurements of a particular quantity (for example $\sin^2\theta^*_w$) at different q^2 does not fit the data then the particle content/or physics content of the Standard Model is incorrect. The reader is referred to reports by Dallas Kennedy in these proceedings and also in the earlier Granlibakken Proceedings (SLAC-REP-306). A detailed discussion can be found in B.W.Lynn and D.C.Kennedy 'Effective Lagrangian for Electroweak Radiative Corrections in Four Fermion Processes' SLAC-PUB-4039 (submitted to Phys. Rev. D
6. 'On-shell' refers to the choice of measurements made on-pole as defining parameters. A reader interested in more detailed information on renormalization schemes, or on electroweak radiative corrections in general, is referred to the review by A.Barroso et al, on this subject which will form part of the ECFA-LEP 200 proceedings (This report is available as a preprint; CERN-EP/87-70).

7. Review of Particle Properties, PL 170B.
8. For ease of comparison between different working groups 93 GeV was chosen as the standard Z^0 mass.
9. A lot of data is already available about the peak position ranging from the direct measurements of UA1 and UA2 to inferred positions based on the values of $\sin^2\theta_W$ extracted form low energy neutrino scattering. The particle data book estimate based on these results is $M_z \approx 92.5$GeV A very recent re-evaluation of all the available data by Amaldi et al(UPR-0331T), prefers a value of $\sin^2\theta_W$ closer to 0.23 corresponding to a lower Z^0 mass of about 92.0 GeV.
10. This uses a line shape corrected for the effects of photon bremsstrahlung and the MINUIT fitting package.
11. Gary Feldman, Asilomar proceedings, SLC/Mark II working group note 1-1.
12. For more details of this and other possible measurements see; Mark II Collaboration and SLC Final Focus Group, *Extraction-Line Spectrometers for SLC Energy Measurement*, SLAC-SLC-PROP-2 (1986).
13. Dave Bannon and Joel Kent, 'Statistical errors from Extraction line Spectrometer Data Sampling', Mark II/SLC- Physics Working Group 1 note 1-8.
14. The SAM is discussed in more detail in Mark II/SLC note:164, information on the mini-SAM can be found in Mark II/SLC notes 150,152.
15. Several Monte Carlos have been compared and made to agree within a percent (see John Matthews, SLC/Mark II Working Group 2 note:2-13).
16. SLC/Mark II Working group 1 note 1-12, a contribution to these proceedings.
17. Robert Cahn, LBL-22601.
18. D.R.Yennie, S.C.Frautschi, and H.Suura; Ann Phys 13,379(1961).
19. A recent review of the work in progress can be found in B.Ward,' Renormalization Group Improved Yennie - Frautschi - Suura Theory ', to appear in Phys. Rev. D.
20. This is certainly true for the Z^0line shape measurements, its also possible that the existing Bhabha monte carlos need improving. Finally, although interesting polarization measurements may be insensitive to the effects of initial state bremsstrahlung, luminosity measurements and/or cross section measurements for polarized beams will need correction.

21. See the contribution due to W.Wetzel in the CERN LEP report 86-02 (p40) and the report of Dallas Kennedy (1-11) in these proceedings for useful comments.

22. B.W.Lynn et al, SLAC-PUB-3725.

23. W.Wetzel, ibid.

24. B.W.Lynn and C.Verzegnassi, SLAC-PUB-3967

25. I would like to repeat an interesting comment made by Bill Marciano at a SLAC seminar. The corrections depend on $\ln(M_z^2/m_x^2)$ for the quarks and leptons that the Z^0 decays to. He pointed out that the correction is not a purely QED one since the scale is set by the weak interaction, in this case by M_z.

26. B.W.Lynn et al, SLAC-PUB-3742; F. Jegerlehner BI-TP 85/28.

27. John Matthews, SLC/Mark II working group 2 note 2-11. A routine by Burkhart (TASSO note: 192 (1981)) is recommended. Some differences in the cross-section calculated by different Monte Carlos can be traced to the Bhabha codes use of more up to date (but possibly not better) code used by s-channel Monte Carlos.

28. W.J.Marciano and Z.Parsa, Cornell Z0 workshop, CLNS 81-485(p127).

29. This allows one to vary the final state mass and quantum numbers and is described briefly in Mark II/SLC physics working group 1 notes 1-4,1-11, which can be found in SLAC-REP-306,and in these proceedings respectively.

30. The same fitting function was used as was used in the statistical studies.

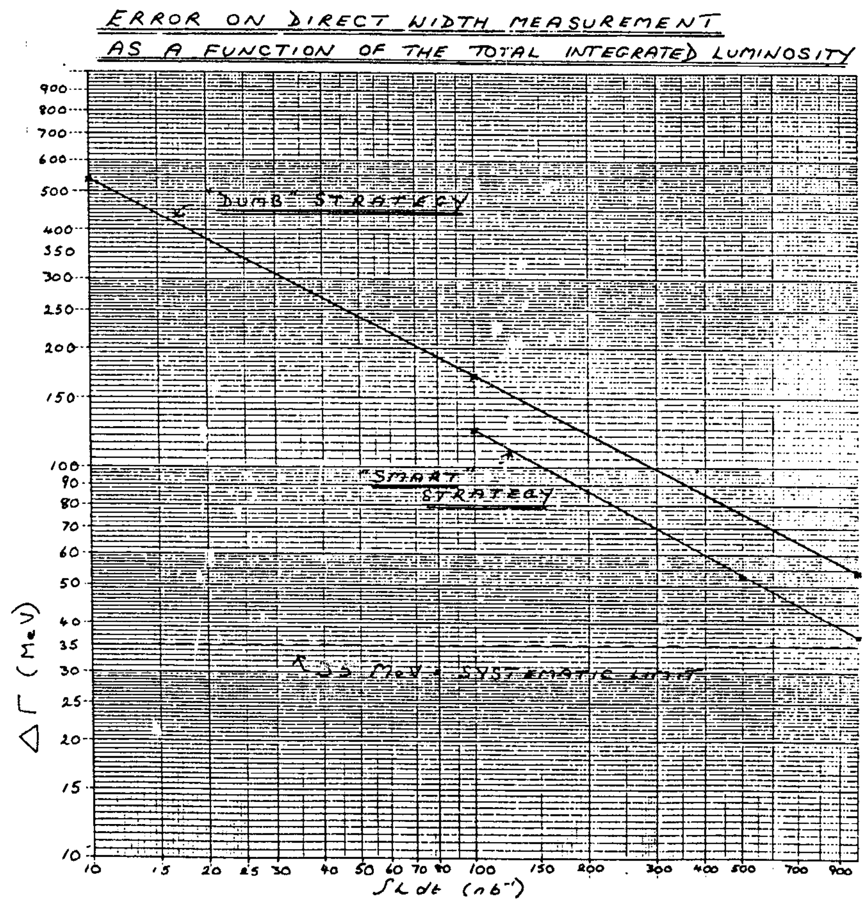

FIGURE 1

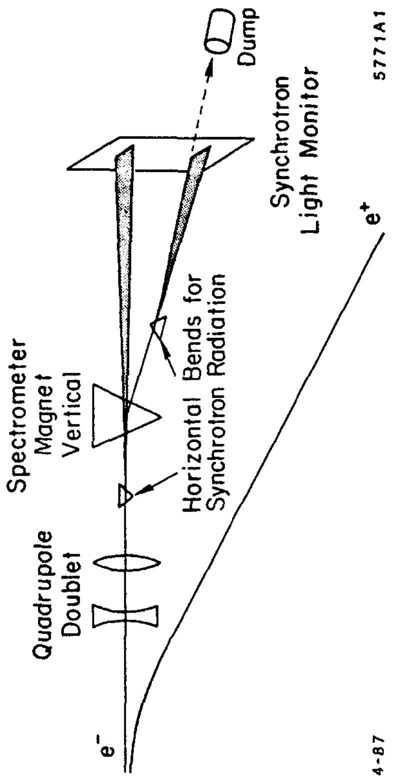

FIGURE 2

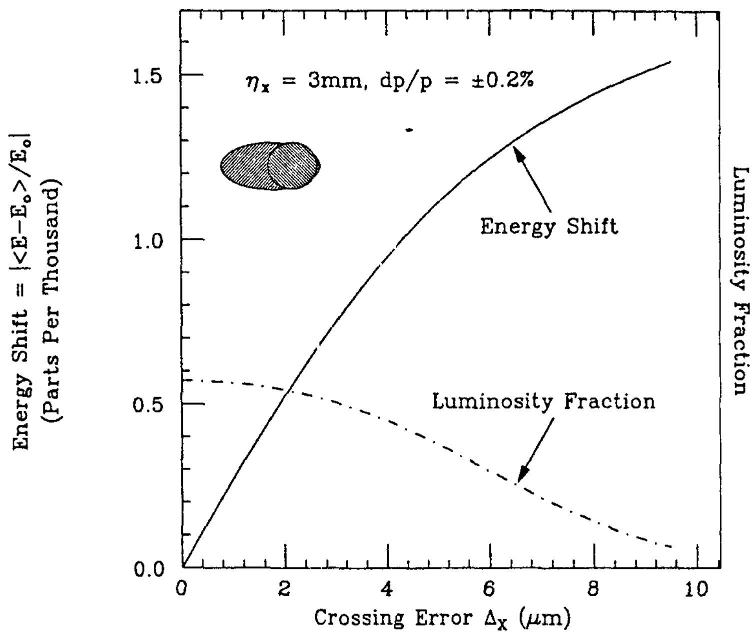

FIGURE 3a

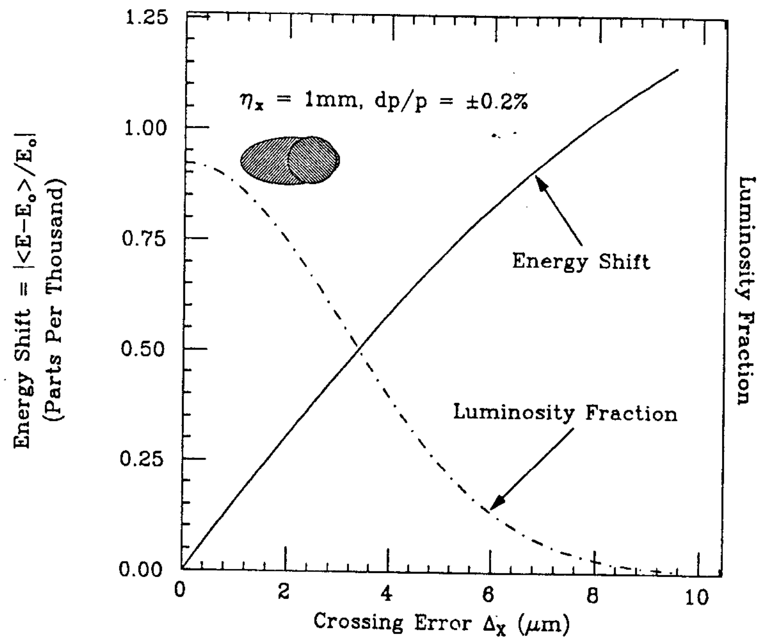

FIGURE 36

A BEGINNERS GUIDE TO RADIATIVE CORRECTIONS

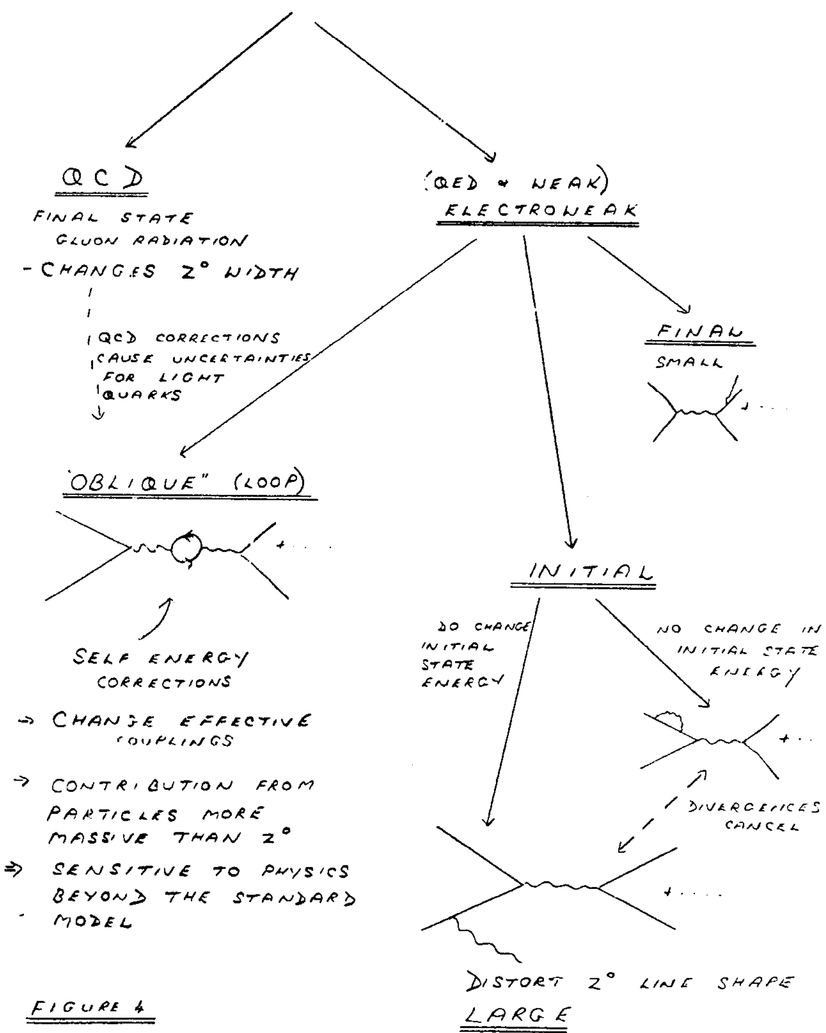

FIGURE 4

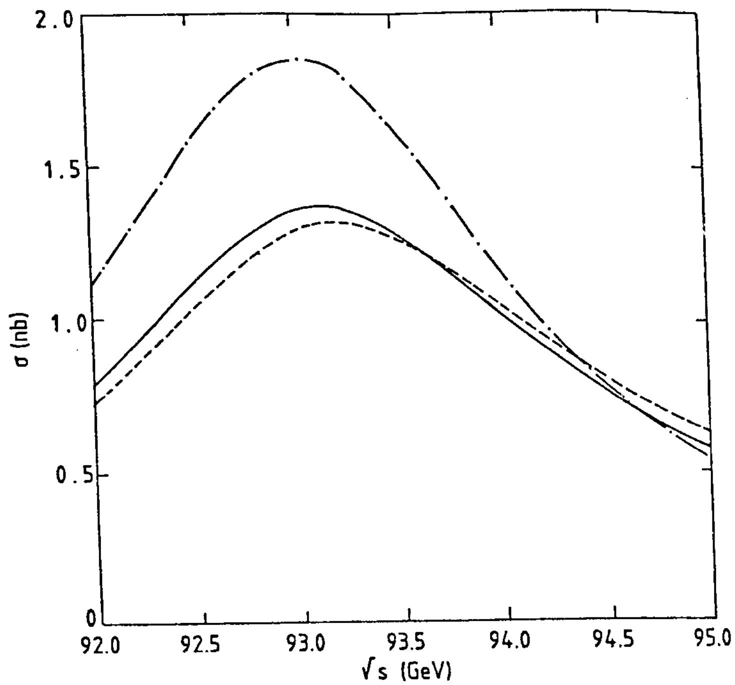

The total cross section σ for $e^+e^- \to \mu^+\mu^-$ as a function of the c.m.s. energy. The dotted, solid, and dashed lines represent the Born approximation, the $O(\alpha)$ corrected, and up to $O(\alpha^2)$ corrected calculations.

FIGURE 5a (SEE 5b FOR DETAILS AROUND PEAK)

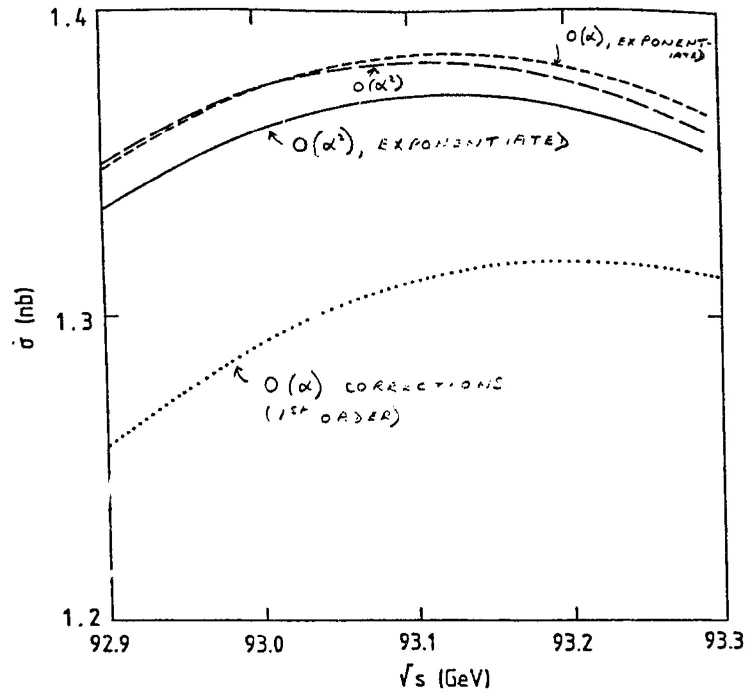

FIGURE 5b

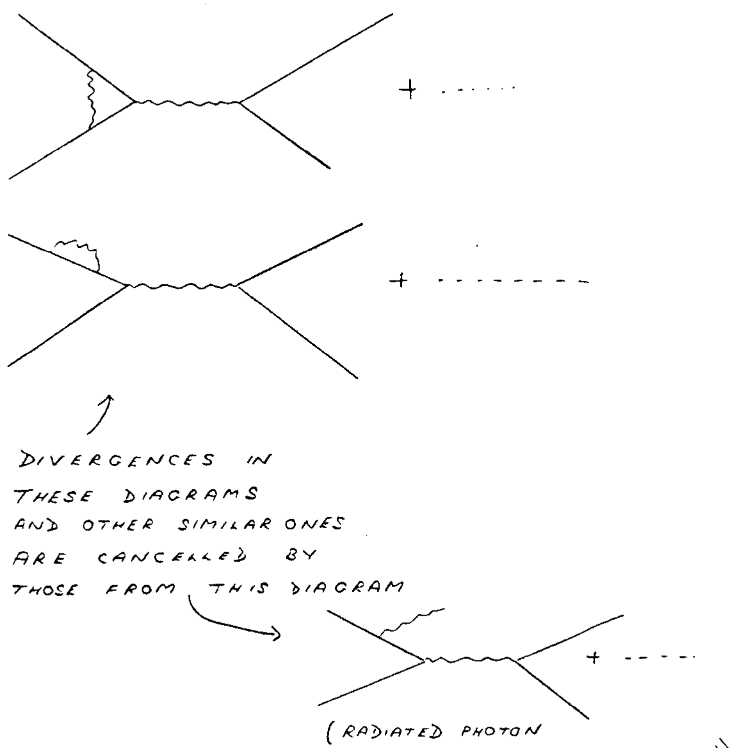

FIGURE 6

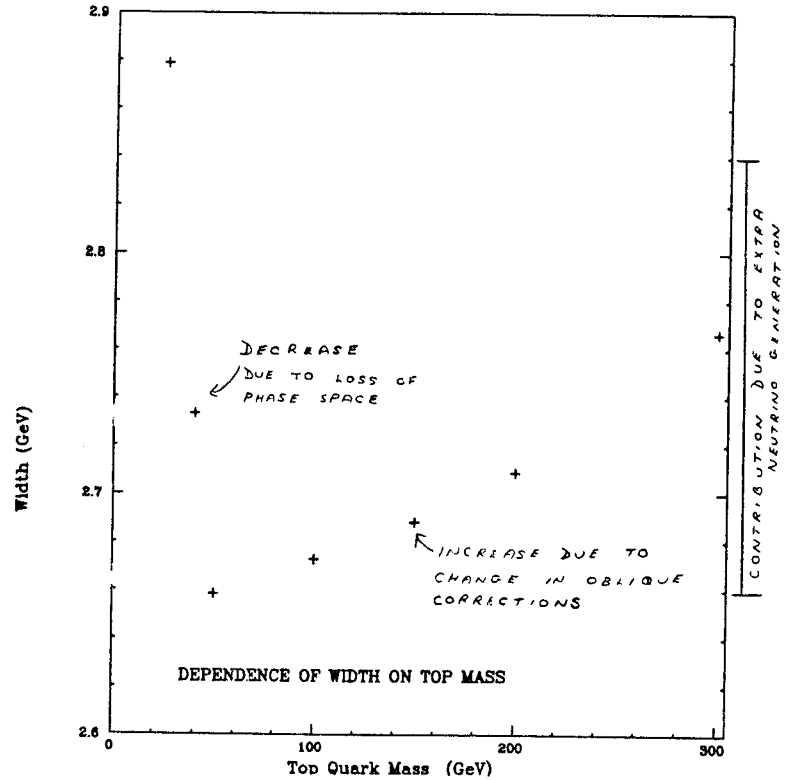

FIGURE 7

Mark II/SLC-Physics Working Group Note # 1–10

AUTHOR: Guy Wormser

DATE: April 9, 1987

TITLE: Beam energy measurements for the first 3 months of SLC operation

---

1. Introduction

The present schedule allows 3 months of data taking for the MarkII collaboration in the summer 1987. 1000 Z^o events may be recorded during that period. Even with this limited sample, the statistical error on the Z^o mass will be as good as 150 MeV. Therefore, systematics errors may become dominant. In fact, during this data taking period, the Beam Energy Spectrometer will not be ready. Thus, the only information available will come the SLC machine itself and more precisely, from its three distinct elements, the Linac, the Arcs and the Final Focus systems. The following sections deal with the quality of the measurement performed in each of these systems

There are 2 different sources of systematic errors :

1. The *relative* errors are the errors associated with 1 measurement compared to another one :they include all the time dependant effects and the statistical precision of each measurement. Those errors govern the *width* resolution of the Z^o .
2. the *absolute* errors are the quadratic sum of the relative errors and all sources of errors which are not time dependant, i.e the reference magnetic field mapping, the positions of the detectors,... Those errors govern the *mass* resolution of the Z^o.

It is also worthwile to notice that some errors can be reduced if the sum of the electron and the positron beams energy is measured, instead of measuring each energy separately. We will use this sum,when available.

2. The Arcs measurement

The arcs are not a very good place to measure the absolute energy nor the relative energy of the beams for the reasons listed below,and therefore it is not planned to use the arcs information.

1. The arcs system has been designed to be as achromatic as possible to be able to transport a $\pm$ .5% energy passband. Moreover, the dispersion has be designed to be small in all the system. Systematics readings of the BPMs before and after the reverse bend can be used to mesure the beam energy with a moment to moment energy resolution of .3 % for a 100 micron BPM displacement. The accuracy is therefore dominated by BPM statistical fluctuations.
2. The magnetic field integral cannot be measured to a very good precision (5 10^{-3})
3. There is a systematic 2 GeV discrepancy between the energy measurement in the arcs and the one performed in the Switch Yard, which is not understood at this time. This discrepancy is probably due to misalignment problems in the Beam Switch Yard ,which are under investigation.
4. Finally,the acquisition rate is rather slow, and the energy has to be averaged on many bursts.

3. The Final Focus measurement

The chromatic correction section of the Final Focus system is a very high dispersive region (η= 240 mm for $\frac{\delta p}{p}$ = 100%). Therefore, it is a good place to measure the energy of the beams. Unfortunately , the beam size is also large in that region, of the order of 2 mm .The position measurement then may be sensitive to the beam shape.This shape may change from burst to burst and is difficult to monitor. The scheme of the chromatic correction section is displayed on Fig.1. There are 4 BPMs on either side of B2, and each pair will provide an independant energy measurement. Each pair will be read every four pulses. A complete determination of the errors attached to such a measurement has not been made yet because some experience of the influence of the beam shape is needed. Otherwise,the prospects are good because the magnetic field integral is well known, up to .1% precision level and the high dispersion makes the errors coming from the intrinsic resolution of the BPMs rather small.

It is therefore planned to read these data as often as possible and to use them as a check of the Switch Yard measurement,which is described below.

4. The Switch Yard measurement

At the end of the linac, the two beams are splitted by a large dipole magnet, with a dispersion power $\eta = 80$ for each beam.(Fig 2) Using a simple set of 4 BPMs, 2 before the magnet and 2 after,it is possible to measure the beams energy on a burst-by-burst basis.This system will effectively be used as a feedback to stabilize the energy of the beams.For the 2 BPMs before the magnet,the electronics is duplicated with a time delay of 50 ns,in order to be able to measure separately the position of the electron and the positron beams,which are 50 ns apart.

However, the absolute energy measurement for a single beam is subject to misalignment inaccuracies. This problem is under intensive study and should be solved when survey data in the Beam Switch Yard are better understood.

To get the energy at the interaction point,the energy loss in the arcs has to taken into account .This loss, 1.3 GeV per beam, can be computed with an accuracy of a few percent,thus leading to a negligible contribution to the overall error.

4.1 The sources of the relative errors on the beam energy

In this section, we will study the different contributions to the relative or time dependant errors on the beam energy. In fact,those errors are related to the BPMs reading.

1. The statistical jitter of a BPM ,i.e. the width of the BPM output when the beams are perfectly stable is typically 40 μm. This is easily measured with the calibration system.
2. Because of nonlinear effects in the BPMs electronics, a intensity variation of the beam may fake a displacement of the beam. This effect can be seen on Fig.3 where a BPM offset is plotted versus the intensity of the test pulse. (the BPM offset is the value which is readout when equal test pulses are send on each electrode, simulating a centered beam).

Although the raw effect may be large,the net contribution is expected to be small because this effect is taken into account in the calibration procedure and the expected beam intensity variations are not very large. Thus, this effect should contribute to about 20 μm .

3. The sensitivity to the beam shape should be small because the beam size is small in that region.This error should be less than 20 μm.

In summary ,we expect a relative error on the BPM readings of 50 to 80 μm.

4.2 The sources of absolute errors on the beam energy

Those errors involve the different position errors in the BPMs and also the errors on the magnetic field integral.

The absolute errors on BPMs reading

1. The external position error is the error with which the absolute position of the BPMs are known. This error is of order of 100 μm subject to coordinate reference problem. However, when measuring the sum of the 2 beams,it is sufficient to measure the relative distance between the 2 BPMs placed after the splitter magnet. This can be done to a precision of 50 micron. In this case also, the effect of the error on the absolute position of the first 2 BPMs become negligible.
2. The position of the true mechanical center relative to the external reference is not known to better than 10 to 20 μm.
3. There can be also a systematic displacement between the mechanical and electrical center of the BPMs. This effect has been measured by inducing a test pulse on a wire positionned at the center of the BPMs.It is of the same order of magnitude as the previous one,40 to 70 μm.
4. A different attenuation length or a different length of the cables can lead to systematic displacement.This effect is expected to be of the order of 25 μm.

Finally,the uncertainty in the calibration of the BPMs leads to an uncertainty of 20 to 50 μm.It has to be stated that this number will remain small only if the calibration procedure is done often enough. Fig.4 shows the day to day variation of the calibration constant of 1 BPM. A 100 μm step occured and could not be explained.

Therefore ,in principle and after a BPMs resurvey, The total BPM accuracy lies in the range 150-250 μm ,after taking into account the relative errors discussed above.The different contributions relative to BPMs reading are summarized in Table 1.

We have now to convert the errors made on the BPMs reading to errors on the beam energies. This is done using the formula :

$$p(e^-) = \frac{K}{x_3 + 1.38x_1 - 3.08x_2}$$

$$p(e^+) = \frac{K}{-x_3 - 1.43x_1 + 1.79x_2}$$

where x_i are the BPMs readings in the plane i.

Using the absolute BPM resolution to compute the error on each beam separately ,one obtains a very large uncertainty.

$$(\frac{\Delta p}{p})_{each} = .6 - 1\%$$

Fortunately, the situation improves a lot when the sum is measured. This is due to the almost complete cancellation of absolute position errors. The result is then

$$(\frac{\Delta E}{E})_{BPM} = .2 - .4\%$$

The absolute errors on the magnetic field

1. The magnetic field integral is known to .1%, giving thus a .1% contribution to the energy estimation
2. The position of the magnetic center of the splitter magnet is known to 2 mm, giving rise also to an error of .1%.

Finally,we obtain the absolute overall resolution :

$$(\frac{\Delta E}{E})_{abs} = .3\% - .5\%$$

leading to :

$$(\frac{\Delta m(Z^o)}{m(Z^o)})_{abs} = 300 - 500\ MeV$$

while the relative resolution is typically 2 times better :

$$(\frac{\Delta m(Z^o)}{m(Z^o)})_{rel} = 150 - 200\ MeV$$

5. Technical implementation

We describe briefly here what will be available on the MarkII tapes.

1. At each burst, the energy and intensity of each beam will be computed in the Switch Yard by the FeedBack microcomputer FB31. The energy spread will also be computed on an average of 10 bursts. These informations will be received by the MarkII acquisition system and will be read every trigger (including of course random triggers)
2. Every 2 or 4 minutes ,the MarkII VAX will send a request to the SLC VAX to read the actual BPMs reading in the Switch Yard and also in the Final Focus. This will allow offline checks of FB31 computations and also comparison between the Switch Yard measurement and the Final Focus one.

6. Conclusion

The essential requirement of the MarkII collaboration

The knowledge of the beam energies for each Z^o candidate

will be satisfied with a absolute precisison of 300 to 500 MeV. The relative mass precision, useful to perform a width measurement will be 150 to 200 MeV.

Table 1

BPMs Errors (in μm)

Relative

Statistical	40 – 70
Non – linearity	20 – 50
Beam shape	10 – 20

Absolute

External survey	100 – 150
Internal	10 – 20
Electrical center	40 – 70
Cables	40 – 70
Calibration	20 – 50

Total relative	50 – 80
Total absolute	150 – 250

Table 2

Contributions to the absolute overall error (in %)

Magneticfield	.1 – .15
Magnetic center	.1 – .15
Absolute BPM resol. on a single beam	.6 – 1.
Absolute BPM resol on total energy	.2 – .4

FIGURE CAPTIONS

1. Scheme of the final focus chromatic correction cross section
2. Scheme of the energy measurement in the Switch Yard
3. Variation of a BPM offset with the intensity of the beam
4. Day-to-day variation of the calibration constants

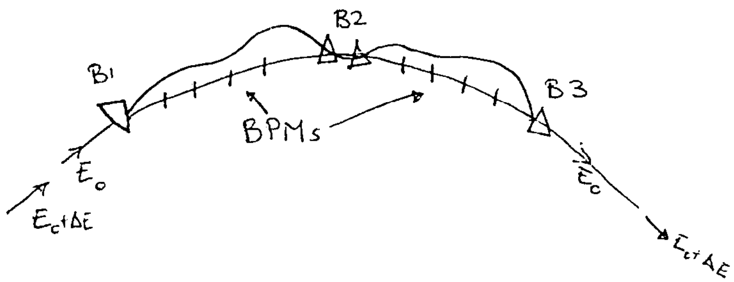

Fig 1 Chromatic correction Section

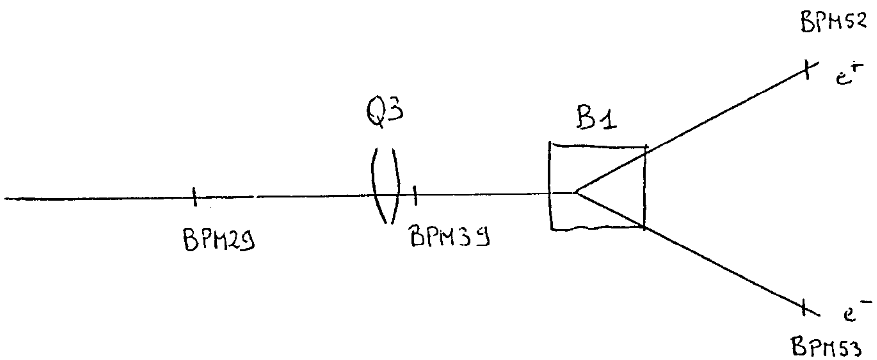

Fig.2 Beam Switch Yard

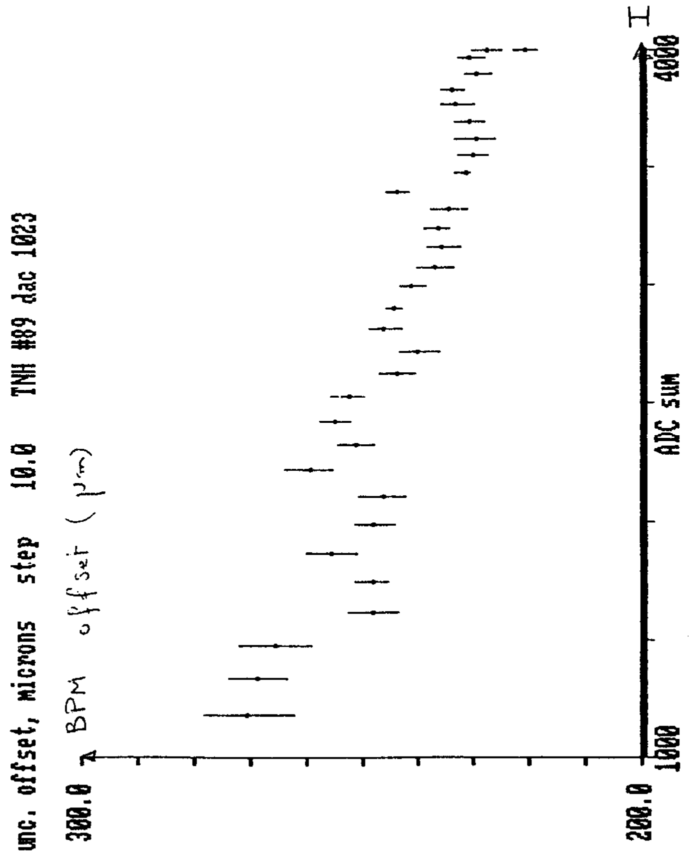

Fig 3. Variation of a BPM offset with beam intensity

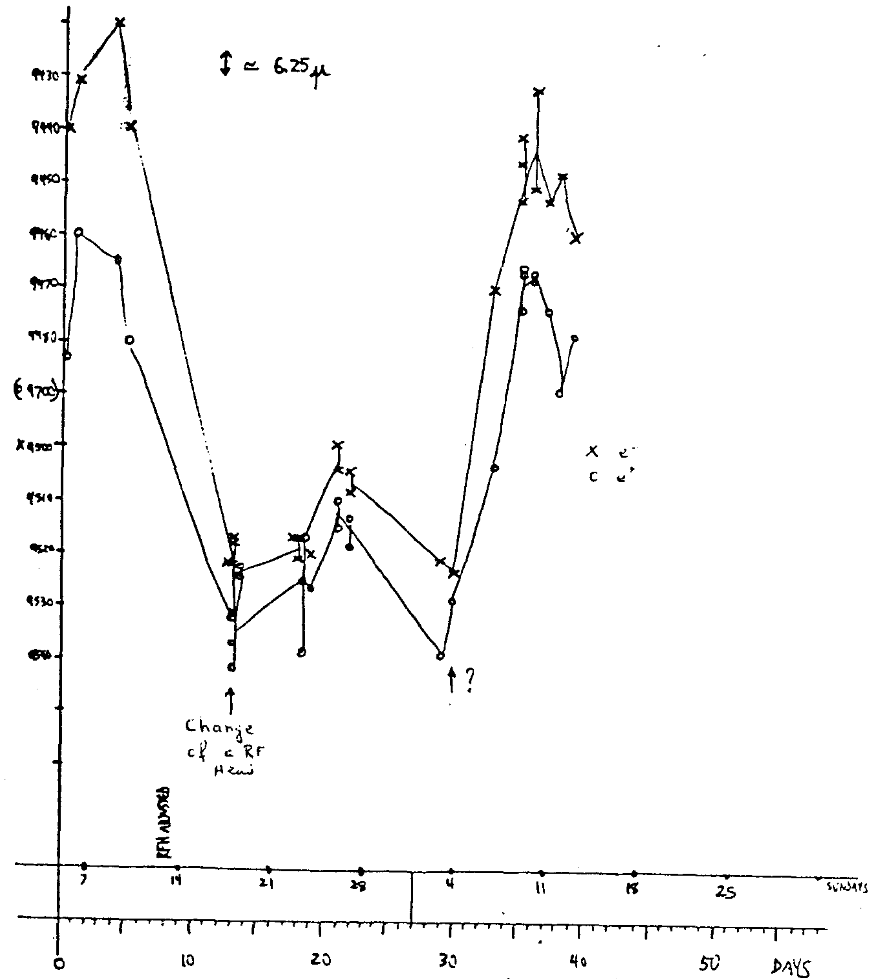

Fig 4. Day-to-day Variation of a BPM offset

Mark II/SLC-Physics Working Group Note # 1–11

AUTHOR: Dallas C. Kennedy II

DATE: June 8, 1987

TITLE: The BREM5 Electroweak Monte Carlo

This is an update on the progress of the BREMMUS Monte Carlo simulator, particularly in its current incarnation, BREM5. The present report is intended only as a follow-up to the Mark II/Granlibakken proceedings, and those proceedings should be consulted for a complete description of the capabilities and goals of the BREMMUS program.

The new BREM5 program improves on the previous version of BREMMUS, BREM2, in a number of important ways. In BREM2, the internal loop ("oblique") corrections were not treated in consistent fashion, a deficiency that led to *renormalization scheme-dependence*; i.e., physical results, such as cross sections, were dependent on the method used to eliminate infinities from the theory. Of course, this problem cannot be tolerated in a Monte Carlo designed for experimental use. BREM5 incorporates a new way of treating the oblique corrections, as explained in the Granlibakken proceedings, that guarantees renormalization scheme-independence and dramatically simplifies the organization and calculation of radiative corrections. This technique is to be presented in full detail in a forthcoming paper. BREM5 is, at this point, the only Monte Carlo to contain the entire set of one-loop corrections to electroweak four-fermion processes and renormalization scheme-independence.

The neutral-current matrix element with the full one-loop oblique corrections is:

$$M_{NC} = \frac{{e_*}^2 QQ'}{q^2} + \frac{{e_*}^2 (I_3 - {s_*}^2 Q)(I'_3 - {s_*}^2 Q')/{s_*}^2 {c_*}^2}{q^2 + \dfrac{{e_*}^2}{4\sqrt{2}{s_*}^2 {c_*}^2 G_{\mu_*} \rho_*}} .$$

The functions ${e_*}^2$, ${s_*}^2$, ${c_*}^2$, G_μ, and ρ_* are related to the usual parameters of electroweak physics (e^2, $\sin^2\theta_W$, etc.) by the oblique corrections, which cause the

"starred" functions to run with q^2. Note that in the corrected matrix element, the starred functions simply replace the "tree-level," or unrenormalized, parameters. There are, in addition, the "direct" corrections, which include box and vertex diagrams; and the bremsstrahlung contribution, which must be added to the purely elastic cross section because of the emission of soft photons that go undetected. The bremsstrahlung corrections are large to lowest order in α, changing the total cross section by over 30% . Thus a certain class of the bremsstrahlung diagrams must be taken into account to higher order by the procedure of "exponentiation," described elsewhere in these proceedings. This method has been worked out for our purposes by B. F. L. Ward and will be implemented soon in BREMMUS. The processes $e^+e^- \to e^+e^-$ (Bhabba scattering) and $e^+e^- \to \nu_e\bar{\nu}_e$, which involve some extra Feynman diagrams, can also be easily put into BREMMUS.

For the first two years of Mark II/SLC operation, a relatively simple way can be used to include the effect of oblique corrections in analytic forms and less elaborate Monte Carlos such as MMGE (MMG1). Near the Z pole, the corrected matrix element can be reduced to the following:

$$\frac{1}{(s - {M_Z}^2)(1 - \kappa) - is(\frac{\Gamma}{\sqrt{s}})}$$

This form is slightly different from that usually used. First is the presence of the term κ, summarizing the effect of the oblique corrections on the resonance shape: κ is about one to two percent in the standard model. The other change, a crucial one normally ignored, is the variation of the imaginary part of the resonance with s. The usual, but incorrect, way of writing the imaginary part is $M_Z\Gamma$, but the variation of phase space away from the pole changes this to the form shown. In fact, $\frac{\Gamma}{\sqrt{s}}$ is (almost) constant with s. (Besides another factor of $\sqrt{s}$, Γ has the starred functions embedded in it, which renormalizes the couplings in the width to their correct values at the Z pole; the starred functions then vary almost not at all if we stay near the pole. The renormalization, mainly due to vacuum polarization, contibutes a correction of about seven percent, for top mass less than 200 GeV.) The effect of radiative corrections in the couplings should be visible after the accumulation of 10^3 Z's and the effect in κ with 10^5 Z's.

The direct and bremsstrahlung corrections are numerically the most important radiative corrections to processes at the Z resonance. The *physically* interesting radiative corrections come from the oblique sector, which can contain a variety of new particles too heavy to be produced at SLC energies but which can affect SLC measureables indirectly. Normally such effects would be swamped by the larger direct corrections, but the left-right polarization asymmetry A_{LR}, measured at the

Z pole, is quite sensitive to the presence of oblique corrections, while being almost completely insensitive to direct corrections:

1. bremsstrahlung;
2. final state QCD (for hadrons);
3. flavor dependence (and the effect is calculable); and
4. hadronization.

The use of hadrons greatly improves the statistical error. A_{LR} directly measures the value of $s_*^2(q^2)$ at the Z pole, and $s_*^2(Z)$ in turn is directly sensitive to heavy particles, as exemplified in Figure 1, which shows the variation of $s_*^2(Z)$ with the top quark mass. Fixing $s_*^2(Z)$ also tells us about grand unified theories at much higher energies (Figure 2) and the possibility of proton decay. The physical importance of the oblique corrections is also reflected in their sensitivity to the new types of physics, such as supersymmetry and technicolor, postulated by theorists over the last decade to extend to the standard model. BREM5 can predict A_{LR} to better than 0.005 now, and, with hadrons, A_{LR} can be measured as accurately as 0.01 (or perhaps even 0.005) at the SLC (Figure 3). A_{LR} will give the physics community a strong foretaste of the physics to come in the next generation of accelerators and illustrates the importance of polarization at the SLC.

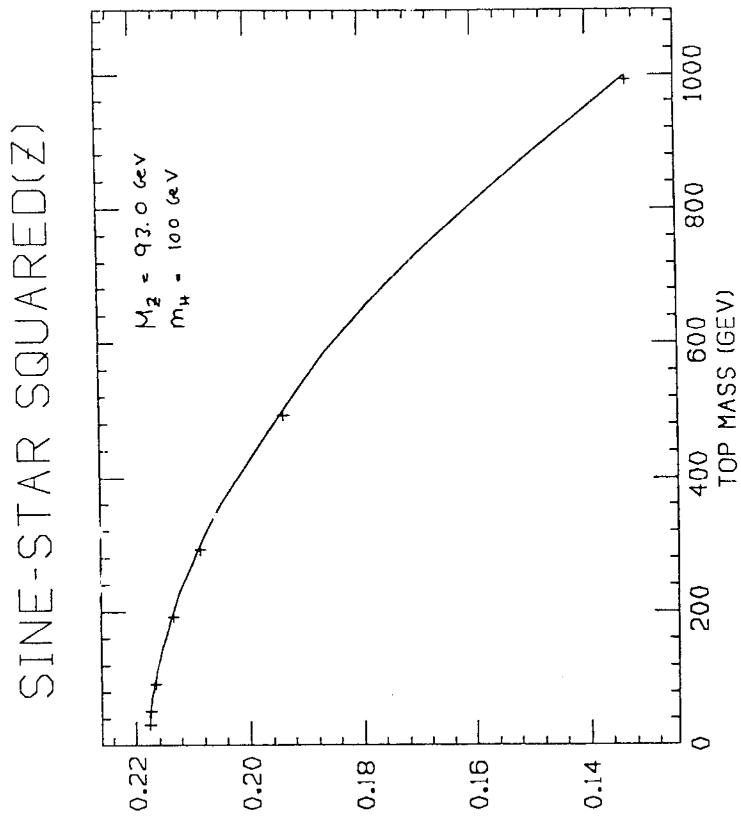

Figure 1

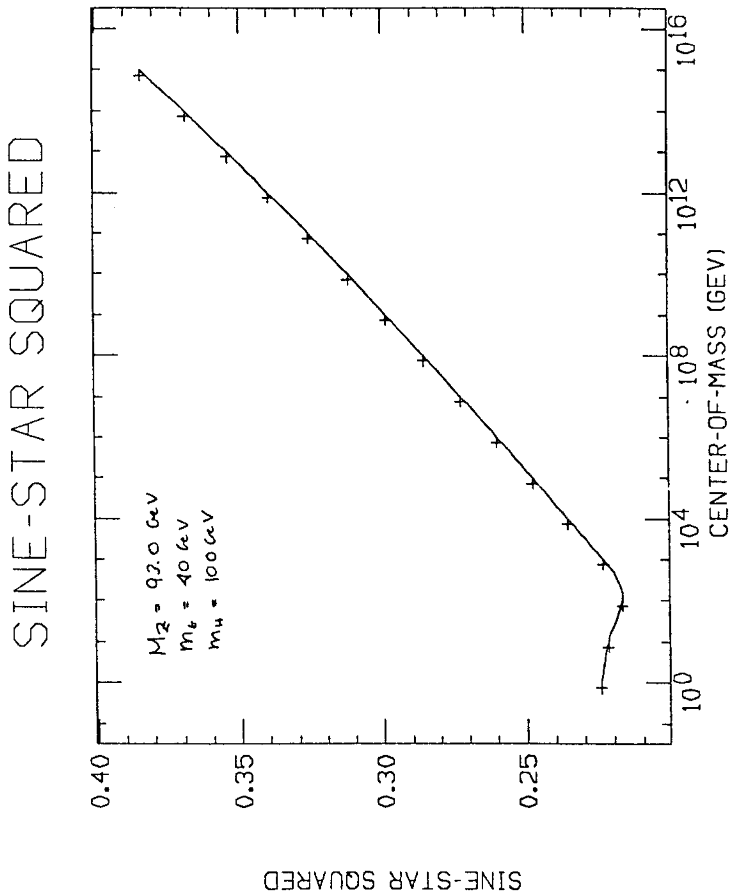

Figure 2

Experimental Uncertainty in A_{LR}

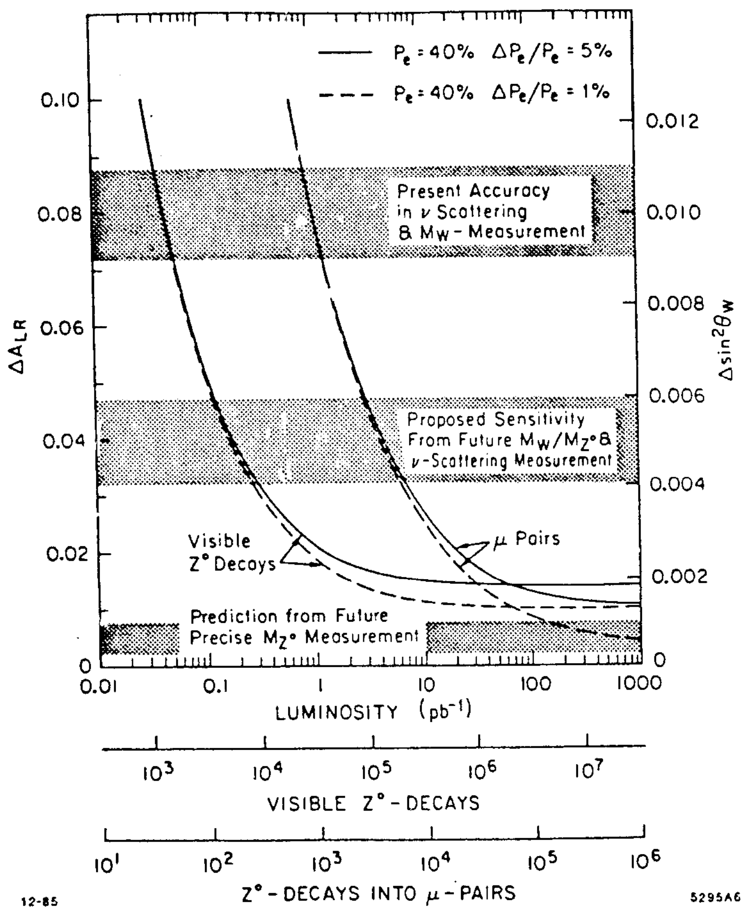

Figure 3

Mark II/SLC-Physics Working Group Note # 1–12

AUTHOR: Jim Alexander, Giovanni Bonvicini, Persis Drell, and Ray Frey

DATE: July 16, 1987

TITLE: Radiative Corrections to the Z^0 Resonance

The experimental evidence supporting the standard model of electroweak interactions is impressive. Perhaps most spectacular of all has been the direct observation of the Z^0, the heavy gauge boson predicted by the model, at the $p\bar{p}$ collider at CERN. Once one can directly produce Z^0s, one is in an excellent position to do detailed studies of the electroweak interaction, both by studying in Z^0 decays how the Z^0 couples to the matter field of quarks and leptons, and by precision measurements of the resonance itself.

The Z^0 resonance, in lowest order, has a Breit-Wigner line shape which is characterized by experimentally measurable quantities: the peak position or mass, the width, and the peak cross section. From an experimental point of view the three parameters, mass, width, and cross section, are independent quantities to be determined. Within the context of the standard model, however, they take on deeper significance that both motivates their measurement and sets the scale of precision at which the measurements may be considered interesting. The mass is related to $\sin^2\theta_W$; the width depends on the number of particles of mass less than half the mass of the Z^0 which couple to the Z^0; and the peak cross section is related to the vector and axial vector couplings, and hence $\sin^2\theta_W$.

Precision studies of the Z^0 resonance have not been forthcoming from the $Sp\bar{p}S$ where the Z^0 was first discovered. The broad spectrum of parton energies in $p\bar{p}$ collisions means that only a small portion of the total luminosity manifests itself in production of the relatively narrow Z^0 peak, and the resonance is difficult to extract from the much larger nonresonant QCD background. Furthermore, in the exclusive leptonic decay modes of the Z which have fairly clean signatures and can be extracted from the background events, the mass of the Z^0 can only be determined from the invariant mass of the lepton pair, since the initial state energy is unknown.

At the SLC and LEP, the situation is quite different. Because the electron and positron are pointlike, the center of mass energy of the interaction is defined by the beam energy. The beam energy spread is small compared to the resonance width, and all the luminosity contributes to the signal. The background is small and all visible decay modes of the Z^0 can be used.

Since it is the beam energy which will be used to determine the mass and width of the Z^0, it is crucial to know the absolute beam energy and energy spread. For the MarkII at SLC, a pair of spectrometers[1] located just upstream of the beam dumps will measure the central value of the beam energies to 0.06%, and will provide information on the beam energy spread, expected to be about 0.2%. Systematic errors on the mass and width of the Z^0 are expected to be around 45 MeV. The measurement of the peak cross section of the resonance will be limited by systematic errors in the monitoring of the machine luminosity. The luminosity monitors[2] measure the reaction $e^+e^- \to e^+e^-$ at small angles where it is dominated by the QED t-channel scattering. In this steeply falling region of the cross section the acceptance determination dominates the systematic error, which is not expected to be better than $\sim 2\%$ overall. Long term stability should be much better, and point-to-point variations in an energy scan will be low.

The Z^0 resonance is profoundly altered from its zeroth order Breit-Wigner shape by radiative corrections. In particular, bremsstrahlung from the annihilating e^+ and e^- alters the effective center of mass energy and significantly changes any quantity that varies strongly with $\sqrt{s}$. This results in shifts of hundreds of MeV in the mass and width of the resonance, and lowers the peak cross section by tens of percent. This paper will review in detail the physics of these corrections, the existing calculations, available Monte Carlos, and the level of precision finally expected in QED radiative corrections to Z^0 line shape measurements. Since we will have excellent energy resolution for the Z^0 mass and width measurement but cruder luminosity monitoring for the cross section measurement, radiative corrections which affect the line shape and peak position must be quite carefully considered, while corrections to the overall normalization at or below the 1% level are less urgent. Recent work extending the calculations to second order has given confidence that QED radiative corrections are well understood and that the precision achievable in these corrections is better than the 45 MeV currently expected to limit experimental measurements.

In section 1 we will review radiative corrections to first order. Results will be extended to higher orders in section 2, and we will discuss, quantitatively, the necessary accuracy of the calculations. The third section will present the radiative corrections from a structure function point of view. The advantages of this method will be discussed, and in section 4, we will present a numerical comparison of all the available calculations, with the conclusion that the agreements and disagreements between the different calculations are well understood, and the theoretical uncertainties are well below the anticipated experimental systematic errors. Section 5 will discuss currently available MC event generators, and in section 6 we will use the new calculations to refit the J/ψ resonance.

1. QED Radiative Corrections to First Order

In lowest order, $e^+e^- \to f\bar{f}$ proceeds by photon exchange and by Z^0 exchange as shown in Fig. 1 . The total cross section is given in the standard model by

$$\sigma(s) = \frac{4\pi\alpha^2}{3s} N \left[Q^2 - \frac{2Qs(s-M_Z^2)v_e v_f}{(s-M_Z^2)^2 + s\Gamma_Z^2} + \frac{s^2(v_e^2+a_e^2)(v_f^2+a_f^2)}{(s-M_Z^2)^2+s\Gamma_Z^2} \right] \qquad (1)$$

where the vector and axial vector coupling strengths for the electron and for the final fermion are

$$v = \frac{-1+4Q^2\sin^2\theta_W}{2\sin 2\theta_W}, \quad a = \frac{-1}{2\sin 2\theta_W}.$$

N and Q denote the number of colors and charge of the fermion. At SLC energies, the first two terms in Eq. (1), the QED and interference contributions, are negligible compared to the third, resonant, term. To an excellent approximation, therefore, one writes the lowest order cross section, $\sigma_0(s)$ as

$$\sigma_0(s) = \sigma_Z \frac{s\Gamma_Z^2}{(s-M_Z^2)^2 + s\Gamma_Z^2}. \qquad (2)$$

This form illustrates the experimentally accessible parameters, M_Z, Γ_Z, and σ_Z and the relativistic Breit-Wigner used to characterize the resonance. The peak cross section, σ_Z, is related to the standard model coupling strengths by $\sigma_Z = 4\pi\alpha^2 N(v_e^2+a_e^2)(v_f^2+a_f^2)/3\Gamma_Z^2$.

In practice, the lowest order line shape defined by Eq. (2) is distorted by radiative effects. The set of diagrams contributing to the first order corrections are shown in Fig. 2. The diagrams 2a and 2b represent the radiation emitted by one initial state electron in the field of the other one. Since this initial state radiation carries energy away, leaving the annihilation center of mass energy below the nominal value, it is principally responsible for the distortions to the resonance line shape. Vertex corrections to the initial state and vacuum polarization graphs (figs. 2c and 2d) represent the electron form factor and charge screening terms, respectively. As they do not change the kinematics, they enter as overall factors to change the scale of the cross section. The vacuum polarization diagrams may be easily summed to all orders in the leading log approximation, but the vertex corrections are complicated and have been only recently calculated to second order .[3] [4] Final state radiation and vertex corrections (Figs. 2e- 2g) differ from the corresponding initial state diagrams in that they do not alter the center of mass energy, and may be summed over inclusively. This summing cancels large logarithmic effects associated with the initial state,[5] leaving a correction of $1+3\alpha Q^2/4\pi$. This is slightly

larger than 1 because there is slightly more phase space available to a three body final state than two body final state. The final set of diagrams in Fig. 2 are box and interference graphs, Fig. 2h-j. These diagrams, if they contain photons only, are known to be odd in $\cos\theta$, so that they contribute to the forward-backward asymmetry, A_{FB}, but make no change to the total cross section. The $\gamma - Z$ pieces have almost the same effect, but in addition contribute a small correction to the cross section. We will omit these pieces in the rest of this paper.

There are other first order radiative corrections which, a priori, must be considered. Corrections coming from one-loop electroweak effects are of order[6] $\alpha/\pi \sim$ .1%. Since these modify the coupling strengths, but have no effect on the kinematics, only the cross section is altered, and that at a level to which experiments will be insensitive. QCD corrections arising from final state gluon radiation introduce corrections of α_s/π, where uncertainty in the value of α_s leaves a residual uncertainty of about 1%. This 1%, however, is on the normalization. It is clear that for the mass and width measurement, and measurements of the total cross section, our greatest concerns are the QED corrections coming from initial state radiation.

Since bremsstrahlung from the initial state electrons means that the actual center of mass energy available for the annihilation is reduced from the nominal $\sqrt{s} = 2E$ set by the beam energies, one is sampling all energies below $\sqrt{s}$ according to a sampling function determined by the physics of bremsstrahlung. For photons of energy kE, the actual center of mass is $\sqrt{s(1-k)}$ and the observed cross section is given by a convolution,

$$\sigma_{obs}(s) = \int f(k,s)\sigma_0(s(1-k))dk \qquad (3)$$

where the function $f(k,s)$ must be computed from the QED diagrams. With $f(k,s)$ in hand, one may use Eq. (3) to extract the three parameters of the underlying Breit-Wigner.

The emission of a single photon from the initial state, as in figs. 2a-b, modifies the amplitude for the hard annihilation process, A_0, by a kinematic factor:

$$A_1 = \left(\frac{p^+}{k\cdot p^+} - \frac{p^-}{k\cdot p^-} \right) A_0. \qquad (4)$$

Summing over photon polarizations and integrating over photon angular variables, one finds the change in the cross section due to initial state radiation is:

$$d\sigma \sim \sigma_0 \left[\frac{2\alpha}{\pi} \left(\log\frac{s}{m_e^2} - 1 \right) \frac{dk}{k} \right], \qquad (5)$$

where we have assumed the emitted photon energy, kE, is small compared to the beam energy in going from Eq. (4) to Eq. (5). It is customary to define an effective coupling constant for bremsstrahlung: $\beta \equiv \frac{2\alpha}{\pi}\left(\log\frac{s}{m_e^2}-1\right)$. This factor is associated with every bremsstrahlung vertex and is large ($\beta = .109$ at SLC energies) due to the large phase space for an electron to disintegrate into an electron and a nearly collinear photon. A large effective coupling constant is the first of two major reasons that QED corrections are so large at the Z^0.

Integrating Eq. (5) over a range of bremsstrahlung energies from k_{min} to k_{max} and adding in the zeroth order cross section, one finds the total cross section including single photon emission from the initial state is:

$$\sigma_1 = \sigma_0(1+\beta\log\frac{k_{max}}{k_{min}}).$$

The infrared divergence as $k_{min} \to 0$ is removed with the inclusion of the vertex correction Fig. 2c, leaving

$$\sigma_1 = \sigma_0(1+\delta_1+\beta\log\frac{k_{max}}{E}), \tag{6}$$

where $\delta_1 = \frac{3}{4}\beta+\frac{2\alpha}{\pi}\left(\frac{\pi^2}{6}-\frac{1}{4}\right)$ is sometimes called the first-order electron form factor. In order to evaluate Eq. (6), we need to know what k_{max} is. In general, photon energies may extend up to the kinematic limit, just shy of the beam energy E, but a resonant cross section will cut off contributions from hard photons. This means that in the vicinity of the peak, ($2E = M$), the resonance imposes an effective upper limit at $k_{max} \sim \Gamma/2$, so that

$$\sigma_1 \sim \sigma_0\left(1+\delta_1+\beta\log\Gamma/M\right).$$

The correction δ_1 arises from the effect of the virtual photon cloud, and has a magnitude at the Z^0 of $\delta_1 = +8.7\%$, while the logarithmic term $\beta\log\Gamma/M$ is due to real radiation, and has a magnitude at the Z^0 of about $\beta\log\Gamma/M \approx -38\%$. The second term is negative because the resonance cuts off the contribution of hard photons, effectively limiting one to only part of the total cross section, and depends on the fractional width of the resonance, Γ/M. This is particularly large for a narrow resonance, such as the J/ψ, and is still quite significant at the Z^0 where $\Gamma/M \sim 3\%$. This is the second reason why the QED corrections are large: the narrow resonance simply cuts off contributions from all but the softest radiative events, which, in turn, constitute only a fraction of the total cross section. More physically, the harder radiation simply moves the center of mass energy off the resonance into a region of low cross section.

Eq. (6) may be rewritten as

$$\sigma_1 = \sigma_0(1+\delta_1)(1+\beta\log\frac{k_{max}}{E}), \tag{7}$$

where terms that are higher than first order are dropped. Eq. (7) clearly separates the virtual corrections $(1+\delta_1)$ from the real $(1+\beta\log\frac{k_{max}}{E})$.

To this point, we have only considered changes to the cross section due to soft photon ($k \leq k_{max} << E$) emission. In this region one may safely ignore the variations of the cross section, and σ_0 can be treated as a constant in Eq. (6) . The contributions from photons radiated with $k_{max} < k < E$ must be included, however, and the variation of the cross section with $\sqrt{s}$ taken into account. The bulk of this so-called hard photon contribution could be handled by writing $\sigma_0 = \sigma_0(s')$ where $s' = s(1-k/E)$ is the center of mass energy remaining for the annihilation after the photon is radiated, and by allowing $k_{max} \to E$ in the integration of Eq. (5). There are, however, bremsstrahlung terms which go not as k^{-1}, but as k^0 and k^1. These terms were lost in the approximation between Eq. (4)and (5), and must be reinstated. The full differential cross section is

$$\frac{d\sigma(s)}{dk} = \beta(\frac{1}{k}-1+\frac{k}{2})\sigma_0(s'), \tag{8}$$

where now k is the scaled photon energy previously denoted k/E. Denoting k_{max}/E by k_0, we write the complete cross section to first order as follows:

$$\sigma_1(s) = \sigma_0(1+\delta_1+\beta\log k_0)+\int_{k_0}^{1}\frac{d\sigma}{dk}dk, \tag{9}$$

with $d\sigma/dk$ being given by Eq. (8). The division of the cross section in Eq. (9) is driven by the need to combine bremsstrahlung and vertex diagrams analytically as $k \to 0$, but leads to the unfortunate presence of an unphysical parameter, k_0. For analytic calculations, the value chosen for k_0 is of no consequence, but in Monte Carlo work, where the "soft" cross section (the first term of Eq. (9)) and the "hard" cross section (the second term in Eq. (9)) may be treated separately, difficulties can arise. The desire to set k_0 as low as possible is hampered by fact that the first order soft cross section becomes negative. At the same time, values of k_0 comparable to, or larger than, Γ_Z are prohibited.[7] These problems all evaporate when higher orders are included.

2. Higher Order QED Corrections

Several recent publications have extended calculations of the QED radiative corrections to the Z^0 resonance to second order.[3][8-10] For $k_{max} << 1$

$$\sigma_2 = \sigma_0(1 + \delta_1 + \delta_2 + \beta \log k_{max} + \delta_1 \beta \log k_{max} + \frac{1}{2}\beta^2 \log^2 k_{max}), \qquad (10)$$

where photon energy variable, k_{max} is understood to refer to the *total* radiated energy due to both photons. The second order virtual correction δ_2 is given by[11]

$$\begin{aligned}\delta_2 = \left(\frac{\alpha}{\pi}\right)^2 \Bigg\{ &\left[\frac{9}{8} - 2\varsigma(2)\right] \log^2 \frac{s}{m_e^2} \\ + &\left[-\frac{45}{16} + \frac{11}{2}\varsigma(2) + 3\varsigma(3)\right] \log \frac{s}{m_e^2} \\ - &\frac{6}{5}[\varsigma(2)]^2 - \frac{9}{2}\varsigma(3) - 6\varsigma(2)\log 2 + \frac{3}{8}\varsigma(2) + \frac{57}{12}\Bigg\}\end{aligned} \qquad (11)$$

where $\varsigma(2) = \frac{\pi^2}{6}$, and $\varsigma(3) = 1.202$.

As was done for the first order case, this result may be written in product form, again assuming one drops the cross terms that exceed second order.

$$\sigma_2 = \sigma_0(1 + \delta_1 + \delta_2)(1 + \beta \log k_{max} + \frac{1}{2}\beta^2 \log^2 k_{max}). \qquad (12)$$

The terms take the following values, (using $k_{max} = \Gamma/M$): $\delta_1 = +8.7\%$, $\delta_2 = -0.5\%$, $\beta \log k_{max} = -38\%$, and $\frac{1}{2}\beta^2 \log^2 k_{max} = +7.5\%$. The virtual corrections (δ_1, δ_2,...) are falling rapidly, and already the second order virtual correction, at -0.5%, is below the level of our experimental sensitivity. This is fortunate, because these terms can be gotten only through direct calculation, a daunting task in third order. The real corrections, on the other hand, are larger and falling more slowly, so one reasonably expects the next order to be significant. For these terms, however, a technique exists to deal with all orders.

The real photon terms are such that at n^{th} order, the term contributed is of the form

$$(\frac{\alpha}{\pi})^n (\log \frac{s}{m_e^2})^n (\log k_{max})^n.$$

These terms are the well-known leading logs and dominate the contribution from

each order. Nonleading terms of the form

$$(\frac{\alpha}{\pi})^n (\log \frac{s}{m_e^2})^m$$

with $m \leq n$ appear in the virtual correction, and other nonleading terms show up in the cross terms. The fact that the leading logs may be summed to all orders[12] allows one to make the extension known as exponentiation:

$$\begin{aligned}\sigma &= \sigma_0(1 + \delta_1 + \delta_2)\left(1 + \beta \log k_{max} + \frac{1}{2!}\beta^2 \log^2 k_{max} + \frac{1}{3!}\beta^3 \log^3 k_{max} + \ldots\right) \\ &= \sigma_0(1 + \delta_1 + \delta_2)\, exp\,(\beta \log k_{max}) \\ &= \sigma_0(1 + \delta_1 + \delta_2)\,(k_{max})^\beta\end{aligned} \qquad (13)$$

For the extraction of the Z^0 line shape, this is a particularly powerful result, because it takes precisely those terms responsible for the line shape distortions, and sums them to all orders. This bodes well for the extraction of M_Z and Γ_Z. Virtual corrections are computed only to second order, but they affect mostly the overall normalization, and at a level already below experimental systematic errors. It is worth noting that through the product with δ_1 and δ_2, the next-to-leading and next-to-next-to-leading terms are also included.

As with the first order calculation, it is necessary to include the contribution from cases where the total radiated energy, k lies in the range $k_{max} < k < 1$. To second order, the differential cross section, analogous to the first order result in Eq. (8) is given in reference 8:

$$\begin{aligned}\frac{d\sigma}{dk} = \sigma_0(s')\Bigg[&\beta\left(\frac{1}{k} - 1 + \frac{k}{2}\right)(1 + \delta_1 + \beta \log(k)) \\ &+ (\frac{\alpha}{\pi})^2 \left(\frac{1 + (1-k)^2}{k} A(k) + (2-k)B(k) + (1-k)C(k)\right)\Bigg],\end{aligned} \qquad (14)$$

where $s' = s(1 - k)$, and the functions $A(k)$, $B(k)$, and $C(k)$ are included for convenience in the appendix. The purely second order $(\frac{\alpha}{\pi})^2$ pieces augment the total cross section slightly at values of $\sqrt{s} > M_Z$, but their impact is small. At values of $\sqrt{s}$ up to 5 GeV above the resonance, the net effect is less than 0.4%.

For the terms with k^{-1} dependence, the results of exponentiation may be used to improve both Eq. (14) and Eq. (8). Differentiating Eq. (13), one finds

$$\frac{d\sigma}{dk} = \beta\sigma_0(1+\delta_1+\delta_2)k^{\beta-1}.$$

This equation illustrates the correct form for $d\sigma/dk$ in the limit $k \to 0$, when leading logs are summed to all orders. In effect, a factor $k^{\beta}(1+\delta_1+\delta_2)$ has been introduced by the exponentiation of higher orders. To include the higher orders in Eq. (14), one must put this factor in by hand. Thus,

$$\begin{aligned}\frac{d\sigma}{dk} = \sigma_0(s')\Bigg[\beta\left(k^{\beta-1}(1+\delta_1+\delta_2) - 1 + \frac{k}{2}\right)\\ +(\frac{\alpha}{\pi})^2\left(\frac{1+(1-k)^2}{k}A(k) + (2-k)B(k) + (1-k)C(k)\right)\Bigg].\end{aligned} \tag{15}$$

A similar result holds for Eq. (8).

For a complete result with all corrections to second order, and leading logs summed to all orders, we have

$$\sigma_{obs}(s) = \sigma_0(s)(1+\delta_1+\delta_2)\,k_0^{\beta} + \int_{k_0}^{1}\frac{d\sigma}{dk}\,dk, \tag{16}$$

with $d\sigma/dk$ taken from Eq. (15). The k_0 problem that arose in the first order calculation is no longer present in Eq. (16) because the soft term vanishes in a well-behaved fashion as $k_0 \to 0$. This allows one to set k_0 arbitrarily small. In fact, under the (good) approximation that $A(k) = B(k) = C(k) = 0$, one may set k_0 to zero and the integral can be solved analytically. This has been done by Cahn,[18] with the additional but not necessary approximation that $\delta_2 = 0$. The result is an analytic expression for $\sigma_{obs}(s)$ that is suitable for fitting acceptance-corrected data. For the reader's convenience, it is reproduced in the appendix.

At this point it is instructive to review what has been accomplished by the inclusion of higher order corrections, and ask whether the primary goal of bettering the experimental systematic errors on M_Z, Γ_Z, and σ_Z has been achieved. Following Ref. 8, we illustrate in Fig. 3 the expected line shape, $\sigma_{obs}(s)$, under four levels of radiative correction: (1) pure first order, (2) first order with exponentiation, (3) pure second order, and (4) second order with exponentiation. For clarity, the full expressions for $\sigma_{obs}(s)$ are given in the appendix. The underlying Breit-Wigner in these calculations has $M_Z = 93.0$ GeV$/c^2$, $\Gamma_Z = 2.5$ GeV, and $\sigma_Z = 1.86$ nb.

The peak of the first order calculation is shifted to 93.180 GeV$/c^2$, and peak cross section lowered to 1.313 nb, a 29% drop relative to the cross section of the underlying resonance. These numbers are consistent with expectations. When exponentiation is included with the first order calculation, the peak position moves back to 93.108 GeV$/c^2$, and the peak height to 1.382 nb. The line shape with exponentiation more closely resembles the underlying shape because exponentiation weights the soft radiation more heavily than the pure first order calculation. The first order calculation properly represents hard radiation, but badly underrepresents the soft components. In first order, for instance, approximately 50% of the cross section occurs below $k_0 = 0.01$, while the inclusion of exponentiation changes this to 90%. Thus the first order correction shifts the peak position too much to the high side and smears the narrow profile into a lower, broader one.

It is interesting to compare second order with exponentiation to first order with exponentiation. Figure 3 shows there is *no* difference in the peak position, which also occurs at 93.108, but there is a drop in the peak height from 1.382 to 1.372 nb. This latter effect can be traced almost entirely to the inclusion of the second order virtual correction δ_2. The important conclusion here is that *the leading logs dominate all line shape distortions*. The explicit presence of nonleading terms to second order has little effect on the position of the peak.

Finally a comparison of the pure second order with the exponentiated second order rounds out the picture. The second order line shape shows a peak at 93.092, with a peak height of 1.374 nb. This peak position is lower than the 93.108 found for the exponentiated case, indicating that the second order real term has overcompensated the excesses of first order. The peak height is almost identical with that of exponentiated second order, as one would expect since they share identical nonleading terms.

Little can be said about the effect of the various correction schemes on the width, Γ_Z, without a more quantitative approach. To meet this need, a set of "fake data" was generated using an exponentiated second order version of $\sigma_{obs}(s)$ (Eq. (16)) to represent the "true" resonance shape. The relative accuracy of a particular correction scheme can then be determined by fitting this "data". The fitting procedure consists of the minimization of a χ^2 function with respect to the underlying resonance parameters M_Z, Γ_Z, and σ_Z of Eq. (3). Table 1 summarizes the results, given in terms of the differences between the values of the parameters found in the fit and those used to generate the "data". The results were found not to depend in any significant way on the choice of scan strategy, *i.e.* the particular set of center of mass energies and their statistical weights. Nor do they depend on details of the χ^2 minimization procedure. The results therefore represent a reasonable comparison of the intrinsic accuracy of the correction schemes. This procedure is used here (Table 1) to compare general levels of approximation relative to the most complete level presently available (reference 8). It is also invoked later to compare the results of various authors.

Table 1 indicates that a first order calculation is clearly inadequate, as it misses the true mass by 121 MeV/c^2, almost three times the expected experimental systematic error, and misses the width by 152 MeV, which is equivalent to almost one light neutrino generation. By contrast, both the exponentiated first order and pure second order perform acceptably well, the former being somewhat better, but both being within the limits of experimental systematics.

From these observations we draw the following conclusions. First, the virtual corrections affect mostly normalization, so accounting for them to second order is quite adequate given the known systematic errors on luminosity measurements. Second, the real terms account for the distortion of the line shape, and must be summed to all orders. Once this summation is done, the mass and width can be properly extracted with an accuracy of a few MeV. Third, the nonleading terms at second order have been shown explicitly to play no significant role in the extraction of mass and width.

To this point we have dealt only with the corrections arising from initial state radiative effects, on the justifiable grounds that the other contributions, from final state radiation, box diagrams, and so forth, are small even in first order. The ability to factorize the initial state effects from the remainder of the cross section is a powerful tool. One may carry this notion further to assign these radiative effects to a *structure* of the initial state. In this view, the sampling function, $f(k,s)$ in Eq. (3), arises from the product of electron structure functions,

$$\int dk_1 D(k_1,s) D(\frac{k-k_1}{1-k_1},s) = f(k,s),$$

which describe the probability to find the electron having radiated off an amount of energy k_1 or $k-k_1$. Without changing the results, this alteration of one's point of view introduces a very useful technique long familiar in hadron physics, but only recently applied to e^+e^- physics.

3. The Structure Function Approach

An electron radiating a photon of energy k is left with a fraction $x = 1-k$ of its original energy. This electron may go on to participate in the annihilation, $e^+e^- \to Z^0, \gamma$, or may split off more photons. The photons themselves may split into e^+e^- pairs, members of which may participate in the annihilation. Either way, the electron finally annihilating carries only a fraction x of the nominal beam energy E. The cascading of electrons and photons is illustrated in Fig. 4. In the standard notation, the probability distribution for finding a electron of momentum fraction x in an interaction with center of mass energy $\sqrt{s}$ is written $D(x,s)$. For an electron and positron of momentum fractions x_1 and x_2, respectively, the total center of mass energy is $\sqrt{x_1 x_2 s}$, and the cross section is $D(x_1,s)\sigma_0(x_1x_2s)D(x_2,s)$. The total observed cross section is then

$$\sigma_{obs}(s) = \int_\epsilon^1 dx_1 \int_\epsilon^1 dx_2 D(x_1,s)\sigma_0(x_1x_2s)D(x_2,s); \tag{17}$$

the lower integration limit depends on the mass of the final state particles. The $D(x,s)$ satisfy the normalization and momentum conservation equations:

$$\begin{aligned} \int D(x,s) &= 1, \\ \sum_i \int x D_i(x,s) &= 1. \end{aligned} \tag{18}$$

The first integral includes all electron components (*i.e.*, valence and sea electrons), while the sum in the second formula runs over all the available partons, photons included. It is safe to neglect all other components, because real heavy fermion pairs are strongly suppressed, and one more pair of electrons can be produced only in fourth order.

The concept of the structure function has been borrowed from QCD where its application in the description of hadrons has proven fruitful. Evolution equations were written for a vectorial theory in the early 1970s[14-17] and were first applied to QCD in reference 17. More recently, they have been used to calculate QED radiative corrections in Ref. 3; subsequently, other calculations have been done[9][10] for specific application to the Z^0 energy region. By including a complete second order evolution of the initial state, including the graphs of Fig. 5, the structure function is

$$D(x,s) = D_\gamma(x,s) + D_{ee}(x,s). \tag{19}$$

$D_\gamma(x,s)$ refers to the probability of finding an electron of momentum fraction x plus an arbitrary number of photons, while $D_{ee}(x,s)$ refers to the probability of finding an electron of momentum fraction x, plus an electron-positron pair, plus an arbitrary number of photons. Reference 3 yields the following result for $D_\gamma(x,s)$ and $D_{ee}(x,s)$:

$$\begin{aligned} D_\gamma(x,s) = {} & \frac{\beta}{2}(1-x)^{\frac{\beta}{2}-1}\left(1+\frac{3}{8}\beta-\frac{\beta^2}{48}\left(\frac{1}{3}L+\pi^2-\frac{47}{8}\right)\right)-\frac{1}{4}\beta(1+x) \\ & +\frac{1}{32}\beta^2\left(4(1+x)\log\frac{1}{1-x}-\frac{1+3x^2}{1-x}\log x-5-x\right), \\ D_{ee}(x,s) = {} & \theta\left(1-x-\frac{2m_e}{E}\right)\left(\frac{\alpha}{\pi}\right)^2\Big[\frac{1}{12}\frac{(1-x-2m_e/E)^{\beta/2}}{1-x}\left(L_1-\frac{5}{3}\right)^2 \\ & \left(1+x^2+\frac{1}{6}\beta\left(L_1-\frac{5}{3}\right)\right)+\frac{1}{4}L^2\left(\frac{2}{3}\frac{(1-x^3)}{x}+\frac{1-x}{2}+(1+x)\log x\right)\Big], \end{aligned} \tag{20}$$

where $L=\log(s/m_e^2)$, β has been defined above, $L_1 = L+2\log(1-x)$ and θ is the Heavyside function. Substituted into Eq. (17), one may derive the form of $f(k,s)$ in Eq. (3), as given in the appendix.

These calculations of $D(x,s)$ in QED assume *collinear* radiation, so the (small) effect of photons emitted at large angles is not included. The collinear and nearly-collinear radiation dominate the center of mass energy shifts and the μ−pair acollinearities, but the μ−pair aplanarity is determined by photons of large transverse momentum. For a full treatment of the kinematics, this transverse momentum must be accounted for. Two approaches may be considered, for example to improve a Monte Carlo based on structure functions as the one described below.

1. The first is to assume the photon p_T distribution is properly simulated by first-order calculations. Since the only photons that will have significant kinematic impact are those with large p_T, this is a very good approximation. One may then include the matrix element for hard photon emission[18] in the σ_0 of Eq. (17).
2. The second is to directly compute the structure function $D(x,p_T,s)$ as has been done in the QCD case.[19]

In either case, the non-factorizable pieces, such as box and interference terms, may be added by hand. These will then modify the σ_0 of Eq. (17).

The removal of energy by bremsstrahlung photons changes not only the center of mass energy, $\sqrt{s}$, but also the center of mass momentum. In general the annihilation center of mass is no longer at rest with respect to the reference frame of the detector. For μ−pair final states, the resulting acollinearities and aplanarities are detectable kinematic effects which provide the only experimental check one has on the radiative correction calculations. Since collinear radiation of energy kE results in a μ−pair acollinearity $\varsigma \approx k$, an acollinearity resolution of 10 mr allows one to

check the corrections directly for $0.01 < k < 1$. The bulk of the corrections arise from infrared radiation, $k \le 0.01$, but the normalization constraints such as those of Eq. (18) impose a relationship between the hard and soft pieces so that the kinematic effects may remain useful checks on the entire calculation. A bremsstrahlung photon of transverse momentum $k_T E$ results in an aplanarity $\eta \approx k_T$, and thus offers a similar check on the transverse elements of the calculation.

On may hope to exploit these kinematic manifestations to measure the structure function $D(x,s)$. If such a measurement is performed on PEP/PETRA data, the resulting structure functions may be evolved to SLC energies and used as input to an SLC Monte Carlo. Amplifying on these ideas, one notes that the center of mass energy is given by $\sqrt{x_1x_2s}$, and additionally, the Lorentz boost, β, of the center of mass is given by $\beta=(x_1-x_2)/(x_1+x_2)$. With the Lorentz dilation given by $\gamma=(x_1+x_2)/2\sqrt{x_1x_2}$, one can directly write down the acollinearity of a μ−pair final state arising from the annihilation of an electron and positron of momentum fractions x_1 and x_2, respectively, as

$$\varsigma = \left|\frac{2\beta\gamma\sin\theta'}{1+\beta^2\gamma^2\sin^2\theta'}\right|, \tag{21}$$

where θ' is the emission angle of the μ^+ in the μ−pair rest frame. The moments of the acollinearity distribution of a μ−pair sample will then be given by

$$f^n(\varsigma,s) = \int dx_1dx_2d\theta'\frac{1}{\sigma}\frac{d\sigma_0}{d\theta'}D(x_1,s)D(x_2,s)\varsigma^n. \tag{22}$$

In the PEP/PETRA region, and in other energy regions where a good amount of data on the continuum has been collected, the underlying Born cross section is known much better than 1%, and with a suitable Monte Carlo, the acollinearity distribution for μ pairs gives a direct measurement of the electron structure function, using Eq. (22). In the same way, the measurement of the p_T dependence of the structure functions can be measured from aplanarity distributions, where the aplanarity η is defined as

$$\eta = \frac{|\vec{p}_{T+}\times\vec{p}_{T-}|}{|\vec{p}_{T+}|\cdot|\vec{p}_{T-}|}. \tag{23}$$

In the SPEAR region, the abundance of resonant states and the large α_s imply that there are non perturbative and theoretically unpredictable QCD effects affecting the total hadronic cross section. Most of the results published used Ref. 20 to extract the QED effects, where the lack of proper form factors can affect the normalization at the 10% level, and missing hard pieces have the side effect of changing the total cross section when hard radiation can take s' down to the region of a large resonance. Besides the interest of reviewing old data using new calculations, there is a small change on the correction Δr[21] to $\alpha(M_Z^2)$ obtained with a dispersion relation fit of the low energy data.

4. Comparison of Existing Calculations

We have cited several works (references 3, 8, 9, 10, 13) in which QED corrections beyond first order have been calculated. Broad differences of approach (matrix element, structure function) have been noted, but differences of detail and discrepancies in results have been reserved for this section. Since the treatment of real pairs differs between authors,[11] we have adopted the following convention for the sake of consistency in these comparisons: real pairs are ignored in Ref. 3, and the electron form factor of Ref. 10 was set equal to the δ_2 of Ref. 8. Hence these results all include virtual pairs, but not real pairs. We have not attempted here to include all existing calculations. In particular, evaluation of the results displayed in references 9 and 22 are expected to be numerically similar to the aforementioned papers. To complete the review and establish a familiar reference point, we include the classic work of Jackson and Scharre, reference 20, where we have modified the virtual correction to exclude the (small) photon vacuum polarization, which is not relevant at the Z^0.

Two types of comparison are made. The first is done by choosing three parameters, $M_Z = 93.0$ GeV/c^2, $\Gamma_Z = 2.5$ GeV, and $\sin^2\theta_W = 0.230$ and generating the profile σ_{obs} according to the corrections given in each of these references. For the $\mu^+\mu^-$ final states, table 2 gives the cross sections at several values of $\sqrt{s}$ in terms of a deviation from the prediction of reference 8 in percent. The very close agreement between reference 8 and references 10 and 3 is quite striking in view of the fact that the former is strict matrix element calculation plus exponentiation, and the latter are structure function results. The large disagreement between reference 8 and reference 20 may be attributed to incomplete treatment of virtual terms, as discussed below.

The "fake data" test used earlier to compare levels of radiative correction may be applied here to compare the agreement on M_Z, Γ_Z, and σ_Z that use of various authors' works would yield. Table 3 shows the results. Again we see the close agreement between Refs. 8, 3, and 10. The shape of the resonance is also well described by Ref. 13. This result has the advantage of a compact, analytic formulation. We have used the sum of the "hard" and "soft" photon results from Ref. 13 for this comparison.

We see that the result of Ref. 20 has substantial discrepancy compared to the more recent calculations, for which the overriding cause is as follows. The corrected cross section with exponentiation of soft photons to all orders, and with

virtual and hard-photon corrections to first order can be taken from Eq. (15) and Eq. (16) (dropping the δ_2 and $(\alpha/\pi)^2$ terms, and letting $k_0 \to 0$):

$$\sigma_{obs}(s) = \beta \int \sigma_0(s')\, k^{\beta-1}(1+\delta_1)\, dk \;-\; \beta \int \sigma_0(s')\,(1-\frac{k}{2})\, dk,$$

where $s' = s(1-k)$, as before. The second term (hard-photon bremsstrahlung), is ignored for the remainder of this discussion. This convolution then takes on the general form

$$\sigma_{obs}(s) = \int \sigma_0(s')\, f(k,s)\,(1+\delta_1)\, dk. \tag{24}$$

However, in Ref. 20 the integral is broken up into two terms

$$\sigma_{obs}(s) = \int \sigma_0(s')\, f(k,s)\, dk \;+\; \delta_1\, \sigma_0(s). \tag{25}$$

In this case, the virtual correction δ_1 modifies the cross section only at the energy $\sqrt{s}$. The reason that this approximation breaks down is illustrated by considering a situation where the center of mass energy is slightly above a narrow resonance of mass M_R, so that $\sqrt{s} = M_R + \Delta E$. The virtual correction shown in Fig. 6 has a small effect which is correctly included in the δ_1 term in both Eq. (24) and Eq. (25). The emission of bremsstrahlung radiation of energy near ΔE represents, on the other hand, a very large effect, and the process depicted in Fig. 7 of a virtual correction along with emission of photons down to the resonance peak is relatively important. Such contributions are not included in Eq. (25). The numerical significance of this omission can be seen in Tabs. 2 and 3 by comparing Ref. 20 to Ref. 13, wherein the most significant difference is the distinction between Eq. (24) and (25). Because Ref. 20 has been used extensively to extract physics results, this distinction is potentially important. It is discussed further in the last section.

Previous discussion indicated that several calculations possess sufficient accuracy for the extraction of the parameters of the Z^0 resonance. We now see that there is excellent agreement between the most complete of these results, *i.e.* Refs. 3, 8, and 10. The simplified result of Ref. 13 is, in fact, also sufficiently accurate, given the expected experimental errors. Although the authors represented in tables 2 and 3 include different levels of approximation for the virtual and hard-photon contributions to the cross section, they all include some form of exponentiation of the soft photons. This is not too surprising, as Tab. 1 shows that an excellent approximation is achieved by including exponentiation of soft photons along with other corrections to only first order.

5. Monte Carlos

In the course of this work, two Monte Carlo programs have been developed. The first is based on the MMG1 program[18] which embodies the complete first order calculation, and has been widely used in analysis of PEP and PETRA data. MMG1 has been modified to include the second order and exponentiation corrections, as in Eq. (16), and shall be referred to here as MMGE. The second program is based on the structure function analysis of reference 10. We give a brief review of each program here.

The starting point of MMG1 is the radiation spectrum, $d\sigma/dk$, which is used to generate the photon energy. All other kinematic variables are generated subsequently. The final result is a set of four-vectors for the produced fermion pair, and a four vector for the photon if its energy was generated above k_0. Normally[7] $k_0 = 0.01$. In MMGE, the radiation spectrum is taken from Eq. (16). The energy generated from this spectrum is then assigned to a single photon, and the remainder of the program proceeds in the usual fashion. Final state radiation, box diagrams, initial/final state interference, and photon vacuum polarization corrections are turned off. The use of exponentiation allows k_0 to be set arbitrarily small, and typically $k_0 = 0.0001$ is used. As an example of this program's application, Fig. 8 shows the effect of higher order corrections on the forward-backward $\mu-$pair asymmetry, calculated with MMGE. One sees that, characteristically, the first order calculation exaggerates the correction, and with higher orders, the final result lies between the lowest order and the first order expectation.

A drawback to a program of MMGE's nature lies in the approximation that all the radiated energy is carried by one photon. In fact it should be spread over infinitely many photons. In practice, if the radiated energy is large, then it certainly is carried predominantly by one photon, while if the radiated energy is small, the kinematic effects are negligible anyway, so it doesn't matter. In the middle ground where one might have two photons of comparable energy, the approximation is poorest, and one may expect to see discrepancies between acollinearity data and predictions of this Monte Carlo.

Equation (19) provides the starting point for the structure function Monte Carlo. With this method one may generate an initial state that already contains all the important radiative corrections, and add further radiative corrections of lesser impact to first order in the matrix element for the hard annihilation process. The kinematics of the final state are largely accounted for by the initial state radiation.

In the structure function Monte Carlo, the momentum fractions x_1 and x_2 are generated first. The center of mass frame is then defined, and the fermion four-vectors are generated back-to-back in that frame, and boosted to the lab frame.

No photon variables are generated; effectively, all radiation is assumed collinear with the beam axis. The fact that collinear radiation accounts for the bulk of the kinematic effects ($\mu-$pair acollinearities, chiefly) make this a useful program. The absence of photon variables may hinder it in some applications. As with MMGE, final state radiation, boxes, and so forth are not presently included.

In both Monte Carlos the k_0 problems that plague first order programs are eliminated by the exponentiation of infrared photons. The value of k_0 may be pushed arbitrarily low. The structure function approach has the additional strength that the radiative corrections are explicitly decoupled from the annihilation process. This means that one may use the same program for different processes, simply by substituting the σ_0 of one's choice into Eq. (17). By the same token, beam energy spreads of arbitrary shape are easily included in this program. Both programs are expected to give negligible errors on predictions of total cross sections for fermion pairs.

6. Applications

In Section 4 we explored the consequences of a separation between soft/virtual terms and radiation terms in the Z^0 energy region. As an interesting application of the current radiative correction calculations, data on the hadronic cross section at the J/ψ resonance[23] were exhumed and refitted.

For this particular case, the beam energy spread $\sigma_E/\sqrt{2}$ is much larger than the natural width of the resonance, and a further integration over all annihilation energies should be considered. Eq.(3) becomes

$$\sigma_{obs}(s_0) = \int dk f(k, s_0) \int d(\sqrt{s}) G(\sqrt{s} - \sqrt{s_0}) \sigma_0((1-k)s).$$

The dependence of f on s is dropped in practice, and the energy distribution G is assumed to be gaussian with standard deviation σ_E. The use of such a formula as a fitting function is technically almost impossible for this particular case. On one hand, a repeated numerical evaluation of a double integral is prohibitively CPU-time consuming; on the other, the available integration algorithms do not easily allow a precise determination ($\lesssim 1\%$) of the integral, because of the almost singular shape of the cross section and of its first derivative respect to s.

It is interesting instead to use the formula given by Cahn[13] and reported in the Appendix, and check the results against the formula given by Ref. 20. In fact, these two recipes are equal but for the different treatment of the virtual terms mentioned in section 4. We checked that the formula by Cahn, integrated over the beam energy spread, was equivalent within $\approx 1\%$ to the results of the structure function Monte Carlo, which is numerically stable. The photon vacuum polarization was taken into account.

For this work we have made first a fit to the resonance using five free parameters, the branching ratio of the J/ψ into electrons B_{ee}, the mass M, the beam energy spread $\sigma_E/\sqrt{2}$, the total width Γ and the background cross section σ_{bk}. The hadronic cross section at the peak from unitarity considerations is

$$\sigma_{had} = \frac{12\pi}{M^2}\frac{\Gamma_{ee}\Gamma_{had}}{\Gamma_{tot}^2} = \frac{12\pi}{M^2}B_{ee}B_{had}. \qquad (26)$$

As a partial constraint to the fit, the sum $(2B_{ee}+B_{had})$ was set equal to one. The minimization program was observed to find three close minima ($\approx 5\%$ apart) along the hyperbola defined by

$$B_{ee}\Gamma = \Gamma_{ee} \sim \text{constant} \sim 4.8\text{keV}.$$

These two parameters, B_{ee} and Γ, could not be constrained separately without using data for e^+e^- and $\mu^+\mu^-$ final states from the same scan. The other three parameters, M, σ_E and σ_{bk} were tightly constrained. The fit performed with the algorithm of Ref. 20 behaved similarly and gave a partial width into electrons approximately equal to 4.5 keV. These numbers should not be taken as new measurements of the J/ψ leptonic width, because we did not use the leptonic data and there could be differences in the details of this analysis and that of Ref. 23; their interest is only in the comparison between the two results. The present error on Γ_{ee} is .3 keV[24], and we plan to discuss this discrepancy in a future paper. Finally, the Monte Carlo was run to produce the fit of Fig. 9 with the following parameters: $B_{ee} = .0675$, $M = 3095.02$ MeV, $\sigma_E/\sqrt{2} = .75$ MeV, $\Gamma = 71.0$ keV and $\sigma_{bk} = 21.5$nb, which correspond to the best fit obtained.

In a separate application of the J/ψ data, we may turn around the classic problem of radiative corrections to a resonance, and instead of using radiative corrections calculations to probe the resonance, use the resonance to probe the radiative corrections. The J/ψ, being much narrower than the combined beam spread and radiative spread of the beam, may be regarded as a delta function. This makes an excellent probe. We take the graph of Fig. 9, subtract the QED background, and replace the abscissa with $2E' = 2(E - E_{nominal})$. What one obtains (Fig. 10) is a mirror image of the resonance that is a precise measurement of a (new) convolution function where beam energy spread effects are taken into account,

$$f'(k,M^2) = \int dx_1 d(\Delta E_1)d(\Delta E_2) \quad D(x_1,s)D(\frac{1-k}{x_1},s)D'(\Delta E_1)D'(\Delta E_2), \quad (27)$$

where $k = 1 - x_1x_2$ and M is the resonance mass. We have assumed that $s \lesssim M^2$, so that $f(k,s)$ does not change during the scan. D' is the beam energy spread

(and can include, for example, beamstrahlung as well), and the integration must be performed on ΔE first to take into account the time ordering correctly. Comparing this with Eq. (17) we see that the cross section has dropped out after an integration over $\sqrt{s}$, as the resonance is effectively a Dirac δ-function in this case. Substitution of $f'(k,s)$ above into Eq. (3) could then be used as a test of the structure functions, as it is relatively insensitive to small changes of the J/ψ resonance parameters. Measurements of this kind could also be performed at the Υ, which is narrower and sits on a very smooth continuum. However, there beam energy spread effects are much larger because of the increased critical energy of the synchrotron radiation emitted by the beams.

7. Conclusions

We conclude that there will be no significant theoretical errors at SLC/LEP due to QED radiative corrections. We have shown that the photon bremsstrahlung is a large distortion to the Z^0 resonance because of the large effective coupling constant for a 50 GeV electron to emit a nearly collinear photon, and because the resonance is relatively narrow. We find that we can sum to all orders (exponentiate) just those terms (real photon emission) that are responsible for the line shape distortions, and the virtual corrections, calculated to second order, will mostly affect the overall normalization of the resonance, and that at a level below the expected experimental systematic error.

The ability to factorize the initial state effects from the remainder of the cross section has led to the description of the initial state radiative corrections in terms of structure functions and evolution equations. We discuss this approach and show how the structure function formalism allows us to include effects like beam spread in a natural way.

At least three papers have calculated radiative corrections using independent matrix element and structure function methods. We have directly compared these calculations and several others by using them to fit a resonance shape. The agreements and disagreements between the calculations are understood, and we find that all calculations that include exponentiation of the soft photons and virtual corrections to at least first order are adequate for the measurement of the parameters of the Z^0 resonance. We also find that the analytic fitting function derived by Cahn is suitable for fitting the data. However, an absolute precision of better than 1% everywhere around the resonance can be achieved only by including form factors and hard pieces to second order, real pairs to lowest order and soft photons to all orders, plus box diagrams and final state corrections.

We describe Monte Carlos that have been developed in the course of this work. We illustrate the use of a structure function Monte Carlo with the ability to include beam spread by refitting the J/ψ resonance.

It is a pleasure to thank R. Cahn, B. Lynn and F. Berends for many useful discussions; special thanks to S. Brodsky and L. Trentadue for illuminating the physics content of evolution equations, and to V.Luth for helping exhume the data on the J/ψ.

Appendix

In this section we collect those formulae the reader may find useful. These include the functions $A(k)$, $B(k)$, and $C(k)$ from Eq. (14), taken from reference 8; the function $f(k,s)$ from Eq. (3), taken from reference 13; the four forms of $\sigma_{obs}(s)$ used to make Fig. 3; and the function $f(k,s)$ from Eq. (3) derived from the structure function analysis of reference 3.

$A(k)$, $B(k)$, and $C(k)$ are given below:

$$\begin{aligned}
A(k) = &-\log^2\frac{s}{m_e^2}\log(1-k) + \log\frac{s}{m_e^2}\Big[Li_2(k) - \frac{1}{2}\log^2(1-k) \\
&+ \log(1-k)\log(k) + \frac{7}{2}\log(1-k)\Big] + \frac{1}{2}\log^2(1-k)\log(k) \\
&+\frac{1}{2}Li_2(k)\log(1-k) - \frac{1}{3}\log^3(1-k) + \varsigma(2)\log(1-k) - \frac{3}{2}Li_2(k) \\
&-\frac{3}{2}\log(1-k)\log(k) - \frac{17}{6}\log(1-k) + \frac{1}{6}\log^2(1-k) - \frac{1}{k}\log^2(1-k) \\
&-\frac{1}{3} - \frac{2}{3k}\log(1-k) - \frac{1}{3k^2}\log^2(1-k)
\end{aligned}$$

$$\begin{aligned}
B(k) = &\log^2\frac{s}{m_e^2}\left[\frac{1}{2}\log(1-k) - 1\right] + \log\frac{s}{m_e^2}\left[\frac{1}{4}\log^2(1-k) - \log(1-k) + \frac{7}{2}\right] \\
&+\frac{3}{2}Li_3(k) - 2S_{1,2}(k) - \log(k)Li_2(k) - \varsigma(2) + \frac{1}{6}\log^2(1-k) \\
&+\frac{1}{2}\log(1-k)\log(k) - \frac{1}{4}log^2(k) + \frac{5}{2}\log(1-k) + \frac{3}{2}\log(k) - \frac{1}{6}
\end{aligned}$$

$$\begin{aligned}
C(k) = &2\log^2\frac{s}{m_e^2} + \log\frac{s}{m_e^2}\left[\log(1-k) - \frac{13}{2}\right] + \frac{16}{3}\varsigma(2) \\
&-\frac{25}{6}Li_2(k) - \frac{13}{12}\log^2(1-k) - 4\log(1-k)\log(k) \\
&+\frac{3}{2}\log^2(k) - \frac{5}{6}\log(1-k) - \frac{15}{6}\log(k) - \frac{2}{3}
\end{aligned}$$

The polylogarithms, $Li_j(k)$, and Spence functions, $S_{1,2}(k)$ are defined in the first paper of reference 4.

The form of $\sigma_{obs}(s)$ given in reference 13 is given below in the notation of this paper.

$$\sigma_{obs}(s) = \sigma_Z(1+\delta_1)\frac{\Gamma_Z^2}{\Gamma_Z^2+M_Z^2}\left[\frac{s}{M_Z^2}a^{\beta-2}\Phi(\cos\theta,\beta) - a^{\beta-1}\frac{\beta}{1+\beta}\Phi(\cos\theta,1+\beta)\right]$$

$$-\sigma_Z\beta\frac{\Gamma_Z}{\sqrt{s}}\left[\tan^{-1}\frac{2M_Z}{\Gamma_Z} - \tan^{-1}\frac{2(M_Z-\sqrt{s})}{\Gamma_Z}\right]$$

In this equation we make the approximation $\delta_1 \approx \frac{3}{4}\beta$. The quantities a, $\cos\theta$, and $\Phi(\cos\theta,\beta)$ are defined as follows:

$$a^2 = \frac{M_Z^2(s/M_Z^2-1)^2 + \Gamma_Z^2(s/M_Z^2)^2}{\Gamma_Z^2+M_Z^2}$$

$$\cos\theta = -\frac{M_Z^2(s/M_Z^2-1) + \Gamma_Z^2(s/M_Z^2)}{a(\Gamma_Z^2+M_Z^2)}$$

$$\Phi(\cos\theta,\beta) = \frac{\pi\beta\sin((1-\beta)\theta)}{\sin\pi\beta\sin\theta}$$

The following four equations give $\sigma_{obs}(s)$ for four different levels of radiative correction, corresponding to the four curves in Fig. 3.

Pure first order:

$$\sigma_{obs}(s) = \sigma_0(s)(1+\delta_1+\beta\log k_0) + \int_{k_0}^{1}\beta(\frac{1}{k}-1+\frac{k}{2})\sigma_0(s')dk.$$

As noted earlier, $s' = s(1-k)$. The Born cross section, $\sigma_0(s)$, is given in Eq. (1).

First order with exponentiation:

$$\sigma_{obs}(s) = \sigma_0(s)(1+\delta_1)k_0^\beta + \int_{k_0}^{1}\beta(k^{\beta-1}(1+\delta_1)-1+\frac{k}{2})\sigma_0(s')dk.$$

Pure second order:

$$\sigma_{obs}(s) = \sigma_0(s)(1+\delta_1+\delta_2+\beta\log k_0+\delta_1\beta\log k_0+\frac{1}{2}\beta^2\log^2 k_0)+$$

$$\int_{k_0}^{1}\sigma_0(s')\left[\beta\left(\frac{1}{k}-1+\frac{k}{2}\right)(1+\delta_1+\beta\log(k))\right.$$

$$\left.+(\frac{\alpha}{\pi})^2\left(\frac{1+(1-k)^2}{k}A(k)+(2-k)B(k)+(1-k)C(k)\right)\right]dk$$

Second order with exponentiation:

$$\sigma_{obs}(s) = \sigma_0(s)(1+\delta_1+\delta_2)k_0^\beta + \int_{k_0}^{1}\sigma_0(s')\left[\beta\left(k^{\beta-1}(1+\delta_1+\delta_2)-1+\frac{k}{2}\right)\right.$$

$$\left.+(\frac{\alpha}{\pi})^2\left(\frac{1+(1-k)^2}{k}A(k)+(2-k)B(k)+(1-k)C(k)\right)\right]dk$$

Finally, we give the expression for the $f(k,s)$ in Eq. (3) as given by the structure function analysis of reference 3.

$$f(k,s) = \beta k^{\beta-1}\left[1+\delta_1-\frac{\beta^2}{24}(\frac{1}{3}\log\frac{s}{m_e^2}+2\pi^2-\frac{37}{4})\right] - \beta(1-\frac{1}{2}k)$$

$$+\frac{1}{8}\beta^2\left[-4(2-k)\log k - \frac{(1+3(1-k)^2)}{k}\log(1-k) - 6 + k\right]$$

$$+(\frac{\alpha}{\pi})^2\left\{\frac{1}{6k}(k-\frac{4m_e}{\sqrt{s}})^\beta\left(\log(\frac{sk^2}{m_e^2})-\frac{5}{3}\right)^2\left(2-2k+k^2+\frac{1}{3}\beta\left(\log(\frac{sk^2}{m_e^2})-\frac{5}{3}\right)\right)\right.$$

$$\left.+\frac{1}{2}\log^2\frac{s}{m_e^2}\left[\frac{2(1-(1-k)^3)}{3(1-k)}+(2-k)\log(1-k)+\frac{1}{2}k\right]\right\}\theta(k-\frac{4m_e}{\sqrt{s}})$$

REFERENCES

1. MarkII Coll. and SLC Final Focus Group, SLAC-SLC-PROP-2(1986).
2. MarkII Proposal for SLC, SLAC-PUB 3561.
3. E.A.Kuraev and V.S.Fadin, SJNP 41(3) 466, 1985.
4. R. Barbieri, J.A. Mignaco and E. Remiddi, Nuovo Cim. 11A:824, 1972; G.J.H.Burgers, PL 164B:167, 1985.
5. T. Kinoshita, J. Math. Phys. 3:650, 1962; T.D. Lee and M. Nauenberg, Phys. Rev. 133B:1549, 1964.
6. See for example B.W.Lynn, M.E.Peskin and R.G.Stuart, SLAC-PUB-3725.
7. J. Alexander *et al.*, SLAC-REP-306, pag. 45.
8. F.A.Berends, G.J.H.Burgers and W.L.Van Neerven, PL 185B: 395, 1987.
9. G.Altarelli and G.Martinelli, CERN/EP 86-02, pag. 47.
10. O. Nicrosini and L. Trentadue, UPRF-86-132.
11. The δ_2 given in the text (Eqn. (11)) is from Ref. 10, where real and virtual pairs are consistently ignored throughout the paper. Ref. 8 includes virtual pairs but not real pairs, thereby generating a term proportional to $\alpha^2 \log^3(\frac{s}{m_e^2})$ as well as affecting the coefficients of the terms proportional to $\alpha^2 \log^n(\frac{s}{m_e^2})$, where $n = 0, 1, 2$. Ref. 3 consistently adds real and virtual pairs, resulting in a cancellation of the $\alpha^2 \log^3(\frac{s}{m_e^2})$ term in $D_{ee}(x, s)$.
12. D.R.Yennie, S.C.Frautschi and H.Suura, Ann. of Phys. 13:379, 1961.
13. R.N.Cahn, LBL-22601.
14. L.N.Lipatov, SJNP 20:94, 1975.
15. L.N.Lipatov and V.N.Gribov, SJNP 15:438, 1972.
16. J.Kogut and L.Susskind, Phys.Rep. 8:75, 1973.
17. G.Altarelli and G.Parisi, NPB 126:298, 1977.
18. F.A.Berends, R.P.Kleiss and S.Jadach, NP B202:63, 1982; Comp. Phys. Comm. 29:185 1983.
19. Y.L.Dokshitser, D.I.Dyakonov and S.I.Troian, Phys. Rep. 58:269, 1980.
20. J.D.Jackson and D.L.Scharre, NIM 128:13, 1975.
21. B.W.Lynn, G. Penso and C. Verzegnassi, PRD 35: 42, 1987; F. Jegerlehner, Z. Phys.C 32: 195, 1986.
22. M. Greco, CERN/EP 86-02, pag. 186.
23. A. M. Boyarski *et al.*, PRL 34:1357, 1975.
24. Particle Data Book, PL 170B, 1986.

TABLE CAPTIONS

1. Accuracy of various levels of approximation on the fit parameters M_Z, Γ_Z, and σ_Z relative to the exponentiated second order calculation of Ref. 8. δQ, with $Q = M_Z$, Γ_Z, or σ_Z, is defined as $Q - Q_8$, where Q_8 is from Ref. 8.
2. Comparison of cross section values, stated as a percent deviation from the cross section of Ref. 8.
3. Results of comparing different calculations for extraction of M_Z, Γ_Z, and σ_Z given data generated by Ref. 8. The differences are defined as in Tab. 1.

Table 1

Fitting Function	δM_Z (MeV/c^2)	$\delta\Gamma_Z$ (MeV)	$\frac{\delta\sigma_Z}{\sigma_Z}$ (%)
1st order	−121	−152	5.63
Exp. 1st order	1	2	−0.54
2nd order (Ref. 8)	14	12	−0.11

Table 2

Fitting	$\frac{\delta\sigma_Z}{\sigma_Z}$ (%) at $\sqrt{s}$ (GeV) =			
Function	91	93	95	97
Berends, *et al* (Ref. 8)	–	–	–	–
Jackson and Scharre (Ref. 20)	4.56	4.31	−0.098	−3.07
Cahn (Ref. 13)	−0.670	−0.034	−0.156	−0.681
Trentadue and Nicrosini (Ref. 10)	0.019	0.025	−0.051	−0.203
Fadin and Kuraev (Ref. 3)	< 0.001	0.003	0.017	0.014

Table 3

Fitting Function	δM_Z (MeV/c^2)	$\delta\Gamma_Z$ (MeV)	$\frac{\delta\sigma_Z}{\sigma_Z}$ (%)
Berends, *et al* (Ref.8)	–	–	–
Jackson and Scharre (Ref.20)	35	69	−4.45
Cahn (Ref.13)	−0.2	8.9	−0.01
Trentadue and Nicrosini (Ref.10)	1.1	1.4	−0.84
Fadin and Kuraev (Ref.3)	< 0.1	0.2	−0.01

FIGURE CAPTIONS

1. Lowest order diagrams for the process $e^+e^- \to f\bar{f}$.
2. Diagrams for the first order correction.
3. The Z^0 line shape with various levels of radiative corrections. Dashed curve: first order. Dotted curve: first order with exponentiation. Dot-dash curve: second order. Solid curve: second order with exponentiation.
4. An electron-photon cascade of the sort described by structure functions.
5. Diagrams of real pair emission.
6. A lowest order virtual correction incorporated in δ_1.
7. Photon bremsstrahlung down to a resonance. In this case the virtual correction has a relatively large effect on the overall cross section.
8. Forward-backward asymmetry as a function of $\sqrt{s}$ for levels of correction. Dotted curve: lowest order; dashed curve: first order; solid curve: second order with exponentiation.
9. The J/ψ resonance shape from Ref. 23. The fit has been obtained using one of the Monte Carlos described in the text.
10. The function $f'(k,s)$ as measured in Ref. 23.

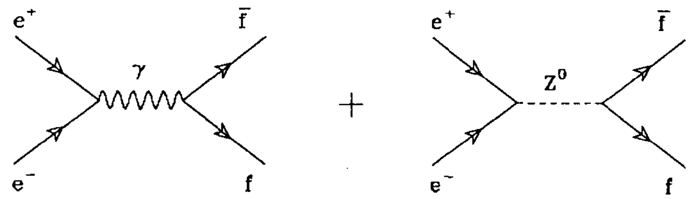

Fig. 1

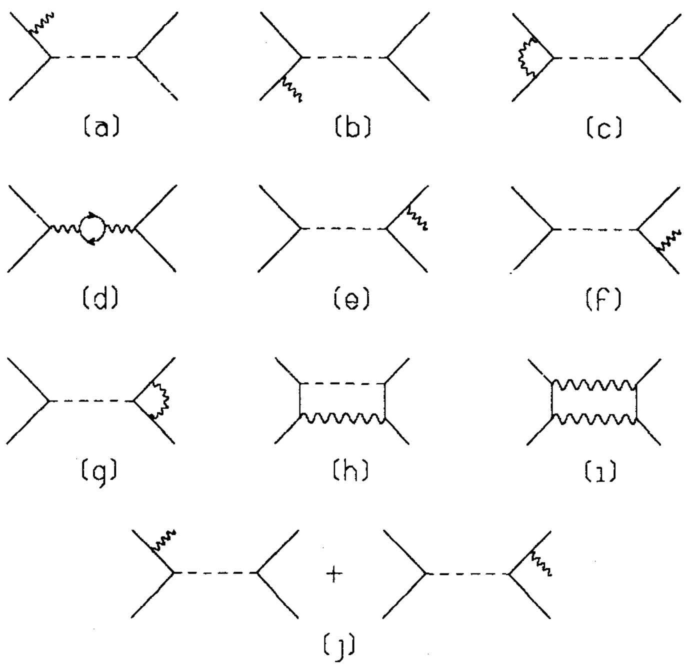

Fig. 2

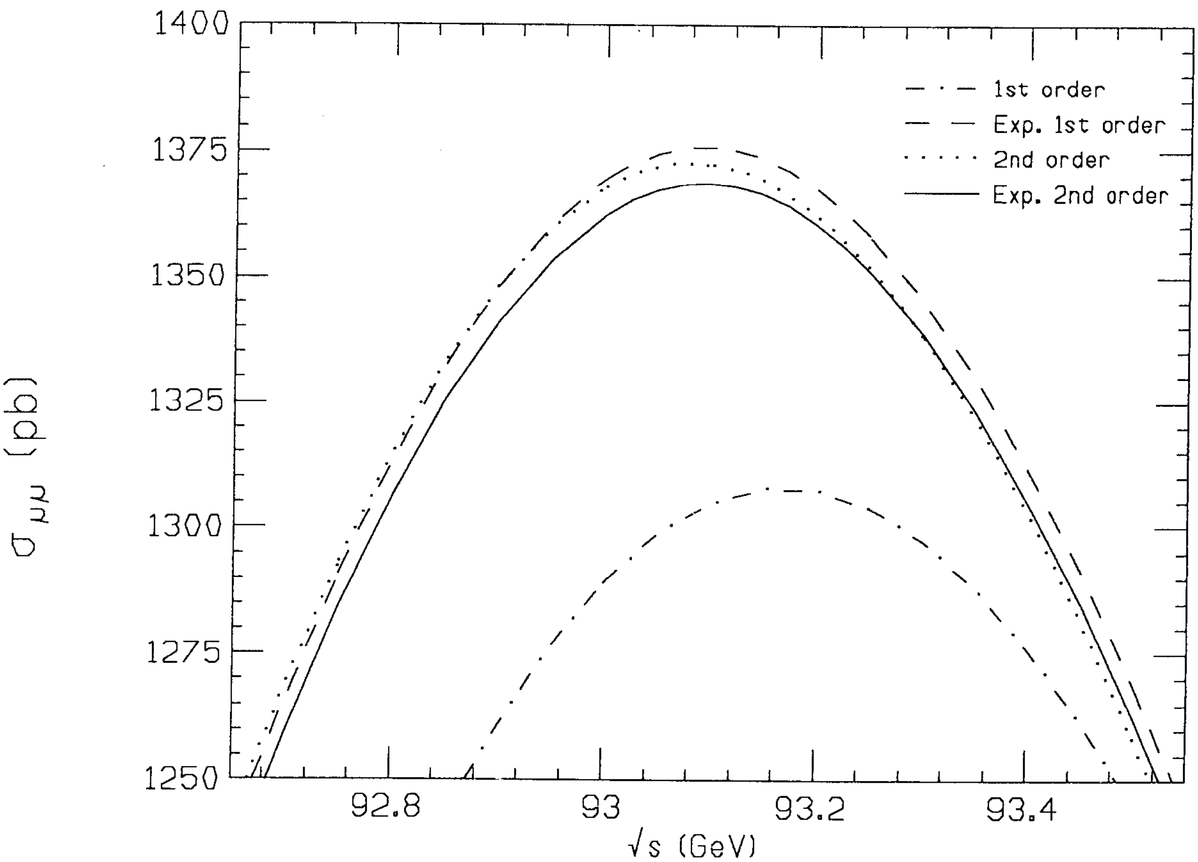
1400
1375
1350
1325
1300
1275
1250
$\sigma_{\mu\mu}$ (pb)
92.8
93
93.2
93.4
$\sqrt{s}$ (GeV)
1st order
Exp. 1st order
2nd order
Exp. 2nd order

Fig. 3

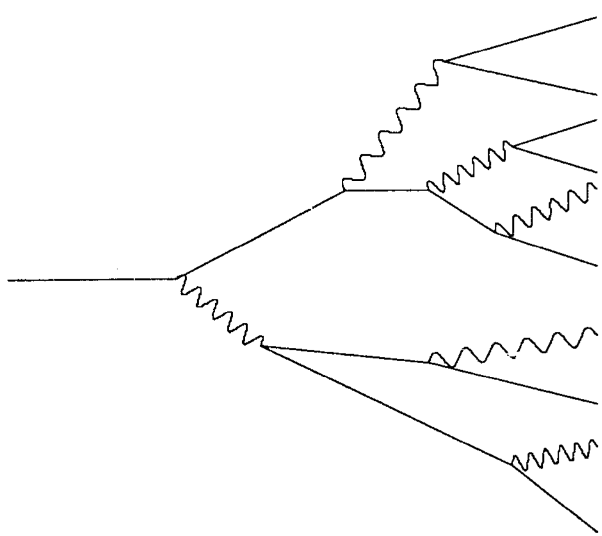

Fig. 4

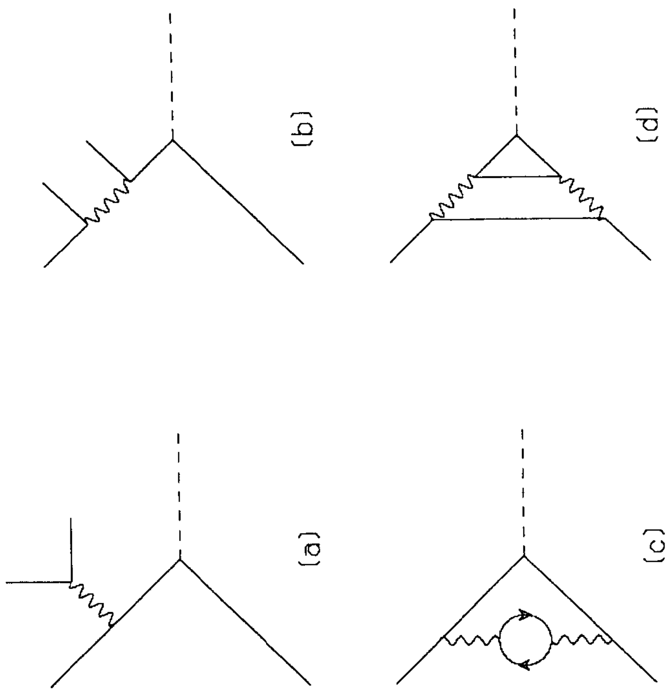

Fig. 5

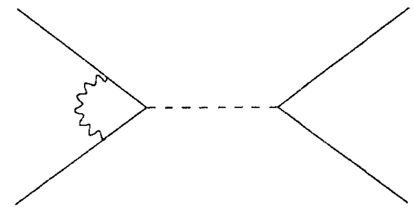

Fig. 6

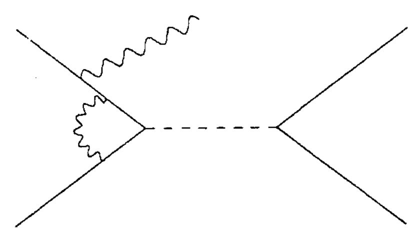

Fig. 7

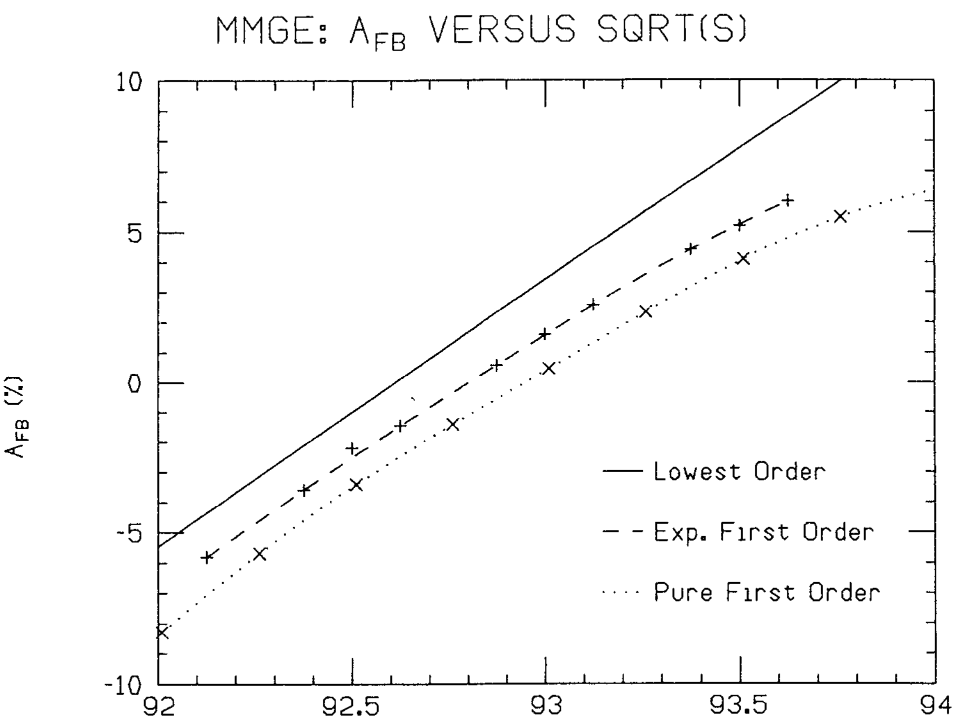
MMGE: A_{FB} VERSUS SQRT(S)
A_{FB} (%)
10
5
0
-5
-10
92
92.5
93
93.5
94
SQRT(S)
Lowest Order
Exp. First Order
Pure First Order

FIG. 8

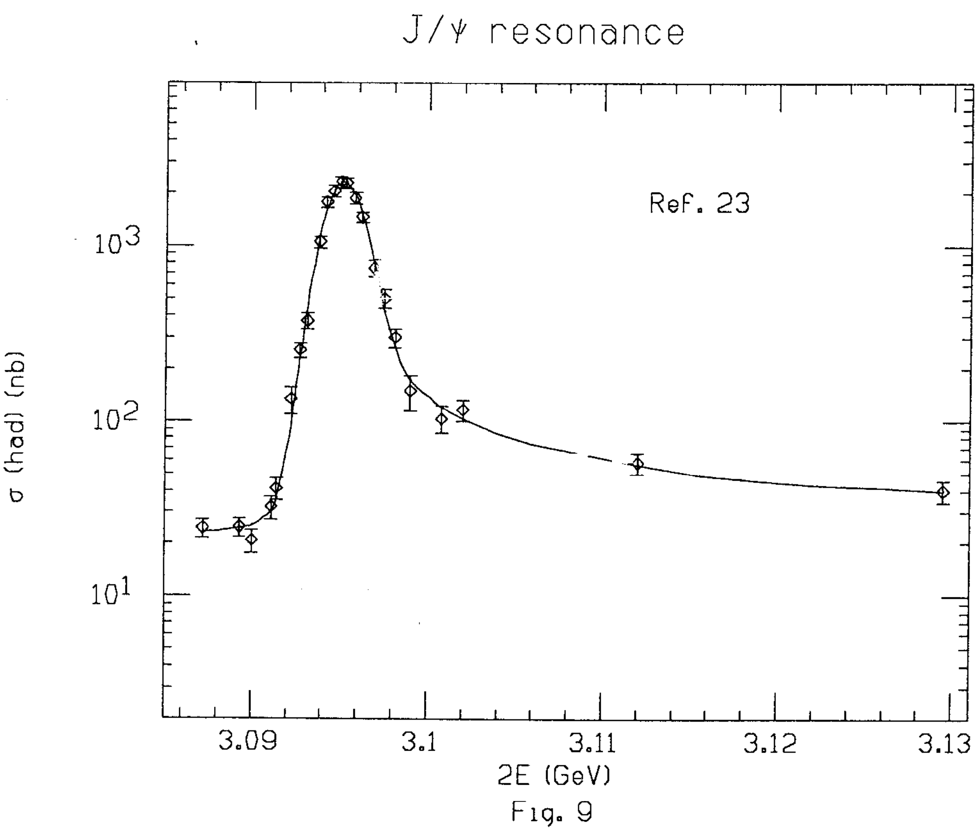
J/ψ resonance
σ (had) (nb)
10^3
10^2
10^1
Ref. 23
3.09
3.1
3.11
3.12
3.13
2E (GeV)

Fig. 9

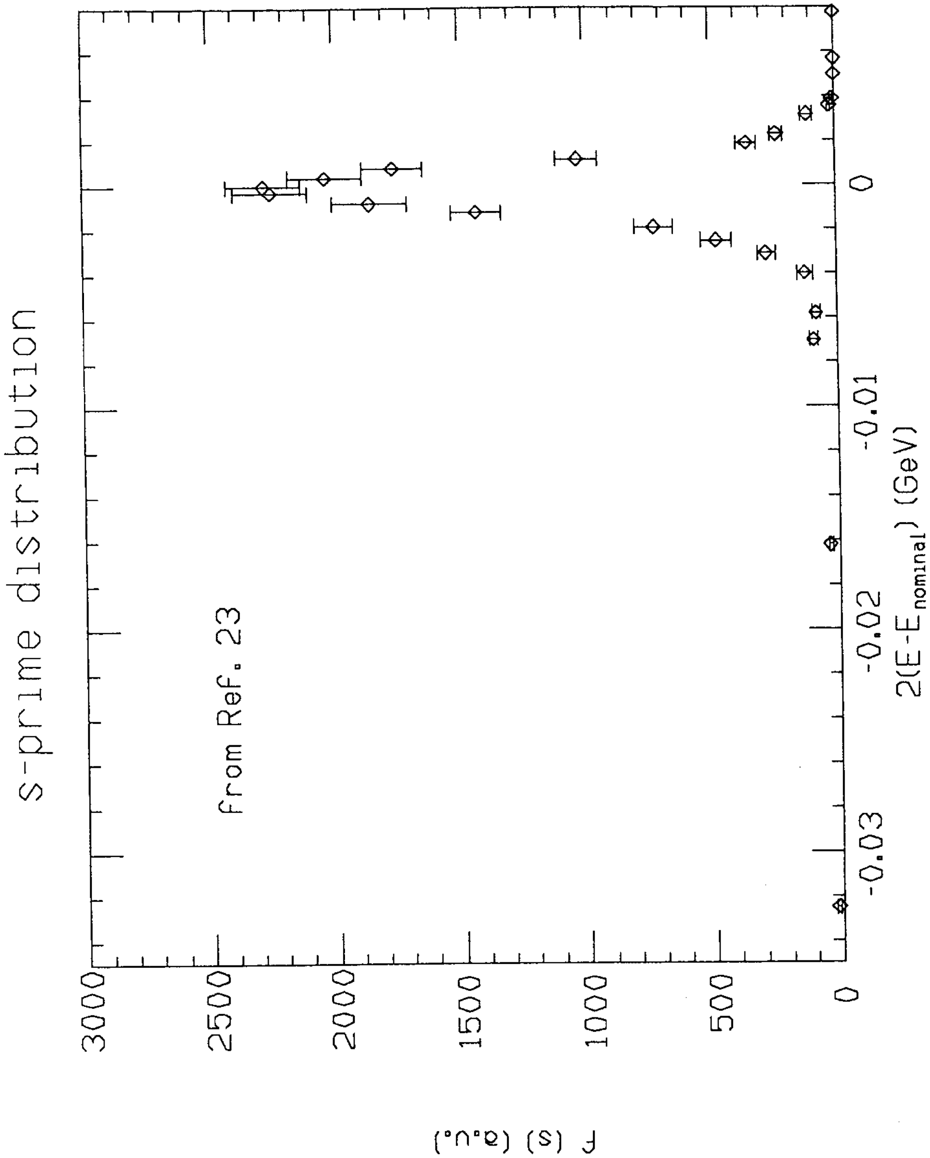
s-prime distribution
from Ref. 23
3000
2500
2000
1500
1000
500
0
f (s) (a.u.)
-0.03
-0.02
-0.01
0
2(E-E$_{nominal}$) (GeV)

Fig. 10

MARK II/SLC-Physics Working Group Note #2 - 22
Author: John Matthews
Date: April 10, 1987
Title: Mark II/SLC Luminosity Measurements

I. Introduction:

The luminosity requirements for Z0 physics have been studied for a number of the major Mark II/SLC physics topics. For at least some of the physics, the luminosity should be measured with an absolute precision better than 2%, and any systematic dependance of the luminosity on the beam energy should be less than 1% "across the Z0". These requirements are reviewed in Section II. The Mark II/SLC luminosity monitors are presented in Section III, as well as the results of the analyses of the systematic uncertainties in the luminosity measurements. Finally, the results are summarized in Section IV. The people contributing to this work are given in Ref. 1.

II. Precision Requirements for Luminosity Measurements for Z0 Physics:

It is useful to review the luminosity requirements for a number of Z0 physics topics. For this discussion I have chosen: the left-right polarization asymmetry denoted A(L-R), neutrino counting using the radiative annihilation channel, the measurement of the Z0 mass and width, and finally the measurement of the hadronic and mu-pair cross sections. The required precision from the luminosity measurement is as follows:

1) A(L-R):

For the measurement of A(L-R), the luminosity monitoring must be stable in time (at least over short time intervals) and should have equal sensitivity to left and right handed electrons. These requirements are "minimal" for a small angle Bhabha luminosity system.

2) e+e- —> $\nu\bar{\nu}\gamma$:

The uncertainty in the luminosity should be small in comparison to the "expected" statistical precision of about 6% for the neutrino counting experiment, Ref. 2.

3) Z0 mass and width:

The Z0 mass and width measurement is insensitive to the absolute luminosity, however systematic dependences on the center of mass energy should be less than 1% for a center of mass energy variation of plus or minus one Z0 width; see Ref. 3.

4) Hadronic and mu-pair cross sections:

The mu-pair cross section can be used to make precision "measurements" of interesting quantities including: leptonic neutral current couplings, and/or the Z0 total width. The determination of the Z0 total width using the mu-pair cross section, at root(s) = M(Z0), is sketched in Fig. 1. Since the Z0 width will be determined to a precision of about 1% by an energy scan over the peak, Ref. 4, any other measurement should achieve a similar precision. To achieve this using the mu-pair cross section requires a 2% luminosity measurement, and 1% would be desirable.

Similar measurements can be done with limited integrated luminosity, and thus early in the Mark II program, using the hadronic cross section. In comparison to measurements using the mu-pair cross section, measurements using the hadronic cross section will have larger "theoretical uncertainties" as well as possible model dependences. As an example, a determination of the total Z0 width into "neutrinos" is shown in Fig. 2. The results depend on the assumed unknown top mass (model dependance), and include a 2% "theoretical uncertainty" from the calculation of the hadronic width of the Z0. Also included in this calculation is a 2% systematic uncertainty from the luminosity measurement as well as an additional 2% systematic from other quantities in the hadronic cross section determination.

In summary, cross section measurements typically require absolute luminosity measurements with a precision better than, or about, 2%.

III. Mark II Luminosity Measurements:

The Mark II/SLC luminosity will be measured using small angle Bhabhas in the Small Angle Monitor, SAM, and in the mini-Small Angle Monitor, miniSAM. The SAM covers the angular region of approximately 50 mrad to 150 mrad and includes precision charged particle tracking and calorimetry. The miniSAM covers the angular region of 15 mrad to 25 mrad and only includes calorimetry. For more details see recent notes on the SAM, Ref. 5, and on the miniSAM, Ref. 6.

To obtain a luminosity measurement with a systematic uncertainty less than 2% is nontrivial. Contributions to the uncertainty come from the luminosity monitor system "acceptance" and from the calculation of the "accepted" Bhabha cross section. These will be discussed in the following subsections.

1) Acceptance Issues:

The lowest order cross section for Bhabha scattering is given by:

$$\sigma_{LO} = \frac{16\pi\alpha^2}{s}\left(\frac{1}{\theta^2_{min}} - \frac{1}{\theta^2_{max}}\right)$$

where theta(min) and theta(max) are the angular acceptance limits for the luminosity monitors. For an uncertainty in the accepted cross section of less than 1%, theta(min) must be known to better than 0.075 mrad (miniSAM) and 0.25 mrad (SAM). This corresponds to a systematic

spacial uncertainty of less than 150 microns radially (miniSAM) and 350 microns radially (SAM). Baring alignment problems, the tungsten collimators used by the miniSAM should permit the miniSAM to meet this tolerance, Ref. 6. This is also the case for the SAM where the wire placement is known to better than 150 microns, Ref. 7.

Luminosity monitor systems should be insensitive to beam motion, and should be self monitoring. The procedures for minimizing the dependance of the luminosity on varying beam conditions have been discussed in the literature, Ref. 8 and previously in the Mark II/SLC Physics Workshops, Ref. 9. The SAM, with precision charged particle tracking, uses "fiducial regions" in the data analysis to achieve this. As a result, the contribution to the systematic uncertainty in the luminosity from beam variation should be less than 1%. For the miniSAM to be insensitive to transverse motion of the beam, the acceptance collimators have been designed to have a different acceptance aperture for outgoing (scattered) e+ and e−. This design compromise, dictated by spacial constraints, means that the miniSAM has some sensitivity (at the < 3% level dominated by e+/e− energy inequalities) to motion of the interaction point along the beam line and/or to inequalities in the e+ and e− energies. However, the pulse by pulse monitoring of the beam energies should allow the miniSAM luminosity to be corrected to the 1% level.

Systematic uncertainties in the SAM and miniSAM luminosity as a function of center of mass energy are expected to be below the 1% level. Possible sources of energy dependant systematic errors that have been considered include the following:

a) variation with center of mass energy of the relative energy of the e+ and e− beams (for example the miniSAM luminosity requires an explicit correction, and the SAM acceptance will be altered slightly due to changes in the e+/e- acolinearity angles),

b) variation with energy of detector backgrounds (for example synchrotron radiation backgrounds into the miniSAM),

c) variation with time of the detector performance due to radiation damage or component failure,

d) incorrect correction for the small (< 1%) contribution from the Z0 to the Bhabha cross section in the SAM, and

e) e+ and e- multiple scattering in the material before the SAM.

Studies of the accepted Bhabha cross section as a function of the detector energy cuts and acolinearity cuts are continuing. In the SAM the charged particle tracking and fine calorimeter segmentation are important aids in understanding the effects of Bhabha event selection "cuts" on the determination of the luminosity. The preliminary results are consistent with a systematic error in the luminosity less than 1% for "loose" data cuts. For example a possible Bhabha selection criteria in the SAM includes e+/e- energies greater than 1/2 the beam energy and e+/e- acolinearity angle less than 10 mrad.

2) Bhabha Cross Section:

The Bhabha monitoring cross section should be known to better than 1% for experiments at the Z0. This requires a QED calculation with the required precision that has been thoroughly checked, preferably with experimental data. Fortunately, Bhabha scattering at small angles is dominated by photon exchange. Thus, the extensive experience with Bhabha Monte Carlo programs at lower energies can be carried over to the SLC. Four order "alpha-cubed" Monte Carlos are studied in Ref. 10. The results are as follows:

a) The "soft" cross sections (that is the cross section including all virtual corrections and real photon emission below 1% of the e+/e-

energy) are found to agree to 5-figures once the same vacuum polarization calculation is used in each program.

b) The "hard" cross sections (that is for the three body e+ e- gamma final state) are consistent with being the same. However at this time these comparisons have only been made at the 1% level, limited by Monte Carlo statistics.

A review of the vacuum polarization calculations indicates that the exact calculation should be used for the leptonic contributions; see for example Ref. 11. The parameterization of the hadronic contribution to the vacuum polarization by Burkhardt, Ref. 12, is in good agreement with other determinations, see Fig. 3a, 3b and Ref. 13, and is recommended for use at this time.

Although the existing Bhabha Monte Carlos agree well in the angular region of the miniSAM and SAM luminosity monitors, and have been well tested at PEP and PETRA energies, the cross sections may not be accurate at the 1% level. Order "alpha-forth" Bhabha Monte Carlos, and order "alpha-cubed" Monte Carlos with exponentiation are needed to determine that the accepted cross sections are "stable" to better than 1%.

IV. Summary:

A review of the luminosity requirements of a number of the major measurements at the Z0 indicate that the luminosity should be known to an absolute precision better than 2% and with a systematic energy dependance of less than 1% "across the Z0 energy region". Present estimates and studies indicate that this should be possible for the SAM, and could be possible for the miniSAM luminosity monitors. The calculation of the "accepted" Bhabha cross section requires order "alpha-forth" Monte Carlos or equivalent.

References:

1) The people working on luminosity measurements in the Mark II, or on the Bhabha Monte Carlo programs include: B. Barnett, G. Bonvicini, J. Chapman, R. Frey, B. Harral, C. Hawkes, J. Hylen, J. Matthews, D. Nitz, M. Petradza, D. Stoker, and R. Thun.

2) R. Thun, Proceedings of the Mark II/SLC Physics Workshop, Granlibakken, SLAC-Report 306 (1986).

3) D. Bannon and J. Kent, Mark II/SLC Working Group Note #1-8 (1986); A. Blondel, F. Dydak, A. Para, and W. Blum, Physics at LEP, Vol. I, 35, CERN 86-02 (1986).

4) M. Levi, Proceedings of the Mark II/SLC Physics Workshop, Granlibakken, SLAC-Report 306 (1986).

5) M. Petradza, R. Thun, G. Bonvicini, J. Chapman, R. Frey, J. Hylen, J. Matthews, and D. Nitz, Mark II/SLC Note #164 (1986).

6) D. Stoker, B.A. Barnett, B.D. Harral, J. Hylen, and J.A.J. Matthews, Mark II/SLC Note #150 (1986); Mark II/SLC Note #152 (1986).

7) R. Thun, private communication.

8) J. Crawford et. al., NIM 127, 173 (1975); B. Heltsley, Thesis (1983).

9) J. Matthews, Mark II/SLC Physics Workshop, Asilomar (1986).

10) J. Matthews, Mark II/SLC Working Group Note #2-13 (1986).

11) F.A. Berends and R. Gastmans, Electromagnetic Interactions of Hadrons, Vol II, Eds. A. Donnachie and G. Shaw, 471 (1978).

12) H. Burkhardt, Tasso Note #192 (1981). This analysis is used by the HOWLEEG Monte Carlo, see Fig. 3b.

13) F.A. Berends and G.J. Komen, Phys. Lett. 63B, 432 (1976); B.W. Lynn, G. Penso, and C. Verzegnassi, SLAC-PUB-3742 (1985).

Figures:

1) Use of the mu-pair cross section at root(s)=M(Z0) to determine the Z0 total width.

2) Use of the hadronic cross section to determine the total width for Z0 decays into "neutrinos" as a function of the top mass. The errors, discussed in the text, correspond to an integrated luminosity of 200/nb.

3) Hadronic contribution to the vacuum polarization from Ref. 13. In a) are shown the comparison of the determinations by Lynn et al, Berends and Komen, and by Paschos. In b) the hadronic vacuum polarization calculations used by three Bhabha Monte Carlo programs are compared to the analysis of Lynn et al. For a description of the Monte Carlo programs see Ref. 10.

$\sigma_{\mu\mu}$ "CLEAN" TEST OF E-W MODEL

$$\sigma_{\mu\mu}(\sqrt{s}=M_Z) = \frac{4\pi\alpha^2}{3M_Z^2} + \frac{G_\mu^2 M_Z^4}{96\pi\Gamma_Z^2}(v_e^2+a_e^2)(v_\mu^2+a_\mu^2)$$

THEN (FOR EXAMPLE):

$$\Gamma_Z = \frac{G_\mu M_Z^2 (v^2+a^2)_{e,\mu}}{\sqrt{96\pi(\sigma_{\mu\mu}-\sigma_{\mu\mu}^{QED})}}$$

WHERE $\delta\Gamma_Z/\Gamma_Z$ TOTALLY DOMINATED BY $\delta\sigma_{\mu\mu}/\sigma_{\mu\mu}$.

$$\frac{\delta\Gamma_Z}{\Gamma_Z} \sim \frac{1}{2}\sqrt{\frac{1}{N_{\mu\mu}}+\frac{1}{N_{BHABHA}}+\left(\frac{\delta\sigma_{\mu\mu}}{\sigma_{\mu\mu}}\right)^2_{\substack{\text{RAD.}\\ \text{CORR.}\\ \text{SYSTEMATIC}}}+\left(\frac{\delta\mathcal{L}}{\mathcal{L}}\right)^2_{\text{SYSTEMATIC}}}$$

∴ TO ACHIEVE $\delta\Gamma_Z/\Gamma_Z \sim 1\%$ REQUIRES $\left(\delta\mathcal{L}/\mathcal{L}\right)_{\text{SYSTEMATIC}} < 2\%$.

Fig. 1: Use of the mu-pair cross section at root(s)=M(Z0) to determine the Z0 total width.

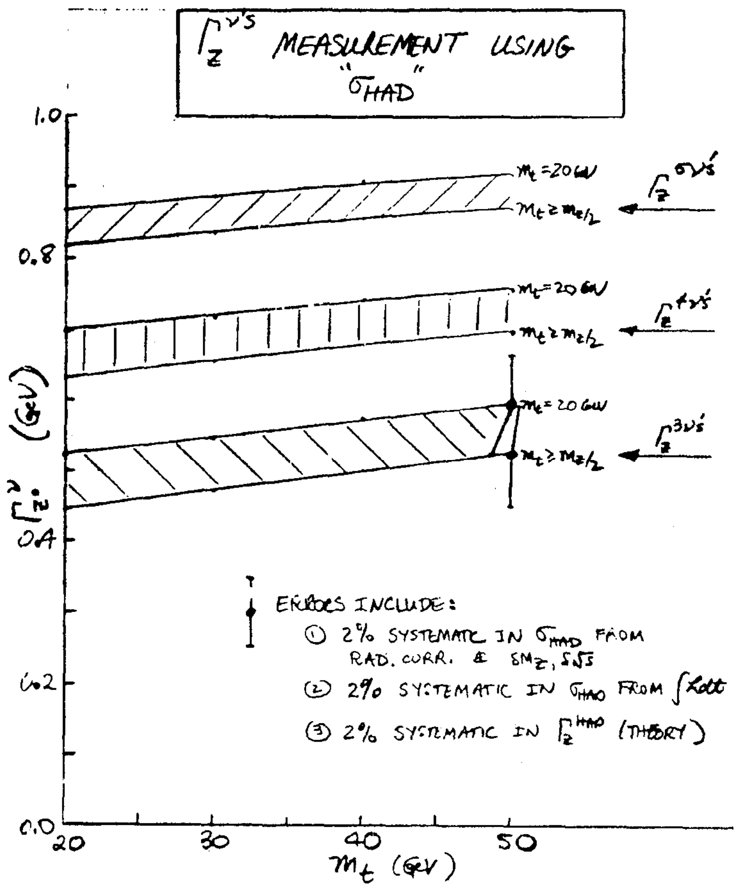

Fig. 2: Use of the hadronic cross section to determine the total width for Z0 decays into "neutrinos" as a function of the top mass. The errors, discussed in the text, correspond to an integrated luminosity of 200/nb.

HADRONIC CONTRIBUTION TO VACUUM POLARIZATION

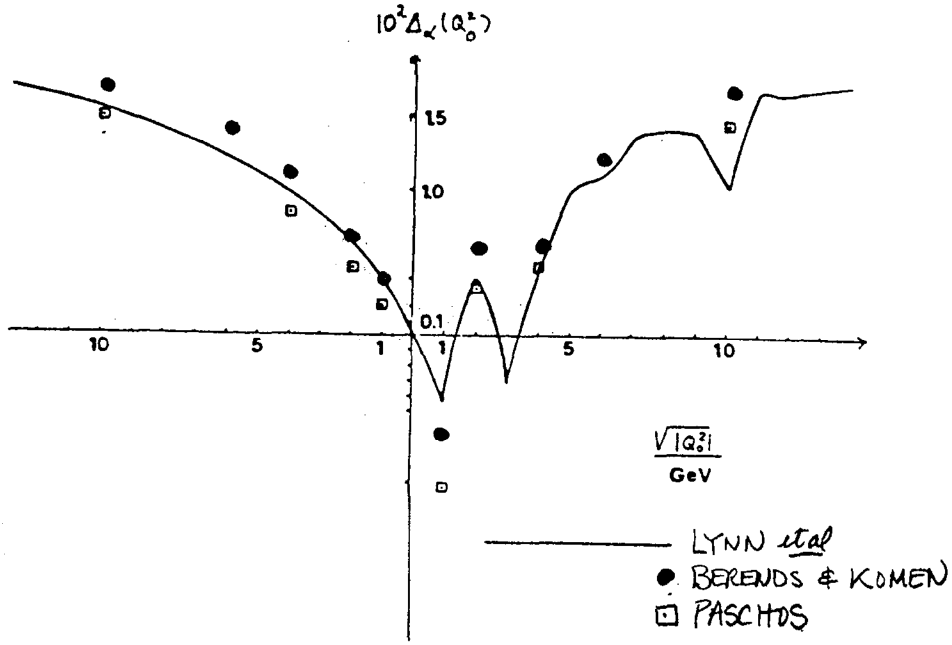

Fig. 3a: Hadronic contribution to the vacuum polarization from Ref. 13. This figure compares the determinations by Lynn et al, Berends and Komen, and by Paschos.

HADRONIC CONTRIBUTION TO VACUUM POLARIZATION

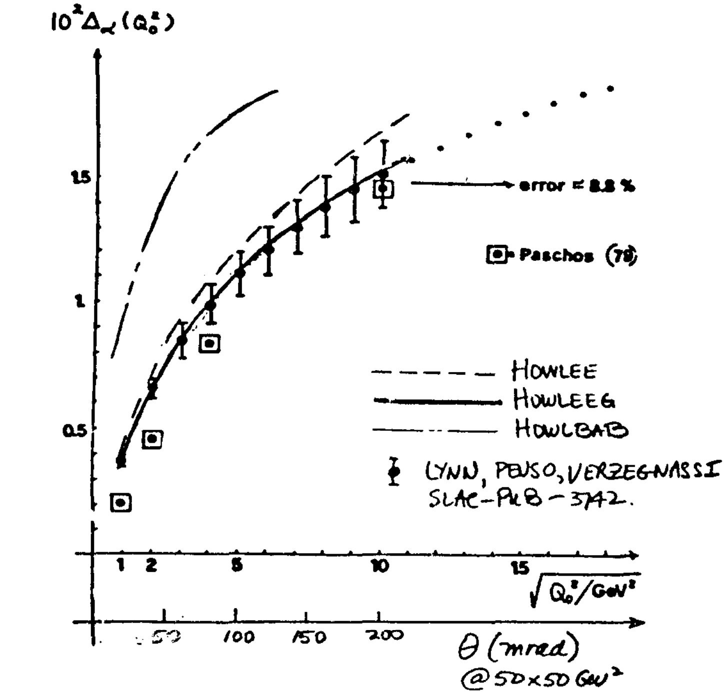

Fig. 3b: Hadronic contribution to the vacuum polarization from Ref. 13. This figure compares the hadronic vacuum polarization calculations used by three Bhabha Monte Carlo programs to the analysis of Lynn et al. For a description of the Monte Carlo programs see Ref. 10.

Mark II/SLC-Physics Working Group Note # 2–23

AUTHOR: Gary Feldman

DATE: June 7, 1987

TITLE: Measurement of the Total Hadronic Cross Section

Introduction

The message of this note is simple. It is to point out that at the SLC we should be able to measure the total hadronic cross section with very high efficiency, and thus with very small systematic error.

Motivation

We want to measure the total hadronic cross section very accurately for several reasons:

1. R' on the Z is just like R in the continuum — it measures the visible particle content of Z decays and is a basic test of QCD. On the Z peak (or for that matter on any resonance), the cross section for producing any state x is given by

$$\sigma_x = \frac{12\pi}{m_Z^2}\frac{\Gamma_{ee}\Gamma_x}{\Gamma_{tot}^2}. \tag{1}$$

The width to any state x is given to first order by

$$\Gamma_x = \frac{G_F\, m_Z^3}{24\sqrt{2}\,\pi}\,(v_x^2 + a_x^2), \tag{2}$$

where v_x and a_x are the vector and axialvector coupling constants for the state x. Using Eqs. (1) and (2) we have

$$R' \equiv \frac{\sigma_{had}}{\sigma_{\mu\mu}} = \frac{\sum_i (v_{q_i}^2 + a_{q_i}^2)(1+\frac{\alpha_s}{\pi})}{v_\mu^2 + a_\mu^2}, \tag{3}$$

where the summation is over all quark colors and flavors. Note that

(a) R' has no dependence on the luminosity measured by Bhabha scattering at small angles.

(b) With loose cuts on the $\mu^+\mu^-$ final states, most of the radiative corrections cancel.

(c) For the Mark II running, the limiting precision will probably be given by the statistics on the muon pairs (plus electron and τ pairs, which can also be used). For 100,000 Z events, the statistical error will be about 1%, which, as we will argue below, should be larger or comparable to the systematic error from the hadronic measurement.

2. We need Γ_{had} to measure the invisible particle content of Z decay:

$$\Gamma_{invis} = \Gamma_{tot} - \Gamma_{vis}, \tag{4}$$

where

$$\Gamma_{vis} = \Gamma_{ee} + \Gamma_{\mu\mu} + \Gamma_{\tau\tau} + \Gamma_{had}. \tag{5}$$

Thus Eq. (4) can be written

$$\Gamma_{invis} = \Gamma_{tot} - (R' + 3)\Gamma_{\mu\mu}. \tag{6}$$

Γ_{tot} can be determined either from a direct measurement or from a measurement of $\sigma_{\mu\mu}$, using Eq. (1). The latter approach appears to be superior due to a fortuitous cancellation of statistical errors.* It, however, is sensitive to a measurement of absolute luminosity, while the former approach does not depend on this measurement. In either case it is desirable to keep the systematic error on σ_{had} to the level of about 1% so that it will not contribute significantly to the overall error.

Sources of Error

What are the sources of error in measuring the total hadronic cross section (other than the determination of luminosity)?

1. The knowledge of the efficiency. We always have to use a Monte Carlo model of the production of hadronic events to evaluate the efficiency. This model is inherently imperfect, so we must reduce our dependence on it as much as possible. The easiest way to do this is to have as high an efficiency as possible. Then, even a relatively high uncertainty on the inefficiency will not be important. Luckily, there is little beam-beam background on the Z peak. Thus, we can relax the cuts that we had to impose at lower energy. For example, the following simple cuts

$$n_{ch} \geq 3$$

and

$$E_{vis} \geq 0.1 E_{cm}$$

result in an efficiency of 98.1%. A Monte Carlo simulation of the visible

* This is the subject of the following note in these proceedings, Mark II SLC-Physics Working Group Note #2-24.

energy spectrum is shown in Fig. 1.

2. Backgrounds.

   (d) Lepton pairs. These are very small for $n_{ch} \geq 3$. τ pairs give about a 1% background which is easy to calculate and remove.

   (e) Two photon events. Since the two photon process is not enhanced by the Z pole, it is quite small. With the above cuts, it is calculated to contribute only 0.1%. This calculation can be tested by observing the spectrum below the visible energy cut. This spectrum is also displayed on Fig. 1.

   (f) Non-beam-beam backgrounds. We will need some running experience before we can discuss these backgrounds intelligently. If they are small, we can remove them by a z subtraction. If they are large, we may have to make more restrictive cuts.

Figure Caption

1. Total visible energy for three or more detected charged particles. The data points represent annihilation data and the histogram represents the two-photon events.

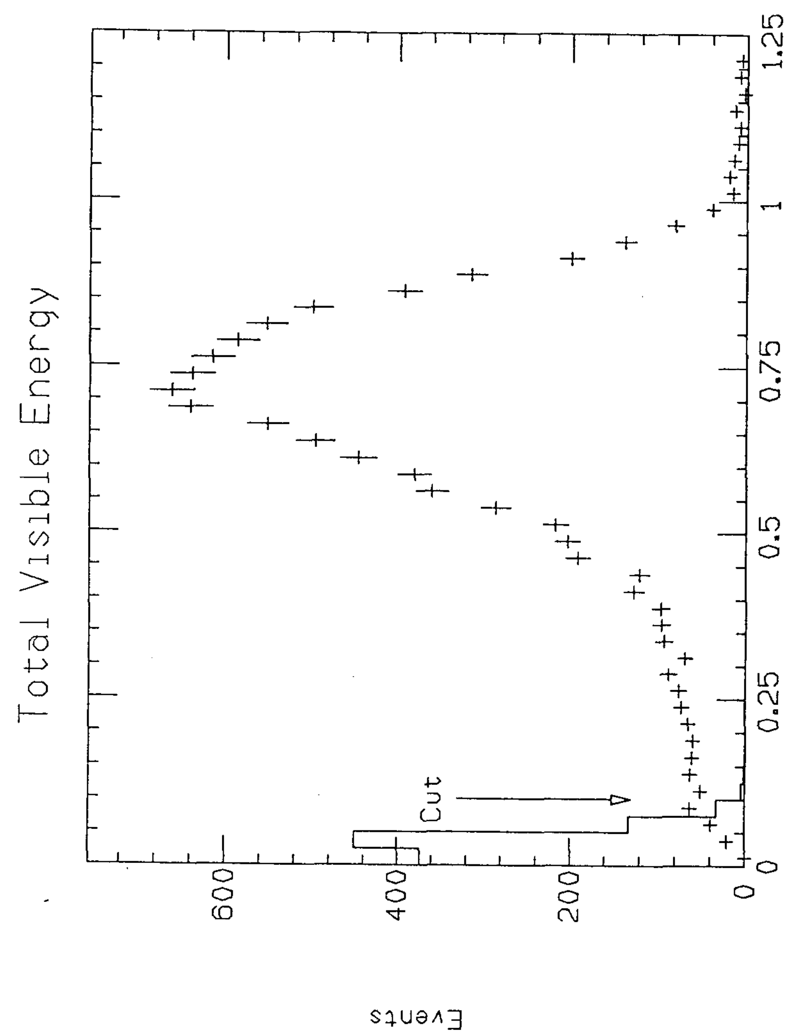

Fig. 1

Mark II/SLC-Physics Working Group Note # 2–24

AUTHOR: Gary Feldman

DATE: June 7, 1987

TITLE: On the Possibility of Measuring the Number of Neutrino Species to a Precision of $\frac{1}{2}$ Species with Only 2000 Z Events.

This note is to show that due to a fortuitous cancellation of statistical errors it will be possible to measure the number of neutrino species during our first runs with much more precision than had been previously thought possible. The partial Z width to invisible particles, Γ_{invis}, will turn out to be better determined than the total Z width, Γ_{tot} by about a factor of $\sqrt{2}$. Furthermore, this measurement will not presuppose the existence or non-existence of the top quark or any other new physics that yields hadronic-like events.

For the purpose of this calculation I will assume that we have collected N_Z Z decays in the region of the Z peak and that we understand the shape and location of the Z sufficiently well that it is not a factor in the analysis — in other words, that all N_Z events could have equivalently been taken at the peak of the Z.

We want to measure Γ_{invis}. The number of neutrino species, N_ν, is related to Γ_{invis} by

$$N_\nu = \frac{12\sqrt{2}\,\pi}{G_F\, m_Z^3}\,\Gamma_{invis} = \frac{\Gamma_{invis}}{176 \text{ MeV}} \quad \text{for } m_Z = 93 \text{ GeV}/c^2. \tag{1}$$

Of course, if other undetectable particles are produced in Z decay they will be experimentally indistinguishable from neutrinos and will contribute to the sum.

Γ_{invis} will be determined from

$$\Gamma_{invis} = \Gamma_{tot} - \Gamma_{vis}, \tag{2}$$

where

$$\Gamma_{vis} = \Gamma_{ee} + \Gamma_{\mu\mu} + \Gamma_{\tau\tau} + \Gamma_{had}. \tag{3}$$

Γ_{ee}, $\Gamma_{\mu\mu}$, and $\Gamma_{\tau\tau}$ will be taken to be equal to their theoretical value for this analysis,

$$\Gamma_{ee} = \Gamma_{\mu\mu} = \Gamma_{\tau\tau} = \frac{G_F\, m_Z^3}{24\sqrt{2}\,\pi}\,(v_e^2 + a_e^2), \tag{4}$$

since there is little uncertainty in this value. Γ_{had}, on the other hand, must be measured, since the top quark or other new physics could contribute to it. Γ_{had}

will be determined from

$$\Gamma_{had} = \frac{N_{had}\,\varepsilon_{\mu\mu}}{N_{\mu\mu}\,\varepsilon_{had}}\,\Gamma_{\mu\mu}, \tag{5}$$

where N_{had} and $N_{\mu\mu}$ are the number of detected hadrons and muon pairs and ε_{had} and $\varepsilon_{\mu\mu}$ are the corresponding detection efficiencies. ($N_{\mu\mu}$ will actually be determined from the sum of μ, e, and τ pairs to achieve higher statistical precision.)

Γ_{tot} will be determined from a measurement of $\sigma_{\mu\mu}$ by inverting the equation

$$\sigma_{\mu\mu} = \frac{12\pi}{m_Z^2}\,\frac{\Gamma_{ee}\Gamma_{\mu\mu}}{\Gamma_{tot}^2} \tag{6}$$

to obtain

$$\Gamma_{tot} = \sqrt{12\pi}\,\frac{\Gamma_{\mu\mu}}{m_Z}\,\sigma_{\mu\mu}^{-1/2}. \tag{7}$$

$\sigma_{\mu\mu}$ is determined from

$$\sigma_{\mu\mu} = \frac{N_{\mu\mu}}{\mathcal{L}\,\varepsilon_{\mu\mu}}, \tag{8}$$

where $\mathcal{L}$ represents the integrated luminosity as measured by the SAM.

Thus, there are five numbers to be determined, $N_{\mu\mu}$, N_{had}, $\mathcal{L}$, $\varepsilon_{\mu\mu}$, and ε_{had}, the first three of which contribute to the statistical error, and the last three of which contribute to the systematic error. Putting together the previous equations, Γ_{invis} can be written in terms of these five numbers as

$$\Gamma_{invis} = \left[\frac{\sqrt{12\pi}}{m_Z}\left(\frac{\mathcal{L}\,\varepsilon_{\mu\mu}}{N_{\mu\mu}}\right)^{\frac{1}{2}} - \frac{N_{had}\,\varepsilon_{\mu\mu}}{N_{\mu\mu}\,\varepsilon_{had}} - 3\right]\Gamma_{\mu\mu}, \tag{9}$$

Differentiating Eq. (9) to obtain the error in terms of the the experimental uncertainties, and rewriting it in terms of Γ_{tot} and Γ_{had}, we have

$$\begin{aligned}\Delta\Gamma_{invis} = {} & (-\frac{1}{2}\Gamma_{tot} + \Gamma_{had})\left(\frac{\Delta N_{\mu\mu}}{N_{\mu\mu}} \oplus \frac{\Delta\varepsilon_{\mu\mu}}{\varepsilon_{\mu\mu}}\right) \\ & \oplus \frac{1}{2}\Gamma_{tot}\frac{\Delta\mathcal{L}}{\mathcal{L}} \oplus \Gamma_{had}\left(\frac{\Delta N_{had}}{N_{had}} \oplus \frac{\Delta\varepsilon_{had}}{\varepsilon_{had}}\right),\end{aligned} \tag{10}$$

where $\oplus$ means addition in quadrature. The above-mentioned fortuitous cancellation occurs in the first term of Eq. (10): $\Gamma_{had} \approx 0.7\,\Gamma_{tot}$, so there is a large cancellation in the coefficient of the largest error, $\Delta N_{\mu\mu}/N_{\mu\mu}$.

Rewriting Eq. (10) in terms of Γ_{tot}, we have

$$\Delta\Gamma_{invis} \approx \left[0.2\left(\frac{\Delta N_{\mu\mu}}{N_{\mu\mu}} \oplus \frac{\Delta\varepsilon_{\mu\mu}}{\varepsilon_{\mu\mu}}\right) \oplus 0.5\frac{\Delta\mathcal{L}}{\mathcal{L}} \oplus 0.7\left(\frac{\Delta N_{had}}{N_{had}} \oplus \frac{\Delta\varepsilon_{had}}{\varepsilon_{had}}\right)\right]\Gamma_{tot}. \quad (11)$$

For comparison, the error on the determination of Γ_{tot} by this method [Eq. (7)] is given by

$$\Delta\Gamma_{tot} = \left[0.5\left(\frac{\Delta N_{\mu\mu}}{N_{\mu\mu}} \oplus \frac{\Delta\varepsilon_{\mu\mu}}{\varepsilon_{\mu\mu}}\right) \oplus 0.5\frac{\Delta\mathcal{L}}{\mathcal{L}}\right]\Gamma_{tot}. \quad (12)$$

I assume that $N_{\mu\mu}$ is measured by the sum of e, μ, and τ pairs with $|\cos\vartheta| < 0.8$ and that $\varepsilon_{\mu\mu}$ can be determined to 2%. I have argued previously that we should be able to determine ε_{had} to a precision of 1%.* The statistical error on $\mathcal{L}$ will be about the same as that on N_{had} and I will assume that the systematic error will be about 3%. This last error will be the dominant component of the error for $N_Z > 2500$.

The table below gives numerical values for $\Delta\Gamma_{invis}$ and $\Delta\Gamma_{tot}$ from Eqs. (11) and (12) and for $\Delta\Gamma_{tot}$ determined from a direct measurement.† (The comparison between the two techniques for measuring Γ_{tot} depends on the relative amount of time scanning and sitting on the peak. I have assumed here that all of the time is spent scanning.)

N_Z	$\Delta\Gamma_{invis}$, Eq. (11) (MeV)	$\Delta\Gamma_{tot}$, Eq. (12) (MeV)	$\Delta\Gamma_{tot}$, Direct Meas. (MeV)
500	142	215	248
1000	105	156	175
2000	81	115	124
5000	62	82	78
10000	54	67	55

* G. J. Feldman, Pajaro Dunes transparencies.

† G. J. Feldman, Mark II SLC-Physics Working Group Note #1-1.

Mark II/SLC-Physics Working Group Note # 2–25

AUTHOR: D. Cords, P. Burchat, P. Grosse-Wiesmann, C. Heusch, J. Matthews, J. Smith, D. Stoker, S. Watson

TITLE: Tau Physics at the Z°

DATE: July 15, 1987

---

1. Introduction

The precision study of tau-pair production at the Z° is an essential ingredient in the investigation of the Standard Model, and in searches for deviations from the Standard Model. Present measurements of $a_{\tau,e}$[1] and $v_{\tau,e}$[2,3] are consistent with lepton universality and with the Standard Model. Unfortunately the PEP and PETRA measurements suffer from rather large uncertainties, especially in the determination of $v_{\tau,e}$, and do not provide a test to better than the 10% level. Similar measurements at the Z° will provide a test at approximately the 1% level.

The plan of this note is as follows. First we review in section 2 the "asymmetry" measurements which, in addition to the precision measurement of the tau pair cross section, provide information on the tau (and electron) neutral current couplings. The measurement of the mean polarization of the taus, P^τ, and the tau polarization forward-backward asymmetry, A_{FB}^{pol}, is summarized in section 3. The Monte Carlo programs that have been developed for tau analysis are discussed in section 4, and the procedures for data selection developed with the Mark II/SLC PEP data are presented in section 5. Completing the discussion of experimental details, we present in section 6 an analysis of the systematic errors relevant to the measurement of the tau "polarization". Finally in section 7 we present a number of possibilities for "new" physics that might be visible in the tau data at the Z°.

2. Asymmetries

Using the following pairs of cross sections:

1. σ_F, σ_B, which are the differential cross sections integrated over the forward or backward hemispheres,
2. σ_L, σ_R, which are the cross sections for left- and right-handed (beam) electrons, and
3. σ_R^τ, σ_L^τ, which are the cross sections for production of right- and left-handed taus,

we define the following asymmetries:

$$A_{FB}^{ch} = \frac{\sigma_F - \sigma_B}{\sigma_F + \sigma_B} \text{ (Charge asymmetry)}$$

$$A_{LR} = \frac{\sigma_L - \sigma_R}{\sigma_L + \sigma_R} \text{ (Left-right asymmetry)}$$

$$P^\tau = \frac{\sigma_R^\tau - \sigma_L^\tau}{\sigma_R^\tau + \sigma_L^\tau} \text{ (Mean } \tau \text{ polarization)}$$

$$A_{FB}^{pol} = \tfrac{1}{2}(P_F^\tau - P_B^\tau) \text{ (} \tau \text{ polarization forward-backward asymmetry).}$$

The actual beam polarization asymmetry, A_{beam}, is simply related to A_{LR} by $A_{beam} = -P_e A_{LR} = P_e P_0^Z$. P_e is the degree of electron beam polarization (+1 for positive helicity (right-handed) electrons), and P^τ and P_0^Z, the intrinsic τ and Z° polarizations, are given by $P^\tau = \frac{-2v_\tau a_\tau}{v_\tau^2+a_\tau^2}$ and $P_0^Z = \frac{-2v_e a_e}{v_e^2+a_e^2}$.[4] With beam polarization, the Z° polarization, P^Z, is $\frac{P_0^Z+P_e}{1+P_e P_0^Z}$. For the Standard Model, $v_{\tau,e} = -(1-4\sin^2\theta_W)$, $a_{\tau,e} = -1$, and P^τ and P_0^Z are -0.24 for $\sin^2\theta_W = 0.22$. We assume unpolarized positron beams. The sensitivity with which the vector coupling or the Weinberg angle can be extracted from these asymmetries can be seen from the following table:

	e⁻Beam Polarization		
On the Z°	$P_e = 0$	$= 0.5$	$= 1.0$
$A_{FB}^{ch} \simeq \frac{3}{4}P^\tau P^Z$	$\frac{3}{4}P^\tau P_0^Z$	$\sim \frac{3}{4}P^\tau(P_0^Z + \frac{1}{2})$	$\frac{3}{4} P^\tau$
$A_{beam} = -P_e A_{LR} = P_e P_0^Z$	0	$\frac{1}{2}P_0^Z$	P_0^Z
$P^\tau = P^\tau$	P^τ	P^τ	P^τ
$A_{FB}^{pol} \simeq \frac{3}{4}P^Z$	$\frac{3}{4}P_0^Z$	$\sim \frac{3}{4}(P_0^Z + \frac{1}{2})$	$\frac{3}{4}$

Depending on the level of electron polarization, typically one asymmetry is sensitive only to the electron couplings and one asymmetry to the tau couplings.

The τ charge asymmetry measures the product of two small vector couplings, except for 100% e$^-$beam polarization where the dependence on the electron couplings drops out. The left-right (polarization) asymmetry is sensitive only to electron couplings, and the mean τ polarization is sensitive only to the τ couplings. Finally, the τ polarization forward-backward asymmetry is sensitive to electron couplings and for 100% e$^-$beam polarization approaches a constant value, thereby indicating that the τ helicities are fully aligned w.r.t the e$^-$helicity. If the beam polarization is assumed to be small, the sensitivity of the Weinberg angle measurements to the various asymmetry errors is given by the following relations:

$$\begin{aligned}\delta \sin^2\theta_W &\simeq \frac{\delta A^{ch}_{FB}}{24(1-4\sin^2\theta_W)} \simeq \begin{cases} \frac{1}{3}|\delta A^{ch}_{FB}| & \text{for } \sin^2\theta_W = 0.22 \\ |\delta A^{ch}_{FB}| & \text{for } \sin^2\theta_W = 0.24\end{cases} \\ &= \tfrac{1}{8}|\delta P^\tau| \\ &= \tfrac{1}{6}|\delta A^{pol}_{FB}| \ .\end{aligned}$$

With polarized beams, we find for the beam polarization asymmetry measurement,

$$\delta \sin^2\theta_W \simeq \tfrac{1}{8P_e}|\delta A_{beam}| = \tfrac{1}{8}|\delta A_{LR}| \ .$$

For a comparison of the different measurements see Ref. 5.

In summary, we note that a measurement of $\sin^2\theta_W$ can be obtained from the angular asymmetry of the τ decay products quite independently of its determination by a precise measurement of the Z° mass. Such an independent measurement constitutes an important test of the standard model. In addition, τ polarization measurements allow determination of the vector couplings of electrons and taus independently and, therefore, a check of lepton universality. The mean tau polarization itself will present an excellent laboratory to observe parity violating effects. These parity violating effects manifest themselves only if the measurements are sensitive to helicity states (as is the case for the mean polarization) and if the vector and axial couplings are both different from zero. With this observational tool available it will be a challenge to probe for "new physics" (see section 7).

3. Measurement of tau polarization

The tau polarization as a function of the τ production polar angle θ on the Z° resonance peak is given by:

$$P^\tau(\cos\theta) = \frac{P^\tau + P^Z \frac{2\cos\theta}{1+\cos^2\theta}}{1 + P^\tau P^Z \frac{2\cos\theta}{1+\cos^2\theta}} \ .$$

$P^\tau(\cos\theta)$ is shown in Fig. 1, for P_e=0, to vary from zero in the backward direction to -45% (-31%) in the forward direction for $\sin^2\theta_W$= .22(.23).

The degree of τ polarization can be determined by analyzing the momentum distributions of its decay products; this has been discussed in some detail previously.[6] For example, the normalized average energy of the decay particle is a linear function of the tau polarization:

$$\bar{x}(\cos\theta) = \frac{2\bar{E}(\cos\theta)}{\sqrt{s}} = x_0 + \alpha\ P^\tau(\cos\theta) \ ,$$

where, for the various decay modes, the parameters x_0 and α are given by:

Decay mode	x_0[7]	α
e, μ	0.35	-0.05
π, K	0.5	$+\frac{1}{6}$
$V(\rho, K^*, a_1)$	0.5	$+\frac{1}{6}\left(\frac{M_\tau^2-2M_V^2}{M_\tau^2+2M_V^2}\right)$

We note that it is important to clearly identify the τ decays. As an example, the sign of α is different for the decays $\tau \to \mu\nu\bar{\nu}$ and $\tau \to \pi\nu$. This results in opposite trends in the charged particle momentum spectra, as shown in Fig. 2. Furthermore, the "analyzing power" of the different decays varies, with the π and K decay modes being the most sensitive to the tau polarization.

In practice the tau polarization analysis is done by forming two independent linear combinations of the particle energies $\bar{x}_F$ and $\bar{x}_B$ averaged over the forward and backward directions:

$$\langle \bar{x} \rangle_\theta = \tfrac{1}{2}(\bar{x}_F + \bar{x}_B) = x_0 + \alpha\ P^\tau$$

$$\bar{x}_{FB} = \tfrac{1}{2}(\bar{x}_F - \bar{x}_B) = \alpha\ A^{pol}_{FB} \simeq f_c \alpha\ P^Z \ ,$$

where f_c is the integral of $P^\tau(\cos\theta)$ over the detector acceptance, which is $\frac{c}{1+c^2/3}$ if the efficiency is uniform out to some maximum $\cos\theta$, c ($f_c = \frac{3}{4}$ for full acceptance).

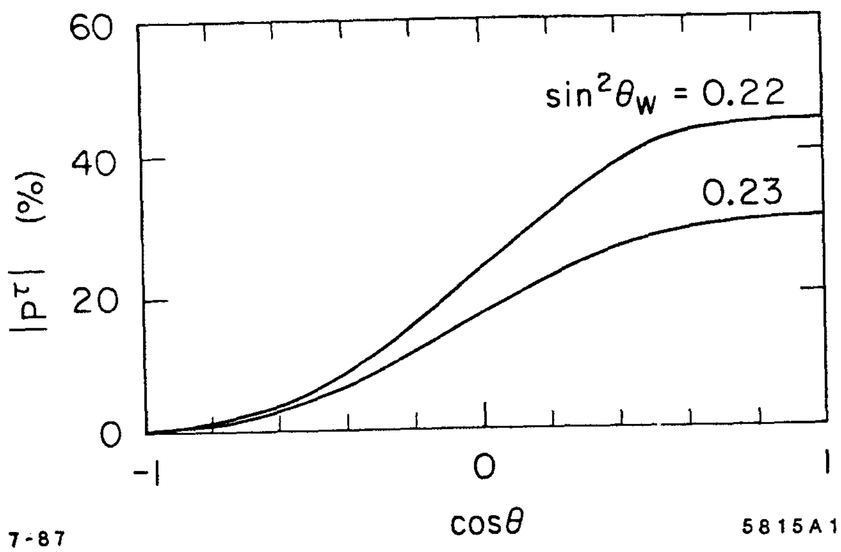

Figure 1. Polarization of the produced τ's as a function of the τ production angle for $\sqrt{s} = M_{Z^0}$.

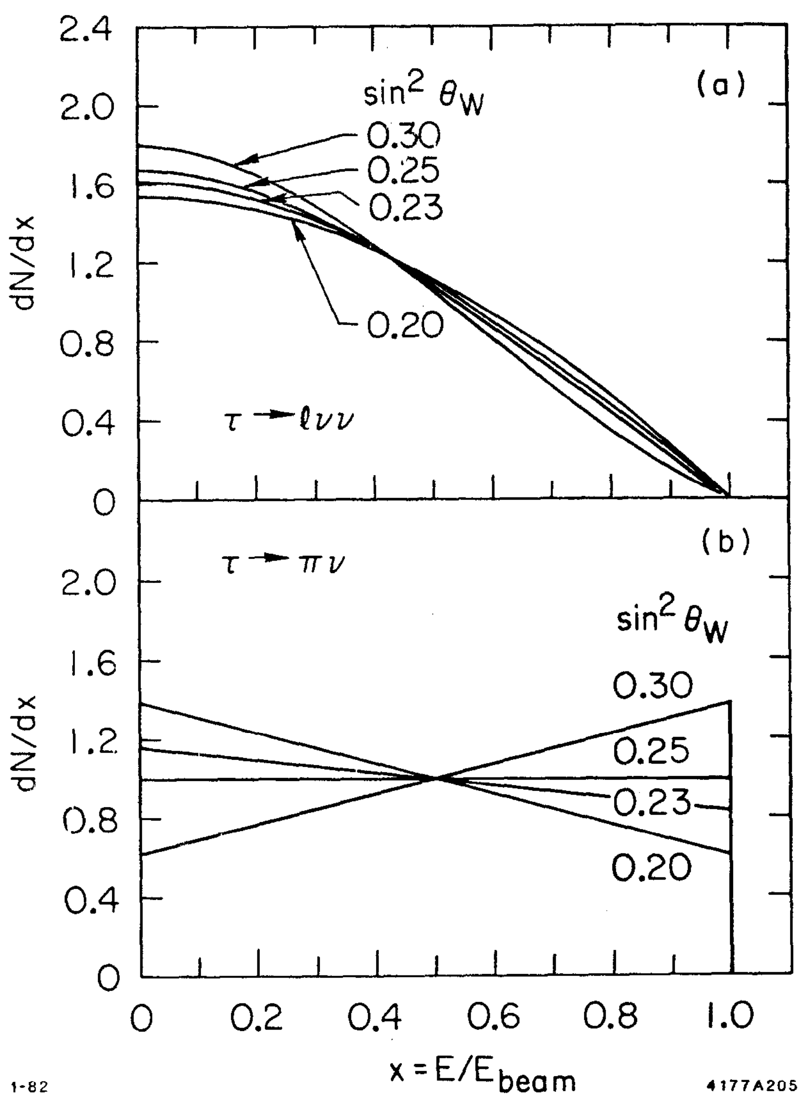

Figure 2. Momentum spectra for τ decay products for different values of the weak parameter $\sin^2\theta_W$ for (a) charged leptons from the decay $\tau \to l\nu\nu$, and (b) pions from the decay $\tau \to \pi\nu$.

From the measurement of the tau polarization, it is difficult to make important improvements in the knowledge of weak parameters with less than 10^5 produced Z°'s. In Table 1, assuming P_e=0, we summarize, for each decay mode, the estimated precision with which we expect to measure the various quantities. We have included our best estimates of the efficiency of the detector, but have not yet done detailed Monte Carlo estimates. For the measurement of v_τ, we assume that the uncertainty in a_τ is small (as mentioned above, we really measure the ratio v_τ/a_τ).

Decay mode	$\delta\langle\bar{x}\rangle$, $\delta\bar{x}_{FB}$	δP^τ	δA_{FB}^{pol}	δv_τ from $\langle\bar{x}\rangle$	$\delta\sin^2\theta_W$ from $\langle\bar{x}\rangle(\bar{x}_{FB})$
e	0.008	0.16	0.26	0.08	0.020(.033)
μ	0.011	0.22	0.37	0.11	0.028(.047)
π	0.019	0.11	0.18	0.06	0.014(.023)
ρ	0.009	0.14	0.24	0.07	0.018(.031)

Table 1. Expected statistical errors for the various decay modes

4. τ pair Monte Carlos

The formula for τ pair production can be written as

$$d\sigma = d\sigma_0[1 + c_\mu s^\mu + \bar{c}_\mu \bar{s}^\mu + c_{\mu\nu} s^\mu \bar{s}^\nu]$$

where s^μ ($\bar{s}^\mu$) is the spin of the τ^- (τ^+) and the coefficients c are functions of the momenta of the incoming and outgoing fermions. The terms involving only s^μ or $\bar{s}^\mu$ result in net polarization of the τ while the terms involving both result in spin correlations between the two τ's. The formulae for τ decay can be written as

$$d\Gamma(\tau^-) = d\Gamma_0(\tau^-)[1 + b_\mu s^\mu]$$

and

$$d\Gamma(\tau^+) = d\Gamma_0(\tau^+)[1 + \bar{b}_\mu \bar{s}^\mu] \ ,$$

where the coefficients b depend on the decay mode, the τ momentum, and the momenta of the decay products. The result of combining the production and decay formulae is

$$d\sigma_{final} = 4d\sigma_0[1 - c_\mu b^\mu - \bar{c}_\mu \bar{b}^\mu + c_{\mu\nu} b^\mu \bar{b}^\nu] \frac{d\Gamma_0(\tau^+)}{\Gamma(\tau^+)} \frac{d\Gamma_0(\tau^-)}{\Gamma(\tau^-)}$$

It is important to note that production and decay do not completely factorize; *i.e.* the constants c which depend on the momenta of the e^+, e^-, τ^+ and τ^- are multiplied by the constants b which depend on the momenta of the decay products and cannot be factored out. This means that in order to incorporate the complete spin effects in the Monte Carlo, the generator cannot be separated from the decay routines.

Generator	KORALZ	LULEPT
Decay Routine	TAUOLA	LULEPT
Lowest order diagrams ($Z^\circ - \gamma$ interference)	Yes	Yes
Initial state radiation incl. resonance	Yes	Yes
Final state radiation	Yes	No
Higher order QED corrections	No	No
Higher order weak corrections	Yes	No
Initial state $e^\pm$ longitudinal polarization	Yes	Yes
Initial state $e^\pm$ transverse polarization	No	No
Longitudinal τ polarization	Yes	Yes
Transverse τ polarization	No	Yes
Longitudinal τ spin correlations	Yes	Yes
Transverse τ spin correlations	No	Yes
Decay Modes:		
$\pi\nu_\tau$, $K\nu_\tau$	Yes	Yes
$e\nu_e\nu_\tau$	Yes	Yes
$\mu\nu_\mu\nu_\tau$	Yes	Yes
$\rho\nu_\tau$, $K^*\nu_\tau$	Yes	Yes
ρ helicity effects	Yes	Yes
arbitrary mixture of V and A at τ vertex	Yes	Yes
arbitrary ν_τ mass	Yes	Yes
multi-prong decays	in progress	*via* $\bar{u}d$ frag.

Table 2. Present Monte Carlo status

There are two fairly complete Monte Carlos for τ pair production and decay at SLC energies: LULEPT[8] and KORALZ.[9] The main features of LULEPT and KORALZ are given in Table 2. The major differences are that KORALZ neglects transverse tau spin effects while LULEPT includes them, and that LULEPT neglects final state radiation and higher order weak corrections in the tau production process while KORALZ includes them. These Monte Carlos were compared by Pat Burchat at the Granlibakken Workshop[10] at which time LULEPT was called LUND/τ. It was concluded that without radiative corrections LULEPT and KORALZ are in agreement with each other and with theoretical predictions within statistical errors. With radiative corrections included, some small differences appear to be caused by the absence of final state radiation in LULEPT. Final state radiation may be included in LULEPT at a later date.

5. Analysis of PEP Upgrade data

To prepare for doing analysis with data at the SLC, we have measured the total cross-section for τ pair production and the topological branching fractions of the τ with PEP Upgrade data. We tried to answer the following questions: Which parameters are most efficient for removing background events while retaining τ pair events, given the detector capabilities? How well do the distributions which are observed in the data and predicted by the Monte Carlo agree? How are the analyses at PEP and SLC different? For example, should we consider cutting on different parameters at the SLC?

Approximately 32 pb^{-1} of data accumulated with the PEP Upgrade detector were used for this analysis. The events analysed come from the filtered data summary tapes (DST's) produced for this run. For both PEP (29 GeV) and SLC (93 GeV) energies, 10,000 Monte Carlo (MC) events were generated with the LULEPT τ pair generator. These events correspond to 74 pb^{-1} at PEP and 8.3 pb^{-1} , or about 300,000 Z°'s, at SLC.

A. Selection Criteria

Events are selected as τ-pair events if they meet certain criteria determined by comparing events on the DST's with MC τ-pair events. The following is a list of quantities used in the selection. The 4-vectors for good tracks are filled using the routines FILCH$ (for charged particles) and FILNE$ (for neutrals) from the VECSUB package of subroutines. The variables in parentheses are quantities calculated in the selection program and used to label the histograms in the figures.

1. For each charged track, the angle with respect to the beam axis (COS) and the difference between the expected and measured time-of-flight (DLTTOF)

is determined. Also, the event vertex is found and compared to the beam vertex.

2. The combined 4-vector for all tracks in the event is computed. The total energy (ETOT), momentum (PTOT), etc. are found. The total energy and net momentum perpendicular to the beam axis (PXYTOT) are good discriminators against two-photon events. Additionally the sum of the Liquid Argon (LA) energy and the net z component of the LA energy is found (ELATZ). Radiative Bhabhas with photons which went down the beam pipe will have ELATZ approximately equal to twice the beam energy.

3. The thrust (THRST) is calculated using all charged tracks and neutrals with at least 500 MeV of energy. The event is divided into the positive and negative thrust hemispheres based on this axis. The number of charged tracks in each hemisphere (NCPHEM, NCMHEM) is found. $\tau^+\tau^-$ events have a topology of 1 vs. 1, 1 vs. 3, etc. since the decay products from the two sides are well separated.

4. The acoplanarity angle (ACOPL) between the total momentum vectors for each side is measured. This angle is defined to be the angle between the planes formed by each total momentum vector combined in turn with the beam axis. A non-zero acoplanarity angle is expected to be very useful for τ event selection because of the missing energy and momentum carried off by the neutrinos in the event.

5. In hemispheres that contain three charged tracks, the net momentum in the rest frame of a τ moving along the hemispheric thrust axis is determined (PBTOT). For true τ decays the net momentum should only reflect the missing ν while non-τ events will have a large PBTOT.

We compare the distributions of the above variables for the DST's and MC to determine where the cuts should be made. In this analysis two sets of cuts are made. The first preliminary set consists of fairly straightforward criteria which select events with the proper topology, missing momentum, etc. Table 3 lists these cuts and shows the number of events which pass each successive cut for DST's, PEP MC, and SLC MC.

Cut Criteria	DST	PEPMC	SLC MC
# events	122,942	10,000	10,301
At least 1 charged track	119,991	9365	9383
DLTTOF $<$ 5 nsec	118,097	9365	9383
Vertex R$<$ 8 cm, Z$<$ 10 cm	110,252	9359	9379
net charge $=$ 0	81,801	7342	8121
$2 \leq$ (# of charged particles) ≤ 6	77,193	7265	8088
ETOT $\geq$ 6 GeV	70,631	6711	8055
PXYTOT $\geq$ 0.5 GeV	47,539	6410	7947
Topology (1 v 1, 1 v 3, 3 v 3, 1 v 5)	45,164	6208	7923
ACOPL $\geq$ 0.01 radians	11,297	5813	6476
PBTOT $\leq$ 1.5 GeV	10,695	5641	6383

Table 3. Number of events passing preliminary selection criteria

In figures 3, 4, and 5, some of the quantities of interest are shown for each of the three data sets after this first set of cuts. Note that PLOW is the momentum of the lowest momentum track in each event and MHEM is the invariant mass of the tracks in the hemisphere with the larger mass. These plots clearly show that there are many background events remaining in the data sample. The distributions are used to determine final cuts to remove these backgrounds.

Table 4 shows the effect of each of these cuts on the number of events remaining and on the PEP calculated total cross-section (neglecting backgrounds). For each cut, the number in parenthesis refers to the cut value which we assume for SLC energies. In particular, the τ events will be much narrower and so an extremely high thrust cut can be made. The acoplanarity angle will be smaller for the same reason.

During the PEP Upgrade running the charged particle trigger required at least two charged tracks with a certain number of hits in the main and inner drift chambers along with TOF information for each. This means that at least two tracks must be within the TOF fiducial volume. Requiring $|\cos\theta|$ to be less than 0.7 for at least two tracks approximates the charged particle trigger in the MC.

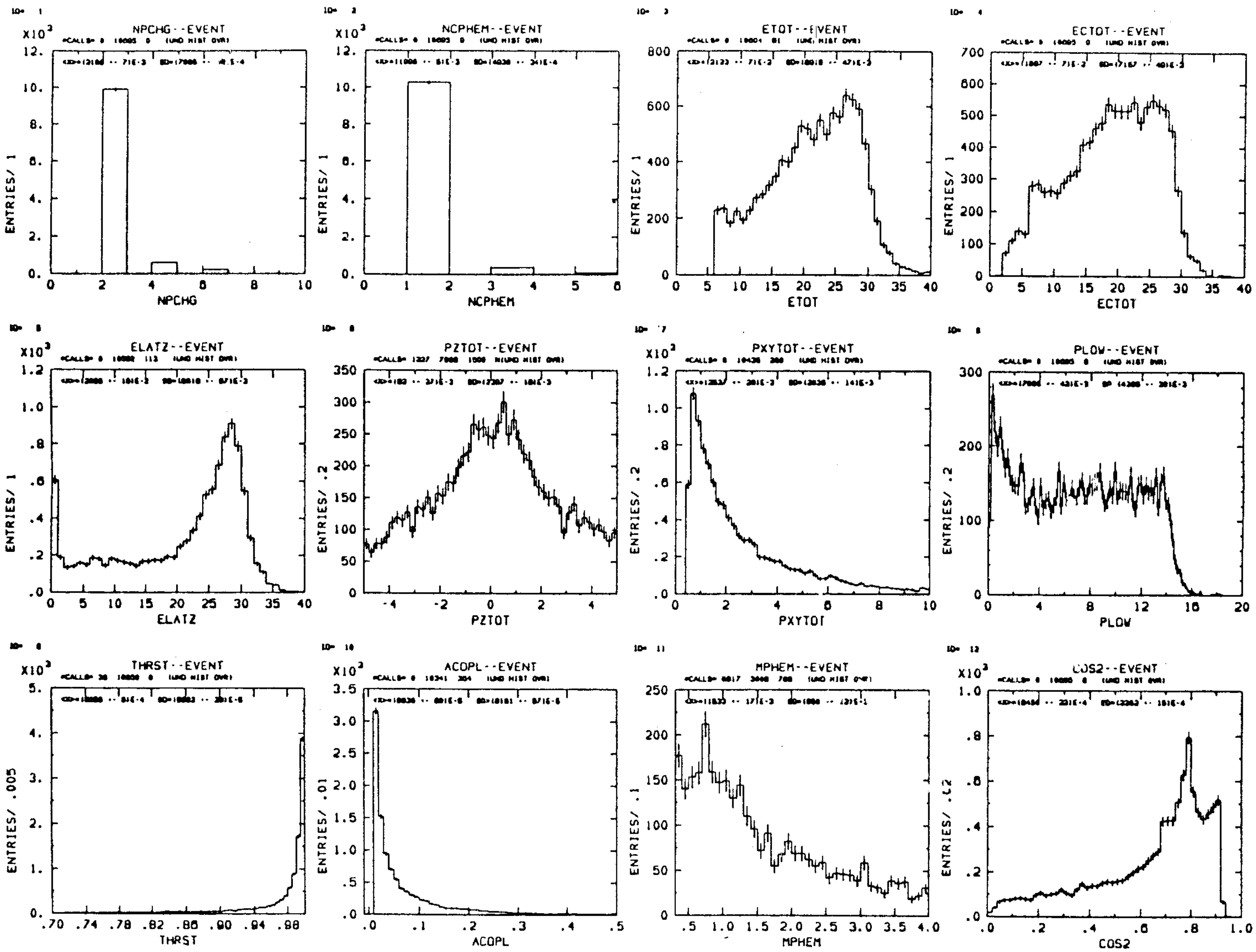

Figure 3. Distributions for upgrade data after preliminary cuts.

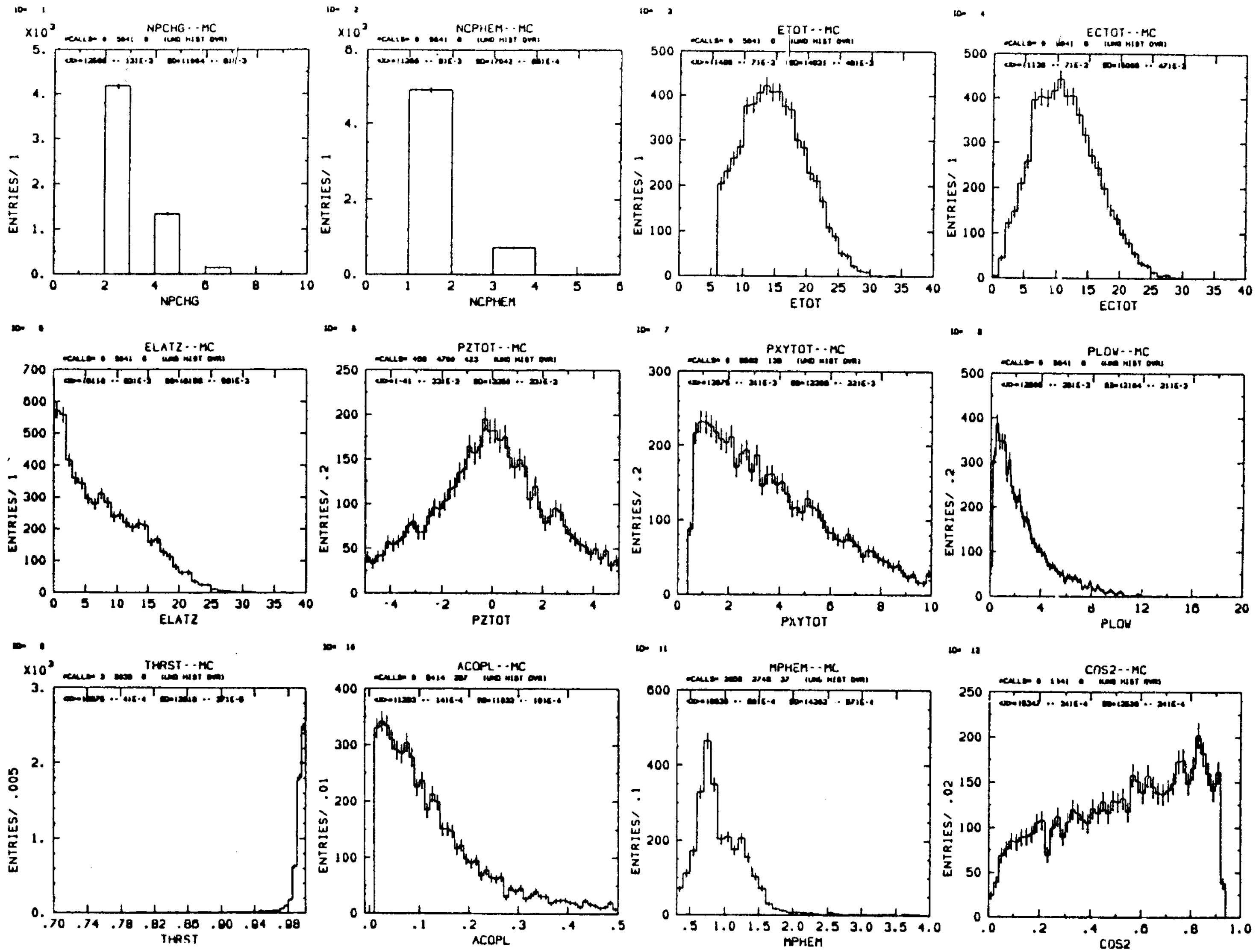

Figure 4. Distributions for PEP Monte Carlo after preliminary cuts.

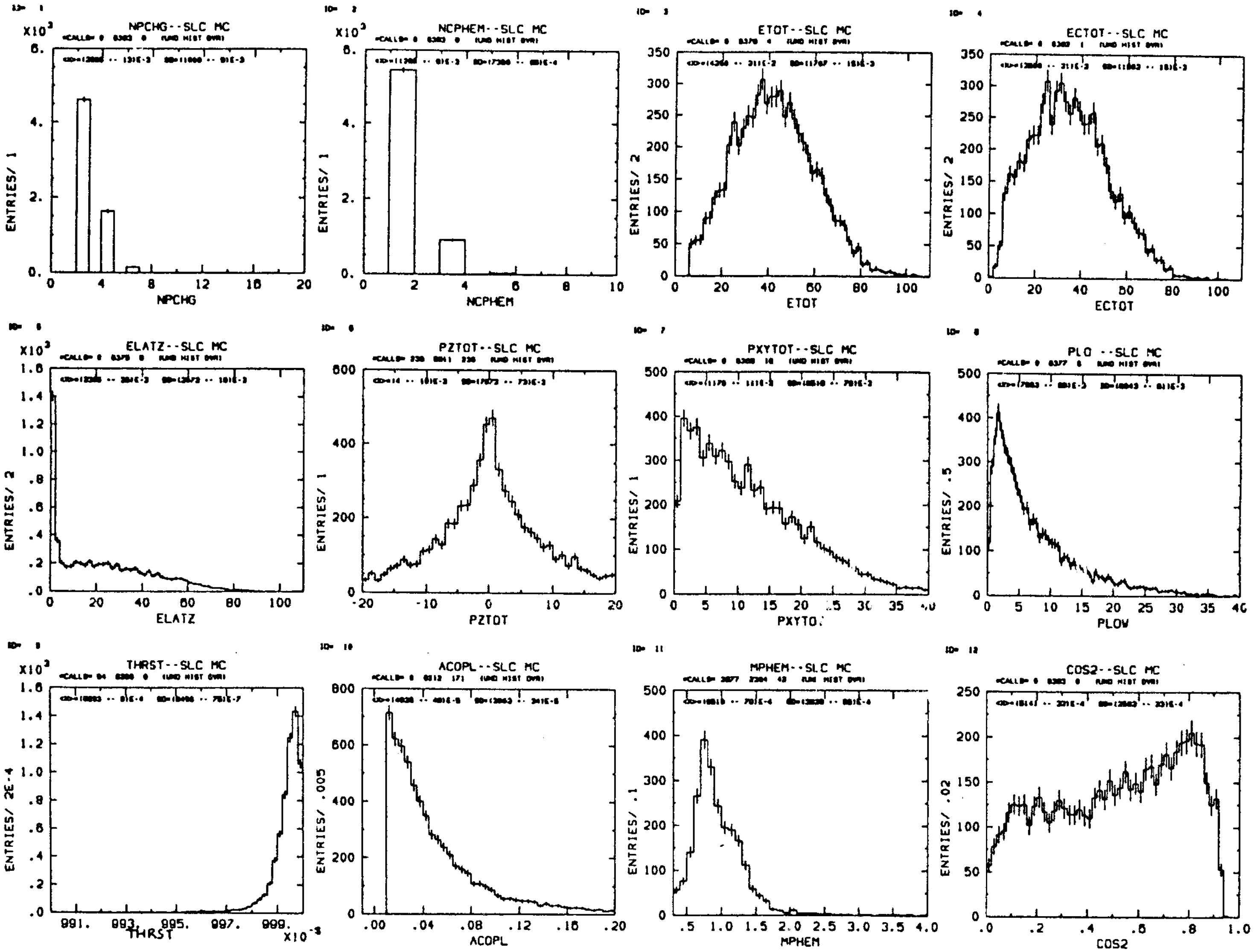

Figure 5. Distributions for SLC Monte Carlo after preliminary cuts.

Cut Criteria	DST	PEP MC	σ(pb)	SLC MC
THRST $\geq .95(.997)$	8514	5378	502	6151
ACOPL $\geq .04(.01)$ radians	3518	4408	253	6151
PLOW $\leq 8.0(20.0)$ GeV	2300	4290	170	5719
ELATZ $\leq 20.0(60.0)$ GeV	1533	4141	117	5376
MHEM ≤ 2.0 GeV	1454	4086	113	5348
$\lvert\cos\theta\rvert \leq 0.7$ for ≥ 2 tracks	1189	2733	138	3765

Table 4. Events passing final selection criteria

Figures 6, 7, and 8 show the same distributions for DST, PEP MC, and SLC MC after the final selection. Comparison of DST and PEP MC shows that the samples have very similar distributions, indicating that a clean sample of $\tau^+\tau^-$ events has been selected. The efficiency for PEP and SLC $\tau^+\tau^-$ events to pass these cuts is 27.3% and 36.5%, respectively. At SLC the trigger requirements can probably be loosened, significantly improving the efficiency.

B. Results

With this sample of τ events, the cross-section (σ_{tot}) and the topological branching fractions $B(\tau \rightarrow 1 \text{ prong})$ and $B(\tau \rightarrow 3 \text{ prongs})$ are measured. From the total integrated luminosity of 31.5 pb^{-1}, the number of events observed, and the efficiency, the cross-section is found to be:

$$\sigma_{tot} = \frac{N_{obs}}{\epsilon \int L dt} = 138.0 \pm 4.0 \, {}^{+2.8}_{-13.5} \text{ pb} .$$

The first error is statistical and the second is systematic. The systematic error is estimated by varying the selection criteria. The asymmetry in the error is probably due to the presence of background events which are sensitive to the cuts. This measurement is in good agreement with the radiatively corrected theoretical cross-section of 136 pb at 29 GeV. The number of observed one and three prong decays are used to measure the topological branching fractions: $B(\tau \rightarrow 1 \text{ prong}) = 0.87 \pm 0.01$ and $B(\tau \rightarrow 3 \text{ prongs}) = 0.13 \pm 0.01$. The errors are statistical only. The world average is $B(\tau \rightarrow 1 \text{ prong}) = 0.865 \pm 0.003$.[11]

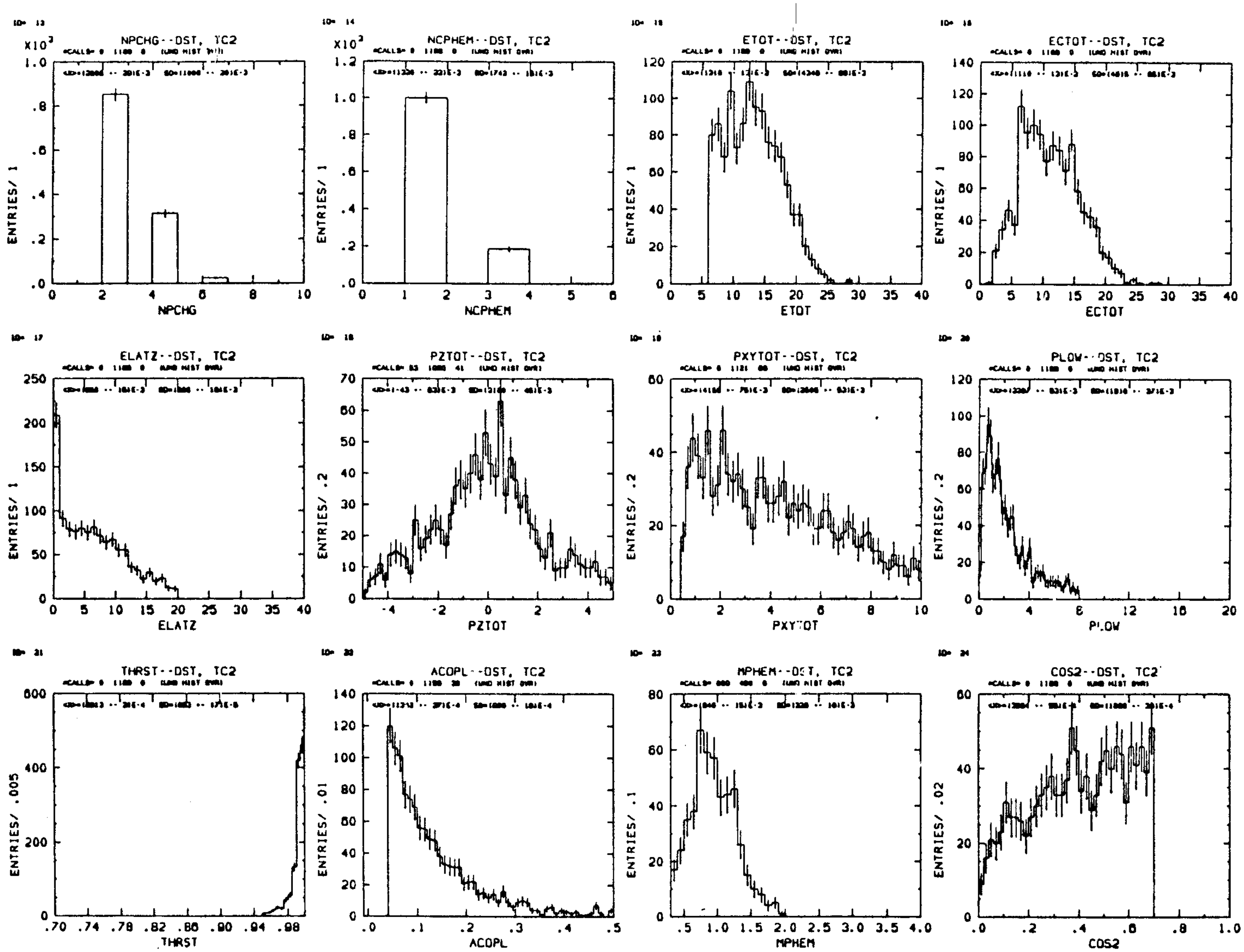

Figure 6. Distributions for upgrade data after final cuts.

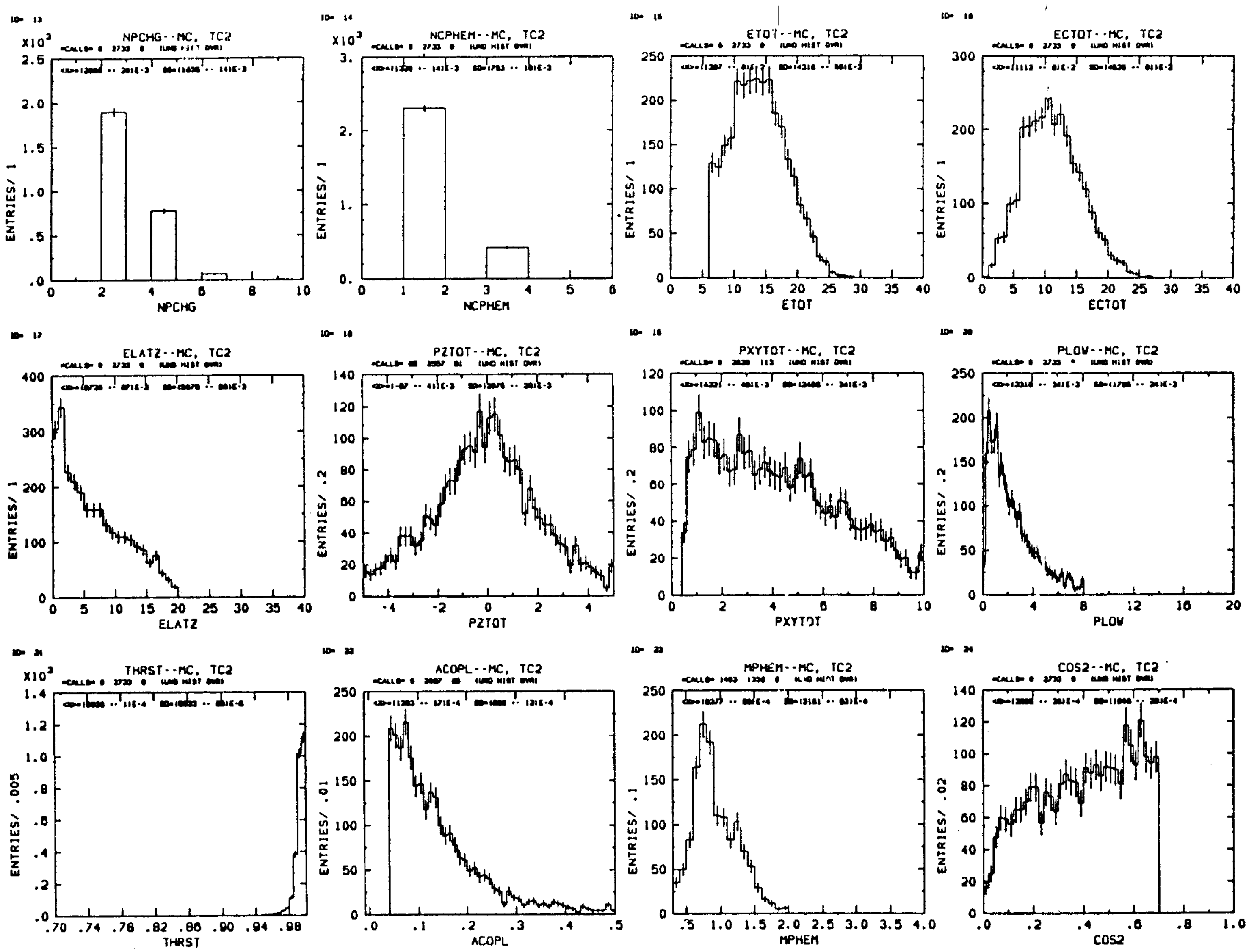

Figure 7. Distributions for PEP Monte Carlo after final cuts.

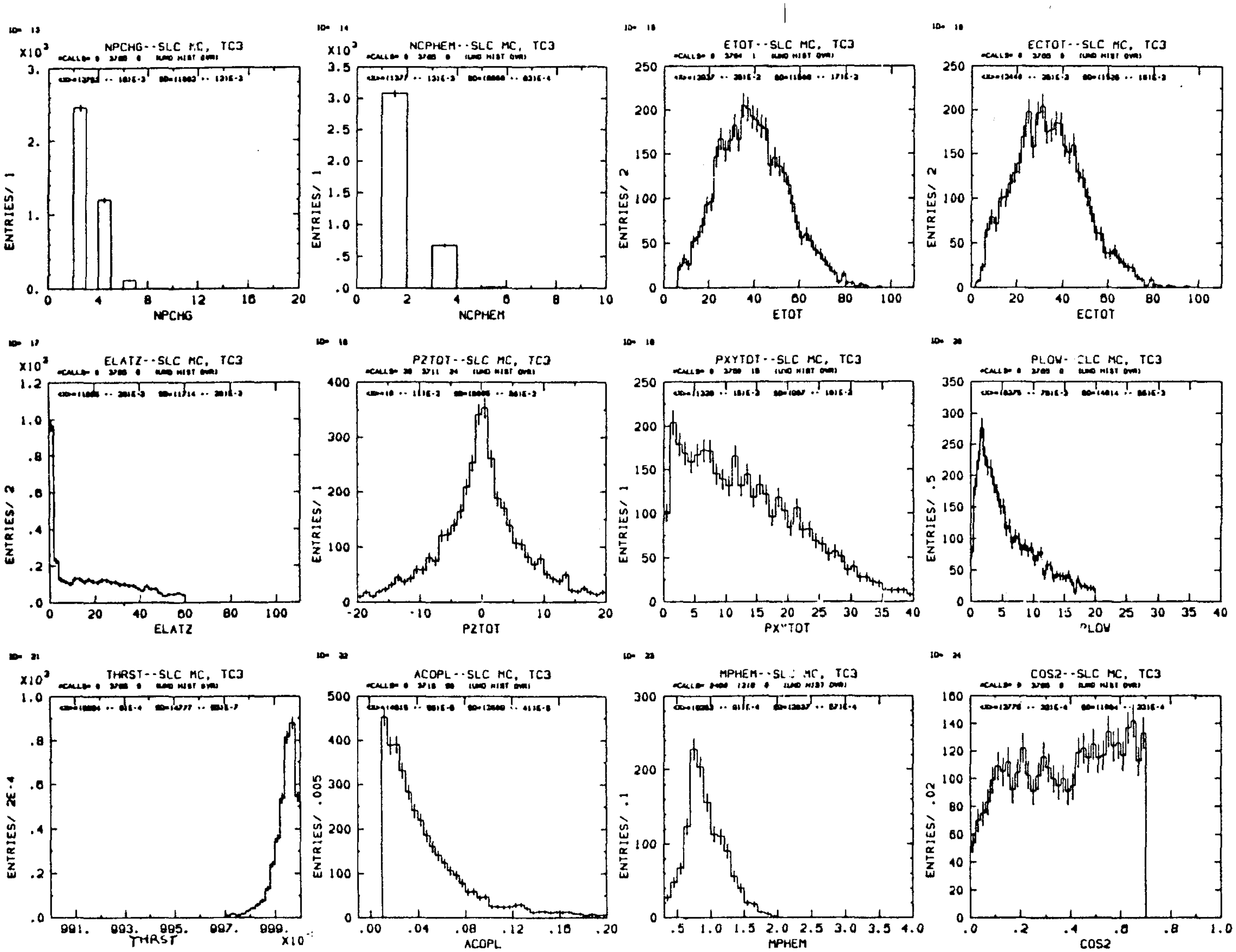

Figure 8. Distributions for SLC Monte Carlo after final cuts.

6. Systematic errors

Systematic errors are likely to be quite important (perhaps dominant) for the mean polarization measurement though, due to many cancellations, the systematics for the polarization asymmetry should be small. The systematic error estimates discussed here rely heavily on the MAC tau polarization measurement[3] performed at a center-of-mass energy of only 29 GeV, where the polarization is expected to be too small to be observed.

Since the expected shift in the mean energy is between 3 and 8% for the various decay modes, and the expected statistical uncertainties are 2-4% (see Table 1), we consider systematic effects smaller than 0.3% to be negligible (effects at this level will be significant only for samples of more than 10^6 produced Z°'s). Effects that we have considered which should be quite negligible include beam energy calibration, charged particle momentum calibration (including magnetic field uncertainties), and radiative corrections (both production and decay). For the ρ decay mode, the electromagnetic calorimeter calibration is also important, but that too can probably be understood with the required accuracy. Misassignment of the charge of both tau decay products, relevant for the energy asymmetry, should also be negligible even for high energy particles.

The most important contributions to the systematics will be due to uncertainties in the detector efficiencies and backgrounds. For the mean energy measurement, considerable work will be required to understand the energy dependence of the efficiencies. Non-tau background will probably be negligible, so background difficulties will involve distinguishing the decay modes of interest from other tau decays. The amount of such backgrounds is uncertain, not only due to uncertainties in the efficiencies of the cuts, but also due to uncertainties in the tau branching fractions. We have no control over the latter since refinement of these branching fractions will be difficult with our limited statistics. The problem is especially severe for the ρ decay mode, where extra neutrals must be rejected and the experimental understanding of decays to π plus multiple neutrals is especially poor. Thus reducing the multiple-neutral background in the ρ sample will be essential to the success of the measurement with this mode.

With the notation defined in section 3, we write the measured mean energy fraction in the presence of background as

$$\begin{aligned}\langle\bar{x}\rangle_{meas} &= f_{sig}\langle\bar{x}\rangle_{sig} + f_{bg}\langle\bar{x}\rangle_{bg} \\ &= \langle\bar{x}\rangle_{sig} - f_{bg}(\langle\bar{x}\rangle_{sig} - \langle\bar{x}\rangle_{bg}) \\ &= x_0^{sig} - f_{bg}(x_0^{sig} - x_0^{bg}) + P^\tau \alpha_{sig}\{1 - f_{bg}(1 - \frac{\alpha_{bg}}{\alpha_{sig}})\} \ .\end{aligned}$$

Similarly, the measured forward-backward energy asymmetry can be written

$$(\bar{x}_{FB})_{meas} = P^Z f_c \alpha_{sig}\{1 - f_{bg}(1 - \frac{\alpha_{bg}}{\alpha_{sig}})\}$$

From these formulae the errors in $\sin^2\theta_W$ are found to be

$$\delta\sin^2\theta_W = \{f_1^2\delta^2\langle\bar{x}\rangle + f_2^2\delta^2 f_{bg}\}^{\frac{1}{2}}$$

from the mean energy measurement and

$$\delta\sin^2\theta_W = \{g_1^2\delta^2\bar{x}_{FB} + g_2^2\delta^2 f_{bg}\}^{\frac{1}{2}}$$

from the energy asymmetry measurement, where

$$\begin{aligned}f_1 &= \frac{1}{8\alpha_{sig}}\frac{1}{1 - f_{bg}(1 - \frac{\alpha_{bg}}{\alpha_{sig}})} \\ f_2 &= f_1(\langle\bar{x}\rangle_{sig} - \langle\bar{x}\rangle_{bg}) \\ g_1 &= \frac{f_1}{f_c} \\ g_2 &= g_1(\bar{x}_{FB})_{meas}(1 - \frac{\alpha_{bg}}{\alpha_{sig}}) \ .\end{aligned}$$

The factor $1 - \frac{\alpha_{bg}}{\alpha_{sig}}$, which appears repeatedly above, is tabulated in Table 5. When this factor is large and positive, the background is potentially quite troublesome; if it is less than one or negative, the background mode is relatively harmless. If the size of the systematic error contribution for each decay mode is arbitrarily required to be less than one-third of the corresponding statistical error given in Table 1, and we assume that the momentum measurements of the particles are not biased, we find the tolerable background levels given in Table 6. Most of these should not be difficult to achieve. The numbers for ρ background are underestimates since the measured momentum will be only the charged pion from the ρ decay. If the π° is missed because it is soft, the bias is small, but if there is undetected overlap or the π° is lost in detector cracks, the bias can be large. Similarly, the numbers for the ρ signal are underestimates since there is a bias when a e, μ, or π picks up a spurious π°. The largest background for the ρ decay mode is expected to be from pi plus multiple neutrals, as discussed above. This is not included in the table, since as for the case of ρ background, there may be a significant detector momentum bias due to undetected π°'s.

Background decay mode	Signal decay mode e	μ	π	ρ
e	-	-	1.30	1.75
μ	-	-	1.30	1.75
π	4.33	4.33	-	-1.50
ρ	2.33	2.33	0.60	-

Table 5. Values of $1 - \frac{\alpha_{bg}}{\alpha_{sig}}$ for the four major decay modes.

Background decay mode	Signal decay mode e	μ	π	ρ
e	-	large	6(15)	3(15)
μ	large	-	6(15)	3(15)
π	3(6)	3(12)	-	12(18)
ρ	3(12)	3(18)	24(33)	-

Table 6. Tolerable background levels (%) for the major decay modes for measurement of $\langle\bar{x}\rangle$. Levels for the $\bar{x}_{FB}$ measurement are given in parentheses.

7. New physics

Experimentation at the SLC will concentrate on two equally fascinating aspects of studies initiated by electron-positron annihilation at or near the Z° peak. The first is an attempt to study in considerable detail the parameters of the Standard Model of the fundamental interactions, based on the gauge group $SU_2 \times U_1 \times SU_3$. This is of the greatest interest because all presently established experimental phenomena are compatible with this model, although noone expects it to be more than a low-energy manifestation of a higher symmetry. Precision tests of its parameters are therefore of the greatest importance. The second is the equally vital search for phenomena that can not be explained by the Standard Model, that will therefore show the way toward the appropriate extension of this model toward a more generally valid framework. For both of these basically important pursuits, the study of e^+e^-annihilation into final states involving tau leptons will be fruitful. Let us enumerate why:

1. Standard Weak Interaction theory sufficed to predict essentially all features of production and decay of the third-generation lepton τ once its mass was

assumed.[12] The accuracy to which these predictions are met is therefore a measuring stick of the validity of the theory.

2. The tau lepton, as a "sequential lepton" in the third fermion generation, has the distinct advantage that its mass suffices to open up a great variety of hadronic channels. It is therefore a prime laboratory for a detailed study of weak-hadronic as well as leptonic currents.
3. It is well known that the third generation of the standard model fermions, with left-handed weak isospin doublets

$$\binom{t}{b} \quad \binom{\nu_\tau}{\tau}$$

is much less well determined than its lower-mass relatives: the t quark remains unobserved as of early 1987; for ν_τ, there is only indirect evidence; the long lifetime of the b quark indicates a small mixing angle for coupling to other generations. Consequently, recent indications that all may not be totally standard with the τ lepton, such as missing one-prong branching fractions,[13] should be taken as a harbinger that the most closely studied of the third generation fermions deserves an even closer look.

In particular, recall that the point-like behavior and V-A current structure of the tau have been studied up to now only at energies where the process $e^+e^- \to \tau^+\tau^-$ proceeds almost exclusively *via* virtual photon exchange. At $\sqrt{s} = m_Z$, the process mediated by the Z° pole may well display features previously unobserved. Foremost among the features to be investigated must be those that may point the way past the standard model phenomenology: flavor non-diagonal weak neutral currents are likely to show up at some level; and compositeness might be accessible to some new tests in experiments involving τ pair production near the Z° pole.

Lepton flavor violation can occur via a number of different extensions of the Standard Model. A first statistically meaningful test at $q^2 = m_Z^2$ will be sensitive to mechanisms beyond the reach of rare decay experiments.[14] They may include the effects of new gauge bosons or of the possible compositeness scale of the Z°.

Size effects altogether provide another important testing ground for τ experimentation. Form factor effects in the effective weak Lagrangian may change the differential cross-section[15] by sizable amounts (as much as 10% for a reasonable set of assumptions). Another effect of size that will be easy to observe[16] is a shift in the peak cross-section energy for the process $e^+e^- \to (Z^\circ \to)\, l_j^+\, l_j^-$, which depends on the generation index, j. Lastly, form factor effects due to composite models can lead to particularly striking effects if we make the (reasonable) assumption that t quark and τ share a generation-defining sub-fermion. It has been shown[17] in particular that if the toponium mass is close to, but smaller than, the Z° mass, and if the generation-defining sub-fermion determines the "size" of a composite τ and t, then striking interference effects are to be expected both in the energy dependence of the ratio $\Gamma(\tau^+\tau^-)/\Gamma(\mu^+\mu^-)$ and in the measurable forward-backward asymmetry of τ pair production.

While individual models serve only to indicate where deviations from the Standard Model *might* be found, they certainly help to emphasize where experimental sensitivity has to be enhanced. They also illustrate the promise that precision study of our only heavy lepton offers when entering into a new realm of energy and momentum transfers, together with a clearly defined initial state.

REFERENCES

1. A recent review of tau forward-backward asymmetry measurements can be found in B. C. Barish and R. Stroynowski, CALT-68-1425 (to be published in Physics Reports).
2. See, for instance, B. Adeva *et al.*, Phys. Lett. 179B, 177 (1986).
3. See W. T. Ford *et al.*, SLAC-PUB-4066 (1987, to be published in Phys. Rev. D) and A. L. Read, Univ. of Colorado Ph.D. Thesis, COLO-HEP-122 (1986).
4. It is possible to rewrite this as $P^{\tau,Z} = \frac{-2v_{\tau,e}/a_{\tau,e}}{1+(v_{\tau,e}/a_{\tau,e})^2}$. This makes it explicitly clear that measurements of the polarizations determine the *ratio* of the couplings.
5. J. Matthews, SLAC Report No. 306, 100 (1986).
6. Proceedings of the SLC Workshop on Experimental Uses of the SLAC Linear Collider, SLAC Report No. 247 (1982).
7. The tabulated values of x_0 do not include mass effects, which increase the quoted values by more than 20% for the more massive mesons.
8. D. Stoker, MARK II/SLC Note 161.
9. KORALZ was written by S. Jadach, Z. Was, and R. Stuart. The implementation for Mark II is described in R. Van Kooten, MARK II/SLC-Physics Working Group Note 2-15.
10. P. Burchat, MARK II/SLC-Physics Working Group Note 2-16 and also contained in SLAC Report No. 306 (1986).
11. The Particle Data Group, M. Aguilar-Benitez *et al.*, Phys. Lett. **170B** (1986).
12. Y. S. Tsai, Phys. Rev. D**4**, 2821 (1971).
13. See, for example, F. J. Gilman and S. H. Rhie, Phys. Rev. D **31**, 1066 (1985). Evidence that, within the Standard Model, the problem cannot be completely resolved with η decays is given in F. J. Gilman, Phys. Rev. D **35**, 3541 (1987) and A. Pich, CERN-TH-4717 (1987).
14. C. A. Heusch, MARK II/SLC-Physics Working Group Note 2-21 and also contained in SLAC Report No. 306 (1986).
15. L. J. Hall and S. F. King, Nucl. Phys. B**287**, 551 (1987).
16. J. Pati and H. Stremnitzer, Phys. Rev. Lett. **56**, 2152 (1986).
17. J. Pati and H. Stremnitzer, University of Maryland preprint MdDP-PP-87-135 (1987).

Mark II/SLC-Physics Working Group Note # 3–18

AUTHOR: Gail G. Hanson

DATE: April 13, 1987

TITLE: Searches for the Top Quark

1. Introduction

This Report for the Mark II Pajaro Dunes Workshop summarizes the work of the Open Top Subgroup[1]. The status of searches for the top quark is presently somewhat ambiguous and a bit discouraging. UA1 now seems to see no signal attributable to top production, but they still have not set a limit. I have heard that not everyone in UA1 believes that top at a mass less than half the Z^0 mass will be ruled out, but we will have to wait and see. Possibly more serious evidence against the top quark at a mass accessible to the SLC comes from the ARGUS Collaboration[2]. They have just reported the observation at the $\Upsilon(4s)$ of B_d^0–$\overline{B}_d^0$ mixing at the 20% level. Ikaros Bigi[3] has calculated the relationship, shown in Fig. 1, between the top mass and B_d mixing in terms of the parameter F calculated from Kobayashi-Maskawa matrix elements, assuming three generations of quarks. Bigi says that the maximum value of F is 8, but it is more likely to be near 4. This puts a limit on the top mass (M_t) of $\gtrsim$ 60–120 GeV/c^2, unless there are four generations.

However, the Open Top Subgroup is still optimistic that top may be found at the SLC. The search methods we have used could also be applied to other heavy particles and so are worth trying on SLC data. Our work has been divided into three main topics:

1. Establishing a "top" signal.
2. Measuring the top mass.
3. Establishing that what we find is really top.

In the following Chapters we will first discuss the Monte Carlo models, cross sections and analysis procedures, followed by the specific work on these topics.

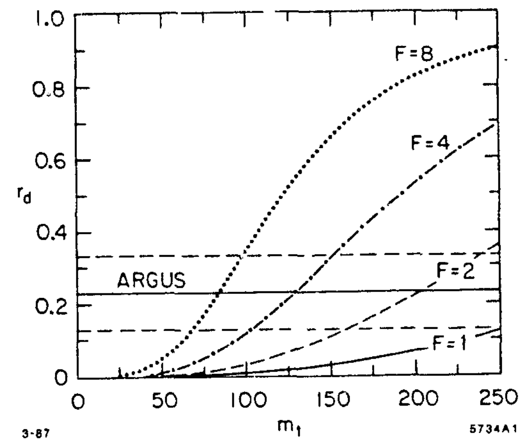

Fig. 1. r_d as a function of M_t in the Standard Model with three families. The theoretical uncertainties are expressed in terms of a factor

$$F = \frac{\mathrm{Re}(V\,(td))^2}{(0.01)^2}\,\frac{B\,f_B^2}{(100\,MeV)^2}.$$

2. Review of Models, Cross Sections and Analysis Procedures

2.1 Monte Carlo Models

The Monte Carlo models used for multihadronic background from u, d, s, c, and b quarks are the Lund model with order α_s^2 QCD matrix elements and symmetric string fragmentation of the partons, the Lund model with leading log parton shower evolution and symmetric string fragmentation, and the Webber model, which also uses leading log parton shower evolution but uses a combination of string and cluster fragmentation. These models were described by Alfred Petersen[4] at this Workshop. The two models with leading log shower evolution have been found to fit multihadronic data from e^+e^- annihilation at PEP/PETRA energies significantly better than models using order α_s^2 QCD matrix elements. Differences between these models as extrapolated to the Z^0 were described by Petersen.

The models used for $t\bar{t}$ production are the Lund model with order α_s^2 QCD matrix elements with either symmetric string fragmentation or Peterson fragmentation and the Webber model. These models were discussed by Kathy O'Shaughnessy[5] at the Granlibakken Workshop. In the Lund model with symmetric fragmentation

Table I. Top branching ratios.

Lund				
$t\bar{q} \rightarrow$	$bu\bar{d}$	+	Spectator	33%
	$bc\bar{s}$	+	"	26%
	$ub\bar{d}$	+	"	4%
	$cb\bar{s}$	+	"	3%
	$be^+\nu_e$	+	"	12%
	$b\mu^+\nu_\mu$	+	"	12%
	$b\tau^+\nu_\tau$	+	"	10%
Webber				
$t \rightarrow$	$bu\bar{d}$			1/3
	$bc\bar{s}$			1/3
	$be^+\nu_e$			1/9
	$b\mu^+\nu_\mu$			1/9
	$b\tau^+\nu_\tau$			1/9

pairs of top mesons are produced usually with no other particles because the top mesons are very hard. In the Lund model with Peterson fragmentation the top mesons are somewhat less hard and one can see some evidence of gluon radiation and production of other particles. Because of the difference in fragmentation there are observable differences between the two models for $25 < M_t < 35$ GeV/c^2, as will be pointed out in later Sections. Present data on heavy quarks does not distinguish between the two types of fragmentation. The effect will be more pronounced for top because it goes as mass squared. There appears to be no problem with using the Lund model with order α_s^2 matrix elements as compared with the Lund model with leading log parton shower evolution for $t\bar{t}$ production since the top quark is very heavy. In any case, we address these variations by using the Webber model. In the Webber model decays are on the quark level ($t \rightarrow bW^+$) as opposed to the Lund model in which top mesons decay. Mesons and baryons are formed only at the ends of the decay chains. Also, in the Webber model the quarks can radiate

gluons, even at intermediate stages of the decays. The branching ratios used for top decay in the Lund and Webber models are shown in Table I.

2.2 Normalization – $t\bar{t}$ Production Cross Section

At the Granlibakken Workshop[6] we presented the $t\bar{t}$ production cross section including the first-order radiative QCD corrections (Schwinger terms)[7]. The effect of these corrections is shown in Fig. 2. We have assumed $M_Z = 93$ GeV/c^2 and $\sin^2\theta_W = 0.22$. These corrections are quite large: they increase the cross section by 15% at $M_t = 25$ GeV/c^2, by 39% at $M_t = 40$ GeV/c^2, and by a factor of 2 at $M_t = 45$ GeV/c^2. We wondered how accurate these corrections are and, since they are so large, how large the higher-order corrections are. Ikaros Bigi and Bennie Ward have looked into this question, and they agree that these corrections are accurate to ~ 10%, unless M_t is very close (< 50 MeV/c^2) to $M_Z/2$.

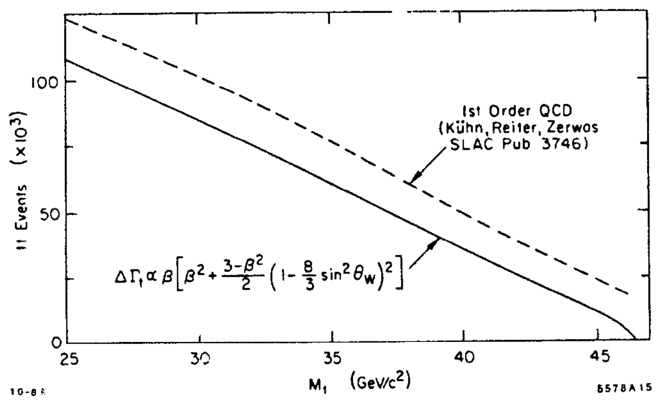

Fig. 2. Number of produced $t\bar{t}$ events for one year at a luminosity of 10^{30} cm^{-2} s^{-1} as a function of M_t without and with first-order QCD corrections. A factor of 0.80 for QED radiative corrections is included.

We have used the QCD-corrected cross sections, listed in Table II, in this report. They include a factor of 0.80 for QED radiative corrections. The cross section for multihadronic events from u, d, s, c, and b quarks, including the factor of 0.80 for QED radiative corrections, is taken to be 30.68 nb.

Table II. $t\bar{t}$ production cross sections for various top masses including first-order QCD corrections and a factor of 0.80 for QED radiative corrections.

M_t (GeV/c^2)	$t\bar{t}$ Production Cross Section (nb)
25	3.94
30	3.24
35	2.44
40	1.57
42.5	1.14
45	0.74
46	0.60

2.3 ANALYSIS PROCEDURES

2.3.1 MCMADE "Analysis"

Much of the Monte Carlo analysis work we have done has been based on using the produced four-vectors in COMMON/MCMADE/ with appropriate cuts or smearing to simulate the detector. For charged particles we choose the final decay particles unless the decay occurs very far from the interaction point. To simulate the acceptance of the drift chamber we require that the transverse momentum relative to the beam direction be greater than 150 MeV/c and $|\cos\theta| < 0.85$, where θ is the polar angle relative to the beam direction.

The only neutral particles used are photons. They are required to have at least 200 MeV energy and $|\cos\theta| < 0.95$. The total visible energy is the sum of the detected charged particle momenta and photon energies and is required to be greater than the beam energy (E_{Beam}). The main purpose of this cut is to suppress the background from events which go out the end of the detector. These events can fake a heavy particle signal because the only particles detected are at large angles to the $q\bar{q}$ axis. We tried to lower this cut to 80% of the beam energy but found that the events with lower visible energy tended to have larger angles between the thrust or sphericity axis and the true $q\bar{q}$ axis. We also make a loose cut on the polar angle of the thrust axis, θ_T: $|\cos\theta_T| < 0.95$.

Electrons and muons are identified by their true identity in the Monte Carlo. Electrons are required to have $|\cos\theta| < 0.85$, and muons are required to have $|\cos\theta| < 0.50$.

2.3.2 Detector Simulation

Some of the Monte Carlo data for $t\bar{t}$ production and for the background has been passed through the full HOWL detector simulation. The Monte Carlo simulated "data" has been passed through the full PASS2 analysis using TRKFIT[8] for charged particle tracking.

Cuts are then made on the track list quantities just as for real data. For charged tracks the transverse momentum relative to the beam direction is required to be greater than 150 MeV/c. Photons are required to have energy greater than 200 MeV. The distance of a photon from a charged track is required to be greater than 7 cm, and there is also a sharing cut. The total visible energy is required to be greater than E_{Beam}. The event is required to have at least 5 charged tracks (0.03% of $t\bar{t}$ events are lost by this cut). We also require $|\cos\theta_T| < 0.95$.

An attempt is made to identify electrons and muons in a realistic manner. For electrons we

CALL LAELEC(I, TEST1, ICLASS).[9]

Electron candidates must have momentum > 1 GeV/c. However, since there is no LAELEC for the endcaps yet, we use ICLASS to decide whether a particle is within the liquid argon fiducial volume and then use the Monte Carlo identification to decide that the particle is an electron. To simulate the endcaps, we call a particle an electron if $0.70 < |\cos\theta| < 0.96$ and it is identified as an electron by the Monte Carlo.

For muons we can use the actual muon identification scheme. A particle with momentum > 2 GeV/c is a muon if

MULEVE = 4 and
NUSTAT(I, 2.0) = 15.

3. Establishing a "Top" Signal

We have considered the following methods for establishing a top signal:

- Shape parameters
- High-p_T leptons
- Isolated leptons
- Multilepton events
- Cluster counting
- Total hadronic cross section.

O'Shaughnessy[5] discussed cluster counting, that is, counting the number of jets in events, at the Granlibakken Workshop. Unfortunately, indications are that the number of events in the background with large numbers of jets is quite high relative to the signal from $t\bar{t}$ events and is also model dependent. We may be able to reduce the background by adjusting the criteria used in the identification of the clusters, but no further work has been done since the Granlibakken Workshop. We have not yet studied in detail using the total multihadronic cross section to establish the existence of top.

We will report here on the use of shape parameters, high-p_T leptons, isolated high-p_T leptons, and lepton counting to establish a top signal. We will also discuss the possibility that top decays to a Higgs boson.

3.1 Establishing a Top Signal Using Shape Parameters

The use of shape parameters to establish a top signal is an obvious method and has been discussed at both the Asilomar and Granlibakken[5] Workshops. The idea, of course, is that $t\bar{t}$ events will be "fat" and easily distinguishable from the ordinary multihadronic background. We will summarize here the results of using the parameter aplanarity to try to establish a top signal. Table III shows the number of events with aplanarity > 0.12 for the multihadronic background models and for $t\bar{t}$ production for the different models and at various top masses.

One can see from the table that the number of high aplanarity events is model dependent both for the multihadronic background and for $t\bar{t}$ production, particularly for relatively low top masses of 25–30 GeV/c^2. For the *udscb* background there is a factor of two difference between the Lund leading log and the Webber models, both of which fit e^+e^- data in the PEP/PETRA energy range rather well. The differences for $t\bar{t}$ production between the Lund model with symmetric fragmentation and the Lund model with Peterson fragmentation can be understood in terms the differences in fragmentation. For the lower top masses the Lund model with symmetric fragmentation produces more back-to-back top mesons with no extra particles leading to fewer events with high aplanarity. It is encouraging that the Lund model with Peterson fragmentation and the Webber model agree for $t\bar{t}$ production.

Our conclusion is that a large number of high-aplanarity events may be a sign of new physics, but one cannot trust the Monte Carlo calculations for the number of events with high aplanarity for either the multihadronic background or the signal from $t\bar{t}$ production. We have also investigated other shape parameters. Thus shape parameters are not a reliable method for establishing a top signal.

Table III. Number of events with aplanarity > 0.12 for different multihadronic background models and for $t\bar{t}$ production for the different models and at various top masses normalized to the same number of Z^0's. QCD corrections were used for the $t\bar{t}$ cross sections. Error bars reflect the statistical errors of the Monte Carlo runs. The MCMADE analysis was used.

M_t (GeV/c^2)		Number of Events Produced	Number of Events With Aplanarity > 0.12
Background			
	Lund Order α_s^2	10,000 *udscb*	12 ± 3.5
	Lund Leading Log	(1.4 × 10^4 Z^0's)	37 ± 5.6
	Webber		76 ± 9.1
25	Lund Symmetric	1283	27 ± 6
	Lund Peterson		112 ± 12
	Webber		94 ± 7.8
30	Lund Symmetric	1058	71 ± 8.7
	Lund Peterson		138 ± 3.8
	Webber		126 ± 8.2
35	Lund Symmetric	795	129 ± 10
	Lund Peterson		147 ± 3.4
	Webber		132 ± 7.2
40	Lund Symmetric	512	108 ± 2.6
	Lund Peterson		116 ± 2.4
	Webber		112 ± 5.3
42.5	Lund Symmetric	372	79 ± 5.4
	Lund Peterson		84 ± 1.8
45	Lund Symmetric	240	40 ± 3.1
46	Lund Symmetric	195	29 ± 2.4

3.2 Establishing a Top Signal Using High-p_T Leptons

The semileptonic decay of top mesons provides a source of high-p_T leptons which can be used to establish a top signal. The use of high-p_T leptons to tag production of heavy quarks has been exploited extensively in PEP/PETRA analyses. This method was discussed at both the Asilomar and Granlibakken[6] Workshops. For completeness, we will review the results of this method.

We always calculate p_T relative to the thrust axis since this gives a distribution which is more similar to the p_T relative to the original top meson direction than is p_T relative to the sphericity axis. As discussed at Asilomar, the sphericity axis tends to be too close to very high-momentum, high-p_T particles so that the very high-p_T particles appear to be at lower p_T. If one uses the sphericity axis, one tends to lose the effect that leptons from higher-mass top mesons populate higher p_T. We calculate the thrust variable using all detected charged and neutral particles for either the MCMADE analysis or the track list quantities from the full detector simulation. For events in general, however, the sphericity axis and the thrust direction approximate the original top direction equally well.

At Granlibakken[6] we showed that there is no difference in the shape of the lepton p_T distribution for $p_T > 3$ GeV/c between the MCMADE analysis and the analysis using full detector simulation. By lepton we always mean an e or a μ. This is useful because we can save computer time by using only the MCMADE analysis for some of the work. The total numbers of leptons with $p_T > 3$ GeV/c are slightly different using the MCMADE quantities as compared with the detector-simulated quantities because the fiducial regions for the real detector are more complicated than the approximations used in the MCMADE analysis. In the detector simulation more charged and neutral particles are detected and the visible energy is higher because the fiducial region cuts used in the MCMADE analysis are tighter than the actual edges of detectors. In a real analysis, however, one might want to use these more severe cuts; here we simply used the detector simulation to indicate which particles were accepted. Of course, the detector simulation probably overestimates overall efficiencies at this point. On the other hand, fewer leptons are identified in the detector simulation because the cracks in the calorimeters and the muon system are put in realistically. At Granlibakken we also showed that the lepton p_T distributions for $p_T > 3$ GeV/c were consistent with being the same for the Lund model with symmetric fragmentation, the Lund model with Peterson fragmentation, and the Webber model. The lepton p_T distribution was also the same for the three models if the cut aplanarity > 0.02 was used on the event.

The numbers of e's and μ's with $p_T > 3$ GeV/c for the different models and for various top masses are shown in Table IV both for no aplanarity cut and for the cut aplanarity > 0.02. Also shown are the predictions for the background from

Table IV. Number of e's and μ's with $p_T > 3$ GeV/c relative to the thrust direction for various top masses. QCD corrections were used for the $t\bar{t}$ cross sections. Error bars reflect the statistical errors of the Monte Carlo runs. 10,000 $udscb$ events can be obtained in 38 days of running at a luminosity of 10^{29} cm^{-2} s^{-1}. The MCMADE analysis was used.

M_t (GeV/c^2)		Number of Events Produced	No Aplanarity Cut	Aplanarity > 0.02
Background				
	Lund Order α_s^2	10,000 $udscb$	81 ± 9	16 ± 4
	Lund Leading Log	(1.4 × 10^4 Z^0's)	79 ± 8.2	42 ± 6.0
	Webber		89 ± 9.4	46 ± 6.8
25	Lund Symmetric	12[illegible]3	325 ± 20	189 ± 16
	Lund Peterson		347 ± 21	258 ± 18
	Webber		316 ± 6.6	238 ± 5.8
30	Lund Symmetric	1058	299 ± 18	222 ± 15
	Lund Peterson		301 ± 5.6	239 ± 5.0
	Webber		287 ± 14	231 ± 13
35	Lund Symmetric	795	232 ± 14	184 ± 12
	Lund Peterson		243 ± 4.4	203 ± 4.0
	Webber		241 ± 11	206 ± 10
40	Lund Symmetric	512	151 ± 3.1	124 ± 2.8
	Lund Peterson		160 ± 2.9	137 ± 2.7
	Webber		162 ± 3.0	141 ± 2.8
42.5	Lund Symmetric	372	112 ± 6.5	93 ± 5.9
	Lund Peterson		123 ± 2.1	107 ± 2.0
45	Lund Symmetric	240	79 ± 4.4	65 ± 4.0
46	Lund Symmetric	195	57 ± 3.3	44 ± 2.9

multihadronic events from u, d, s, c, and b quarks using the Lund order α_s^2, Lund leading log, and Webber models. The error bars reflect the statistics of the various Monte Carlo data sets, which contained from 1000 to 10,000 produced $t\bar{t}$ events. The MCMADE analysis was used.

One can see that if no aplanarity cut is used the numbers of high-p_T leptons are quite model independent, both for the background and for $t\bar{t}$ events. One would expect this for the $t\bar{t}$ events since one is really looking at the characteristics of the top semileptonic decay. It is encouraging that the Webber model gives the same numbers of high-p_T leptons since it decays the top differently. However, it is surprising that the various background models are so similar since one might expect that introducing higher-order QCD effects would yield more high-p_T leptons.

Using only the Lund order α_s^2 model for background, we found that the cut aplanarity > 0.02 reduced the background by a large factor without reducing the signal very much. Just before the Granlibakken Workshop we began investigating the models with leading log parton shower evolution and found that the aplanarity cut was much less effective in reducing the background. Also, for $t\bar{t}$ production the aplanarity cut reduces the signal more for the Lund model with symmetric fragmentation than it does for either the Lund model with Peterson fragmentation or the Webber model for top masses from 25 to 35 GeV/c^2. The Lund model with Peterson fragmentation and the Webber model give very similar results.

Table V. Hadron misidentification backgrounds for leptons with $p_T > 3$ GeV/c. The numbers of particles with $p_T > 3$ GeV/c are given for leptons from $t\bar{t}$, leptons from $udscb$, misidentified hadrons from $t\bar{t}$, and misidentified hadrons from $udscb$ for 10,000 $udscb$ events and the corresponding number of 512 $t\bar{t}$ events for $M_t = 40$ GeV/c^2.

	Leptons From $t\bar{t}$	Leptons From $udscb$	Hadrons From $t\bar{t} \times$ C	Hadrons From $udscb \times$ C
Electrons				
(C = 0.005)				
No Aplanarity Cut	106.8	64.9	4.3	11.2
Aplanarity > 0.02	90.5	23.9	4.0	4.4
Muons				
(C = 0.01)				
No Aplanarity Cut	46.4	38.4	3.8	10.6
Aplanarity > 0.02	40.4	12.8	3.5	4.1

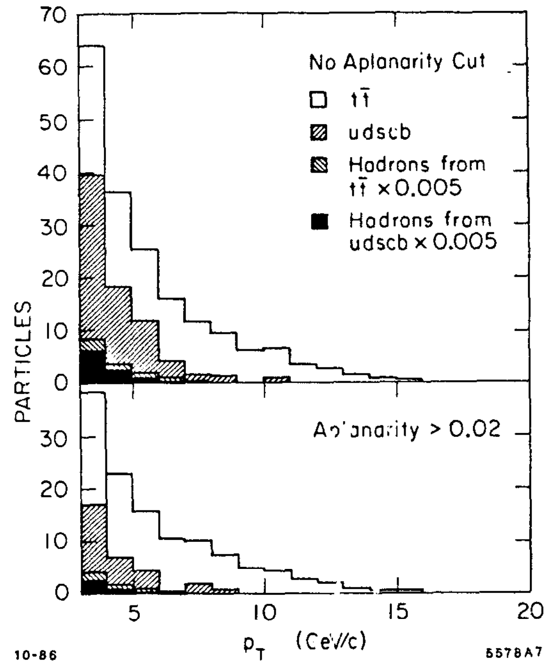

Fig. 3. Hadron misidentification backgrounds for electrons. The p_T distributions are shown for electrons from $t\bar{t}$, electrons from $udscb$, hadrons misidentified as electrons from $t\bar{t}$, and hadrons misidentified as electrons from $udscb$. The numbers of particles are given for 10,000 $udscb$ events from the Lund leading log Monte Carlo and the corresponding number of 512 $t\bar{t}$ events for $M_t = 40$ GeV/c^2 from the Lund model with Peterson fragmentation.

We have looked at backgrounds to high-p_T leptons from $t\bar{t}$ production due to misidentified hadrons. We have used detector simulation Monte Carlo data for both the background from u, d, s, c, and b multihadronic events and for $t\bar{t}$ production. The Lund leading log model was used for the background event production. We used $t\bar{t}$ production from the Lund model with Peterson fragmentation for $M_t = 40$ GeV/c^2.

We looked at electrons and muons separately. To calculate the background from hadrons which are misidentified as electrons, we multiplied the number of

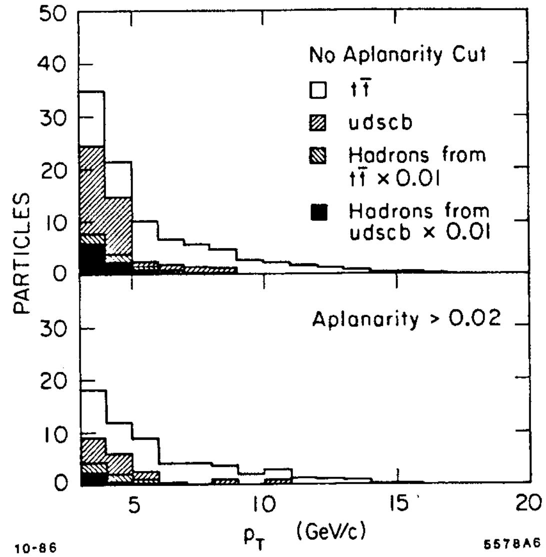

Fig. 4. Hadron misidentification backgrounds for muons. The p_T distributions are shown for muons from $t\bar{t}$, muons from *udscb*, hadrons misidentified as muons from $t\bar{t}$, and hadrons misidentified as muons from *udscb*. The numbers of particles are given for 10,000 *udscb* events from the Lund leading log Monte Carlo and the corresponding number of 512 $t\bar{t}$ events for $M_t = 40$ GeV/c^2 from the Lund model with Peterson fragmentation.

hadrons within the fiducial region of the calorimeters by 0.005. To calculate the number of hadrons misidentified as muons we multiplied the number of hadrons with MULEVE = 4 by 0.01. The misidentification probabilities are rough approximations to those measured at PEP[9]. More accurate misidentification probabilities as functions of p and p_T will have to be obtained for the SLC range of p and p_T. The results as a function of p_T are shown for electrons in Fig. 3 and for muons in Fig. 4. We have normalized to 10,000 non-top multihadronic events and to the appropriate number of $t\bar{t}$ events given by the production cross section. The total numbers of particles with $p_T > 3$ GeV/c are given in Table V.

The conclusion is that high-p_T leptons provide a model-independent signal for $t\bar{t}$ events if the aplanarity cut is not used; however, the background from non-$t\bar{t}$ events is rather large: the signal to background is 2 to 1 for $M_t = 40$ GeV/c^2. One can reduce the background by making an aplanarity cut, but the effect is not as large when background models which are probably more realistic are used; also, the

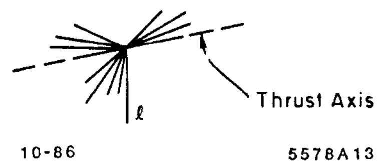

Fig. 5. Multihadronic event with gluon radiation showing how the p_T of a lepton in a jet can be increased because the thrust axis is not along the jet direction.

effect of the cut on $t\bar{t}$ events is model dependent, although the model dependence is not large for the larger top masses. The background from misidentified hadrons is not large: 15% of the $t\bar{t}$ signal for electrons and 31% for muons with no aplanarity cut at $M_t = 40$ GeV/c^2. The largest background is real leptons from non-top multihadronic events.

3.3 Establishing a Top Signal Using Isolated High-p_T Leptons

Another approach to reducing the background to high-p_T leptons from non-top multihadronic events is to require that the high-p_T leptons be isolated. Isolated leptons were used, for example, by UA1[10]. The philosophy is to look for leptons which are not in jets in order to reduce the background from *udscb* multihadronic events in which gluons have been radiated. The thrust axis in such events is not along the $q\bar{q}$ axis, which causes leptons from heavy quark decays (especially b's) to appear to have higher p_T, as shown in Fig. 5. For top meson decays one would select the lepton from the direct top semileptonic decay, but one would reject leptons which come from the semileptonic decay of the b from the top decay. Thus the signal would be reduced as compared with simply counting high-p_T leptons.

There are several methods one could use to select isolated leptons: requiring the energy to be less than some cut within a cone around the lepton, requiring the number of particles to be less than some cut within a cone around the lepton, and requiring that the lepton have no nearby clusters. Here we will employ the isolation method used by Tim Barklow for searches for supersymmetric particles[11]. First we select a lepton with $p_T > 3$ GeV/c as described in Section 3.2. In order to determine whether the lepton is isolated, we find clusters using all the other particles detected, charged and neutral. The VECSUB routine LCLUS$ is used. Then we calculate the quantities ρ_j defined[12] as

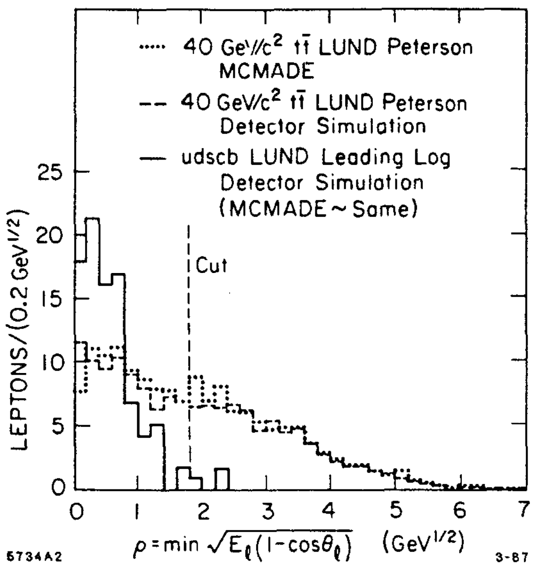

Fig. 6. Isolation criterion for leptons with $p_T > 3$ GeV/c. Distribution of ρ (defined in text) for leptons with $p_T > 3$ GeV/c for 10,000 *udscb* events from the Lund leading log model with full detector simulation and for 512 $t\bar{t}$ events with $M_t = 40$ GeV/c^2 from the Lund model with Peterson fragmentation for both the MCMADE analysis and the analysis using full detector simulation.

$$\rho_j = \sqrt{E_\ell \left(1 - \cos\theta_{\ell j}\right)},$$

where E_ℓ is the energy of the lepton and $\theta_{\ell j}$ is the angle between the lepton and the j^{th} cluster. We then examine

$$\rho = \min(\rho_j).$$

Figure 6 shows the distribution of ρ for leptons with $p_T > 3$ GeV/c for 10,000 *udscb* events from the Lund leading log Monte Carlo with full detector simulation

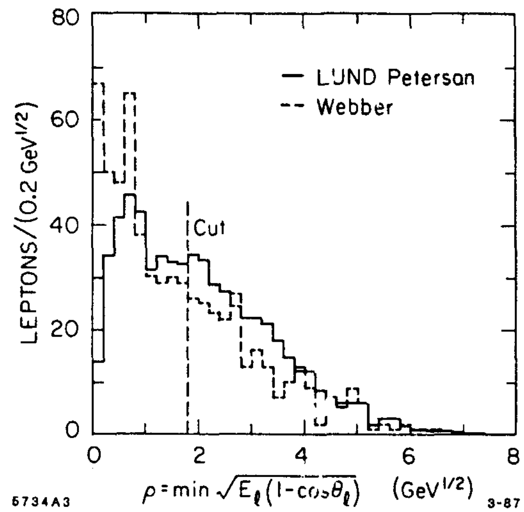

Fig. 7. ρ distributions for leptons with $p_T > 3$ GeV/c for $t\bar{t}$ production with $M_t = 35$ GeV/c^2 for the Lund model with Peterson fragmentation and for the Webber model. The distributions are normalized to the same number of leptons with $p_T > 3$ GeV/c.

and for the corresponding number of 512 $t\bar{t}$ events for $M_t = 40$ GeV/c^2. We make the cut $\rho > 1.8$ GeV$^{1/2}$ (it could be made as low as 1.4 GeV$^{1/2}$).

Table VI shows the number of e's and μ's with $p_T > 3$ GeV/c for the different models and for various top masses with and without the isolation cut. Also shown are the predictions for the two models with leading log parton shower evolution for the background from *udscb* multihadronic events. The background rejection is excellent. The top signal is reduced by about a factor of two as compared with counting the number of leptons with $p_T > 3$ GeV/c. There is, however, some model dependence in the isolation cut. For top masses between 25 and 35 GeV/c^2 the isolation criterion removes more leptons with $p_T > 3$ GeV/c in the Webber model than in either version of the Lund model. Figure 7 shows the ρ distributions for leptons with $p_T > 3$ GeV/c for 35 GeV/c^2 $t\bar{t}$ production for both the Lund model with Peterson fragmentation and the Webber model. The leptons in the Webber model are less isolated, probably because of more gluon emission, resulting in about 20% fewer leptons passing the isolation cut.

Table VI. Number of e's and μ's with $p_T > 3$ GeV/c relative to the thrust direction for various top masses with and without isolation. QCD corrections were used for the $t\bar{t}$ cross sections. Error bars reflect the statistical errors of the Monte Carlo runs. 10,000 *udscb* events can be obtained in 38 days of running at a luminosity of 10^{29} cm^{-2} s^{-1}. The MCMADE analysis was used, except for the *udscb* multihadronic background for which full detector simulation was used.

M_t (GeV/c^2)		Number of Events Produced	$p_T > 3$ GeV/c	Isolated ($\rho > 1.8$ GeV$^{1/2}$) $p_T > 3$ GeV/c
Background				
	Lund Leading Log	10,000 *udscb*	79 ± 8.2	2.6 ± 1.5
	Webber	(1.4×10^4 Z^0's)	87 ± 9.8	3.3 ± 1.9
	Lund Symmetric		325 ± 20	177 ± 15
25	Lund Peterson	1283	344 ± 21	145 ± 14
	Webber		307 ± 14	121 ± 8.8
	Lund Symmetric		298 ± 18	149 ± 13
30	Lund Peterson	1058	299 ± 5.6	150 ± 4.0
	Webber		291 ± 12	125 ± 8.1
	Lund Symmetric		230 ± 14	109 ± 9.3
35	Lund Peterson	795	240 ± 4.4	122 ± 3.1
	Webber		250 ± 10	97 ± 6.2
	Lund Symmetric		150 ± 3.1	76 ± 2.2
40	Lund Peterson	512	158 ± 2.8	76 ± 2.0
	Webber		170 ± 6.5	74 ± 4.3
42.5	Lund Symmetric	372	111 ± 6.4	61 ± 4.7
	Lund Peterson		122 ± 2.1	62 ± 1.5
45	Lund Symmetric	240	78 ± 4.4	38 ± 3.1
46	Lund Symmetric	195	57 ± 3.3	30 ± 2.4

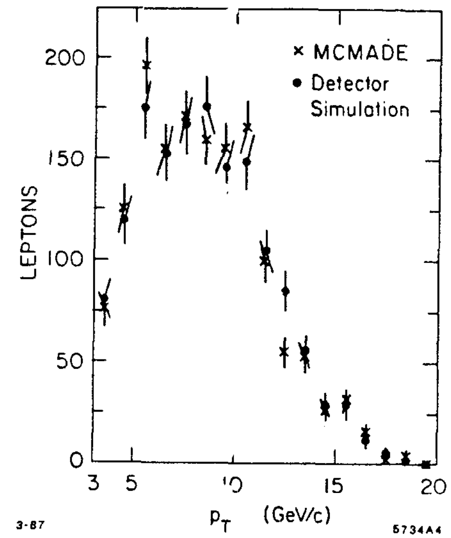

Fig. 8. Comparison of shapes of p_T distributions for isolated leptons for MCMADE analysis and analysis using full detector simulation for M_t = 40 GeV/c^2. The $t\bar{t}$ production model is the Lund model with Peterson fragmentation. The distributions are normalized to the same number of isolated leptons with $p_T > 3$ GeV/c.

As we did for the lepton p_T distributions with no cuts or with an event aplanarity cut, we have compared the shapes of the lepton p_T distributions with the isolation cut for the MCMADE analysis *vs.* full detector simulation and for differences among the various $t\bar{t}$ production models. Figure 8 shows the lepton p_T distributions for isolated leptons with $p_T > 3$ GeV/c for the MCMADE analysis and for the analysis using full detector simulation for $M_t = 40$ GeV/c^2. The Lund model with Peterson fragmentation was used. The two distributions are normalized to the same number of leptons with $p_T > 3$ GeV/c. The shapes of the two distributions are the same within statistics. The numbers of isolated leptons with p_T > 3 GeV/c are slightly different using the MCMADE quantities as compared with the detector-simulated quantities for the reasons given in Section 3.2. Figure 8 also illustrates the difference in shape of the lepton p_T distribution when the isolation criterion is applied (compare with Figs. 3 and 4). The isolation cut mainly removes leptons with $p_T \lesssim 8$ GeV/c. The resulting p_T distribution looks more like the p_T distribution of leptons from the top semileptonic decay. The leptons removed tend to be from cascade decays of b quarks coming from top decays. Since the very high p_T leptons remain, the isolated lepton p_T distribution is just as sensitive, if not more so, to the top mass.

Figure 9 shows the p_T distributions for isolated leptons for 40 GeV/c^2 $t\bar{t}$ production for the Lund model with symmetric fragmentation, the Lund model with Peterson fragmentation, and the Webber model. Within the statistical errors there is no difference in shape between the three models, although the Webber model does tend to have somewhat more leptons at lower p_T. We have shown that the shape of the p_T distribution for isolated leptons is the same for the MCMADE analysis and for the detector simulation analysis and is independent (within statistics) of the production model.

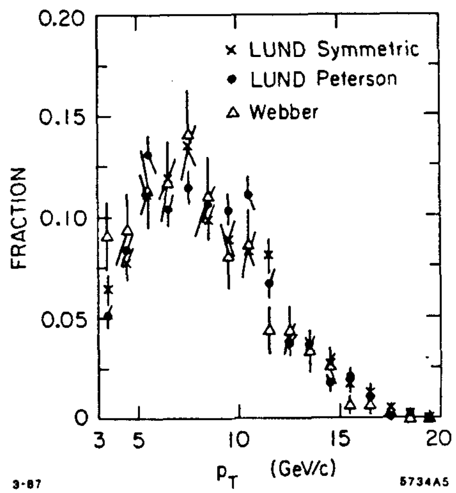

Fig. 9. Comparison of the p_T distributions for isolated leptons for the three $t\bar{t}$ production models for $M_t = 40$ GeV/c^2. The MCMADE analysis is used.

We have looked at backgrounds to isolated high-p_T leptons from $t\bar{t}$ production due to misidentified hadrons. The method used is the same as that described in Section 3.2, except that there are so few isolated hadrons that one has to take care that the particles within the fiducial regions of either the calorimeters or muon detection system are really hadrons and not leptons. For example, isolated particles within the fiducial region of the calorimeters are likely to be muons which were not identified by the muon system; these muons are not likely to be misidentified as

Table VII. Hadron misidentification backgrounds for isolated leptons with $p_T > 3$ GeV/c. The numbers of isolated particles with $p_T > 3$ GeV/c are given for leptons from $t\bar{t}$, leptons from $udscb$, misidentified hadrons from $t\bar{t}$, and misidentified hadrons from $udscb$ for 10,000 $udscb$ events and the corresponding number of 512 $t\bar{t}$ events for $M_t = 40$ GeV/c^2.

	Isolated Leptons From $t\bar{t}$	Isolated Leptons From $udscb$	Isolated Hadrons From $t\bar{t} \times$ C	Isolated Hadrons From $udscb \times$ C
Electrons (C = 0.005)	49.0	2.6	0.1	0.2
Muons (C = 0.01)	22.4	0.0	0.1	0.2

electrons. The backgrounds from misidentified hadrons are given in Table VII. There is no problem at all with background from isolated misidentified hadrons.

Isolated high-p_T leptons appear to be the best method for establishing a top signal since the background from u, d, s, c, and b multihadronic events is reduced to a negligible level. The problems are a loss of statistics by a factor of two compared with high-p_T leptons and some model dependence.

3.4 Establishing a Top Signal Using Lepton Counting

In view of the loss of statistics involved in the isolated high-p_T lepton method for establishing a top signal, Chang Kee Jung has begun to look into a method which might require fewer events for a statistically significant signal. He looks at the average number of leptons per event, making no cuts other than those required for lepton identification. His results are shown in Table VIII and Fig. 10. There is a statistically significant increase in average number of leptons per event if $t\bar{t}$ production is included for $M_t \lesssim 40$ GeV/c^2 if one stays within the same model. Jung also looks at the enhancement if the highest momentum lepton has momentum ($p_{leading}$) > 4 GeV/c. He has not yet looked into backgrounds from hadron misidentification, which will be more severe if no p_T or isolation cuts are made on the leptons. This analysis has uncovered a problem with the Monte Carlo models: the Webber model gives more leptons than the Lund model. This difference does not show up for leptons with $p_T > 3$ GeV/c and is probably due to a difference in charm or bottom quark decay. At least one of the models must disagree with known physics for this to happen. This will have to be investigated further.

Table VIII. Average number of leptons per event with and without requiring that the highest momentum lepton have momentum ($p_{leading}$) > 4 GeV/c for *udscb* background and for various top masses.

M_t (GeV/c^2)	Number of Events Produced	Average Number of Leptons per Event No Cuts	Average Number of Leptons per Event $p_{leading} > 4$ GeV/c
Background			
Lund Leading Log	10,000	0.200 ± 0.004	0.120 ± 0.003
Webber	*udscb*	0.228 ± 0.004	0.134 ± 0.003
25 Lund Peterson	11,283	0.279 ± 0.005	0.179 ± 0.004
Webber	*udscbt*	0.305 ± 0.005	0.192 ± 0.004
35 Lund Peterson	10,795	0.248 ± 0.005	0.160 ± 0.004
Webber	*udscbt*	0.284 ± 0.005	0.178 ± 0.004
40 Lund Peterson	10,512	0.233 ± 0.005	0.146 ± 0.004
Webber	*udscbt*	0.263 ± 0.005	0.163 ± 0.004
40 Lund Peterson ($t \to b\,H^+$, $H^+ \to c\bar{s},\ \tau^+\nu_\tau$)	10,512 *udscbt*	0.223 ± 0.005	0.130 ± 0.004
40 Lund Peterson ($t \to b\,H^+$, $H^+ \to c\bar{b}$)	10,512 *udscbt*	0.243 ± 0.005	0.143 ± 0.004

3.5 Establishing a Top Signal If Top Decays to a Higgs Boson

If there are two Higgs doublets and the charged Higgs mass is in the right range relative to top, the dominant decay of top could be $t \to bH^+$. The Higgs then decays into either $c\bar{s}$ and $\tau^+\nu_\tau$ or $c\bar{b}$, depending on the Kobayashi-Maskawa mixing angles. The branching ratio for top decay through the W would then be small, and the searches for top using its semileptonic decays would not work. Don Fujino has done some preliminary work on this possibility.

Fujino chooses events with five or six clusters and tries to reconstruct the Higgs and top masses from combinations of two or three clusters. He makes cuts,

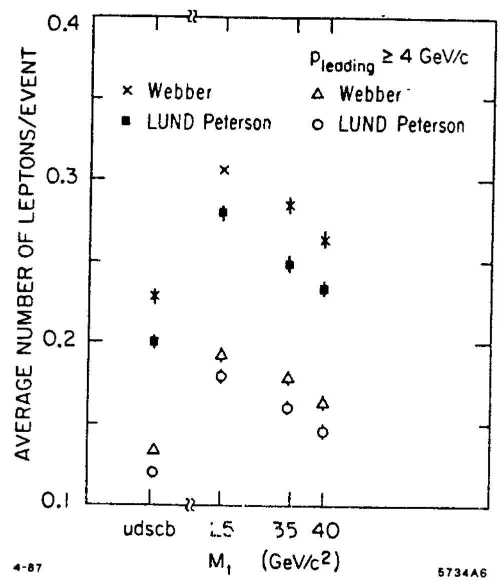

Fig. 10. Average number of leptons per event for *udscb* background and including top for various top masses. The background models are the Lund leading log and Webber models. The $t\bar{t}$ production models are the Lund model with Peterson fragmentation and the Webber model.

described in Section 4.5, to reduce the background from non-top multihadronic events and reduce the number of wrong combinations of clusters considered. Sachio Komamiya wrote the Monte Carlo used. Fujino's results for $M_t = 40$ GeV/c^2 and $M_H = 30$ GeV/c^2 are shown in Fig. 11. He uses the scaled mass as described in Section 4.5. Figure 11(a) shows the three-cluster mass distribution which does peak at 40 GeV/c^2. Figure 11(b) shows the two-cluster mass which peaks at 30 GeV/c^2. The difference, shown in Fig. 11(c), peaks at 10 GeV/c^2. The method seems to work well, except that Fig. 12 shows the same method applied to a Monte Carlo simulation with $M_t = 40$ GeV/c^2 and standard decays of top. Evidently three-cluster masses tend to peak at ~ 40 GeV/c^2, or about half the center-of-mass energy, and two-cluster masses tend to peak at about one-third the center-of-mass energy. There is also a problem with background from *udscb* multihadronic events, which is described in Section 4.5. Clearly much more work is needed to find top if it decays predominantly into a charged Higgs.

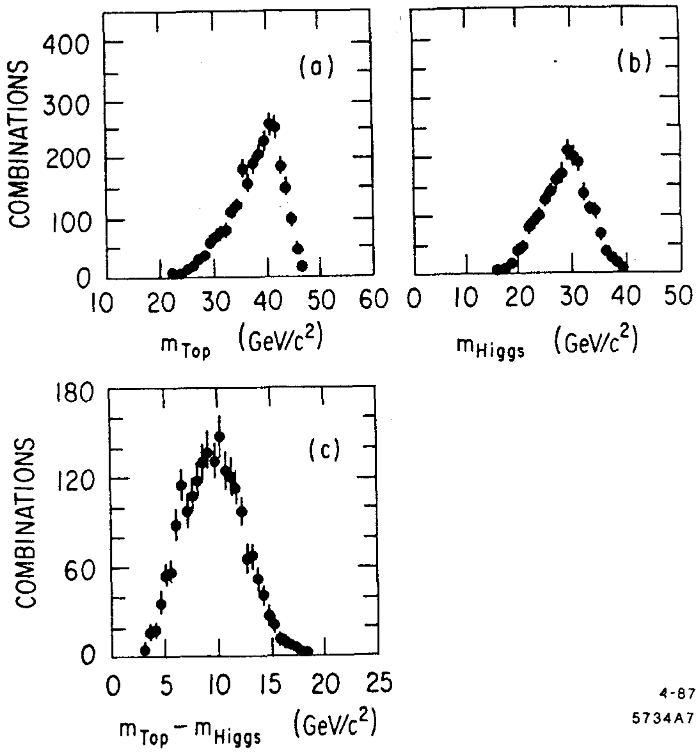

Fig. 11. Cluster masses for a Monte Carlo simulation in which $t \rightarrow bH^+$ and $H^+ \rightarrow c\bar{s}$ (75%) + $\tau^+\nu_\tau$ (25%). M_t = 40 GeV/c^2 and M_H = 30 GeV/c^2. (a) Three-cluster mass distribution. (b) Two-cluster mass distribution. (c) Difference between three- and two-cluster mass distributions.

4. Measuring the Top Mass

We are studying various methods for measuring the top mass, once we have (with some luck!) established a top signal. They are:

- Number of high-p_T or isolated high-p_T leptons
- Shape of the p_T distribution for isolated leptons
- Hadronic jet mass in events with a single semileptonic decay
- Reconstructed jet masses in events with double semileptonic decays
- Reconstructed jet masses in events with double hadronic decays.

We will discuss these methods in detail in the following Sections.

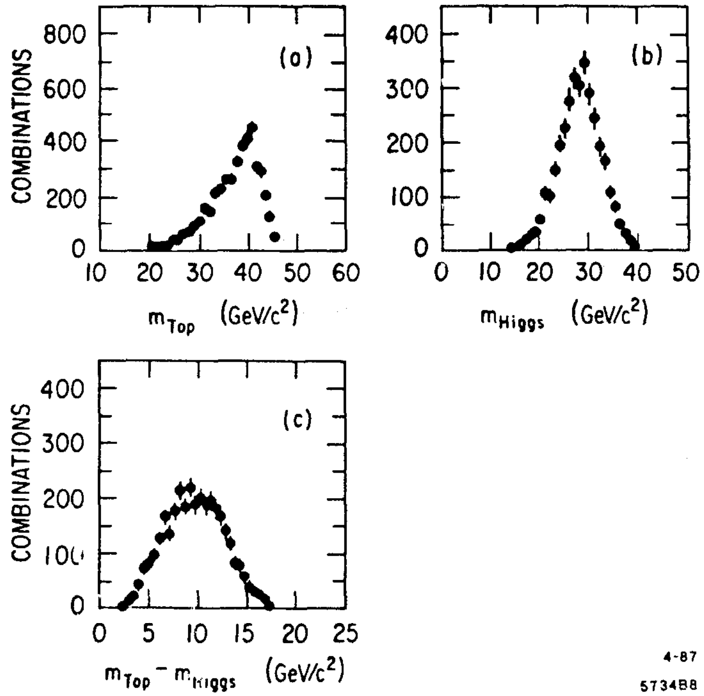

Fig. 12. Cluster masses for the Lund model with Peterson fragmentation in which $t \rightarrow bW^+$. (a) Three-cluster mass distribution. (b) Two-cluster mass distribution. (c) Difference between three- and two-cluster mass distributions.

4.1 Measuring the Top Mass From the Number of High-p_T or Isolated High-p_T Leptons

The mass of the top might be measured simply by counting the number of leptons or isolated leptons with $p_T > 3$ GeV/c and comparing with the prediction for each M_t. However, there are several serious problems with this method:

- The $t\bar{t}$ production cross section as a function of M_t must be known. The largest error in calculating this cross section is the QCD correction, which is probably accurate to 10%.
- The top semileptonic branching ratio must be assumed, but it can probably be calculated reliably.
- There is an $\sim$ 20% model dependence in the predicted number of isolated leptons with $p_T > 3$ GeV/c for a given number of produced $t\bar{t}$ events for $M_t \lesssim 35$ GeV/c^2.
- One must know the e and μ identification efficiencies.
- The background from non-$t\bar{t}$ must be known, but this appears to be under control for isolated high-p_T leptons, unless there is a background from other new physics.
- The hadron misidentification backgrounds must be known, but this also does not appear to be a problem, especially for isolated high-p_T leptons.

Assuming we can solve all of these problems, then we would simply count the number of leptons or isolated leptons with $p_T > 3$ GeV/c and compare with the predictions as in Table VI, normalized to the number of Z^0's produced. For example, if we measured 70 $\pm$ 8.4 isolated leptons with $p_T > 3$ GeV/c for 10,000 produced *udscb* multihadronic events, we could measure $M_t = 41.5\ ^{+1.3}_{-1.5}$ GeV/c^2. This method is less sensitive for lower top masses because there is more model dependence and because the number of high-p_T leptons varies less rapidly with top mass. It is interesting to note that one can obtain M_t with slightly less error with higher background since the differences for different M_t are more significant – one only has to know the background. In practice, one would use other methods, such as the shape of the p_T distribution for isolated leptons, and then check the number of isolated high-p_T leptons against the prediction for consistency.

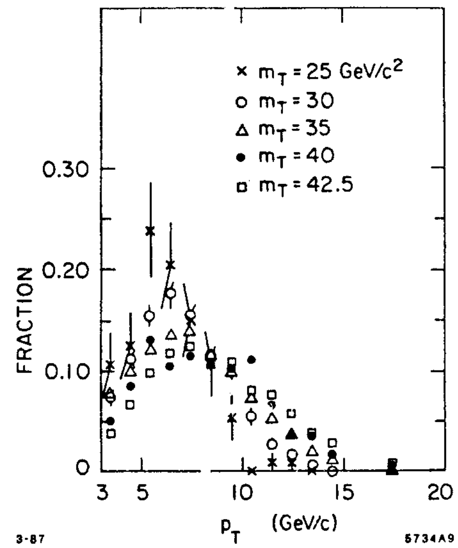

Fig. 13. p_T distributions for isolated leptons for various top masses for the Lund model with Peterson fragmentation. The distributions are given as fractions of the total number of isolated leptons with $p_T > 3$ GeV/c at each top mass. The MCMADE analysis is used.

4.2 Measuring the Top Mass from the Shape of the p_T Distribution for Isolated Leptons

At the Granlibakken Workshop[6] we discussed measuring the top mass from the shape of the lepton p_T distribution. Here we use instead the shape of the p_T distribution for isolated leptons since the background from *udscb* multihadronic events is much less.

The shape of the lepton p_T distribution varies with the mass of the top meson due to the kinematics of the semileptonic decay. If one requires that the lepton be isolated, the p_T distribution becomes more like that from the semileptonic decay of the top: the leptons removed have mainly $p_T < 8$ GeV/c and tend to be from the cascade decays of b quarks coming from top decays. We show in Fig. 13 the p_T distributions for isolated leptons for various top masses given as the fraction of the total number of isolated leptons with $p_T > 3$ GeV/c at each top mass. Of course, the p_T distribution shifts to higher p_T as the top mass increases. We have

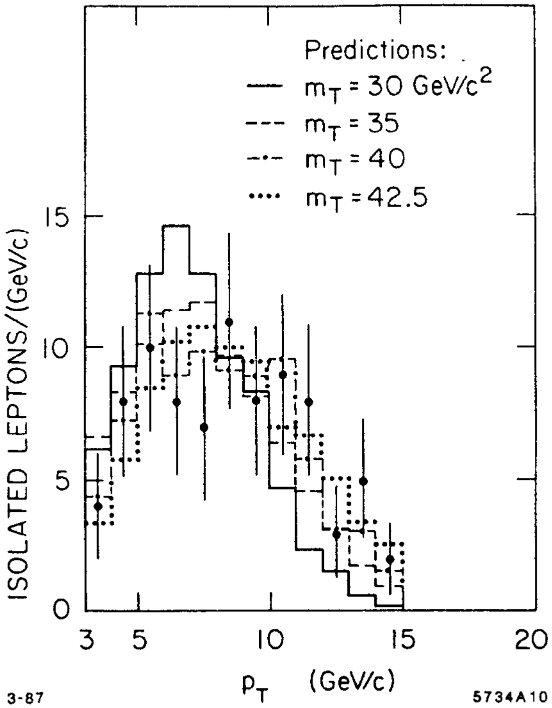

Fig. 14. p_T distribution for isolated leptons from 512 $t\bar{t}$ events at $M_t = 40$ GeV/c^2 from the Lund model with Peterson fragmentation compared with predictions for $30 < M_t < 42.5$ GeV/c^2. There are 83 isolated leptons with $3 < p_T < 15$ GeV/c.

used a likelihood method to study the differences in shapes for various top masses. One could also look at the average p_T, but the likelihood method should give the maximal information.

In order to use a likelihood method, one needs to know the predicted shape of the p_T distribution very well. For this study we generated 10,000 $t\bar{t}$ events for each top mass $30 < M_t < 42.5$ GeV/c^2 using the Lund model with Peterson

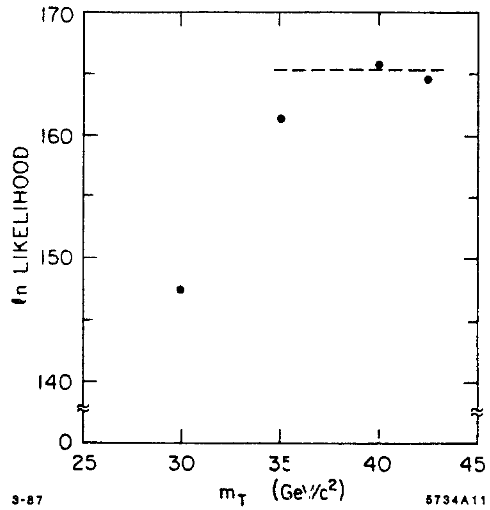

Fig. 15. The ln likelihood that each of four mass hypotheses fits the shape of the p_T distribution for the 512 $t\bar{t}$ events from the Lund model with Peterson fragmentation at $M_t = 40$ GeV/c^2. The dashed line is drawn 0.5 unit of ln likelihood lower than the largest ln likelihood of the four hypotheses at $M_t = 40$ GeV/c^2.

fragmentation. We used the MCMADE analysis in order to save computer time. In Section 3.3 we showed that there is no difference in the shape of the p_T distribution for isolated leptons between the MCMADE analysis and the analysis using full detector simulation.

To study the method, we generated fake data by looking at the number of isolated leptons in each p_T bin for the first 512 $t\bar{t}$ events (corresponding to 10,000 *udscb* events) in one of the $M_t = 40$ GeV/c^2 runs and compared this distribution with the high-statistics predictions for each of the various top masses. We assumed a Poisson distribution, so the ln likelihood is given by

$$\ln \text{likelihood} = \sum n \ln \bar{n},$$

where n is the measured number in each bin and $\bar{n}$ is the predicted number in each bin. The normalization is fixed by

$$\sum n = \sum \bar{n}.$$

We are studying the shape only; the number of isolated leptons for $p_T > 3$ GeV/c is the same for each of the predictions. We have to use only those p_T bins for all of the mass hypotheses for which we have a reliable prediction for each mass hypothesis. For example, if we include the hypothesis $M_t = 25$ GeV/c^2 and there are no isolated leptons with $p_T > 13$ GeV/c for that mass hypothesis, then for testing all hypotheses we would include only those bins $3 < p_T < 13$ GeV/c in the ln likelihood calculation.

The fake data for $M_t = 40$ GeV/c^2 compared with the predictions for $30 < M_t < 42.5$ GeV/c^2 are shown in Fig. 14. The ln likelihood for each mass hypothesis is shown in Fig. 15. Note that even with only 512 events (83 isolated leptons with $3 < p_T < 15$ GeV/c), we can see a distinct difference in ln likelihood between the different mass hypotheses. Remember that 0.5 unit of ln likelihood corresponds to one standard deviation difference in M_t. One would need to run more Monte Carlo data to map out the shape of the ln likelihood near the maximum. It looks as if one could measure M_t to $\pm \sim 1.5$ GeV/c^2 for $M_t \sim 40$ GeV/c^2.

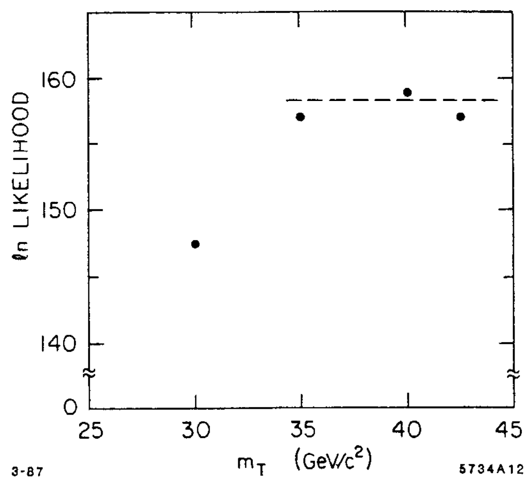

Fig. 16. The ln likelihood that each of four mass hypotheses fits the shape of the p_T distribution for the 512 $t\bar{t}$ events from the Webber model at $M_t = 40$ GeV/c^2. There are 80 isolated leptons with $3 < p_T < 15$ GeV/c. The dashed line is drawn 0.5 unit of ln likelihood lower than the largest ln likelihood of the four hypotheses at $M_t = 40$ GeV/c^2.

As an additional test of this method we compared 512 $t\bar{t}$ events from the Webber model with $M_t = 40$ GeV/c^2 with the predictions calculated from the Lund model with Peterson fragmentation. The ln likelihood for each mass hypothesis is shown in Fig. 16. The ln likelihood is still largest for the 40 GeV/c^2 hypothesis, but there is less separation between the 35 and 40 GeV/c^2 hypotheses than there was for the fake data generated with the Lund model. This may be due to a statistical fluctuation, or it may be due to differences in the shape of the p_T distribution for isolated leptons between the Lund model and the Webber model. We did see some evidence for this in Fig. 9, but higher statistics Monte Carlo runs would be needed to clarify the situation.

In any case, except for possible differences between models, the shape of the p_T distribution for isolated leptons is just as sensitive to the top mass for the same number of produced $t\bar{t}$ events as without the isolation cut even though there are fewer leptons in the distribution.

4.3 Measuring the Top Mass from the Hadronic Jet Mass in Events with a Single Semileptonic Decay

This method, developed by Tim Barklow, has not changed since the Granlibakken Workshop. It is repeated here for completeness. The philosophy is to select events with an isolated lepton and then reconstruct the mass of three clusters assumed to come from the hadronic decay of a top meson. One selects events with an isolated lepton and four clusters. Then one forms the quantity

$$M_{Hadron} = \frac{E_{Beam}}{\gamma_{Measured}}.$$

$\gamma_{Measured}$ is the γ of the resultant four-vector of the three clusters assumed to come from the hadronic top decay. This definition reduces the smearing due to varying amounts of missing energy. Fig. 17 shows the distribution of M_{Hadron} for $M_t = 25$ GeV/c^2. The peak at high mass ($\sim E_{Beam}$) is due to wrong combinations. One sees an asymmetric peak at ~ 25 GeV/c^2 with an rms width of ~ 1 GeV/c^2. Fig. 18 shows the same distribution for $M_t = 40$ GeV/c^2. There is a peak at ~ 40 GeV/c^2 which is somewhat obscured by the high-mass peak from wrong combinations. The method is probably the most promising of the jet mass reconstruction methods, but we need to find cuts to remove the background from wrong combinations.

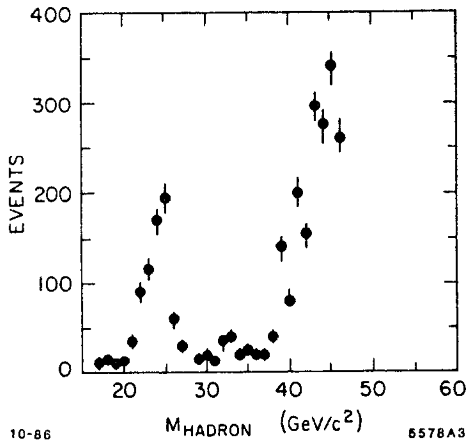

Fig. 17. Distribution of M_{Hadron} for M_t = 25 GeV/c^2.

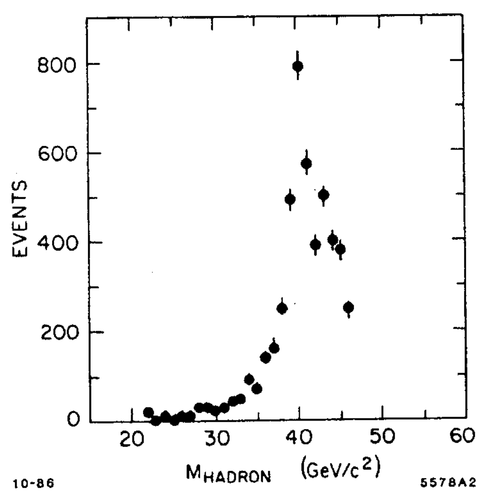

Fig. 18. Distribution of M_{Hadron} for M_t = 40 GeV/c^2.

4.4 Measuring the Top Mass Using Events with Double Semileptonic Decays

John Bartelt worked on this analysis, which was suggested in Ref. 7. One selects events with two isolated leptons and at least two jets. The missing four-momentum (assumed to be the two neutrinos) is then calculated. The event is boosted to the rest frame of the missing four-momentum. The neutrino energy is assumed to equal half the missing mass. For an array of polar and azimuthal angles (θ, ϕ), which are assumed to be the neutrino direction, one calculates the mass of the jet, lepton, and neutrino on each side of the event. One then plots all masses which pass some cut on the difference in masses between the two sides, or, alternatively, one plots the average mass for the θ, ϕ value which gives the smallest mass difference. Such a mass plot using the first method is shown in Fig. 19 for 1000 produced $t\bar{t}$ events for M_t = 40 GeV/c^2. There is a wrong combination peak at $\sim$ 25 GeV/c^2. One problem with this method is that a large number ($\geq$ 1000) of $t\bar{t}$ events are needed because of the requirement that both top mesons decay semileptonically. However, there is no problem with background from *udscb* multihadronic events. This method can probably best be used to confirm other methods.

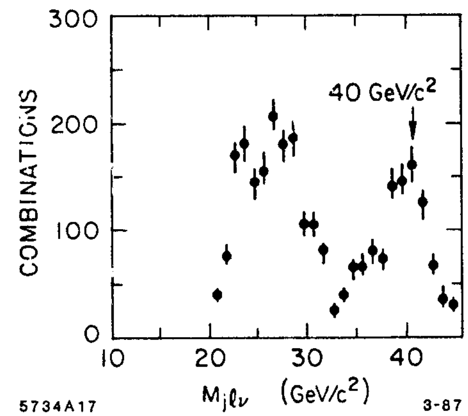

Fig. 19. Distribution of the masses of jet, lepton, and neutrino for 1000 $t\bar{t}$ events with full detector simulation at M_t = 40 GeV/c^2.

4.5 Measuring the Top Mass Using Events with Double Hadronic Decays

Don Fujino developed this method as a complement to the methods involving top semileptonic decays. This method is also used for the analysis described in Section 3.5. One looks for events in which both top mesons decay hadronically, typically five- or six-cluster events. One needs to apply tight cuts to remove the background from *udscb* multihadronic events and from wrong combinations in $t\bar{t}$ events. The analysis is described in detail in Ref. 13 and summarized here.

The cuts used are the following:

- Total visible energy > E_{Beam}
- $\geq$ 5 clusters
- No isolated e's or μ's
- Event shape cuts
- Cuts on missing energy and momentum
- Combinatorics cuts
- Cuts to require that the two top mesons be back-to-back
- A cut on the mass difference between the two sides of the event.

The energy (E_{Top}) and momentum (p_{Top}) of three-cluster combinations which pass the cuts are then calculated. The top mass (M_{Top}) is then calculated using a rescaling technique to make up for missing energy:

$$M_{Top} = \frac{E_{Beam}}{E_{Top}}\sqrt{E_{Top}^2 - p_{Top}^2}.$$

Distributions of this quantity for various top masses and Monte Carlo models are shown in Fig. 20. Figure 20(a), which shows M_{Top} for M_t = 25 GeV/c^2 for the Lund model with symmetric fragmentation, shows a very clear peak at 25 GeV/c^2. The peak is broader and there is a larger wrong combination peak at $\sim E_{Beam}$ in Fig. 20(b), which shows M_t = 25 GeV/c^2 but for the Lund model with Peterson fragmentation. The explanation for the difference is that $t\bar{t}$ production with symmetric fragmentation is more consistent with the hypothesis of back-to-back top meson production. For M_t = 35 GeV/c^2, shown in Fig. 20(c), there is still a peak at 35 GeV/c^2, but it is on the shoulder of a large wrong combination peak. For M_t = 40 GeV/c^2, shown in Fig. 20(d), the top peak is totally obscured by the wrong combination peak. Figure 20(e) shows the M_{Top} distribution for the *udscb* multihadronic background for the worst case, the Webber model. The number of combinations in this plot is about four times as many as for 40 GeV/c^2 $t\bar{t}$

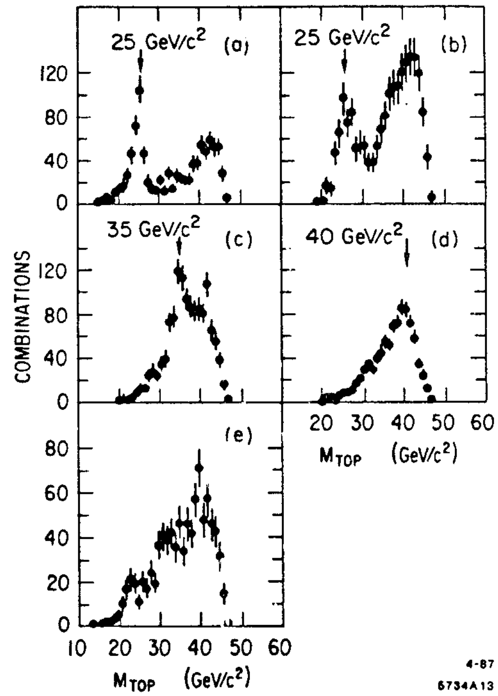

Fig. 20. Distributions of M_{Top} (defined in text) for (a) 1000 $t\bar{t}$ events for M_t = 25 GeV/c^2 using the Lund model with symmetric fragmentation, (b) 1000 $t\bar{t}$ events for M_t = 25 GeV/c^2 using the Lund model with Peterson fragmentation, (c) 1000 $t\bar{t}$ events for M_t = 35 GeV/c^2 using the Lund model with Peterson fragmentation, (d) 1000 $t\bar{t}$ events for M_t = 40 GeV/c^2 using the Lund model with Peterson fragmentation, and (e) 10,000 *udscb* multihadronic events using the Webber model.

normalized to the same number of produced Z^0's and would swamp the top signal for $M_t \gtrsim$ 35 GeV/c^2. Fujino is working on cuts to reduce this background. The mass peaks for lower-mass top look quite hopeful, though.

5. Establishing That What We Find Is Really Top

If we find a signal for some type of new particle which seems to fit the criteria for top production, we have to establish that it is really top. The methods which we have considered are the following:

- Establish the decay $T \rightarrow B\bar{\ell}\nu X$
- Measure the semileptonic inclusive branching ratios
- Measure the $t\bar{t}$ forward-backward asymmetry using lepton tags
- Explicitly rule out other possibilities such as B′, heavy lepton, or supersymmetry
- Measure the lepton momentum distribution.

We have not yet worked on measuring the semileptonic branching ratios; there are the obvious normalization difficulties, similar to those listed in Section 4.1. The other methods are described in detail in the following Sections.

5.1 Establishing the Decay $T \rightarrow B\bar{\ell}\nu X$ and Explicitly Ruling Out Some Other Possibilities

If we can establish that we have observed a new particle which decays into $B\bar{\ell}\nu X$ with parameters which agree with those for the top meson, then it is very unlikely that the new particle is something else. We would already have studied the shape of the p_T distribution for isolated leptons, as described in Section 4.2. We would go on from there to establish that the isolated high-p_T lepton was produced along with a cluster which has an impact parameter consistent with a bottom meson. Steve Wagner and Wayne Koska have worked on this problem. In Fig. 21 we show the impact parameter of the lepton *vs.* the impact parameter of the jet for various hypotheses for a 25 GeV/c^2 heavy quark. If the heavy quark is top, we would expect it to decay with a short lifetime into a B with a long lifetime. Therefore the impact parameter of the lepton would be small while the impact parameter of the jet would be large. This is what we see for the case $t \rightarrow bW^+$ for the Lund model with symmetric fragmentation or Peterson fragmentation. There are differences between the two models due to the harder t-quark fragmentation in the symmetric fragmentation model. If, on the other hand, the new particle is a short-lived particle which decays into cW^-, both impact parameters will be small, as shown in Fig. 21. If the new particle is long-lived, both impact parameters will be large, which is also shown in Fig. 21.

The dependences of the jet impact parameter on the top mass and on the two fragmentation models are shown in Fig. 22. The impact parameter decreases slightly as M_t increases. Also, the difference between the two fragmentation models

April 13, 1987

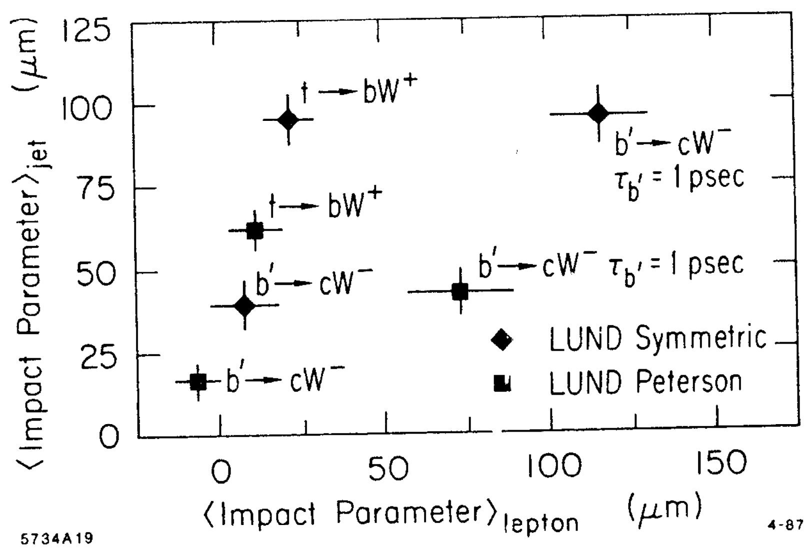

Fig. 21. Impact parameter of the lepton *vs.* impact parameter of the jet for various hypotheses for a 25 GeV/c^2 heavy quark.

disappears for $M_t \geq 35$ GeV/c^2. For the two cases $b' \rightarrow cW^-$ and $t \rightarrow dW^+$ the jet impact parameter is much smaller.

According to these studies we should be able to establish the decay $T \rightarrow B\bar{\ell}\nu X$ by examining the impact parameters of the lepton and the jet coming from the decay. However, this analysis was done using MCMADE quantities and needs to be made more realistic using detector simulation.

5.2 Measuring the $t\bar{t}$ Forward-Backward Asymmetry

The $t\bar{t}$ forward-backward asymmetry was discussed at the Asilomar and Granlibakken Workshops[6]. Since then we have made improvements in reducing the background and in increasing the sensitivity of the measurement.

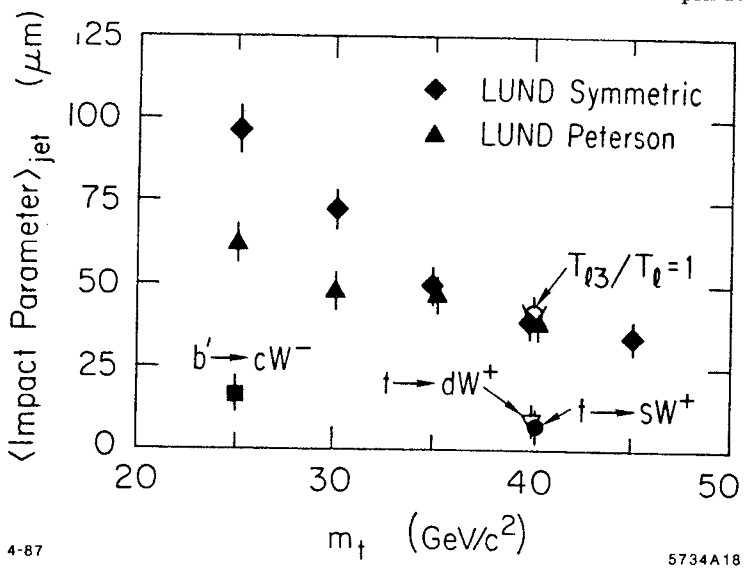

Fig. 22. Impact parameter of the jet *vs.* mass of the top or heavy quark for the Lund model with symmetric or Peterson fragmentation or for other hypotheses for the decay of the heavy quark.

The polar angle distribution for any fermion pair from Z^0 decay is given by

$$\frac{d\sigma}{d\cos\theta} = \frac{\pi\alpha^2}{2s}(1+\cos^2\theta) + \frac{G_F^2 M_Z^4}{256\pi\Gamma_Z^2}\left[(v_e^2+a_e^2)(v_f^2+a_f^2)(1+\cos^2\theta) + 8a_e v_e a_f v_f \cos\theta\right],$$

where α is the fine structure constant, s is the center-of-mass energy squared, G_F is the Fermi coupling constant, M_Z and Γ_Z are the mass and width of the Z^0, respectively, and $a_{e,f}$ and $v_{e,f}$ are the axial vector and vector weak coupling constants for the electron and fermion.

Integrating over $\cos\theta$ for the forward and backward regions, we obtain the forward-backward asymmetry:

$$A_{FB} = \frac{3a_e v_e a_f v_f}{(a_e^2+v_e^2)(a_f^2+v_f^2)}.$$

The forward-backward asymmetry can be used to distinguish between charge-1/3 and charge-2/3 quarks. The forward-backward asymmetry is 0.12 for the t quark and 0.17 for the b quark at the Z^0 peak (assuming $\sin^2\theta_W = 0.22$). These would be rather difficult to distinguish experimentally, except that the charge asymmetries of the leptons from the semileptonic decays have different signs. This happens because a top quark decays into a positively-charged lepton, whereas a bottom quark decays into a negatively-charged lepton. The $t\bar{t}$ forward-backward asymmetry may be reduced by the effects of the large top mass or by other details of top meson production; nevertheless, it is an important physical measurement to make to establish the identity of the top meson.

The sphericity axis is a surprisingly good measure of the top quark direction, even for top masses as large as 40 GeV/c², as shown in Fig. 23. The lepton from the top semileptonic decay is in the same hemisphere as the top meson ~ 75% of the time for M_t = 40 GeV/c². Therefore, the sphericity axis pointed in the hemisphere of the positively-charged lepton from the top semileptonic decay (or in the opposite hemisphere to the negatively-charged lepton) can be used to measure the top forward-backward asymmetry. One needs to use cuts to ensure that the leptons come only from the top semileptonic decay since the major background is leptons from b-quark decays, which have the opposite asymmetry. At Granlibakken we had determined the following cuts to select leptons from the top semileptonic decay:

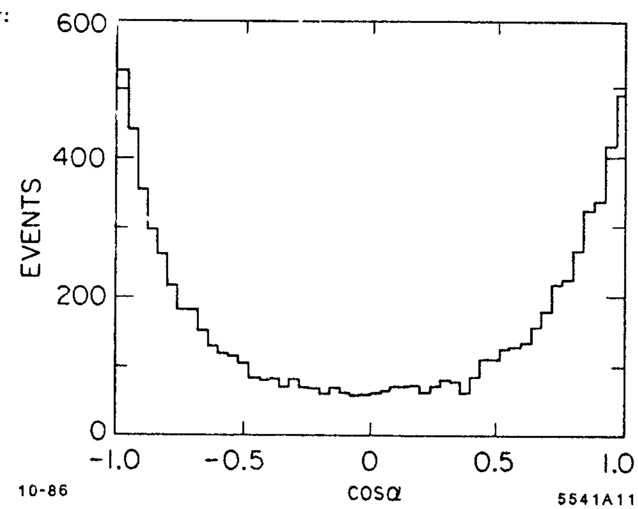

Fig. 23. Cosine of the angle between the produced quark direction and the reconstructed sphericity axis for M_t = 40 GeV/c².

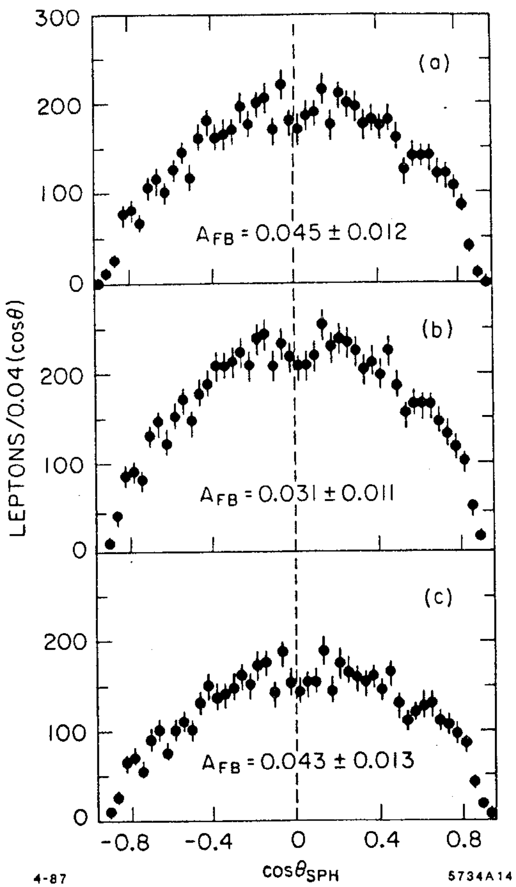

Fig. 24. Cos θ distribution of the lepton-signed sphericity axis for 50,438 $t\bar{t}$ events at $M_t = 40$ GeV/c^2 for (a) high-p, p_T leptons, (b) isolated leptons with $p_T > 3$ GeV/c, and (c) isolated high-p, p_T leptons.

$$p_T \geq 8.0\ GeV/c \text{ or}$$

$$5.0 < p_T < 8.0\ GeV/c \text{ and } p \geq 14\ GeV/c \text{ or}$$

$$3.0 \leq p_T \leq 5.0\ GeV/c \text{ and } p \geq 18\ GeV/c.$$

From Monte Carlo data with detector simulation we found that these cuts give leptons which come from the top semileptonic decay 94% of the time for $M_t = 40$ GeV/c^2. We will refer to leptons which satisfy these cuts as high-p, p_T leptons. In order to study how to make the forward-backward asymmetry measurement more sensitive, we generated 50,438 $t\bar{t}$ Monte Carlo events with $M_t = 40$ GeV/c^2 with only MCMADE quantities. Using high-p, p_T leptons from this sample, we obtain the lepton-signed sphericity axis cos θ (cos θ_{SPH}) distribution shown in Fig. 24(a). The forward-backward asymmetry from this distribution is 0.045 ± 0.012 using e's and μ's together. Clearly this is not a measurement for the first year of running at the SLC! The Muon Upgrade improves this measurement by doubling the number of identified μ's so that the numbers of identified e's and μ's are about the same.

Table IX. Number of leptons from $t\bar{t}$ compared with background from *udscb* multihadronic events for various requirements on the leptons. The Lund model with Peterson fragmentation with $M_t = 40$ GeV/c^2 was used for $t\bar{t}$ production, and the Lund leading log model was used for *udscb* production. 10^5 *udscb* events were assumed with the corresponding number of 5120 $t\bar{t}$ events. Full detector simulation was used.

Lepton Requirement	$t\bar{t}$ Signal	*udscb* Background
High p, p_T	576 ± 17	221 ± 43
Isolated	679 ± 19	25 ± 15
Isolated High p, p_T	483 ± 16	17 ± 12

The estimated background to high-p, p_T leptons from *udscb* multihadronic events is larger than expected, however, considering the severity of the high-p, p_T cuts, as shown in Table IX. This is especially unfortunate because the background events tend to be $b\bar{b}$ events and so have the opposite asymmetry. One must find a better set of cuts to reduce this background. Our work on establishing a top signal using isolated leptons led us to look at the forward-backward asymmetry for the lepton-signed cos θ_{SPH} distribution using isolated leptons with $p_T > 3$

GeV/c, shown in Fig. 24(b). The forward-backward asymmetry from this dist bution is 0.031 $\pm$ 0.011, somewhat less than for the high-p, p_T leptons probab because only about 90% of the isolated leptons with $p_T > 3$ GeV/c are from t top semileptonic decay. Of course, the problem of background from $udscb$ mul hadronic events has been solved, as shown in Table IX. Thus we are led to go o step further to using isolated high-p, p_T leptons to measure the forward-backwa asymmetry. The lepton-signed cos θ_{SPH} distribution for isolated high-p, p_T lepto is shown in Fig. 24(c) and has a forward-backward asymmetry of 0.043 $\pm$ 0.01 which is as good as for high-p, p_T leptons. The background situation is now ev better, as shown in Table IX. For a data set corresponding to 10^5 $udscb$ mult hadronic events, one would measure a forward-backward asymmetry of 0.043 0.046 for M_t = 40 GeV/c^2.

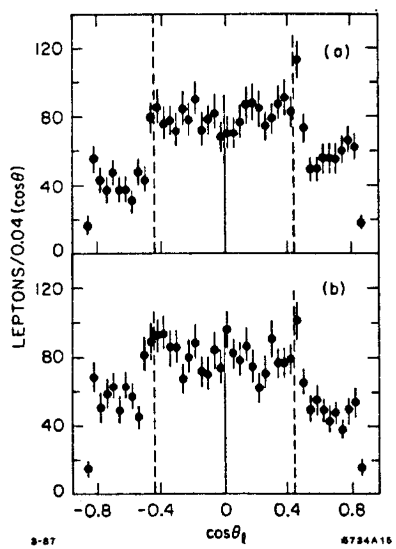

Fig. 25. Cos θ distribution for (a) positively-charged isolated high-p, p_T e's and μ's and (b) negatively-charged isolated high-p, p_T e's and μ's for 50,438 $t\bar{t}$ events at M_t = 40 GeV/c^2.

We have also found ways to improve the sensitivity of the forward-backward asymmetry measurement. Figures 25(a) and (b) show the cos θ distributions for the positively- and negatively-charged isolated high-p, p_T leptons which were used

to point the sphericity axis for Fig. 24(c). (The reason for the depletion of leptons for $|\cos\theta| > 0.50$ is the lack of muon detection in that region.) If one calculates the forward-backward charge asymmetry from these distributions, one obtains 0.052 $\pm$ 0.013, about the same as for the lepton-signed sphericity axis. The forward-backward asymmetry is a function of cos θ and is largest for large $|\cos\theta|$. If one divides up the lepton cos θ distribution into two regions, one obtains:

$$A_{FB} = 0.013 \ \pm \ 0.017 \text{ for } |\cos\theta| < 0.44$$

$$A_{FB} = 0.112 \ \pm \ 0.021 \text{ for } |\cos\theta| \geq 0.44.$$

Thus one can increase the sensitivity of the forward-backward asymmetry measurement simply by using only isolated high-p, p_T leptons with large $|\cos\theta|$. For 10^5 $udscb$ multihadronic events one would have 230 isolated high-p, p_T leptons with $|\cos\theta| \geq 0.44$ from 5120 $t\bar{t}$ events with M_t = 40 GeV/c^2 and would have a measured A_{FB} = 0.112 $\pm$ 0.066, which is an improvement of about a factor of two in statistical significance. (The Muon Upgrade would approximately double the number of leptons in this region.) The background from $udscb$ multihadronic events would be $\sim 9 \pm 9$ isolated high-p, p_T leptons.

Another method of measuring the $t\bar{t}$ forward-backward asymmetry has been reported by Ray Frey. He reconstructs the top meson direction from the three clusters opposite isolated $p_T > 3$ GeV/c leptons for 10,000 $t\bar{t}$ events at M_t = 30 GeV/c^2 and finds A_{FB} = 0.140 $\pm$ 0.016. Since this is a rather low top mass, we will have to find out how well this method works for higher mass top for which it is more difficult to choose the correct clusters to make up the top meson.

And finally, Paul Grosse-Wiesmann[14] has reminded us in his talk that longitudinally polarized electrons increase the forward-backward asymmetries for fermion pairs:

$$A_{FB}^{POL} \ = \ (3-5) \ \times \ A_{FB}^{UNPOL}$$

for $t\bar{t}$ production.

5.3 Measuring the Lepton Momentum Distribution

Ray Frey and Dave Stoker have been working on distinguishing a top quark from a b' quark by measuring the momentum distribution of the lepton from the semileptonic decay. Figure 26 shows the momentum distributions for isolated high-p_T leptons from either b' or t decay. The average momentum is significantly higher for a b' quark than for a t quark with 1000 $t\bar{t}$ events.

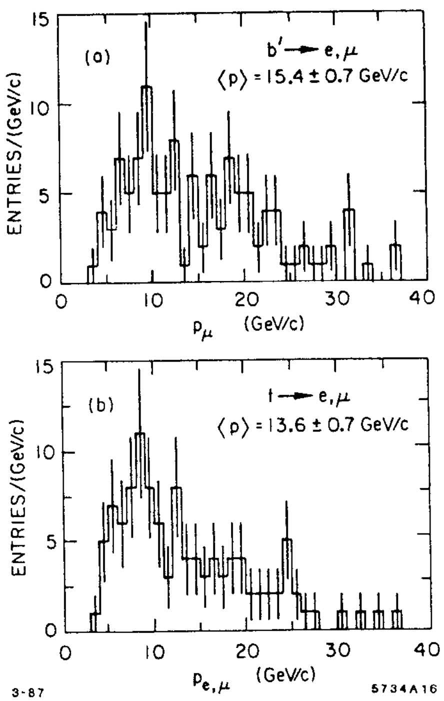

Fig. 26. Momentum distributions for isolated high-p_T leptons from (a) b' decay or (b) t decay for 1000 $t\bar{t}$ or $b\bar{b}'$ events. The mass of the heavy quark is 25 GeV/c^2, but there is little mass dependence.

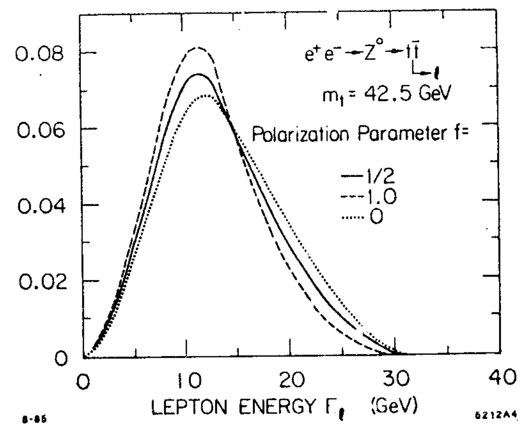

Fig. 27. Dependence of the energy distribution of the charged lepton from semileptonic decay of the t-quark on polarization effects. Distributions are given for three values of the polarization parameter f. $f = 0$ indicates complete depolarization, and $f = 1$ indicates no depolarization. (From Ref. 7.)

This measurement is complicated by the effects of top quark polarization. The top quarks from Z^0 decay are produced with a high degree of longitudinal polarization, even if the beams are not polarized. However, depolarization[7] takes place in the process of fragmentation and decay. Figure 27 shows the effect of the polarization parameter f on the lepton energy distribution. Dave Stoker is working on incorporating top polarization into the Lund Monte Carlo in a manner similar to that already used for $\tau^+\tau^-$ production (LULEPT[15]). The production and decay of the $t\bar{t}$ are given by

$$d\sigma_{tot} = d\sigma_0\left[1 - c_\mu b^\mu - \bar{c}_\mu \bar{b}^\mu + c_{\mu\nu} b^\mu \bar{b}^\nu\right]\left(\frac{d\Gamma_0(t)}{\Gamma_t}\right)\left(\frac{d\Gamma_0(\bar{t})}{\Gamma_t}\right),$$

where c_μ, $c_{\mu\nu}$ are components of the polarization density matrix, which describes the production of the $t\bar{t}$, and the b_μ describe the decay of the top quark. Bennie Ward calculated the components of the polarization density matrix. Production and decay of the top quark do <u>not</u> factorize. The Lund generator handles the production of the $t\bar{t}$, fragmentation of the top quarks to top mesons/baryons, selection of the top meson/baryon decay modes, and the subsequent fragmentation. LULEPT calculates the polarization density matrix, with beam polarization, if any, and decays the top mesons/baryons using the polarization density matrix and the $V - A$ interaction. The software package is nearly finished.

6. Conclusions

Isolated leptons with $p_T > 3$ GeV/c appear to be the most background-free method for establishing a top signal. We should be able to establish a top signal using this method with $\sim$ 7000 Z^0's for $M_t \lesssim 43$ GeV/c^2. It is crucial that the electron and muon identification systems be operational for the first substantial running at the SLC, both for the top search and for many other new-particle searches.

We can probably measure M_t to $\pm$ 1–2 GeV/c^2 with 10,000 Z^0's, depending on the value of the top mass. We can average several methods if they are consistent with each other. With 10^5 Z^0's we can probably measure the top mass to < 1 GeV/c^2. Methods for measuring the top mass involving reconstructing masses of groups of particles need more work.

With 10^5 Z^0's we should be able to establish that what we find is really top, assuming we find something, using the following methods:

- Establish the decay $t \to b\ell^+\nu X$ with an impact parameter analysis
- Measure the $t\bar{t}$ forward-backward asymmetry
- Measure the average momentum for isolated leptons.

We are all looking forward to finding top at the SLC. We could use some data!

References

1. The members of the Open Top Subgroup are: T. Barklow, B. Barnett, J. Bartelt, I. Bigi, P. Dauncey, G. Feldman, R. Frey, D. Fujino, G. Hanson, C. Jung, S. Komamiya, W. Koska, K. O'Shaughnessy, A. Petersen, D. Stoker, S. Wagner, B. Ward, A. Weir, and E. Wicklund.
2. H. Albrecht, in *Proceedings of the International Symposium on the Fourth Family of Quarks and Leptons, Santa Monica, California, February 26–28, 1987.*
3. I. I. Bigi, in *Proceedings of the International Symposium on the Fourth Family of Quarks and Leptons, Santa Monica, California, February 26–28, 1987*, SLAC-PUB-4269.
4. A. Petersen, "QCD at the Z^0," in these Proceedings.
5. K. O'Shaughnessy, "Monte Carlo Models for Top Production," Mark II/SLC–Physics Working Group Note #3–9, in *Proceedings of the Second Mark II Workshop on SLC Physics*, SLAC Report No. SLAC-306 (1986).
6. G. Hanson, "Finding Open Top," Mark II/SLC–Physics Working Group Note #3–10, in *Proceedings of the Second Mark II Workshop on SLC Physics*, SLAC Report No. SLAC-306 (1986).
7. J.H. Kühn, A. Reiter, and P.M. Zerwas, Nucl. Phys. **B272**, 560 (1986), SLAC-PUB-3746.
8. TRKFIT was written by George Trilling specially for use on Monte Carlo analysis. It uses the Monte Carlo information to associate the correct hits with tracks at the pattern recognition stage. The usual track fitting is then done.
9. P. Burchat and M. Nelson, MKII/SLC Note #114.
10. G. Arnison, *et al.*, Phys. Lett. **122B**, 103 (1983).
11. T. Barklow, "Supersymmetric Particle Searches," in these Proceedings.
12. Our definition of ρ_j is smaller than Barklow's by a factor of $\sqrt{2}$.
13. D. Fujino, "Finding the Hadronic Decay Mode of Top," Mark II/SLC–Physics Working Group Note # 3–13.
14. P. Grosse-Wiesmann, "Physics with Polarized Beams," in these Proceedings.
15. D. Stoker, Mark II/SLC Note #161.

Mark II/SLC-Physics Working Group Note # 3–19

AUTHOR: K.K. Gan

DATE: April 15, 1987

TITLE: Heavy Charged Lepton Search

This paper describes a study of some search methods for a new heavy charged lepton at SLC.

1. Introduction

The Z^0 boson provides a new opportunity for a new charged lepton search. However, the search at the Z^0 posts a new problem. The problem is that we must use the hadronic decay mode of the new lepton in order to achieve a reasonable detection efficiency. But the background from original hadronic events is enormous. The disadvantage of using the leptonic decay modes is that the leptonic decay width is small. The electron and muon decay modes of the lepton each accounts for $\sim 11\%$ of the total decay width, therefore the $e-\mu$ final state contributes only 2.4% of the total heavy lepton sample. Taking detection efficiency into account, the efficiency for $e-\mu$ events is $\sim 1\%$. For a sample of $10^5 Z^0$'s, this yields 13.4 $e-\mu$ events for a heavy lepton with mass of $M_L = 30$ GeV/c^2 and 3.9 events for a lepton of $M_L = 40$ GeV/c^2.

The large background from the original hadronic events in the heavy lepton search using the hadronic decay mode is due to the fact that the dominate decay mode of the Z^0 boson is hadronic. Assuming five species of quarks, the ratio of the heavy lepton cross-section to the total hadronic cross-section is,

$$\frac{\sigma^{L^+L^-}}{\sigma^{q\bar{q}}} = 0.021, \tag{1.1a}$$

for $M_L = 30$ GeV/c^2, and

$$\frac{\sigma^{L^+L^-}}{\sigma^{q\bar{q}}} = 0.007, \tag{1.1b}$$

for $M_L = 40$ GeV/c^2. These are to be compared with those expected in the normal

γ^* continuum,

$$\frac{\sigma^{L^+L^-}}{\sigma^{q\bar{q}}} = 0.25,$$

for $M_L = 30$ GeV/c^2, and

$$\frac{\sigma^{L^+L^-}}{\sigma^{q\bar{q}}} = 0.19,$$

for $M_L = 40$ GeV/c^2. With the enormous hadronic contamination, a efficient set of selection criteria is needed. One possibility is to use events with one charged particle in one hemisphere recoiled against a jet of particles in the other (1-N topology). This takes advantage of the fact that it is unlikely at SLC energy for a quark to fragment into a jet containing one charged particle.

2. KNO Prediction on 1-N events

We can use the KNO scaling[1] of the charged particle multiplicity to calculate the probability, P_1, that a quark will fragment into a jet containing one charged particle. To calculate the probability, we need to know the average charged particle multiplicity $< N >$ of the hadronic events at SLC energy. This can be extrapolated from the measurement[2] at lower energies shown in Fig. 1. The TASSO experiment parameterizes the charged multiplicity dependent on the center-of-mass energy $\sqrt{s}$ as

$$< N >= a + b \ln s + c \ln^2 s,$$

where $a = 3.33 \pm 0.11$, $b = -0.40 \pm 0.08$, and $c = 0.26 \pm 0.01$. At $\sqrt{s} = 93$ GeV, this yields $< N >= 21.1$. With this value as input, we can use the KNO scaling distribution[3] shown in Fig. 2 to estimate the probability,

$$P_1 = 0.0028.$$

From Eq. (1.1), the fraction of 1-N events is now

$$\frac{\sigma^{L^+L^-}}{\sigma^{q\bar{q}}} = 3.8,$$

for $M_L = 30$ GeV/c^2, and

$$\frac{\sigma^{L^+L^-}}{\sigma^{q\bar{q}}} = 1.3,$$

for $M_L = 40$ GeV/c^2. Therefore a reasonable signal to noise can be achieved using 1-N events.

3. 1-N Event Analysis

The heavy charged lepton Monte Carlo[4] installed by D. Stoker is used in the analysis. The backgrounds are studied using the Lund hadronic events generated by A. Peterson, the tau events produced by P. Burchat, and the two-photon events produced by T. Barklow. The event selection criteria are:

1. 1-N topology with N $\geq$ 3
2. net charge $\leq$ 1
3. total charged energy > 14 GeV
4. jet mass > 2.0 GeV/c^2 for N $\leq$ 5
5. acollinearity angle > 15^0
6. $|\cos\theta| < 0.8$.

Criterion (2) is designed to reject hadronic events since most of hadronic events misidentified as 1-N topology are those with unreconstructed tracks near the edge of the detector. These background events usually have large net charge as shown in Fig. 3. As evidence from the figure, the cut is effective in rejecting the background while causing small lost of signal. Criterion (3) takes further advantage of the unreconstructed tracks: 1-N hadronic events have, on the average, lower total charged energy (see Fig. 4). Criteria (4) and (5) are designed to reduce tau contamination. Criterion (6) is used to eliminate the remaining hadronic contamination (see Fig. 5).

For a data sample corresponding to an integrated luminosity of 1 pb^{-1}, 57 heavy lepton events pass the selection criteria for $M_L = 30$ GeV/c^2, and 10 events for $M_L = 40$ GeV/c^2. The Monte Carlo predicts a background of 1.3 events: 0.0 events from hadron, 0.6 events from tau, and 0.7 events from two-photon. The detection efficiencies are 12.5 and 7.0% for the two lepton masses, respectively. We have therefore obtained a signal with low background and good detection efficiency.

The lepton content of the 1-prong jet provides a powerful consistency check. The Monte Carlo predicts the probability for the charged particle in the 1-prong jet to be an electron is 0.38 and to be a muon is 0.16, for $M_L = 30$ GeV/c^2. The corresponding probabilities for $M_L = 40$ GeV/c^2 are 0.35 and 0.13, respectively. Here an electron is defined to be a particle with shower energy to momentum ratio, E/P > 0.7, and a muon is a particle that penetrats four layers of muon chamber (MULEVE = 4 and MUSTAT = 15). The Monte Carlo therefore predicts that $\sim$ 50% of the 1-prongs are leptons. In the event of an excess of 1-N events is observed over the predicted background and the lepton content is consistent with that expected for a heavy lepton, then a heavy lepton might be produced. On the other hand, if the number of 1-N events is consistent with the predicted background

and the lepton content is also consistent with that expected for the background, then a heavy lepton may not be produced.

4. 3-N Event Analysis

Since it is somewhat unlikely for a quark to fragment into a jet containing three charged particles at Z^0, I have also studied the feasibility of a search using 3-N events. Although a good signal to background ratio can be obtained with a set of reasonable cuts, this topology gives only $\sim$ 10% improvement in statistic. This search method is therefore not very effective. This could be useful at higher energies.

5. Two-jet Event Analysis

I have also studied the feasibility of a search using acollinear 2-jet events with missing transverse momentum, P_T. The selection criteria are:

1. four or more charged particles
2. total charged energy > 14 GeV
3. jet mass > 2.0 GeV/c^2 for events with six or less charged particles
4. acollinearity angle > 40^0
5. $P_T/E_{TOT} > 0.6$.

The minimum total charged energy requirement, criterion (2), is chosen to be identical to that used in the 1-N events. A slightly lower value could be used. But the increase in efficiency is only a few percent. The effect of the acollinearity angle cut, criterion (4), is shown in Fig. 6. It is evidence from the figure that the hadronic background is formidable. The 40^0 acollinearity cut causes a lost of 60% of the signal. It is also evidence from the figure that an additional cut is needed. The cut chosen is the normalized P_T, criterion (6). Fig. 7 shows the normalized P_T of the events passing the acollinearity cut but before the normalized P_T cut is imposed. 81% of the signal is lost due to the normalized P_T cut.

For a data sample corresponding to an integrated luminosity of 1 pb^{-1}, 27 heavy lepton events satisfy the selection criteria for $M_L = 30$ GeV/c^2, and 9.6 events for $M_L = 40$ GeV/c^2. The hadronic background is 1.9 events and the backgrounds from tau and two-photon are negligible. The detection efficiency is 5.9 and 6.8% for the two lepton masses, respectively. Therefore a reasonable efficiency is obtained for this search technique and the background is under control.

Combining the events in this data sample with those selected in the 1-N search yields a total of 75.1 events for $M_L = 30$ GeV/c^2, and 17.2 events for $M_L =$ 40 GeV/c^2. The total background is 3.2 events, with 1.9 events from hadron, 0.6 events from tau, and 0.7 events from two-photon. The total detection efficiency is 16.5 and 12.0% for the two masses, respectively. Therefore by using two different sets of selection criteria, a good detection efficiency is obtained and the background is under control.

6. Future Studies

More studies are needed in the heavy lepton search. One is to study how well the Lund Monte Carlo predicts the number of 1-N events. Some studies have already been conducted. I have compared the number of 1-N events predicted by the Lund with that expected from KNO scaling. The comparison is restricted to the central region of the detector, $|\cos\theta| < 0.7$, to minimize the number of unreconstructed tracks. The Lund predicts 19 events of 1-N topology for an integrated luminosity of $\sim 0.5\ pb^{-1}$. This is to be compared with the 41 events expected assuming KNO scaling. Therefore we know the normalization of the 1-N events to within a factor of two. This is acceptable since the background is small. It should be noted that the detector inefficiency is not included in the KNO prediction. More detail study is underway.

I have also compared the number of 1-N events measured at PEP with the Lund expectation. The agreement is good. More study is needed.

It is also very clear from Figs. 6 and 7 that, in the search method using acollinear 2-jet events with missing transverse momentum, we need a good understand of the acollinearity and transverse momentum distributions of the hadronic background. Detail comparisons of the PEP data with Lund expectations are planned.

I am also exploring other event selection techniques to improve the detection efficiency.

7. Conclusion

A Heavy charged lepton can be isolated using events of 1-N topology and acollinear 2-jet events with missing transverse momentum. A good detection efficiency is achieved and the background is under control. We are sensitive to a 30 GeV/c^2 lepton with a data sample of 5,000 Z^0's and a 40 GeV/c^2 lepton with 20,000 Z^0's.

8. Acknowledgement

This work is made possible with the heavy charged lepton Monte Carlo installed by Dave Stoker.

REFERENCES

1. Z. Koba, H. B. Nielsen, and P. Olesen, Nucl. Phys. B40, 317 (1972).
2. M. Althoff *et al.*, Z. Phys. C22, 307 (1984).
3. M. Derrick *et al.*, Phys. Rev. D34, 3304 (1986).
4. D. Stoker, MARK II/SLC Note #161.

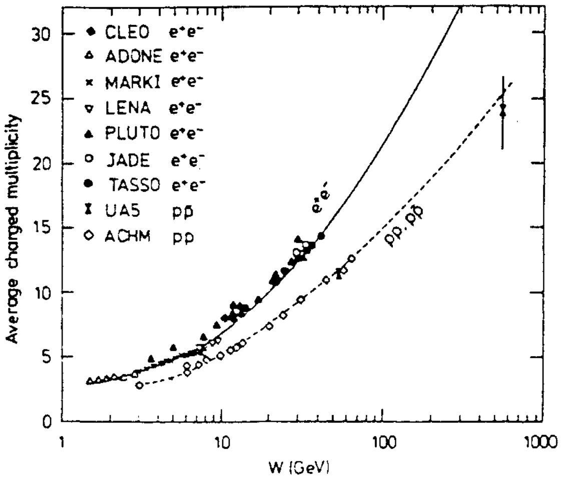

Fig. 1. The energy dependent of the average charged multiplicity. The solid line uses a parameterization given in the text.

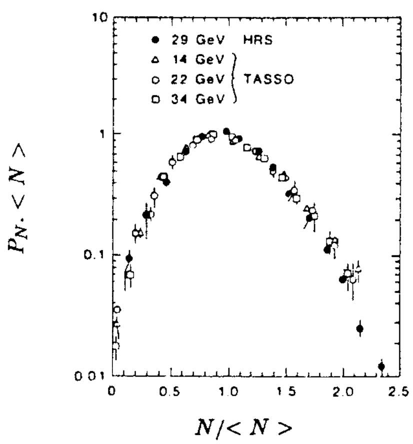

Fig. 2. The KNO scaling of the charged multiplicity of a jet. P_N is the probability of finding a jet with N charged particles.

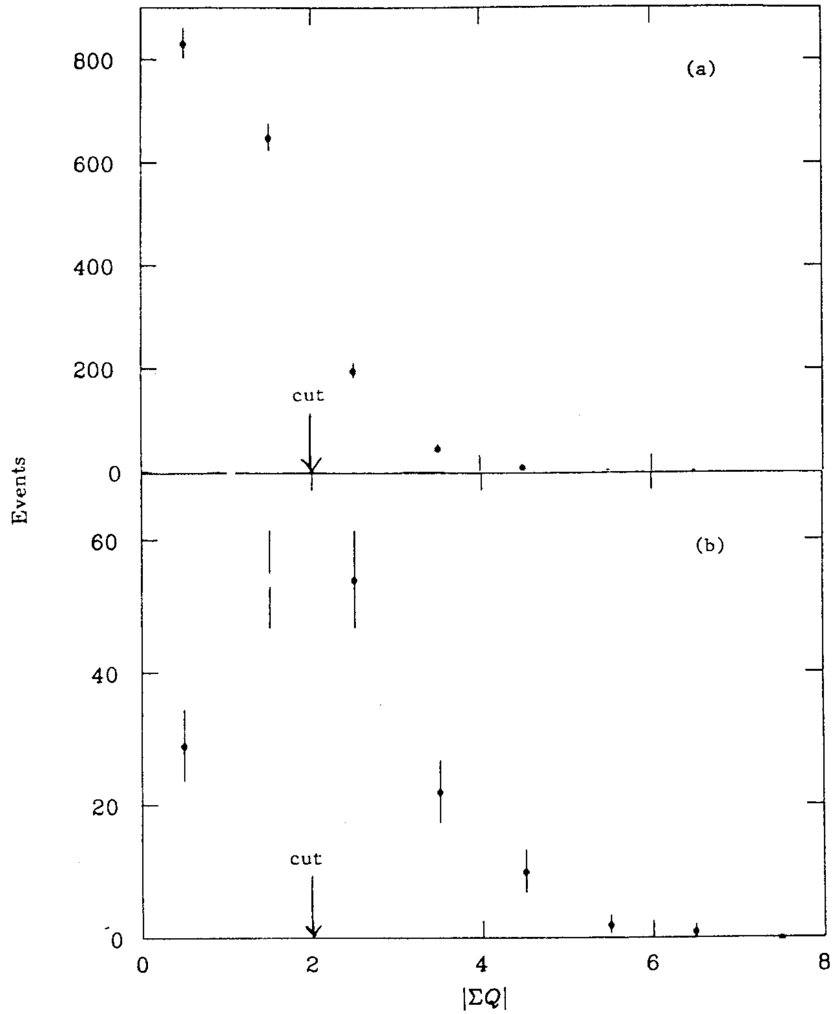

Fig. 3. Net charge distribution of 1-N events, (a) heavy charged lepton events with mass M_L=30 GeV/c^2, (b) hadronic events.

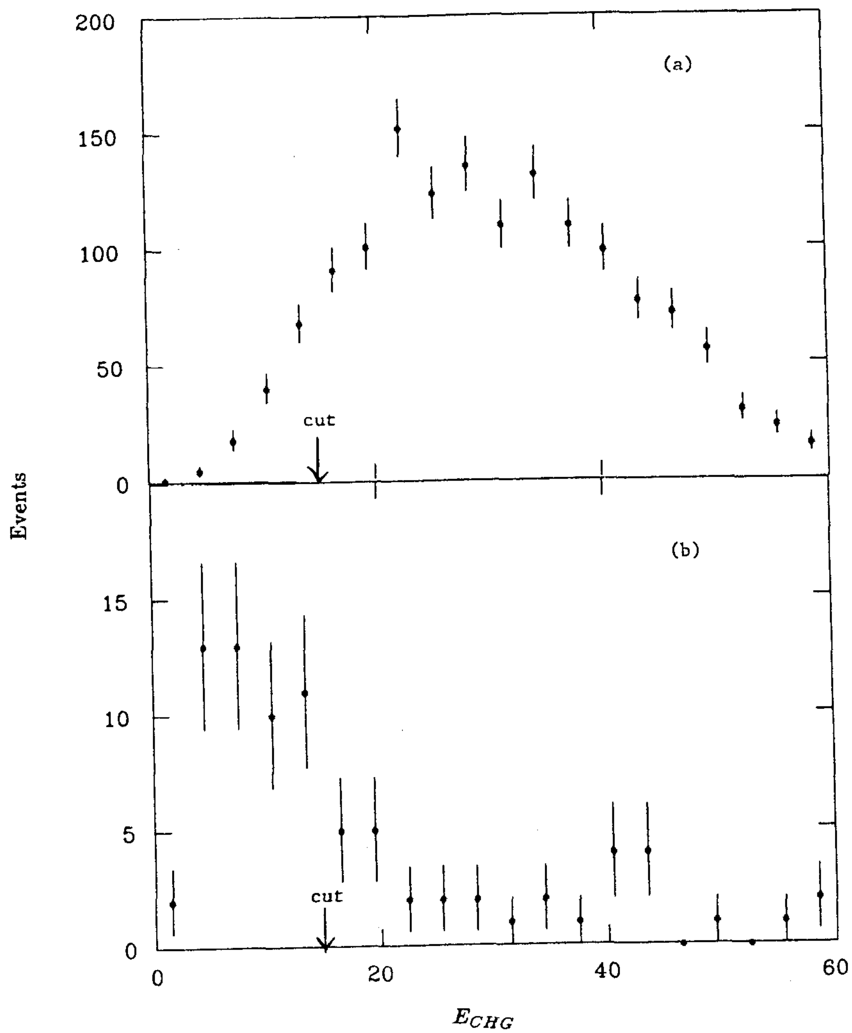

Fig. 4. Total charged energy distribution of 1-N events with net charge ≤ 1, (a) heavy charged lepton events with mass M_L=30 GeV/c^2, (b) hadronic events.

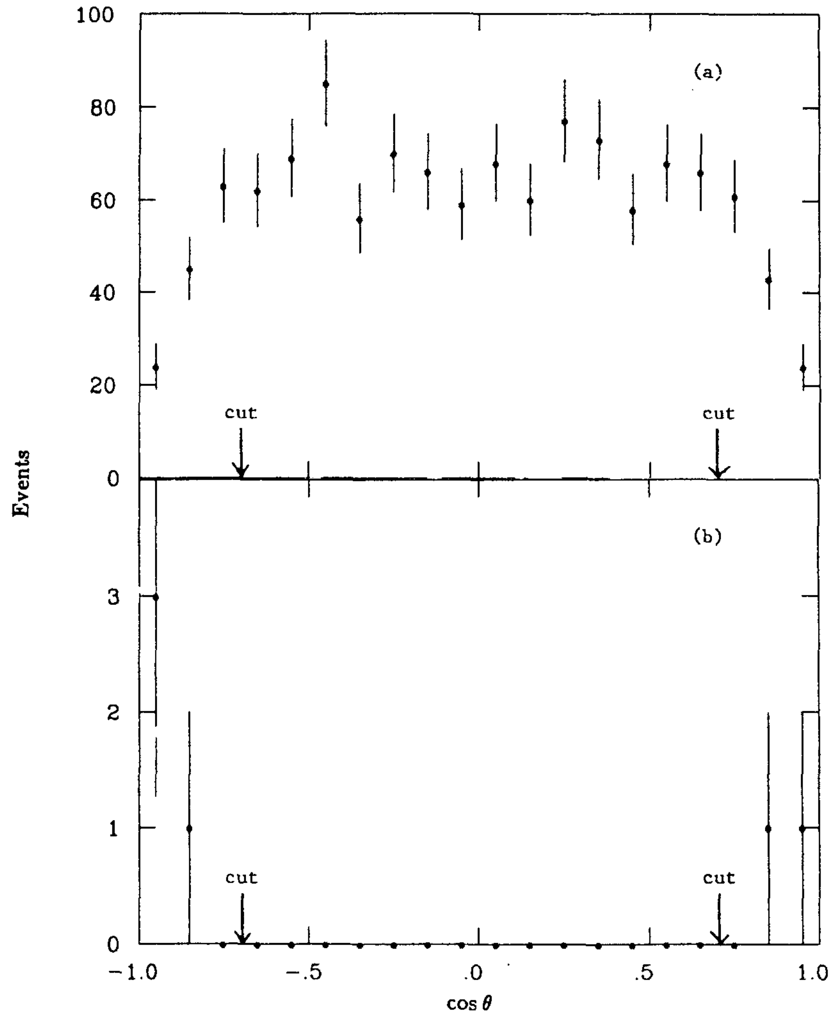

Fig. 5. Angular distribution of 1-N events that passed all the selection criteria described in the text but before the angular cut is imposed. (a) heavy charged lepton events with mass M_L=30 GeV/c^2, (b) hadronic events.

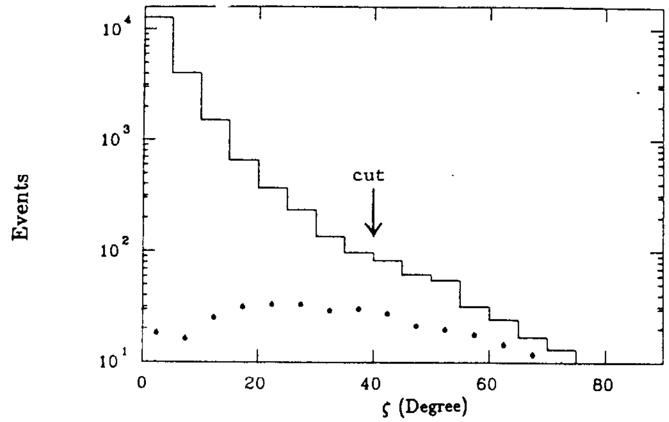

Fig. 6. Acollinearity angle distribution of the 2-jet events that passed selection criteria (1) – (3). The data points are for the heavy charged lepton events with mass M_L=30 GeV/c^2 and the histogram is for the hadronic events.

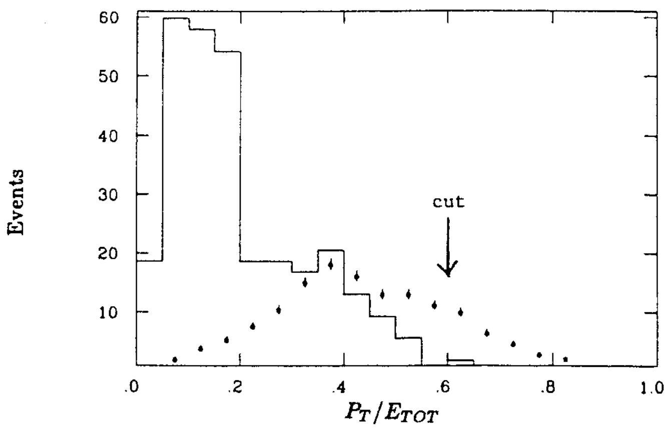

Fig. 7. Normalized transverse momentum distribution of 2-jet events that passed selection criteria (1) – (4). The data points are for the heavy charged lepton events with mass M_L=30 GeV/c^2 and the histogram is for the hadronic events.

Mark II/SLC-Physics Working Group Note # 3–20

AUTHOR: Sachio Komamiya

DATE: April 30, 1987

TITLE: SEARCHES FOR HIGGS PAIRS

ABSTRACT

Possible non-minimal Higgs boson searches at SLC on the Z^o peak are surveyed. Especially, the pair production of charged Higgs bosons ($e^+e^- \to H^+H^-$) and that of two different neutral Higgs bosons ($e^+e^- \to H_i^o H_j^o$) are studied. The expected event topology varies with the mass spectra of the Higgs bosons. With a relatively small number of events in the early SLC running period (with $\approx$ 10,000 Z^o's), we may have a hint of the evidence of the process $e^+e^- \to H^+H^- \to q'\bar{q} + q\bar{q}'$ by reconstructing the jet-jet invariant mass peak. The process $e^+e^- \to H_i^o H_j^o$ is relatively easy to find if one of the Higgs bosons decays into a muon pair (and probably if it decays into a tau pair) and if the suppression of the cross section due to the Higgs mixing is not too severe. Possible strategies to find these events are discussed, and some of them are demonstrated. Higgs bosons from top quark decay are also briefly discussed.

1. Introduction

In the standard model, the Higgs boson is necessary in order to prevent the cross section from violating the unitarity for some fundamental processes (e.g. W^+W^- elastic scattering etc.). Moreover, Higgs bosons play a very important role in determining the masses of fundamental fermions (leptons and quarks) and of the weak gauge bosons: so, it is responsible for all the masses of massive elementary particles. Nevertheless the Higgs boson sector in the standard model appears artificial. Perhaps Higgs bosons are composite particles of more fundamental constituents and the Higgs mechanism can be explained by a possible residual force of more fundamental interactions. Anyway, to look experimentally for such a fundamental particle is an extremely important and exciting task for us [1]. In this note, I try to survey the major phenomenology of non-minimal Higgs bosons from Z^o decays at SLC and discuss possible strategies for detection and identification of them. A lot of work has already been done for the minimal Higgs Boson by the Higgs working group [2], but we have just started to study the non-minimal Higgs cases. This note is based on the Mark-II note No.168. Some new considerations and ideas are added onto it.

1.1 Minimal and Non-Minimal Higgs bosons

In the minimal standard model there is only one SU(2) doublet of Higgs fields. Each component of the doublet has two degrees of freedom, hence there are all together four fields. In the model, however, there is only one physical Higgs boson, since two charged fields are eaten by the W boson and one neutral field is absorbed to the Z^o boson to make these gauge bosons massive by the Higgs mechanism. The coupling constants of the minimal Higgs boson to other fundamental particles are all determined in the minimal theory. What is not known is the Higgs boson mass. There are essentially no direct experimental mass limits for the minimal Higgs boson. The best limit was from the CUSB collaboration ($M_{H^o} < 1.2\ GeV$ or $M_{H^o} > 4.2\ GeV$ with 90% C.L.) from Υ radiative decay. However, the limit is not valid any more since the limit was obtained without taking into account the huge QCD radiative corrections which negatively contribute to the $\Upsilon \to \gamma H^o$ decay width[3]. The most popular way to look for the minimal Higgs boson at SLC/LEP is to look for events $e^+e^- \to Z^o H^o$ [4], where Z^o decays into e^+e^-, $\mu^+\mu^-$ or $\nu\bar{\nu}$ and H^o decays into a heavy fermion pair ($b\bar{b}$ or $t\bar{t}$). On the Z^o resonance H^o cannot be produced accompanied with a real Z^o, so that there is no mass constraint on the e^+e^- pair or $\mu^+\mu^-$ pair which come from a virtual Z^o. Furthermore, the cross section of $e^+e^- \to Z^{o*}H^o \to e^+e^-H^o$, $\mu^+\mu^-H^o$ is a steeply falling function with the Higgs mass. These make the minimal Higgs searches relatively difficult on the Z^o peak [2].

If the Higgs sector is non-minimal, there will be more physical neutral and charged Higgs bosons. The minimal extension of the Higgs sector is to add another SU(2) Higgs doublet:

$$\phi_1 = \begin{pmatrix} \phi_1^+ \\ \phi_1^o \end{pmatrix}, \qquad \phi_2 = \begin{pmatrix} \phi_2^+ \\ \phi_2^o \end{pmatrix},$$

where ϕ_1^+, ϕ_1^o, ϕ_2^+ and ϕ_2^o are complex fields. Therefore there are initially eight fields. The vacuum expectation values (VEV's) are

$$<\phi_1>= \begin{pmatrix} 0 \\ v_1/\sqrt{2} \end{pmatrix}, \qquad <\phi_2>= \begin{pmatrix} 0 \\ v_2/\sqrt{2} \end{pmatrix}.$$

Assuming CP non-violation, the relative phase between two vacuum expectation values is zero.

The quadratic sum of the VEV is equal to the VEV squared (v^2) of the standard Higgs boson, hence $M_{W_\pm} = g \cdot v/2 = g \cdot \sqrt{v_1^2 + v_2^2}/2$.

Since the ρ parameter ($\rho = \frac{Mw^2}{M_Z^2 cos^2\theta_w}$) is experimentally consistent with unity, ($\rho = 1.006 \pm 0.008$) [5] the structure of the Higgs multiplet is likely to be SU(2) doublets (not triplets etc). At least two Higgs doublets are necessary for most of the supersymmetric models [6]. Models with axions need at least two Higgs doublets [7]. Because of the above reasons, for a working hypothesis, the two SU(2) doublet model is assumed in this note. For the two SU(2) doublet models, there are three physical neutral Higgs bosons (H_1^o, H_2^o, H_3^o) and two charged Higgs bosons (H^+ and H^-). Originally there are four neutral and four charged fields but one neutral field is absorbed to give mass to the Z^o and two charged fields to $W^\pm$ by the Higgs mechanism. The mass eigenstates of the physical Higgs bosons can be mixtures of the weak eigenstates. There are two mixing angles for two Higgs doublets since the charged and neutral sector do not mix. One of the mixing angles is related to the ratio of the vacuum expectation values. In general, the physical Higgs bosons in the two doublet model are given by

$$\begin{aligned}
H^\pm &= -\phi_1^\pm \sin b + \phi_2^\pm \cos b, \\
H_1^o &= \sqrt{2}[(Re\phi_1^o - v_1)\cos a + (Re\phi_2^o - v_2)\sin a], \\
H_2^o &= \sqrt{2}[-(Re\phi_1^o - v_1)\sin a + (Re\phi_2^o - v_2)\cos a], \\
H_3^o &= \sqrt{2}[-Im\phi_1^o \sin b + Im\phi_2^o \cos b].
\end{aligned}$$

The mixing angle b is defined by $\tan b = \frac{v_2}{v_1}$. The other angle a is also an arbitrary parameter.

In the case of the neutral Higgs bosons, H_3^o is a pseudoscalar and the other two are scalars, if their parity is defined through the coupling with fermions. To be more precise, H_3^o is CP-odd state and the other neutrals (H_1^o and H_2^o) are CP-even states. The recipe to obtain the above linear combinations is given elsewhere [8]. The interactions of Higgs bosons with fermions can be determined from the fermion mass term in the Lagrangian. The couplings are different from model to model and depend on which Higgs is more responsible for which fermion mass. The important constraint on the Higgs couplings is that flavor changing neutral currents cannot be induced by the neutral Higgs bosons (or at least the FCNC should be suppressed within the experimentally allowed level). To avoid FCNC from the neutral Higgs sector, each fermion is imposed to couple with only one of the two Higgs doublets (only with ϕ_1^o or only with ϕ_2^o).

Since the Higgs couplings with fermions are model dependent, we have to be aware of the underlying assumptions which are specially applied in some models. For example, supersymmetry inspired models [9] have some assumptions which differ from the model where one of the Higgs does not directly couple to any fermions [8]. The masses of the physical Higgs bosons are more model dependent

than the coupling constants. They depend on the structure of the Higgs potential, which contains many free parameters.

2. Charged Higgs Boson Pair Production

The charged Higgs bosons (H^+H^-) are pair produced in e^+e^- annihilation via Z^o or virtual γ. Since they are excluded up to $\sim 18\ GeV$ at PETRA [10], $H^\pm$ masses above the limit are considered. Charged Higgs bosons are heavier than the W bosons in the minimal supersymmetric models [9] but who knows?

The total cross section of the process $e^+e^- \to Z^o \to H^+H^-$ is given by

$\sigma = \sigma_{\nu_\mu \bar{\nu}_\mu}/2 \cdot \cos^2 2\theta_W \cdot \beta^3$, where $\beta = \sqrt{1 - \frac{4M_{H^\pm}^2}{s}}$.

The angular distribution of the $H^\pm$ is $d\sigma/d\Omega \propto \sin^2\theta$.

The cross section relative to that for multihadron events at the Z^o peak is small:

$$\frac{\Gamma(Z^o \to H^+H^-)}{\sum \Gamma(Z^o \to q\bar{q})} = \frac{\Gamma(Z^o \to \nu_\mu \bar{\nu}_\mu)/2 \cdot \cos^2 2\theta_W \cdot \beta^3}{\sum \Gamma(Z^o \to q\bar{q})} \approx 0.016 \cdot \beta^3,$$

where the top quark contribution is neglected.

At PEP/PETRA energies the relative cross section is

$$\frac{R_{H^+H^-}}{R_{hadrons}} = \frac{0.25 \cdot \beta^3}{4} \approx 0.063 \cdot \beta^3.$$

It looks much harder to look for charged Higgs boson on the Z^o peak than at PEP/PETRA. To look for the charged Higgs at SLC, jet reconstruction has to be much better than what TASSO had done at PETRA [11]. Also we need a reliable QCD shower model to understand the multi-jet background from ordinary multihadron events. The possible decay modes are $H^- \to b\bar{c}$, $s\bar{c}$ or $\tau\bar{\nu}_\tau$. If the branching fraction of the decay process $H^- \to \tau\bar{\nu}_\tau$ is large (> 20 %), and if we have a large number of Z^o's ($\approx$100,000) it is not too difficult to isolate the signal from ordinary multihadron events and perhaps from $t\bar{t}$ events by identifying the leptons or the tau decays. If the branching fraction into tau is small, the events are purely hadronic and have four jet topology, and hence they are not so easy to isolate from multijet events due to higher order QCD processes.

$e^+e^- \to H^+H^- \to c\bar{b}$ (or $c\bar{s}$) + $b\bar{c}$ (or $s\bar{c}$)

Isolation of the signal for the charged Higgs boson pair production with subsequent hadronic decay will be discussed in this section.

Energy flows in the ϕ-$\cos\theta$ plane for a typical H^+H^- event are shown in Fig.1a for partons (quarks from the Higgs decay), in Fig.1b for final state stable particles after fragmentation and decay, and in Fig.1c for observed particles after the detector simulation.

Cluster Algorithm

To reconstruct the jet structure of the H^+H^- events, a cluster algorithm is introduced. The method is based on the variable used in the Lund cluster algorithm[12]:

$$d_{ij}^2 = (|\vec{p_i}||\vec{p_j}| - \vec{p_i}\cdot\vec{p_j})(4|\vec{p_i}||\vec{p_j}|)/(|\vec{p_i}| + |\vec{p_j}|)^2.$$

Since there are 4 jets in the lowest order for the processes $H^+H^- \to b\bar{c}c\bar{b}$ ($s\bar{c}c\bar{s}$), the number of reconstructed clusters is forced to be equal to four. The basic scheme goes as follows. Initially each observed particle is assumed to be a cluster by itself. Then the two clusters with smallest d_{ij}^2 are combined by adding vectorially their 4-momenta. This is repeated until the number of clusters is reduced to four. The reconstructed cluster for the typical event is shown in the ϕ-$\cos\theta$ plane in Fig.1d (for the same events as in Fig.1a-c). In the cluster algorithm, all the charged particle masses are assumed to be the pion mass.

Event Reconstruction

Since initial state hard radiations are suppressed at the Z^o peak, we can use beam energy constraint for solving the kinematics. After finding four clusters (j1, j2, j3, j4), the energy of the clusters are calculated assuming the velocity of the clusters $\vec{\beta_i}$ as the observed ones [11],

$$\sum E_i = \sqrt{s},$$
$$\sum E_i\vec{\beta_i} = \vec{0}.$$

The calculated energy E_i can have a negative value for badly reconstructed events.

In the next step, the combination of two clusters which is the best given to form H^+ (or H^-) is searched for. Within the three different combinations i.e. (12)(34),(13)(24) and (14)(23), the combination with the smallest χ^2 is selected, where:

$$\chi^2 = (\frac{\sqrt{s}/2 - E_i - E_j}{\sqrt{s}/2})^2 + \alpha[(\frac{M_{ij} - M_{H^\pm}}{M_{H^\pm}})^2 + (\frac{M_{kl} - M_{H^\pm}}{M_{H^\pm}})^2].$$

The parameter α is optimized so that the reconstructed mass resolution is small for H^+H^- events and, simultaneously, the mass distribution for the background is reasonably wide in order to maximize the signal to background ratio. The value $\alpha = 0.25$ is chosen.

Cuts

To enhance H^+H^- signal from ordinary multihadron background, the following cuts are applied (The cuts are optimized for 30 GeV $H^\pm$'s):

(1) $|\cos\theta_{H^\pm}| < 0.60$, where $\theta_{H^\pm}$ is the reconstructed polar angle of the $H^\pm$ momentum.

(2) Reconstructed energy of each cluster ($E_i, i = 1,2,3,4$) should exceed 7 GeV.

(3) The minimum angle between any pair of cluster momentum should be greater than 60°.

(4) The difference between the H^+ and H^- energies has to be smaller than 3 GeV.

(5) The difference of the reconstructed "H^+mass" and "H^-mass" must be smaller than 4 GeV.

The expected distributions for the observables used for the cuts are shown for H^+H^- events assuming $M_H^\pm = 30$ GeV and for ordinary multihadron events (Lund 6.1 QCD shower model) in Fig.2-6.

After the cuts (1)-(5), the distributions of the averaged invariant mass of the two reconstructed Higgs bosons are shown in Fig.7b for H^+H^- events on top of the QCD background. The same plot for Higgs masses of 25 GeV and 35 GeV are shown in Fig.7a and in Fig.7c, respectively. The numbers of events in Fig.7 correspond to 10,000 Z^o's at the Z^o peak. It is not impossible to find a hint of charged Higgs production at SLC with 10,000 Z^o's* The mass resolution is determined by the jet energy calculation and hence it depends very much on the missing momenta due to unreconstructed or escaped particles.

$e^+e^- \to H^+H^- \to \tau^+\nu_\tau + s\bar{c}(b\bar{c}), \tau^-\bar{\nu}_\tau + c\bar{s}(c\bar{b})$

If we have enough Z^o's, it is worth studying the $\tau\nu+$ hadrons topology since the decay mode $H^- \to \tau^-\bar{\nu}_\tau$ can be as large as 20%. A typical M.C. generated event is shown in Fig.8a.

* If other new heavy particles which decay into hadrons are produced with larger cross section, it would not be easy to dig the signal out from this 'background'.

Strategies to look for these events are the following:

(1) An isolated "tau" is required. The "tau" is defined as an isolated one or three charged high momentum particles with or without photons and the visible invariant mass should be consistent with being $< M_\tau$. No other high momentum particles are in the hemisphere defined by the tau.

(2) Select events with large missing P_T or large acoplanarity angle with respect to the beam axis.

(3) Calculate invariant mass of the hadronic system by rescaling the total energy of the hadrons to $\sqrt{s}/2$ in order to estimate the $H^\pm$ mass.

We have already looked for this mode at PETRA and PEP. With a small number of Z^o's, we should not make the cut too hard cuts. We can try almost the same cuts that JADE applied at PETRA, rescaled for $\sqrt{s} = 93\ GeV$, before doing much sophisticated selection discussed above. The cuts are the following:

(1) $0.25 \cdot \sqrt{s} < E_{vis} < 0.8 \cdot \sqrt{s}$,

(2) $|\cos\theta_{th}| < 0.6$, where θ_{th} is the polar angle of the thrust axis,

(3) $\phi_{acop} > 40° \cdot (|\cos\theta_{th}| + 1)$, where ϕ_{acop} is the acoplanarity angle of the event*. The scatter plot of $\cos\theta_{th}$ vs ϕ_{acop} after the visible energy cut (1) is shown in Fig.9a for 30 GeV H^+H^- events, and the corresponding plot for the background distribution is shown in Fig.9b. The detection efficiency of the H^+H^- events is about 23 % for $M_{H^\pm} = 30GeV$, and the expected number of events is about 4 with 10,000 Z^o's after the cuts for $M_{H^\pm} = 30GeV$ and $B(H^- \to \tau^-\bar{\nu}_\tau) = 0.25$. The expected number of background events is 0.9 ± 0.5, estimated by using the Lund shower model (without top quark). With 10,000 Z^o's, it is not easy to look for H^+H^- by searching for this event topology since the expected branching fraction is small.

$e^+e^- \to H^+H^- \to \tau^+\nu_\tau + \tau^-\bar{\nu}_\tau$

If the tau decay mode is dominant for some reason or if we have a large number of Z^o's, we can study $\tau\nu + \tau\nu$ topology. A typical M.C. generated event is shown in Fig.8b.

The essential requirements to search for these events are:

* Momenta of particles in each hemisphere perpendicular to the thrust axis are summed vectorially. With the two resultant momenta $\vec{p_+}$ and $\vec{p_-}$, the acoplanarity angle ϕ_{acop} is defined as the angle between the plane formed by $\vec{p_+}$ and the beam direction $\vec{e_z}$ and the plane formed by $\vec{p_-}$ and $\vec{e_z}$:

$$\phi_{acop} = -(\vec{p_+} \times \vec{e_z}) \cdot (\vec{p_-} \times \vec{e_z}) / \{|\vec{p_+} \times \vec{e_z}| \cdot |\vec{p_-} \times \vec{e_z}|\}.$$

(1) Select events of two isolated τ's plus nothing else (1+1 or 1+3 charged particle topologies).

(2) Reject $\tau\tau\gamma$ background by requiring no hits in the veto counters or in the hole taggers.

(3) Require large acoplanarity angle (the angle between the plane defined by the τ^+ and the beam, and the plane defined by the τ^- and the beam).

This topology would also be seen for $e^+e^- \to \tilde{\tau}^+\tilde{\tau}^-$. Since the cross section of stau pair production is larger than that for $e^+e^- \to H^+H^-$ and the stau decays into $\tau + \tilde{\gamma}$ with 100% branching ratio if $(M_{\tilde{\tau}} > M_{\tilde{\gamma}})$, event shape for the $\tilde{\tau}$ pair production can be different from that for $H^\pm$ pair production with $H^+ \to \tau^+\nu$ decay. Furthermore, $\tilde{\gamma}$ can be massive, whereas ν_τ is experimentally less than 70 MeV, so that the visible energies of the two processes might be different.

This mode is also studied at PEP and PETRA.

3. Associate Production of Scalar and Pseudoscalar Neutral Higgs Bosons

A scalar Higgs boson (H_s^o) associated with a pseudoscalar (H_p^o) can be produced from Z^o at SLC: $e^+e^- \to Z^o \to H_s^oH_p^o$ ($H_s^o = H_1^o$ or H_2^o, $H_p^o = H_3^o$).

The total cross section of this process is $\sigma = \sigma_{\nu_\mu\bar{\nu}_\mu}/2 \cdot \bar{\beta}^3\cos^2(a-b)$, where $\bar{\beta} = 2P_{CM}/\sqrt{s} = \sqrt{[s-(M_s+M_p)^2][s-(M_s-M_p)^2]}/s$, and a and b are mixing angles. The angular distribution is $d\sigma/d\Omega \propto \sin^2\theta$.

Note that $e^+e^- \to Z^o \to H_i^oH_i^o$ is forbidden by Bose symmetry*. One of the two Higgs bosons must be CP odd and the other must be CP even if CP violation is negligible.

* If a Z^o could decay into two identical spin-zero bosons, the final state wave function would be antisymmetric under the exchange of the two Higgs bosons, since the angular momentum L of the two Higgs bosons must be 1 (total angular momentum conservation). However, the wave function must be symmetric because of the Bose symmetry. Neutral ρ meson cannot decay into two π^o's and ϕ^o cannot decay into two K_S^o's because of the same reason.

The total cross section can be larger than that for the charged Higgs boson pair production, at most by a factor $\frac{1}{\cos^2 2\theta_w}$. The cross section depends, however, on the Higgs mixing angles (by a factor $\cos^2(a-b)$). Therefore it can be also smaller than the charged Higgs cross section, which does not depend on the mixing angles. At SLC on the Z^o peak, the rate of the $Z^o \to H_p^o H_s^o$ events can be as large as that for muon pairs, if both Higgs bosons are light and the mixing angle factor is close to unity. The cross section contours for the most optimistic case ($\cos^2(a-b)=1$) are shown in Fig.10, on the $M_{H^o s} - M_{H^o p}$ plane. The cross section contours at the present TRISTAN energy ($\sqrt{s} = 50\ GeV$) and at PEP energy ($\sqrt{s} = 29\ GeV$) are also shown in the figure.

Decay modes of the scalar and the pseudoscalar Higgs bosons depend on the masses and the mixing angles.

In principle, they decay into the heaviest available fermion pair: $H_i^o \to f\bar{f}$.

The width is given by

$$\Gamma = \frac{N_c}{8\pi}\frac{M_{H_i^o}}{v^2}M_f^2 \cdot \left(1 - \frac{4M_f^2}{M_{H_i^o}^2}\right)^{3/2} \cdot F(a,b) \qquad \text{for the scalars,}$$

$$\Gamma = \frac{N_c}{8\pi}\frac{M_{H_i^o}}{v^2}M_f^2 \cdot \left(1 - \frac{4M_f^2}{M_{H_i^o}^2}\right)^{1/2} \cdot F(a,b) \qquad \text{for the pseudoscalar,}$$

where N_c=3 for quarks and N_c=1 for leptons, and $F(a,b)$ is a function of mixing angles. The function is model dependent. In the minimal supersymmetric models [9],

$$\begin{aligned}
F(a,b) &= \left(\frac{\sin a}{\sin b}\right)^2 && \text{for } i=1, && f = u,c,t \\
F(a,b) &= \left(\frac{\cos a}{\cos b}\right)^2 && \text{for } i=1, && f = d,s,b,e,\mu,\tau \\
F(a,b) &= \left(\frac{\cos a}{\sin b}\right)^2 && \text{for } i=2, && f = u,c,t \\
F(a,b) &= \left(\frac{\sin a}{\cos b}\right)^2 && \text{for } i=2, && f = d,s,b,e,\mu,\tau \\
F(a,b) &= (\cot b)^2 && \text{for } i=3, && f = u,c,t \\
F(a,b) &= (\tan b)^2 && \text{for } i=3, && f = d,s,b,e,\mu,\tau.
\end{aligned}$$

If the scalar mass is more than two times larger than the pseudoscalar mass, $H_s^o \to H_p^o H_p^o$ is the dominant decay mode unless there is a suppression factor due to the Higgs mixing, since the width is, in principle, larger than that for the decay into fermion pair, by a factor $O(\frac{1}{4N_c}\frac{M_{H^o}^2}{M_f^2})$ [13].

In Fig.11a, a schematic mass dependence of the event topologies of the process $e^+e^- \to H_s^o H_p^o$ is shown on the plane of scalar mass vs pseudoscalar mass. Near the decay thresholds, the branching fractions may be affected by the phase space factor. Also the dominant decay modes depend on the mixing angles. In some of the models, couplings of the Higgs bosons with fermions depend on the weak isospin of the fermion. This effect may also vary the decay mode. For example, if charge 2/3 quarks couple only to one of the Higgs doublet and the charge -1/3 ones to the other, in order to avoid the dangerous FCNC caused by the neutral Higgs bosons and if the mixing of those doublets is negligible, the pattern of the event topologies might be simpler (see Fig.11b). The pattern of event topologies which can be observed from Fig.11a are the following:

- If $M_{H^o s} > 2M_{H^o p}$, the events are three pairs of the same fermion species,

$$\begin{aligned}
e^+e^- \to Z^o &\to H_s^o + H_p^o \\
&\to H_p^o + H_p^o + H_p^o \\
&\to f\bar{f} + f\bar{f} + f\bar{f}.
\end{aligned}$$

- If $M_{H^o s} < 2M_{H^o p}$, the events are two pairs of fermions of the same or different species,

$$\begin{aligned}
e^+e^- \to Z^o &\to H_s^o + H_p^o \\
&\to f\bar{f} + f'\bar{f}'.
\end{aligned}$$

Note that the H_i^o cannot decay into two H_s^o's, even if $M_{H_p^o} > 2M_{H_s^o}$, because of CP conservation. In supersymmetric inspired models the latter event topology might be dominant even if $M_{H_s^o} > 2 \cdot M_{H_p^o}$. As shown in the figure, event signatures of the $e^+e^- \rightarrow H_s^o H_p^o$ process depend very much on the mass spectrum. Some of the Monte Carlo generated events are shown in Fig.12 to 16.

$Z^o \rightarrow H_s^o H_p^o$ searches at PEP/PETRA

If the Higgs bosons are very light ($< 2M_\mu$), their lifetime would be quite long, and even long enough such that they are almost stable. At PEP and PETRA, we have already searched for these events.

An example of the above are monojet searches. In 1984, UA1 reported the observation of monojet events [14]. It has been suggested by Glashow and Manohar [15]* that these monojet events can be explained by an anomalous decay of Z^o into two different Higgs bosons ($H_p^o H_s^o$), where H_s^o is very light ($< 2M_\mu$) and hence stable, and the other decays into $f\bar{f}$ or $f\bar{f}H_s^o$. They also suggested that these monojets from virtual Z^o's can be seen at PEP and PETRA. In the beginning of 1985, HRS [17], MAC [18], and Mark-II [19] at PEP, and CELLO [20] and JADE [21] at PETRA studied monojet production due to a virtual Z^o decay. The limit of the Z^o decay width into the monojet mode normalized to that of $Z^o \rightarrow \nu_\mu \bar{\nu}_\mu$ is shown in Fig.17, as a function of H_p^o mass. In Fig.11, the region on $M_{H^o s} - M_{H^o p}$ plane, where we looked for the monojet, is indicated.

Another topology was studied by JADE one year ago, motivated by the axion interpretation of the GSI events. In 1985, correlated monochromatic e^+ and e^- energy peaks were found in heavy ion collision at GSI [22]. The kinematic energy of the peak is about 300 keV, which corresponds to an e^+e^- invariant mass of 1.8 MeV, if the e^+ and e^- come from a neutral particle produced almost at rest. Recently, a non-standard axion model has been proposed by Peccei, Wu and Yanagida [23] and independently by Krauss and Wilczek [24]. The Higgs interaction with fermions in the model is nonstandard: the axion couples mainly to u-quarks and electrons and does not couple to other fermions, so that one can avoid flavor changing neutral current in the tree level, and simultaneously the GSI electron energy peak can be explained.

The axion (H_p^o) can be produced accompanied by a scalar Higgs boson (H_s^o) from a virtual Z^o at PETRA [25]. The scalar Higgs boson mass would most naturally be around the smaller vacuum expectation value ($\approx 3.6\ GeV$), which is calculated from the assumed axion mass of 1.8 MeV [25]. Since the scalar (H_s^o) is very much heavier than the axion (H_p^o), the H_s^o decays immediately into $H_p^o H_p^o$, resulting in three axions in the final state. At PETRA energies, the axion decay length is $O(1m)$. Therefore the final event topology is $\leq 3\ e^+e^-$ pairs seen in the fiducial volume of the tracking chamber, accompanied with or without large missing P_t due

* Prior to the monojet boom, JADE had previously searched for monojet production in the context of a search for the supersymmetric partner of Z^o production accompanied by a photino ($e^+e^- \rightarrow \tilde{Z} + \tilde{\gamma}$), where $\tilde{Z}$ decays into $q\bar{q}\tilde{\gamma}$ or $q\bar{q}\tilde{g}$ [16].

to unseen axions, which decay outside of the detector. The limit from JADE [26] is shown in Fig.18 for the decay width $Z^o \rightarrow H_s^o H_p^o$ normalized to that of $Z^o \rightarrow \nu_\mu \bar{\nu}_\mu$ as a function of H_s^o mass (in the figure, M_{H_s} and M_{H_p} are indicated as M_h and M_a, respectively). For the model by Peccei, et al., the scalar masses up to about 5 GeV are excluded with 90% C.L., but the scalar can be much heavier. Note, however, that the models by Peccei, et al., and Krauss, et al., are now almost excluded by the combined experimental results from pion rare decays [27] and beam dump experiments [28], independent of the scalar mass. Anyway, it is quite interesting that such a light and feebly interacting particle could have been found from a virtual Z^o decay, if it exists at all. In Fig.11, the searched region in the $M_{H^o s} - M_{H^o p}$ plane for this case is indicated.

Although these models (Glashow-Manohar, Peccei, et al., Krauss, et al.), have been excluded, it is worth looking for these processes again at SLC. This is because the theorists chose particular couplings of the Higgs bosons with fermions (because they want to explain the monojet events or the GSI events by the neutral Higgs bosons) and hence the cross section has almost no reduction due to the Higgs mixing angles ($cos^2(a-b) \approx 1$). If the reduction is very severe, it could not be excluded.

$e^+e^- \rightarrow H_i^o H_j^o$ with $H_j^o \rightarrow \mu^+\mu^-$

If the mass of the lighter neutral Higgs boson (H_j^o) is between $2M_\mu$ and $2M_K$, it decays dominantly into a muon pair* . The search is not too difficult for this case. Furthermore, if the heavier Higgs (H_i^o) decays into two H_j^o's and all the three H_j^o decay into muon pairs, the final state is six muons (see Fig.12). We will not miss these spectacular events if they are produced at SLC. If the $H_i^o \rightarrow H_j^o H_j^o$ decay mode is suppressed, by kinematical reasons or due to mixing angles, H_j^o decays, in principle, into the heaviest possible fermion pair (see Fig.13). We can look for the both cases simultaneously, requiring at least one isolated and low invariant mass (0.2 to 1 GeV) muon pair. If H_i^o,the heavier Higgs boson, is not too heavy, the muon pair has large momentum. For example, even if $M_{H_i^o}$ is 70 GeV, the muon pair momentum is about 20 GeV at $\sqrt{s} = 94\ GeV$. The possible experimental selection criteria for these events are the following:

(1) The total charged multiplicity of the event is larger than or equal to four.

(2) The total visible charged particle energy of the event exceeds $\sqrt{s}/2$.

(3) At least one oppositely charged pair (i,j) with opening angle ψ_{ij} satisfying $\cos\psi_{ij} > 0.99$.

* Even above the kaon pair threshold and below the tau pair threshold, the decay branching fraction into muon pair can be as large as 3 %, since the Higgs couples to the current quark masses (not to the constituent quark masses).

(4) The pair should be in the barrel part, $|\cos\theta_i| < 0.6$ and $|\cos\theta_j| < 0.6$, where θ_i and θ_j are the polar angles of the charged particles i and j, respectively.

(5) The momenta of the two charged particles are above 2 GeV: $|\vec{p_i}|$, $|\vec{p_j}| > 2$ GeV.

(6) The scalar sum of the momenta is larger than 10 GeV: $|\vec{p_i}| + |\vec{p_j}| >10$ GeV.

(7) Except for the particles i and j, no charged particles ($p > 0.2$ GeV) are within a 60 degree cone from the momentum vector of the pair ($\vec{p_i} + \vec{p_j}$).

(8) The total shower energy within the 60 degree cone, including the energy deposit due to the pair, is less than 1.5 GeV.

(9) At least one of them is a muon, requiring that all the four layers of the muon tubes have hits within 3σ of the track extrapolation from the central drift chamber, taking into account fit and multiple scattering errors.

After all the cuts, except for the momentum sum cut (6) and for the muon selection cut (9), the scatter plot of the two momenta, $|\vec{p_i}|$ and $|\vec{p_j}|$ is plotted for the M.C. generated $H_i^oH_j^o$ events with $M_{H_i^o} = 30$ GeV and $M_{H_j^o} = 0.7$ GeV in Fig.19a and that with $M_{H_i^o} = 70$ GeV and $M_{H_j^o} = 0.7$ GeV in Fig.19b. The background from ordinary multihadron events (Lund 6.1 QCD shower model) is shown in Fig.19c. The number of the events in Fig.19 are normalized to 20,000 $Z^o \rightarrow hadrons$ (u,d,c,s,b). The most optimistic branching fraction of $\Gamma(Z^o \rightarrow H_i^oH_j^o) = \Gamma(Z^o \rightarrow \nu_\mu\bar{\nu}_\mu)/2 \cdot (\frac{2p_{H^o}}{\sqrt{s}})^3$ is used, and the decay modes $H_i^o \rightarrow b\bar{b}$ and $H_j^o \rightarrow \mu\bar{\mu}$ are assumed. After requiring one of the particles of the pair to be a real muon, the corresponding momentum scatter plots are shown in Fig20a and Fig.20b. For the multihadron events, there are no events after the requirement that one of the pair particles to be a real muon, for the total 20,000 events generated. The detector simulation of the events is described in section 3.1. The muon detectors are not fully simulated. Assuming a geometrical acceptance cut of $|\cos\theta| <0.5$ and muon identification efficiency of 75% in the acceptance, the total number of events expected after the cuts is 113 events for 10,000 Z^o decays for $M_{H_i^o} = 30$ GeV and $M_{H_j^o} = 0.7$ GeV. The corresponding number of background events from multihadrons is 1.2, assuming the faking probability of a charged particle to be a muon to be 0.02, for momentum above 2 GeV. One can conclude that it is not difficult to find these events, if the main background is due to multihadrons. The other background which has to be carefully considered is two photon processes. The contribution from the ordinary multiperipheral diagram is negligible, if we reject $e^+e^-\mu^+\mu^-$ events. The dominant one is the two photon conversion diagram, namely the case that one photon is converted into a muon pair and the other one into a quark pair. The cross section is negligiblly small on the Z^o peak, estimated by using the Berends-Daverfeldt-Kleiss Monte Carlo event generator for two photon processes [29]. The reliability of the Monte Carlo is tested by analysing the PEP

data.

For a higher H_i^o masses, the cross section gets smaller by a factor $(\frac{2p_{H^o}}{\sqrt{s}})^3$ and hence the momenta of the muons are smaller, and the isolation of the muon pair may have problems. As one can see from Fig.20b, it is not impossible to detect these events even for $M_{H_i^o} = 70$ GeV. Even for the case that $M_{H_j^o}$ is just above the $\mu^+\mu^-$ threshold, the two muon tracks are well separated in the outer layers of the drift chamber. In the layer 12, the muon tracks are separated at least 12 mm, whereas the double track resolution is 4.2 mm. In the inner layers the double tracks can be recognized by the doubled dE/dx values. If the $M_{H_j^o}$ is just above the muon pair threshold, the shower energy and muon hits of the low invariant mass charged particle pairs have to be examined, otherwise the pairs can be rejected as a photon conversions.

The six muon events ($H_i^oH_j^o \rightarrow H_j^oH_j^oH_j^o \rightarrow \mu^+\mu^-\mu^+\mu^-\mu^+\mu^-$) can to be selected from the above sample by requiring additional muons. This process is background free and is easy to identify.

Carrie Fordham and S.K. have already searched for isolated muon pairs in the PEP data. The selection was started from the data summary tapes (DST's). The integrated luminosity which corresponds to the data we analysed is 266 pb^{-1}. The cross section of the process $e^+e^- \rightarrow H_s^oH_p^o$ via a virtual Z^o is $0.174 \cdot \bar{\beta}^3\cos^2(a-b)$ pb^{-1}, where $\bar{\beta} = 2 \cdot p_{H_s^o}/\sqrt{s} = 2 \cdot p_{H_p^o}/\sqrt{s}$, and a and b are the Higgs mixing angles. The number of events expected is $46 \cdot \bar{\beta}^3\cos^2(a-b)$. The selection criteria for the events are the same as those in the previous page, except for the following cuts:

(3) $\cos\psi_{ij} > 0.97$,

(5) $|\vec{p_i}|$, $|\vec{p_j}| > 1$ GeV,

(8) The total shower energy within the 60 degree cone, including the energy deposit due to the pair, is less than 1.0 GeV.

In addition to the cuts in the previous page, off-timing cosmic muons, which are reconstructed as two parallel tracks in the chamber, are rejected by using the TOF counter information. After all the cuts two events survived. They are shown in Fig.21. The main background source is the two photon processes, where one of the photon is converted into a muon pair and the other into a quark pair. The expected number of background within the cuts from these processes is 2.9 ± 1.0, estimated by using the Berends- Darverfeld- Kleiss Monte Carlo program, in which the hadronic fragmentation of the quark pair is incorporated by Tim Barklow. Therefore the surviving events are consistent with being the background. The detection efficiency of the Higgs events is about 60 %* for $M_{H_s^o} = 0.7\ GeV$, $M_{H_p^o} = 5.0GeV$, $H_s^o \to \mu^+\mu^-$ and $H_p^o \to c\bar{c}$.

If the $M_{H_s^o}$ is just above the muon pair threshold ($M_{H_s^o} = 0.22GeV$), the efficiency (for the original Mark-II detector) is decreased to 13 % because of the double track resolution of the old Mark-II chamber. For the most optimistic case (no reduction of the cross section by the mixing), the heavier Higgs mass can be excluded up to about $15GeV$ with 95 % C.L. for $M_{H_s^o} = 0.7\ GeV$.

$e^+e^- \to H_i^o H_j^o$ and $H_j^o \to \tau^+\tau^-$

This case was already studied by the LEP physics working group for a special case: $H_i^o H_j^o \to \tau^+\tau^- + b\bar{b}$ [30]. They require at least one of the taus to decay leptonically and look for a invariant mass peak of the $b\bar{b}$ system. A typical M.C. event is shown in Fig.14. Since we have to look for these events with relatively small luminosity in the early SLC running period, it is better to study more general tau pair selection criteria. An efficient way to select isolated tau pairs is to require topologies of 1+1 or 1+3 charged particle configurations with or without photons in one hemisphere. The hard photons in the tau hemisphere have to be very close to the charged tracks (i.e. they come from the tau decays). If the invariant mass of H_i^o is relatively small, $< 30\ GeV$, the efficiency would be high, since all the high momentum particles from the H_i^o decay are in the opposite hemisphere of the tau pair. The number of background events from multihadrons is comparable with that of the signal, estimated roughly by using the Lund shower model. If one requires that at least one of the two taus decays leptonically, more than 50 % of the tau pairs will be rejected. However, the requirement of a lepton is necessary to get rid of the background efficiently. If the lepton detection and identification efficiencies are taken into account, the detection efficiency would be $\approx$ 20 % and the signal to background ratio is increased to about five. After selecting the events containing an isolated tau pair, the mass of the Higgs boson is estimated in the following way.

The opposite hemisphere of the tau pair is divided into two jets. Energies of taus and the two jets are calculated from the directions of two taus, $\vec{n_1}$ and $\vec{n_2}$, and the velocities of the two jets, $\vec{\beta_3}$ and $\vec{\beta_4}$, by using the energy-momentum conservation.

$$\sqrt{p_1^2 + m_\tau^2} + \sqrt{p_2^2 + m_\tau^2} + E_3 + E_4 = \sqrt{s},$$
$$p_1\vec{n_1} + p_2\vec{n_2} + E_3\vec{\beta_3} + E_4\vec{\beta_4} = \vec{0}.$$

If the taus are approximated to be massless, then the equations are linear and the energies are easily calculated. After calculating the energies, a correlated peak

* Although the muon chamber geometrical acceptance is about 50 % of 4π, the efficiency is higher than 50 % due to the angular distribution ($\propto \sin^2\theta$).

in tau-tau mass vs jet-jet mass plane would be found. The detail of the method is still under study.

$e^+e^- \to H_i^o H_j^o \to q\bar{q} + q'\bar{q}'\ (+\ q''\bar{q}'')$

This is the most tough case to look for. For the case of the charged Higgs pair production, resolution of the averaged mass ($\frac{M_{H^+}+M_{H^-}}{2}$) is quite good (see Fig.7), because some soft particles are combined into wrong clusters and hence there is a compensation between the two reconstructed Higgs masses. This trick of averaging cannot be used for the neutral Higgs case, since the two Higgs bosons have different masses. Improvement of the jet algorithm, the energy calculation and the two (or three) Higgs mass reconstruction strategies have to be studied in the future. Some M.C. events are shown in Fig.15 and 16.

4. Higgs Bosons from Open Top

4.1 CHARGED HIGGS FROM OPEN TOP DECAY

This topic is not fully studied yet. Don Fujino and I have just started to work on it. Some of the results of the Don's analysis are presented by Gail Hanson in this workshop[31]. The idea is that the charged Higgs bosons can be looked for in the top quark decays, if the Z^o peak is above the open top threshold and the charged Higgs boson is lighter than the top quark. The cross section of $t\bar{t}$ events is greater than that for charged Higgs boson pair production approximately by an order of magnitude:

$$\frac{\Gamma(Z^o \to H^+H^-)}{\Gamma(Z^o \to all)} \approx 0.01 \cdot \beta^3 \approx 0.0035 \qquad (\text{for} \quad m_{H^\pm} = 30GeV),$$
$$\frac{\Gamma(Z^o \to t\bar{t})}{\Gamma(Z^o \to all)} \approx 0.035 \qquad (\text{for} \quad m_t = 40GeV).$$

If the charged Higgs boson is lighter than the top quark, the decay branching fraction of the process $t \to H^+b$ is almost 100%. The ordinary top search strategy, searching for isolated high p_T leptons, does not work for this case since the leptons from the decay chain $H^+ \to \tau^+\nu_\tau \to \ell^+\nu_\ell\bar{\nu}_\tau\nu_\tau$ are significantly softer than those from the semileptonic decay of top quark. The combined branching fraction of $t \to H^+b \to \tau\nu_\tau b \to \ell\nu_\ell\bar{\nu}_\tau\nu_\tau b$ is at most about 4 % for each lepton species (e or μ). The majority of the top pair events with subsequent top decay into H^+b are hadronic multijet events, since H^+ decays predominantly into $c\bar{b}$ or $c\bar{s}$. Of course these events are more spherical than the ordinary multihadrons, but the tail of distributions due to the higher order QCD processes is large and the estimation of the tail by jet models have a large ambiguity. For example, the distribution predicted by the Lund model [12] is signicantly shifted to the softer side compared with the Webber model [32] prediction.

Perhaps we can see a bump in distributions of jet variables on the top of the smooth QCD background. For example, the distribution of p_T^{out} sum normalized by the visible energy shows a bump due to the top events on the top of the smooth exponetial QCD background of the light quarks as shown in Fig.22a ($B(H^+ \rightarrow c\bar{b}) = 100\%$). If $B(H^+ \rightarrow \tau^+\nu_\tau) = 25\%$ and $B(H^+ \rightarrow s\bar{c}) = 75\%$, the distribution (Fig.22b) is as soft as for that of ordinary top decay via W^+ (Fig.22c). The variable p_T^{out} is the transverse momentum from the event plane which is defined by the two major sphericity axes. I choose this variable since the tail from the higher order QCD processes is relatively small, compared with those for sphericity or thrust distributions. It is necessary to tune up the QCD shower models by using the non-spherical region of the jet variable distributions, where the contamination of possible heavy new particles is relatively small.

4.2 Neutral Higgs from Open Top

Neutral Higgs bosons can be produced like Bremsstrahlung process from $t\bar{t}$ events. However, the cross section is a few % of $t\bar{t}$ cross section even for a very light standard Higgs boson[33]. For non-minimal Higgs bosons, the cross section depends on the mixing angles and the Higgs coupling with the top quark.

The other possibility of the neutral Higgs production from top quark is the decay process $t \rightarrow c + H_i^o$ via a loop of $b - W^\pm - b$ or $b - H^\pm - b$ (This is not a tree level FCNC decay).

If this decay mode is dominant, by some reason, again the top quark cannot be found through its semi-leptonic decay mode.

These processes are not yet studied.

4.3 Comments on the QCD shower models

To study the hadronic decays of Higgs bosons, it is crucial to control the background from the higher order QCD processes and it is better to have reliable models to estimate the multi-jet background. The QCD parton shower models are needed, even at the PEP/PETRA energies, since the models based on the $O(\alpha_s^2)$ exact matrix elements and on phenomenological hadronic fragmentation (like the Lund non-shower model) cannot describe consistently the muti-jet rate[34]. The QCD shower models became fashionable since a few years ago. The incorporation of the soft- and collinear- gluon- interference effect is investigated by many theorists, and as a result, Webber and Marchesini include the interference effects, approximated by the angular ordering of the partons, into their Monte Carlo[32]. The model describes, so called, the string effects for three jet events [35], but there are mainly two problems. One of the problems is that the model does not have an exact energy-momentum conservation. This is due to the over-constraint on the kinematical variables: The final state parton masses are fixed to the nominal values depending on their flavors and the total energy-momentum is calculated backward along the cascade branches. The other problem is common to all the shower models: the model cannot describe the hard processes since it is based on the leading-log approximation, which works well in the infinite momentum frame. These two problems seem to be cured in the Lund shower model, but they are treated in an inconsistent way. In fact, the Lund shower model (with angular ordering) is in principle, using the same parton shower scheme as the Webber model. The energy-momentum conservation is artificially done by adjusting the momenta: an event is boosted to have zero net momentum and the momenta of all the particles are rescaled with a common factor to have a net energy of $E_{cm} = \sqrt{s}$*

This kind of adjustment destroys the distributions of particles and effectively deforms the correct matrix element. In addition to this, in order to have a reasonable rate of hard three jet events, the ratio between the exact differential three jet cross section and that for the leading-log approximation is effectively weighted in each branching. The distributions for the soft processes where the approximation works well might be destroyed by the weighting, since the interference effects are already simulated by the angular ordering.

To avoid this confusion, I have proposed to use the exact matrix element for the hard processes and the leading-log shower models for the soft processes and combine the two parts in a consistent way[36]. The soft part and the hard part can be clearly defined by the invariant mass of the system. Technically this is done by a trick, that the $O(\alpha_s)$ exact matrix element is incorporated into the Webber model. The

* *The newest version of the Lund shower model (version 6.3) has an exact momentum conservation.*

combined model describes the energy-energy-correlation better than the original Webber model does[36], but the hard four jet events are not yet described, since the incorporation is up to $O(\alpha_s)$. In principle, the $O(\alpha_s^2)$ matrix elements can be incorporated into the model in a similar way, but it is not worth doing it now because the model has another problem of the momentum non-conservation.

The energy momentum conservation can be satisfied in the Webber model by loosening the kinematical constraints: the branching can be terminated also when the invariant mass of a parton gets smaller than the nominal value, without fixing the final state parton masses after the termination of the cascade processes. Of cource, the termination of the branchings should also be controlled by the Sudakov form factor. These ideas are not yet included in the Monte Carlo program.

I agree that the good model is defined to be one which describes the data better. I would also like to stress that the models in the market still need improvements and even if the predicted distributions can fit the data it can be accidental, unless we have good reasons to believe the results.

5. Conclusions

(1) With 10,000 Z^o's, we may have a hint of the evidence of charged Higgs boson pair production, if the mass is below 35 GeV, by reconstructing the jet-jet invariant mass peak.

(2) For the neutral Higgs boson production ($e^+e^- \rightarrow Z^o \rightarrow H_i^o + H_j^o$, $i \neq j$), the cross section depends on the Higgs mixing angles. If at least one of the Higgs bosons decays into a lepton pair and there is almost no suppression due to the mixing, it is possible to find the evidence with 10,000 Z^o's. If two of them decay into hadrons, it is very difficult to look for them with a small number of Z^o's.

(3) If the charged Higgs boson is lighter than top quark, top quark decays into $H^+ + b$. Even if we cannot find the top quark through their semileptonic decay modes, top quarks can be produced at SLC. We have just started to investigate this case.

APPENDIX

Monte Carlo Event Simulation

Monte Carlo event generator programs for the process $e^+e^- \rightarrow H^+H^-$ and $\rightarrow H_i^oH_j^o$ are coded under the framework of the Lund 6.1 generator. The production and decay processes are simulated according to the differential cross section and the decay matrix element. For the scalar pair production, the angular distribution is proportional to $\sin^2\theta$. For the decay, it is an isotropic distribution in the scalar particle rest frame. Hadronic fragmentation is simulated using the Lund

string model and the higher order QCD effects in the decay processes ($H^- \rightarrow b\bar{c}g$ or $H^o \rightarrow c\bar{c}g$ etc) are included by applying the Lund shower model for the decay processes [12]. The initial state radiation effect is included in the simulation. On the Z^o peak, the effect is mainly that of the lowering of the total cross section and the events have almost no hard photon radiations ($E_\gamma \gg \Gamma_{Z^o}$).

The detector effects are not fully simulated, but the Mark-II acceptance cuts, momentum and energy smearings are applied to each particle, according to the following parameters.

For stable charged particles ($e^\pm$, $\mu^\pm$, $\pi^\pm$, $K^\pm$, p and $\bar{p}$):

$$\sigma_{p_t}/p_t = 0.004p_t \quad (p_t \text{ in } GeV, \quad \text{for } |\cos\theta| < 0.7)$$
$$\sigma_{p_t}/p_t = (0.115\,|\cos\theta| - 0.0748)\cdot p_t \qquad (\text{for } |\cos\theta| \geq 0.7)$$
$$\sigma_\theta = 1.5\ mrad,$$
$$\sigma_\phi = 0.5\ mrad,$$

For photons:

$$\sigma_E/E = 0.15/\sqrt{E} \qquad (E \text{ in } GeV, \text{ for } |cos\theta| < 0.7),$$
$$\sigma_E/E = 0.20/\sqrt{E} \qquad (E \text{ in } GeV, \text{ for } |cos\theta| \geq 0.7),$$
$$\sigma_\theta = 3.5\ mrad,$$
$$\sigma_\phi = 3.5\ mrad.$$

Acceptance of each detector component is:

$|cos\theta| < 0.85$, for the tracking chamber

$|cos\theta| < 0.7$ and $|\phi - n\cdot 45^\circ| < 3^\circ$ $\quad (n = 0, 1, ..., 7)$ for LA

$0.7 \leq |cos\theta| < 0.95$ for EC.

It was assumed in the simulation that neutral hadrons (K_L^o, n and $\bar{n}$) and neutrinos escape the detector undetected.

FIGURE CAPTIONS

*Fig.*1 Energy flow of a typical $e^+e^- \rightarrow H^+H^-$ event in $\cos\theta$-ϕ plane,

(a) for partons ($b\bar{c}c\bar{b}$ from H^+H^-),

(b) for final state stable particles ($\gamma, e^\pm, \mu^\pm, \pi^\pm, K^\pm, K_L^o, p, \bar{p}, n, \bar{n}$ and neutrinos),

(c) for observed particles after Mark-II detector simulation (there is missing energy-momentum in this case), also the reconstructed four clusters are indicated,

(d) for adjusted cluster energies by using the energy-momentum conservation as described in the text.

Fig.2 The distribution of $|\cos\theta_{H^\pm}|$, where $\theta_{H^\pm}$ is the polar angle of the reconstructed charged Higgs boson,

(a) for $H^+H^- \to b\bar{c}c\bar{b}$ events with $M_{H^\pm} = 30\ GeV$,

(b) for multihadron events (Lund shower model).

Fig.3 Energy distribution of the smallest energy cluster (the cut is indicated in the figure), after the cut (1),

(a) for $H^+H^- \to b\bar{c}c\bar{b}$ events with $M_{H^\pm} = 30\ GeV$,

(b) for multihadron events (Lund shower model).

Fig.4 The distribution of the minimum angle between any pair of the cluster momenta, after the cuts (1) and (2),

(a) for $H^+H^- \to b\bar{c}c\bar{b}$ events with $M_{H^\pm} = 30\ GeV$,

(b) for multihadron events (Lund shower model).

Fig.5 The distribution of the energy difference between reconstructed two Higgs bosons, after the cuts (1),(2), and (3),

(a) for $H^+H^- \to b\bar{c}c\bar{b}$ events with $M_{H^\pm} = 30\ GeV$,

(b) for multihadron events (Lund shower model).

Fig.6 The distribution of the mass difference between two reconstructed Higgs bosons, after the above cuts,

(a) for $H^+H^- \to b\bar{c}c\bar{b}$ events with $M_{H^\pm} = 30\ GeV$,

(b) for multihadron events (Lund shower model).

Fig.7 Invariant mass distrubution of reconstructed charged Higgs bosons for the process $H^+H^- \to b\bar{c}c\bar{b}$ on top of the background from multihadron events (Lund shower model), after applying all the cuts. The cuts are optimized for $M_{H^\pm} = 30\ GeV$.

(a) $M_{H^\pm} = 25\ GeV$,

(b) $M_{H^\pm} = 30\ GeV$,

(c) $M_{H^\pm} = 35\ GeV$.

Fig.8

(a) A typical M.C. event for the process $H^+H^- \to s\bar{c}\tau^+\nu_\tau$ with $M_{H^\pm} = 30\ GeV$ and $\sqrt{s}$ =94 GeV, reconstructed in the upgrade Mark-II detector.

(b) A typical M.C. event for the process $H^+H^- \to \tau^-\bar{\nu}_\tau\tau^+\nu_\tau$ with $M_{H^\pm} = 30\ GeV$ and $\sqrt{s}$ =94 GeV.

Fig.9 Distributions of ϕ_{acop} vs $\cos\theta_{th}$ after the visible enrgy cut ($0.25 < E_{vis}/\sqrt{s} < 0.8$),

(a) for events in which one of the charged Higgs decays into $\tau + \nu_\tau$ and the other decays into $c + s$, assuming $M_{H^\pm} = 30\ GeV$,

(b) for background events due to light quark (udscb) production.

Fig.10 The cross section contours for the process $e^+e^- \to H_s^o + H_p^o$ on the Z^o peak in the $M_{H_s^o} - M_{H_p^o}$ plane, where H_s^o and H_p^o are a scalar and a pseudoscalar Higgs boson, respectively. The expected cross section contours at TRISTAN energy (50 GeV) and at PEP energy (29 GeV) are also shown.

Fig.11 A schematic diagram of event topologies for the process $e^+e^- \to H_s^o + H_p^o$ on the Z^o peak in the $M_{H_s^o} - M_{H_p^o}$ plane.

(a) In the case that the Higgs bosons couple to the heaviest possible fermion and H_s^o decays into two H_p^o's, if kinematically allowed.

(b) For supersymmetric models, the $H_s^o \to H_p^oH_p^o$ mode is suppressed by the choice of the mixing angles, so the two fermion pair final state might be dominant, even in the region $M_{H_s^o} > 2M_{H_p^o}$.

Fig.12 A typical M.C. event for the process $H_s^oH_p^o \to H_p^oH_p^oH_p^o \to \mu^+\mu^-\mu^+\mu^-\mu^+\mu^-$ with $M_{H_s^o} = 30\ GeV$, $M_{H_p^o} = 0.7\ GeV$ and $\sqrt{s}$ =94 GeV.

Fig.13 A typical M.C. event for the process $H_s^oH_p^o \to \mu^+\mu^- + b\bar{b}$ with $M_{H_p^o} = 30\ GeV$, $M_{H_s^o} = 0.7\ GeV$ and $\sqrt{s}$ =94 GeV.

Fig.14 A typical M.C. event for the process $H_s^oH_p^o \to \tau^+\tau^- + b\bar{b}$ with $M_{H_p^o} = 50\ GeV$, $M_{H_s^o} = 10\ GeV$ and $\sqrt{s}$ =94 GeV.

Fig.15 A typical M.C. event for the process $H_s^oH_p^o \to H_p^oH_p^oH_p^o \to c\bar{c} + c\bar{c} + c\bar{c}$ with $M_{H_s^o} = 30\ GeV$, $M_{H_p^o} = 0.7\ GeV$ and $\sqrt{s}$ =94 GeV.

Fig.16 A typical M.C. event for the process $H_s^oH_p^o \to b\bar{b} + b\bar{b}$ with $M_{H_s^o} = 30\ GeV$, $M_{H_s^o} = 15\ GeV$ and $\sqrt{s}$ =94 GeV.

Fig.17 PEP and PETRA upper limits for the decay $Z^o \to H_s^oH_p^o$ normalized to that for $Z^o \to \nu_\mu\bar{\nu}_\mu$, as a function of $M_{H_p^o}$ mass assuming H_s^o is light and stable ($M_{H_s^o} \leq 0.2\ GeV$). The widths are calculated at the Z^o peak. The curve predicted by the Glashow-Manohar model is also shown. In the figure, h_1^o and h_2^o mean H_s^o and H_p^o, respectively.

Fig.18 Preliminary JADE upper limit of the decay width for $Z^o \to H_s^oH_p^o$ normalized to that for $Z^o \to \nu_\mu\bar{\nu}_\mu$, as a function of $M_{H_p^o}$ mass assuming H_p^o is an axion, which decays into e^+e^- with a lifetime of about 10^{-13} sec. In the figure, h and a mean H_s^o and H_p^o, respectively ($M_{H_s^o} \leq 0.2\ GeV$). The width are calculated at the Z^o peak. The broken curve is the theoretical prediction of the axion model by Peccei et al.

Fig.19 A scatter plot of the two momenta, p_i vs p_j, which form an isolated oppositely charged particle pair selected as in the text (without requiring muons),

(a) for $Z^o \rightarrow H_s^o H_p^o \rightarrow \mu^+\mu^- + b\bar{b}$ event with $M_{H_s^o} = 0.7\ GeV$ and $M_{H_p^o} = 30\ GeV$. The number is normalized to 20,000 multihadrons at the Z^o peak.

(b) for $Z^o \rightarrow H_s^o H_p^o \rightarrow \mu^+\mu^- + b\bar{b}$ event with $M_{H_s^o} = 0.7\ GeV$ and $M_{H_p^o} = 70\ GeV$. The number is normalized to 20,000 multihadrons at the Z^o peak.

(c) for multihadron background after cuts (originally 20,000 events generated).

Fig.20 A scatter plot of two momenta, p_i vs p_j, of an isolated oppositely charged particle pair selected as in the text (at least one of the pair particles is a muon).

(a) for $Z^o \rightarrow H_s^o H_p^o \rightarrow \mu^+\mu^- + b\bar{b}$ event with $M_{H_s^o} = 0.7\ GeV$ and $M_{H_p^o} = 30\ GeV$. The number is normalized to 20,000 multihadrons at the Z^o peak.

(b) for $Z^o \rightarrow H_s^o H_p^o \rightarrow \mu^+\mu^- + b\bar{b}$ event with $M_{H_s^o} = 0.7\ GeV$ and $M_{H_p^o} = 70\ GeV$. The number is normalized to 20,000 multihadrons at the Z^o peak.

Fig.21 Two survived events after all the cuts for selecting small opening angle high momentum muon pairs.

Fig.22 A distribution of the p_T^{out} sum normalized by visible energy for $Z^o \rightarrow t\bar{t}$ events on the top of the smooth background from light quark production (udscb). The number is normalized to 10,000 Z^o's (Z^o's decay into light fermions).

(a) With the decay of $t \rightarrow b + H^+$ with 100 % branching fraction and the subsequent decay of $H^+ \rightarrow c\bar{b}$ with 100 % branching fraction.

(b) With the decay of $t \rightarrow b + H^+$ with 100 % branching fraction and the subsequent decay of $H^+ \rightarrow c\bar{s}$ with 75 % branching fraction and $H^+ \rightarrow \tau^+\nu_\tau$ with 25 % branching fraction.

(c) With the ordinary weak decay of $t \rightarrow b + W^{+*}$.

REFERENCES

[1] G.J. Feldman, Proc. of Conf. on Physics in Collision VI, Chicago (1986), SLAC-PUB-4143

[2] D. Wood, Proc. of Mark-II SLC-Physics Workshop at Granlibakken, September 1986, p320;

A. Schwarz, Proc. of Mark-II SLC-Physics Workshop at Granlibakken, September 1986, p327;

W. Innes, Proc. of Mark-II SLC-Physics Workshop at Granlibakken, September 1986, p341;

A. Weir, Proc. of Mark-II SLC-Physics Workshop at Granlibakken, September 1986, p348;

[3] M.I. Vysotsky, Phys. Lett., 97B(1980)159

[4] J.D. Bjorken, Proc. 1976 SLAC Summer Institute on Particle Physics, SLAC-PUB-198 (1977)

[5] G. Altarelli, Proc. of Int. Conf. on High Energy Physics, Berkeley (1986) to be published

[6] H.E. Haber and G.L. Kane, Phys. Reports, 117(1984)279

[7] R.D. Peccei and H.R. Quinn, Phys Rev. Lett., 38(1977)1440;

Phys. Rev., D16(1977)1791

W.A. Bardeen and S.-H.H. Tye, Phys. Lett., 74B(1978)229

W.A. Bardeen, S.-H.H. Tye and J.A.M. Vermaseren Phys. Lett., 76B(1978)580

[8] H.E. Haber, G.L. Kane and T. Sterling, Nucl. Phys. B161(1979)493 Phys. Rev., D16(1977)1791

[9] J.F. Gunion and H.E. Haber, Nucl. Phys. B272(1986)1 Phys. Rev., D16(1977)1791

[10] JADE Collab., W. Bartel et al., Z. Physik, C31(1986)359;

S. Komamiya, Proc. of Int. Conf. on Lepton and Photon Interactions at High Energies, Kyoto, (1986) p612

[11] TASSO Collab., M. Althoff et al., Phys. Lett., 122B(1983)95

[12] T. Sjostrand, Lund preprint, LU-TP 85-10 (1985);

A. Petersen modified the decay routine of the Lund model so that the QCD shower model can be used in the decay of heavy particles.

[13] Ying Liu, Z. Physik, C30(1986)631

[14] UA1 Collab., G. Arnison et al., Phys. Lett., 139B(1984)115

[15] S.L. Glashow and A. Manohar, Phys. Rev. Lett., 54(1985)526

[16] JADE Collab., W. Bartel et al., Phys. Lett., 146B(1984)126

[17] HRS Collab., C. Akerlof et al., Phys. Lett., 156B(1985)271

[18] MAC Collab., W.W. Ash et al., Phys. Rev. Lett., 54(1985)2477

[19] Mark-II Collab., G.J. Feldman et al., Phys. Rev. Lett., 54(1985)2289

[20] CELLO Collab., H.J. Behrend et al., Phys. Lett., 161B(1985)182

[21] JADE Collab., W. Bartel et al., Phys. Lett., 155B(1985)288, and updated result for the Berkeley Conference (1986).

[22] T. Cowan et al., Phys. Rev. Lett., 56(1986)446

[23] R.D. Peccei, T.T. Wu and T. Yanagida, Phys. Lett., B172(1986)435

[24] L.M. Krauss and F. Wilczek, Phys. Lett., B173(1986)189

[25] K. Hagiwara, DESY/KEK, private communication

[26] JADE Collab., preliminary result presented by S. Wittaker at the Int. Conf. on High Energy Physics, Berkeley, (1986)

[27] S. Egli et al., SIN preprint, PR-86-08 (1986)

[28] A. Konaka et al., Phys. Rev. Lett. 57(1986)659

C.N. Brown et al., Phys. Rev. Lett. 57(1986)2101

[29] F.A. Berends, P.H. Daverfeld and R. Kleiss, Phys. Lett. 148B(1984)489; Nucl. Phys. B253(1985)441

Tim Barklow corrected the errors in the Monte Carlo and that in the paper.

[30] Edited by J. Ellis and R.D. Peccei, CERN 86-02(1986) p340

[31] G. Hanson, in this proceedings

[32] G. Marchesini and B.R. Webber, Nucl. Phys. B238(1984)1;

B.R. Webber, Nucl. Phys. B238(1984)492;

[33] K.J.F. Gaemers and G.J. Gounaris, Phys. Lett., 77B(1978)379

[34] JADE Collab., W. Bartel et al., Z. Physik, C33(1986)23

[35] A. Petersen, DESY 84-082(1984);

JADE Collab., W. Bartel et al., Phys. Lett., 157B(1985)340;

TPC Collab., H. Aihara et al., Phys. Rev. Lett., 54(1986)270

[36] S. Komamiya, DESY 86-065(1986)

278

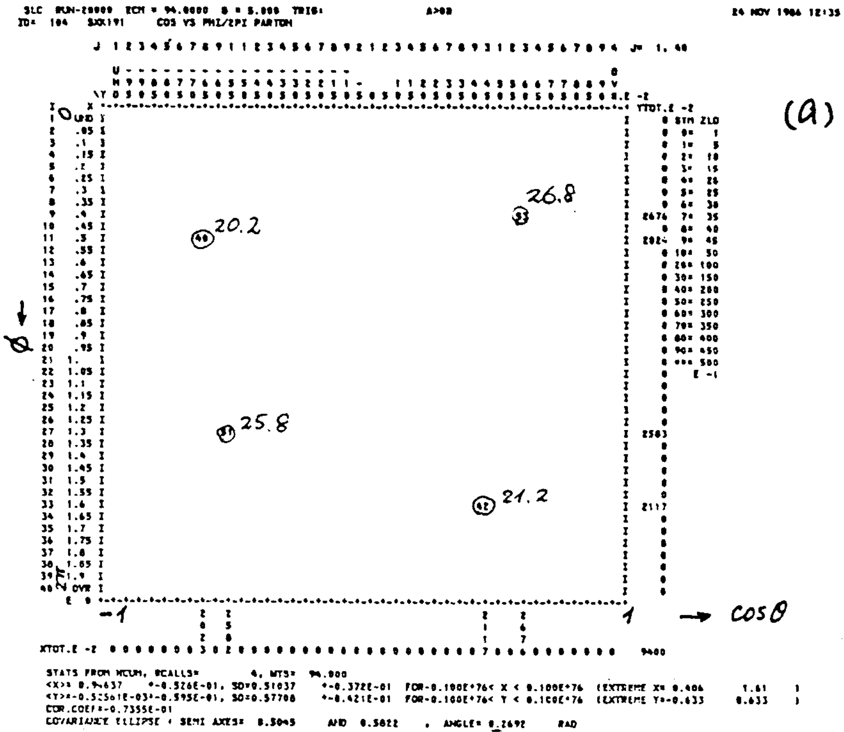

(a)

279

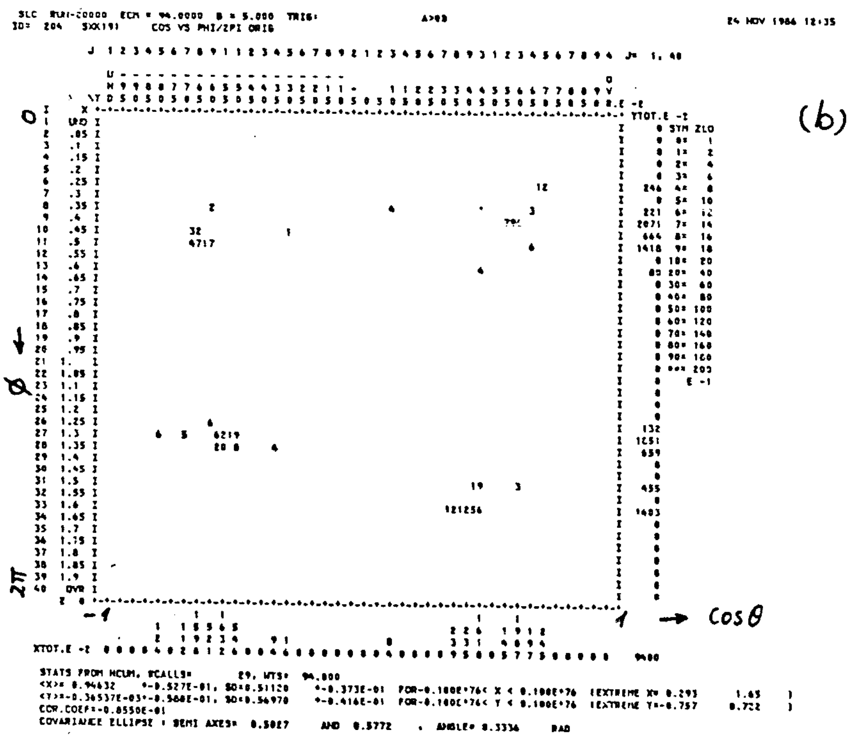

(b)

Fig. 1

280

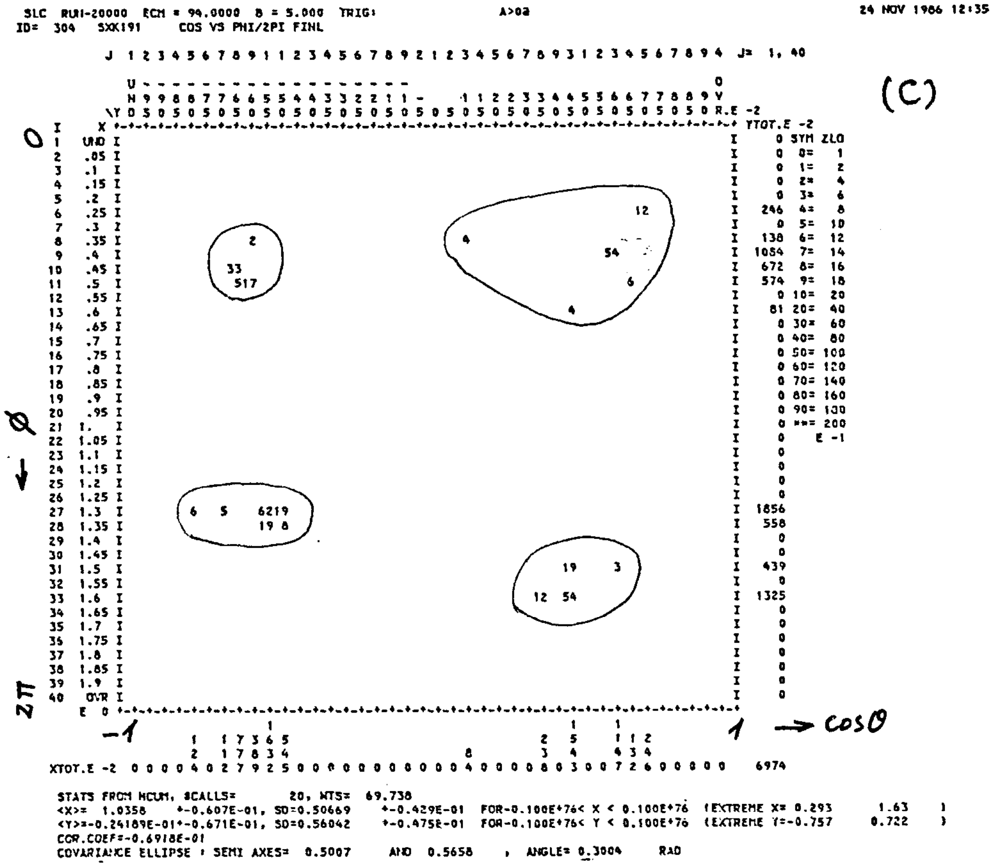
SLC RUN-20000 ECM = 94.0000 B = 5.000 TRIG: A>0a 24 NOV 1986 12:35
ID= 304 SXX191 COS VS PHI/2PI FINL
(C)
0
ϕ
2π
-1
1
→ cosθ
STATS FROM HCUM, #CALLS= 20, WTS= 69.738
<X>= 1.0358 +-0.607E-01, SD=0.50669 +-0.429E-01 FOR-0.100E+76< X < 0.100E+76 (EXTREME X= 0.293 1.63)
<Y>=-0.24189E-01+-0.671E-01, SD=0.56042 +-0.475E-01 FOR-0.100E+76< Y < 0.100E+76 (EXTREME Y=-0.757 0.722)
COR.COEF=-0.6918E-01
COVARIANCE ELLIPSE : SEMI AXES= 0.5007 AND 0.5658 , ANGLE= 0.3004 RAD

281

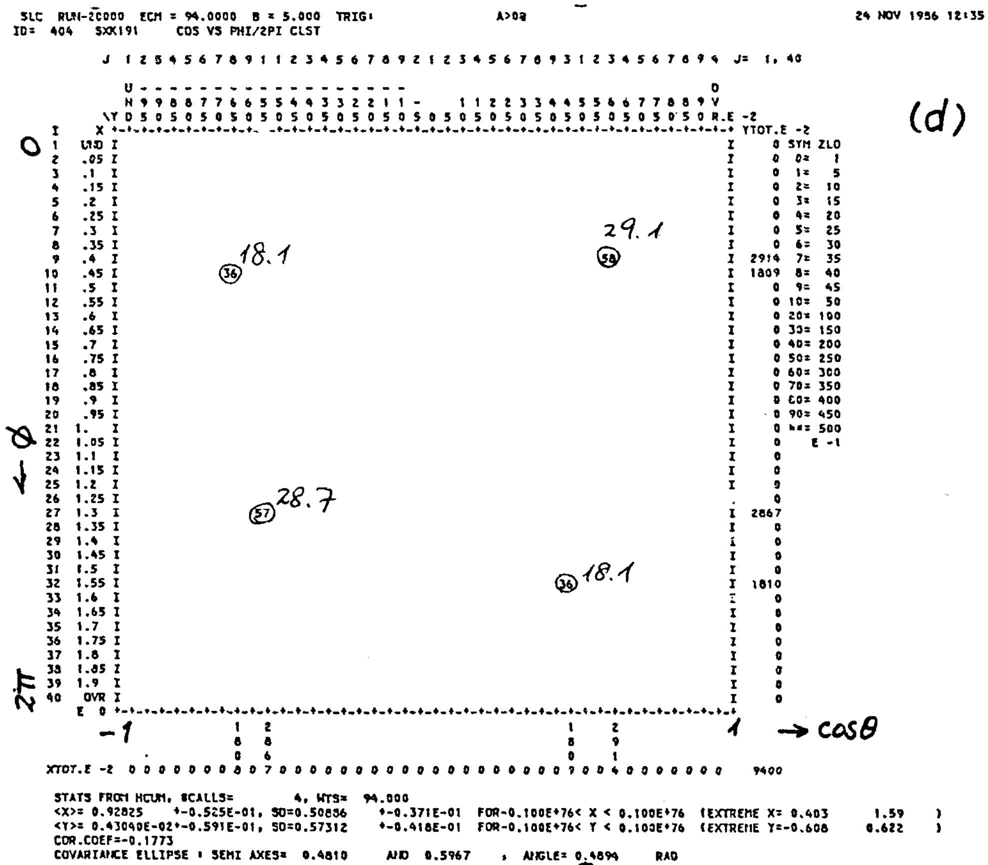
SLC RUN-20000 ECM = 94.0000 B = 5.000 TRIG: A>0a 24 NOV 1986 12:35
ID= 404 SXX191 COS VS PHI/2PI CLST
(d)
0
18.1
29.1
28.7
18.1
ϕ
2π
-1
1
→ cosθ
STATS FROM HCUM, #CALLS= 4, WTS= 94.000
<X>= 0.92825 +-0.525E-01, SD=0.50836 +-0.371E-01 FOR-0.100E+76< X < 0.100E+76 (EXTREME X= 0.403 1.59)
<Y>= 0.43040E-02+-0.591E-01, SD=0.57312 +-0.418E-01 FOR-0.100E+76< Y < 0.100E+76 (EXTREME Y=-0.608 0.622)
COR.COEF=-0.1773
COVARIANCE ELLIPSE : SEMI AXES= 0.4810 AND 0.5967 , ANGLE= 0.4894 RAD

Fig 1

282

SLC RUN-20000 ECM = 94.0000 B = 5.000 TRIG: A>0a 22 DEC 1986 23:53
ID= 51 SXK316 COS(TH)

BIN	YCUM	Y	YERR	LO EDGE X
1	81	81	9.0	UND
2	161	80	8.9	.02
3	233	72	8.5	.04
4	326	93	9.6	.06
5	420	94	9.7	.08
6	519	99	9.9	.1
7	616	97	9.8	.12
8	714	98	9.9	.14
9	806	92	9.6	.16
10	895	89	9.4	.18
11	984	89	9.4	.2
12	1083	99	9.9	.22
13	1167	84	9.2	.24
14	1242	75	8.7	.26
15	1317	75	8.7	.28
16	1392	75	8.7	.3
17	1480	88	9.4	.32
18	1562	82	9.1	.34
19	1637	75	8.7	.36
20	1693	56	7.5	.38
21	1759	66	8.1	.4
22	1824	65	8.1	.42
23	1881	57	7.5	.44
24	1943	62	7.9	.46
25	1999	56	7.5	.48
26	2053	54	7.3	.5
27	2122	69	8.3	.52
28	2174	52	7.2	.54
29	2222	48	6.9	.56
30	2277	55	7.4	.58
31	2316	39	6.2	.6
32	2351	35	5.9	.62
33	2408	57	7.5	.64
34	2447	39	6.2	.66
35	2500	53	7.3	.68
36	2523	23	4.8	.7
37	2560	37	6.1	.72
38	2600	40	6.3	.74
39	2636	36	6.0	.76
40	2660	24	4.9	.78
41	2683	23	4.8	.8
42	2711	28	5.3	.82
43	2730	19	4.4	.84
44	2748	18	4.2	.86
45	2761	13	3.6	.88
46	2775	14	3.7	.9
47	2789	14	3.7	.92
48	2795	6	2.4	.94
49	2799	4	2.0	.96
50	2803	4	2.0	OVR
	E 0	E 0	E 0	E 0

0 |cos θH±| 1

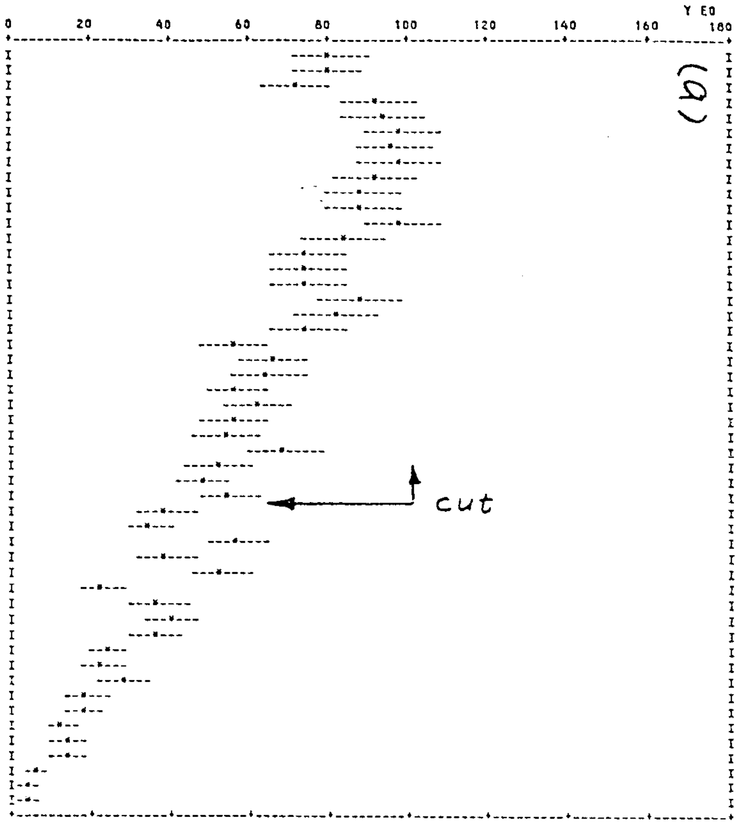

STATS FROM HCUM, #CALLS= 2803, WTS= 2803.0
<X>= 0.35955 +-0.454E-02, SD=0.24042 +-0.321E-02 FOR-0.100E+76< X < 0.100E+76 (EXTREME X= 0.395E-03 0.996)

SLC RUN-20000 ECM = 94.0000 B = 5.000 TRIG: A>0a 23 DEC 1986 25: 3
ID= 51 SXK317 COS(TH)

BIN	YCUM	Y	YERR	LO EDGE X
1	367	367	19.2	UND
2	719	352	18.8	.02
3	1088	369	19.2	.04
4	1481	393	19.8	.06
5	1881	400	20.0	.08
6	2264	383	19.6	.1
7	26[illegible]0	356	18.9	.12
8	2977	357	18.9	.14
9	3332	355	18.8	.16
10	3718	356	19.6	.18
11	4116	398	19.9	.2
12	4503	387	19.7	.22
13	4887	384	19.6	.24
14	5267	380	19.5	.26
15	5636	369	19.2	.28
16	6024	388	19.7	.3
17	6432	40[illegible]	20.2	.32
18	6832	40[illegible]	20.0	.34
19	7216	38[illegible]	19.6	.36
20	7596	380	19.5	.38
21	7993	397	19.9	.4
22	8404	411	20.3	.42
23	8818	414	20.3	.44
24	9267	449	21.2	.46
25	9699	432	20.8	.48
26	10151	452	21.3	.5
27	10581	430	20.7	.52
28	11020	439	21.0	.54
29	11476	456	21.4	.56
30	11944	468	21.6	.58
31	12408	464	21.5	.6
32	12894	486	22.0	.62
33	13421	527	23.0	.64
34	13933	512	22.6	.66
35	14458	525	22.9	.68
36	14994	536	23.2	.7
37	15540	546	23.4	.72
38	16077	537	23.2	.74
39	16637	560	23.7	.76
40	17270	633	25.2	.78
41	17897	627	25.0	.8
42	18511	614	24.8	.82
43	19131	620	24.9	.84
44	19698	567	23.8	.86
45	20216	518	22.8	.88
46	20512	296	17.2	.9
47	20720	208	14.4	.92
48	20870	150	12.2	.94
49	20981	111	10.5	.96
50	21088	107	10.3	OVR
	E 0	E 0	E 0	E 0

0 |cos θH±| 1

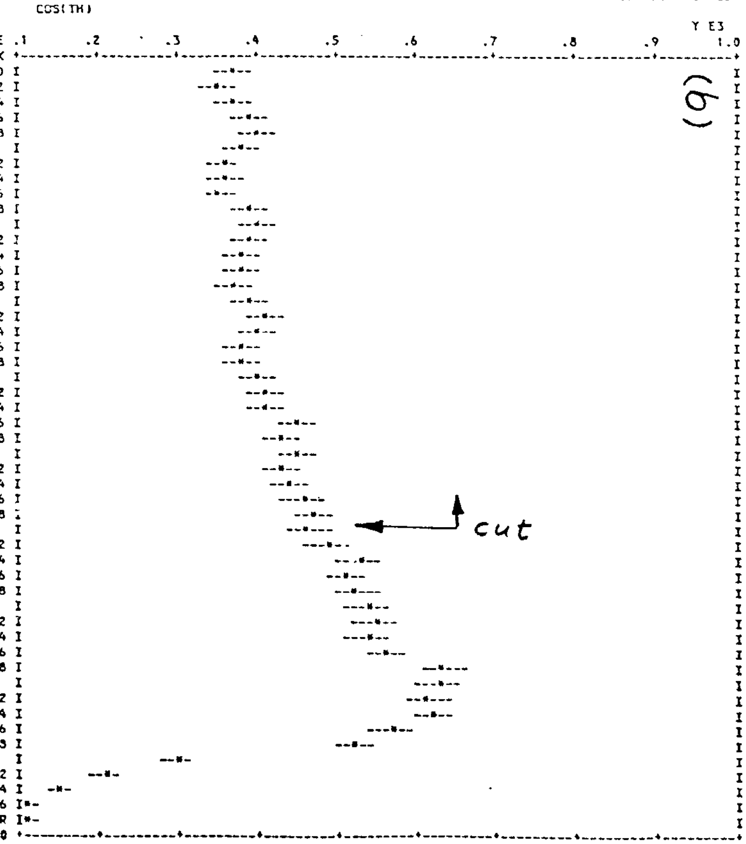

STATS FROM HCUM, #CALLS= 21088, WTS= 21088.
<X>= 0.51155 +-0.187E-02, SD=0.27148 +-0.132E-02 FOR-0.100E+76< X < 0.100E+76 (EXTREME X= 0.138E-03 1.00)

283

Fig. 2

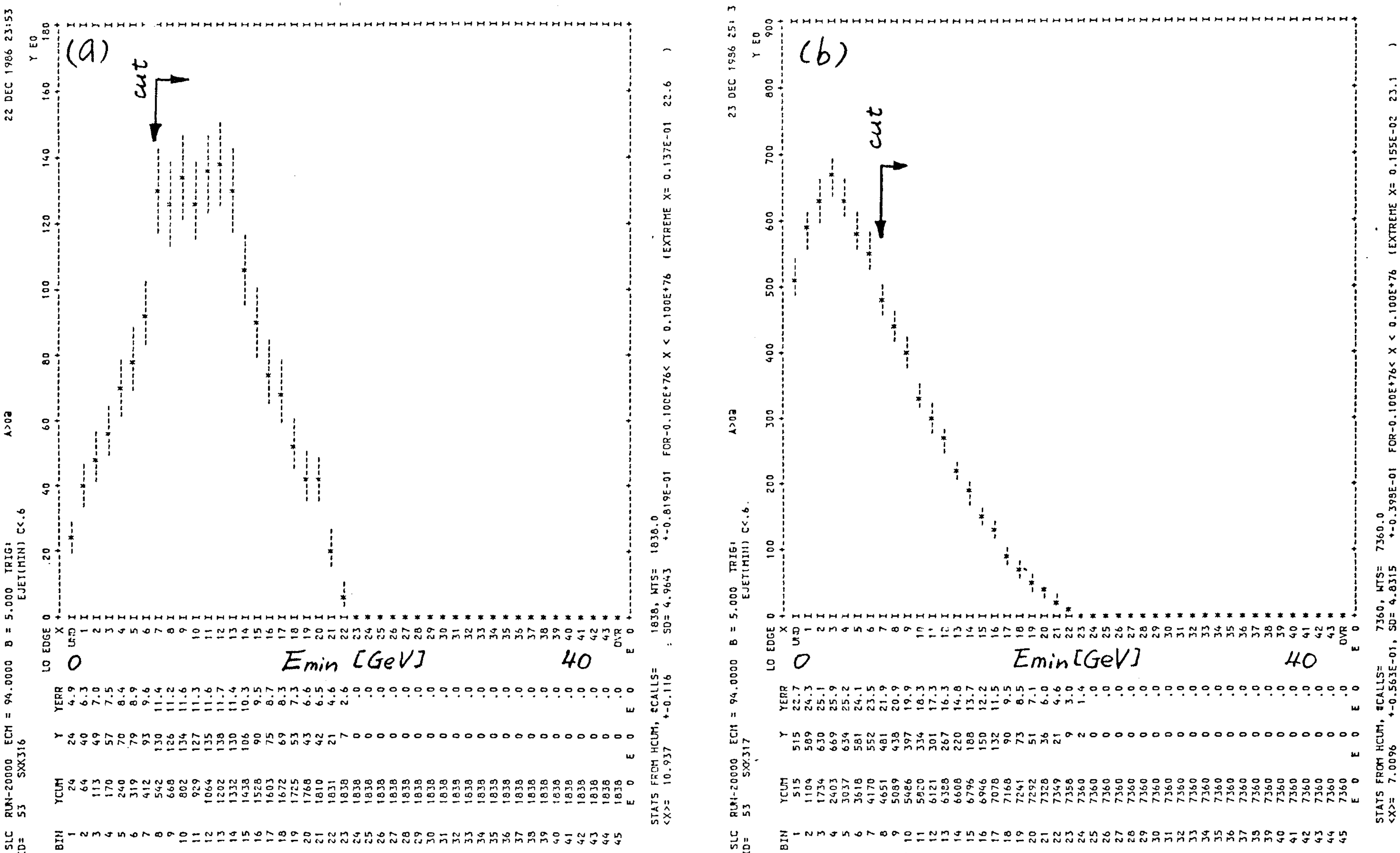

Fig. 3

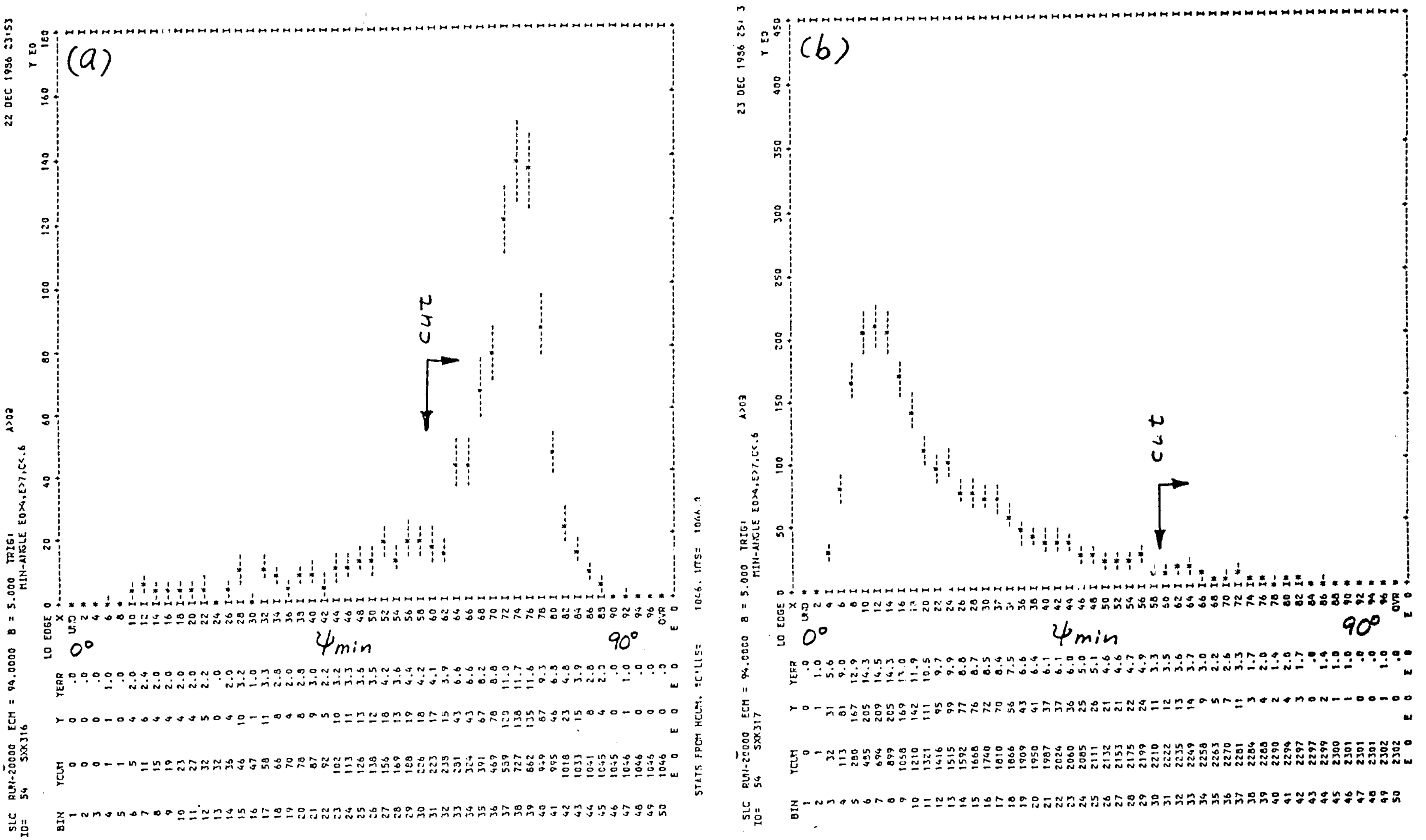

Fig 4

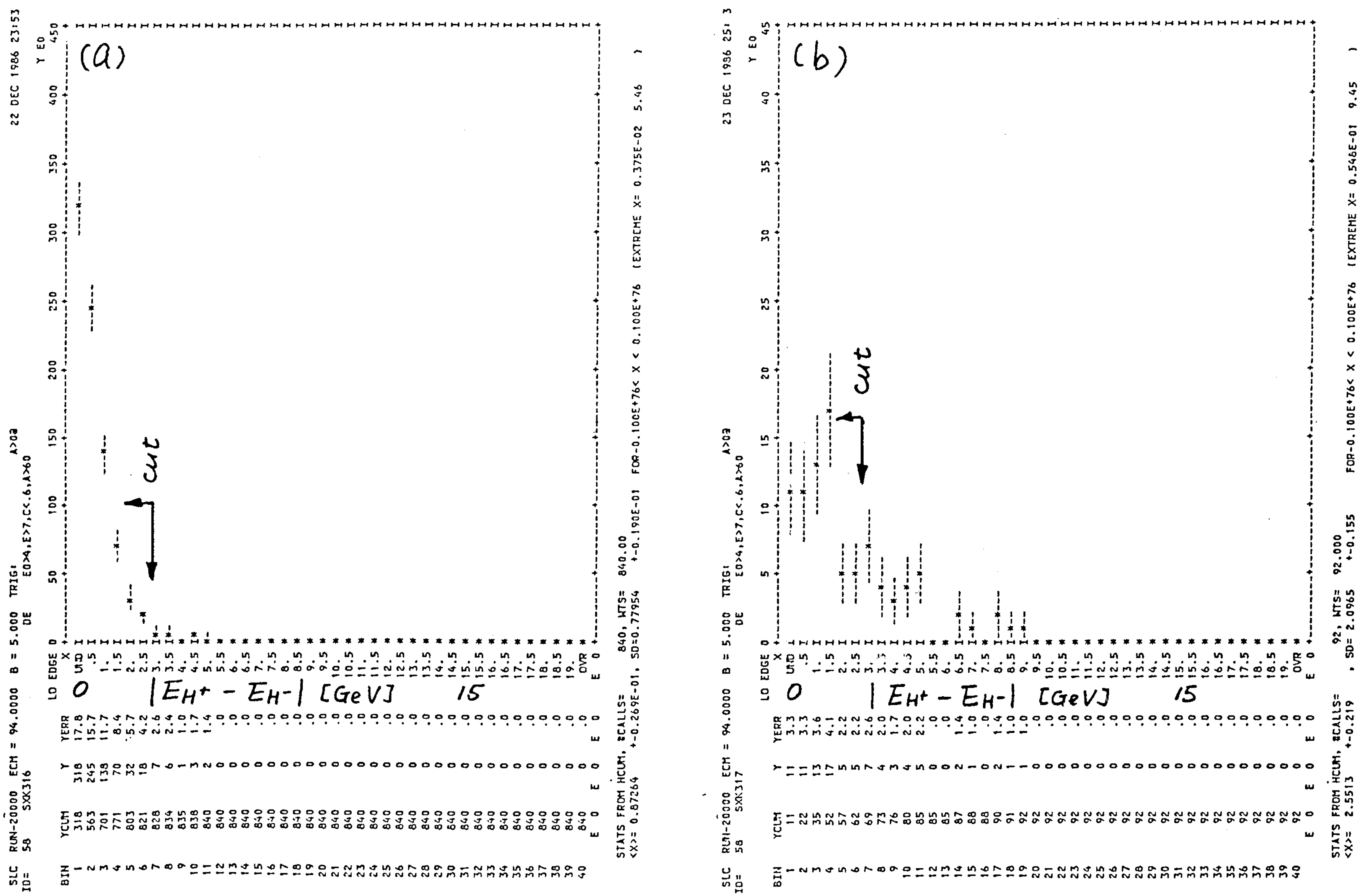

(a)
SLC RUN-20000 ECM = 94.0000 B = 5.000 TRIG:
22 DEC 1986 23:53
cut
0
|EH+ - EH-| [GeV]
15
(b)
SLC RUN-20000 ECM = 94.0000 B = 5.000 TRIG:
cut
0
|EH+ - EH-| [GeV]
15

Fig.5

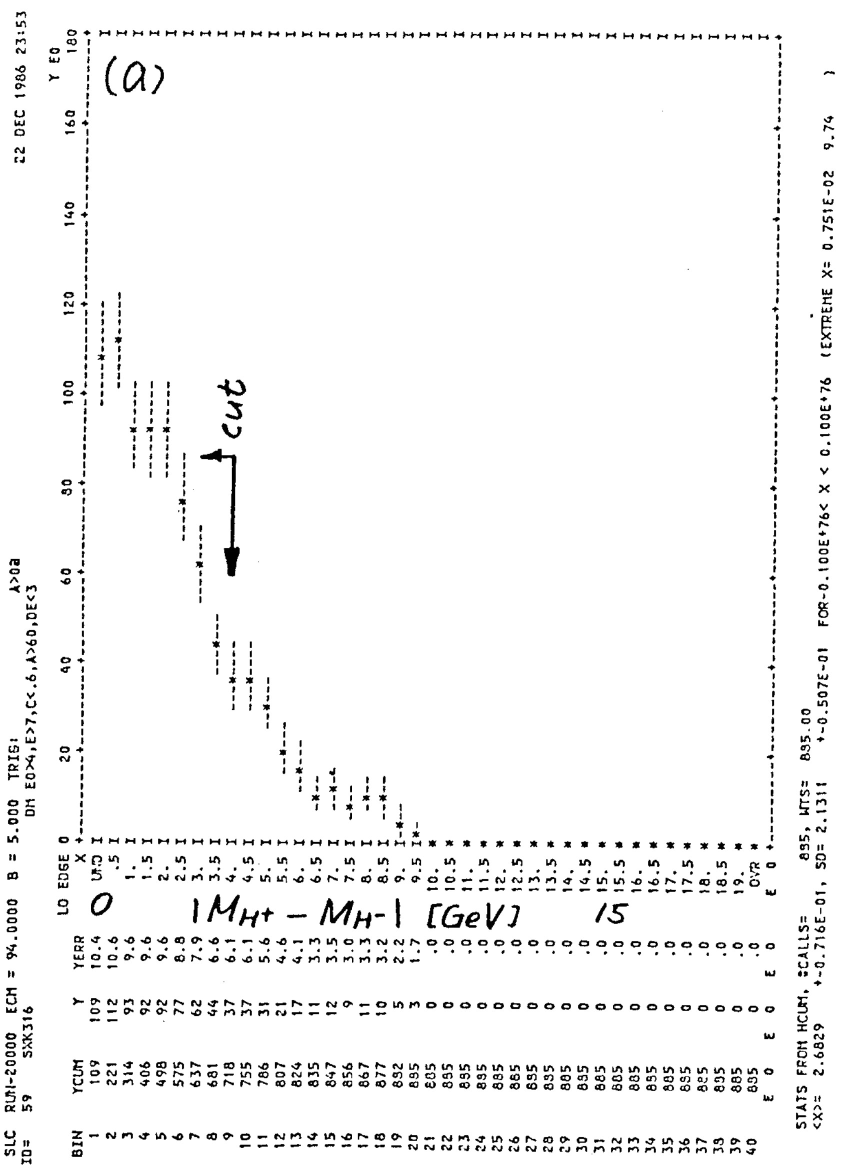

SLC RUN-20000 ECM = 94.0000 B = 5.000 TRIG:
ID= 59 SXX316
DM E0>4,E>7,C<.6,A>60,DE<3
22 DEC 1986 23:53
(a)
cut
0
|M_H+ − M_H-| [GeV]
15

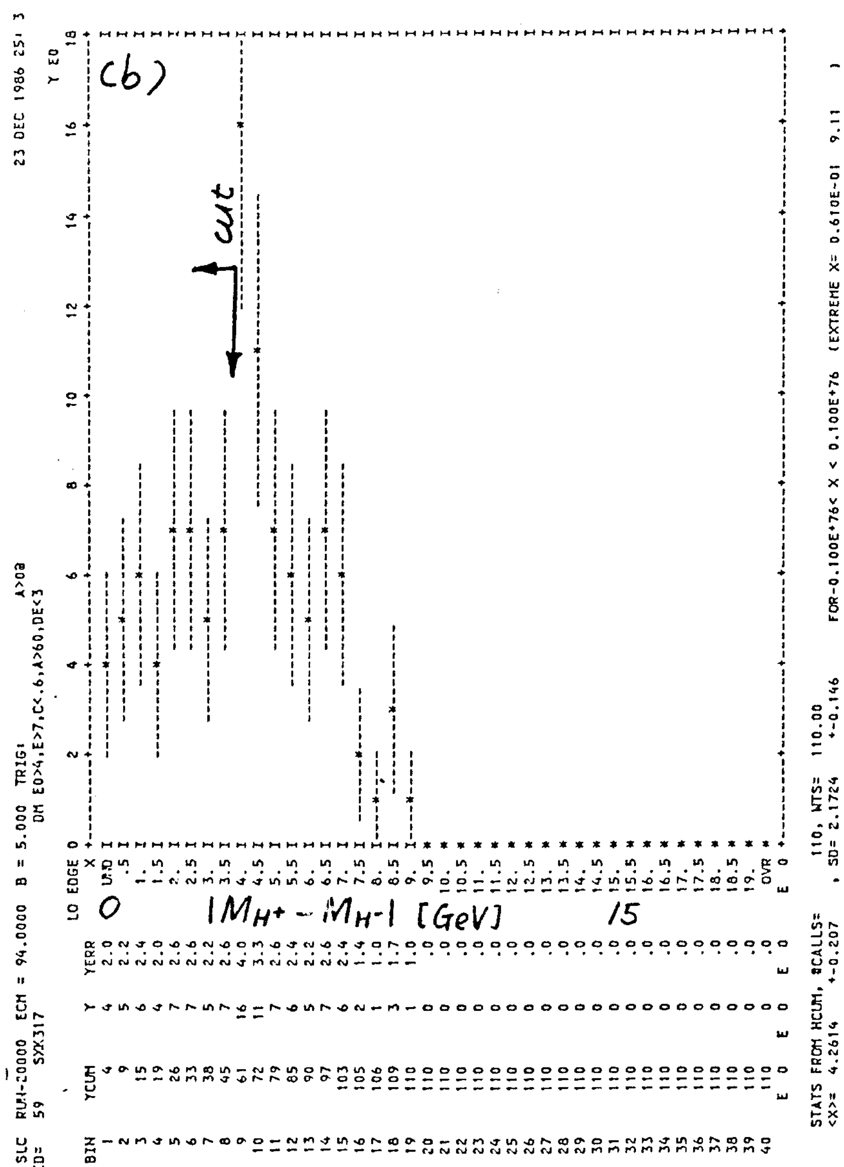

SLC RUN-20000 ECM = 94.0000 B = 5.000 TRIG:
ID= 59 SXX317
DM E0>4,E>7,C<.6,A>60,DE<3
23 DEC 1986
(b)
cut
0
|M_H+ − M_H-| [GeV]
15

Fig.6.

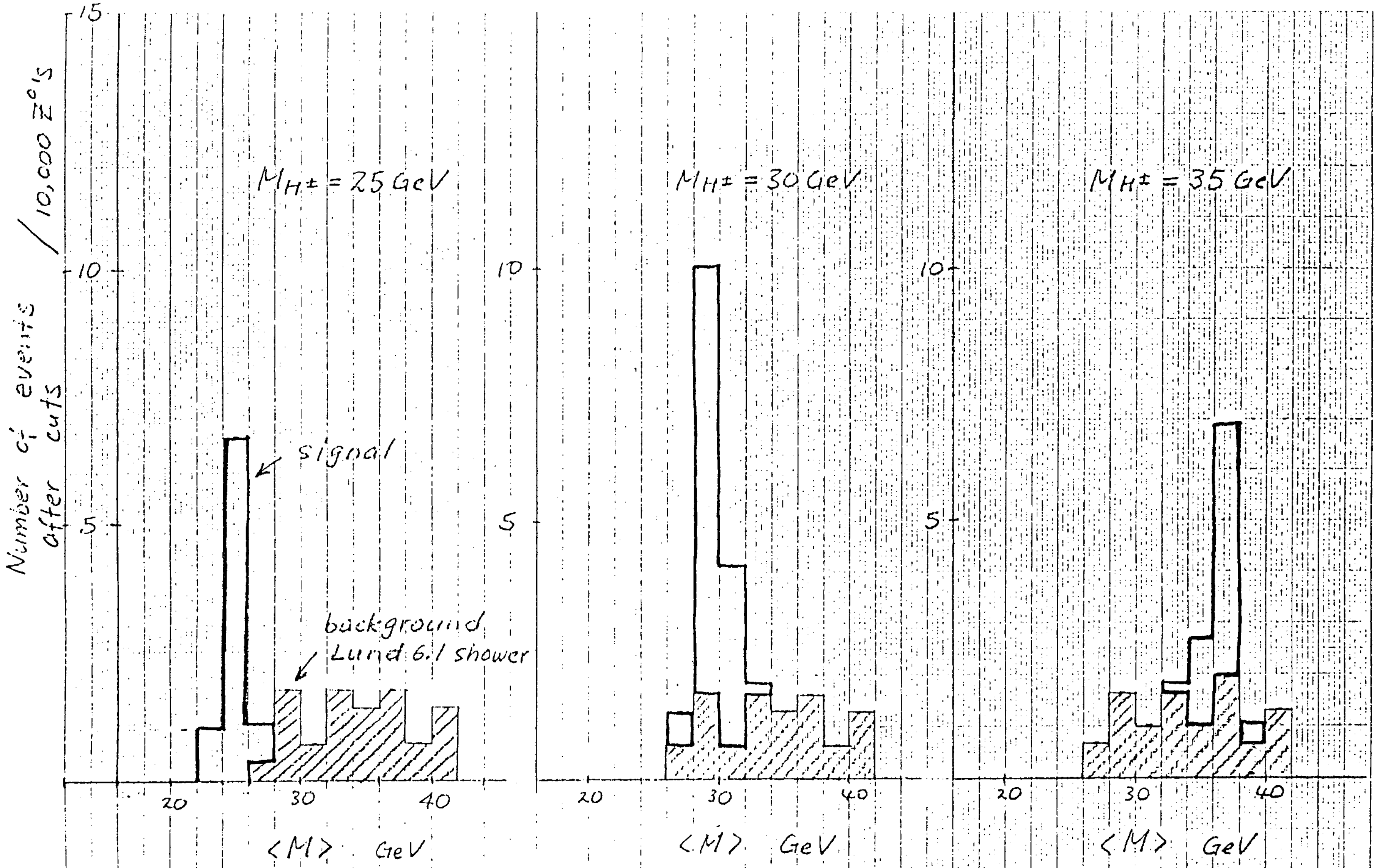

$$\langle M \rangle = \frac{M_{H^+}\,(\text{reconstructed}) + M_{H^-}\,(\text{reconstructed})}{2}$$

Fig. 7

293

RUN-22000 REC 1 E= 94.00 0 PRONG NO VERTEX (0-0)
TRIGGER 0 00F CCHAR MARK II - SLC/PEP

TRK	P	ELATOT	ID
1	0.2	0.1	PI-
2	0.4	0.1	PI+
3	6.9	0.4	PI+
4	2.7	2.1	E-
5	1.6	0.1	PI-
6	2.8	0.3	PI+
7	0.4	0.0	PI-
8	4.3	0.1	PI+
9	11.0	0.0	PI-
10	4.3	0.1	PI+
11	5.2	0.2	PI+
12	0.6	0.1	PI-
13	0.2		PI-
14	2.0		MU+
15		0.2	G
16		0.4	G
17		0.6	G
18		0.4	G
19		0.2	G

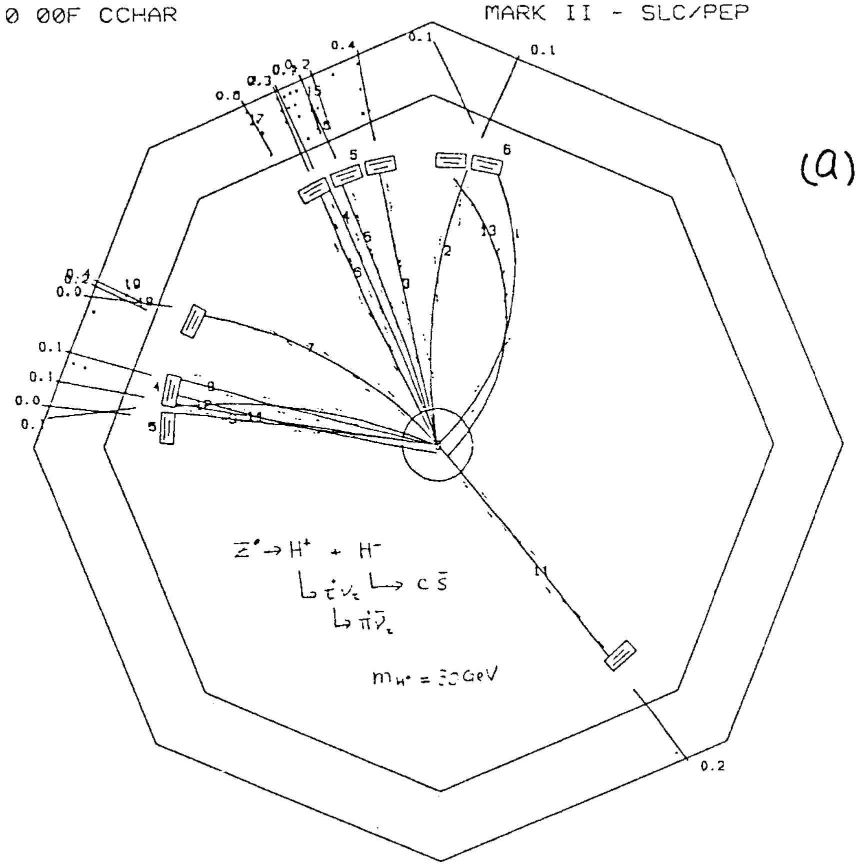

294

RUN-22000 REC 6 E= 94.00 0 PRONG NO VERTEX (0-0)
TRIGGER 0 00F CCHAR MARK II - SLC/PEP

TRK	P	ELATOT	ID
1	1.2	0.0	PI-
2	5.4	0.3	PI+
3	6.7	0.3	PI+
4	1.4	0.3	PI-
5		3.7	G
6		21.3	G
7		0.2	G

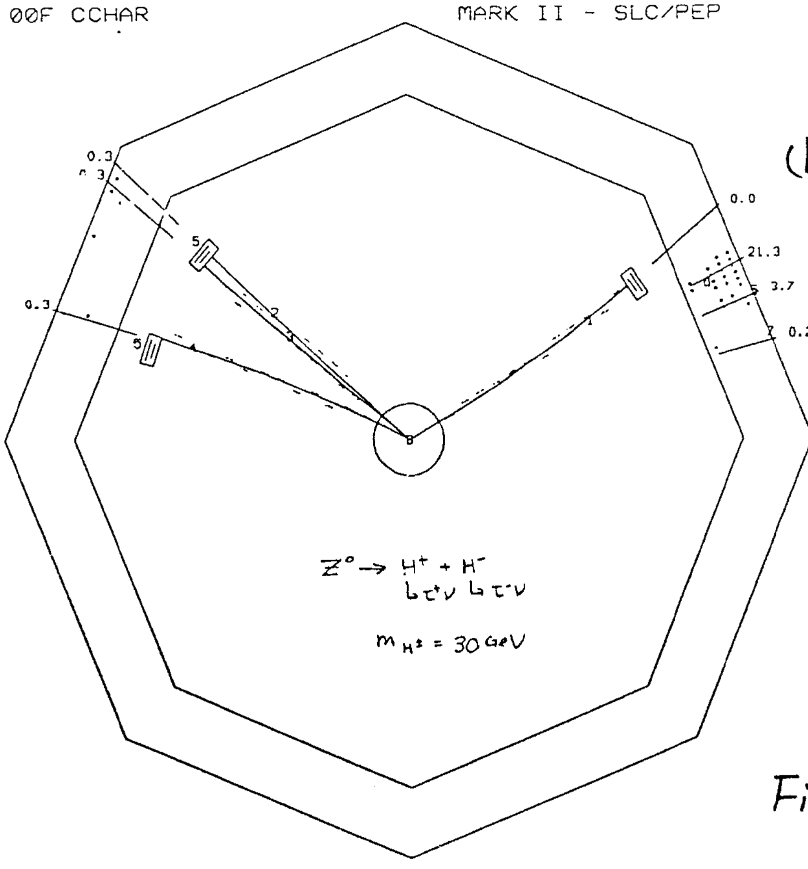

Fig. 8

295

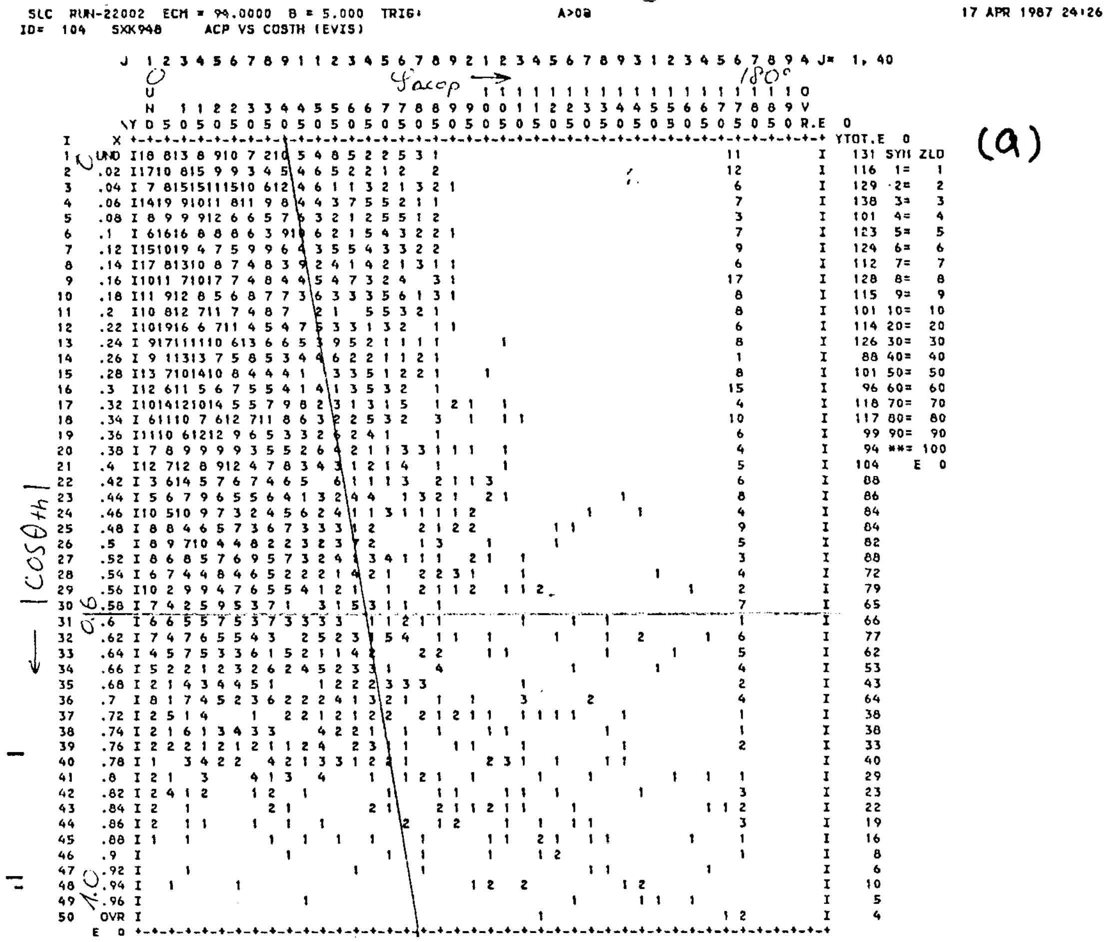

(a)

296

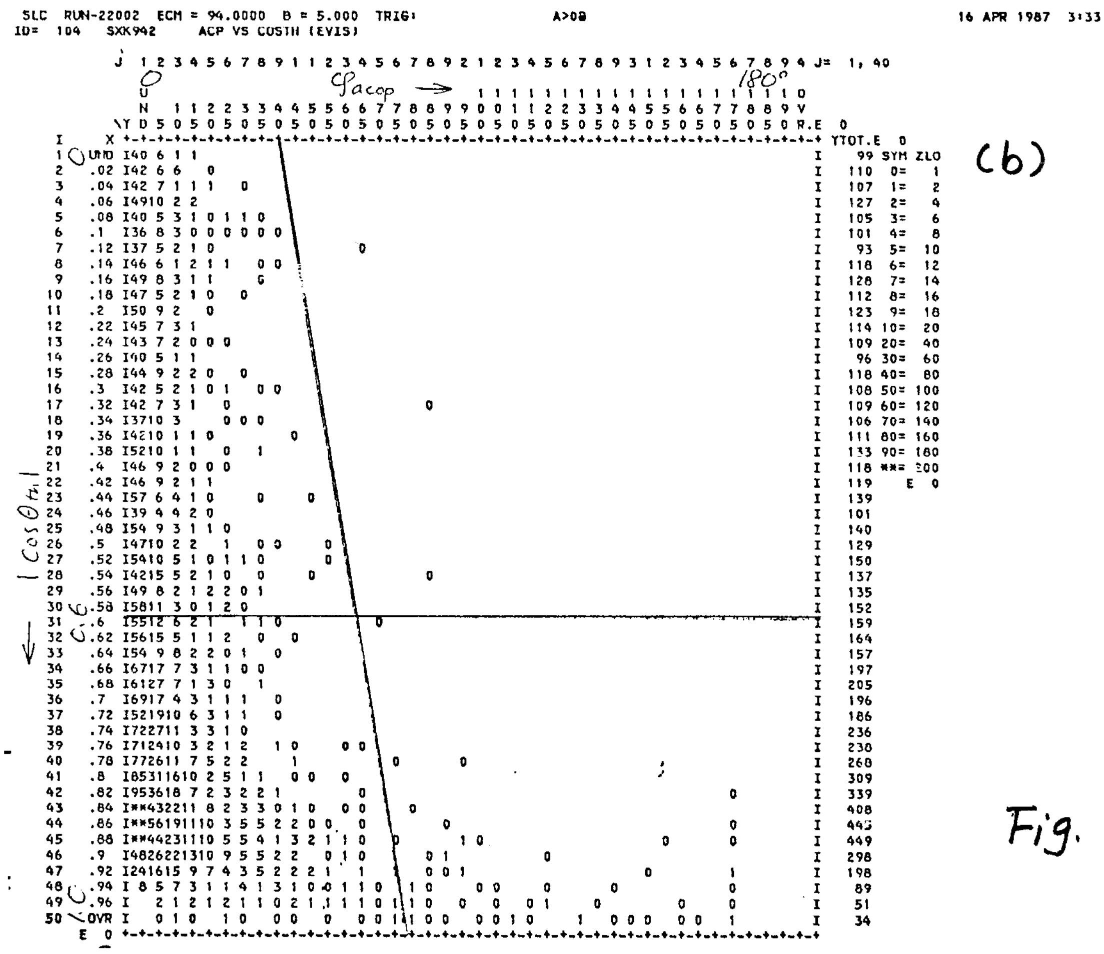

(b)

Fig. 9

297

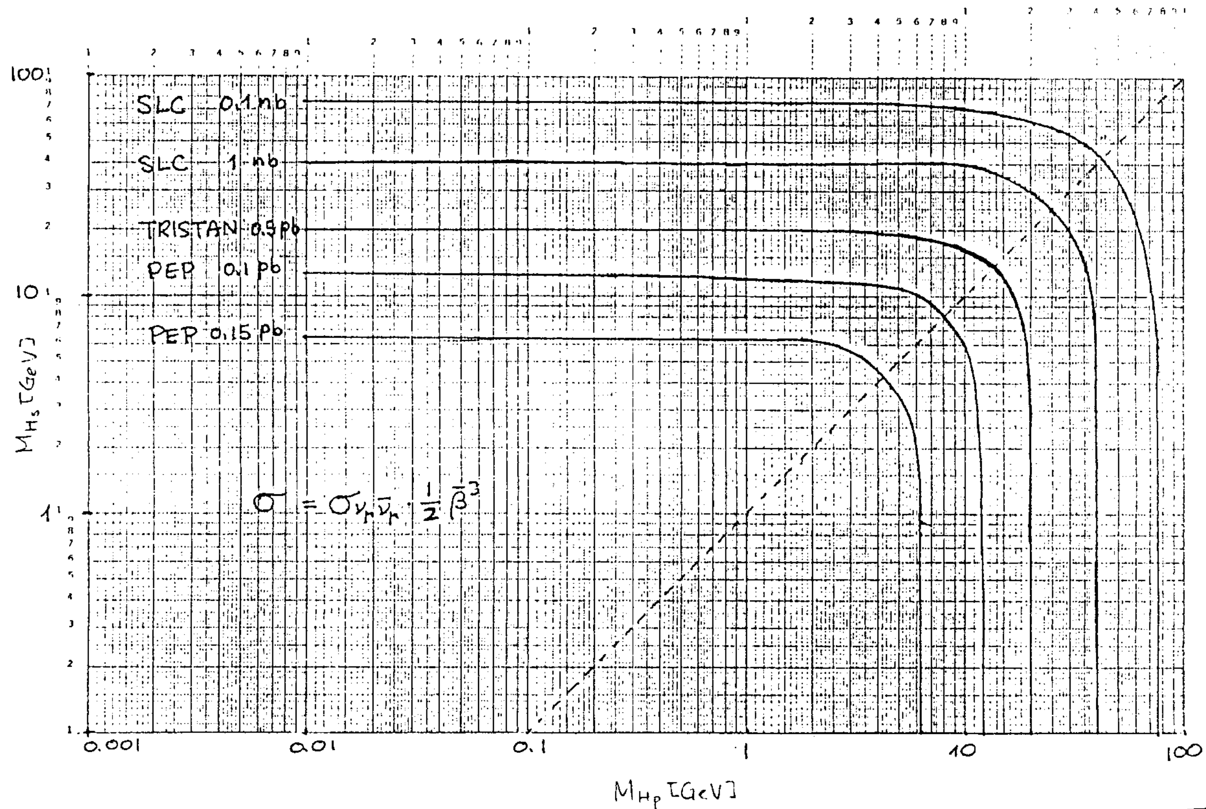

Fig. 10

298

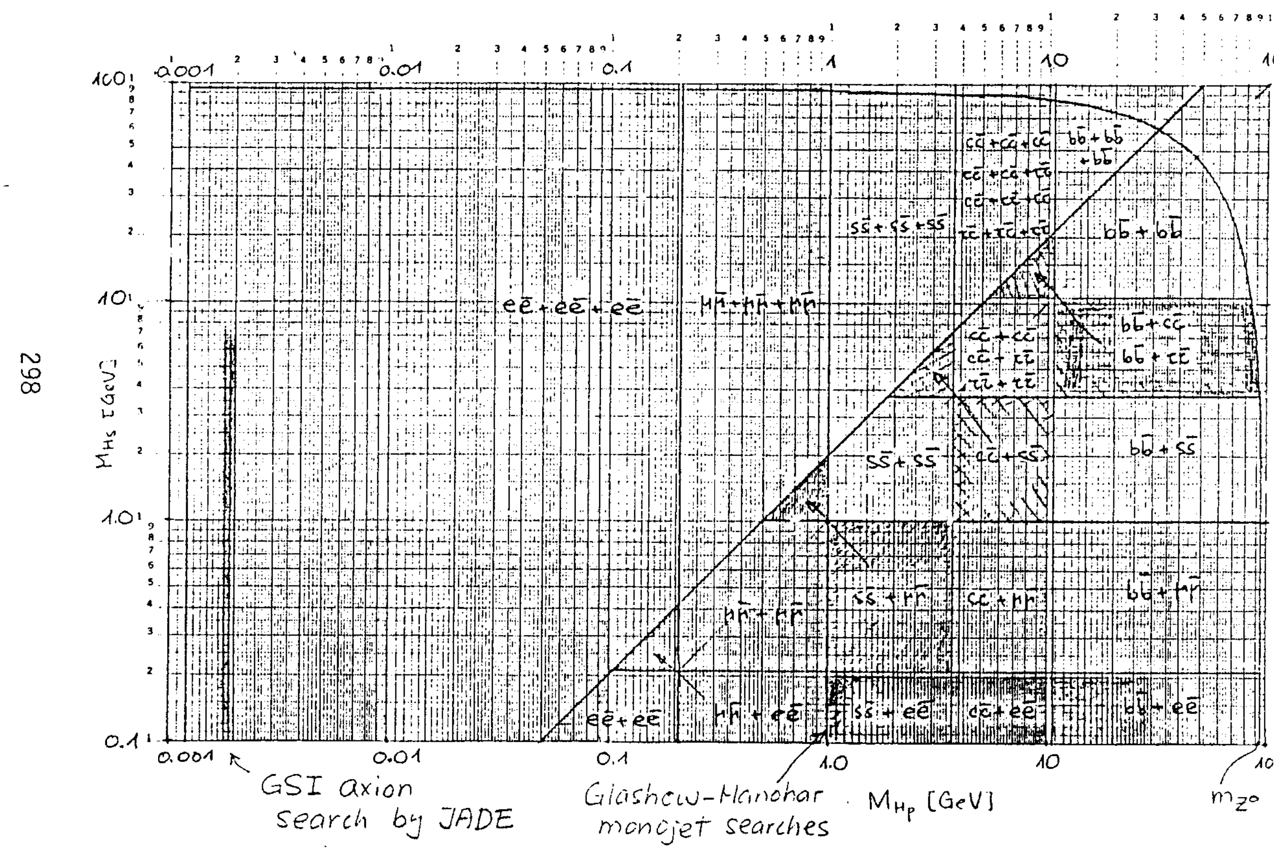

Fig. 11a

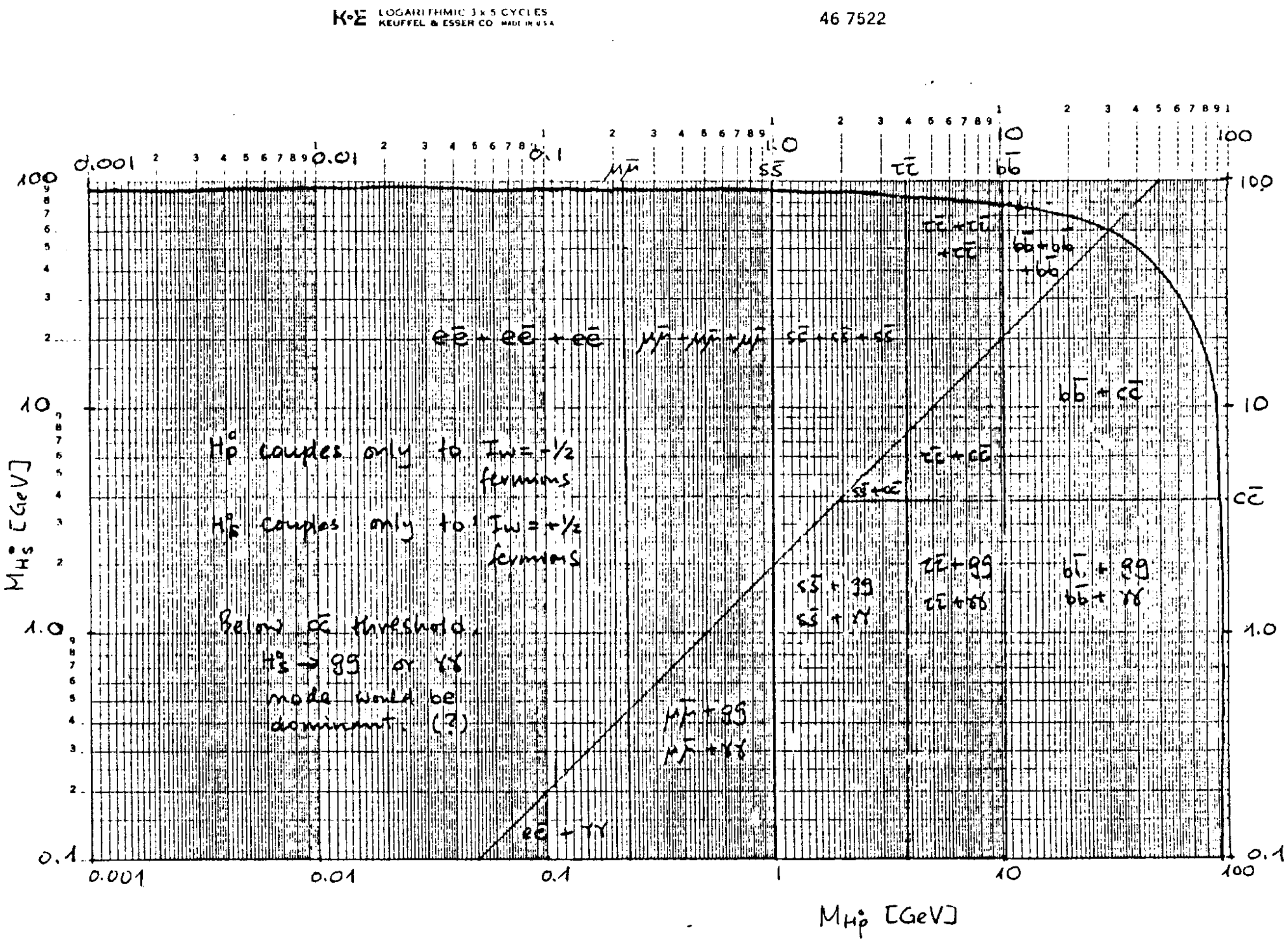
K+E LOGARITHMIC 3 x 5 CYCLES
KEUFFEL & ESSER CO. MADE IN U.S.A.
46 7522
Hp° couples only to Iw = -½ fermions
Hs° couples only to Iw = +½ fermions
Below cc̄ threshold Hs° → gg or γγ mode would be dominant. (?)
MHs° [GeV]
MHp° [GeV]

Fig.11.b

RUN-22000 REC 1 E= 94.00 0 PRONG NO VERTEX (0-0)
TRIGGER 0 00F CCHAR MARK II - SLC/PEP

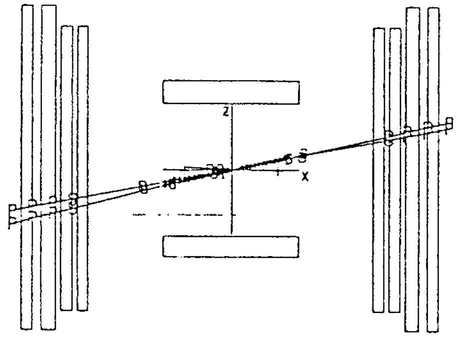

TRACKLIST TABLE

94.000	-22000	1	0
1	15.839	-0.878	61999.000
-1	5.106	0.063	65999.000
1	5.353	-1.266	65 3.267
-1	24.775	-4.539	72 3.052
1	33.236	4.940	72999.000
-1	12.000	2.091	72999.000

$Z^0 \to H_s^0 H_p^0$
$\to H_p^0 H_p^0 H_p^0$
$\to \mu^+\mu^-\mu^+\mu^-\mu^+\mu^-$

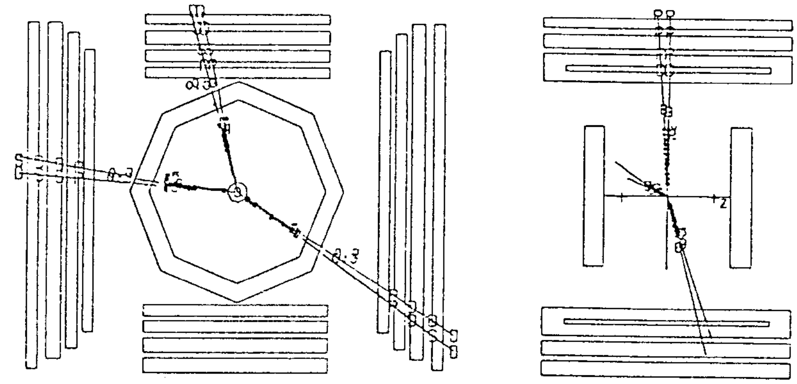

$m_{H_s^0} = 30\,GeV$

$m_{H_p^0} = 0.7\,GeV$

Fig. 12

RUN-22000 REC 3 E= 94.00 0 PRONG NO VERTEX (0-0)
TRIGGER 0 00F CCHAR MARK II - SLC/PEP

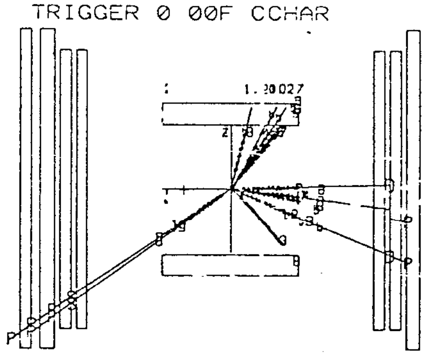

TRACKLIST TABLE

94.000	-22000	3	0
1	1.658	-0.293	72999.000
1	0.890	0.027	61 3.033
-1	0.729	-0.577	64999.000
-1	2.152	3.085	25
1	5.913	5.594	59999.000
1	3.297	3.454	47999.000
-1	2.612	2.354	52999.000
-1	3.849	5.496	35
1	10.009	-5.927	71999.000
-1	25.577	-13.979	61999.000
-1	0.751	-0.090	72999.000
1	4.472	-1.705	69 4.060

$Z^0 \to H_s^0 H_p^0$
$\to \mu^+\mu^- b\bar{b}$

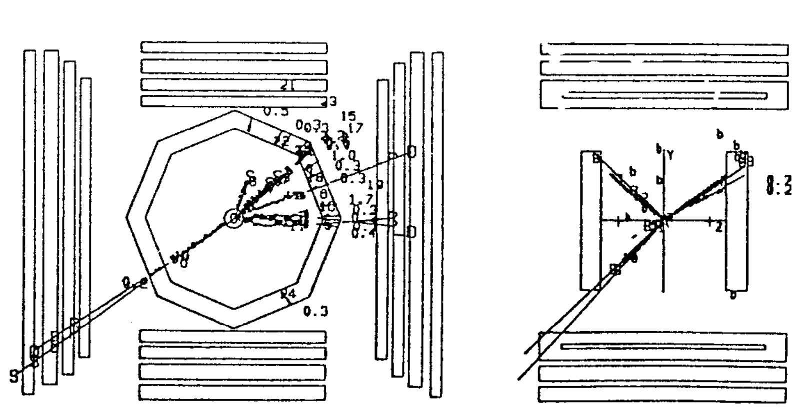

$m_{H_s^0} = 0.7\,GeV$

$m_{H_p^0} = 30\,GeV$

Fig. 13

RUN-22000 REC 1 E= 94.00 0 PRONG NO VERTEX (0-0)
TRIGGER 0 00F CCHAR MARK II - SLC/PEP

TRK	P	ELATOT	ID
1	2.1	0.3	PI-
2	1.0	0.1	PI+
3	1.0	0.1	PI-
4	0.2		PI+
5	0.4		PI-
6	0.9	0.8	E+
7	0.9	0.0	PI-
8	0.7	0.1	PI+
9	0.4	0.1	PI-
10	0.8	0.3	PI+
11	4.7	0.3	PI+
12	2.7	0.1	PI+
13	0.2	0.0	PI+
14	1.0	0.4	PI-
15	4.7	0.0	PI-
16	0.2		PI-
17	0.7	0.2	PI-
18	3.0	1.2	PI+
19	1.0	0.3	PI-
20	0.5	0.3	PI+
21		1.5	G
22		0.1	G
23		0.4	G
24		0.6	G
25		0.2	G
26		0.1	G
27		0.1	G
28		1.6	G
29		2.5	G
30		1.2	G
31		0.3	G
32		0.3	G
33		0.5	G
34		0.2	G

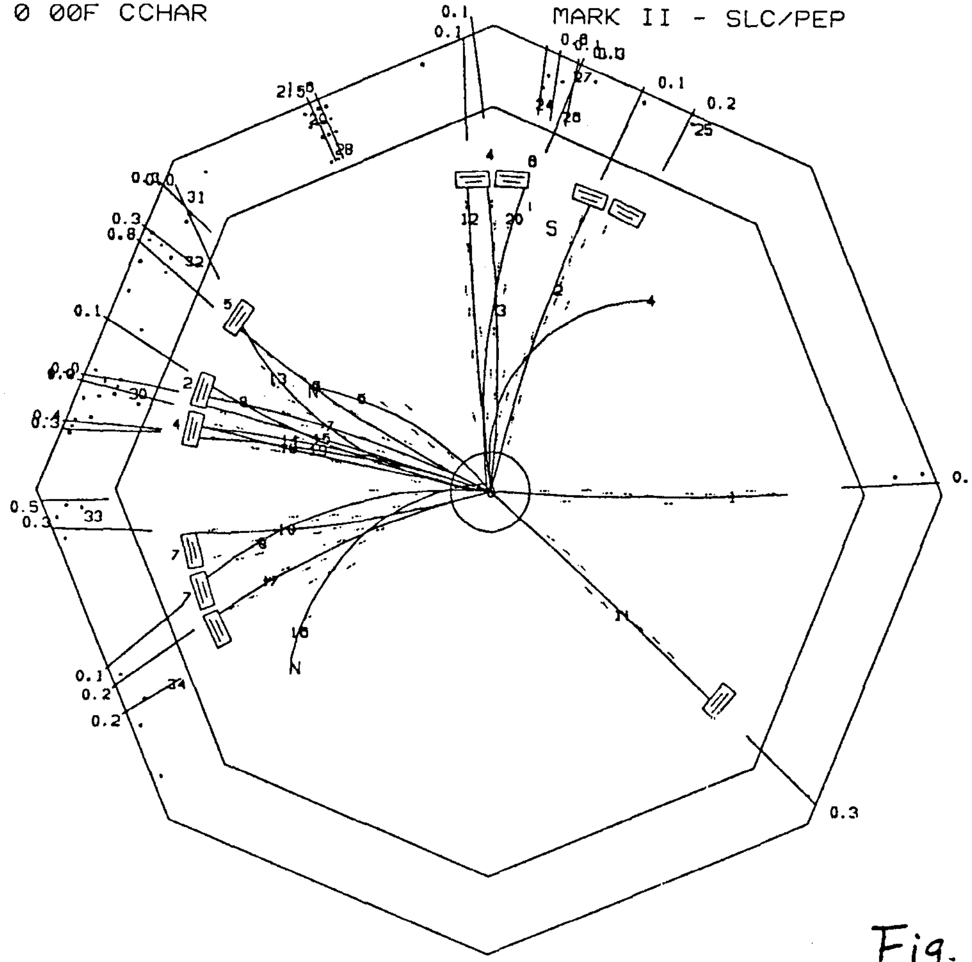

Fig. 14

RUN-22000 REC 1 E= 94.00 0 PRONG NO VERTEX (0-0)
TRIGGER 0 00F CCHAR MARK II - SLC/PEP

TRK	P	ELATOT	ID
1	0.7	0.1	PI-
2	2.7	0.3	PI+
3	2.1	0.3	PI+
4	1.1	0.0	PI-
5	0.9	0.2	PI+
6	3.0	0.2	PI+
7	5.3	0.1	PI+
8	3.7	0.1	PI+
9	0.2	0.2	PI-
10	0.9	0.8	E+
11	1.4	0.1	PI-
12	0.2	0.1	E-
13	8.9	0.3	PI+
14	13.0	0.1	MU-
15	4.8	0.0	PI-
16	5.5	0.0	PI+
17	0.7	0.2	PI-
18	3.4	0.2	PI-
19	0.2		PI-
20		0.2	G
21		1.3	G
22		0.2	G
23		0.3	G
24		1.4	G
25		2.1	G
26		1.0	G
27		0.2	G
28		0.5	G
29		0.1	G
30		0.7	G
31		3.8	G
32		1.3	G
33		0.1	G
34		0.3	G

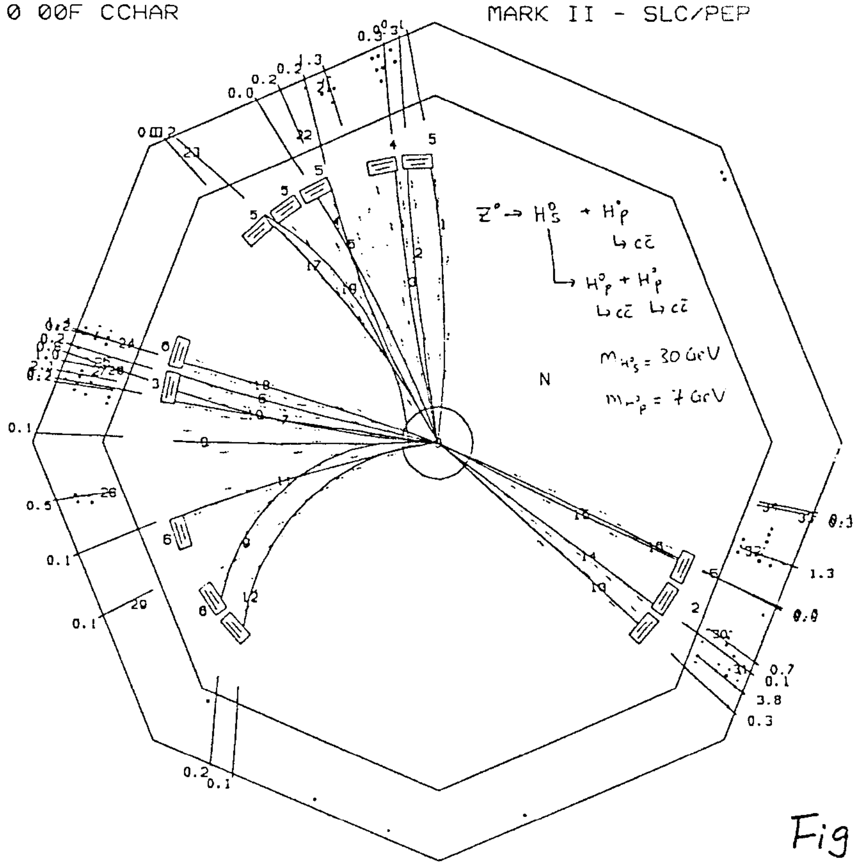

Fig. 15

RUN-22000 REC 2 E= 94.00 0 PRONG NO VERTEX (0-0)
TRIGGER 0 00F CCHAR MARK II - SLC/PEP

TRK	P	ELATOT	ID
1	0.4	0.1	PI+
2	2.4	7.8	E+
3	0.8	0.2	PI-
4	1.2	0.4	PI-
5	0.7	0.3	PI+
6	2.9	5.1	E-
7	0.5	0.0	PI+
8	0.7	0.1	PI-
9	1.2	0.3	PI+
10	7.6	0.3	MU-
11	1.7	0.1	PI+
12	0.2	0.1	E+
13	5.1	0.2	PI+
14	2.3	0.2	PI-
15	1.1	0.0	PI-
16	0.5	0.7	PI-
17	1.8	0.0	PI-
18	1.7	0.4	PI-
19	2.7	0.0	PI+
20	2.9	0.1	PI-
21	0.6	0.1	PI+
22	2.6	0.1	PI-
23		2.6	G
24		6.8	G
25		0.2	G
26		3.9	G
27		2.5	G
28		0.5	G
29		0.2	G
30		0.3	G
31		0.1	G
32		0.3	G
33		0.5	G
34		0.3	G

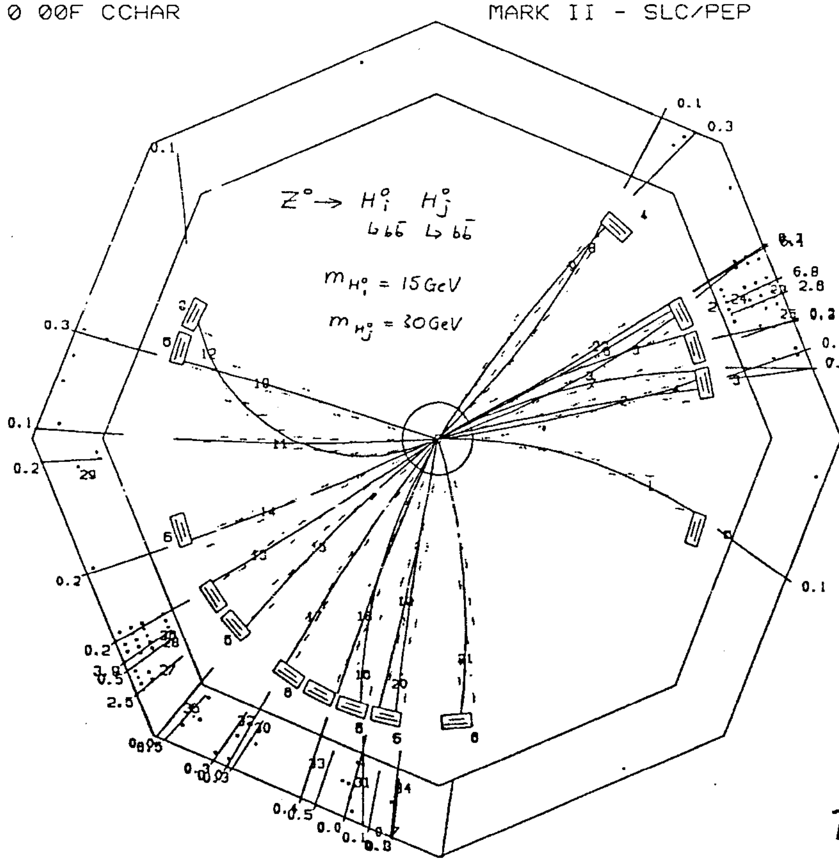

Fig. 16

305

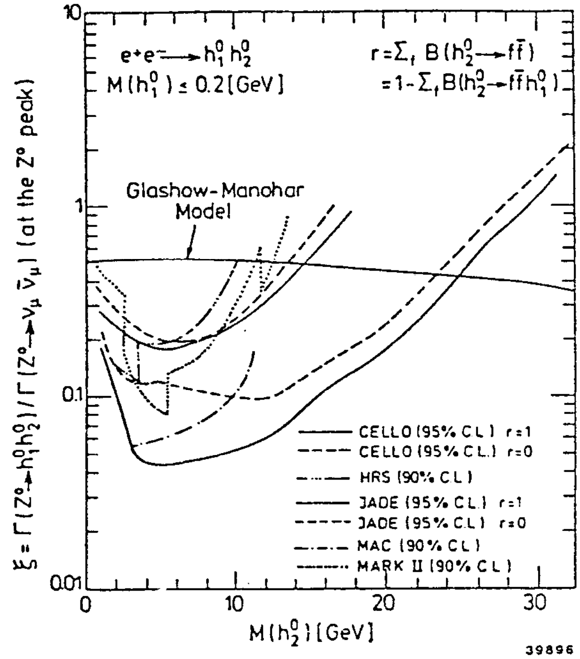

Fig. 17

306

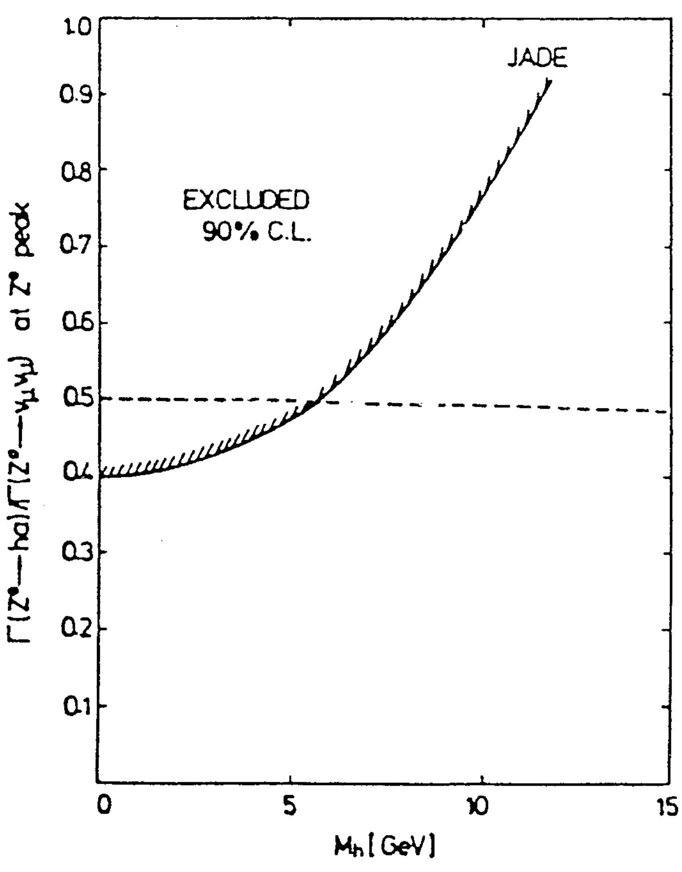

Fig. 18

SLC RUN-20000 ECM = 94.0000 B = 5.060 TRIG: A>0= 16 DEC 1986 17: 6
ID= 52 SXX292 PI VS PJ ISOL H+H-

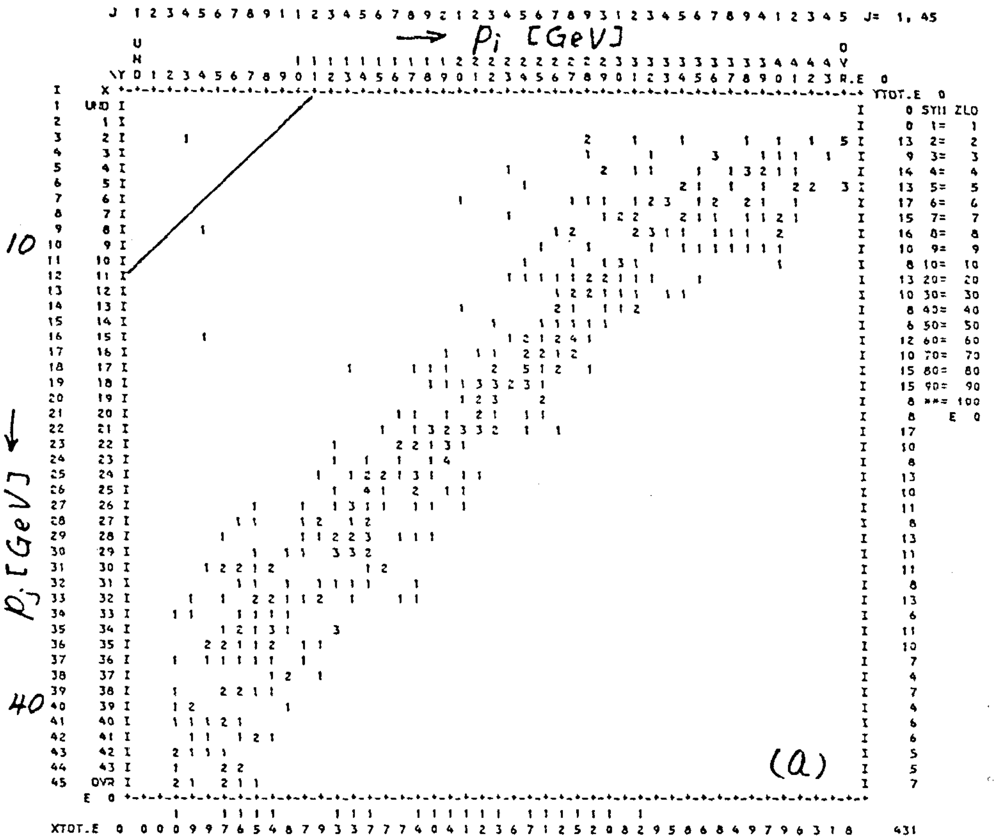

STATS FRCM HCUM, #CALLS= 431. WTS= 431.00
<X>= 20.890 +-0.571 , SD= 11.851 +-0.404 FOR-0.100E+76< X < 0.100E+76 (EXTREME X= 2.01 48.8)

SLC RUN-20000 ECM = 94.0000 B = 5.000 TRIG: A>0a 16 DEC 1986 17: 1
ID= 52 SXX291 PI VS PJ ISOL H+H-

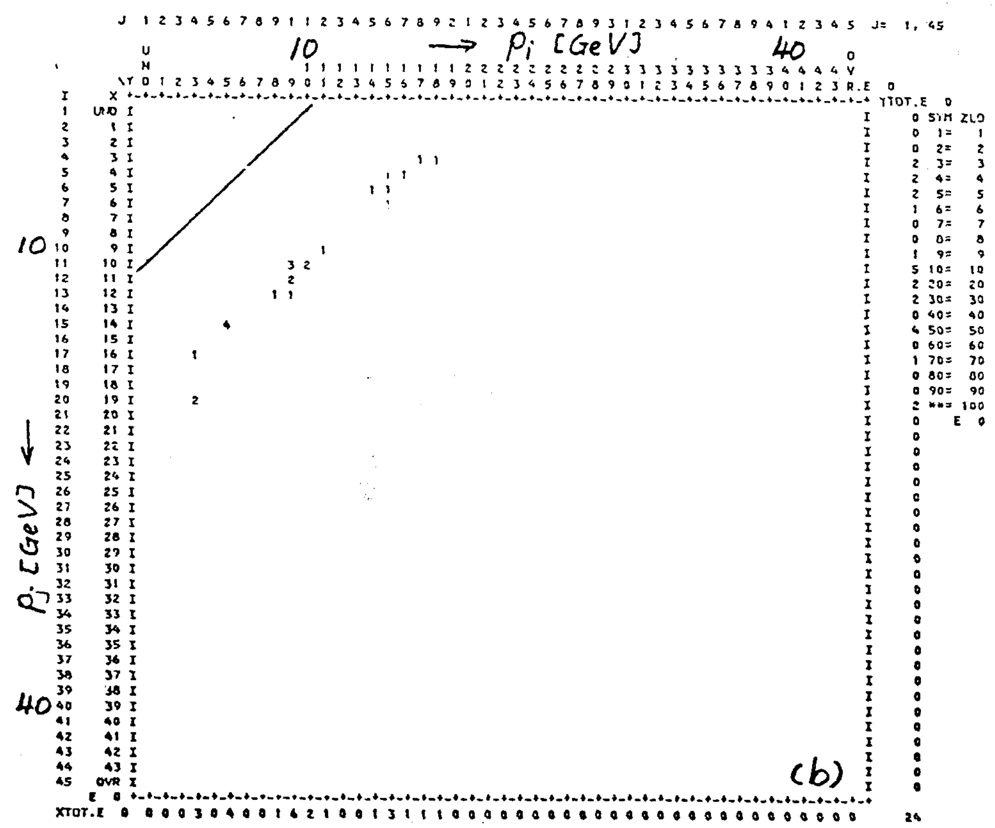

STATS FROM HCUM, #CALLS= 24, WTS= 24.000
<X>= 10.690 +-0.943 , SD= 4.6217 +-0.667 FOR-0.100E+76< X < 0.100E+76 (EXTREME X= 3.24 19.8)
<Y>= 10.213 +-0.935 , SD= 4.5810 +-0.661 FCR-0.100E+76< Y < 0.100E+76 (EXTREME Y= 3.20 18.7)

Fig. 19

SLC RUN-20000 ECM = 94.0000 B = 5.000 TRIG: A>0B 16 DEC 1986 21
ID= 52 SXK290 PI VS PJ ISOL H+H-

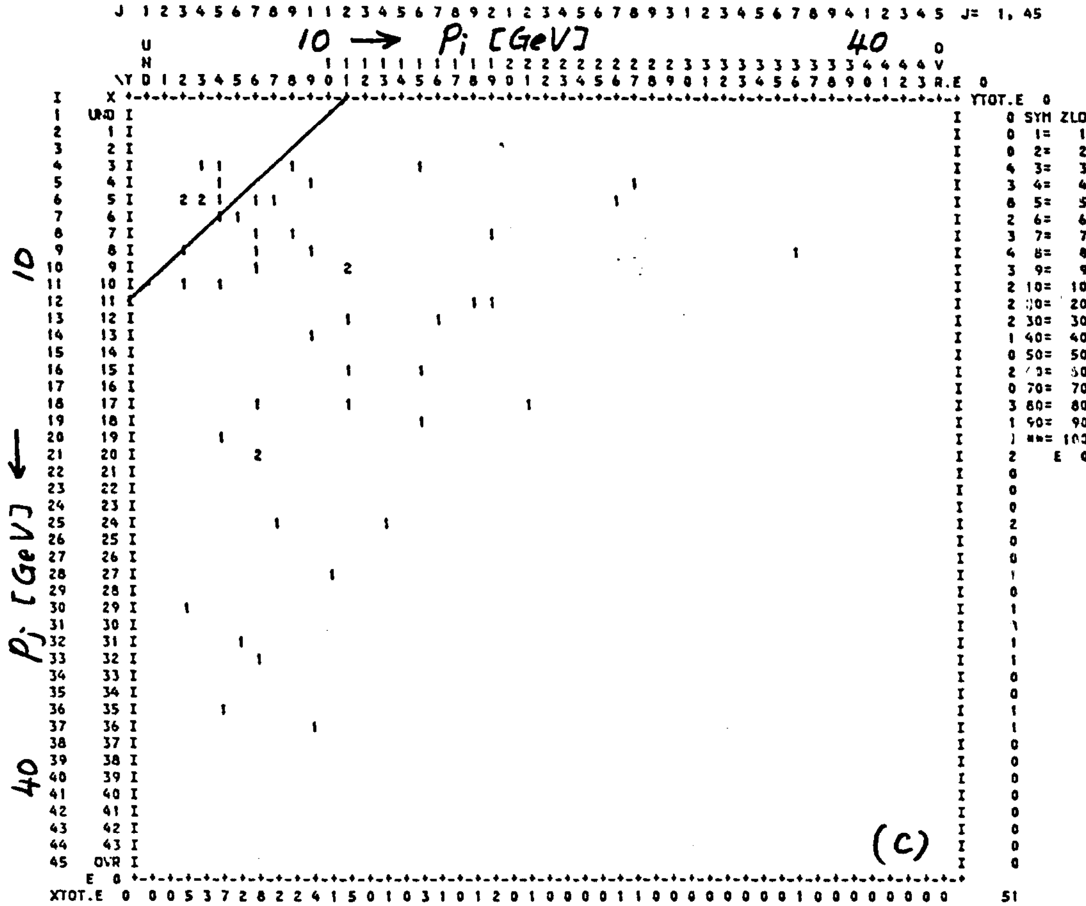

STATS FROM HCUM, #CALLS= 51, WTS= 51.000
<X>= 12.874 +- 1.26 , SD= 9.0043 +-0.892 FOR-0.100E+76< X < 0.100E+76 (EXTREME X= 3.09 36.7)
<Y>= 9.8157 +-0.999 , SD= 7.1310 +-0.706 FOR-0.100E+76< Y < 0.100E+76 (EXTREME Y= 2.39 36.3)

Fig. 19

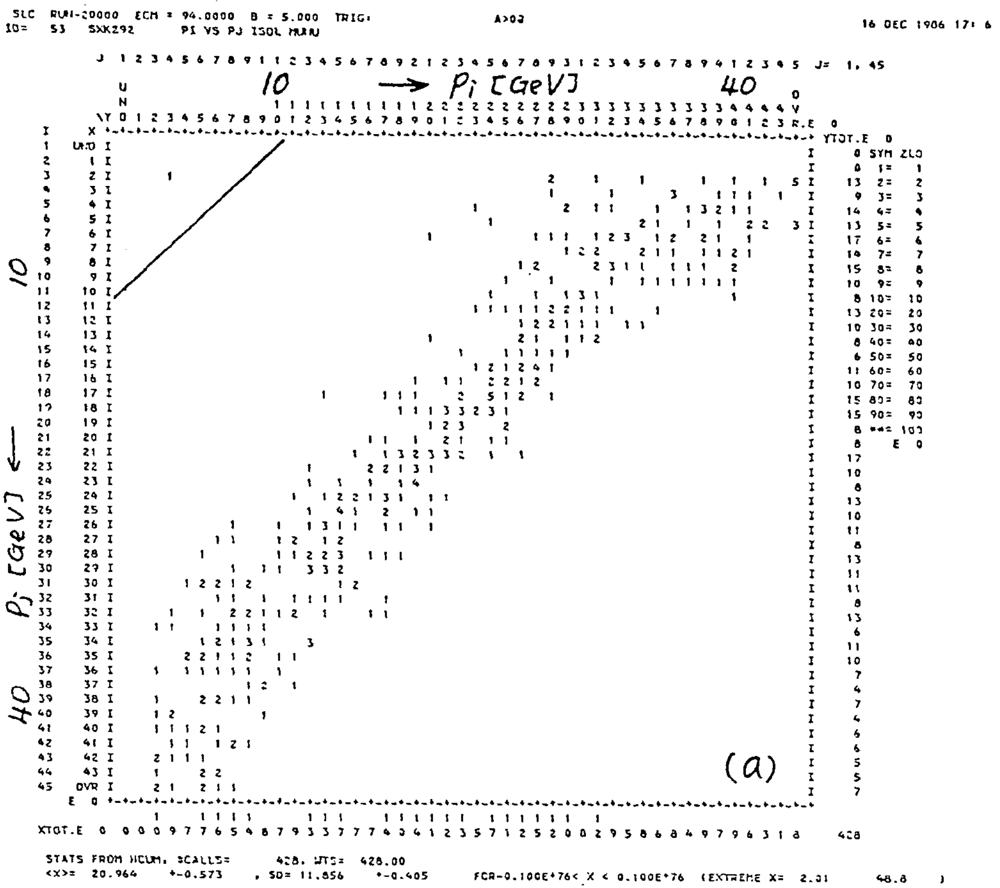

SLC RUN-20000 ECM = 94.0000 B = 5.000 TRIG: A>02 16 DEC 1986 17: 6
ID= 53 SXX292 PI VS PJ ISOL MUMU
10 → p_i [GeV] 40
p_j [GeV] ←
10
40
(a)
STATS FROM HCUM, SCALLS= 428. WTS= 428.00
<X>= 20.964 +-0.573 , SD= 11.856 +-0.405

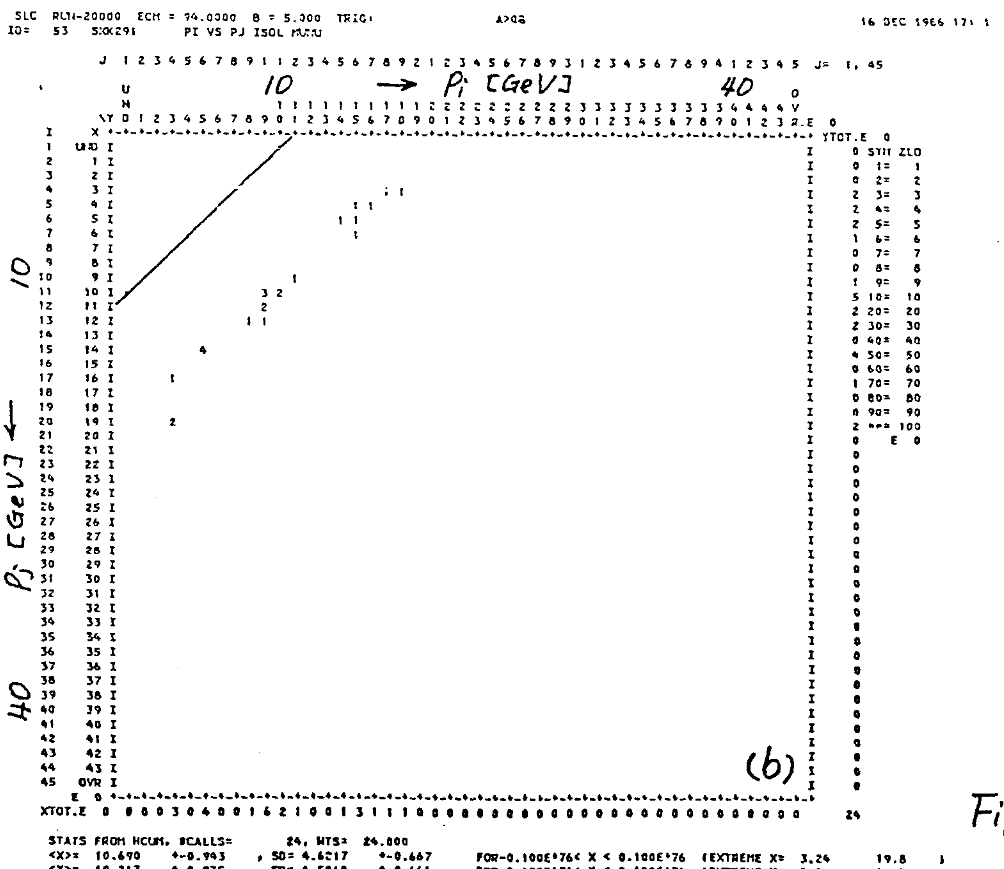

SLC RUN-20000 ECM = 94.0000 B = 5.000 TRIG: A>02 16 DEC 1986 17: 1
ID= 53 SXX291 PI VS PJ ISOL MUMU
10 → p_i [GeV] 40
p_j [GeV] ←
10
40
(b)
STATS FROM HCUM, SCALLS= 24. WTS= 24.000
<X>= 10.690 +-0.943 , SD= 4.4217 +-0.667
<Y>= 10.213 +-0.935 , SD= 4.5810 +-0.661

Fig. 20

RUN 9391 REC 444 E= 29.00 10 PRONG HADRON (5-0)
TRIGGER 04F V MARK II - PEP

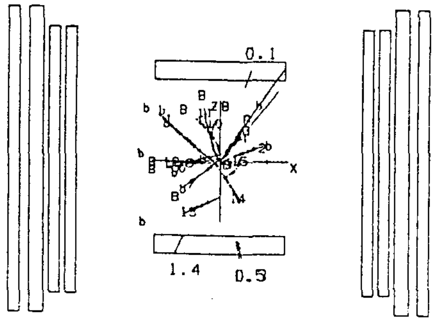

TRACKLIST TABLE

29.000	9391	444	5	
0	-0.006	-0.003	-0.011	
-1	0.597	0.459	17	5.919
-1	0.190	0.042	8	5.274
-1	6.211	3.100	20	5.075
1	2.284	0.902	17	4.420
1	1.471	-0.209	11	5.107
-1	1.324	-0.189	12	1.335
1	1.168	-0.488	12	4.875
1	0.122	0.073	9	4.418
-1	1.050	-0.034	14	5.635
-1	0.141	0.088	11	7.355
-1	0.379	0.295	9	9.582
1	1.130	0.017	8	5.022
1	26.995	-6.867	8	4.892
1	0.513	-0.352	10	10.552
1	0.141	0.044		9999.000

312

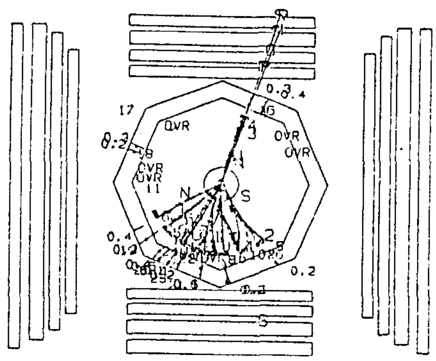

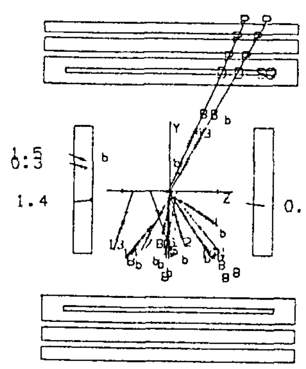

RUN 11419 REC14666 E= 29.02 5 PRONG HADRON (5-0)
TRIGGER 85A V MARK II - PEP

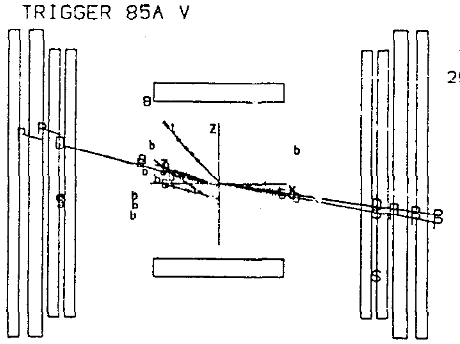

TRACKLIST TABLE

29.020	11419	14666	5	
0	-0.004	-0.001	-0.006	
1	0.244	0.234		9999.000
-1	5.775	1.703		15999.000
-1	2.327	0.587	13	4.599
-1	2.869	-0.365	21	5.266
1	10.020	-1.674	23	5.056
-1	19.036	4.390		7999.000
1	0.313	0.201		7999.000

313

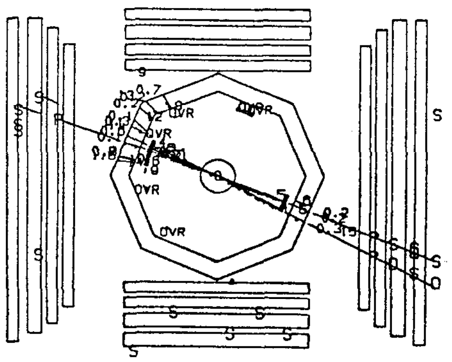

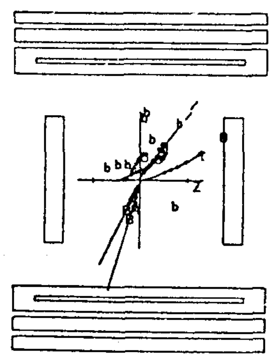

Fig. 21

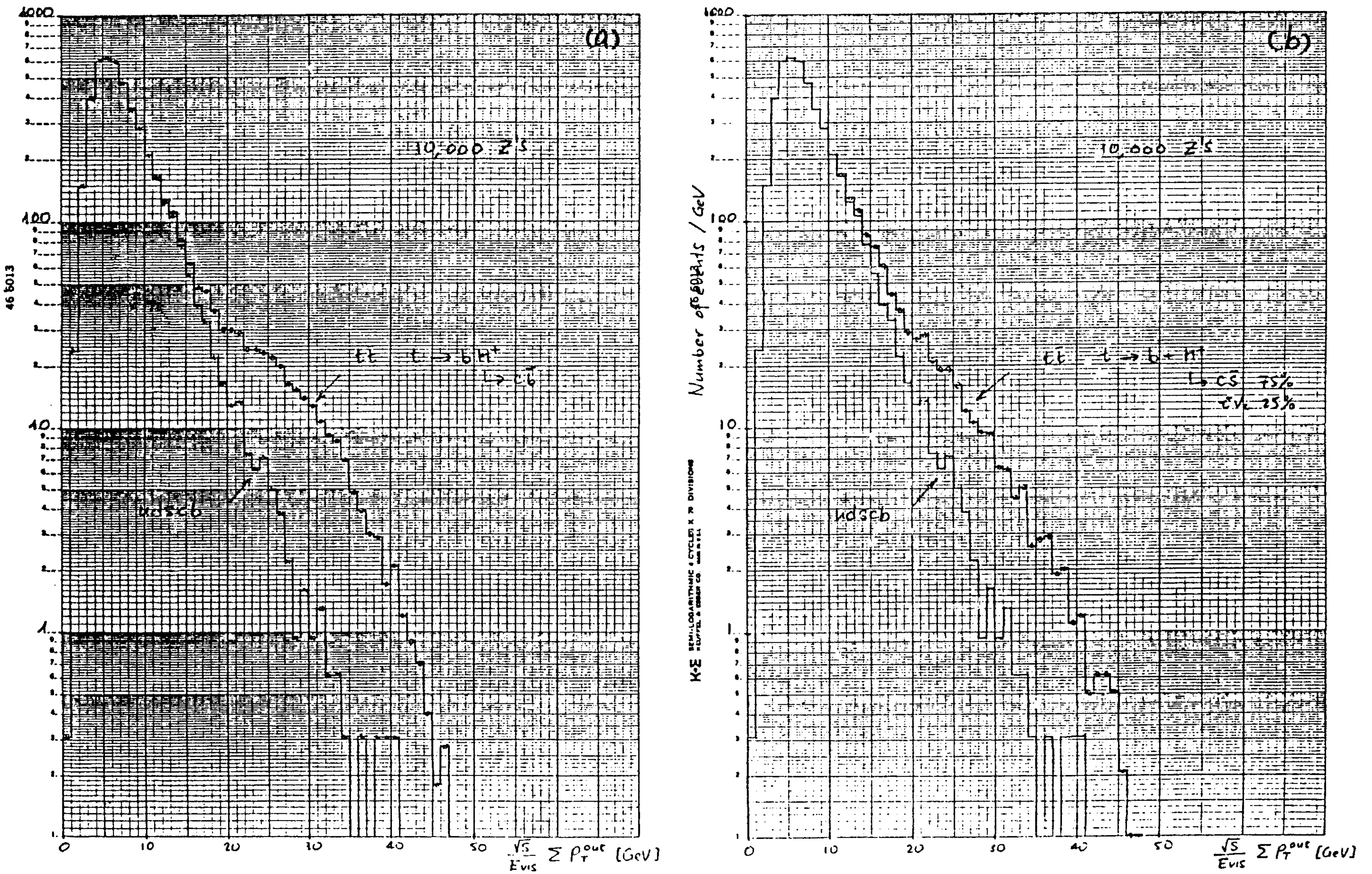

314 315

Fig. 22

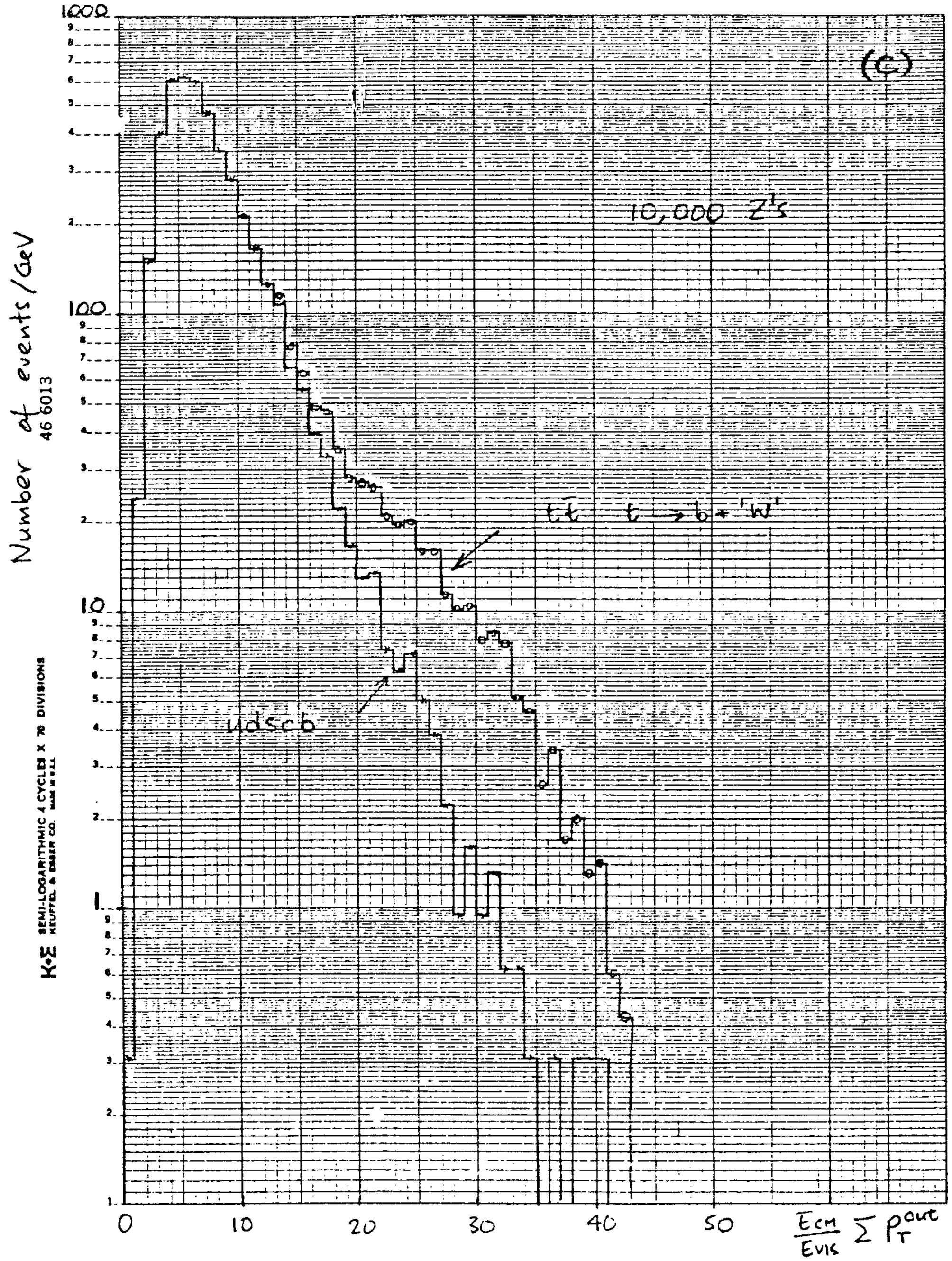
(c)
10,000 Z's
$t\bar{t}$ $t \to b + 'W'$
udscb
Number of events / GeV
$\frac{E_{CM}}{E_{VIS}} \sum P_T^{out}$
1000
100
10
1
0
10
20
30
40
50
K+E SEMI-LOGARITHMIC 4 CYCLES X 70 DIVISIONS
KEUFFEL & ESSER CO.
46 6013

Fig. 22

Mark II/SLC-Physics Working Group Note # 3–21

AUTHOR: Tim Barklow

DATE: July 25, 1987

TITLE: Searches for Supersymmetric Particles

Table of Contents

1. THE MINIMAL SUPERSYMMETRIC EXTENSION TO THE STANDARD MODEL

If supersymmetric (SUSY) particles exist with masses on the order of 1 TeV or less, and if nature's gauge group structure in this energy range is limited to the standard model's $SU(3) \times SU(2) \times U(1)$, then there is a minimal set of supersymmetric particles that is common to all supersymmetric extensions to the standard model[1]. It is the purpose of this chapter to introduce the general minimal supersymmetric extension to the standard model. As part of this introduction the minimal set of fundamental parameters will be enumerated and the consequences for SLC physics of certain choices for these parameters will be discussed.

1.1 THE MINIMAL SET OF PARTICLES

We list the the additional particles required by any supersymmetric extension to the standard model:

1. Two additional neutral Higgs particles and a charged Higgs particle. These arise from the extra Higgs doublet that is needed to ensure that the Higgs superpotential is supersymmetric[2].
2. One scalar neutrino for each of the three ordinary neutrinos and a left and right-handed sfermion for each massive fermion.
3. Four neutralinos $\tilde{\chi}_1^0$, $\tilde{\chi}_2^0$, $\tilde{\chi}_3^0$, and $\tilde{\chi}_4^0$. Each neutralino is a mixture of the SUSY partners of the photon, the Z^0 and the neutral components of the Higgs doublets. The neutralinos are Majorana fermions.
4. Two charginos $\tilde{\chi}_1^+$ and $\tilde{\chi}_2^+$. Each chargino is a mixture of the fermion partners of the $W^\pm$ and the charged components of the Higgs doublets.
5. The gluino, which is the fermion partner of the gluon.

1.2 THE MINIMAL SET OF UNKNOWN PARAMETERS

Neglecting Cabibbo-like mixing in the sfermion sectors there are, at a minimum, 36 unknown parameters in any SUSY extension to the standard model. We list them:

1. 3 neutrino masses $M_{\tilde{\nu}_e}$, $M_{\tilde{\nu}_\mu}$, and $M_{\tilde{\nu}_\tau}$
2. In general the sfermion mass eigenstates are of the form

$$\tilde{f}_1 = \tilde{f}_L \cos\theta_f + \tilde{f}_R \sin\theta_f$$
$$\tilde{f}_2 = -\tilde{f}_L \sin\theta_f + \tilde{f}_R \cos\theta_f$$

so that there are 18 sfermion masses $M_{\tilde{f}_i}$ and 9 left-right mixing angles θ_f

for

$$f = e, \mu, \tau, u, d. s, c, b, t \qquad \& \qquad j = 1, 2 \quad .$$

3. 3 Majorana masses M', M, and M_g for the Bino (partner of the U(1) gauge field), W^3ino (partner of the neutral SU(2) gauge field) and gluino respectively.
4. A superpotential parameter μ, the ratio of Higgs vacuum expectation values $v_1/v_2 = \tan\beta$, and the mass of the charged Higgs particle $M_{H^\pm}$.

The parameters M', M, μ, $\tan\beta$ together with the known standard model parameters determine the masses and mixing of the neutralinos and charginos. For example the neutralinos are given by

$$\begin{pmatrix} \tilde{\chi}_1^0 \\ \tilde{\chi}_2^0 \\ \tilde{\chi}_3^0 \\ \tilde{\chi}_4^0 \end{pmatrix} = N' \begin{pmatrix} \tilde{\gamma} \\ \tilde{Z}^0 \\ \tilde{H}^0{}_1 \\ \tilde{H}^0{}_2 \end{pmatrix}$$

where the matrix N' is obtained by diagonalizing the neutralino mass matrix

$$Y = \begin{pmatrix} M' & 0 & -M_Z \sin\theta_W \cos\beta & M_Z \sin\theta_W \sin\beta \\ 0 & M & M_Z \cos\theta_W \cos\beta & -M_Z \cos\theta_W \sin\beta \\ -M_Z \sin\theta_W \cos\beta & M_Z \cos\theta_W \cos\beta & 0 & -\mu \\ M_Z \sin\theta_W \sin\beta & -M_Z \cos\theta_W \sin\beta & -\mu & 0 \end{pmatrix}$$

In a similar way, the charginos are obtained by diagonalizing

$$\begin{pmatrix} M & M_W \sqrt{2} \sin\beta \\ M_W \sqrt{2} \cos\beta & \mu \end{pmatrix}$$

Furthermore, the masses and couplings of the neutral Higgs bosons $H^0{}_1$, $H^0{}_2$, and $H^0{}_3$ are determined by the aforementioned parameters plus $M_{H^\pm}$.

1.3 IMPLICATIONS OF CHOICES FOR THE UNKNOWN PARAMETERS

It is possible to reduce the number of unknown parameters from 36 to 8 by making some simplifying assumptions that are either theoretically motivated or of little consequence for our work. Specifically we assume the following:

1. Define $M_{\tilde{\nu}} \equiv M_{\tilde{\nu}_e} = M_{\tilde{\nu}_\mu} = M_{\tilde{\nu}_\tau}$
2. Set $\theta_f = 0$ and $M_{\tilde{f}_L} = M_{\tilde{f}_R}$
3. Define $M_{\tilde{l}^-} \equiv M_{\tilde{e}} = M_{\tilde{\mu}} = M_{\tilde{\tau}}$
4. Define $M_{\tilde{q}} \equiv M_{\tilde{u}} = M_{\tilde{d}} = M_{\tilde{s}} = M_{\tilde{c}} = M_{\tilde{b}}$
5. Relate the Bino and gluino majorana masses M' and M_g to the W^3ino majorana mass M through the grand unified theory relations

$$M' = \frac{5}{3} M \left(\frac{g_{U(1)}}{g_{SU(2)}} \right)^2$$

$$M_g = M \left(\frac{g_{SU(3)}}{g_{SU(2)}} \right)^2$$

To summarize, our reduced set of fundamental parameters consists of:

$$M_{\tilde{\nu}},\ M_{\tilde{l}^-},\ M_{\tilde{q}},\ M_{\tilde{t}},\ M,\ \mu,\ \tan\beta,\ \&\ M_{H^\pm}$$

We now pose the question, *What is the likelihood that SUSY particles will be kinematically accessible at SLC when the unknown SUSY parameters are chosen at random within a reasonable range?* . We have chosen values for the parameters $M, \mu, \tan\beta, M_{H^\pm}$ at random within the range

$$\begin{aligned} 0 < \ & M && < 500GeV \\ 0 < \ & \mu && < 500GeV \\ -1 < \ & \tan\beta && < 10 \\ M_W < \ & M_{H^\pm} && < M_W + 500\text{GeV} \end{aligned}$$

After making 2000 such choices we observe the following.

650 out of 2000 or 32.5% of the random choices give $\tilde{\chi}_1^0$ masses less than half the Z^0 mass. $\tilde{\chi}_1^0$ is the lightest neutralino and will either be stable or decay to invisible particles $(\nu + \tilde{\nu})$ so that the only way to detect such a particle is through neutrino counting techniques. The second lightest neutralino $\tilde{\chi}_2^0$ has a mass less than half the Z^0 mass for 15.0% of the random choices. Decays of the $\tilde{\chi}_2^0$ will in general be visible and distinctive.

The mass of the $\tilde{\chi}^0_3$ is always greater than half the Z^0 mass and the $\tilde{\chi}^0_4$ is always more massive than the $Z0$.

While the neutral Higgs scalar labelled $H^0{}_1$ is always more massive than the Z^0 , the neutral Higgs scalar $H^0{}_2$ is always less massive. The $H^0{}_2$ is the only particle in our minimal set of SUSY particles with an upper bound on its mass. Unfortunately, the cross-section for singly produced Higgs scalars is prohibitively small for scalar masses greater than about 30 GeV so that this upper bound is not useful for SLC or LEP I .

The gluino has a mass less than half the Z^0 mass 1.8% of the time. The lighter chargino $\tilde{\chi}^+_1$ has a mass less than half the Z^0 mass for 20% of the random choices. The higher mass $\tilde{\chi}^+_2$ is always more massive than the $W^{\pm}$.

In summary the lightest neutralino $\tilde{\chi}^0_1$ has the greatest chance of being kinematically accessible at SLC. However, it can only be seen through measurements of the invisible Z^0 width, making a SUSY interpretation difficult. The next most likely SUSY particle to be kinematically accessible is the chargino $\tilde{\chi}^+_1$ followed by the second lightest neutralino $\tilde{\chi}^0_2$.

2. SUPERSYMMETRY PHENOMENOLOGY ON THE Z^0

2.1 SFERMIONS

The canonical decay of a sfermion is to the partner fermion and the lightest neutralino:

$$\tilde{f} \rightarrow f + \tilde{\chi}^0_1 \tag{2.1}$$

This decay mode should dominate but there can be exceptions. If $M_{\tilde{g}} < M_{\tilde{q}}$ then the squark can decay via

$$\tilde{q} \rightarrow q + \tilde{g}$$

Or, if $M_{\tilde{\chi}^+_1} < M_{\tilde{f}}$ then sfermions can decay via

$$\tilde{f} \rightarrow f' + \tilde{\chi}^+_1$$

If the $\tilde{Z}^0$ component of the $\tilde{\chi}^0_1$ vanishes, then the sneutrino cannot undergo the canonical decay (2.1) and must undergo three or four-body tree-level or two-body loop decays. The same comment could apply to selectrons if the $\tilde{\chi}^0_1$ were a pure Higgsino. As an example you could have

$$\tilde{e}^-{}_L \rightarrow \tau^- + \bar{\nu}_\tau + \tilde{\nu}_e$$

If three-body decays are not allowed then four-body decays could be important. As examples, you might have

$$\tilde{e}^-{}_L \rightarrow e^- + \tilde{\chi}^0_1 + \mu^- + \mu^+$$
$$\tilde{\nu}_e \rightarrow \nu_e + \tilde{\chi}^0_1 + s + \bar{s}$$

Tree-level four-body decays will in general compete with loop two-body decays.

2.2 CHARGINOS AND NEUTRALINOS

Chargino and neutralino production can take place on the Z^0 as follows:

$$
\begin{aligned}
e^+e^- \rightarrow Z^0 \rightarrow & \tilde{\chi}_1^+\tilde{\chi}_1^- \\
& \tilde{\chi}_1^0\tilde{\chi}_1^0 \\
& \tilde{\chi}_1^0\tilde{\chi}_2^0 \\
& \tilde{\chi}_2^0\tilde{\chi}_2^0
\end{aligned}
$$

Chargino Production

Chargino production can be huge. The Z^0 couples to

$$T_3 - Q\sin^2\theta_W$$

where T_3 is the 3rd component of weak isospin of the particle in question and Q is its charge. The $W^\pm$ has $T_3 = \pm 1$ so that the $\tilde{W}^\pm$ has $T_3 = \pm 1$.

$$\Gamma\left(Z^0 \rightarrow \tilde{W}^+ + \tilde{W}^-\right)$$

can be as large as .8GeV .

If the chargino is a pure Higgsino ($\tilde{\chi}_1^+ = \tilde{H}^+$) it will have an enhanced Γ compared to a charged heavy lepton L^- even though

$$\Gamma\left(Z^0 \rightarrow \tilde{H}^+\tilde{H}^-\right) = \Gamma\left(Z^0 \rightarrow L^+L^-\right)$$

in the limit

$$M_{\tilde{H}^+}, M_{L^-} \rightarrow 0 \qquad .$$

Note that

$$\Gamma\left(Z^0 \rightarrow f\bar{f}\right) \propto \beta g_v$$

for $\beta \ll 1$ where g_v is the vector coupling constant for the fermion f . We have in the limit $\sin^2\theta_W = 0.25$

$$
\begin{aligned}
g_{L\tilde{H}^+} &= -1/4 & \qquad g_{LL^-} &= -1/4 \\
g_{R\tilde{H}^+} &= -1/4 & \qquad g_{RL^-} &= +1/4
\end{aligned}
$$

where g_L and g_R are the left and right-handed couplings respectively. From

$$
\begin{aligned}
g_v &= 2(g_L + g_R) \\
g_a &= 2(g_L - g_R)
\end{aligned}
$$

we have

$$
\begin{aligned}
g_{v\tilde{H}^+} &= -1 & \qquad g_{vL^-} &= 0 \\
g_{a\tilde{H}^+} &= 0 & \qquad g_{aL^-} &= -1
\end{aligned}
$$

As an example, if

$$M_{\tilde{H}^+} = M_{L^-} = 40\text{GeV}$$

then

$$
\begin{aligned}
\Gamma\left(Z^0 \rightarrow L^-L^+\right) &= .01\text{GeV} \\
\Gamma\left(Z^0 \rightarrow \tilde{H}^+\tilde{H}^-\right) &= .10\text{GeV}
\end{aligned}
$$

Chargino Decays

The $\tilde{\chi}_1^+$ will decay by one or more of the following decay modes:

$$
\begin{aligned}
\tilde{\chi}_1^+ \rightarrow & \ \tilde{\chi}_1^0 + W^{+*} \\
& \ \tilde{\nu}_l + l^+ \\
& \ \bar{d} + \tilde{u}^* \\
& \ l^+ + \tilde{\nu}_l^* \\
& \ \nu_l + \tilde{l^+}^*
\end{aligned}
$$

Most of these decays can be classified as follows:

1. lepton + missing energy
2. hadrons + missing energy

The one exception is when the $\tilde{u}^*$ couples to a quark and a gluino; in such a case the missing energy can be small and difficult to utilize.

Neutralino Decays

It was mentioned previously that the lightest neutralino, $\tilde{\chi}_1^0$, should be stable or decay invisibly to

$$\tilde{\chi}_1^0 \rightarrow \bar{\nu} + \tilde{\nu}_l$$

The second lightest neutralino $\tilde{\chi}_2^0$ can decay by one or more of the following decay modes:

$$
\begin{aligned}
\tilde{\chi}_2^0 \rightarrow & \ \gamma + \tilde{\chi}_1^0 \\
& \ H^0 + \tilde{\chi}_1^0 \\
& \ \tilde{\chi}_1^0 + Z^{0*} \\
& \ l^- + \tilde{l^+}^* \\
& \ \bar{u} + \tilde{u}^* \\
& \ \bar{\nu}_l + \tilde{\nu}_l^*
\end{aligned}
$$

The event topologies for neutralino pair-production or associated production can be classified as follows:

1. no visible particles
2. 1 or 2 photons + missing energy
3. 2 leptons + missing energy
4. 2 leptons + hadrons + missing energy
5. 4 leptons + missing energy
6. hadrons + missing energy

Associated production of neutralinos $\tilde{\chi}_1^0$ and $\tilde{\chi}_2^0$ will produce beautiful monojets. Pair-production of the $\tilde{\chi}_2^0$ can also produce monojets if decay through the virtual Z^0 is important.

3. DETECTING SUPERSYMMETRIC EVENTS WITH THE MARK II

Our techniques for detecting SUSY events with the MarkII were described in the Granlibakken MarkII workshop report[3] In this chapter we briefly review that work; the reader should consult Ref. 3 for a more detailed discussion.

3.1 GENERAL CHARACTERISTICS OF SUSY EVENTS

The generic SUSY event has the following characteristics:

1. A largish missing energy
2. The missing four-vector moves slowly ($\beta_{\text{miss}} \ll 1$) compared to an event where 1 hard particle dominates the missing four-vector (e.g. an hadronic event with a hard $K^0{}_L$ has $\beta_{\text{miss}} \approx 1$).
3. The visible system does not balance P_T with respect to the beam axis: $\beta_{T\text{vis}} \gg 0$
4. Visible decay products will not be back-to-back, so the event acollinearity will be large.
5. If a lepton is a primary decay product then it will be hard and will be isolated from jets and other leptons.

3.2 SUSY EVENTS WITH ISOLATED LEPTONS

The isolated lepton technique is very powerful because the conventional physics background to isolated leptons is exceedingly small on the Z^0 .

As described in the Granlibakken report we determine whether or not a lepton is isolated based on a variable called ρ. The isolated lepton parameter ρ is defined as follows:

1. Remove the candidate lepton from the track list, where the track list contains both charged and neutral tracks. A neutral track is defined to be any neutral cluster found by the liquid argon or end cap analysis that has not been associated with a charged track.
2. Perform the Lund cluster algorithm[4] (with the distance scale $d_{join} = 0.5$) on the remaining tracks .
3. For each jet j form the quantity

$$\eta_j = \sqrt{2E_l(1 - \cos\theta_{lj})} \tag{3.1}$$

where E_l is the lepton energy and θ_{lj} is the angle between the lepton and the jet, and define

$$\rho \equiv \min_{jets\ j}\{\eta_j\} \tag{3.2}$$

The quantity (3.1) can be thought of as the invariant mass of the lepton and the jet with the jet mass set to 0 and the jet energy set to 1 GeV. We note that equation (2.1) in Ref. 3 is missing a factor of 2 due to a typographical error.

If we require that

$$\begin{aligned} \text{NCHRG} &\geq 5 \\ \text{EVIS} &> 0.1 * \text{ECM} \quad . \end{aligned}$$

and require that there be at least one electron or muon with

$$\rho > 1.8$$

where an electron must have an LAELEC TEST1 parameter of

$$\text{TEST1} > 1.1$$

and a muon must satisfy

$$\text{MULEVE} = 4 \quad \text{and} \quad \text{MUSTAT} = 15 \quad ,$$

then about 0.03% of events from conventional physics processes pass these cuts. These events are almost entirely due to conventional Z^0 decays to hadrons. They can be eliminated by rather loose cuts on thrust or event acollinearity. For example if you require in addition to the above cuts that the event acollinearity ACOLL satisfies

$$\text{ACOLL} > 14^\circ$$

then you obtain the following counts of background and signal processes assuming 1 pb^{-1} of luminosity:

NO. OF EVENTS	PROCESS
0.1	conventional physics
15	40 GeV charged lepton (0 GeV neutrino)
150	40 GeV charged Higgsino (20 GeV photino)
750	40 GeV Wino (20 GeV photino) .

3.3 SUSY EVENTS WITHOUT ISOLATED LEPTONS

SUSY particles often have sizeable branching fractions for decay modes without primary leptons. To separate these decays from background we use the event acollinearity ACOLL and the variable $\beta_{T\text{vis}}$:

$$\beta_{T\text{vis}} \equiv \frac{\left|\sum_{tracks\ i} \vec{P}_{T_i}\right|}{\sum_{tracks\ i} E_i}$$

where $\vec{P}_{T_i}$ is the vector P_T of track i with respect to the beam axis, E_i is the energy of track i, and the sums are over all charged and neutral tracks.

If we require that

$$\begin{aligned} \text{NCHRG} &\geq 5 \\ \text{EVIS} &> 0.1 * \text{ECM} \\ \beta_{T\text{vis}} &> 0.6 \\ \text{ACOLL} &> 40^\circ \quad , \end{aligned}$$

then we obtain the following counts of background and signal processes assuming 1 pb^{-1} of luminosity:

NO. OF EVENTS	PROCESS
.8	conventional physics
438	40 GeV degenerate udscb squarks (20 GeV photino)
48	40 GeV left-handed b squark only (20 GeV photino)
33	40 GeV charged heavy lepton (20 GeV neutrino)
330	40 GeV charged Higgsino (20 GeV photino)
1650	40 GeV Wino (20 GeV photino) .

4. CONCLUSIONS

We should be able to exclude with the MARK II a very large fraction of the kinematically accessible SUSY particles predicted by the minimal SUSY extension to the standard model. If there is a SUSY particle being produced, we should be able to prove that the Z^0 is decaying to a new particle with SUSY-like properties. We also believe that we are in a very good position to extract many of the properties of such a particle.

REFERENCES

1. H. Haber and G. Kane, *Phys.Rept.* **117** (1985) 75 ; this reference is the source of almost all material presented in this chapter
2. J. Gunion and H. Haber, *Nucl.Phys.* **B272** (1986) 1
3. T.Barklow, MarkII/SLC-Physics Working Group Note # 3-11, in SLAC-Report-306 (1986)
4. T. Sjöstrand, *Comput.Phys.Comm.* **28** (1983) 229

Mark II/SLC-Physics Working Group Note # 3–23

AUTHOR: Martin L. Perl

DATE: July 1, 1987

TITLE: Small Multiplicity Events in $e^+ + e^- \rightarrow Z^0$ and Unconventional Phenomena

SLAC – PUB – 4165
December 1986
(E)

SMALL MULTIPLICITY EVENTS IN $e^+ + e^- \rightarrow Z^0$ AND UNCONVENTIONAL PHENOMENA*

Martin L. Perl
Stanford Linear Accelerator Center
Stanford University, Stanford, California 94305

ABSTRACT

Events with two–, four– or six–charged particles and no photons produced through the process $e^+ + e^- \rightarrow Z^0$ provide an opportunity to search for unconventional phenomena at the SLC and LEP electron-positron colliders. Examples of unconventional processes are compared with the expected background from electromagnetic processes and from charged lepton pair production.

Invited paper to be presented at the XXII Recontres de Moriond:
Electroweak Interactions and Unified Theories Conference, Les Arcs, France, March 8-15, 1987

*Work supported by the Department of Energy, contract DE–AC03–76SF00515.

A. INTRODUCTION

At the Z^0, the process

$$e^+ + e^- \rightarrow Z^0 \rightarrow n\text{-charged-particles} + 0\text{-photons} \tag{A1}$$

where $n = 2$, 4 or 6; provides an opportunity to search for unconventional processes. The behavior and rate of background events from conventional processes can be calculated, and the events occupy limited regions in the space of kinematic variables. This paper provides a concise description of this opportunity.

There are several unconventional processes which can yield small multiplicity, 0–photon events. The signatures for some of these processes have been fully discussed, other processes are less known. The discussion here is based on a classification by general production mechanisms and event topology. For example, there are similarities in the signatures for the charged sequential lepton ($L^\pm$) process

$$\begin{aligned} e^+ + e^- &\rightarrow Z^0 \rightarrow L^+ + L^- \\ L^+ &\rightarrow \ell^+ + \nu_\ell + \bar{\nu}_L \\ L^- &\rightarrow \ell^- + \bar{\nu}_\ell + \nu_L \end{aligned} \tag{A2}$$

and the supersymmetric scalar lepton ($\tilde{l}^\pm$) process

$$\begin{aligned} e^+ + e^- &\rightarrow Z^0 \rightarrow \tilde{\ell}^+ + \tilde{\ell}^- \\ \tilde{\ell}^+ &\rightarrow \ell^+ + \tilde{\gamma} \\ \tilde{\ell}^- &\rightarrow \ell^- + \tilde{\gamma} \end{aligned} \tag{A3}$$

if

$$\begin{aligned} m_L \gg m_\ell \quad &, \quad m_L \gg m_{\nu_L} \\ m_{\tilde{\ell}} \gg m_\ell \quad &, \quad m_{\tilde{\ell}} \gg m_{\tilde{\gamma}} \end{aligned} \tag{A4}$$

Here, ℓ means e or μ, ν is a neutrino, $\tilde{\gamma}$ is a photino and m means mass. When m_L and $m_{\tilde{\ell}}$ are greater than about 20 GeV/c^2, these processes yield acollinear two–charged–particle events with substantial energy and missing momentum. There is little background to such events from conventional processes.

On the other hand, suppose $m_L - m_{\nu_L}$ or $m_{\tilde{\ell}} - m_{\tilde{\gamma}}$ is small, of the order of 1 GeV/c^2. Then, depending on m_L or $m_{\tilde{\ell}}$, such events may have small visible energy and two–virtual–photon processes may cause a troublesome background.

I also discuss unconventional processes which might produce four–charged leptons. A well-known example is a neutral lepton L° which mixes with the e or μ:

$$\begin{aligned} e^+e^- &\rightarrow Z^0 \rightarrow L^0 + \bar{L}^0 \\ L^0 &\rightarrow \ell^- + \ell'^+ + \nu_{\ell'} \\ \bar{L}^0 &\rightarrow \ell^+ + \ell'^- + \bar{\nu}_{\ell'} \end{aligned} \tag{A5}$$

An instructive example is to suppose that an unknown, very high energy, interaction has a low energy residual interaction at the Z^0 mass which yields directly

$$e^+ + e^- \rightarrow Z^0 \rightarrow \ell^+ + \ell^- + \ell'^+ + \ell'^- \tag{A6}$$

As I show in sec. E, if the ℓ and ℓ' are required to be μ's, one can search to very small cross sections in the process in eq. A5 or A6.

The comparison of signatures for unconventional processes with the backgrounds from conventional processes depends upon the particle detector. For this paper I use a simplified model of the Mark II detector (sec. B) as it has been upgraded by my colleagues and myself for use at the SLAC Linear Collider (SLC).

Having made many searches for new particles and been successful only once, I know that one cannot precisely set search criteria until the experiment is working and the data is in hand. Usually one does not achieve the expected search sensitivity, unexplained background and imperfect equipment usually intervene first. Therfore, I shall limit myself to indicating general directions for signature selection, and proceed by example.

The plan of the paper is that backgrounds for two–charged–particle events are described in sec. C and compared in sec. D with examples of such events from unconventional processes. In secs. E and F, I discuss the background and unconventional process examples for four–charged– and six–charged–particle events, respectively.

B. SCHEMATIC DETECTOR, ACCEPTANCES AND CROSS SECTIONS

1. Schematic Detector

I discuss and calculate backgrounds and unconventional process systems using a schematic magnetic detector based on the upgraded Mark II detector.[1] In the following list θ is the smallest angle (0°–90°) between the direction of motion of a particle and the e^+e^- beam line, p is the magnitude of a particle momentum and E is its energy.

charged particle momentum measured: $\cos\theta < 0.85$ (B1a)

e identified: $\cos\theta < 0.85$, $E > 1.$ GeV (B1b)

μ identified: $\cos\theta < 0.85$, $E > 1.5$ GeV (B1c)

γ detected and energy measured: $\cos\theta < 0.95$ (B1d) e detected for veto: $\theta > 15$ mrad, $E > 0.2$ GeV (B1e)

γ detected for veto: $\theta > 15$ mrad, $E > 0.2$ GeV (B1f)

2. Acceptances

In the background and signature calculations, the acceptance for charged particles is set by

$$\cos\theta < 0.85 \qquad (B2a)$$

$$p > 1.\ \mathrm{GeV}/c \qquad (B2b)$$

3. Cross Sections

The approximate, radiatively corrected, cross section for

$$e^+ + e^- \to Z^0 \to f + \bar{f} \qquad (B3)$$

is

$$\sigma_{f\bar{f}} \approx 1400\ T_f(\beta)\ \mathrm{pb} \qquad (B4)$$

T_f depends upon the f-Z^0-$\bar{f}$ coupling. For conventional charged leptons

$$T_{L^-} \approx \beta(3-\beta^2)/2 \qquad (B5a)$$

For conventional neutral leptons

$$T_{L^0} \approx \beta(3+\beta^2)/2 \qquad (B5b)$$

C. BACKGROUNDS FOR TWO-CHARGED PARTICLE, 0-PHOTON EVENTS

1. $e^+e^- \to \ell^+\ell^-$

The reaction

$$e^+ + e^- \to \ell^+ + \ell^- \qquad (C1)$$

where ℓ is an e or μ, gives a pair of collinear particles to the extent allowed by radiative corrections and instrumental errors. When ℓ is a τ, the one-charged-particle, 0-photon decay modes

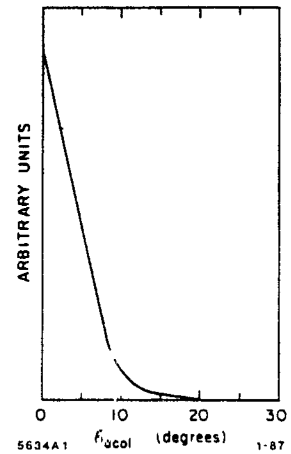

Figure 1

$$\tau^- \to \nu_\tau e^- \bar{\nu}_e \ ,\quad \nu_\tau \mu^- \bar{\nu}_\mu \ ,\quad \nu_\tau \pi^- \ ,\quad \nu_\tau K^- \qquad (C2)$$

yield the acollinearity angle distribution of fig. 1. Here, θ_{acol} is defined[2] to be 0 when the particles have exactly oppposite momenta. When

$$\theta_{acol} > 15^\circ \qquad (C3)$$

is required, about 0.5% of the decays are accepted under the conditions of eqs. B1 and B2. Hence

$$\sigma(ee \to \tau\tau, \text{2-prong, 0-photon} \approx 1.4\ \mathrm{pb}, \qquad \theta_{acol} > 15^\circ \qquad (C4)$$

The efficacy of increasing the lower limit on θ_{acol} to reduce this σ depends upon the level of mistracking in a particular detector.

2. $e^+e^- \to \ell^+\ell^-\gamma, \ell^+\ell^-\gamma\gamma$

The radiative corrections to the reactions in eq. C1 lead to a continuum between lepton pair production and

$$e^+ + e^- \to \ell^+ + \ell^- + \gamma \qquad (C5a)$$

$$e^+ + e^- \to \ell^+ - \ell^- + \gamma + \gamma \qquad (C5b)$$

The completeness of the photon veto (eq. B1f) for the schematic detector controls the level of background from these reactions. For example, in

$$e^+ + e^- \rightarrow \mu^+ + \mu^- + \gamma \tag{C6}$$

the schematic detector does not veto photons with $E_\gamma < 0.2$ GeV or with $\theta_\gamma < 15$ mrad. But events with $E_\gamma < 0.2$ GeV are removed by the acollinearity criterion, eq. C3. Events with $\theta_\gamma < 15$ mrad have acoplanarity angles[2] of the order of a degree, hence they can be removed by a nominal acoplanarity angle[2] criterion of

$$\theta_{acop} > 5^\circ \tag{C7}$$

The practical question is the degree of perfection of the photon veto system. Consider $ee \rightarrow \mu\mu\gamma$ again and suppose no photon veto, only $\theta_{acol} > 15^\circ$ and $\theta_{acop} > 5^\circ$, then

$$\sigma(ee \rightarrow \mu\mu\gamma) = 23.\ \text{pb}, \qquad \theta_{acop} > 15^\circ, \theta_{acol} > 5^\circ \tag{C8}$$

under all other conditions of eqs. B1 and B2. A 1% inefficiency in the photon veto will then leave

$$\sigma(ee \rightarrow \mu\mu\gamma) = 0.2\ \text{pb} \tag{C9}$$

Similar considerations apply to the other reactions in eq. C5.

3. $e^+e^- \rightarrow e^+e^-e^+e^-, e^+e^-\mu^+\mu^-, e^+e^-\pi^+\pi^-$

The two-virtual-photon processes

$$e^+ + e^- \rightarrow e^+ + e^- + e^+ + e^- \tag{C10a}$$

$$e^+ + e^- \rightarrow e^+ + e^- + \mu^+ + \mu^- \tag{C10b}$$

$$e^+ + e^- \rightarrow e^+ + e^- + \pi^+ + \pi^- \tag{C10c}$$

give two-charged-particle, 0-photon events when one e^+ and one e^- are not detected because their angles with the beamline, $\theta_e{}^+$ and $\theta_e{}^-$, are very small. This kinematic situation has been studied in several experiments[3,4] and the results confirm the calculation methods developed by Berands, Daverveldt and Kleiss.[5]

With the acceptance conditions of eq. B2, the cross section in the pion pair process (eq. C10c) is a small fraction of the cross sections for the lepton pair processes (eqs. C10a and C10b), hence the former is ignored here. We use the mnemonic $ee \rightarrow (ee)\ell\ell$ to represent the sum of the processes in eqs. C10a and C10b when one e^+ and one e^-, represented by the symbols (ee), are not detected by tracking or veto devices. The observed cross section,

$\sigma(ee \rightarrow (ee)\ell\ell)$ depends upon the charged particle acceptance criteria and the angular extent of the $e^\pm$ veto devices. For example, with $\theta_{acol} > 15^\circ, \theta_{acop} > 5^\circ, p > 1$ GeV/c:

$$\sigma(ee \rightarrow (ee)\ell\ell) \approx 60\ \text{pb} \quad , \quad \theta_{e^\pm,veto} > 15\ \text{mrad} \tag{C11a}$$

$$\sigma(ee \rightarrow (ee)\ell\ell) \approx 150\ \text{pb} \quad , \quad \theta_{e^\pm,veto} > 555\ \text{mrad} \tag{C11b}$$

Here, $\theta_{e^\pm,veto}$ is measured from the beamline. Figures 2 and 3 give the E_{vis} and p_T distributions when the $\theta_{acol} > 15^\circ, \theta_{acop} > 5^\circ, p > 1.$ GeV/c criteria are applied. Here E_{vis} is the total energy of the two observed charged particles and p_T is the vector sum of their momenta transverse to the beamline.

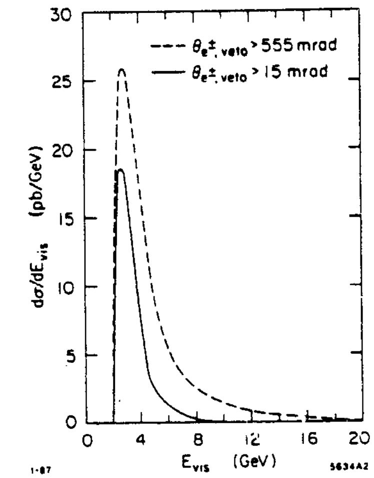

Fig. 2

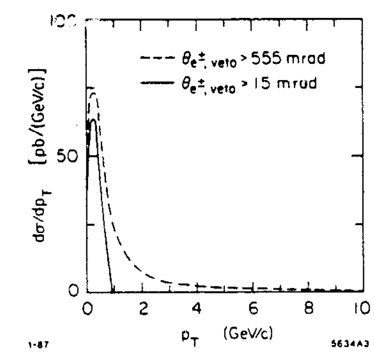

Fig. 3

The $ee \to (ee)\ell\ell$ cross section can be a serious background when one is searching for processes with small E_{vis}, such as the close-mass lepton pair model in sec. D2. This background can also be a problem in searches involving very small cross sections, such as occurred in the search of Perl *et al.*,[6] for neutral leptons in e^+e^- annihilation events produced at 29 GeV total energy.

When an $e^\pm$ is detected with $\theta_{e,veto} > 15$ mrad with perfect efficiency (eq. B1f), the remaining events with $\sigma = 60$ pb (eq. C11a) can be removed with a p_T criterion such as

$$p_T > 0.8 \text{ GeV/c} \tag{C12}$$

However, if the $e^\pm$ veto is inefficient there will be a background from a fraction of the dN/dp_T distribution in fig. 3 for $\theta_{e,veto} > 555$ mrad. For example, 1% inefficiency would give $\theta(ee \to (ee)\ell\ell) \approx 0.7$ pb for events where p_T exceeds the criterion in eq. C12. Such events would have p_T values up to 8 GeV/c and E_{vis} values up to 20 GeV/c. Of course, a larger p_T criterion could be used, but that reduces the efficiency of some searches for unconventional processes.

4. Summary

With criteria

$$\begin{aligned} \theta_{acol} &> 15^\circ \\ \theta_{acop} &> 5^\circ \\ p_T &> 0.8 \text{ GeV/c} \end{aligned} \tag{C13}$$

in the schematic detector, the two-charged particle, 0-proton backgrounds have cross sections of the order of a few tenths of a pb to several pb. Inefficiencies in γ and $e^\pm$ vetoes can substantially increase these cross sections. Special criteria such as requiring an $e\mu$ pair can substantially decrease some of these cross sections.

D. SIGNATURES FOR TWO-CHARGED PARTICLE, 0-PHOTON EVENTS FROM UNCONVENTIONAL PROCESSES

In this discussion the unconventional processes are classified according to the effect of the production mechanism on the kinetic variable distributions.

1. Pair Production of Charged Particles with Large Decay Energies

The general process is production of an x^+x^- pair followed by the decays of x^+ and x^- through the weak interaction:

$$e^+ + e^- \to x^+ + x^- \tag{D1}$$

$$x^\pm \to y^\pm + n_1 + n_2 + \ldots \tag{D2}$$

with the energy released in the decay of the x, large compared to the masses of the y and the $n_1, n_2 \ldots$. Here, $n_1, n_2 \ldots$ are neutral, weakly interacting particles; there may be one or more

in the decay. And y^- means e^-, μ^-, π^- or K^-. It can also indicate τ^- when the τ decays into a one-charged-particle, 0-photon mode. The general kinematics are determined by two parameters: (i) the mass of x, called m_x and (ii) the difference, called δ, between m_x and the sum of all the masses of the particles on the right side of the reaction in eq. D2. Explicitly

$$\delta = m_x - \left(m_y + \sum m_n\right) \tag{D3}$$

The case usually discussed is

$$m_x \approx \delta \tag{D4}$$

The best known example[7] is a heavy sequential lepton, L^-, with a near-zero-mass neutrino partner ν_L. Then the decay process in eq. D2 is

$$L^- \to \ell^- + \bar\nu_\ell + \nu_L \quad ; \quad \ell = e, \mu \tag{D5}$$

A similar example is the chargino, χ^- proposed in supersymmetric models, when the χ^- decays to a near-zero-mass photino, $\tilde\gamma$:

$$\chi^- \to \ell^- + \nu_\ell + \tilde\gamma \quad , \quad \ell = e, \mu \tag{D6}$$

A two-body example, also from supersymmetric models, is the pair production of scalar leptons

$$\begin{aligned} e^+ + e^- \to Z^0 \to \tilde\ell^+ + \tilde\ell^- \\ \tilde\ell^- \to \ell^- + \tilde\gamma \end{aligned} \tag{D7}$$

To illustrate the case of a three-body decay

$$x^- \to \ell^- + n_1 + n_2 \tag{D8}$$

I use the following simplified model: (i) the production process in eq. D1 is isotropic, the decay process in eq. D8 is calculated using relativistic phase space, and the masses of the final particles are set to zero. The θ_{acol} distribution is given in fig. 4 for $m_x = 20$, 30 and 40 GeV/c^2. Replacing the phase space calculation by one using some combination of V and A couplings changes these distributions slightly. A feeling for the observed cross section can be obtained by using eq. B4 with $\beta = 1$, using the branching fractions

$$B(x^- \to e^- n_1 n_2) = B(x^- \to \mu^- n_1 n_2) = 0.1 \quad , \tag{D9}$$

and using an acceptance of 0.7 for the criteria of eqs. B2 and C11:

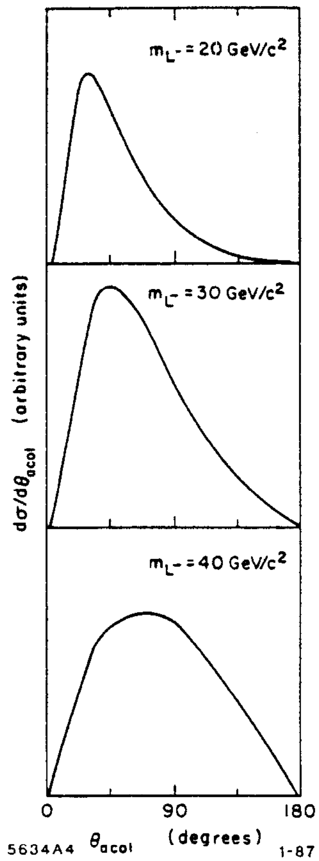

Figure 4

$$
\begin{aligned}
|\cos\theta| &< .85 \\
p &> 1.\ \mathrm{GeV/c} \\
\theta_{acol} &> 15^\circ \\
\theta_{acop} &> 5^\circ
\end{aligned}
\tag{D10}
$$

Then

$$\sigma = (ee \to L^+L^- \to \ell^+\ell^-, \text{observed}) = 39 \text{ pb} \tag{D11}$$

As is well known this is much larger than the background examples given in eqs. C4 and C9, hence such searches are straightforward. Incidently, the lower limit from the UA1 collaboration[8] of

$$m_{L^-} > 41 \text{ GeV/c}^2 \qquad (90\% \text{ CL})$$

on a charged heavy lepton with a near-zero-mass neutrino partner limits this search using Z° decay to a small mass range.

Summarizing, the events produced by processes defined by eqs. D1, D2 and D4 have the following properties:

1. As m_x approaches $m_Z/2$, the acollinearity increases. Acollinearity and acoplanary criteria such as $\theta_{acol} > 15^\circ, \theta_{acop} > 5^\circ$ separate most of the events from the $ee \to \ell\ell$ and $ee \to \ell\ell\gamma$ backgrounds.
2. For all m_x values the events have large E_{vis} values, hence they separate from $ee \to (ee)\ell\ell$ events.
3. For all m_x values the events have large p_T values.

There have been several detailed discussions[9,10] of how to search for new particles produced by the processes defined by eqs. D1, D2 and D4. I turn to a less known case.

2. Pair Production of Charged Particles with Small Decay Energies

We have recently begun to study models[11] where the production and decay processes are given by eqs. D1 and D2 but

$$m_x \gg \delta \tag{D12}$$

I will concentrate on what I call the close-mass lepton pair model[11,12] The reader can easily extend the discussion to other hypothetical particles, for example, charginos and photinos.

Consider the lepton pair L^-, L° with masses m_- and m_0, respectively. Suppose $m_- > m_0$ but

$$m_- - m_0 = \delta \ll m_- \tag{D13}$$

The charged particle in the decay modes

$$L^- \to \ell^- + \bar{\nu}_\ell + L^\circ \quad ; \quad \ell = e, \mu \tag{D14a}$$

$$L^- \to \pi^- + L^\circ \tag{D14b}$$

has maximum laboratory momentum

$$P_{max} = E_b \left[1 - \left(\frac{m_0}{m_-}\right)^2\right] \left[1 + \left(1 - \left(\frac{m_-}{E_b}\right)^2\right)^{1/2}\right] \Big/ 2 \tag{D15}$$

Here E_b is the beam energy $m_Z/2$. The ℓ, ν_ℓ and π masses have been set to zero. Using eq. D12

$$E_{vis} < (\delta/m_-) m_Z \tag{D16}$$

Here E_{vis} is the total useable energy.

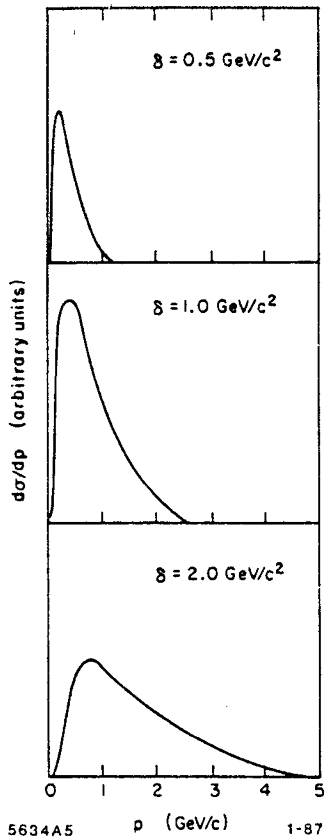

Figure 5

If δ is of the order of a few GeV/c^2 or less, and m_- is of the order of tens of GeV/c^2, E_{vis} is small. Then the $ee \to (ee)\ell\ell$ background (sec. C3) becomes important. A general discussion is unwieldy because there are now two parameters, m_- and δ; I proceed by example.

Suppose $m_- = 30$ GeV/c^2; consider the decay modes of eq. D14a; set $m_\ell = 0, m_{\nu_\ell} = 0$, and let $\delta = m_- - m_0$ have the values 0.5, 1.0 and 2.0 GeV/c^2. Using the pair production cross section in eqs. B4 and B5a and conventional weak interaction theory with V–A coupling, we calculate kinematic distributions, branching fractions and the observed cross sections for the classic signature

$$e^+ + e^- \to L^+ + L^- \to e^\pm + \mu^\mp + \text{ missing energy} \tag{D17}$$

The e and μ momentum distributions are given in fig. 5. Table 1 gives the observed cross sections under the usual criteria

Table 1. Branching fractions and observed cross sections for $e^+e^- \to L^+L^- \to e^\pm\mu^\mp +$ missing energy via $L^- \to L^0 e^- \bar{\nu}^e, L^+ \to \bar{L}^0\mu^+\nu_\mu$, with $m_- = 30$ GeV/c^2.

$m_- - m_0$ (GeV/c^2)	$B(L^- \to L^0 e^- \bar{\nu}_e)$	$B(L^+ \to \bar{L}^0\mu^+\nu_\mu)$	Observed σ (pb) p > 0. GeV/c	Observed σ (pb) p > 1. GeV/c
2.0	.19	.19	71.	.29
1.0	.17	.16	50.	4.
0.5	.18	.15	51.	0.

$$\begin{aligned} |\cos\theta| &< 0.85 \\ \theta_{acol} &> 15^\circ \\ \theta_{acop} &> 5^\circ \end{aligned} \tag{D18}$$

but with

$$\begin{aligned} &p > 0.\ \text{GeV/c} \\ &\text{or} \\ &p > 1.\ \text{GeV/c} \end{aligned} \tag{D19}$$

Figure 5 and Table 1 lead to several comments:

1. As $\delta = m_- - m_0$ decreases below 2. GeV/c^2, the $p > 1.$ GeV/c criterion must be abandoned. But then, according to eqs. B1b and B1c, the e and μ can no longer be identified.
2. Without e and μ identification the observed cross sections are the same size as the $ee \to (ee)\ell\ell$ background cross sections in eq. C11.
3. Comparing fig. 6, the p_T distributions for this model, with fig. 3, one sees that for small values of δ this signature will be submerged by the $ee \to (ee)\ell\ell$ background.

There are, of course, other signatures for the process under discussion: $\ell^\pm\pi^\mp, \ell^\pm\rho^\mp$ and four-charged particles, depending upon δ. And the Z^0 width, when carefully measured, would reflect the existence of an additional L^- and L^0. But when $\delta \lesssim 1.5$ GeV/c^2, it could be very difficult to elucidate the type of process discussed in this section. Incidently, when $\delta \lesssim m_\pi$, the charged particle lifetime becomes sufficiently long for the L^- to appear stable.

3. Production of Two Neutral Particles

Various types of hypothetical leptons[11,13,14] illustrate how two–charged–particle, 0–photon events could come from the decay of the Z^0. If there is a heavy neutral lepton, L^0, which mixes with the e, μ or τ generation then the following could occur

$$\begin{aligned} e^+ + e^- &\to L^0 + \bar{\nu}_1 \\ L^0 &\to \ell_1^- + \ell_2^+ + \nu_2 \end{aligned} \tag{D20}$$

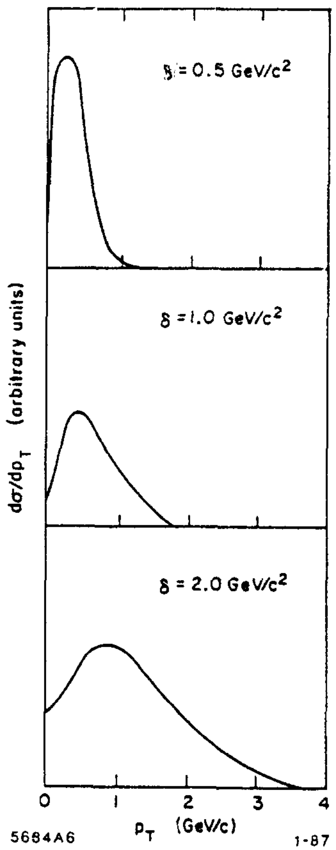

Figure 6

Here ℓ means e, μ or τ and ν is the corresponding neutrino. In a more exotic scheme, consider a pair of neutral leptons L^0, ν_L with the unconventional decay $L^0 \rightarrow \nu_L + \ldots$, then

$$\begin{aligned} e^+ + e^- &\rightarrow L^0 + \bar{\nu}_L \\ L^0 &\rightarrow \nu_L + \ell^+ + \ell^- \end{aligned} \tag{D21}$$

or

$$\begin{aligned} e^+ + e^- &\rightarrow L^0 + \bar{L}^0 \\ L^0 &\rightarrow \nu_L + \ell^+ + \ell^- \\ \bar{L}^0 &\rightarrow \bar{\nu}_L + \nu + \bar{\nu} \end{aligned} \tag{D22}$$

will give two–charged–particle, 0–photon events.

Another possibility is a weakly decaying neutral boson[6], N^0, with

$$\begin{aligned} e^+ + e^- &\rightarrow N^0 + \bar{N}^0 \\ N^0 &\rightarrow \ell^+ + \ell^- \\ \bar{N}^0 &\rightarrow \nu + \bar{\nu} \end{aligned} \tag{D23}$$

In all these processes, as in the process in sec. D1, the events will have

1. large values of θ_{acol}
2. large values of E_{vis}
3. large values of p_T

Although here the large values of θ_{acol} occur for a different reason than the processes in sec. D1. Indeed in contrast to the latter processes, these processes give events which become more collinear as m_0 approaches m_Z or $m_Z/2$. Figure 7 illustrates this for the reactions in eq. D22. Here the masses of ν_L, ℓ and ν are set to zero, and once again relativistic phase space is used for the decay process. The L^0 mass is given for each curve.

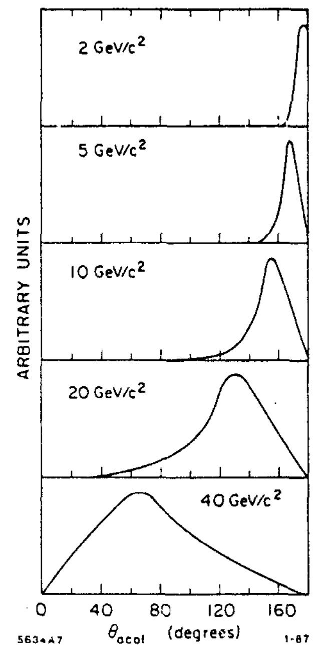

Figure 7

To illustrate what an observed cross section might be, I use eqs. B4 and B5b with $\beta = 1$, and I take the branching fractions from fig. 3 in ref. 6.

$$\begin{aligned} B(L^0 \to \nu_L \nu_i \nu_i) &= 0.25 \\ B(L^0 \to \nu_L \ell\ell) &= 0.07 \end{aligned} \tag{D24}$$

Before any θ_{acol} or θ_{acop} cuts, the acceptance is 0.7 for

$$\begin{aligned} |\cos| &< .85 \\ p &> 1.\ \mathrm{GeV/c} \end{aligned} \tag{D25}$$

Then

$$\sigma(ee \to L^0 \bar{L}^0 \to \ell^+ \ell^-,\ \text{observed}) = 69\ \text{pb} \tag{D26}$$

Like the result in eq. D11, this σ allows a straightforward search with respect to the background discussed in sec. C, providing the production cross section and branching fractions are as assumed here.

4. Production through a Central Process

As a final example I consider a central process, perhaps the low energy residual of some much higher energy interaction, where the Z^0 decays to four fermions

$$Z^0 \to f_1 + \bar{f}_1 + f_2 + \bar{f}_2 \tag{D27}$$

If f_1 is a neutrino, and f_2 is a lepton

$$Z^0 \to \nu + \bar{\nu} + \ell^+ + \ell^- \tag{D28}$$

yields two–charged particle, 0–photon events.

The question is how small a cross section could be found in view of the background described in sec. C: e^+e^- and $\mu^+\mu^-$ pairs from $ee \to \tau\tau, ee \to \ell\ell\gamma$ and $e^+e^- \to (ee)\ell\ell$. Important separation criteria are: (i) the lower limit on θ_{acol}, called $\theta_{acol,min}$ and (ii) the lower limit on E_{vis}, called $E_{vis,min}$. The former discriminates against all backgrounds, the latter against $ee \to (ee)\ell\ell$. Figure 8 gives the acceptance as a function of these criteria. Relativistic phase space is used and all lepton masses are zero. Useable acceptances can be obtained with large values of $\theta_{acol,min}$ and $E_{vis,min}$ and such large values discriminate against the background discussed in sec. C. The lower limit on the detectable cross section from the reaction in eq. D28 will probably be set by detector inefficiencies and malfunctions.

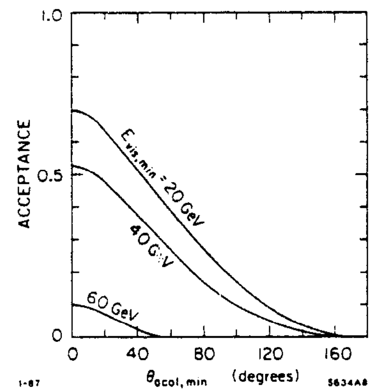

Figure 8

E. BACKGROUND FOR FOUR–CHARGED AND SIX–CHARGED PARTICLE, 0–PHOTON EVENTS

1. $e^+e^- \to \tau^+\tau^-$

The process

$$e^+ + e^- \to \tau^+ + \tau^- \tag{E1}$$

gives four–charged or six–charged particles and 0–photons when one or both τ's decay

$$\tau^- \to \pi^- + \pi^+ + \pi^- \tag{E2}$$

But these events will be obvious and easily separated out.

2. $e^+e^- \to e^+e^-\ell^+\ell^-$

The two–virtual–photon process

$$e^+ + e^- \to e^+ + e^- + \ell^+ + \ell^- \tag{E3}$$

with all particles detected is the main known background from conventional processes for four–charged particle, 0–photon events. The process in eq. E3 has been studied at PETRA[15,16] and compared with calculations using the Monte Carlo methods of ref. 5. Measurement and calculations agreed in the use of ref. 15, but not in that of ref. 16. The latter discrepancy has not been confirmed.

Using the Monte Carlo program from ref. 5, with the criteria

$$|\cos\theta| < 0.85 \quad \text{(E4a)}$$

$$p > 1. \quad \text{(E4b)}$$

$$m_{\ell\ell} > 1.\ \mathrm{GeV/c^2} \quad \text{(E4c)}$$

the observed cross section is

$$\sigma(ee \to eeee, ee\mu\mu; \text{observed}) = 0.084 \pm 0.019 \text{ pb} \quad \text{(E5)}$$

Here, $m_{\ell\ell}$ represents the invariant masses of $e^+e^-, \mu^+\mu^-$ and $e^\pm\mu^\mp$ pairs; the lower limit eliminates uninteresting events. The uncertainty in σ is from the statistics of the Monte Carlo calculation.

All the $ee \to ee\mu\mu$ events contributing to σ in eq. E5 have one $m_{\ell\ell}$ close to the lower limit in eq. E4c, the other $m_{\ell\ell}$ is usually close to m_Z^0, an expected distribution. For example, if

$$m_{\ell\ell} > 5.\ \mathrm{GeV/c^2} \quad \text{(E6)}$$

is required, the observed cross section is reduced to

$$\sigma(ee \to eeee, ee\mu\mu, \text{observed}) = 0.022 \pm 0.008 \text{ pb} \quad \text{(E7)}$$

Thus, the criteria in eqs. E4a, E4b and E6 limit $\sigma(ee \to ee\ell\ell$, observed) to very small values.

3. $e^+e^- \to$ hadrons

A possible, albeit very small, background is four–charged or six–charged particle, 0–photon hadronic events from quark-antiquark pair production. I do not know how to calculate this. The cross section for such events in the PETRA–PEP region is not measured to my knowledge. And one cannot depend upon the empirical quantum chromodynamic calculational methods used in the several Monte Carlo programs currently applied to $e^+e^- \to$ hadrons. Such programs are designed and adjusted to fit the behavior of the bulk of hadronic events; not the rare events of interest here.

F. FOUR–CHARGED OR SIX–CHARGED PARTICLE, 0–PHOTON EVENTS FROM UNCONVENTIONAL PROCESSES

Here, as in sec. D, the unconventional processes are classified according to the affect of the production mechanism on the kinematic variable distribution. The background has been discussed in sec. E. Excepting the easily recognized $\tau\tau$ background, the known background is 0.1 to 0.01 pb, eqs. E5 and E7. The limitations on search sensitivity will probably come from a combination of the unknown hadronic background (sec. E) and detector malfunctions and inefficiencies.

1. Four–Charged Particle, 0–Photon Events from Two Neutral Particles

Using the L^0, ν_L model of eq. D22

$$\begin{aligned} &e^+e^- \to Z^0 \to L^0 + \bar{L}^0 \\ &L^0 \to \nu_L + \ell^+ + \ell^- \\ &\bar{L}^0 \to \bar{\nu}_L + \ell^+ + \ell^- \end{aligned} \quad \text{(F1)}$$

or the neutral boson model of eq. D23

$$\begin{aligned} &e^+ + e^- \to Z^0 \to N^0 + N^0 \\ &N^0 \to \ell^+ + \ell^- \quad (\text{both } N^0) \end{aligned} \quad \text{(F2)}$$

four–charged particle, 0–photon events can be produced. Here ℓ means e, μ or the one–charged–particle, 0–photon decay modes of the τ. Of course the ℓ's could be replaced by π or K mesons, but such decay modes would probably have very small branching fractions for the L^0 or N^0 masses of interest—above several GeV/c^2.

The L^0, ν_L model with the $\nu_L\ell^+\ell^-$ branching fraction of eq. D24, with the production cross section of eqs. B4 and B5b with $\beta = 1$, and with an acceptance of 0.4 for

$$\begin{aligned} &|\cos\theta| < .85 \\ &p > 1.\ \mathrm{GeV/c} \end{aligned} \quad \text{(F3)}$$

gives

$$\sigma(ee \to L^0\bar{L}^0 \to \ell^+\ell^-\ell^+\ell^-, \text{ observed}) = 5 \text{ pb} \quad \text{(F4)}$$

This is a relatively small cross section, but still much larger than the known background cross sections.

The N^0 model would give obvious events with $E_{vis} = m_Z$ within detector precision and radiative corrections. The distributions of pair masses would indicate m_{N^0}, and be very different from the $ee \to ee\ell\ell$ distributions (Sec. E2).

A generalization of the L^0 and N^0 models would add additional neutral, weakly-interacting, particles to the decay modes in eqs. F1 or F2.

2. Production through a Central Process

The central process model in sec. D4 would also give

$$e^+ + e^- \to \ell_1^+ + \ell_1^- + \ell_2^+ + \ell_2^- \quad \text{(F5)}$$

Using relativistic phase space, the acceptance under the criteria of eq. F3 is 0.5, again $E_{vis} = m_Z$.

3. Four-Charged or Six-Charged Particle, 0-Photon Events from Charged Particle Production

Here I follow the scheme of the $\tau\tau$ production and decay process. Consider

$$e^+ + e^- \to Z^0 \to f^+ + f^- \tag{F6}$$

with the decay modes

$$f^- \to \ell^- + \nu + \bar{\nu} \tag{F7a}$$

$$f^- \to \ell^- + \ell^+ + \ell^- \tag{F7b}$$

Here, as before, ℓ means e, μ or the one-charged-particle, 0-photon τ decay modes; ν means ν_e, ν_μ or ν_τ.

Such events will be distinctive, particularly the six-charged-particle events with $E_{\text{vis}} = m_Z$.

ACKNOWLEDGEMENTS

I am greatly indebted to Timothy Barklow for many valuable conversations and insights on small multiplicity of events, to David Stoker for conversations and calculations on close-mass pairs, to Alfred Peterson for his development of, and knowledge of, Monte Carlo programs for e^+e^- annihilation, and to Bruce LeClaire for his construction of general computer programs for executing analysis of real and simulated data. I am also indebted to my other colleagues in the new Mark II collaboration who are preparing our experiment on the SLC.

REFERENCES

1. Proposal for the Mark II at SLC, SLAC-PUB-3561 (1985).
2. $\cos\theta_{\text{acol}} = -\vec{n}_1 \cdot \vec{n}_2$ and $\cos\theta_{\text{acop}} = -(\vec{n}_1 \times \vec{n}_+) \cdot (\vec{n}_2 \times \vec{n}_+) / |\vec{n}_1 \times \vec{n}_+||\vec{n}_2 \times \vec{n}_+|$ where $\vec{n}_1, \vec{n}_2$ and $\vec{n}_+$ are the unit momentum vectors for observed particle 1, observed particle 2 and the incident e^+, respectively.
3. R. P. Johnson, Ph. D. Thesis, Stanford Univ., SLAC-REP-294 (1986).
4. M. L. Perl *et al.*, Phys. Rev. **34D**, 3321 (1986).
5. F. A. Berands, P. H. Daverveldt and R. Kleiss, Nucl. Phys. **B253**, 441 (1985).
6. M. L. Perl *et al.*, Phys. Rev. **32D**, 2859 (1985).
7. For discussions of search methods for sequential, heavy, charged leptons from Z^0 decay, see D. Stoker, Mark II/SLC-Physics Working Group Note 0-2 (1986), p. 475; Physics at LEP, CERN 86-02 (1986), edited by J. Ellis and R. Peccei, Vol. 1, p. 424.
8. A. Honma, Proc. 23rd Conf. High-Energy Physics (Berkeley, 1986), to be published; also issued as CERN-EP/86-153 (1986).
9. Mark II/SLC-Physics Working Group Note 0-2 (1986), unpublished.

10. Physics at LEP, CERN 86-02 (1986), edited by J. Ellis and R. Peccei.
11. M.L. Perl, Proc. 23rd Int. Conf. High-Energy Physics (Berkeley, 1986), to be published. Also issued as SLAC-PUB-4092 (1986).
12. S. Raby and G. B. West, Los Alamos Preprint LA-UR-86-4151 (1986). This work proposes a close-mass lepton pair in connection with solar neutrino and dark matter questions.
13. F. J. Gilman, Comments Nuclear and Particle Physics, **16**, 231 (1986).
14. S. Komamiya, Proc. Int. Symp. Lepton and Photon Interactions at High Energies (Kyoto, 1985), edited by M. Konuma and K. Takahashi, p. 612.
15. W. Bartel *et al.*, Z. Phys. **C30**, 545 (1980).
16. H. J. Behrend *et al.*, DESY 84-103 (1984).

Mark II/SLC-Physics Working Group Note #4-5

AUTHOR: B. F. L. Ward

DATE: February 28, 1987

TITLE: Single Quark Decays in Toponium

Abstract

We consider single quark decays in toponium from the standpoint of the physics possibilities for the MkII detector at the SLC. Accordingly, we focus on the theoretical uncertainties associated with various estimates of $\Theta \to T_b^{(*)} + X$, $\bar{T}_b^{(*)} + X'$ when $m_t \sim 40$ GeV. Three types of estimates are considered: non-relativistic potential model estimates, vector dominance model estimates, and Lepage-Brodsky perturbative QCD estimates. We argue that the difference between the estimates may be traced to the large squared momentum behavior of the respective wavefunctions of the $T_b^{(*)}$ meson. Thus, the MkII, operating at the SLC, may be able to discriminate between these wavefunctions.

I. Introduction

The UA1 Collaboration[1] has recently emphasized that the top quark mass m_t has only the lower limit of the PETRA experiments: $m_t \gtrsim 24$ GeV. Such large values of m_t imply that single quark toponium decays, in which either the t or the $\bar{t}$ in $\Theta \equiv {}^3S_1(t\bar{t})$ undergoes a weak decay, are significant. Thus, it is natural to ask whether a detector such as the MkII, operating at the SLC, might be able to exploit some of the unique characteristics of such single quark decays (SQD's) from the standpoint of possible new physical phenomena?

An immediate response which comes to one's mind is the particular type of SQD in which the b (or $\bar{b}$), which is produced when the t (or $\bar{t}$) decays, binds with the untransformed $\bar{t}$ (or t) to make a $\bar{T}_b^{(*)}(T_b^{(*)})$ meson. We refer to this type of Θ SQD as $\bar{T}_b^{(*)}(T_b^{(*)})$ exclusive SQD. Because $b\bar{b}$ pairs are very rarely provided by the vacuum for fragmenting quarks, Θ SQD may be the only practical source of $T_b^{(*)}(\bar{T}_b^{(*)})$ mesons. For this reason, we feel it is indeed appropriate to quantify the type of rate one can expect for $\Theta \to \bar{T}_b^{(*)} + X', T_b^{(*)} + X$ for $m_t \sim 40$ GeV.

Accordingly, we shall discuss three different approaches for estimating $\Theta \to T_b^{(*)} + X$, $\bar{T}_b^{(*)} + X'$: non-relativistic potential model estimates, as they are typified by the work of Bigi and Krasemann[2], vector dominance estimates, and estimates based on the methods of Lepage and Brodsky.[3] In this way, we hope to isolate the key theoretical uncertainites involved in such estimates.

Our discussion will proceed as follows. In the next section, we discuss the methodologies of Bigi and Krasemann, of the vector dominance formalism, and of the Lepage-Brodsky theory as they relate to $\Theta \to T_b^{(*)} + X$, $\bar{T}_b^{(*)} + X'$. In Sect.

III, we compare these methods in the space of the momentum transferred in the $\textcircled{H} \to T_b^{(*)}(\bar{T}_b^{(*)})$ transition. Section IV contains some concluding remarks.

II. Three Approaches to $\textcircled{H} \to T_b^{(*)} + X, \bar{T}_b^{(*)} + X'$

In this section, we wish to present three different approaches to $\textcircled{H} \to T_b^{(*)} + X$, $\bar{T}_b^{(*)} + X'$. We begin with the method of Bigi and Krasemann, as it typifies the non-relativistic potential model approach to the type of transition under discussion.

Specifically, Bigi and Krasemann compute the non-relativistic wavefunctions of $\textcircled{H}$ and $T_b^{(*)}(\bar{T}_b^{(*)})$ by solving the respective Schroedinger equations with their favorite potential for QCD. The rate for $\textcircled{H} \to T_b^{(*)} + X, \bar{T}_b^{(*)} + X'$ is then represented as

$$BR(\textcircled{H} \to T_b^{(*)} + X, \bar{T}_b^{(*)} + X') = BR(SQD)|I_{overlap}|^2 \tag{1}$$

where BR(SQD) is the branching fraction of $\textcircled{H}$ to all SQD final states and $I_{overlap}$ is the overlap integral of the $\textcircled{H}$ state and the $T_b^{(*)}(\bar{T}_b^{(*)})$ state boosted by the recoil momentum Q of the W. This is illustrated in Fig. 1. For $m_t \cong 40$ GeV, Bigi and Krasemann find

$$|I_{overlap}|^2 \cong .03 \quad . \tag{2}$$

Thus, according to this type of estimate one expects

$$BR(\textcircled{H} \to T_b^{(*)} + X, \bar{T}_b^{(*)} + X') \cong 1.5\% \tag{3}$$

if we take Γ_{tot} ($\textcircled{H}$) ~ 100 KeV and BR(SQD) ~ 49% as typical non-relativistic potential model results[4] for $m_{\textcircled{H}} \sim 80$ GeV.

A natural question to ask is whether the representation (1) is adequate for a highly relativistic b quark such as that generated by the $t \to b + W^+$ transition involved in Fig. 1 at the $\textcircled{H} \to \bar{T}_b^{(*)} + W$ vertex. The typical $|\vec{Q}|$ is ~ 13 GeV. This issue can be addressed by computing the process in Fig. 1 in a relativistically invariant model such as the vector dominance model. To this type of estimate we turn next.

More precisely, we consider the process illustrated in Fig. 2. For simplicity, we treat $\textcircled{H} \to T_b + X, \bar{T}_b + X'$ since this will allow us to illustrate the relevant physical ideas. The W-T_b^* mixing parameter $f_{WT_b^*}$ is related to the T_b^*-$\textcircled{H}$-$\bar{T}_b$ coupling $g_{T_b^*}$ via

$$f_{WT_b^*} = m_{T_b^*}^2 g_W / 2 g_{T_b^*} \sqrt{2} \quad , \tag{4}$$

where g_W is the usual weak SU_{2L} coupling and $m_{T_b^*}$ is the rest mass of the T_b^* . Hence, the amplitude corresponding to Fig. 2 taken together with the axial current contribution is, using the free quark mode',

$$A(\textcircled{H} \to \bar{T}_b + X) = \frac{iG_F}{\sqrt{2}} \bar{u}_{f_1} \gamma^\mu (1-\gamma_5) v_{f_2} \frac{M_W^2}{M_W^2 - Q^2} \left(g_A \left(\frac{E_{\bar{T}_b} + m_{\bar{T}_b}}{2E_{\bar{T}_b}} \right) \epsilon_{\textcircled{H}\mu} \right.$$
$$\left. + \frac{i g_V}{2E_{\bar{T}_b} m_{\textcircled{H}}} \frac{m_{T_b^*}^2}{(m_{T_b^*}^2 - Q^2)} \epsilon_{\mu\alpha\beta\gamma} \epsilon_{\textcircled{H}}^\alpha P_{\bar{T}_b}^\beta P_{\textcircled{H}}^\gamma \right) \tag{5}$$

where the weak vector and axial charges g_V and g_A are taken to be 1 here, G_F is the Fermi constant, M_W is the W_μ^+ rest mass and $m_{\bar{T}_b(\textcircled{H})}$ is the rest mass of the $\bar{T}_b$ ($\textcircled{H}$) . Entirely standard manipulations may be used to see that, for $m_t \cong 40$ GeV, (5) yields

$$\Gamma(\textcircled{H} \to \bar{T}_b + X', T_b + X) \cong 17.4 \text{ KeV} \tag{6}$$

which represents a discrepancy of a factor greater 10 when compared with the non-relativistic potential model result (3) .

Now, the vector dominance ansatz, taken together with the free quark model, is obviously at best an approximation, since it treats the T_b^* as a point-particle, for example, whereas the Q which are involved in Figs. 1 and 2 clearly probe the distances well-within the interior of the T_b^*. But, clearly, (6) indicates that the large value of $|\vec{Q}|$ compared to the b rest mass and to the typical momenta in the T_b^* wavefunction may cause relativistic corrections to be important in $\textcircled{H} \to T_b^{(*)} + X, \overline{T}_b^{(*)} + X'$. Accordingly, we turn next to the method of Lepage and Brodsky - a manifestly relativistically invariant bound-state methodology.

The method of Lepage and Brodsky is based on the diagrams in Fig. 3. The respective amplitudes, to leading order in the Lepage-Brodsky expansion, are easily obtained when one follows the rules in Ref. 3. For example, for $\textcircled{H} \to \overline{T}_b + X'$, we have the amplitude

$$A(\textcircled{H} \to \overline{T}_b + X') = 4 i g_s^2 C_F \frac{G_F}{\sqrt{2}} \left(\frac{M_W^2}{M_W^2 - Q^2} \right) a_{\textcircled{H}} a_{\overline{T}_b} m_{\textcircled{H}} \Big\{ g_A F_{\parallel} P_{\overline{T}_b \nu} \epsilon_{\textcircled{H}} \cdot P_{\overline{T}_b}$$
$$+ g_A F_{\perp}^{(1)} \epsilon_{\textcircled{H} \nu} + i g_V F_{\perp}^{(2)} \epsilon_{\nu}{}^{\alpha\beta\gamma} \epsilon_{\textcircled{H} \alpha} P_{\overline{T}_b \beta} P_{\textcircled{H} \gamma} \Big\} \bar{u}_{f_1} \gamma^{\nu} (1 - \gamma_5) v_{\bar{f}_2} \tag{7}$$

where g_s is the QCD coupling constant and the form factors $a_{\textcircled{H}} a_{\overline{T}_b} F_{\parallel} C_F$ and $a_{\textcircled{H}} a_{\overline{T}_b} F_{\perp}^{(i)} C_F$ are given by the standard manipulations and have been recorded elsewhere[5] for reasons of length. Proceeding in this same manner for $\textcircled{H} \to \overline{T}_b^* + X', T_b^* + X$, we find, always using the standard methods,

$$\Gamma(\textcircled{H} \to \overline{T}_b^{(*)} + X', T_b^{(*)} + X) \cong 23\,KeV \tag{8}$$

for $m_t \cong 40$ GeV. Hence, we find a large probability, ~ 47%, that $\textcircled{H}$ SQD's lead to $T_b^{(*)} (\overline{T}_b^{(*)})$ mesons.

The large discrepancy between (8) and (3), which is a factor of ~ 15, leads us to try to isolate, then, its origin. We turn to this issue in the next section.

III. Comparison of the Approaches

In this part of our discussion, we would like to compare the three approaches to $\textcircled{H} \to T_b^{(*)} + X, \overline{T}_b^{(*)} + X'$ which we considered in the previous section. Our objective is to try to isolate the source of the discrepancy between the non-relativistic methods, as they are represented by (3), and the relativistic methods of the vector dominance lore and of Lepage and Brodsky, as they are represented by (6) and (8).

More precisely, the common feature of the vector dominance and Lepage-Brodsky approaches to the processes $\textcircled{H} \to \overline{T}_b^{(*)} + X'$ is that there is no severe suppression in the effective wavefunction for the b quark in Fig. 3 because its typical momentum is ~ 13 GeV. On the other hand, the non-relativistic wavefunction used to compute $I_{overlap}$ in (2) is highly damped at such values of $|\vec{Q}|$ because the typical momentum inside the $\overline{T}_b^{(*)}$ is $\stackrel{<}{\approx} .9$ GeV. Thus, we would like to quantify this by comparing the behaviors of the wavefunctions, at $|\vec{Q}| \sim 13$ GeV, of the typical QCD potential model for $T_b^{(*)}$ and of the Lepage-Brodsky theory for $T_b^{(*)}$. We will use the Cornell model[6] for the QCD potential V(r) so that

$$V(r) = -4\alpha_s/3r + r/a^2 \tag{9}$$

with $\alpha_s \cong .168$, $a = 2.34$ GeV^{-1}, $m_b = 5.17$ GeV and $m_t = 40$ GeV, as usual, in this discussion. In this way, we find the reduced radial wavefunction $u(\rho)$ shown in Fig. 4 for the lowest orbital angular momentum L = 0 state, where $u(\rho)$ is related to the radial wavefunction $R(r)$ via

$$R(\vec{r}) = \frac{1}{\sqrt{4\pi}}\,\frac{1}{r}\left(\frac{2\mu}{a^2}\right)^{1/6} u\left(\left(\frac{2\mu}{a^2}\right)^{1/3} r\right) \qquad (10)$$

with $\mu = m_b m_t/(m_t+m_b)$ and $r = |\vec{r}|$. To obtain the respective Lepage-Brodsky wavefunction $\psi_{\text{Lepage-Brodsky}}(x_i,Q)$ in momentum space, we iterate the Fourier transform $\psi_{NR}(Q)$ of the wavefunction $u(\rho)$ against the Lepage-Brodsky kernel as we have illustrated in Fig. 5. In this way, we find the results for $\psi_{NR}(Q)$ and $\psi_{\text{Lepage-Brodsky}}(x_i,Q)$ listed in Table I. For completeness, we have also included in Table I the Q^2 dependence of the vector dominance model form factor effect, so that one can have a view of the type of relative Q^2 variation of the vertex in Fig. 2 in comparison with the Q^2 variation of the other approaches.

The results in Table I show that the key difference between the relativistic approaches and the non-relativistic approach is that, at the typical value of $|\vec{Q}|$ in Fig. 1, the relativistic wavefunctions are substantially larger than their non-relativistic analogue. In fact, the ratio of $\psi^2_{\text{Lepage-Brodsky}}/\psi^2_{NR}$ for $11\,\text{GeV} \lesssim |\vec{Q}| \lesssim 16\,\text{GeV}$ is $\sim$13-130, and, hence, is precisely of the right size to explain the difference between (3) and (8). We feel, therefore, that we have indeed isolated the key difference between the non-relativistic and relativistic approaches to $\Theta \to T_b^{(*)} + X, \bar{T}_b^{(*)} + X'$. Presumably, experiment will ultimately discriminate between these two types of approaches.

V. Conclusions

In this discussion we have considered three approaches to $\Theta \to T_b^{(*)}+X, \bar{T}_b^{(*)}+X'$, the non-relativistic potential model approach, the vector dominance model approach and the approach of Lepage and Brodsky. We have found that the relativistic models, such as the latter two approaches, give a rate which is $\gtrsim$15 times the non-relativistic approach. We have traced this discrepancy to the behavior of the respective wavefunctions at squared momentum transfers ~ (13 GeV)^2. Thus, a detector such as the MkII (or SLD) at the SLC may be able to discriminate between the two types of predictions in the not-too-distant future.

Acknowledgements

The author is grateful to the members of the MkII SLC Toponium Physics Working Group for many fruitful discussions on the material in the text. The author would also like to acknowledge fruitful discussions with I. I. Y. Bigi, S. J. Brodsky and A. Schwarz.

References

1. D. Cline, talk presented at SLAC, June, 1986
2. I. I. Y. Bigi and H. Krasemann, Zeit. fur Phys. C7, 127 (1981) and references therein.
3. G. P. Lepage and S. J. Brodsky, Phys. Rev. D22, 2157 (1980).
4. See, for example, S. Gusken et al., SLAC-PUB-3580, 1985, and references therein.
5. B. F. L. Ward, University of Tennessee preprint, 1987, in preparation.
6. E. Eichten et al., Phys. Rev. D21, 203 (1980).

Table I

Comparison of the Three Approaches

Q(GeV)	$\psi_{NR}(Q)$	$\psi_{Lepage-Brodsky}(x_i, Q)$	$m^2_{T_b^*}/(m^2_{T_b^*} - Q^2)$
1	1.34	.884	1
6	5.25×10^{-3}	.0387	1.02
11	1.685×10^{-3}	.0191	1.06
16	-4.48×10^{-3}	.016	1.14

Figure Captions

1. $\textcircled{H} \to \bar{T}_b^{(*)} + f_1 + \bar{f}_2$ where $\binom{f_1}{f_2}_L$ is a SU_{2L} weak doublet.
2. Vector-dominance model for $\textcircled{H} \to \bar{T}_b + f_1 + \bar{f}_2$ where $\binom{f_1}{f_2}_L$ is a SU_{2L} weak doublet.
3. Lepage-Brodsky approach to $\textcircled{H} \to \bar{T}_b^{(*)} + f_1 + \bar{f}_2$, where $\binom{f_1}{f_2}_L$ is a weak SU_{2L} doublet. G denotes a gluon in our analysis.
4. Cornell model reduced radial wavefunction for $T_b^{(*)}$. $u(\rho)$ is normalized to unity: $\int_0^\infty d\rho\, u^2(\rho) = 1$.
5. Lepage-Brodsky equation for $\psi(x_i, Q)_{\text{Lepage-Brodsky}}$, where we use the non-relativistic wavefunction as approximate input.

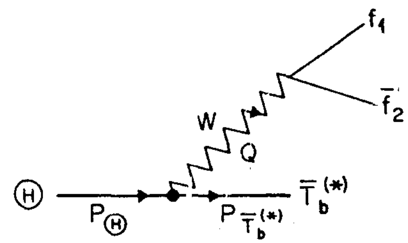

FIG. 1

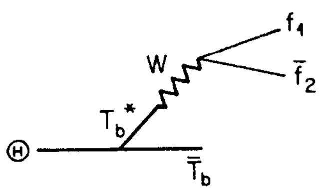

FIG. 2

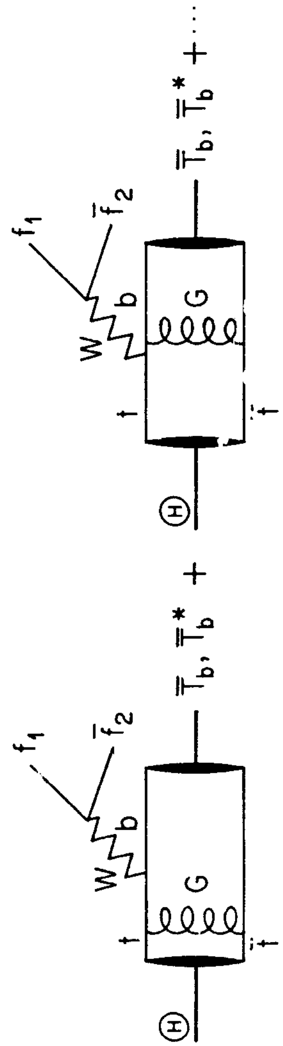

FIG. 3

REDUCED RADIAL WAVEFUNCTION
FOR T_b IN THE CORNELL MODEL

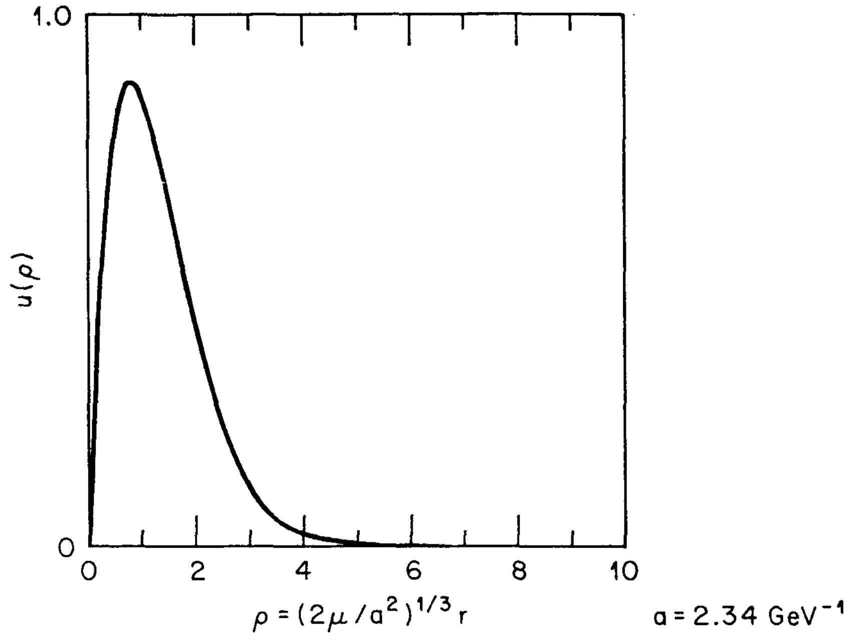

FIG. 4

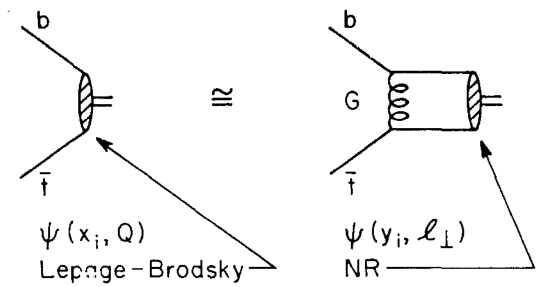

FIG. 5

MARK II/SLC–Physics Working Group Note # 4–6

AUTHOR: Hartmut F.-W. Sadrozinski*

DATE: May 18, 1987

TITLE: View from the Top(onium)

---

1. Introduction

Because of the large mass of the top quark, physics at the toponium resonance Θ will be very exciting and very different from the lower mass vectors J/ψ and Υ.[1] The mass of toponium will also determine at which Collider facility toponium physics will be carried out : for $m_\Theta < 75$ GeV TRISTAN, for 75 GeV$< m_\Theta < 100$ GeV SLC and LEP and for 100 GeV $< m_\Theta <$ 200 GeV LEP II.

As discussed below more in detail, other parameters besides the CM energy will be important: the luminosity and the energy spread of the beams. The CERN workshop on LEP Physics[2] has devoted a large section to toponium physics under the assumption that data samples of $10^5\Theta$ events might be ultimately accumulated.

In the framework of the MARK II/SLC Physics Workshop, we investigated toponium physics topics which could be relevant in the early running of SLC: the duration of a toponium run and the luminosity will be limited and basically we confined ourselves to physics with 1000 toponium events. At a luminosity of $\mathcal{L} = 10^{30}$ cm^{-2}sec^{-1} and an energy spread of $\sigma_{E_{CM}} = 0.0008E_{CM}$ this could be accomplished in 3 months. The physics topics relevant to such a small data sample are discussed in the second part. The third part will be devoted to toponium searches. We conclude with a critical assessment of our assumptions.

2. Physics at Toponium

Even with a small data sample there are several crucial measurements which can be proposed at toponium Θ but not at the Z_0. They have been described in detail in Workshop Notes and discussed by F. Porter at the Granlibakken meeting in September, 1986.[3]

---

* For the TOPONIUM Group of the MARK II/SLC Physics Workshop F.Porter, Z.Li, B.Ward, A.Seiden, F.Gilman, P.Franzini, A.Peterson

2.1. Higgs Search[4]

The process to detect a standard Higgs H^0 is the Wilczek mechanism $\Theta \to \gamma H^0$. For toponium masses m_Θ of about 70 to 80 GeV and small Higgs masses m_H it has a branching ratio of 2-3 %, not including potentially large first order corrections. The signal, a monochromatic isolated photon, has little background for m_H between about 10 GeV and 50 GeV and would yield about 15 photons over background of 4 for 1000 Θ events.

2.2. Determination of the K–M matrix element $|V_{tb}|$ to 30%[5]

At toponium the semileptonic width of the decay $t \to be\nu$ can be determined from the total width $\Gamma_{tot} = \frac{\Gamma_{ee}}{B_{ee}}$ and the branching ratio $B(t \to be\nu)$, and is related to the K–M matrix element $|V_{tb}|$:

$$\Gamma_{t\to be\nu} = G_F^2 m_t^5 f\left(\frac{m_b}{m_t}\right) |V_{tb}|^2$$

A 20%–30% measurement of $|V_{tb}|$ should be possible with 1000 Θ events, which would be interesting in the case of 4 generations and a larger than Cabibbo like mixing between t and b'.

2.3. Charge of a New Quark[6]

The onium rate of a new quark is determine both by its charge and by its vector coupling to the Z_0. This means that if a new quark is found, the rate into toponium/bottonium can in most cases reveal its charge. For example, far away from the Z_0 the rate for a quark of charge 2/3 is a factor 4 larger than for a charge 1/3 quark. If, on the other hand, one wants to determine the charge of a new quark on the Z_0, the difference of the rates is less pronounced. In addition the threshold factor of a heavy quark reflects the uncertainty in the mass determination into uncertainties in the predicted rate. One might have to measure the lepton asymmetry or the specific momentum spectrum to distinguish between a new quark with $\frac{2}{3}$ charge and one with $\frac{1}{3}$ charge.

2.4. Quark Potential[3]

The splitting of the lower lying triplet S states of toponium depends strongly on the model for the quark potential.

2.5. QCD in Weak Decays[7]

There are QCD predictions that weak toponium decays lead to T_b mesons and to Υ decays. Because the single quark decay (SQD) of toponium is of the order 20–30% for $m_\Theta \simeq$70–80 GeV, these QCD models could conceivably be tested at toponium.

3. Toponium Search

3.1. Event Rates

The total cross section integrated over the center of mass energy E is a constant related to the leptonic width Γ_{ee}:

$$\int \sigma_{tot} dE = \frac{6\pi^2}{m_\Theta^2}\,\Gamma_{ee}\ .$$

Because the width of the resonance Γ_Θ is smaller than the energy spread of the beam $\sigma_{E_{CM}}$, the counting rate N depends on both the luminosity $\mathcal{L}$ and the energy spread :

$$N = \sigma_{peak} \cdot \mathcal{L} = \frac{6\pi^2}{\sqrt{2\pi}}\,\frac{\Gamma_{ee}}{m_\Theta^2}\,\frac{\mathcal{L}}{\sigma_{E_{CM}}}\ .$$

We have assumed $\mathcal{L} = 10^{30}$ cm^{-2} sec^{-1} and $\sigma_{E_{CM}} = 0.0008 \cdot E_{CM}$, but we have come to realize that these requirements will be hard to meet during MARK II's stay at SLC.[8]

3.2 Scan Strategies

Depending on the mass m_t of the top quark, we distinguish between 3 different mass regimes:

3.2.1. $m_\Theta > m_Z + 2\Gamma_Z$

If toponium is heavier than the Z_0, no direct observation will be possible and we leave it as a challenge to Working group # 1 to extract the top mass from radiative corrections.[9]

3.2.2. $m_Z - 2\Gamma_Z < m_\Theta < m_Z + 2\Gamma_Z$[10]

If the mass of toponium coincides with the Z mass, interference effects will be showing up which can be used to determine the mass of toponium to the accuracy of the energy spectrometer. As pointed out by F. Porter,[6] one would scan with steps of $\sqrt{2}\sigma_{E_{CM}}$ across the Z_0 resonance which with $\sigma_E = 74$ MeV means 100 steps between $E_{CM} = M_Z - 2\Gamma$ to $M_Z + 2\Gamma$. The largest deviation from smooth shape of the Z resonance are 3–4%, and one day of running gives a 2% measurement. This scan would require an excellent monitoring of the luminosity to a fraction of a percent.

In this case there would be no open top dacays of the Z_0 and the interference effects would lead to the discovery of top. The physics of toponium would be dull because it will be doninated by standard Z_0 physics because of the $Z_0 - \Theta$ mixing.

3.2.3. $m_\theta < m_Z - 2\Gamma_Z$

If toponium is below the Z_0, a search will entail a continuum scan. The size of the toponium signal in events/day is compared to the background from udscb continuum in Fig. 1.[3] We will assume that the top quark has been discovered on the $Z_0$and the top mass is known to ± 1 GeV. If $m_\Theta = 70$ GeV we need about $1\frac{1}{2}$ day per scan point and about 25 steps to cover 2 GeV. The total scan would take 40 days. The counting rate per day as function of E_{CM} is shown in Fig. 2a. For $m_\Theta = 80$ GeV, the signal/noise gets poorer and we need about 5 days/scan point (Fig. 3a). For 22 steps, this means 100 days. For larger toponium masses we are running out of running time. After finding $\Theta(1S)$ the mass of the $\Theta(2S)$ can be estimated with ones favorite potential model and a miniscan done for it. At $m_\Theta = 80$ GeV the Richardson potential predicts 0.9 GeV for the $\Theta(1S) - \Theta(2S)$ mass difference while the "V_T" potential predicts 0.5 GeV for the same mass difference.

3.2.4. Effect of the SQD on Scans

The single quark decay of toponium (SQD) has unique signatures : while the quark-anti quark events have a multiplicity of 2.5, the SQD events have a mean multiplicity of 4.2. We can use this fact and shape parameter like aplanarity, sphericity, thrust, and isolated leptons to distinguish between SQD events from toponium and $q\bar{q}$ events from the continuum background.

Our philosophy has been to use two-dimensional cuts in shape parameters. This is illustrated in Fig. 4 where the aplanarity (APL) *vs.* thrust (THR) is shown for SQD events in Fig. 4a and for $q\bar{q}$ events in Fig. 4b. The indicated cut at (APL > 0.04 or THR < 0.82) leaves about 80% of the SQD event and only 15% of $q\bar{q}$ events. In similar fashion one cuts in two dimensions on sphericity SPH and thrust THR: THR < 0.9 or SPH > 0.1 . If we require additionally that the event contains at least 4 jets, 65% of the SQD events survive while only 3% of the $q\bar{q}$ background are kept. With these efficiencies the rates/day for a toponium mass of $m_\Theta = 70$ GeV is shown in Fig. 2b and for $m_\Theta = 80$ GeV in Fig. 3b. In both cases the signal/noise improved drastically but the counting rate dropped resulting in about the same statistical significance for the SQD search as for the measurement of the total rate. The observation of the SQD decays will thus confirm the existence of toponium .

6. Conclusion

In order to propose a physics program on toponium with the MARK II at SLC (if the toponium mass is in the SLC range), the performance of the machine has to be improved , such that, for example, the luminosity is $\mathcal{L} \geq 10^{30}$ cm^{-2} sec^{-1} and the energy spread $\sigma_{E_{CM}} \leq 0.0008 E_{CM}$. Then a search for toponium would take between 1 month and 3 months. An additional run of 3 months would yield 1000 events for toponium physics.

It will depend on the performance of the SLC whether SLD, LEP and/or TRISTAN will have all the fun with toponium.

REFERENCES

1. E. Eichten, Proc.of the XII SLAC Summer Institute, SLAC (1984)
2. Physics at LEP, CERN 86-02
3. F. Porter, Proceedings of the Second MarkII Workshop at Granlibakken, MarkII/SLC Note # 4-02
4. H.F.-W. Sadrozinski, MarkII/SLC Note # 4-04
5. F. Gilman and H.F.-W. Sadrozinski, MarkII/SLC Note # 4-03
6. F. Porter, MarkII-SLC Physics Note #4-01
7. B. Ward, These Proceedings, MarkII/SLC Note # 4-05
8. B. Richter, these Proceedings.
9. P. Rankin, these Proceedings.
10. P. Franzini and F. Gilman, Phys.Rev. D 32, 237 (1985)

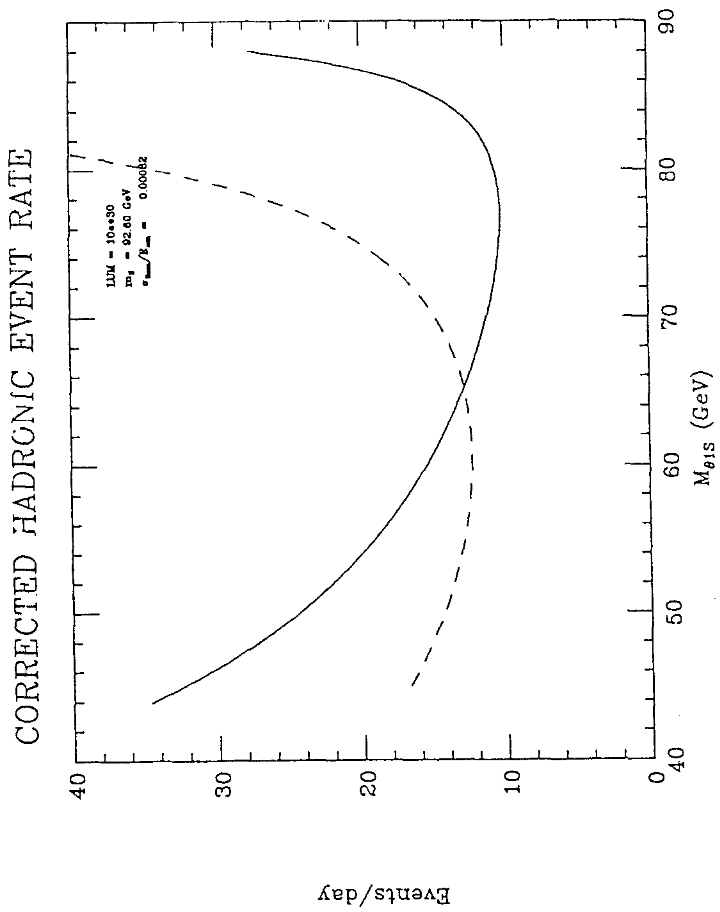

Fig. 1. Hadronic event rate for toponium (solid curve) and *udscb* continuum (dashed curve). Radiative corrections are applied.

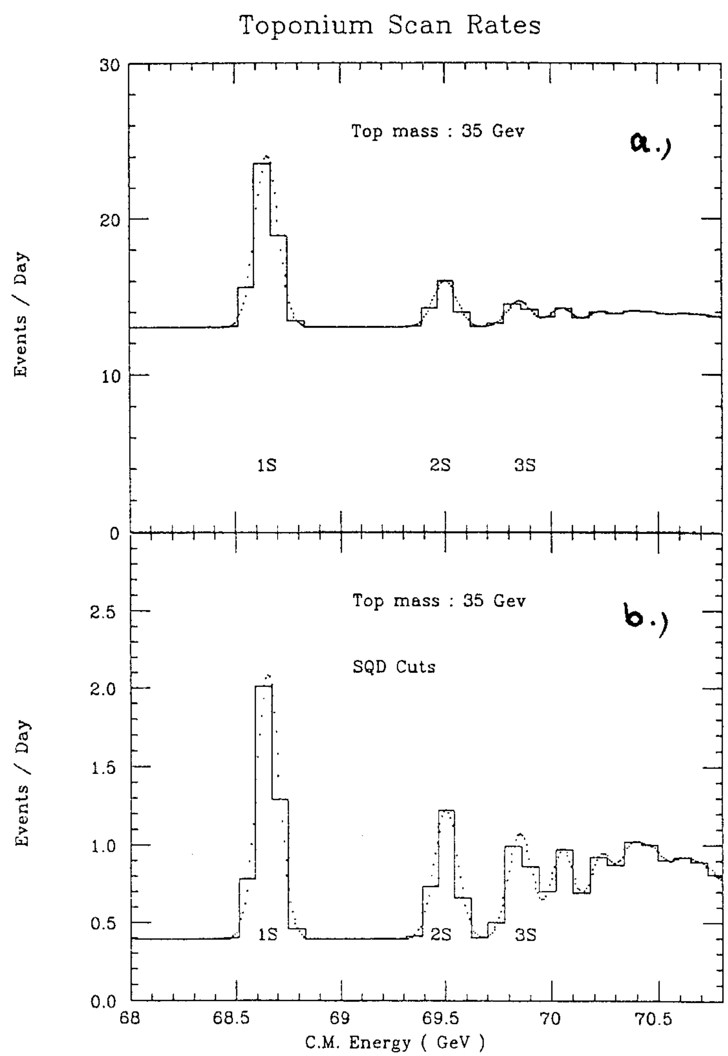

Fig. 2. Hadronic event rate per day for toponium search at $E_{CM} = 70$ GeV a.) all events , b.) after SQD cuts. The binsize is $\sqrt{2}\sigma_{E_{CM}}$.

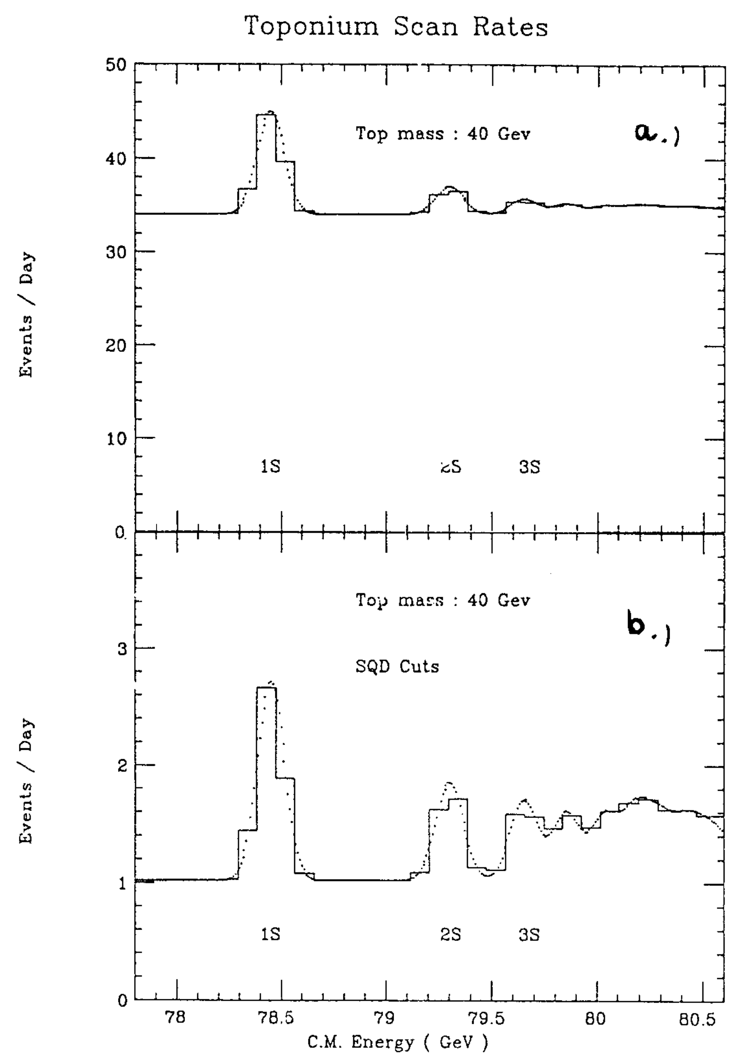

Fig. 3. Hadronic event rate per day for toponium search at $E_{CM} = 80$ GeV a.) all events , b.) after SQD cuts. The binsize is $\sqrt{2}\sigma_{E_{CM}}$.

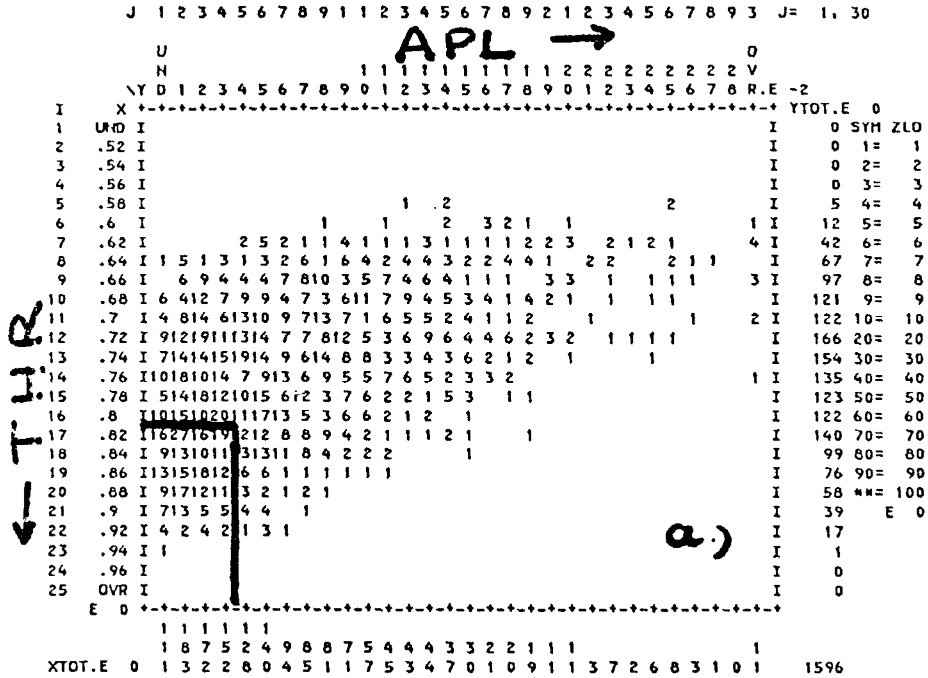

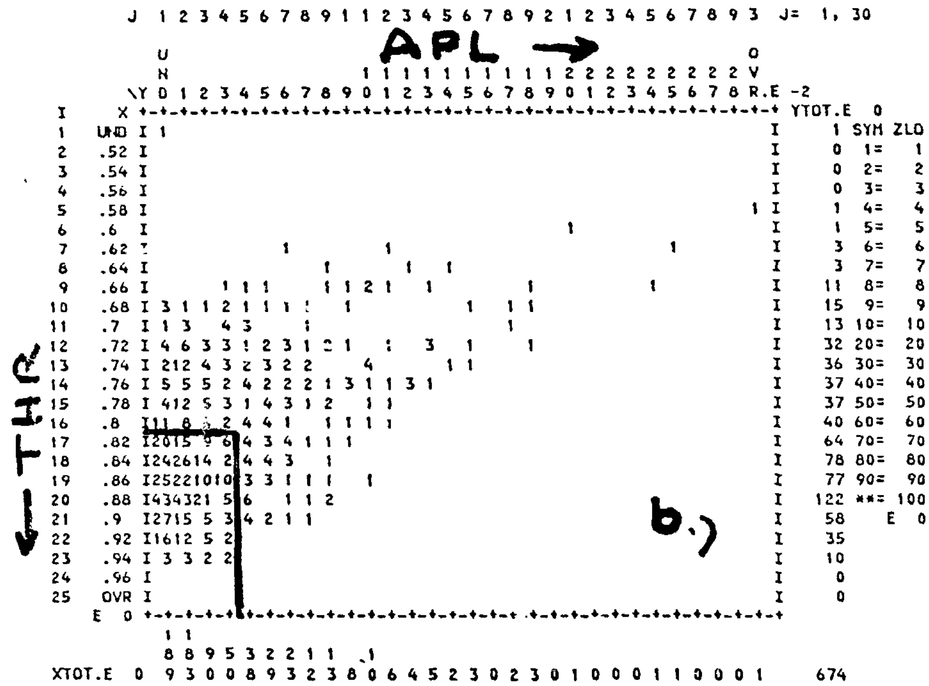

Fig. 4. Aplanarity (APL) vs thrust (THR) for a.) SQD events and b.) $q\bar{q}$ events. The cuts are indicated.

Mark II/SLC-Physics Working Group Note # 5–2

AUTHOR: Spencer Klein

DATE: April 9, 1987

TITLE: Detection and Identification of (Long Lived) Neutral Particles

---

This report summarizes work done by the Mark II/Upgrade Working Group on long lived neutral particles. The active members of the group were Gerry Abrams, Gerson Goldhaber, Spencer Klein and Alan Weinstein, aided by a group of theorists, most notably Bob Cahn.

The group explored a variety of models which postulate the production of one or more neutral particles. We focused on models where the neutrals were long lived, producing separated vertices. Most of the work was based on a model of neutral heavy lepton pair production, but much of it could be easily adapted to other models of long lived particle production.

The topics discussed are: physics models, triggering problems, tracking and reconstruction difficulties, backgrounds, and neutral heavy lepton identification.

1. Physics Models

The model most actively considered was that of neutral heavy lepton (L^0) production and decay. L^0 phenomenology has been considered by many authors[1,2]

L^0's are produced at SLC in the reaction $Z^0 \rightarrow L^0\overline{L}^0$. The expected branching ratio for this decay is roughly 6% times a mass dependent threshold factor: $(\beta/4)(3+\beta^2)$. For 1000 produced standard model Z^0, there are

Mass	$N(L^0\overline{L}^0)$
5 GeV/c^2	60
20 GeV/c^2	52
40 GeV/c^2	27

So, a L^0 search is something that can be done with a small number of Z^0's.

The simplest L^0 model postulates a new lepton doublet (one charged, one neutral). If the L^0 is the lighter of the two, it is stable, and will only be detectable indirectly via neutrino counting experiments. If the charged lepton is lighter, the L^0 decays into l^-W^+. The l^- is stable, and may be identifiable by stable particle searches. Alternatively, the decay topology of 2 stable penetrating particles plus two decaying W's will look like two muons plus two W's.

The standard model may be easily extended slightly to allow mixing with one or more of the known leptons. Theory gives us no clues as to the size of this mixing. However, the size of the mixing angle determines the L^0 lifetime. The lifetime is

$$\tau_{L^0} = \tau_\mu\left(\frac{m_\mu}{m_{L^0}}\right)^5 \frac{Br(L^0 \rightarrow l^-\nu e)}{|U_{e4}|^2}$$

where $|U_{e4}|$ is matrix element which mixes the L^0 and electrons. These decays can be found by searching for separated vertices. Figure 1 shows a typical event; a separated vertex is visible. The mixing angle can be found from the measured L^0 lifetime, mass and branching ratio. A separated vertex search at PEP yielded a negative result[3] . Since the detector size is constant, such at SLC a similar search will cover a similar region, but extending to higher masses at smaller mixing angles. Figure 2 shows the limit for $|U_{e4}|$ set by the PEP search, along with results from other types of searches for L^0. The region which can be searched at SLC is also shown.

O(10) grand unified theories suggest another type of L^0 decay. In it, a weak isospin singlet L^0 will mix with one of the three generations via the mass matrix:

$$\begin{pmatrix} 0 & \mu \\ \mu & M \end{pmatrix}$$

where μ is the mass of one of the known charged lepton and M is the mass of the L^0. This gives the light neutrinos a mass of μ^2/M. In this theory, there is no GIM mechanism, so the L^0 can decay via the flavor changing neutral current. In that case, it can also be produced via a flavor changing neutral current: $Z^0 \rightarrow L^0\nu_l$. The light neutrinos are invisible, so these decays appear as monojets. However, the rate for this process is suppressed by $|U_{l4}|^2$.

Many other L^0 models have been proposed. Space limitations do not allow a full discussion, but many of them are detectable using the techniques proposed here.

Other potential new physics can produce long lived neutral particles. Certain versions of supersymmetry can lead to long lived neutral particles. In particular, if the Higgsino is the lightest SUSY particle, the photino will decay via $\tilde{\gamma} \rightarrow \gamma\tilde{H}$ and $\tilde{\gamma} \rightarrow ff\tilde{H}$[4] . The $\tilde{\gamma}$ lifetime is

$$\tau \sim 10^{-11}\left(\frac{1GeV/c^2}{m_{\tilde{\gamma}}}\right)sec$$

so at SLC separated vertices should be detectable for $m_{\tilde{\gamma}} < 3GeV/c^2$.

will produce separated vertices. Because of the large boost, and the tiny opening angle ($\approx$ .01 degree), the two electron tracks will probably not be resolvable as two separate tracks. Instead, they will appear as a single, doubly ionizing track, which deposits a large amount of energy in the calorimeter. The lifetime can be found by looking for tracks like this which appear to start partway out in the drift chamber.

2. Triggering

L^0 decays involve low multiplicities and separated vertices, both of which can provide a challenge to the Mark II trigger. There are two independent triggers which are for L^0 decays; the total energy trigger and the charged particle trigger.

The energy trigger is best for detecting final states involving electrons, which deposit most of their energy into the calorimeter. For L^0 decays, the energy threshold is relatively unimportant, since the particles produced have high momenta. The solid angle is important, however, so it is important to include the endcaps in the trigger. It would be useful to have a muon trigger to complement the electron trigger.

The charged particle trigger complements the energy trigger, detecting charged particle final states. Through a specialized pattern recognition processor, it searches for tracks which come from the vicinity of the interaction region. It is essentially 100% efficient for high multiplicity final states, which will not be considered further here. For low multiplicity states, consider the reaction

$$e^+e^- \to L^0\overline{L}^0 \to w^+x^-y^+z^-(\nu)$$

where energy is lost to one or more neutrinos.

The efficiency for triggering on this decay is a function of the radius of decay from the origin and the decay opening angle. These two variables are closely related to the particles mass and lifetime. We shall consider two L^0 lifetimes, 6.6 psec and 300 psec. The former is just long enough to be comfortably identifiable via secondary vertex techniques, while the latter will provide a real challenge to the trigger.

The trigger setup used at SLC will be determined by many factors. The most important of these is the background noise level; the trigger will be as loose as noise levels allow. To get an idea of the possibilities, we will consider 3 possible trigger setups with varying noise rejection capabilities:

High Noise Scenario
- 5/6 axial layers
- 3/5 stereo layers
- 1 TOF Layer

High Noise Scenario
- 5/6 axial layers
- 3/5 stereo layers
- 1 TOF Layer

Standard (ala PEP)
- 2/3 inner axial layers
- 2/3 outer axial layers
- 2/5 stereo layers
- 1 TOF Layer

Low Noise Scenario
- 1/3 inner axial layers
- 1/3 outer axial layers
- 1/5 stereo layers
- 1 TOF Layer

In all cases, a supercell is considered hit if three or more wires in it fired. All three cases are based on a two track requirement.

Table 1 shows the probability of a 4 pronged short lived (6.6 psec) $L^0\overline{L}^0$decay triggering for these three configurations, for 5, 20, and 40 GeV/c^2 L^0 masses.

Mass	$\gamma\beta c\tau$	Tight	Standard	Loose
5 GeV/c^2	18.5 mm	63%	65%	68%
20GeV/c^2	4.3 mm	79%	79%	82%
40GeV/c^2	1.2 mm	91%	89%	91%

Table I Triggering Probability for Short Lived L^0
Statistical Error $\pm 2\%$

All three triggers give similar results. This is because the trigger probability is mainly a function of solid angle; any particle within the active solid angle will trigger the detector with all three triggers. This solid angle is limited by the $\cos(\theta)$ limits of the drift chamber outer layers; the exact limit depends on how many layers are required in the trigger.

The triggering probability decreases for smaller L^0 masses. This is because, at smaller L^0 masses, the opening angle is small. If a low mass L^0 is produced at high $\cos(\theta)$, then it will disappear into the endcap, without producing a charged trigger. At higher masses, the larger opening angle spreads out the decay products, increasing the chance that 2 tracks will be in the active region.

Table II shows the $L^0\overline{L}^0$ triggering probability for long lived (300 psec) $L^0\overline{L}^0$ pairs. Also shown is the mean decay distance, $\gamma\beta c\tau$.

Mass	$\gamma\beta c\tau$	Tight	Standard	Loose	Tight Outer	Std. Outer
5 GeV/c^2	85 cm	28%	29%	42%	37%	50%
20GeV/c^2	20 cm	73%	72%	77%	71%	-
40GeV/c^2	5.8 cm	89%	89%	91%	84%	-

Table II - Triggering Probability for Long Lived L^0
Statistical Error ±2%

At the largest decay distances, the loose trigger has a significantly higher efficiency. This is because these decays occur far enough out in the drift chamber that tracks are lost because they miss many layers. To see what we can do about this problem, we consider two triggers which are designed to catch these decays. They are:

High Noise Scenario Long Lived Particle Trigger

- 3/3 outer axial layers
- 1/2 outer stereo layers
- 1 TOF Layer

Standard Noise Scenario Long Lived Particle Trigger

- 2/3 outer axial layers
- 1/3 outer stereo layers
- 1 TOF Layer

These triggers have a higher efficiency than their standard counterparts for long lived particles For shorter lifetimes, they are slightly less efficient. This is because, by requiring more hits in the outermost drift chamber layers, they slightly reduce active solid angle. Further, in many noise models, the noise is worst in the inner layers. In these situations, these triggers have excellent noise rejection.

The initial SLC trigger should resemble one of the three standard choices. However, there are many small changes being considered, some of which could affect these results. The most likely change is the TOF counters may be removed from the trigger. This would increase the trigger acceptance somewhat, because the TOF system has 4 holes in it for the drift chamber support fins. For the 5 GeV/c^2 short lived L^0, removing the TOF requirement increased the trigger acceptance about 2 %.

Another possible change would be to include the vertex chamber in the trigger. This will reduce the acceptance for tracks from long lived particles in three ways. Requiring vertex chamber hits will eliminate tracks from L^0 which decay outside the instrumented layers. The vertex chamber hits will allow the tracks to be projected back to the interaction region more accurately, reducing the acceptance for tracks whose projections miss the origin. Finally, this will reduce the number of trigger channels that can be used for outer stereo drift chamber layers, reducing our sensitivity in that region.

A third option would be to add one of the long lived particle triggers described above, in addition to the normal trigger. This would eliminate the bad effects of including the vertex chamber in the trigger. However, there are some technical difficulties in doing this.

3. Selection and Reconstruction

Alan Weinstein has studied the problems of reconstructing L^0 decays. These decays can be divided into two classes; high and low multiplicity. High multiplicity decays are those where one or both of the W's produced decays into a hadronic shower. Alan discussed the reconstruction of these decays at Granlibakken[6] .

Briefly, these events are selected by requiring at least 1 (or 2) high momentum leptons. The thrust axis is found. The event is divided into hemispheres, and each hemisphere is assumed to contain one L^0. Unfortunately, for the higher L^0 masses this can lead to particles being assigned to the wrong L^0. This probability varies from 0.3 % up to 20% as the mass varies from 10 to 40 GeV/c^2 .

These misassignments lead to poor mass resolution for the higher mass L^0, as Figure 3 shows. Figure 3a is a plot of 10 GeV/c^2 L^0 mass resolution, while Figure 3b shows 40 GeV/c^2 L^0 mass resolution.

The mass resolution may be improved somewhat by calculating a beam constrained mass, constraining the L^0 using $E_{beam} = E_{L^0}$ as a constraint. This compensates for the missing energy due to neutrinos, etc. Each calculated mass is scaled up by E_{beam}/E_{seen}. to compensate for this missing energy. Figure 4 shows the effects of this scaling; the 10 GeV/c^2 mass resolution is much improved and is now centered at the L^0 mass. The 40 GeV/c^2 mass resolution is also much improved, but still suffers from the effects of particles crossing into the wrong hemisphere.

Low multiplicity decays are reconstructed by a similar procedure. The thrust axis is found, and the event is divided up by hemisphere. The low multiplicity decays are defined by requiring exactly 2 oppositely charged particles in a hemisphere, where the highest momentum track is a lepton.

The efficiency for reconstructing these decays depends on several factors, among them the requirement that the highest momentum particle be a lepton. Figure 5 shows the reconstruction efficiency for one example, a 20 GeV/c^2 $\tau=$ 300 psec L^0 as a function of cos(θ). Because of the uncertainty in the production models, the absolute scale should be regarded as arbitrary. For higher L^0 masses, the plot is much flatter because of the larger opening angles. At smaller L^0 masses, the plot is box shaped, cutting off quickly at the edges of the effective tracking volume.

Another important parameter is the radius of the decay from the interaction region. A 5 GeV/c^2 L^0 with a 300 psec lifetime has $\gamma\beta c\tau$ of 85 cm, providing a good test of reconstruction. Figure 6 shows the reconstruction efficiency as a function of decay radius. The efficiency is constant out to a radius of 80 cm, and good out to 1 meter in radius. Figure 7 shows this in another way, plotting the number of reconstructed, efficiency corrected L^0 versus decay radius in the xy plane. The line through the histogram is an exponential fit. The decay lengths found are in generally good agreement with the generated distributions. Table III shows the decay lengths found in the exponential fits, compared with similar fits to the generated distributions.

Mass	Lifetime	$c\tau_{gen}$	$c\tau_{recon}$	Decay Length Resolution	Mass Resolution
5 GeV/c^2	6.6 psec	14 mm	13 mm	1.6 mm	.11 GeV/c^2
5 GeV/c^2	300 psec	532 mm	542 mm	1.6 mm	.25 GeV/c^2
20 GeV/c^2	6.6 psec	3.1 mm	3.5 mm	.76 mm	.27 GeV/c^2
20 GeV/c^2	300 psec	95 mm	137 mm	.76 mm	.34 GeV/c^2
40 GeV/c^2	300 psec	40 mm	41 mm	.31 mm	-

Table 3 - Decay Reconstruction Characteristics

Figure 8 shows the accuracy differently, plotting the reconstructed radius minus the monte carlo generated radius, fit to a gaussian plus a constant. The 5th column of Table 3 shows the widths of these peaks for the different samples. For the low masses, the vertexing accuracy is low because the opening angles are small. In the long lifetime cases, the peaks have large tails, because the charged tracks are tracked over a shorter distance, reducing tracking accuracy.

The reconstruction accuracy is a strong function of the individual decay points, since it depends heavily on the distance from the decay point to the nearest DAZM, and the accuracy of that DAZM. Thus, decays which occur in the vertex chamber will be found with the highest accuracy, while those in the main chamber or near the origin will be found less accurately.[7] Finally, the results for the 40 GeV/c^2

case should not be taken too seriously because the efficiency is very low, for reasons that will be discussed below.

The low multiplicity decays also give good mass measurements, since we can reconstruct the entire final state by repeating the mass scaling trick used in the high multiplicity sample. Figure 9 shows the reconstructed mass found by this procedure for a 20 GeV/c^2 generated mass. As before, this can be scaled up by E$_{beam}$/ E$_{seen}$, producing Figure 10. Figure 11 and 12 show similar plots for a 5 GeV/c^2 L^0. The final column in Table 3 shows the mass peak widths for the different cases. The relative error in the 5 GeV/c^2 short lived sample is large because it decays far out in the drift chamber, so that its decay products tracks have few DAZMs and are poorly measured.

This procedure fails completely at high L^0 masses, because the opening angles are so large that the division into hemispheres usually leads to a misassignment. Figure 13 shows an event where this occurs. The thrust axis is obvious, yet examination (and MCMADE) shows that the L^0 flight directions are almost perpendicular to it, as can be seen from the slightly displaced decay vertex. Figure 14 shows the mass plot for a 40 GeV/c^2 L^0 (not scaled by the beam energy). Here, however, only 4 prong events have been selected. No peak is visible. For 4 prong decays, we can get around this problem by calculating the invariant masses of all opposite sign combinations. Figure 14 shows this. A peak centered at 40 GeV/c^2 is seen. Unfortunately, since this method is limited to 4 prong events, it has inherently reduced efficiency.

4. Backgrounds

In considering backgrounds, we may divide $L^0\overline{L}^0$events into three types, depending on how the W decays.

1. $L^0\overline{L}^0 \rightarrow$ 2 leptons; 2 leptons
2. $L^0\overline{L}^0 \rightarrow$ 2 leptons; lepton + jet
3. $L^0\overline{L}^0 \rightarrow$ lepton+jet; lepton + jet.

Figure 1 was an example of a type 1 decay. The largest backgrounds for these decays are from $e^+e^- \rightarrow e^+e^-l^+l^-$ and possible new physics. The QED background is expected to be small since it is not enhanced by the Z^0 pole. Also, the QED background can be reduced by requiring missing momentum, which will suppress everything except $e^+e^-\tau^+\tau^-$.

The major backgrounds for type 2 and type 3 are similar, except that the type 2 decays will have a more unusual topology. Fig. 13 shows an example of a type 3 decay, while Fig. 16 is a type 2 decay. For both cases, the major backgrounds are heavy quark decays. For lighter L^0 masses, this could be the bottom quark; for heavier L^0 it is the top quark. The L^0 decays will be marked by an increased number of produced leptons. However, since lepton tagging is an important part of tagging both L^0 events and top quark events, the situation will be confused.

If type 1 and type 2 signals are found, they should signal the existence of Type 3 events. However, models that predict only Type 3 reactions will look a lot like heavy quark decay. The situation is further complicated by the fact that lepton tagging is an important tool in finding both reactions.

If the L^0 lifetime is long enough so that separated vertices can be found, these background should essentially disappear. We have seen that these separated vertex searches can find vertices out to a decay path of roughly 1 meter. The lower limit to these searches depends on backgrounds from quark decay, and beam movement, and the amount of data available. We can choose 1 mm (half the value used in the PEP search) as a safe estimate. Using this, figure 17 shows the region in mass - lifetime space that can be ruled out for pair production of neutral particles. The projected SLC search region in Figure 2 is derived from this.

5. Asymmetry

We have shown that we can measure the L^0 mass and, if it is long enough, the L^0 lifetime. However, to really establish the existence of a new neutral heavy lepton, more characteristics would be nice. One thing that would be nice to measure is the $L^0\overline{L}^0$asymmetry.

The asymmetry can be measured because the L^0 always decays into l^-W^+, while the $\overline{L}^0$ always decays to l^+W^-. So, in theory, the asymmetry can be measured by looking at the angle between the electron beam and the positive leptons. However, since the W's can also decay into leptons, either directly, or via heavy quark decays, the situation is complicated. Generally the leptons from the L^0 will have more energy than the leptons from the W decay. This is because the initial lepton and the W divide the available energy, and then the energy is divided again the W decay, reducing the amount available for a non-primary lepton. Unfortunately, this is only true statistically.

One simple approach is to only consider the highest momentum lepton. However, this leads to a wrong assignment about 20 % of the time. When this is coupled with the fact that the detected lepton direction differs from the original L^0 direction, we find that this approach is not good enough, and a more sophisticated approach is needed.

6. Conclusions

If neutral heavy leptons exist with a mass less than $m_Z/2$, they should be produced copiously at SLC. If they decay in the detector, then we can detect them, and measure their mass. If they live long enough to give a separated vertex, we can measure their lifetime.

If we don't find them, we can set limits over a wide range of masses and lifetimes. If the backgrounds are controllable, we can find L^0 down to zero lifetimes. If not, by searching for separated vertices, we can set limits over a wide range of lifetimes. Figure 13 shows the mass- lifetime limits that can be excluded by a separated vertex search, whether for a neutral heavy lepton or any other long lived particle.

If we do find $L^0\overline{L}^0$pair production, we must be careful, because these decays can mimic some heavy quark decays.

REFERENCES

1. F. Gilman, Comments Nucl. Part. Phys., 16, 231 (1986)
2. M.L. Perl, in Proceedings of the Santa Fe Meeting of the Division of Particles and Fields of the American Physical Society, ed. T. Goldman, World Scientific, 1984
3. C. Wendt *et al.*, SLAC-PUB-4177, January, 1987; submitted to Phys. Rev. Lett.
4. H. Haber, in Proceedings of the Thirteenth SLAC Summer Institute on Particle Physics, 1985, SLAC Report 296.
5. See, for example, K. Hagiwara and S. Komimiya, preprint KEK-TH 145/ KEK Preprint 86-95, January, 1987
6. A. Weinstein, Mark II/SLC-Physics Working Group Note 5-1, October 10, 1986.
7. None of this work used the vertex chamber or silicon strips; including these two subsystems will improve these results for short lived L^0.

FIGURE CAPTIONS

1. A $L^0\overline{L}^0$pair decaying to $\mu^-\mu^+\tau^+\pi^-$ plus neutrinos.
2. Limits on $|U_{e4}|^2$ from various sources. The potential SLC separated vertex search is also indicated. The limits for $|U_{\mu 4}|^2$ are similar.
3. Calculated invariant mass for (a) 10 GeV/c^2 and (b) 40 GeV/c^2 generated L^0 masses.
4. Scaled invariant masses for (a) 10 GeV/c^2 and (b) 40 GeV/c^2 generated The masses have been scaled up by $E_{beam}/E_{detect.}$. L^0 masses.
5. Efficiency as a function of cos(θ) for a 20 GeV/c^2 , 300 psec L^0.
6. Efficiency versus decay radius for a 5 GeV/c^2 , 300 psec L^0.
7. Reconstructed, efficiency corrected decay radius for a 5 GeV/c^2 , 300 psec L^0. The straight line is the result of an exponential fit.
8. Reconstructed decay radius minus monte carlo generated decay radius.
9. Reconstructed mass for 20 GeV/c^2 , 300 psec low multiplicity L^0.
10. Scaled mass for 20 GeV/c^2 , 300 psec low multiplicity L^0. The masses have been scaled up by $E_{beam}/E_{detect.}$.
11. Reconstructed mass for 5 GeV/c^2 , 6.6 psec low multiplicity L^0.
12. Scaled mass for 5 GeV/c^2 , 6.6 psec low multiplicity L^0. The masses have been scaled up by $E_{beam}/E_{detect.}$.
13. A 40 GeV/c^2 $L^0\overline{L}^0$decaying to $e^+e^-e^+$jet$^-$. Tracks 8 and 10 are from the first L^0, although they are in opposite thrust hemispheres. This can be seen because they form a separated vertex.
14. Reconstructed mass for 40 GeV/c^2 , 6.6 psec low multiplicity L^0. The mass was reconstructed by hemisphere
15. Reconstructed mass for 40 GeV/c^2 , 6.6 psec low multiplicity L^0. The mass was reconstructed by trying all oppositely charged pairs.
16. A 40 GeV/c^2 type 3 $L^0\overline{L}^0$decaying to lepton+jet;lepton+jet. Such a decay can mimic a top quark decay.
17. The mass-lifetime region that can be excluded for pair produced neutral particles by a Mark II/SLC search for separated vertices.

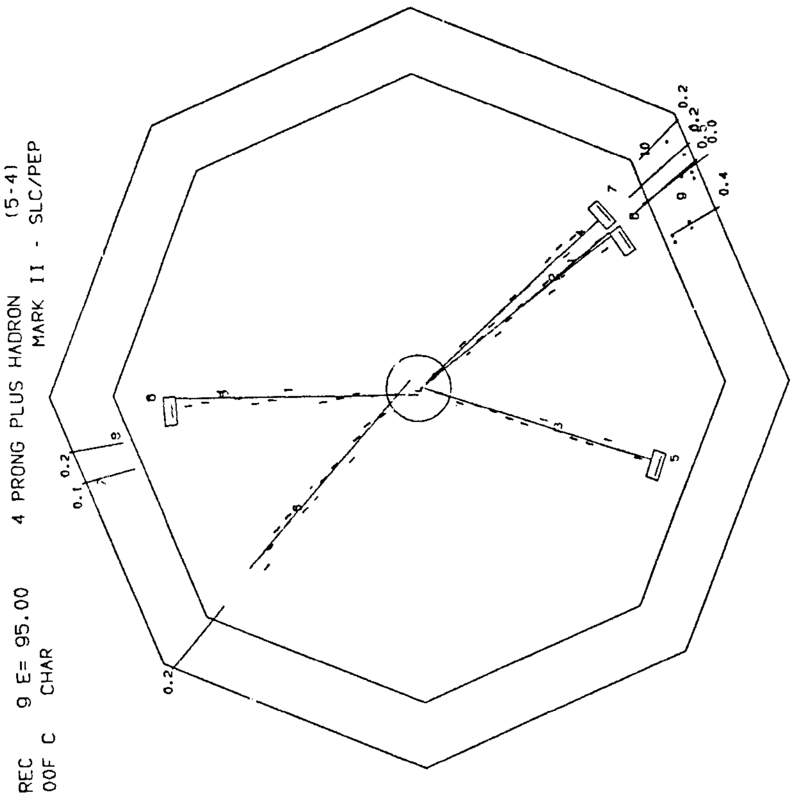

Figure 1 A $L^0\overline{L}^0$pair decaying to $\mu^-\mu^+\tau^+\pi^-$ plus neutrinos.

TRK	P	ELATOT	ID
1	6.9	0.5	PI-
2	10.2	0.0	PI+
3	18.3		PI-
4	7.9	0.2	PI+
5	38.9		MU+
6	14.1	0.2	PI-
7		0.1	G
8		0.2	G
9		0.4	G
10		0.2	G

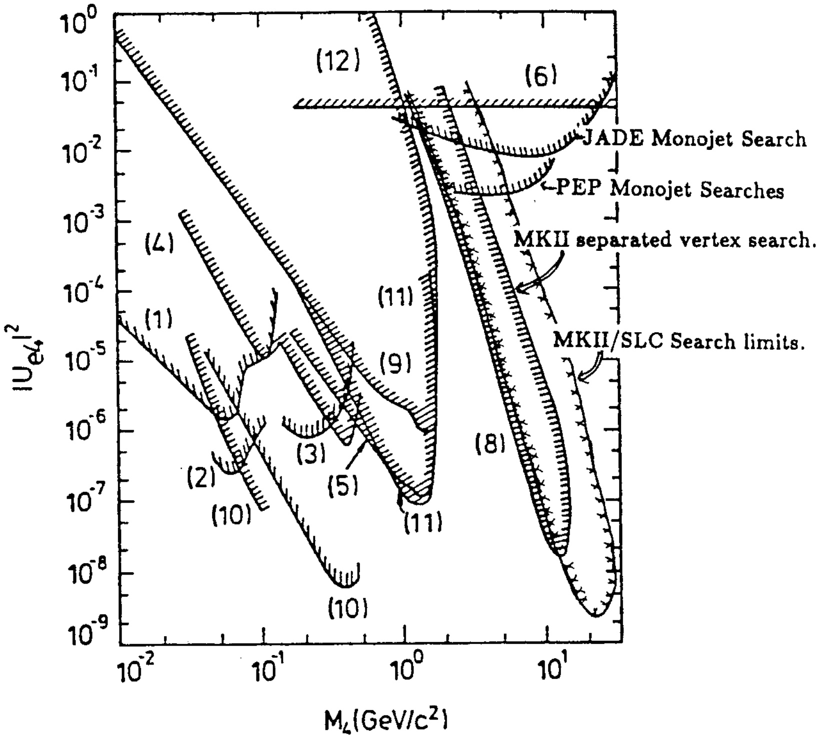

Figure 2 Limits on $|U_{e4}|^2$ from various sources. The potential SLC separated vertex search is also indicated. The limits for $|U_{\mu 4}|^2$ are similar.

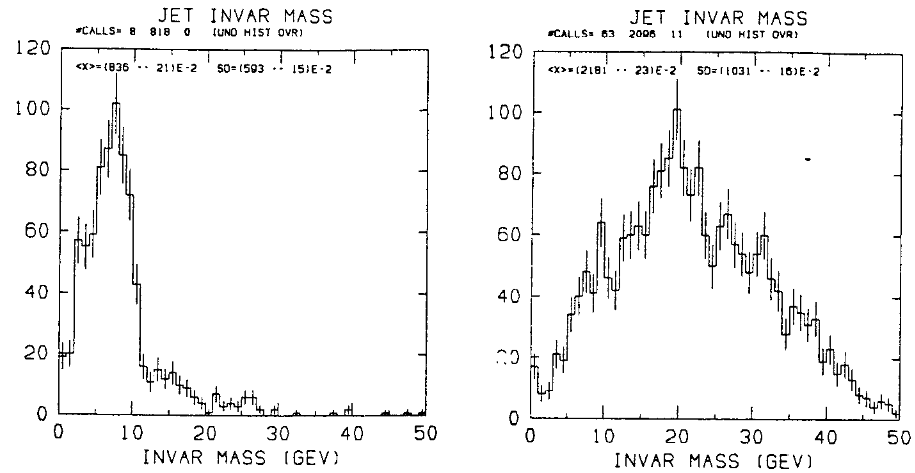

Figure 3 Calculated invariant mass for (a) 10 GeV/c^2 and (b) 40 GeV/c^2 generated L^0 masses.

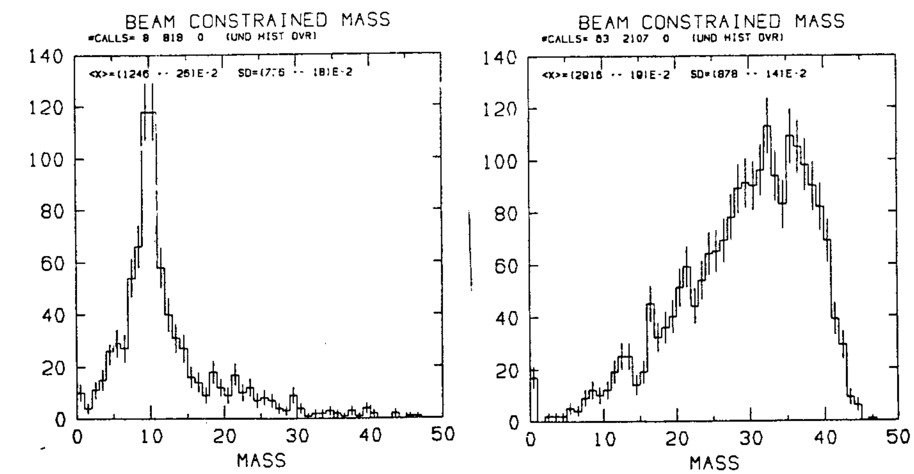

Figure 4 Scaled invariant masses for (a) 10 GeV/c^2 and (b) 40 GeV/c^2 generated L^0 masses.

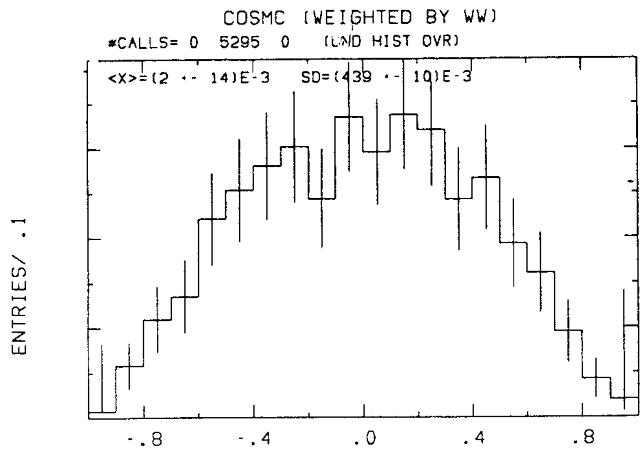

Figure 5 Efficiency as a function of cos(θ) for a 20 GeV/c^2 , 300 psec L^0.

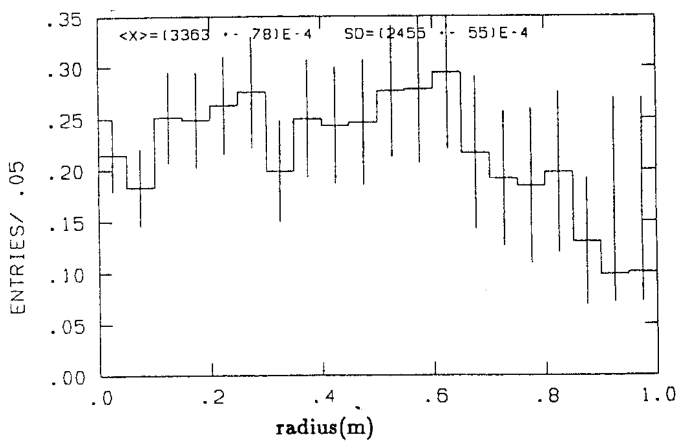

Figure 6 Efficiency as a function of decay radius for a 5 GeV/c^2 , 300 psec L^0.

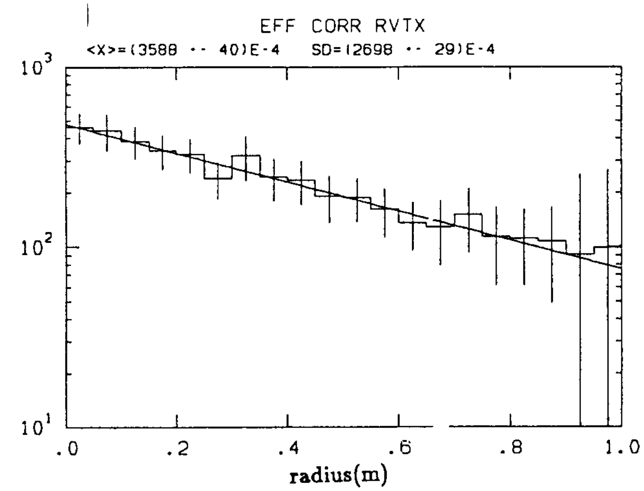

Figure 7 Reconstructed, efficiency corrected decay radius for a 5 GeV/c^2 , 300 psec L^0. The straight line is the result of an exponential fit.

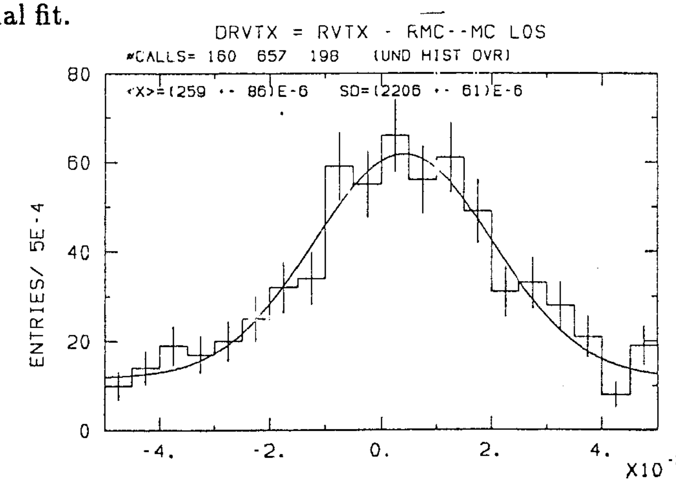

Figure 8 Reconstructed decay radius minus monte carlo generated decay radius for a 5 GeV/c^2 , 300 psec lifetime L^0.

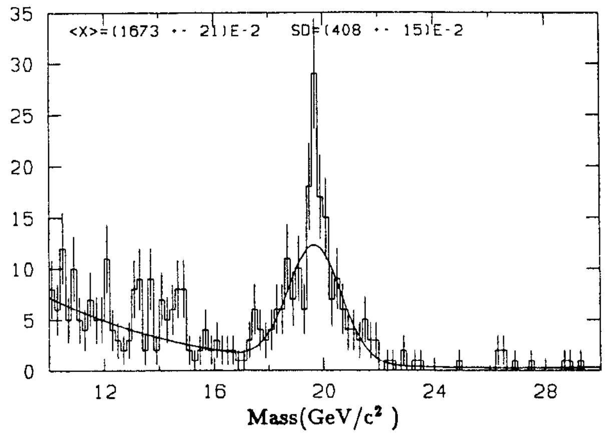

Figure 9 Reconstructed mass for 20 GeV/c^2 , 300 psec low multiplicity L^0.

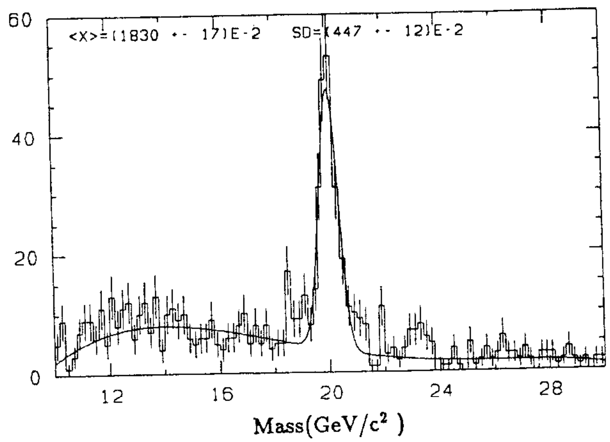

Figure 10 Scaled mass for 20 GeV/c^2 , 300 psec low multiplicity L^0.

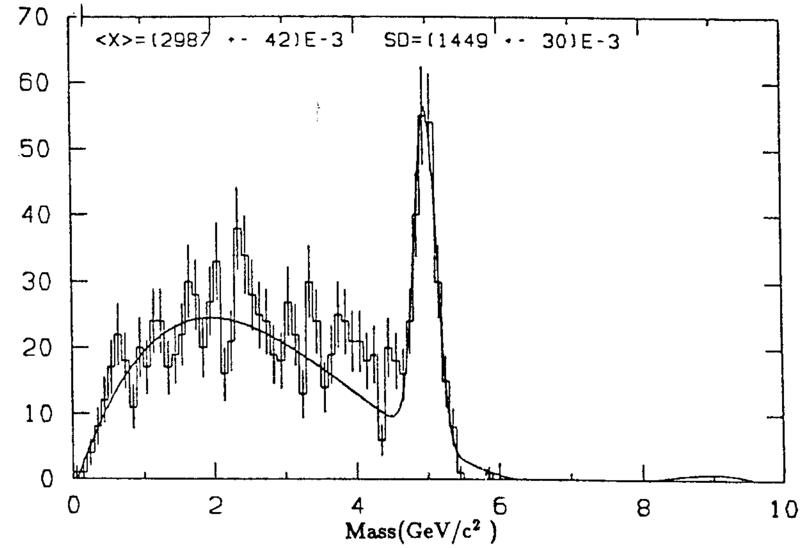

Figure 11 Reconstructed mass for 5 GeV/c^2 , 6.6 psec low multiplicity L^0.

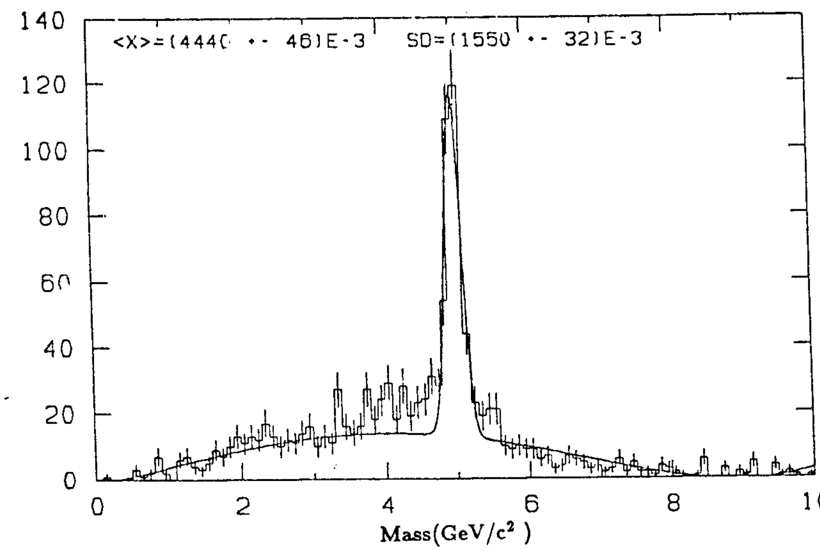

Figure 12 Scaled mass for 5 GeV/c^2 , 6.6 psec low multiplicity L^0.

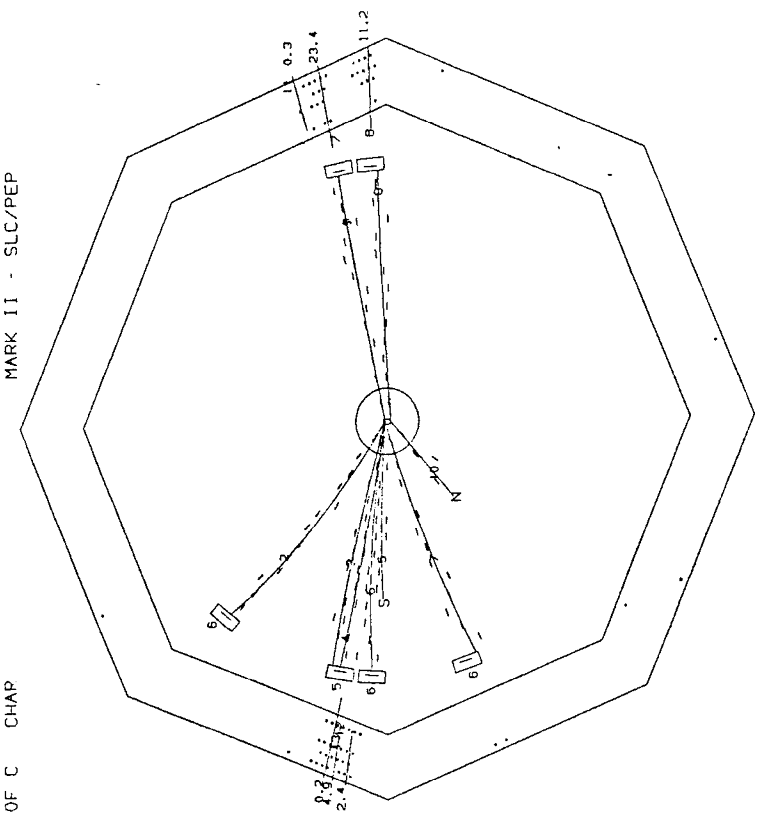

Figure 13 A 40 GeV/c^2 $L^0\overline{L}^0$ decaying to $e^+e^-e^+$jet$^-$. Tracks 8 and 10 are from the first L^0, although they are in opposite thrust hemispheres. This can be seen because they form a separated vertex.

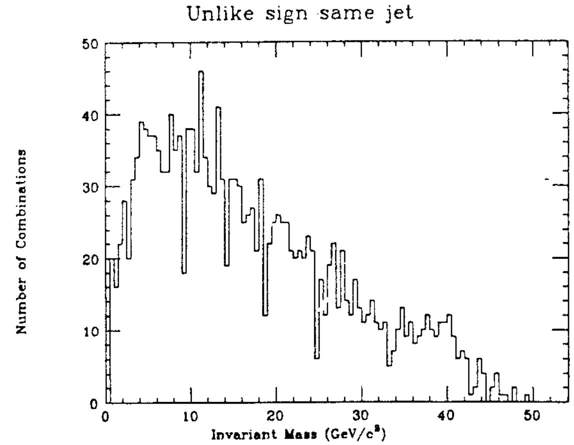

Figure 14 Reconstructed mass for 40 GeV/c^2 , 6.6 psec low multiplicity L^0. The mass was reconstructed by hemisphere.

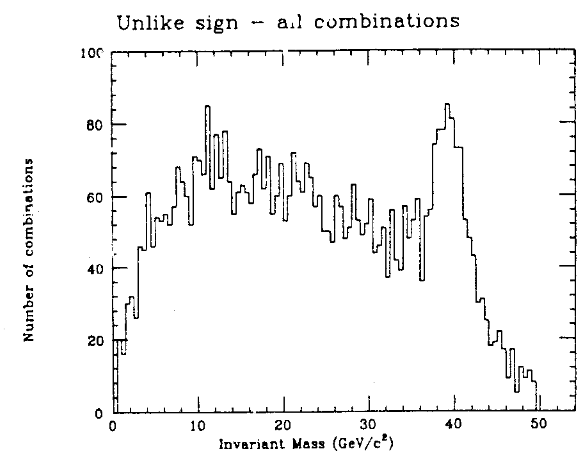

Figure 15 Reconstructed mass for 40 GeV/c^2 , 6.6 psec low multiplicity L^0. The mass was reconstructed by trying all oppositely charged pairs.

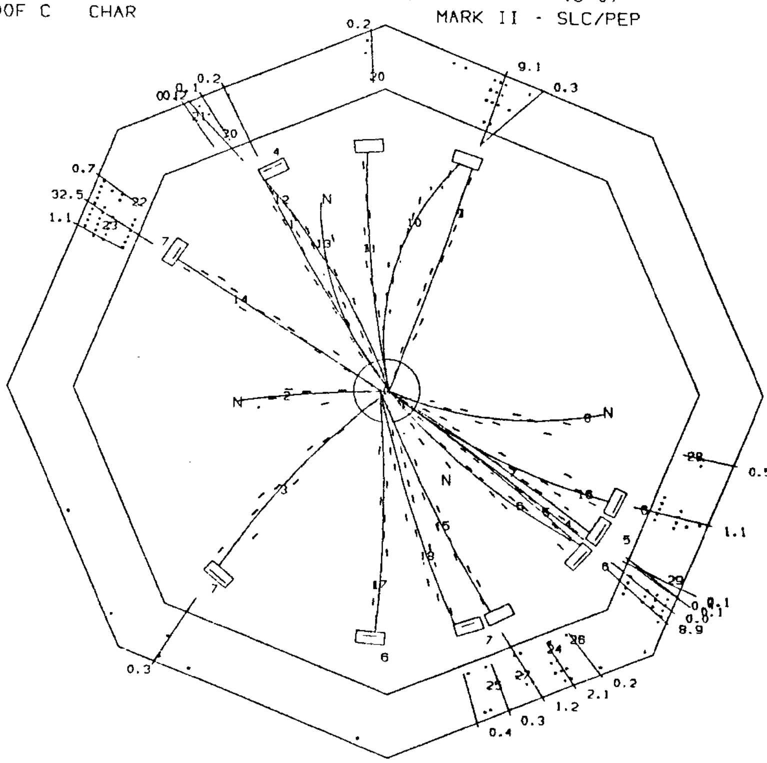

TRK	P	ELATOT	ID
1	1.8	0.2	PI+
2	2.0	0.2	PI-
3	0.8	0.3	K-
4	6.8	0.0	PI+
5	3.2	8.9	E+
6	0.7	0.1	PI-
7	3.9	0.1	PI+
8	0.5	0.1	PI-
9	9.1	9.1	E-
10	0.2	0.3	PI+
11	1.0		PI+
12	0.6	0.2	PI-
13	0.4	0.1	PI+
14	31.6	32.5	E+
15	1.4	1.2	E-
16	0.6	1.1	E-
17	1.3		P+
18	1.2		PI-
20		0.2	G
21		0.1	G
22		0.7	G
23		1.1	G
24		2.1	G
25		0.4	G
26		0.2	G
27		0.3	G
28		0.5	G
29		0.4	G
30		0.1	G
31		0.1	G

Figure 16 A 40 GeV/c^2 type 3 $L^0\overline{L}^0$ decaying to lepton+jet;lepton+jet. Such a decay can mimic a top quark decay.

Fig. 17 Limits for a separated vertex search

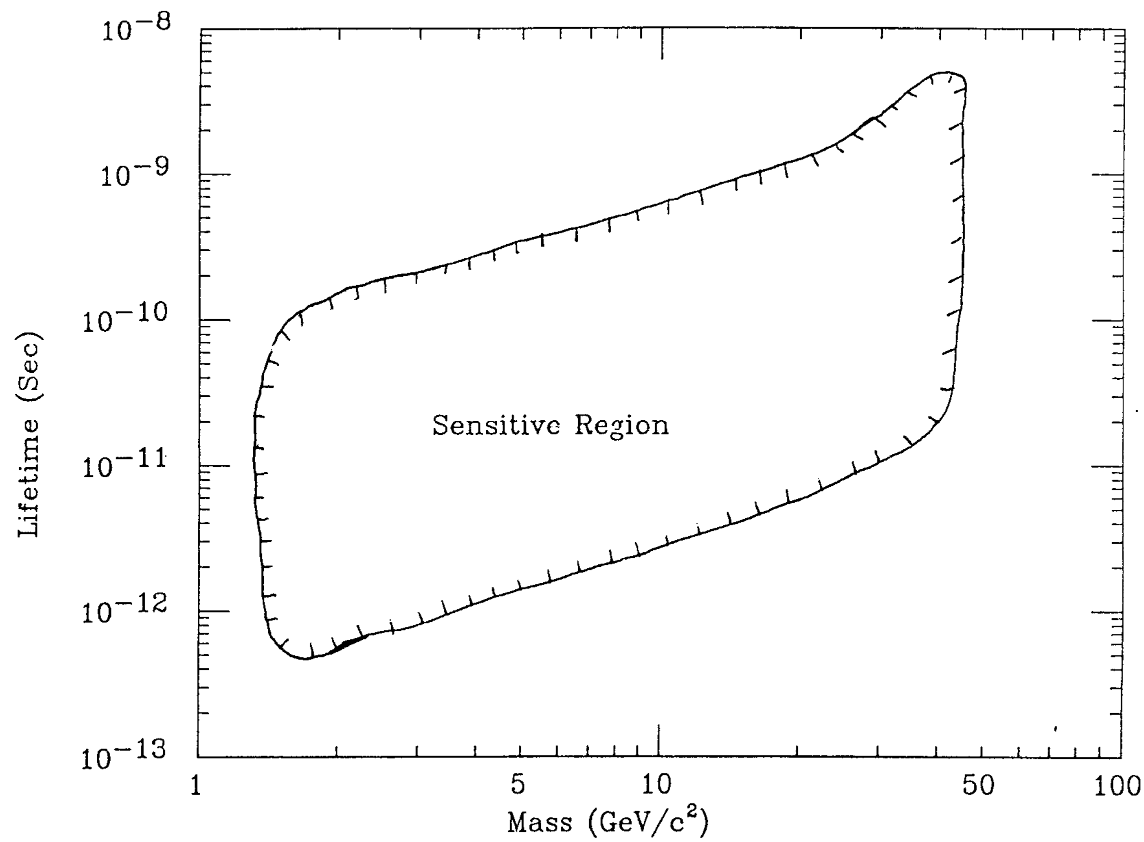

Mark II/SLC-Physics Working Group Note # 8–003

AUTHOR: Alfred Petersen

DATE: June 10, 1987

TITLE: QCD AT THE Z^0

---

1. Introduction

This report summarizes the work of the QCD group[1] as it was presented at the Mark II Pajaro Dunes Workshop. The QCD working group has in principle to cover a large variety of topics addressed by multihadronic events on the Z^0. A lot of the points are not directly related to the production and decay of the Z^0, rather to the new energy range opened up by the SLC or LEP. The large hadronic cross section on the Z^0 will possibly provide us with quite enormous event samples compared to the cross section in the continuum. On the other hand, events from standard QCD predictions will be the background to possible new physics at energies near the Z^0 mass. To gain confidence with the background calculations, we have to be able to understand the "old physics" to a satisfying level. The aim of this working group can be addressed to the following three points:

1) QCD as background for new processes.
2) What can we learn in perturbative QCD at the Z^0?
3) What can we learn in the hadronization at the Z^0?

A goal concerning the first point is the tuning and optimization of the existing QCD plus fragmentation models. This can be partly done by comparing them with existing data at lower energies. We tested mainly the Lund model,[2] the model of Webber *et al.*[3] and that of Gottschalk *et al.*[4] Global shape distributions like thrust, sphericity, aplanarity, minor value, oblateness and the jet masses are taken into account. A good knowledge of the observables can help to get good background estimations for new physics.

The main goals concerning the perturbative and non-perturbative aspects of QCD can be outlined by the following topics:

a) Global shape analysis like thrust, sphericity, Q-plot, major and minor values, oblateness, ...

b) Inclusive particle distributions like x (scaling violation), $p_\perp$, $p_\perp^2$, $p_\perp^{in}, p_\perp^{out}$, rapidity (plateau height, dip at y=0), multiplicity, KNO distribution,

c) α_s determination with e.g. energy-energy correlation and its asymmetry, hemisphere masses $(M_{br}^2 - M_{sl}^2)/s$, multi-jet analysis, ...

d) Test to show that α_s is running with energy.

e) Differences between quark and gluon jets.

f) Evidence for the gluon self-coupling.

g) String and coherence effects.

h) Charm and bottom quarks topics like fragmentation function, scaling violation of charmed meson, production of heavy quarks by $g \rightarrow Q\bar{Q}$, polarization of charm and bottom quarks, ...

The last point will be covered mainly by the c and b quark working group. For points like a), b), c), d), and g) it is interesting to see the E_{cm} dependence, so these analysis should be compared with the existing data in the 30 GeV region. A lot of these observables have been analyzed now, but, for example, the multiplicity and KNO scaling distributions haven't been done at 29 GeV so far. For most of the topics, an analysis can already start with the order of several thousand events. Unfortunately we haven't covered all the topics in our working group. So, for some topics I will only try to outline the direction of search.

2. QCD plus Fragmentation Models

There are several models for multihadron production currently available and, since their authors are continually working to improve them, it is sometimes difficult to keep track of the latest developments. With respect to the QCD calculations, the models can be divided into two groups: those in which partons are produced according to the second order in α_s QCD matrix elements and those in which they are produced by leading log parton shower evolution.

For the fragmentation of the partons into hadrons there are three main schemes available: independent fragmentation (IF)[5], string fragmentation (SF)[6] and cluster fragmentation (CF)[7]. The independent fragmentation scheme is strongly disfavored by the data in certain regions[8], so it will not be discussed further here. We will restrict ourselves mainly to the model of Webber et al.[3] (Version 4.1), the Lund model[2] (JETSET 6.3), and that of Gottschalk et al.[4] (CALTECH II from June 1986). For all the models the purely weak effects which are important at the Z^0 energies and the electroweak interferences on the total cross section, flavor composition and angular distributions are taken into account. The simulations of the weak effects are taken from the Lund generator[2].

The parameter values of the models given below are the results of investigations of the multidimensional parameter space by fits to the distributions of the Mark II data at $E_{cm} = 29$ GeV. A total systematic optimization procedure was not used, since the variety of data sets used did not cover the event topologies uniformly and may bias the χ^2 values from the fits.

2.1 THE LUND MODEL

The Lund model provides us with two options for parton generation: a second order matrix element calculation (Lund MA) and a leading log parton shower (Lund Shower). QCD calculations in second order perturbative theory have been provided by Gutbrod, Kramer and Schierholz[9] (GKS), Ellis, Ross and Terano[10] (ERT), Gottschalk and Shatz[11] (GS) and Kramer and Lampe[12] (KL). Their results differ by up to 10 - 20% . The problems are due to the approximations made in some of the calculations, as well as to the different treatment of soft gluons ("parton dressing"). Some recent comparisons indicate that the calculations of ERT and KL give similar results, whereas those of GKS lead to a $\simeq$ 10% higher value in α_s. Since it has mainly an effect on the value of the coupling constant and not on the shape of the distributions, we still used the Lund model with its GKS calculations.

At low E_{cm} $O(\alpha_s^2)$ matrix elements seem to be adequate, but at SLC or LEP energies the production of at most four partons will certainly be insufficient. Indications at PETRA/PEP energies show that these data also demand higher parton multiplicities[13] than produced by Lund MA. Another problem is implied by the y_{min} cutoff. The production of 2-, 3-, and 4-parton final states is determined by α_s and the lower cutoff y_{min}. If the value M_{ij}^2/E_{cm}^2 of any pair of partons i and j of an event is less than y_{min}, then these two partons are combined to one parton. Using the same y_{min} value at different center-of-mass energies implies a fragmentation scheme which has to be Q^2 dependent. Almost none of the fragmentation schemes is Q^2 dependent. To compensate for this a cutoff defined in $M_{min}^2 = y_{min}E_{cm}^2$ should be used, but covering an energy range from 30 GeV to 90 GeV confronts one then with the following problem: a M_{min}^2 cutoff which describes the data well at 30 GeV leads at high E_{cm} to a 3 + 4-parton rate which exceeds the total cross section, and a cutoff which is well defined at 90 GeV results in no agreement with data at 30 GeV. Table 1 shows the fraction of 2-, 3- and 4-parton events for fixed y_{min} or M_{min} cutoff at 29 GeV and 93 GeV. Due to this problem we will use in this paper a fixed y_{min} cutoff for all energies knowing that the fragmentation scheme had to be Q^2 dependent to get the right scaling.

Table 1. Parton multiplicities for different cutoff values.

E_{cm} (GeV)	α_s	y_{min}	M_{min}	$q\bar{q}$	$q\bar{q}g$	$q\bar{q}gg$
29	0.173	0.015	3.6 GeV	8%	80%	12%
93	0.137	0.015	11.4 GeV	28%	60%	8%
29	0.173	0.15	11.4 GeV	91%	9%	0%

Such a problem does not occur in the parton shower evolution where a fixed cutoff Q_0 is used, rather than a scaled one. The highly excited $q\bar{q}$ system evolves in the first phase (early times) into a system of partons with lower virtuality by radiating gluons and producing new $q\bar{q}$ pairs according to the leading-log QCD probabilities. If the virtual mass of a given parton reaches a certain cutoff (Q_0), the evolution stops for this parton. In the parton shower option in the Lund model the evolution proceeds in the c.m. system. The angular ordering which is needed to correctly take into account the soft gluon interference effects is imposed by a rejection technique at each step. For the first branch on each side no angular ordering is taken, instead the matrix elements are used as a guideline here. By this method more hard 3-jet events are produced than in a standard shower evolution, in better agreement with existing data.

It is still an open question which Q^2 definition in $\alpha_s(Q^2)$ has to be taken to get the right running of the coupling constant with energy. In second order matrix element calculations $Q^2 = s$ is used, but if the two gluons are radiated from the same quark, this definition is probably no more correct for the second branch. In the parton shower model of Lund one can choose between $Q^2 = m^2$, the virtual mass of the parent parton, $Q^2 = p_\perp^2$, the transverse momenta of the daughter partons (the default value) or even use a fixed value of α_s which is a nice toy model for testing the running of the coupling constant. It should be pointed out that the Λ_{LLA} value in a leading log evolution cannot be directly correlated to the $\Lambda_{\overline{MS}}$ value estimated from a first or second order matrix element calculation.

At the end of the parton production, string fragmentation[2] is used in both options. A string is stretched from a quark via gluons to an antiquark. Breaks in the string result in the production of additional $q\bar{q}$ pairs. The breaking can be understood as a tunneling phenomenon, automatically providing a suppression of heavy flavor production and a Gaussian transverse momentum spectrum. As a consequence of the partition into the parton level and the fragmentation, there is a "grey zone" in between that either can be described by soft gluons or by the fragmentation parameters, depending on the cutoff Q_0.

The relevant parameters for the Lund MA option are given in Table 2a and for the Lund shower in Table 2b with the range we tested for the optimization and the best values for describing the data at $E_{cm} = 29$ GeV. The other parameters are used with the default values in JETSET 6.3 except that the results on D^0 and D^+ branching ratios from Mark III are taken into account[14].

Table 2a: The parameters for the Lund MA model

Parameter	Range Tested	Best Value
$\Lambda_{\overline{MS}}$ QCD scale (GeV)	0.3 - 0.6	0.5
y_{min} cutoff for combining partons	fixed	0.015
A fragmentation function parameter	0.5 - 1.3	0.9
B fragmentation function parameter	0.5 - 1.3	0.7
σ_q parameter of the Gaussian[15] $p_\perp$ (GeV)/c	0.2 - 0.3	0.265

Table 2b: The parameters for the Lund shower model

Parameter	Range Tested	Best Value
Λ_{LLA} QCD scale (GeV)	0.2 - 0.6	0.4
Q_0 cutoff for parton evolution (GeV)	1.0 - 2.0	1.0
A fragmentation function parameter	0.1 - 0.5	0.45
B fragmentation function parameter	0.8 - 1.2	0.9
σ_q parameter of the Gaussian[15] $p_\perp$ (GeV)/c	0.18 - 0.27	0.23

The range of the parameters given in the tables were covered by roughly 40 different parameter sets. An increase of Λ by 0.1 GeV leads to the production of $\simeq$ 0.4 more charged particles, whereas increasing σ_q by 50 MeV/c reduces the average number of charged particles by $\simeq$ 0.5. This, and the fact that the parameter A and B are highly correlated, reduces the variation in the parameter space quite drastically if one demands the average multiplicity to be between 12.5 and 13.5 to describe the measured data. The comparisons with the data show that the values for Q_0 and y_{min} should be made as small as possible to get sufficient gluon radiation. The best values given are more or less the kinematic limits in the generators.

2.2 The Webber Model

The Webber model was the first model which used the leading log parton shower evolution and included coherence effects by angular ordering[16]. The coherence effect originates from destructive interferences between Feynman diagrams in a certain approximation (leading log) and is equivalent to an ordering of consecutive opening angles. The soft gluon interferences lead in addition to an azimuthal parton asymmetry. This is at moment only in the Webber model built in as an option. So far, all the shower models do not include the special treatment of the polar distribution for hard 3-parton events, rather all assume the distribution given for normal $q\bar{q}$ events.

At the beginning of the evolution, the initial system is boosted perpendicular to the primary quark direction such that all partons are produced in one hemisphere. This provides an elegant way of handling the angular ordering, but has the problem that the total center-of-mass energy of the system can be found only after the whole shower evolution of the event, and the final state system depends partly on the way it is boosted[17]. At the end of the shower the final gluons are forced to split into $q\bar{q}$ pairs by the same mechanism. Neighboring $q\bar{q}$ pairs along the color flux lines are combined to form colorless clusters. These clusters decay according to a phase space model into one or two particles which can be stable particles or resonances. Another problem is the existence of very massive clusters which cannot be allowed to decay isotropically[18]. A string-like scheme is used to break these clusters into two smaller clusters, each of which may break further if massive enough. Unfortunately this heavy cluster decay produces more particles from a given cluster mass than the parton shower does from a primary gluon of the same invariant mass. This leads to the strange situation, shown in Table 3, that an increase of the QCD scale Λ_{LLA} results in more produced gluons but no increase in the number of final state hadrons[19].

Table 3 The average gluon and charged particle multiplicity for different Λ values.

Λ (GeV)	n_{gluon}	n_{ch}
0.15	1.75	12.86
0.25	2.35	12.67

Since the exact first or second order matrix elements are not included in the leading log approximation, some changes have to be made to account for the right number of hard 3-jet events. The Version 4.1 uses a more thorough treatment of the first splitting of the virtual photon into the primary $q\bar{q}$ pair. This is now performed according to the Altarelli-Parisi splitting function[20] $P(z) = \frac{3}{2}\left(z^2 + (1-z)^2\right)$, where z is the fraction of energy assigned to one quark. It leads to a more asymmetric parton distribution in z which produces more 3-jet events, in better agreement with the data than the older Version 2.0. Another way, used by S. Bethke[21], is to give a higher boost to the initial $q\bar{q}$ system such that the angle between them is 30^0 instead of 90^0. A third way implies the calculations of $q\bar{q}$ and $q\bar{q}g$ events according to first order matrix element and to start the further parton shower from these configurations. But it needs additional cuts against double counting. Work in this direction has been done by S. Komamiya[22] and A. Petersen.

Table 4 shows the three important parameters of the model with the range we tested for the optimization and the best values for describing the data. The additional parameters were used with the default values in the generator. However, the Lund decay routines were used for charmed meson decays. For b and t quarks the weak decays are simulated on the quark level such that no real B or T mesons are produced. Due to this, there is no lifetime implemented for B mesons.

Table 4: The Parameters for the Webber model

Parameter	Range Tested	Best Value
Λ_{LLA} QCD scale (GeV)	0.15 - 0.3	0.2
m_g cutoff for further parton evolution (GeV)	0.6 - 0.85	0.75
m_{cl} cutoff for string breaking of clusters (GeV)	2.5 - 3.8	3.0

2.3 The CALTECH II Model

The CALTECH II model of Gottschalk et al. starts with a leading log parton shower, where the evolution proceeds in the c.m. system. The coherence effect by angular ordering is imposed by rejection techniques at each step. As with the Lund model, a reweighting of the first splitting according to the matrix element is used. At the end of the shower the quarks and gluons are replaced by color strings which break up into substrings according to the Artru-Mennessier scheme.[23] It implies a uniform string breaking with no mass shell constraints, in contrast to the Lund scheme, and it has no limited transverse momentum production during the string breaking. Substrings below a certain cutoff are treated as colorless clusters which decay according to a phase space model optimized with low energy data.

The important parameters are given in Table 5, whereas for the additional parameters the default values are chosen. The parameters t_0 and w_{min} have been fixed to the default values according to the results in Ref. 4.

Table 5: The parameters for the CALTECH II model

Parameter	Range Tested	Best Value
Λ_{LLA} QCD scale (GeV)	0.3 - 0.6	0.5
t_0 cutoff for further parton evolution (GeV^2)	fixed	2.0
ρ string breaking parameter (GeV^{-2})	1.4 - 2.4	1.6
w_{max} cluster decay parameter (GeV)	1.9 - 3.0	2.2
w_{min} cluster decay parameter (GeV)	fixed	0.25

3. Optimization of the Models to the 30 GeV Energy Range

For the tuning of the existing QCD plus fragmentation models we used mainly our data at $E_{cm} = 29$ GeV. In addition the average values of observables are also compared with other existing data from the PETRA energy range. The agreement between the models and the data is discussed in some detail. These results have been published in Ref. 24.

3.1 Particle and Event Selection for Multihadron Events

These are the cuts used at 29 GeV but which have to be further improved for the 90 GeV energy region. The charged track selection criteria are the following: a well-reconstructed track has to pass within 4 cm in radius (distance of closest approach perpendicular to the beam axis) and 6 cm in z from the event vertex and have at least 100 MeV/c of transverse momentum with respect to the incoming beams. The measured momentum is corrected for energy loss in the material in front of the tracking chambers assuming the particle to be a pion. Photons are detected by their electromagnetic showers in the calorimeters. A neutral cluster with energy greater than 150 MeV and a distance (at the radius of the shower counter) of more than 30 cm from the closest charged track is defined as a photon.

Hadronic events were selected by making the requirements given in Table 6. The three numbers at the end of each cut definition show the percentages of multihadronic events that pass that and all the above cuts, as estimated from Monte Carlo calculations. The first number corresponds to the original detector, the second to the Upgrade and the third one to the Upgrade at 93 GeV. The increase in the $cos\theta_T$ cut for the upgrade data is due to the better coverage of the central drift chamber and the new endcaps.

Table 6: The cuts for hadronic event selection

Cut	Cut Definition	PEP5	Upgrade	93 GeV
1	At least 5 well-reconstructed charged tracks.	89%	91%	98%
2	Sum of charged energy $\geq 27.5\%$ of E_{cm}.	67%	87%	94%
3	Sum of charged track and photon energy $\geq 55\%$ of E_{cm}.	48%	70%	77%
4	The z coordinate of the event vertex to be within 20 cm of the measured interaction point.	48%	70%	77%
5	$\mid \cos\theta_T \mid < 0.55$ for the PEP5 data set and $\mid cos\theta_T \mid < 0.8$ for the Upgrade data set with θ_T = angle between thrust axis and incoming beam.	38%	60%	68%
6	$p_{miss} < E_{cm}/4$ with p_{miss} = magnitude of the missing momentum vector.	35%	57%	64%
7	For events with $p_{miss} > 2$ GeV/c, we demand $\mid \cos\theta_{miss} \mid < 0.9$ with θ_{miss} = angle between p_{miss} and incoming beam.	33%	52%	60%
8	In 2-jet events, if both jets have fewer than 5 charged and neutral particles, then the invariant masses of both jets have to exceed 2 GeV/c.	33%	52%	60%
9	Events, with an observed photon of $E_\gamma \geq 3$ GeV as well as $E_\gamma \geq 90\%$ of the observed energy of the jet to which it is assigned are removed.	32.5%	51%	60%

For the jet definition, a cluster algorithm[2)] which utilizes the vector momenta of charged and neutral particles and partitions the events into a number of reconstructed jets is used.

The cuts discriminate against poorly reconstructed events, beam-gas scattering (Cuts 4, 6, 7), two photon events (6, 7), τ pair production (1, 8) and events with initial or final state photon radiation (7, 9). The contamination of the accepted events by these processes at $E_{cm} = 29$ GeV was found to be small: $< 0.2\%$ from τ pair production, $< 1.0\%$, from $\gamma\gamma$ scattering, and a negligible amount from beam-gas scattering.

A total of 22000 events of PEP5 data and 7400 events of Upgrade data passed the selection criteria and were used for the comparison with the models.

3.2 Definition of the Observables

The properties of the events are studied in both global event shape observables and inclusive particle distributions. For calculating event shapes and axes all charged and neutral particles are used.

The eigenvalues of the sphericity tensor[25] are taken to characterize the events according to their shape in momentum space. For each event the eigenvalues Q_1, Q_2, Q_3, ($Q_1 < Q_2 < Q_3$ and $Q_1 + Q_2 + Q_3 = 1$) and the corresponding principal axes $\vec{q_1}$, $\vec{q_2}$, $\vec{q_3}$ of the momentum ellipsoid are calculated. The sphericity axis ($\vec{q_3}$) is usually taken as the event axis and the event plane is defined by ($\vec{q_2}$, $\vec{q_3}$). In terms of the Q_i, the aplanarity is defined by $A = 3/2\,Q_1$, the sphericity by $S = 3/2\,(Q_1 + Q_2)$ and the variable Q_x by $Q_x = (Q_3 - Q_2)/\sqrt{3}$. Due to the fact that the sphericity tensor uses the momenta of the particles quadratically, those observables are more sensitive to the high momentum particles in an event than observables which use momenta linearly.

Another way of measuring the event structure is the thrust[26] which is defined as $T = Max\{\Sigma|p_{\|i}|/\Sigma|p_i|\}$, where $p_{\|i}$ is the longitudinal momentum of particle i relative to the thrust axis, which is chosen such as to maximize $\Sigma|p_{\|i}|$. The axis with the greatest thrust value perpendicular to the thrust axis is defined to be the major axis, and the thrust along this axis is the major value[27]. The minor axis is defined to give an orthonormal system, and the minor value is again the sum of parallel momenta with respect to this axis over the sum of momenta. The oblateness is the difference of the major and minor values. Because these observables use momenta linearly, they are much more sensitive to the soft particle production than those from sphericity analysis, and past experience has shown that their distributions are more difficult to describe using the models.

A third measure of the hadronic final state with sound perturbative properties is the jet invariant mass proposed by Clavelli[28], though we use a slightly different definition. The event is divided into two hemispheres by the plane perpendicular to the sphericity axis, and the invariant mass of all particles in each hemisphere is calculated. The smaller value defines M_{sl}, the mass of the slim jet, and the other M_{br}, the mass of the broad jet. The quantities of interest are M_{br}^2/s, M_{sl}^2/s and $(M_{br}^2 - M_{sl}^2)/s$ with $s = E_{cm}^2$.

Measurements of the inclusive distributions of charged particles within hadronic events are given in $x = 2p/E_{cm}$, $p_\perp$ and $p_\perp^2$ (with respect to the sphericity axis), $p_\perp^{in}$ and $p_\perp^{out}$, the transverse momenta in and out of the event plane, the rapidity $y = 1/2\,\ell n\,[(E+p_\|)/(E-p_\|)]$, where in this case $p_\|$ is the component of momentum parallel to the thrust axis, and the charged particle flow $dn/d\theta$, where θ is the angle between the particle and the sphericity axis. Finally, the energy flow $dE/d\theta$ is used, which is equal to dn/dθ weighted by the energies of the charged and neutral particles.

3.3 CORRECTIONS

To correct the observed distributions for acceptance inefficiencies, other detector imperfections, effects from radiated photons, and the above described cuts, Monte Carlo simulation programs are used. The production of multihadronic events was computed based on the different models for QCD plus fragmentation.

The corrected distribution, $dn_{cor}(x)$, as a function of a variable x is obtained from the measured distribution $dn_{meas}(x)$ by using a bin-by-bin correction function $C(x)$,

$$dn_{cor}(x) = C(x)\, dn_{meas}(x) \quad .$$

where C(x) is determined from the Monte Carlo simulation. At $E_{cm} = 29$ GeV, for most of the distributions $C(x)$ varies between 0.7 and 1.4 with the values being closer to unity for the Upgrade detector than for the PEP5 detector. Even smaller corrections are predicted for $E_{cm} = 93$ GeV. The correction factors are averaged between the results of the different models, but a higher weight is given to those models which describe the uncorrected data best. The differences between the averaged value and those of the different models are taken as measures of the systematic uncertainty in the corrections. The errors shown for the corrected distributions contain the quadratic sum of the statistical error of the data and the systematic error in the correction.

3.4 COMPARISON OF THE DATA AT $E_{cm} = 29$ GEV WITH THE MODELS

The PEP5 data and the Upgrade data are combined into one set by averaging the two values weighted by their errors. The new total error is calculated as the inverse quadratic sum of the statistical errors of the two data sets, and the systematic error from the correction factors is added quadratically.

The averaged distributions of the data are shown in Figures 1 – 15 and compared with the predictions of the Lund MA, Lund Shower, CALTECH II, and Webber models.

The Lund MA model underestimates the tails of the aplanarity (Fig. 1), the minor value (Fig. 6), and the $p_{\perp}^{out}$ distributions (Fig. 11). These indicate that the number of four and higher parton events is not well accounted for. The inclusive particle distribution in x (Fig. 12) is slightly overestimated in the region $0.3 < x < 0.7$. The thrust distribution (Fig. 4), which is often difficult to describe, is well described by this model. The study showed that the $(M_{br}^2 - M_{sl}^2)/s$ distribution

(Fig. 9) is quite sensitive to the value of the scale parameter Λ and relatively insensitive to other parameters, including whether string or independent fragmentation is used. All the other distributions are fairly well described. For 50,000 simulated events the sum of χ^2 of all distributions is 1230 using 450 data points.

The CALTECH II model describes the data less well. It has a sum of χ^2 of 6830 for the same comparison. The number of events with high aplanarity is over estimated. For the sphericity, thrust, minor value, M_{br}^2/s, and M_{sl}^2/s distributions (Figures 3, 4, 6, 7 and 8) it produces too many events with very low values, too few with medium values around the peak of the distributions, and again too many with very high values. A change in the Λ value does not result in better overall agreement. It might be that the two fragmentation schemes, string breaking and cluster decays, used successively in this model lead to a higher probability of extreme event shapes. The particle and energy flow (Figures 15 and 16) are more populated around 20^0 and less in the region perpendicular to the sphericity axis.

For the rapidity (Fig. 13) the model predicts rather a deeper dip at $y = 0$ and a higher peak at $y \simeq 1.5$. It is interesting that the rapidity distributions for the four models look quite different close to zero. Although all three parton shower models take the interference effects into account, they give different predictions for the form of the dip. Problems similar to those described here have also been found in comparisons with other published data by the authors of the model[4].

Trying to understand the problems of the CALTECH II model, we implemented the Lund parton shower or the Lund fragmentation in the CALTECH II model. The combination of the CALTECH II parton shower with the Lund string fragmentation improved the agreement with the data, but, for example, the higher rates with very low and high thrust still remain (Fig. 5), indicating that some of the problems, in particular the overestimation of the number of nearly spherical events, originate in the CALTECH II parton shower model. One surprising feature of the model is that the average number of final quarks of 2.73 is roughly as large as the number of gluons with 2.69 per event in the parton shower.

The use of the Lund parton shower with the CALTECH II hadronization results in better agreements than the previous combination. For this combination the resulting distribution at low thrust describes the data reasonably well (Fig. 5), but the peak at high thrust is still shifted to higher values than measured. Other distributions also indicate that the hadronization of the partons does not seem to be broad enough for pencil-like jets.

The new version of the Webber model gives a good reproduction of the data in $Q_2 - Q_1$ (Fig. 2) which are quite sensitive to hard gluon radiation. The older Version 2.0 substantially underestimated the high $Q_2 - Q_1$ tail. The new version still overestimates the number of events with high thrust, low minor value, low M_{br}^2/s, low M_{sl}^2/s (Figures 4, 6, 7 and 8) and low multiplicity (not shown), probably due to insufficient soft gluon radiation. Lowering the cutoff mass in the parton shower would increase the number of gluons, but would also lower the final multiplicity, again a problem of the special handling of heavy cluster decay. The average $p_\perp^2$ (Fig. 10) is slightly too high and the inclusive x distribution (Fig. 12) lies above the data for large x. The sum of χ^2 is 2870, which is half way between the Lund model and the CALTECH II model.

To see whether these problems come more from the parton shower scheme of the model or the hadronization, we used only the parton shower of the Webber model. Instead of breaking each gluon into a $q\bar{q}$ pair, the Lund string was stretched from a quark via the gluons to the anti-quark and this string then fragmented according to the Lund model. With this scheme we achieved much better agreement with the data (roughly as well as with the Lund shower model) than with the original version. But the cutoff for further parton evolution (m_g) has then to be reduced to 0.6 GeV, the lowest possible value for the generator. These facts indicate that the problems in the Webber model may be due to more to the hadronization side.

The Lund Shower model gives one of the best descriptions of the data, indicated by the sum of χ^2 of 960 which is the lowest value of the models used. There are some slight underestimations in the thrust and M_{br}^2/s distributions (Figures 4 and 7) close to the peak values, and the x distribution (Fig. 12) is somewhat higher around $x = 0.5$.

The branching ratios of the decaying D^0 and D^+ reflect visibly on the observed distributions. We used slightly different decay modes and branching ratios than were originally in the version JETSET 6.3, taking into account some of the later Mark III measurements[14]. With the original version, a change of the parameters A from 0.45 to 0.5 and σ_q from 230 to 250 MeV is necessary to get similar agreement with the data using the different D decay probabilities.

An interesting point is that a low cutoff mass in the parton shower ($Q_0 \sim 1.0$ GeV) is needed to describe the data around the peaks in the global shape distributions. It indicates that multiple gluon radiation within an event is important even in connection with string fragmentation, to get a good transition between the perturbative and non-perturbative part[29]. An average of 4.8 gluons and 2.1 quarks are produced in the parton shower with the given parameters and only 3% (3%) of the events have no (one) gluon radiated.

3.5 Comparison of Energy Behavior of Observables

The description of the data by the models at a given c.m. energy is only one check of the underlying assumptions. Another check is whether the models can give the right prediction of the energy behavior of the data without changing the parameters. In relation to the upcoming Z^0 physics, it is interesting to look at the extrapolation of the models to the 90 GeV region. As a first step we will look at the behavior of the average values of the observables. To increase the sensitivity, we also include published results of the PLUTO[30], TASSO[31], CELLO[32], JADE,[13,33] and HRS[34] collaborations. The average values for some of the observables from the previous section are given in Figures 16 – 21 as a function of E_{cm}. The reader should keep in mind that the models are optimized to the Mark II data points such that deviations between other measurements and the models may occur.

For the average aplanarity, in Fig. 16a, the results from HRS and our measurement differ slightly. The four models all agree at very low E_{cm}, but at high E_{cm} the Lund MA model predicts a factor of 2 lower value than the parton shower models, again due to the incomplete simulation of multiple gluon emission. However, the shower model predictions also differ substantially. The average sphericity (Fig. 16b) of HRS and Mark II agree well, whereas TASSO measures lower values around 30 GeV. All models follow the trend of the data, although Lund MA gives a lower extrapolation to higher E_{cm}. The experimental $< M_{br}^2/s >$ (Fig. 17a) agree relatively well, and the models themselves follow the trend of the data fairly well. The $< (M_{br}^2 - M_{sl}^2)/s >$ value (Fig. 17b) of our measurement is substantially higher than those of PLUTO which might be due to the fact that they calculate the two masses by a minimization process whereas we use the sphericity axis to define the two masses for both our data and the models. The models predict different slopes at higher energies. The three shower models give the same prediction around 70 GeV but diverge at 90 GeV. The values of $< 1 - T >$ (Fig. 18) of the different measurements scatter substantially. The models again predict quite different curvatures.

For Fig. 19a and b, the energy-energy correlations (EEC)[35] and their asymmetry (EECA) have been calculated. Figure 19a shows the integral of the EEC from 57.6° to 122.4°. The agreement of the data points is fairly good. The CALTECH II model has lower values over the whole energy range than the Lund Shower and the Webber model. Reference 4 claims this is due to the neglect of nonleading higher-order corrections in the leading-log shower formalism.

The energy behavior of integrated EECA from 28.8° to 90° (Fig. 19b) is not very conclusive from the experimental point of view. On the other hand, it is interesting to see the different energy behavior of the models. The data look rather flat, but all four models decrease with energy until $E_{cm} \approx 20$ GeV, due to a nonvanishing contribution from the fragmentation of nearly 2-jet events. Above 20 GeV the Lund MA model predicts a continual increase up to 100 GeV. (A model with the same matrix elements to second order in α_s but with independent fragmentation leads to a decrease of the value over the whole region from 10 GeV to 100 GeV, which is naively expected from the running coupling behavior of QCD.) The increase in Lund MA comes mainly from the decreasing power of the string effect with increasing energy. Fewer particles are produced between the quark and antiquark jets than between the quark and gluon jets in 3-jet events. These events look more 2-jet like and hence have less asymmetry. With increasing jet energies the string effect becomes less pronounced, leading to a larger asymmetry. So the energy dependence of the EECA in the Lund MA model behaves oppositely to what one expects naively from the running coupling constant behavior in QCD. The asymmetries of the parton shower models also increase after a dip at 20 GeV, until they reach a slight maximum between 60 GeV and 80 GeV, after which they decrease again. One reason for this might be that events with multiple gluon emission again look more symmetric, decreasing the value of asymmetry.

The average multiplicity in Fig. 20a shows good agreement at the existing energies with all four models, but the differences at high energies are such that their predictions at 90 GeV vary between 18 and 23 charged particles. The average number of reconstructed jets or clusters[36], also shown in Fig. 20a, has a nearly linear increase with E_{cm} for the shower models. The Lund MA model increases more slowly, predicting a value at the Z^0 which is 20% lower. As a direct correlation, the same trend as in the multiplicity is visible in Fig. 20b, where the average particle x is plotted. The agreement between the different data points is quite good.

The average $p_\perp^2$ in Fig. 21a shows fair agreement between the experiments. It is interesting to notice the different $p_\perp^2$ behavior of the models. All the models show an increase in $p_\perp^2$ with energy, but the increase is less rapid for the Lund Shower and CALTECH II than for the Webber model and Lund MA. This is probably partly due to the fact that the last two have a smaller multiplicity. The Lund MA prediction in Fig. 21b indicates that the increase in $p_\perp^2$ is not coming from $(p_\perp^{out})^2$ which has the lowest increase with energy of all, but from $(p_\perp^{in})^2$ which is mainly due to hard gluon radiation.

Overall, the comparison of the average values of observables between the different experiments is satisfying. The largest deviations between experiments are in the aplanarity, sphericity, and 1 - T distributions. The biggest difference in the energy behavior between the models is between the Lund MA model on the one hand and the shower models on the other hand.

4. Prediction of the Models at the Z^0

The figures in the previous section have already presented the average values of the observables at the Z^0 energy. In Figures 22 - 37 the distributions of the model predictions themselves are given for E_{cm} = 93 GeV including the electroweak effects. Again, the same distributions are chosen as in the comparison at E_{cm} = 29 GeV. The usual trend is that the global shape distributions peak more at low values , indicating that the events get narrower in width.

The aplanarity in Fig. 22 shows large differences between the models. This demonstrates that it might be dangerous to use a cut in aplanarity when looking for new particle production[37]. For Q_x, $Q_2 - Q_1$ and sphericity the predictions differ only slightly: as an example, the sphericity is shown in Fig. 23. The CALTECH II model at 93 GeV again indicates for these observables the behavior of larger populations at very low and high values, and somewhat smaller in the medium range, in comparison with the other two shower models. The same trend is visible for thrust in Fig. 24. Events with low thrust are much more suppressed in the Lund MA model. The differences between the model predictions for the minor value distribution in Fig. 25 are also visible at 93 GeV. The lack of multiple gluon events makes the Lund MA curve much narrower than the other three. The differences between the Lund Shower and Webber model are mainly due to differences in hadronization.

The M_{br}^2/s distribution in Fig. 26 again indicates the special form of the CALTECH II model which causes it to be a bit higher on the tail than the other three models. For M_{sl}^2/s in Fig. 27, the Lund Shower and the Webber models give nearly the same prediction whereas the CALTECH II model is far higher in the tail and the Lund MA is visibly lower. All four models give similar predictions for $(M_{br}^2 - M_{sl}^2)/s$ as shown in Fig. 28. Above a value of 0.12 the distributions at E_{cm} = 29 GeV and 93 GeV nearly agree. This is expected if the tail is mainly sensitive to hard gluon radiation.

The number of reconstructed clusters or jets in Fig. 29 shows a clear distinction between the second-order matrix element and the shower models. The shower models will increase drastically the predicted background in the top quark search using jet reconstruction[38]. For the charged multiplicity in Fig. 30, CALTECH II indicates the broadest distribution, probably due to using both string breaking and cluster decay. This model says that events even with more than 50 charged particles are occasionally possible, in contrast to the other models which don't have this high a multiplicity.

The $p_\perp$ distributions in Figs.31, 32 and 33 have similar trends for all models except the $p_\perp^{out}$ of the Lund MA, which is again lower. The particle x distributions in Fig. 34 reflect the difference in multiplicity. Figure 35 shows the ratio R_x of the inclusive particle distribution at E_{cm} = 93 GeV over that at 29 GeV. Due to scaling violation which means more gluon radiation at higher energy the R_x value should be less than unity for high x. The Lund MA with fixed y_{min} cutoff shows no scaling violation at high x, due to the missing Q^2 dependence in the fragmentation function. A scale breaking effect of the order of 25% is visible, if the Lund MA is used with fixed invariant mass cutoff M^2_{cut}. The shower models predict a scaling violation of the order of 30% with still quite different predictions for the Webber and the CALTECH II models.

The different plateau heights in the rapidity distributions in Fig. 36 are due to the different multiplicities of the models. In addition they show quite different behavior in the plateau region and in their approach to the dip at $y = 0$. A dip is predicted by both coherence effects on the parton level and by the string decay mechanism.

The energy flow in Fig. 37 emphasizes the difference between Lund MA and the shower models. The comparisons of the energy flow at $E_{cm} = 29$ GeV and 93 GeV show that for $\theta > 15^0$ the increase in energy is a factor of two over the whole region. The main increase in energy is in a cone of 10^0 around the sphericity axis.

Overall it is interesting to see that the three parton shower models still give somewhat differing predictions at energies around 90 GeV. The differences which appear are often already visible at 30 GeV. A second order matrix element model like Lund MA is probably inadequate to describe data on the Z^0.

5. α_s Determination

A glance back over the last decade shows that the estimation of the strong coupling constant α_s has been a difficult task from both the experimental and the theoretical side. The various QCD calculations in second order perturbation theory result in 10 - 20% differences. These originate from approximations made in some of the calculations and from different treatments of soft gluons. An additional uncertainty comes from the fact that the calculations are done with massless quarks, which afterwards have to get masses. Different fragmentation schemes lead to differences in α_s of up to 40%, if special schemes are not ruled out by the data. The different analysis methods, based on various measured observables, can result in different values of α_s, and methods which were claimed at the beginning to be "gold plated" afterwards showed similar problems with model dependence. All these problems will probably not be one tiny bit easier at 90 GeV than at lower energies. Although the starting Q^2 value is higher, it nevertheless has to evolve down to the same low Q^2 values where the coupling constant increases drastically and where perturbative calculations are no more valid. The production of new particles makes the α_s determination only more difficult. (This is one of the very few good aspects of finding no new particles at the Z^0.)

Since a lot of the problems are on the parton level and in the models, we should try at the beginning to get detector corrected distributions which the theorists can then use to find their values of α_s. Although it is difficult to judge which observables are the best to unravel α_s, my favorites are the energy-energy correlation (EEC) and its asymmetry (EECA), the hemisphere masses $(M^2_{br} - M^2_{sl})/s$ and a multi-jet analysis. D. Wood is working on the first of these topics and S. Bethke[21] on the latter one.

We will discuss here a little bit more the Field method[39] of α_s determination, which was claimed to be model independent. The point is to use observables which can be calculated analytically at the parton level to order α_s^2 like the EECA, thrust, M^2_{br}/s and $(M^2_{br} - M^2_{sl})/s$. Each of these observables is proportional to α_s and has a well-defined perturbative series at the parton level:

$$Obs(W)_{parton} = C_0\alpha_s(W)(1 + C_1\alpha_s(W) + \ldots)$$

where $Obs(W)$ stands for the observable as a function of c.m. energy and where the first two terms in the series have been calculated. Field then assumes that the experimental observable can be written as the sum of two terms:

$$Obs(W)_{Exp} = Obs(W)_{parton} + Had(W)$$

a calculable QCD perturbative series plus an incalculable nonperturbative hadronization piece, $Had(W)$. In addition the assumption is made that the hadronization can be described by:

$$Had(W) = F/W$$

The point is that F can be positive or negative, but it does not change sign for a given observable. For thrust and M^2_{br}/s the sign is positive, which implies these give upper bounds for α_s. The EECA and $(M^2_{br} - M^2_{sl})/s$ have a negative F, and by that provide lower bounds for α_s.

To second order in α_s the observables can be described by:

$$Obs(W)_{Exp} = C_0\alpha_s(W)(1 + C_1\alpha_s(W)) + F/W$$

By fitting this formula to the energy dependence of the observables one can estimate the value of α_s to second order in the limit $W \to \infty$

This method works well for independent fragmentation, but in the assumption of string fragmentation the distortion by the string effect has to be added by:

$$Obs(W)_{Exp} = C_0\alpha_s(W)(1 + C_1\alpha_s(W)) + F/W + G(\alpha_s, W)$$

The point is that the factor $G(\alpha_s, W)$ is always negative for all observables. Due to the bend of the string all $q\bar{q}g$ events look more 2-jet like after fragmentation. The value of G also depends on α_s since only events with a gluon are affected by the string. This implies that the method of upper and lower bounds for α_s does not work if G is unknown. So, even with this method we do not get rid of the model dependence in the α_s determination.

6. Can We Observe a Running α_s?

This question is one of the important topics as experimental tests of QCD. The energy dependence of α_s in second order in the $\overline{\text{MS}}$ scheme is given by:

$$\begin{aligned}
\alpha_s^{(2)} &= \frac{12\pi}{b_0 \cdot ln(Q^2/\Lambda^2_{\overline{MS}}) + \frac{b_r}{b_0}\, ln\, ln(Q^2/\Lambda^2_{\overline{MS}})} \\
b_0 &= 33 - 2\,n_f \\
b_r &= 918 - 114\,n_f \\
n_f &= \text{number of different quark flavors}
\end{aligned}$$

The logarithmic decrease with increasing energy is a unique feature of non-abelian gauge theories. However, the changes are quite small at high energies. At low energies, where the decrease of α_s can be quite substantial, perturbative calculations are not possible and the effects of a running α_s cannot be unraveled from the experimental data.

As shown in the previous chapter, the estimation of α_s is still covered with a lot of problems:

- present second order QCD calculations show differences up to 10 – 20%,
- second order calculations break down at $\sim$ 90 GeV,
- different fragmentation schemes give different results,
- a proper definition of Q^2 is needed, since in finite order perturbation theory the α_s results depend on the definition of Q^2,
- there are problems with production threshold of new quarks (The choice of keeping the physical value of α_s, rather than the scale parameter Λ, constant at the threshold is certainly preferred[40]),
- different analyzing methods might be used by the experiments by comparing α_s from various publications.

Since the individual determination of α_s values at different energies will suffer from the above problems, it is probably better to show that an observable which is closely related to α_s is running with the right expectation than to try unraveling α_s from it. One possibility would be the ratio R of the total hadronic cross section over the muon pair cross section, but the change is only of the order of a few percent and the contributions from electroweak effects start to dominate the change in R.

Another possibility is the relative production rates of n-jet events, which are directly related to the strong coupling strength and the applied jet resolution parameters. For the definition of a reconstructed n-jet events it is nice to have an algorithm which is closely related to the parton resolution cutoffs. We will use the algorithm developed by S. Bethke under the name YCLUS$ available in the VECSUB package. For all pairs of particles k and l of an event, the scaled invariant mass squared

$$y_{kl} = \frac{M^2_{kl}}{E^2_{vis}}$$

is calculated, where E_{vis} is the total visible energy of an event. The two particles with the smallest value of y_{kl} are replaced by a pseudo-particle of four-momentum $(p_k + p_l)$. This procedure is repeated until all y_{kl} exceed a certain threshold value, y_{cut}, and the resulting number of pseudo-particles is called the jet multiplicity of the event. In calculating the invariant pair-masses, M_{kl}, the expression

$$M^2_{kl} = 2\,E_k\,E_l\,(1 - \cos\theta_{kl})$$

is used, where E_k and E_l are the energies and θ_{kl} is the angle between the momentum vectors of pseudo particles k and l.

By using E_{vis} instead of E_{cm} it turns out that the corrections for the detector imperfections is small compared to the algorithm LCLUS$[36] in the VECSUB package. Table 7 shows the values of the correction factors for the two algorithms at E_{cm} = 29 GeV and 93 GeV. For YCLUS$ they are close to unity, whereas for LCLUS$ the corrections can be quite drastic for high jet multiplicities.

Table 7. Correction factor for the fraction of n-jet events for different jet algorithms and energies.

	E_{cm} = 29 GeV		E_{cm} = 93 GeV	
	LCLUS$	YCLUS$	LCLUS$	YCLUS$
2-jet	0.83±0.02	0.97±0.02	0.60±0.02	0.97±0.02
3-jet	1.50±0.05	1.04±0.02	0.87±0.02	1.05±0.03
4-jet	5.20±0.9	1.07±0.07	1.40±0.05	1.04±0.10

By choosing the jet resolution parameter y_{cut} close to the value of the QCD y_{min} cutoff and keeping it constant for all energies, the theoretical expectation for the rates of n-jet events depends mainly on the value of α_s and its predicted energy behavior. The production rate of 3-jet events is expected to decrease with increasing energy with the same proportion as α_s. In Table 8 the n-jet event rates for the Lund shower model are given for the two algorithms and the two energies. The algorithm LCLUS$ shows an increase of the average jet multiplicity with energy. A similar picture would result for YCLUS$ if, instead of the scaled y_{cut}, a fixed cutoff in $M^2_{cut} = y_{cut} \cdot E^2_{cm}$ would have been used. But with a fixed $y_{cut} = 0.04$ for YCLUS$ (as in Table 8) the average jet multiplicity decreases with energy. The number of 3-jet events is reduced by 23% and that of 4-jet events even by 52% in going from 29 GeV to 93 GeV. This reduction is quite close to what is also expected from the second order calculation of 3-parton events.

Table 8. Jet multiplicities for different jet algorithms and energies.

	E_{cm} = 29 GeV		E_{cm} = 93 GeV	
	LCLUS$	YCLUS$	LCLUS$	YCLUS
2-jet	64%	49%	18%	62%
3-jet	33%	46%	38%	35%
4-jet	3%	5.2%	30%	2.5%
5-jet	0%	0%	11%	0%

Figure 38 shows the fractions of 3-jet events (R_3) with $y_{cut} = 0.04$ as a function of E_{cm}. Our data point at E_{cm} = 29 GeV agrees quite well with the JADE results, which show a falling fraction of 3-jet events with increasing energy. The data are well described by the Lund shower model with Λ = 310 MeV. On the other hand, if the same starting value for α_s is used in the shower model for all E_{cm}, then the expected fraction stays more or less constant above an energy of $\sim$ 35 GeV. The increases at lower energies is somewhat expected, since in this regime the minimum required cluster pair mass is too small to discriminate against effects of heavy particle decays and fluctuations in the fragmentation. The energy independent 3-jet value above 35 GeV indicates that the jet algorithm used does not add any energy dependent effects by itself.

The question of how much data are needed to show that R_3 is decreasing with energy, given our data sample at 29 GeV is investigated in Table 9 where the required number of events with a $y_{cut} = 0.08$ for a 3σ, 4σ and 5σ effect are shown. So, on the order of 5000 multihadron events should be sufficient to show a signal for the running α_s.

Table 9. The required number of events for a running 3-jet rate

	29 GeV	44 GeV	60 GeV	93 GeV
R_3	22%	20%	19%	18%
N for 3σ		6400	1900	1000
N for 4σ		18000	3800	2000
N for 5σ		∞	8000	3300

The 4-jet rate should show even stronger running, since it is proportional to α_s^2. The Lund shower model predicts a reduction of 50% going from 29 GeV to 93 GeV, but the statistics will be limited. Other possibilities of testing the α_s running could be the fraction of events with thrust $\lesssim 0.8$, with $M^2_{br}/s \gtrsim 0.1$ or with $M^2_{sl}/s \gtrsim 0.05$. The events with $M^2_{sl}/s \gtrsim 0.05$ are mainly originating from 4-parton events with two partons on each side, whereas for $M^2_{br}/s \gtrsim 0.1$ all 3 and 4-parton events contribute. This implies that the cuts are sensible to special parton configurations and that these fractions will have different energy behavior.

7. String and Coherence Effects

The experimental observation of the string effect, the depletion of particles between the quark and antiquark jets compared to the region between quark and gluon jets in 3-jet events, has been shown by several experiments in the 30 GeV region. It will be interesting whether we can see the string effect at 90 GeV. Since the string effect mainly influences the soft particles, one naively assumes that with a second order matrix element model plus string fragmentation the effect should decrease with increasing energy, but on the other hand a parton shower model with soft gluon interferences included should also predict an effect at high energies. If the string fragmentation is a way to implement coherence on the nonperturbative level, then the question is whether we need in addition to take into account the coherence on the parton level.

T. Sjöstrand[40] tested the string effect with the Lund shower model at E_{cm} = 35 GeV. He showed that the shower model both with and without angular ordering, plus string fragmentation reproduce the string effect. It has to be tested what the result will be, if instead of string fragmentation a cluster decay mechanism like the one of the Webber model is used. This is important, since in previous publications[8] it has been shown that the first Gottschalk model (CALTECH I) with no angular ordering does not exhibit the string effect, whereas the Webber model with angular ordering predicts it. The question is whether this is due to the angular ordering or due to other differences in the two generators. The Lund program gives the opportunity to test all these questions within one generator.

To look for the string effect we use the methods from JADE[8]. Three-jet events are found by the cluster algorithm YCLUS$ with $y_{cut} = 0.04$. In addition, only events with $Q_1 < 0.06$ and Q_2 - $Q_1 > 0.05$ are selected to have distinctive three jets. The three jets are numbered such that jet 1 is opposite the smallest angle between the jet axes and jet 3 is opposite the largest angle. Figure 39 shows the particle flow in the event plane starting from the axis of jet 1 and running via jet 2 and 3 back to jet 1. In Fig. 39a, where the Lund MA with string or independent fragmentation are given, the lower particle production between jets 1 and 2 which are in the majority the two quark jets is still visible at 93 GeV for string fragmentation in connection with a higher production in the valleys neighboring the gluon jet. Table 10a summarizes the ratios between N_{31} and N_{12}, where N_{jk} is the integrated particle or energy flow in the region $0.3 < \Theta_i/\Theta_{jk} < 0.7$, with Θ_{jk} the angle in the event plane between jets j and k and Θ_i the angle between the particle i and jet j. There is a clear distinction in the ratios between string and independent fragmentation, where the gluon fragments like a quark, in Rows 1 and 7. If the gluon fragments softer than a quark jet (Row 2), the ratios get slightly increased. In comparison with results at 30 GeV, the differences are still of the same order at 93 GeV.

Table 10a. The ratio of the number of particles in the angular region $0.3 < \Theta_i/\Theta_{jk} < 0.7$ between jets 1 and 3 to the corresponding number between jets 1 and 2. The calculations are done for different model options and the errors only contain the statistical ones.

row	Lund model scheme	all	$p_\perp^{out}$ >0.3GeV	K,p	energy
1	MA+indep. frag. g=q	1.07±0.01	1.25±0.04	1.18±0.04	1.25±0.02
2	MA+indep. frag. g≠q	1.14±0.02	1.28±0.05	1.27±0.06	1.30±0.02
3	shower inc.+cluster	1.22±0.03	1.47±0.09	1.65±0.26	1.48±0.04
4	shower inc.+string	1.30±0.02	1.52±0.07	1.67±0.10	1.62±0.03
5	shower coh.+cluster	1.33±0.02	1.54±0.07	1.65±0.15	1.67±0.03
6	shower coh.+string	1.39±0.02	1.63±0.07	2.10±0.13	1.84±0.03
7	MA+string frag.	1.50±0.02	1.91±0.07	2.09±0.10	1.96±0.03

Table 10b. The $< p_\perp^{in} >$ for particles with $p_\parallel > 5$ GeV/c within jets 1 and 2.

row	Lund model scheme	n_{ch}	jet 1	jet 2
1	MA+indep. frag. g=q	18.5	-1± 5	28± 5
2	MA+indep. frag. g≠q	19.9	4± 6	22± 6
3	shower inc.+cluster	24.3	-3±12	-18±13
4	shower inc.+string	23.8	19±10	-46±12
5	shower coh.+cluster	19.1	27±10	-38±10
6	shower coh.+string	20.4	46±10	-86±11
7	MA+string frag.	18.2	53± 5	-104± 6

In Fig. 39b the curves are given for the Lund shower model with or without angular ordering and with string fragmentation or the Webber cluster decay mechanism. Overall it is visible that the angular ordering produces less final particles, especially with the cluster decay (see also Column 3 of Table 10b). For the Lund shower with coherence plus string fragmentation the peaks of jets 1 and 3 are slightly more shifted to each other than without coherence.

It is interesting to see in Table 10a that the ratios continuously increase from Row 1 to Row 7. The clear difference with second order matrix elements models between independent (Row 1) and string fragmentation (Row 7) gets more complex going to the leading log parton shower models. The 3-gluon coupling tends to fill some additional particles around jet 3, whereas some of the hard 4-parton events will contribute particles in the region between jets 1 and 2. But nevertheless, the biggest difference with the Lund shower model is between coherent shower plus string and incoherent plus cluster decay. The other two options are lying somewhere in between.

Another way of looking for the string effect is to test the particle distributions within the jets. Within the quark jets, the soft particles will be more pulled to the gluon than the harder ones. JADE[8] looked for the $< p_\perp^{in} >$ of the particles in jets 1 and 2 as a function of $p_\parallel$, parallel to the jet axis. They found that the $< p_\perp^{in} >$ for high $p_\parallel$ points away from the gluon jet. Column 4 (5) in Table 10b shows the $< p_\perp^{in} >$ for particles with $p_\parallel > 5$ GeV/c of jet 1 (2), where the minus sign means it points to (away from) jet 3. With this method we again see steadily increase or decrease from Row 1 to Row 6. It should be noted that the difference in the ratios in Table 10a between coherent and incoherent with string fragmentation gets smaller, when more distinct 3-jet events are used by requiring a higher cut in Q_1 - Q_2, whereas the difference in the $< p_\perp^{in} >$ in Table 10b stays the same.

The results show that at 90 GeV the different schemes in the Lund model give a gradual transition from incoherent shower plus cluster decay to coherent shower plus string fragmentation. Both, the coherence on the parton level in the leading log shower and the coherence on the nonperturbative level, implemented by string fragmentation, are needed to get the highest value for the ratios N_{31}/N_{12} and for $< p_\perp^{in} >$ in jets 1 and 2. The question will be, whether the data will give us a clear answer to puzzle.

8. Quark and Gluon Jets

Another important topic is the differences between jets which originate from high energy quarks and those from gluons. On the parton level, due to the higher probability of radiating further gluons from a primary gluon than from a quark, a gluon jet will be broader and softer in particle spectrum than a quark jet of the same energy. Results in the 30 GeV region from e^+e^- annihilation[42] and also from $p\bar{p}$ in UA1[43] showed evidence for such effects.

Problems in this field are the enrichment of the gluon jets and the need for comparison of jets with nearly the same energy. One method is the comparison of nearly 3-fold symmetric 3-jet at 90 GeV, where two of the jets are quark jets and the other a gluon jet, with all multihadronic events from TRISTAN around 60 GeV, where these originate from two quark jets. Another way is to use tagged charm or bottom quark jets in 3-jet events to get a nearly clean sample of gluon jets. One has to subtract the background of the heavy quark jets carefully, since we want to compare gluon jets with normal light (u, d, s) quark jets. Points of interest to look for in gluon jets are:

- $p_\perp$ distribution of particles within the jet,
- x distribution of particles,
- charge content,
- baryon content,
- isoscalar content,
- gluonium states.

For some of these questions 10,000 multihadronic events might not be enough and so the topic will have to be delayed.

9. Testing the Gluon Self-coupling

An essential feature of the QCD as a non-abelian theory is the existence of the gluon self-coupling, that a gluon can radiate gluons. Some indirect evidence is the observed broadening of gluon jets compared to quark jets. The best test comes from 4-jet events. Methods have been proposed by Körner, Schierholz and Willrodt[44] (KSW) and Nachtmann and Reiter[45] (NS).

For the KSW method, 4-jet events with two jets in each thrust hemisphere are used. The angle ϕ_{KSW} is defined as the angle between the two planes built by jets (1, 2) and (3, 4), where the momenta in each hemisphere are ordered according to $|\vec{p}_1| \geq |\vec{p}_2|$ and $|\vec{p}_3| \geq |\vec{p}_4|$

$$\cos\phi_{KSW} = \vec{n}_{12}\cdot\vec{n}_{34}$$
$$\vec{n}_{ij} = \frac{\vec{p}_i\times\vec{p}_j}{|\vec{p}_i|\cdot|\vec{p}_j|}$$

In QCD, the distribution of ϕ_{KSW} is expected to be more shifted towards 180° than in QED.

The NR method is based on the different helicity structure of the processes $g \to gg$ and $g \to q\bar{q}$ for the configurations in Fig. 39. The emission of a gluon into a gluon pair is forbidden at right angles, whereas the emission of a quark pair is allowed. For parallel emission the opposite is true. So, a very special kinematic configuration of two almost antiparallel jets with high energies (1 and 2) and two antiparallel jets with low energies (3 and 4) has to be demanded. The jets have to be ordered according to $E_1 > E_2 > E_3 > E_4$ and the above arguments are only valid in the limit $E_2 >> E_3$. Nachtmann and Reiter introduced the angle θ_{NR} which basically measures the angle between the vectorial difference of the two highest and the two lowest energetic jets of a 4-jet event. A slightly modified definition has been done by Ali and Rudolph[46]:

$$\cos\theta_{NR} = \vec{n}_{12}\cdot\vec{n}_{34}$$
$$n_{ij} = \left(\frac{\vec{p}_i}{|p_i|} - \frac{\vec{p}_j}{|p_j|}\right)$$

But the fact that E_2 should be at least factor 2 larger than E_3 restricts the useful sample quite drastically.

S. Bethke[21] has made a comparison of the two analyses with 10000 generated 4-parton events at $E_{cm} = 44$ GeV. Figures 40a and b show the differential distributions of $\cos\theta_{NR}$ and ϕ_{KSW} of the 4-parton events according to QCD, an abelian QCD (QED) and a pure phase-space (PS) model without applying any special cuts. On this level, significant differences between QCD and the two other models can be seen in both distributions. In Figures 40c and d, the generated 4-parton events were fragmented into final state hadrons and the observables were calculated from the jet axes using YCLUS$ with $y_{cut} = 0.024$. In the observable θ_{NR}, a detectable difference between the QCD and the QED model is still visible, whereas the difference in ϕ_{KSW} is nearly washed out, even though these samples do not contain background from misidentified 2- and 3-parton events. This analysis should be redone at $E_{cm} = 93$ Gev, where careful checks between the QCD and QED-like models with second order matrix element and the QCD shower models have to be carried out. Part of such studies have been carried out by Ref. 46.

10. Summary

The tuning and optimization of the existing QCD plus fragmentation models has been done in great detail with existing data at lower energies. The Lund shower model gives a quite good reproduction of the experimental distributions. The other parton shower models have still some more problems, show similar energy behavior as the Lund shower model. This will help us to get some confidence in the background calculations for possible new physics at SLC. For the other points of interest in QCD, I think, still more work has to be done.

References

1. The members of the QCD group are: S. Bethke, S. Brodsky, P. Dauncey, T. Hansl-Kozanecki, S. Komamiya, A. Petersen, B. Ward, P. Weber, A. Weigend, and D. Wood.
2. T.Sjöstrand, Computer Phys.Comm. **39**, 347 (1986); T.Sjöstrand and M. Bengtsson, Computer Phys.Comm. **43**, 367 (1987).
3. B.R.Webber, Nucl.Phys. **B238**, 492 (1984), and private communication.
4. T.D.Gottschalk, D.Morris CALT-68-1365 (1986)
5. P.Hoyer *et al.*, Nucl.Phys.**B161**, 349 (1979); A.Ali *et al.*, Phys.Lett.**93B**, 155 (1980).
6. B.Andersson *et al.*, Phys.Rev. **97**, 33 (198?).
7. The first cluster model was from: R.D.Field and S.Wolfram, Nucl.Phys. **B213**, 65 (1983).
8. JADE Collaboration, W. Bartel *et al.*, Phys. Lett. **101B**, 129 (1981); Phys. Lett. **134B**, 275 (1984); Z.Phys. **C21**, 37 (1983); H. Aihara *et al.*, Phys. Rev. Lett. **54**, 270 (1985).
9. F.Gutbrod, G.Kramer and G.Schierholz, Z.Phys. **C21**, (1984) 235.
10. R.K. Ellis *et al*, Nucl.Phys. **B178**421 (1981).
11. T.D. Gottschalk and M.P. Shatz, Phys.Lett. **150B**451 (1985).
12. G. Kramer and B. Lampe, DESY 86-119 (1986)).
13. JADE Collaboration, W.Bartel *et al.*, Z.Phys. **C25**, 231 (1984); W.Bartel *et al.*, Z.Phys. **C33**, 23 (1986).
14. R.Schindler, proceedings of the 1986 SLAC Summer Institute (1986). Very recent results from Mark III show that some branching ratios have to be corrected downwards again.
15. Using the definition of the Lund model the values have to be multiplied by $\sqrt{2}$.
16. G.Marchesini and B.R.Webber, Nucl.Phys. **B238**, 1 (1984).
17. See, e.g., P.Dauncey PhD Thesis, RAL-T-034 (1986)
18. It should be noted that the "string" effect disappears in the Webber model if these large mass clusters are allowed to decay isotropically.
19. See also A.Petersen, Strong Interaction on Gauge Theories, XXIth Rencontre de Moriond 291 (1986).
20. G.Altarelli and G.Parisi, Nucl.Phys. **B216**, 298 (1977).
21. S. Bethke, Habilitationsschrift, to be published (1987).

22. S. Komamiya, Strong Interaction on Gauge Theories, XXIth Rencontre de Moriond 199 (1986).
23. X.Artru and G.Mennessier, Nucl.Phys. **B70**, 93 (1974).
24. A.Petersen *et al.*, SLAC-PUB-4290 (1987), to be published in Phys. Rev. D.
25. J.D.Bjorken, S.J.Brodsky, Phys.Rev. **D1**, 1416 (1970); G. Hanson *et al.*, Phys.Rev.Lett **35**, 1609 (1975); we used the definition from C. Berger *et al.*, Phys.Lett **82B**, 449 (1979).
26. S.Brandt *et al.*, Phys.Lett. **12**, 57 (1964); E.Fahri, Phys.Rev.Lett. **39**, 1587 (1977).
27. A.De Rujula *et al.*, Nucl.Phys. **B138**, 387 (1978). We used the algorithm described in Ref.6.
28. L.Clavelli, D.Wyler, Phys.Lett. **103B**, 383 (1981).
29. See also T.Sjöstrand and M. Bengtsson, LUTP 86-18 (1986).
30. PLUTO Collaboration, C.Berger *et al.*, Z.Phys. **C28**, 365 (1985); PLUTO Collaboration, C.Berger *et al.*, Z.Phys. **C12**, 297 (1982); PLUTO Collaboration, C.Berger *et al.*, Phys.Lett. **95B**, 313 (1980).
31. TASSO Collaboration, M.Althoff *et al.*, Z.Phys. **C22**, 307 (1984).
32. CELLO Collaboration, H.J.Behrend *et al.*, Z.Phys. **C14** , 95 (1982).
33. JADE Collaboration, W.Bartel *et al.*, Z.Phys. **C20**, 187 (1983).
34. HRS Collaboration, D.Bender *et al.*, Phys.Rev. **D31**, 1 (1985).
35. C.Basham, L.Brown, S.Ellis and S.Love, Phys.Rev.Lett **41**, 1585 (978).
36. We use the cluster algorithm of Ref.6.
37. See, e.g., G. Hanson in Proceedings of the Second Mark II Workshop on SLC Physics, SLAC Report No. 306 (1987).
38. See, e.g., K. O'Shaughnessy in Proceedings of the Second Mark II Workshop on SLC Physics, SLAC Report No. 306 (1987).
39. R.D. Field, Proc. International Lepton Photon Symposium, Cornell University 593 (1983).
40. G. Altarelli, Proc. Europhysics Conf. on High Energy Physics, Bari 728 (July 1985).
41. See also M. Bengtsson and T.Sjöstrand, LUTP 86-24 (1986).
42. JADE Collaboration, W. Bartel *et al.*, Z.Phys. **C21**, 37 (1983); Mark II Collaboration, A. Petersen *et al.*, Phys. Rev. Lett. **55**, 1954 (1985).
43. UA1 Collaboration, G. Arnison *et al.*, Nucl. Phys. **B276**, 253 (1986).
44. J. Körner *et al.*, Nucl. Phys. **B185**, 365 (1981).

45. O. Nachtmann and A. Reiter, Phys. Lett. **116**, 42 (1982).
46. A. Ali, DESY 86-032 (1986); CERN 86-02 Vol. 2 (1986).

Figure Captions

1. The aplanarity distribution in comparison with the models.
2. The $Q_2 - Q_1$ distribution in comparison with the models.
3. The sphericity distribution in comparison with the models.
4. The thrust distribution in comparison with the models.
5. The thrust distribution in comparison with the Lund shower model (full line), the CALTECH II model (dotted line), the CALTECH II parton shower with Lund string fragmentation (dot-dot-dashed), and the Lund parton shower with CALTECH II fragmentation (dashed-dashed-dot).
6. The minor value distribution in comparison with the models.
7. The M_{br}^2/s, distribution in comparison with the models.
8. The M_{sl}^2/s, distribution in comparison with the models.
9. The $(M_{br}^2 - M_{sl}^2)/s$ distribution in comparison with the models.
10. The $p_\perp^2$ distribution of charged particles with respect to the sphericity axis in comparison with the models.
11. The $p_\perp^{out}$ distribution of charged particles with respect to the event plane in comparison with the models.
12. The charged particle x distribution in comparison with the models.
13. The rapidity distribution of charged particles with respect to the thrust axis in comparison with the models.
14. The charged particle flow with respect to the sphericity axis in comparison with the models.
15. The energy flow with respect to the sphericity axis in comparison with the models.
16. (a) The <aplanarity> and (b) <sphericity> as a function of E_{cm} in comparison with HRS and TASSO results and the model predictions.
17. (a) The $< M_{br}^2/s >$ and $< M_{sl}^2/s >$, and (b) $< (M_{br}^2 - M_{sl}^2)/s >$ as a function of E_{cm} in comparison with PLUTO and JADE results and the model predictions.
18. The <1 - T> as a function of E_{cm} in comparison with HRS, JADE, PLUTO and TASSO results and the model predictions.

19. (a) the energy-energy correlation (EEC) integrated in the angular region $57.6° < \theta < 122.4°$ and (b) the asymmetry of EEC integrated in the angular region $28.8° < \theta < 90°$ as a function of E_{cm} in comparison with CELLO, JADE, and PLUTO results and the model predictions.
20. (a) The mean multiplicity and number of reconstructed jets or clusters and (b) the mean charged particle x as a function of E_{cm} in comparison with HRS, JADE, PLUTO and TASSO results and the model predictions.
21. (a) The $< p_\perp^2 >$ and (b) the $< (p_\perp^{out})^2 >$ and $< (p_\perp^{in})^2 >$ as a function of E_{cm} in comparison with HRS, PLUTO and TASSO results and the model predictions.
22. The predicted aplanarity of the models at $E_{cm} = 93$ GeV.
23. The predicted sphericity of the models at $E_{cm} = 93$ GeV.
24. The predicted thrust of the models at $E_{cm} = 93$ GeV.
25. The predicted minor distribution of the models at $E_{cm} = 93$ GeV.
26. The predicted M_{br}^2/s distribution of the models at $E_{cm} = 93$ GeV.
27. The predicted M_{sl}^2/s distribution of the models at $E_{cm} = 93$ GeV.
28. The predicted $(M_{br}^2 - M_{sl}^2)/s$ distribution of the models at $E_{cm} = 93$ GeV.
29. The predicted number of reconstructed jets or clusters of the models at E_{cm} = 93 GeV.
30. The predicted multiplicity of the models at $E_{cm} = 93$ GeV.
31. The predicted $p_\perp$ distribution of charged particles with respect to the sphericity axis of the models at $E_{cm} = 93$ GeV.
32. The predicted $p_\perp^{out}$ distribution of charged particles with respect to the event plane of the models at $E_{cm} = 93$ GeV.
33. The predicted $p_\perp^{in}$ distribution of charged particles to the sphericity axis in the event plane of the models at $E_{cm} = 93$ GeV.
34. The predicted charged particle x distribution of the models at $E_{cm} = 93$ GeV.
35. The predicted ratio R_x of the x distribution at $E_{cm} = 93$ GeV over that at $E_{cm} = 29$ GeV.
36. The predicted rapidity distribution of charged particles with respect to the thrust axis of the models at $E_{cm} = 93$ GeV.
37. The predicted energy flow with respect to the sphericity axis of the models at $E_{cm} = 93$ GeV.
38. The 3-jet event rates as a function of E_{cm} for $y_{cut} = 0.04$ and 0.08 compared to the Lund shower model with a constant and a running value of α_s.

39. The charged and neutral particle flow in 3-jet events for different schemes within the Lund model at $E_{cm} = 93$ GeV.
40. Pictorial description of the Nachtmann Reiter selection rule.
41. Model-distributions of $\cos\theta_{NR}$ and ϕ_{KSW}, calculated on the parton level (a and b) and after the fragmentation and jet analysis (c and d).

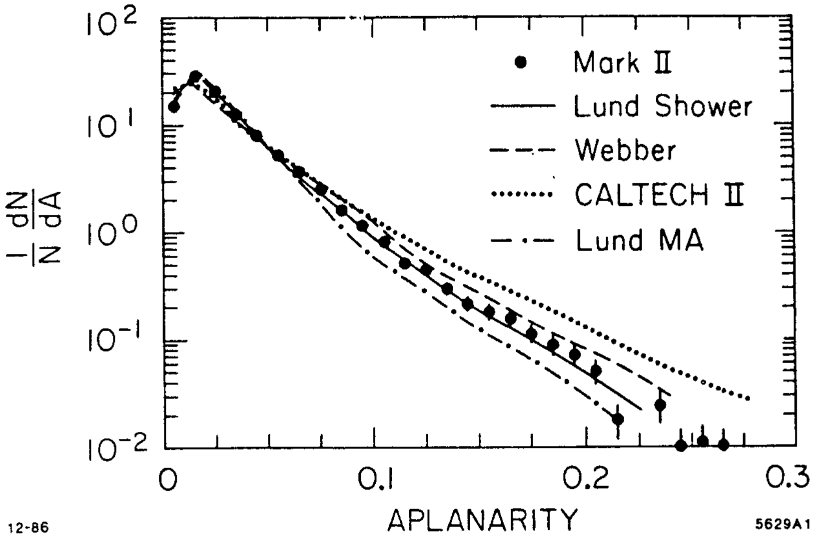

FIG. 1

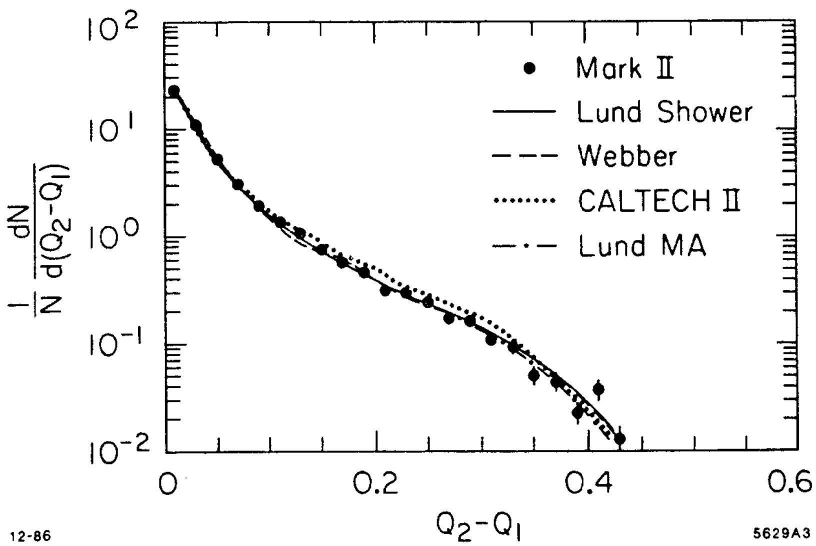

FIG. 2

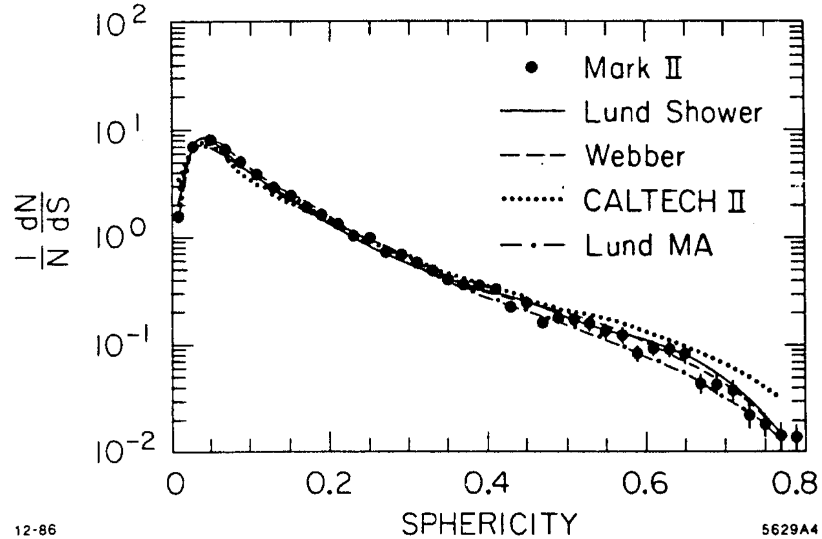

FIG. 3

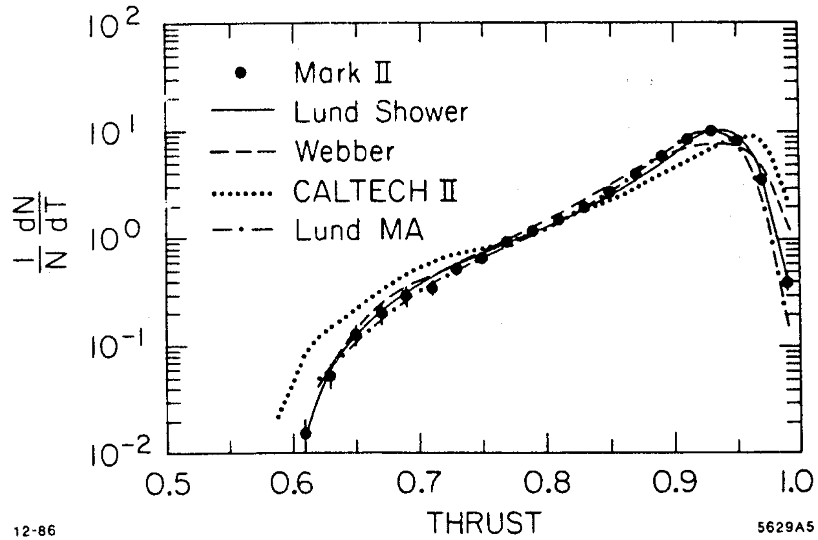

FIG. 4

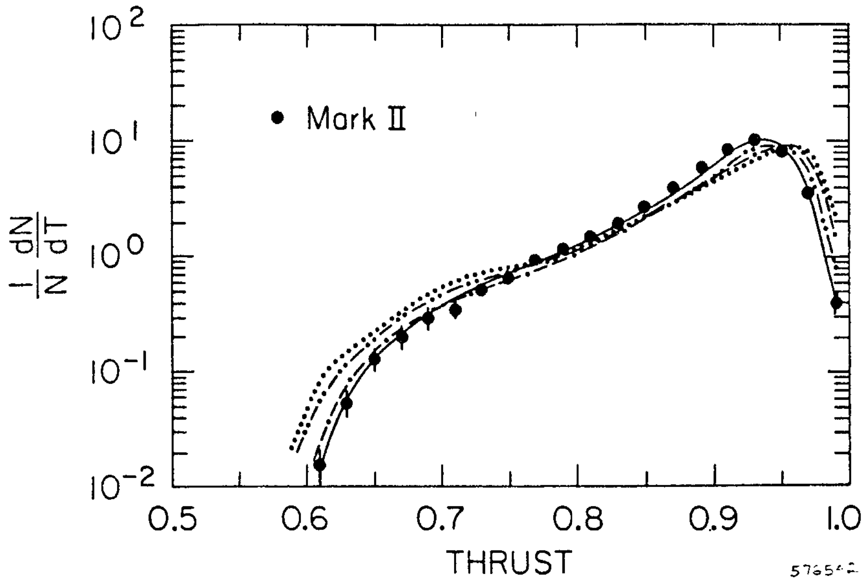

FIG. 5

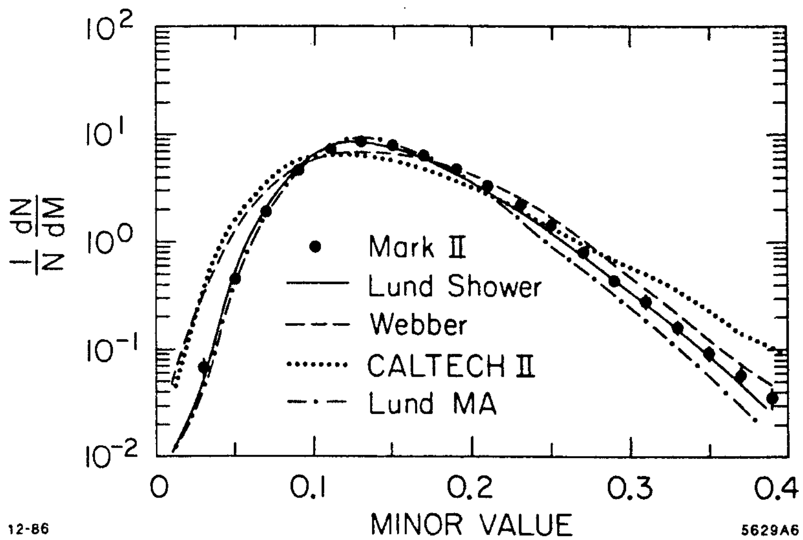

FIG. 6

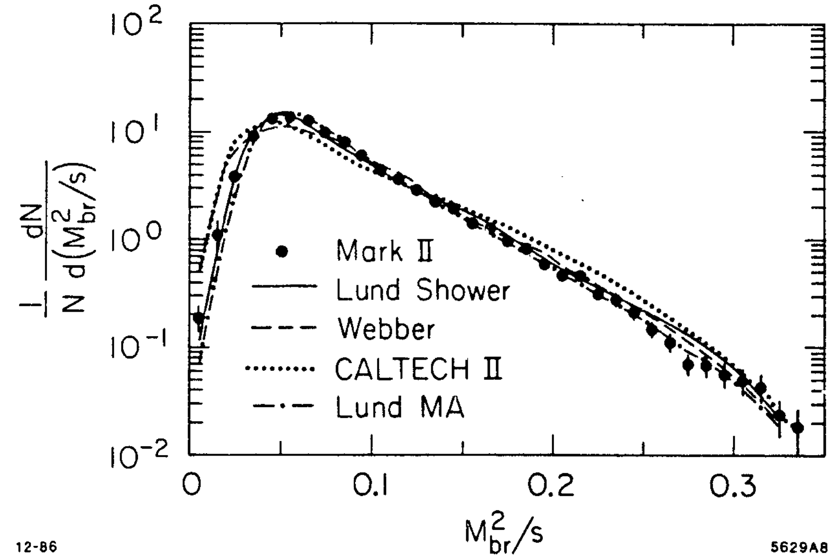

FIG. 7

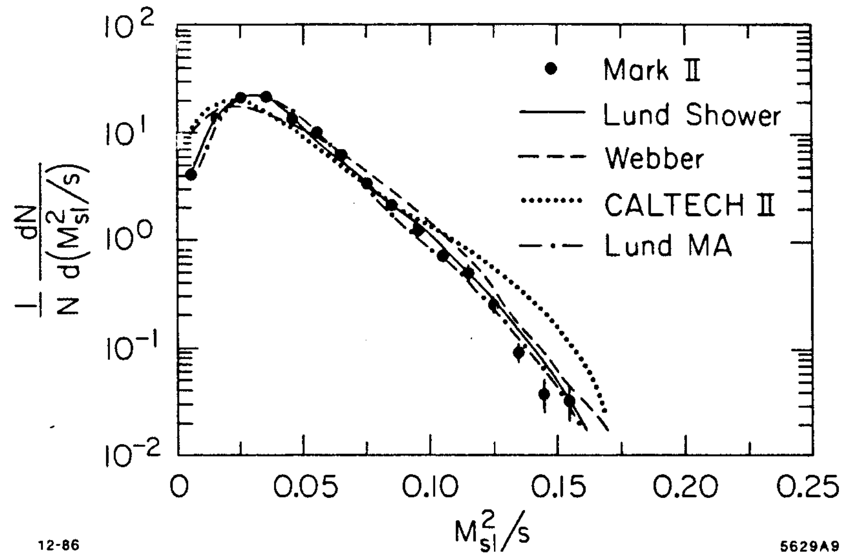

FIG. 8

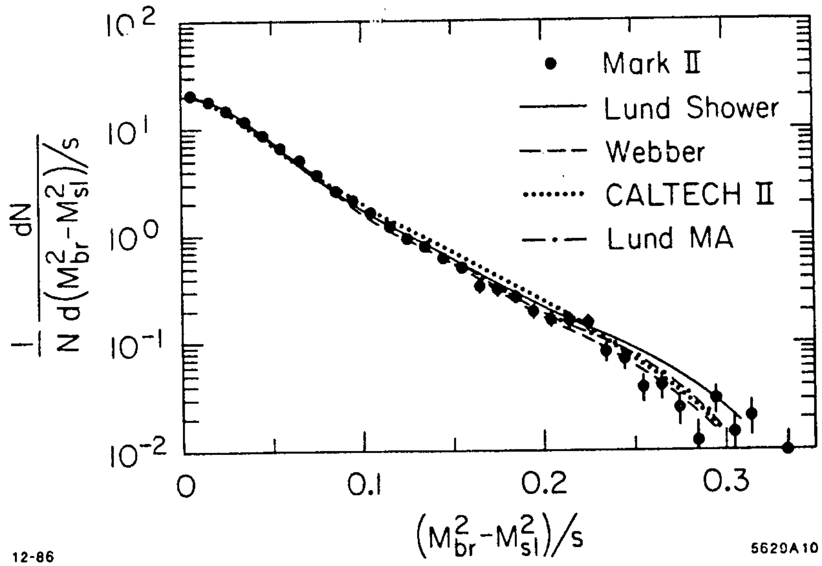

FIG. 9

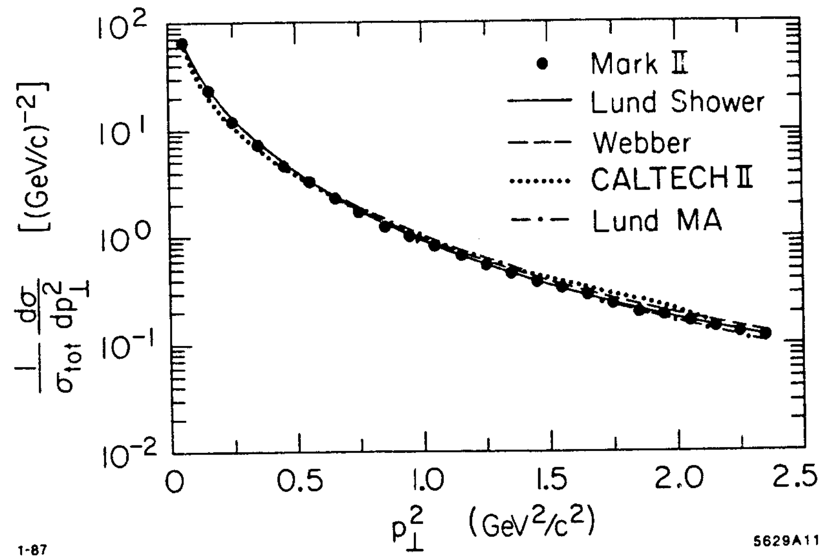

FIG. 10

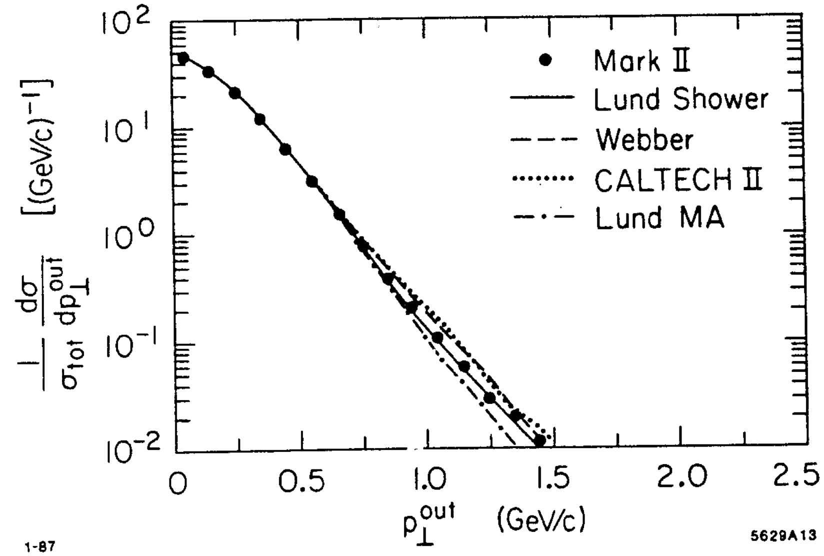

FIG. 11

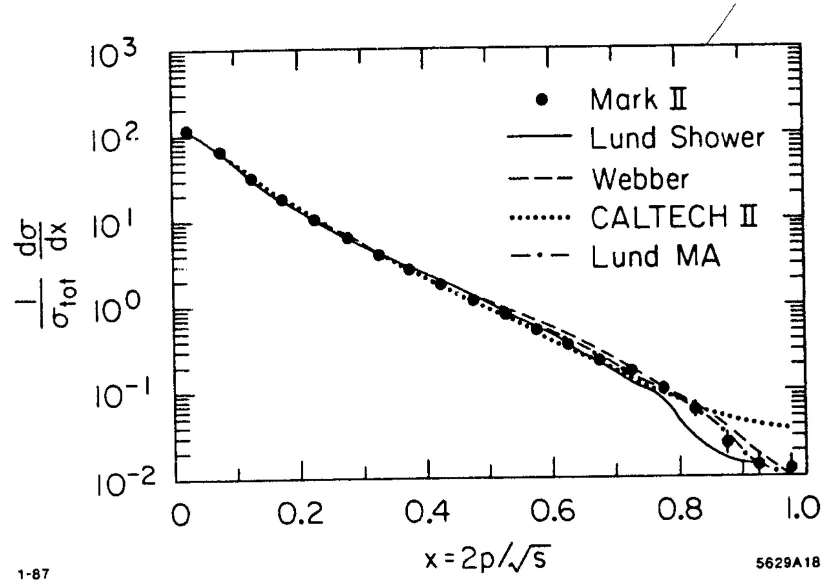

FIG. 12

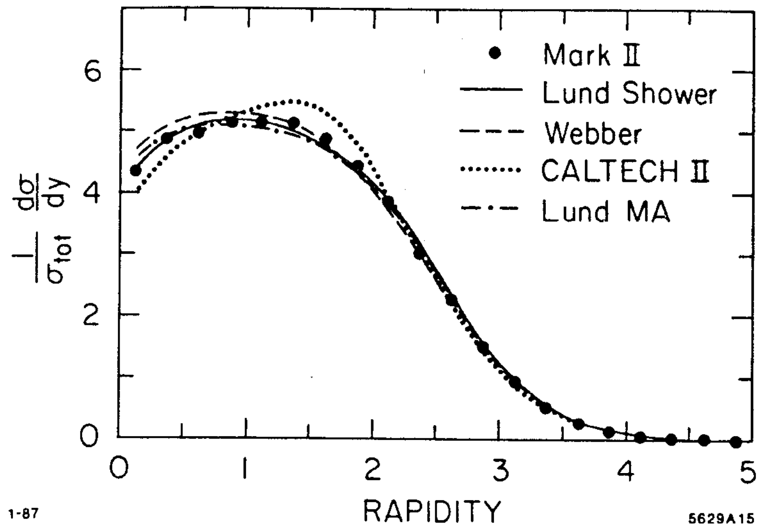

FIG. 13

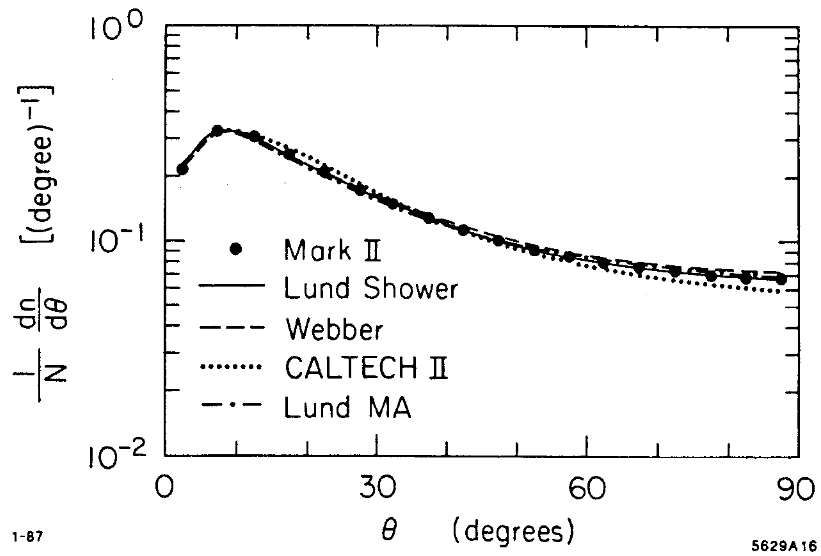

FIG. 14

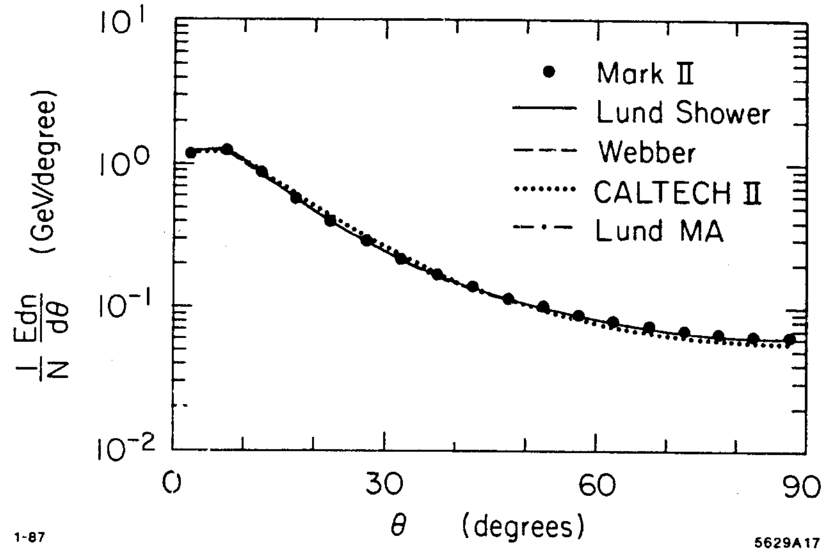

FIG. 15

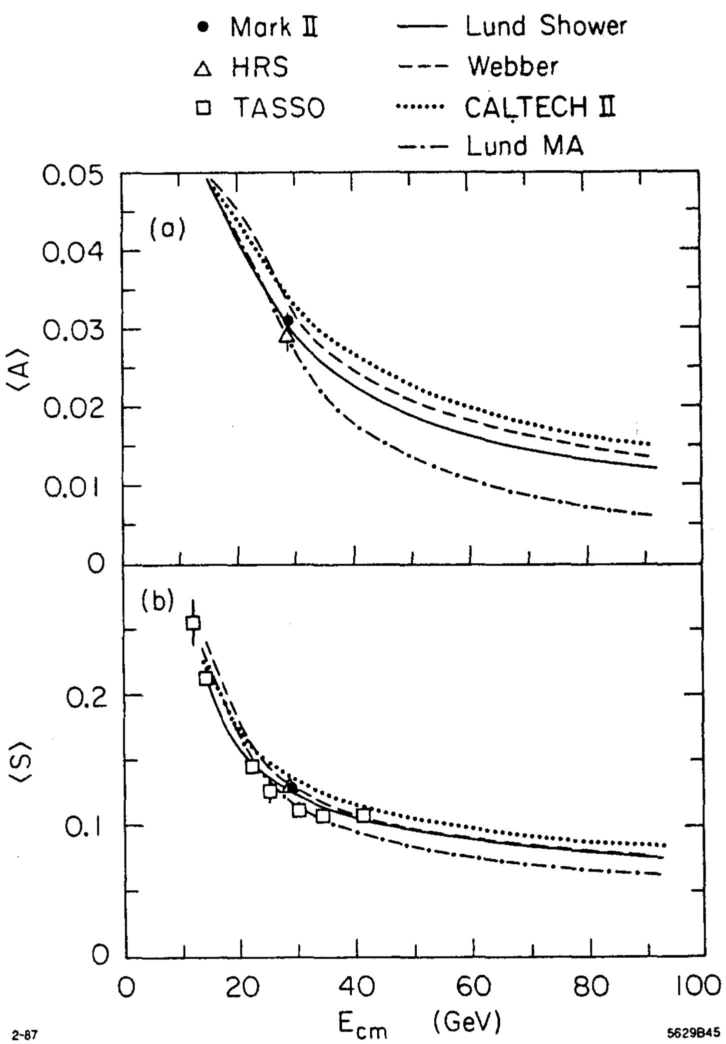

Mark II
HRS
TASSO
Lund Shower
Webber
CALTECH II
Lund MA
(a)
(b)
⟨A⟩
⟨S⟩
0.05
0.04
0.03
0.02
0.01
0
0.2
0.1
0
0
20
40
60
80
100
E_{cm} (GeV)
2-87
5629B45

FIG. 16

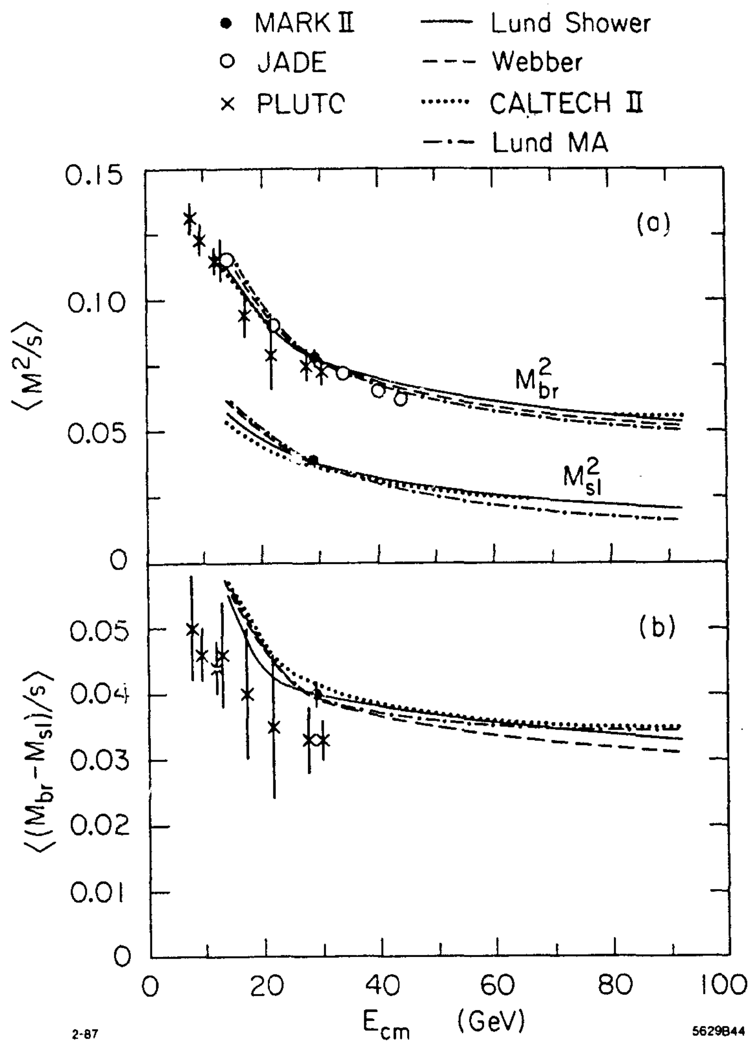

MARK II
JADE
PLUTO
Lund Shower
Webber
CALTECH II
Lund MA
(a)
(b)
M^2_{br}
M^2_{sl}
$\langle M^2/s \rangle$
$\langle (M_{br}-M_{sl})/s \rangle$
0.15
0.10
0.05
0
0.05
0.04
0.03
0.02
0.01
0
0
20
40
60
80
100
E_{cm} (GeV)
2-87
5629B44

FIG. 17

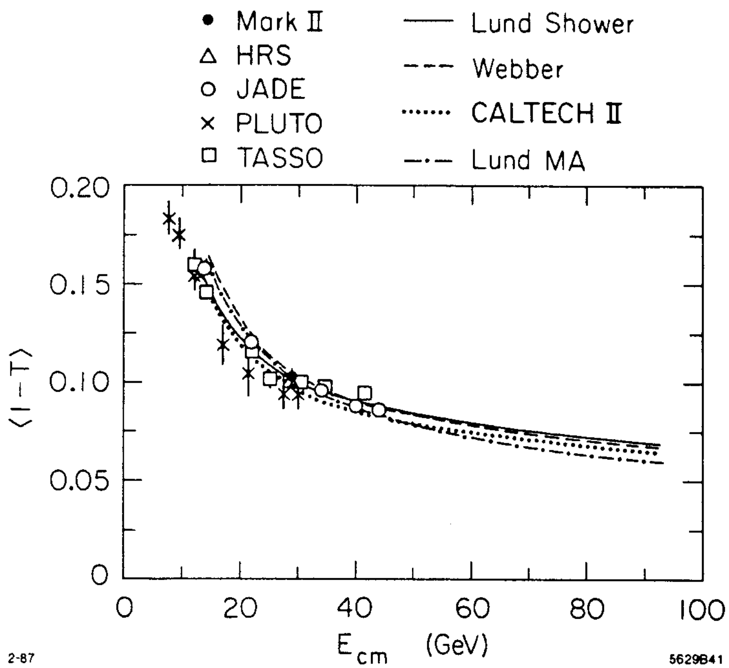

Mark II
HRS
JADE
PLUTO
TASSO
Lund Shower
Webber
CALTECH II
Lund MA
0.20
0.15
0.10
0.05
0
⟨1−T⟩
0
20
40
60
80
100
E_cm (GeV)
2-87
5629B41

FIG. 18

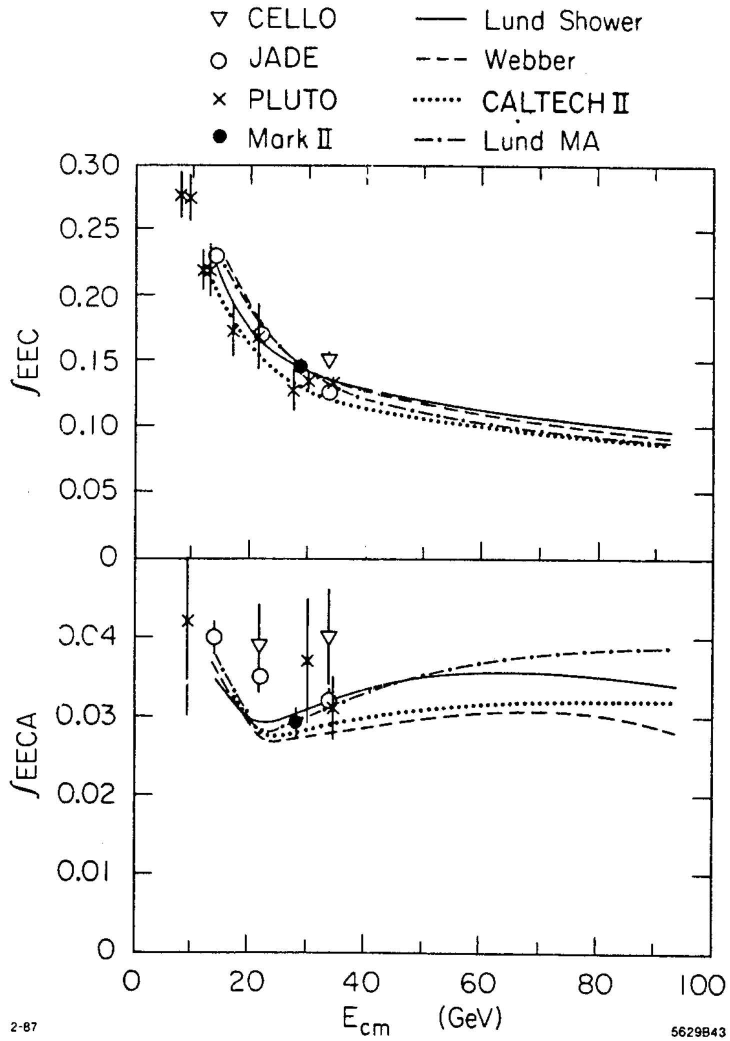

CELLO
JADE
PLUTO
Mark II
Lund Shower
Webber
CALTECH II
Lund MA
0.30
0.25
0.20
0.15
0.10
0.05
0
∫EEC
0.04
0.03
0.02
0.01
0
∫EECA
0
20
40
60
80
100
E_cm (GeV)
2-87
5629B43

FIG. 19

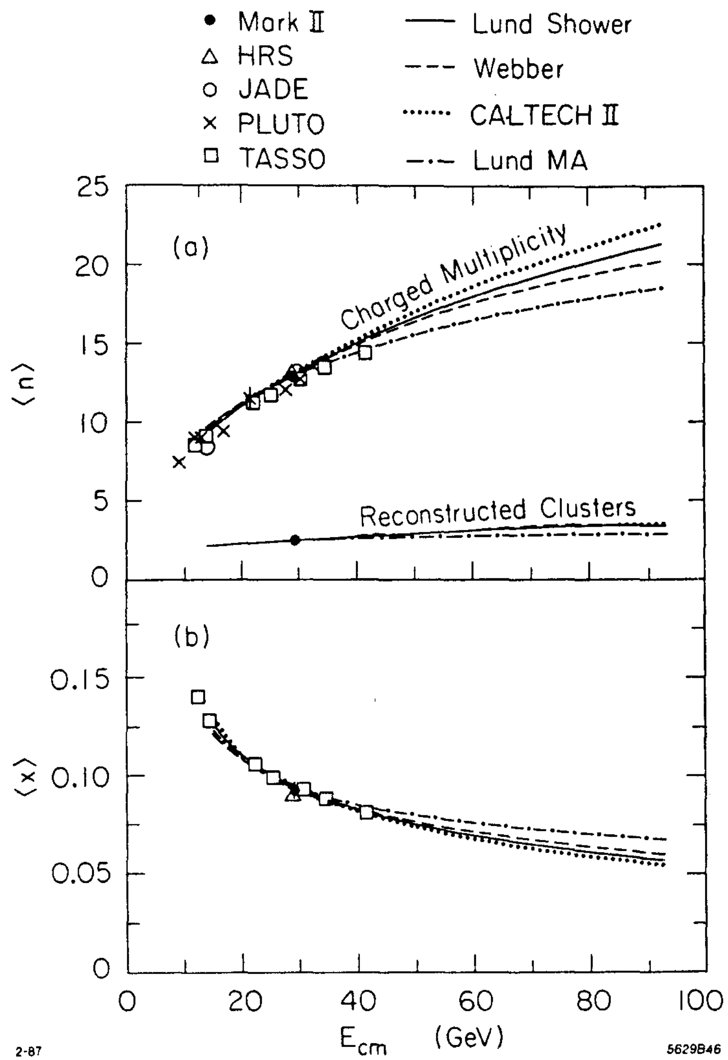
● Mark II
△ HRS
○ JADE
× PLUTO
□ TASSO
Lund Shower
Webber
CALTECH II
Lund MA
(a)
Charged Multiplicity
Reconstructed Clusters
(b)
⟨n⟩
⟨x⟩
25
20
15
10
5
0
0.15
0.10
0.05
0
0
20
40
60
80
100
E_cm (GeV)
2-87
5629B46

FIG. 20

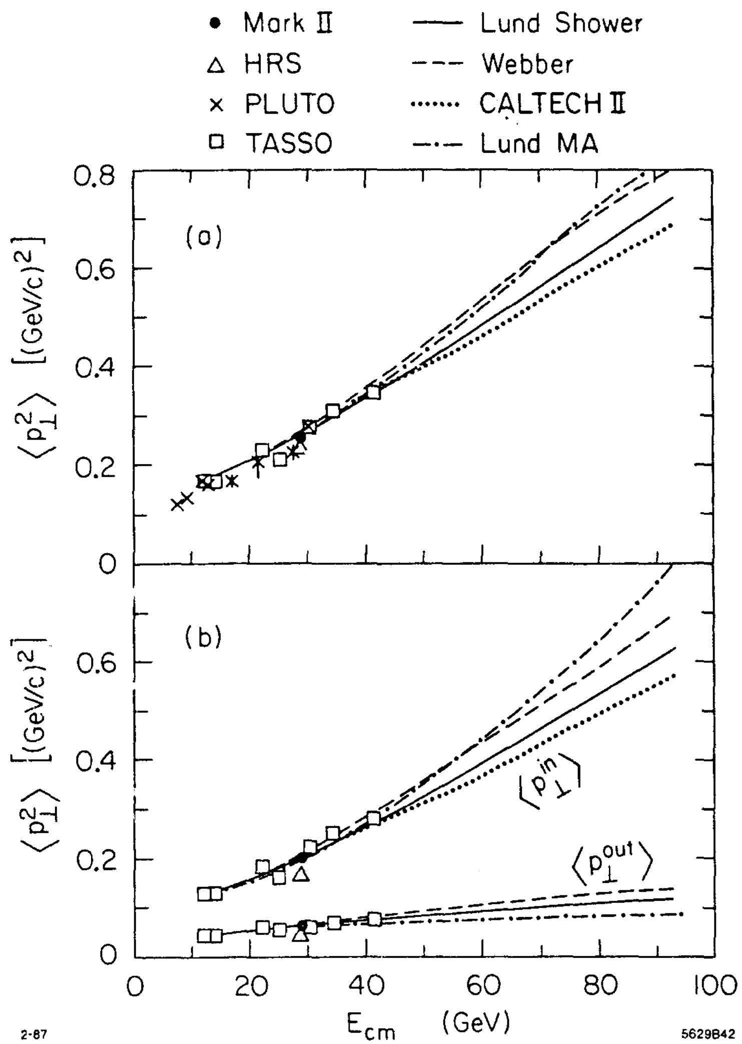
● Mark II
△ HRS
× PLUTO
□ TASSO
Lund Shower
Webber
CALTECH II
Lund MA
(a)
(b)
⟨p⊥²⟩ [(GeV/c)²]
⟨p⊥^in⟩
⟨p⊥^out⟩
0.8
0.6
0.4
0.2
0
0
20
40
60
80
100
E_cm (GeV)
2-87
5629B42

FIG. 21

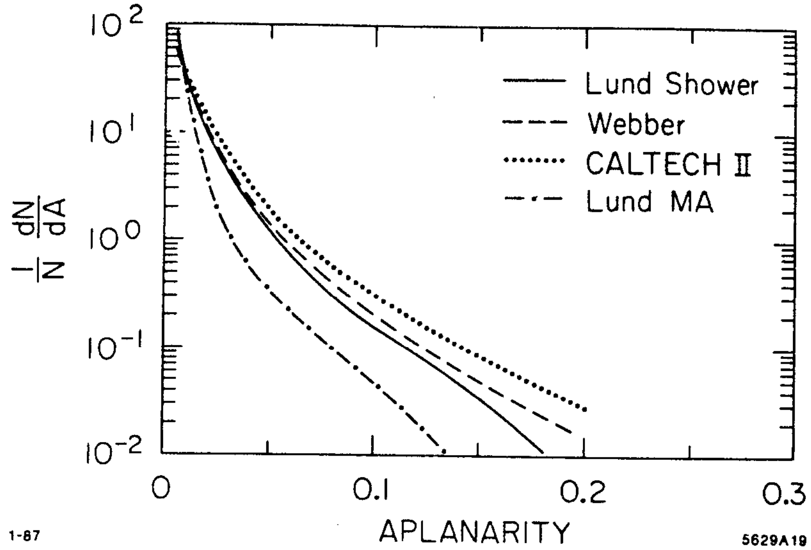

FIG. 22

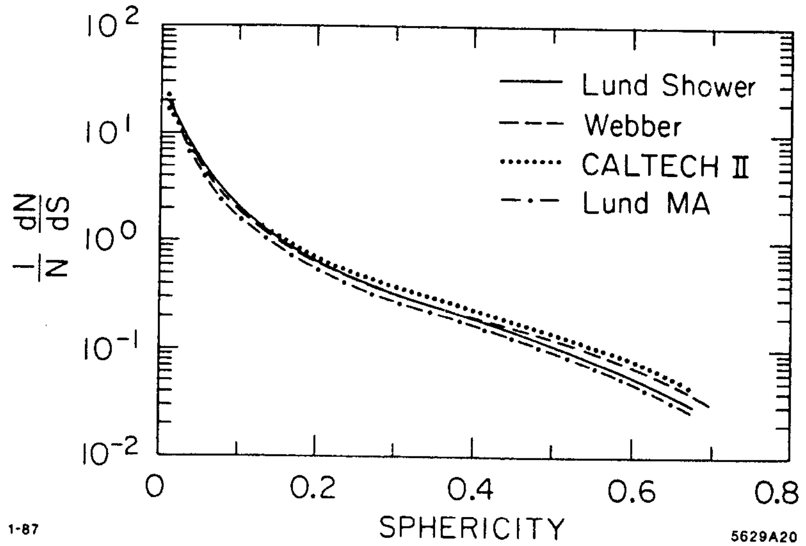

FIG. 23

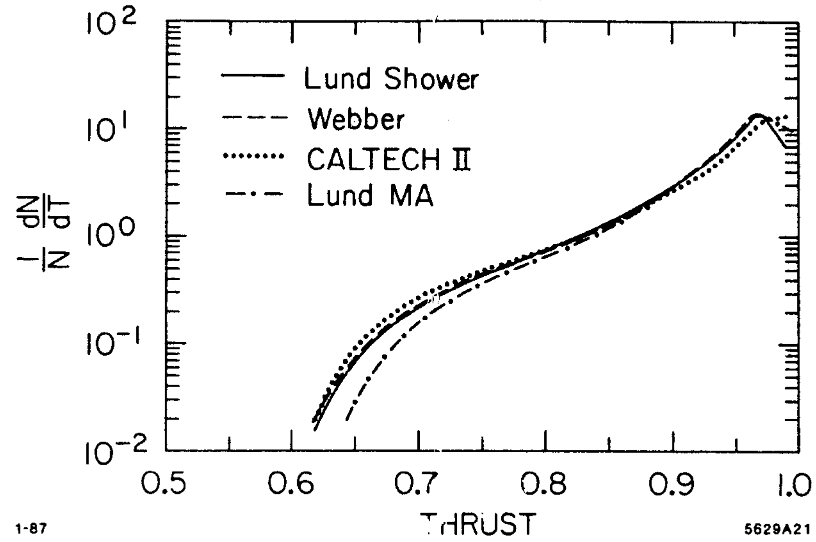

FIG 24

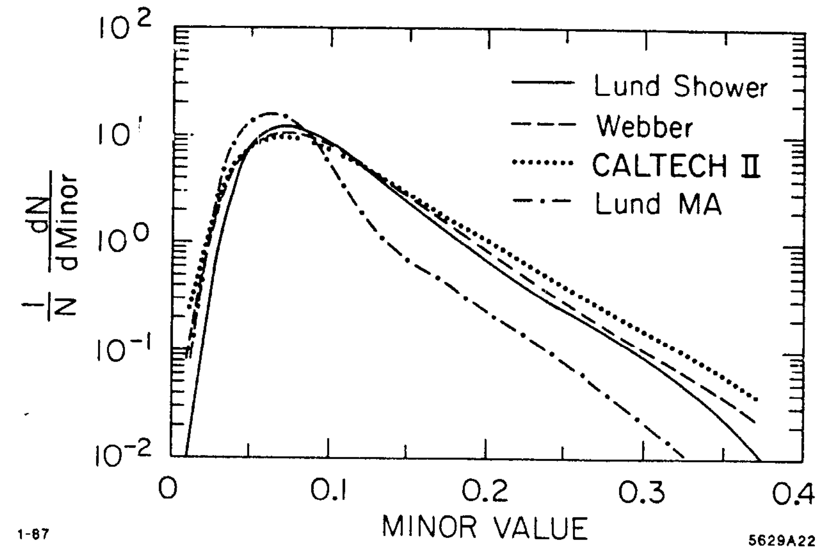

FIG. 25

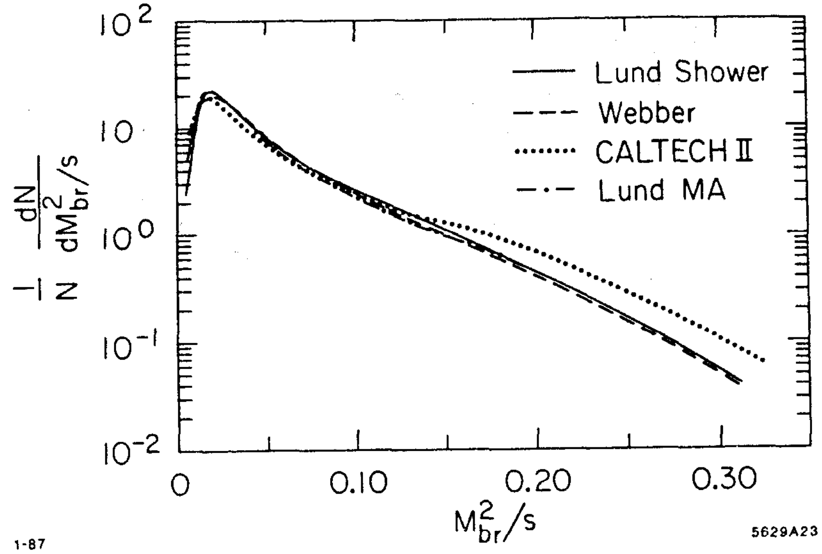

FIG. 26

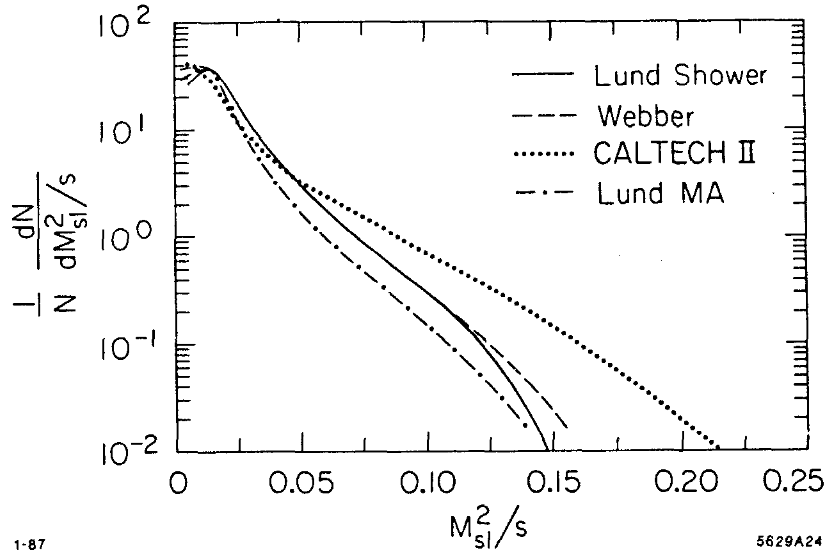

FIG. 27

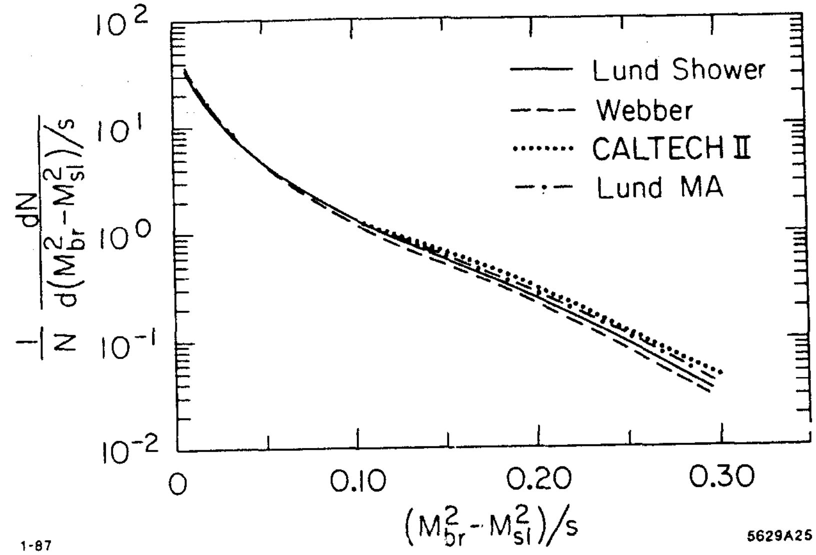

FIG. 28

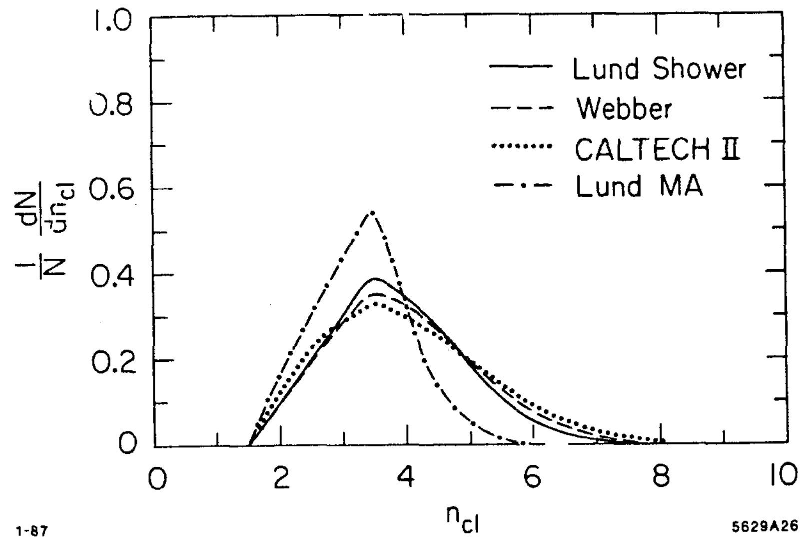

FIG. 29

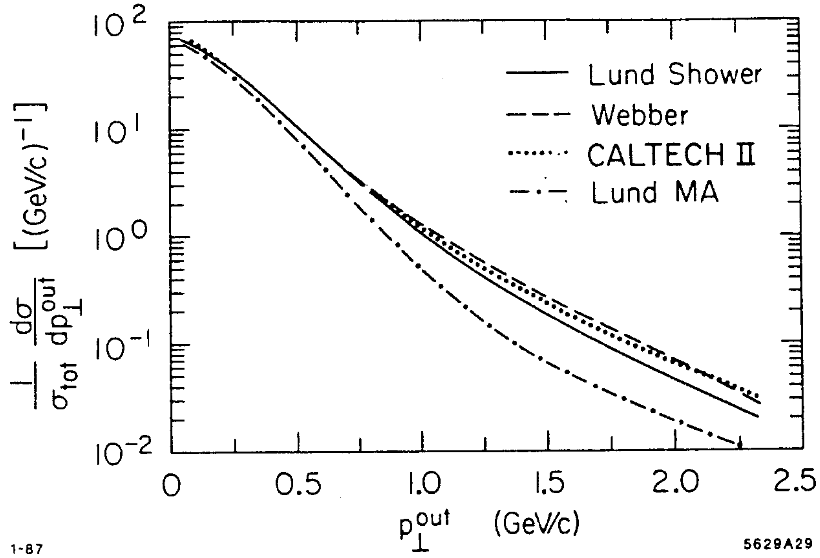

FIG. 32

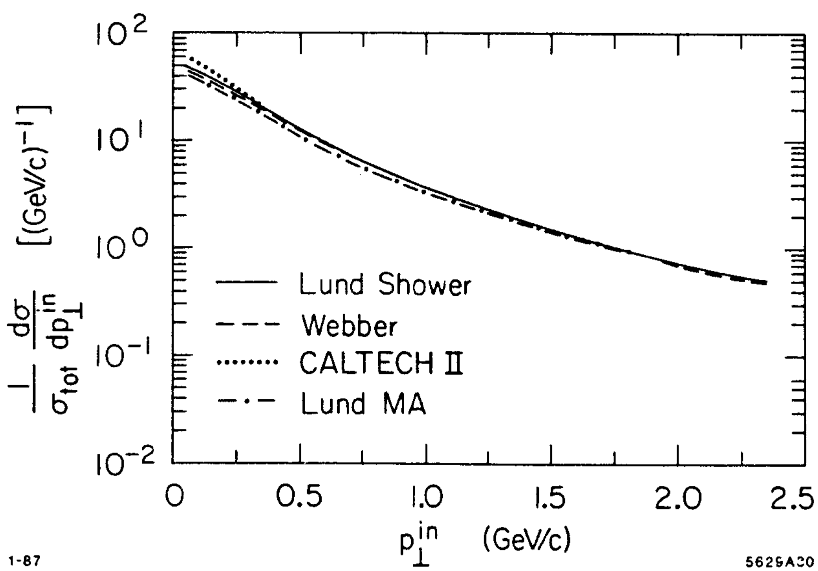

FIG. 33

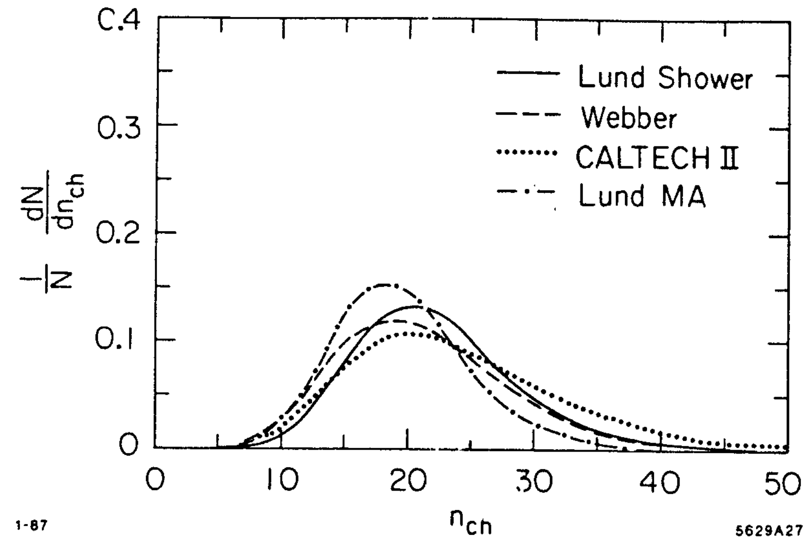

FIG. 30

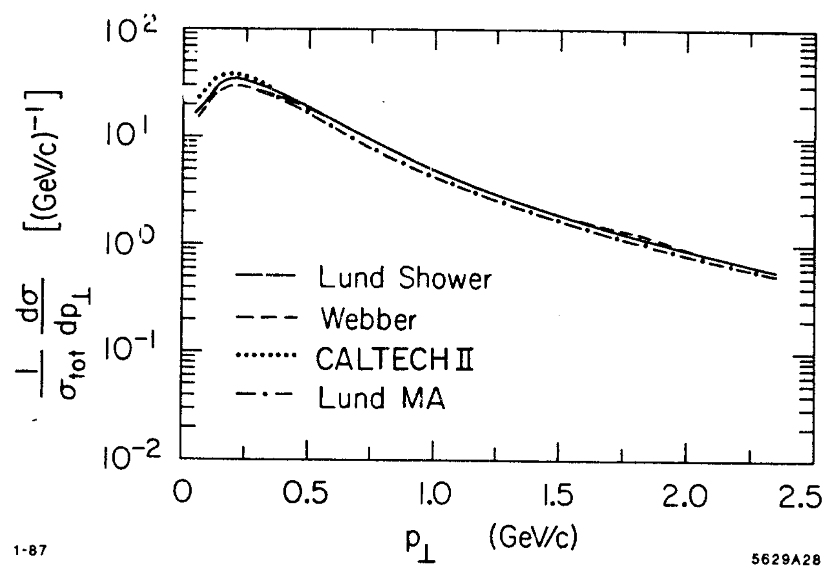

FIG. 31

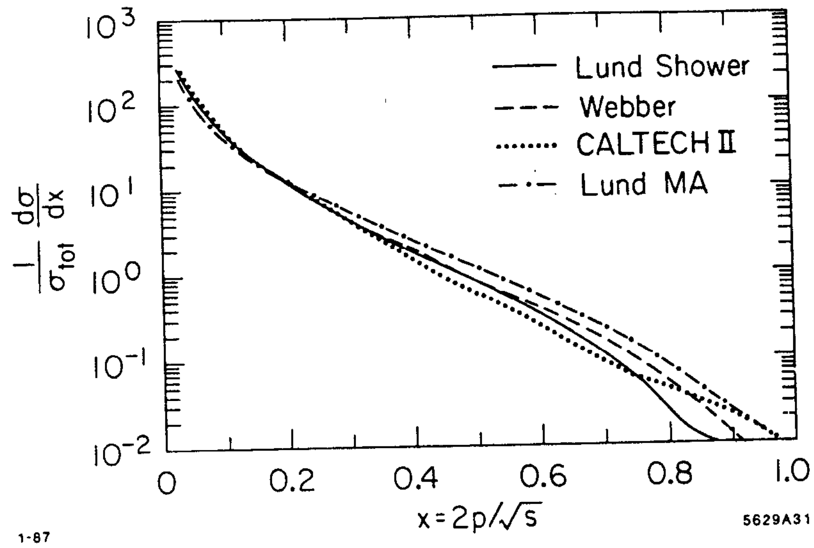

FIG. 34

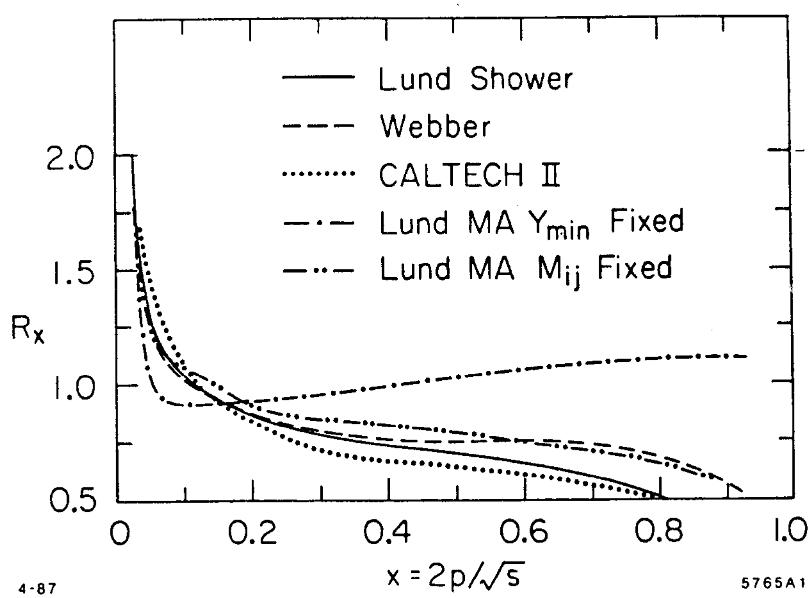

FIG. 35

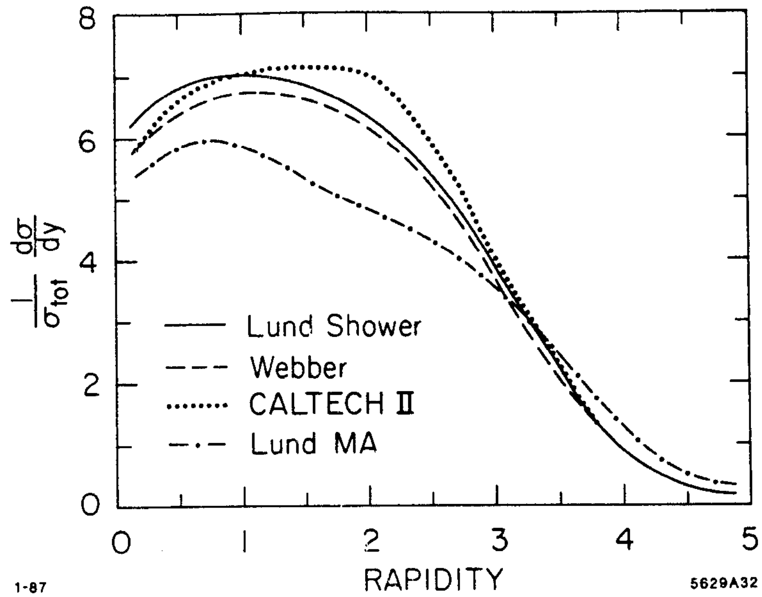

FIG. 36

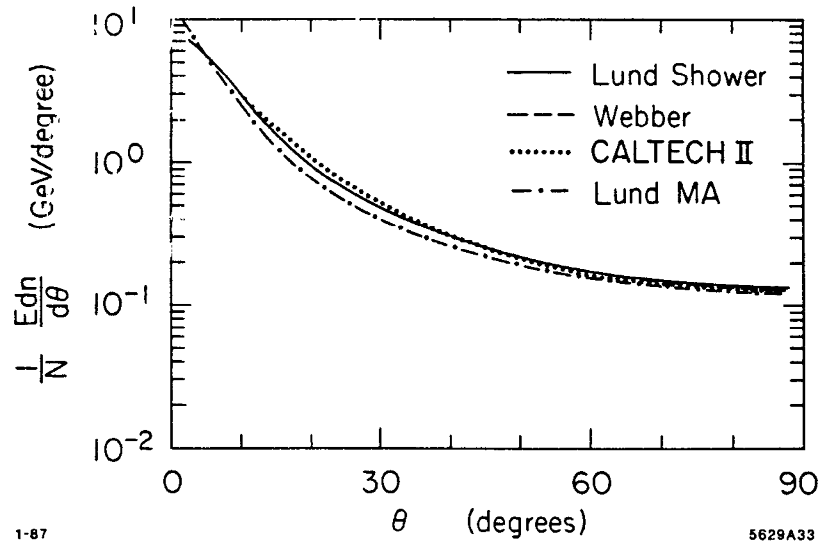

FIG. 37

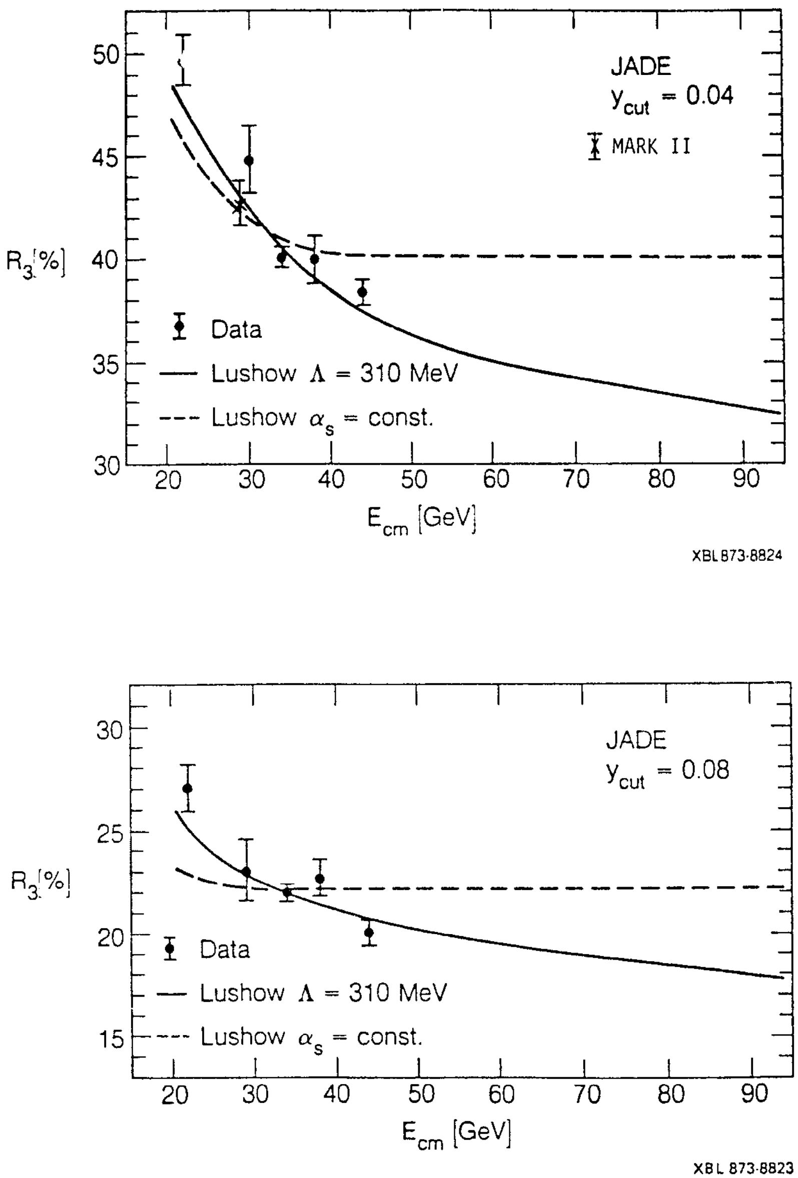
JADE
y_{cut} = 0.04
MARK II
Data
Lushow Λ = 310 MeV
Lushow α_s = const.
R_3 [%]
E_{cm} [GeV]
XBL 873-8824
JADE
y_{cut} = 0.08
Data
Lushow Λ = 310 MeV
Lushow α_s = const.
R_3 [%]
E_{cm} [GeV]
XBL 873-8823

FIG. 38

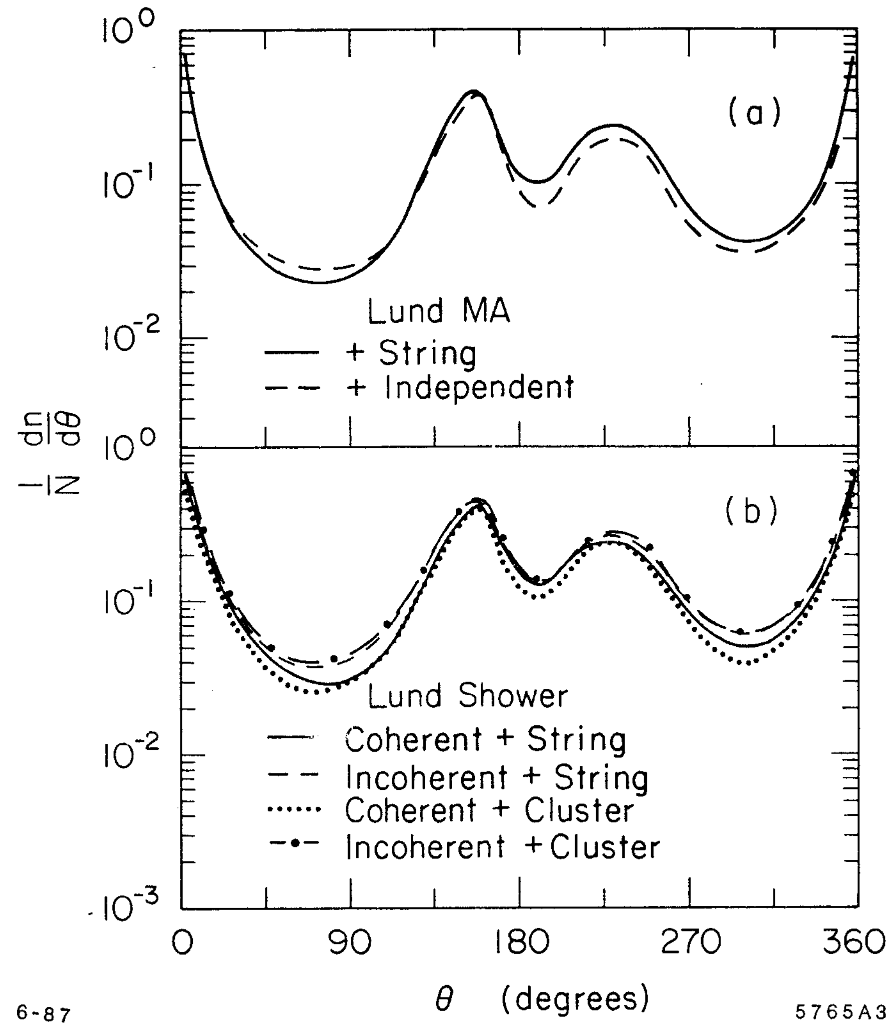
(a)
Lund MA
+ String
+ Independent
(b)
Lund Shower
Coherent + String
Incoherent + String
Coherent + Cluster
Incoherent + Cluster
$\frac{1}{N}\frac{dn}{d\theta}$
θ (degrees)
6-87
5765A3

FIG. 39

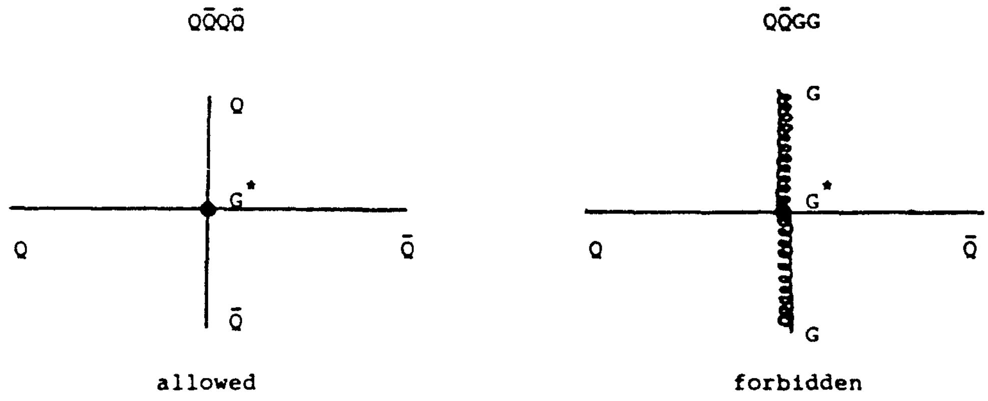

$Q\bar{Q}Q\bar{Q}$
Q
G^*
Q
$\bar{Q}$
$\bar{Q}$
allowed
$Q\bar{Q}GG$
G
G^*
Q
$\bar{Q}$
G
forbidden

FIG. 40

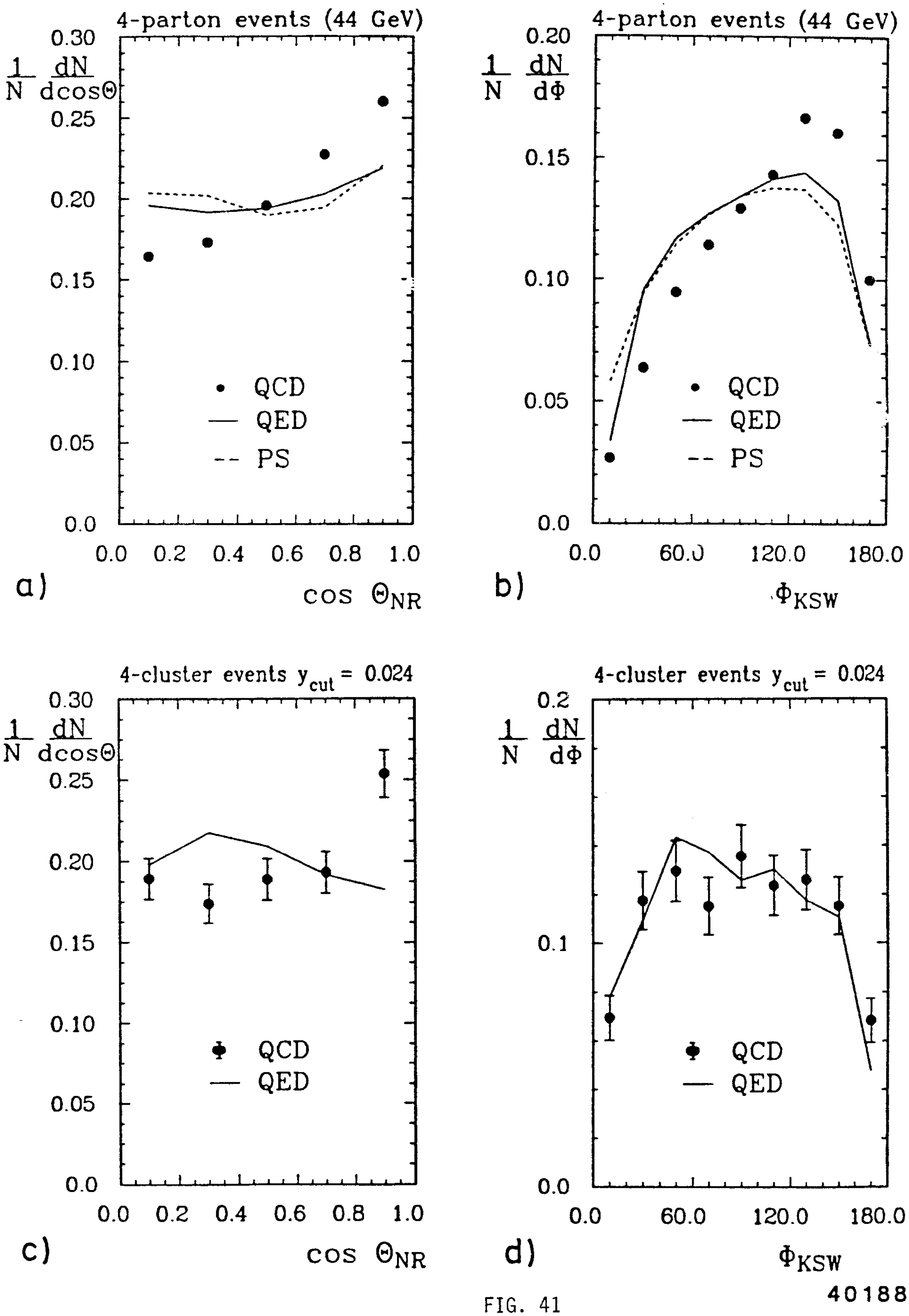
4-parton events (44 GeV)
$\frac{1}{N}\frac{dN}{d\cos\Theta}$
QCD
QED
PS
a)
cos Θ_{NR}
4-parton events (44 GeV)
$\frac{1}{N}\frac{dN}{d\Phi}$
QCD
QED
PS
b)
Φ_{KSW}
4-cluster events y_{cut} = 0.024
$\frac{1}{N}\frac{dN}{d\cos\Theta}$
QCD
QED
c)
cos Θ_{NR}
4-cluster events y_{cut} = 0.024
$\frac{1}{N}\frac{dN}{d\Phi}$
QCD
QED
d)
Φ_{KSW}
40188

FIG. 41

Mark II/SLC-Physics Working Group Note # 9–15

AUTHOR: Guy Wormser

DATE: April 27, 1987

TITLE: ψ tagging and B spectroscopy

1. Introduction

One of the most interesting aspects of standard physics on the Z^o peak is precision measurements of B spectroscopy. Two very challenging results are missing now, namely the separate measurement of B^0_d and B^- lifetimes and exclusive reconstruction of B^0_s . In this note, a simple and powerful way to obtain these results is described, *the ψ tagging*.

Some simple ideas are developped in Section 1. Section 2 is devoted to a search for ψ events in the PEP data, in order to get a feeling of the feasibility of such a method and Section 3 contains the extrapolated results expected at SLC. Although this method will be shown one of the most effective to reach the above goals,it requires however a large amount of Z^o events. This physics begins in fact with 100 to 200 thousand Z^o events (the expected final sample of MarkII) to reach its full strength with 1 million Z^o (a typical LEP luminosity). Thus, in 3 years from now, it is highly probable that the above goals will be reached, since there is almost no unknown parameters in this method.

2. Some simple ideas

2.1 ψ RECONSTRUCTION AND EXCLUSIVE STATES

The inclusive branching ratio of ψ in B decays has been measured at Cornell and Desy (ref 1-2). Using this measured value of 1.25 % and the branching fraction of ψ into lepton pairs -15% -,one obtains the visible branching ratio of a ψ ,detected in e^+e^- or $\mu^+\mu^-$:

$$b.r.\ B \rightarrow \psi \rightarrow e^+e^-\ or\ \mu^+\mu^- = .19\%$$

This branching ratio is the highest available for a "quasi-exclusive" mode. It will be shown below that there is no more extra price to pay to be able to measure separately the B^0_d and the B^- lifetime. For exclusive spectroscopy, inclusive ψ decays are dominated by 2 body decays so the favoured channels are :

1. $B^0 \rightarrow \psi\ K^* \rightarrow K\pi$
2. $B^- \rightarrow \psi\ K^-$
3. $B^0_s \rightarrow \psi\ \phi$

The first 2 decay modes have been observed at Cornell and Desy and their branching ratios have been measured. Taking as a reference sample 10^6 Z^o and taking $Z^o \rightarrow b\ \bar{b}$ branching ratio of 15%, 500 ψ will be produced. It is reasonnable to expect a 40% efficiency as it will be discussed in chapter 3, then 200 ψ are detected. The expected rates for the different meson states are respectively

1. B^0_d : 25 ψ K π fully resconstructed allowing a 20% measurement of the B^0_d lifetime.
2. B^- : 10-15 ψ K^- fully reconstructed allowing a 30% measurement of the B^- lifetime
3. B^0_s :if one assumes B^0_s /B^0_d =.5, 10 events could be seen in the ψ ϕ mode, allowing the discovery of this state. Of course, since nothing is known up to now on the production rates and on the branching ratios,surprises -good or bad - are possible.

The background under the ψ signal will be quite manageable, given the good lepton identification power. It may be possible to ask only a very well identified track and looser conditions on the other one. For the B exclusive states, the background also is expected to be small and can be further reduced by suppressing the combinatorial background using the vertex detector. This has to be contrasted with methods using charm mesons to reconstruct exclusive B states. The ψ is only produced by b quarks while charmed mesons are also produced by $c\bar{c}$ events ,thus generating a large background.

2.2 LIFETIME MEASUREMENTS

The 2 nice properties of the $B \rightarrow \psi$ decays are emphasized below :

1. The ψ has no lifetime of its own, and therefore the observed ψ vertex is indeed the B vertex. Thus, the access to the B vertex is direct and unbiased. This has to be constrasted with the open charm decay mode of the B. Because of the relatively long lifetime of the produced charm mesons, the b vertex is difficult to isolate and if since most of the time, the charm selection needs some vertex cuts, the resulting measurement of B lifetime will be biased. As a consequence, the systematic errors will be small. The main source is the determination of the betagamma and theta paramaters of the B meson using those of the ψ . Because of the large mass of the ψ ,there is a large correlation between the B variables and the ψ ones and no large model dependant effect can occur. Furthermore, experimental results from Cornell and Desy are available.

2. The ψ decay products are 2 large angle energetic tracks. This allows a very good measurement of their intersection, since the multiple scattering will be negligeable -allowing to use the full power of a Silicon Strip Detector- and the relative angle will be large.

This precise knowledge of the B vertex makes possible to count how many tracks are coming from this vertex. B_d^0 or B_s^0 vertices will be formed by 0 or 2 other tracks rattached to this vertex while B^- vertices will show 1 or 3. Since these other tracks have a non zero impact parameter relative to the primary vertex, it is in fact possible to sort B^0 and B^- events with a 75% efficiency (see section 3). Thus, a separate lifetime measurement can be done using the full ψ statistics. This result will then become available with only 200 to 300 thousand Z^o , a possible MarkII final sample.

As a final comment, this ψ tagging method is almost completely independant of most of new physics which may turn up at SLC. This is because it is quite unlikely that new physics manifest itself by ψ production, while, in the other hand, it will certainly do by lepton production which will make lifetime measurement through b semileptonic decay more difficult. The most obvious example is top production. In that case, one will have to sort leptons coming from top - with no impact parameter - from leptons coming from b's, certainly a non trivial problem. With the ψ method, on the contrary, all the b quarks produced by top decays are useful in exactly the same way as directly produced b quarks.

3. ψ search with PEP data

A search for ψ in the data collected by the MarkII detector at the PEP storage ring has been done and is described in detail in ref. 3. A brief summary of these preliminary results is given below.

The data sample consisted of 100,000 hadronic events with a 29 GeV E_{cm}, corresponding to a 200 pb^{-1} luminosity. Events with 2 electron or muon candidates in the *same hemisphere* were selected. The same sign events provide a background monitor for events with 1 or 2 misidentified tracks. The other source of background is cascade events, i.e. events where the B meson decays to a lepton and a charmed meson which, in turn, decays semileptonically. This background is monitored using a cascade MonteCarlo program. The identification cuts are the minimal ones needed to suppress the misidentification background in the ψ mass range. After these cuts, 11 events are found in the data (7 e^+e^- and 4 $\mu^+\mu^-$), with an estimated background of 1.7 ± .5 events. The invariant mass distribution is compatible with MonteCarlo expectations (the expected resolution is about 350 MeV (250 MeV) for electron (muon) channels).

The number of ψ expected from B decays, taking in account the luminosity, the measured branching ratios and our detection efficiency is 5 ±1. The observed number, 9.25, is above this expectation but quite compatible with it . The general characteristics of these events,(multiplicity, visible energy, number of extra leptons,..) is compatible with expectation.

A lifetime measurement was performed with those 11 events. Only 2 have a negative lifetime, and the mean lifetime is 1.75 ± 1. ps . A maximum log-likelyhood fit yields the following result :

$$\tau_B \;=\; 2.2\,^{+1.3}_{-0.7} \pm 0.3 \;\; \mathrm{ps}\,.$$

In summary, preliminary evidence of ψ has been found in the MarkII PEP data. The background has been found quite manageable. The b lifetime measurement has been performed using this new technique.The statistical error is rather large but the relative systematic error (15 %) is comparable to the best measurement using semileptonic decays.

4. Expected results at SLC

In this chapter, the previous analysis is reviewed using now a MonteCarlo program runned at a center of mass energy of 93 GeV with the SLC MarkII configuration. It is important to notice that these 2 changes improve the detection efficiency and resolution by a great factor.

1. The energy boost will make identification easier. At PEP, the slowest track was often in the 1 GeV range where identification efficiencies drop quickly.
2. The dE/dX information will allow to reduce by a factor 10 the misidenfication probability.
3. The mass resolution is significantly improved by the new drift chamber and by the fact that high energy electrons are well measured in the calorimeters.
4. The acceptance is improved by the electromagnetic end-caps (and by the muon upgrade in a near future.)
5. The lifetime measurement will be substantially improved by the small SLC beam size, the new vertex drift chamber and by the Silicon strips device when it will become operationnal.

4.1 Detection efficiency and mass resolution

The Table 1 gives the different sources of detection inefficiencies, according to the MonteCarlo program. For electrons, using only 1 track fully identified,one gets a 58% efficiency. This may be found sufficient if dE/dX information is added. Requiring 2 identified tracks is still quite good, 42% efficiency.

It is worthwile noticing that a non negligeable proportion of electrons are not tracked in the drift chamber but are detected as photons in the endcaps (15%). The necessary software to recover those tracks will be written soon. For the moment, one can use them as photons but the mass resolution is degraded by a factor 2.

For the $\mu^+\mu^-$ channel, the efficiency with 1 and 2 identified tracks are respectively 56 % and 18.5%. These figures do not include the muon upgrade larger acceptance .

The mass distribution is shown in fig. 1 for $\mu^+\mu^-$ and on fig. 2 for e^+e^- . The FWHM is 100 and 150 MeV respectively. In the electron case, this could be improved using the calorimeter energy measurement which has a better energy resolution for energetic tracks. The weighted mean of the calorimeter and the drift chamber momentum is computed to obtain the mass distribution shown in fig. 3 . However,there is some pile-up in the liquid argon which creates a tail at large mass. More work is therefore needed to really reach the intrinsic resolution.

4.2 Lifetime measurement

It is clear that the mean B lifetime measurement will be dominated only by statistical accuracy. Each ψ decay length, of several mm in average, will be measured with a precision of 100 μm (fig. 5) using the Si strips vertex detector. The statistical error on the lifetime measurement will then be given roughly by $1/\sqrt{N}$ so for 1 M Z^o , with 200 ψ , the statistical error will be 7 %.

For the separate lifetime measurements, one has to count the tracks at the ψ vertex. Fig.6 shows the distance and impact parameter of the tracks which are not coming from the ψ vertex while fig.7 shows the same quantities for the tracks indeed coming from the vertex. Requiring both a small distance to the ψ vertex and some impact parameter enables to sort the events properly, as it is shown in the following table, obtained with the 2 requirements

- Distance to the secondary less than 80 μm
- Impact parameter greater than 40 μm

	0 gener. track	1 gener. track	2 gener. tracks
0 track found	448	263	119
1 track found	132	428	152
2 track found	33	62	191

The best result is obtained by looking at the sample with 2 tracks which contains 78% of B^0 . The 1 track sample is also sufficiently pure (60% of B^-) to make a quite good separate lifetime measurement. If one uses the Vertex drift chamber alone, the results are not very different. This happens because the cuts are large compared to the intrinsic resolution of the 2 detectors. This track counting method will be subsantially improved with a 3-D vertex detector like the SLD CCD vertex detector. In that case, removing primary tracks from the secondary vertex is much easier.

5. Conclusion

A simple and powerful way of obtaining 2 challenging new results in the B spectroscopy has been described. This method requires a large but realistic data sample, between 200,000 and 1 M Z^o . The ψ tagging is a method well suited to the MarkII good lepton identification and good spatial resolution. It offers an almost unique way to discover the B_s^0 meson and to measure separately the B_d^0 and B^- life times. The systematical errors associated to the lifetime measurement are expected to be quite small.

This method has been checked successfully on PEP data, where a preliminary ψ signal is found, over a very small background.

Finally, this method contains no unknown parameters and is completely insensitive to new physics, which could make the usual semileptonic lifetime measurement much more difficult.

References

1. M. Alam et al. (CLEO coll.),Physical Review D,34,3279,(1986)

2. H. Albrecht et al. (ARGUS coll.) Physics Letters,162B,395 (1985)

3. G. Wormser,MarkII/PEP-V note,April 13,1987. 4. R. Ong, MarkII Memorandum, Jan. 3,1987

5. R. Ong and K. Riles, MarkII/SLC note # 166,Dec. 19,1986

Table 1

	e^+e^-	$\mu^+\mu^-$
Number of events	1175	1235

Number of events lost for each cut

0 MC tracks linked	87	79
1 forward track lost	173	146
1 central track lost	14	15
$p_{min} < 1$ GeV	102	68
Wrong sign	0	0
Wrong hemisphere	13	11
0 identified tracks	99	401
only 1 identified track	197	287
Good events	490	228
Good events(in %)	42	18.5

FIGURE CAPTIONS

1. Mass $\mu^+\mu^-$
2. Mass e^+e^- using the DC information
3. Mass e^+e^- using DC +LA information
4. Mass e"γ", where the γ is 1 electron seen in the endcaps but missed by the drift chamber
5. Difference between the reconstructed decay length and the generated one
6. Tracks not coming from the secondary vertex

a. Distance to the ψ vertex for tracks not coming from this vertex

b. Impact parameter distribution for those tracks

c. Distance to the ψ vertex after requiring an impact parameter greater than 40 μm

7. Tracks coming from the secondary vertex

a. Distance to the ψ vertex for tracks coming from this vertex

b. Impact parameter distribution for those tracks

c. Distance to the ψ vertex after requiring an impact parameter greater than 40 μm

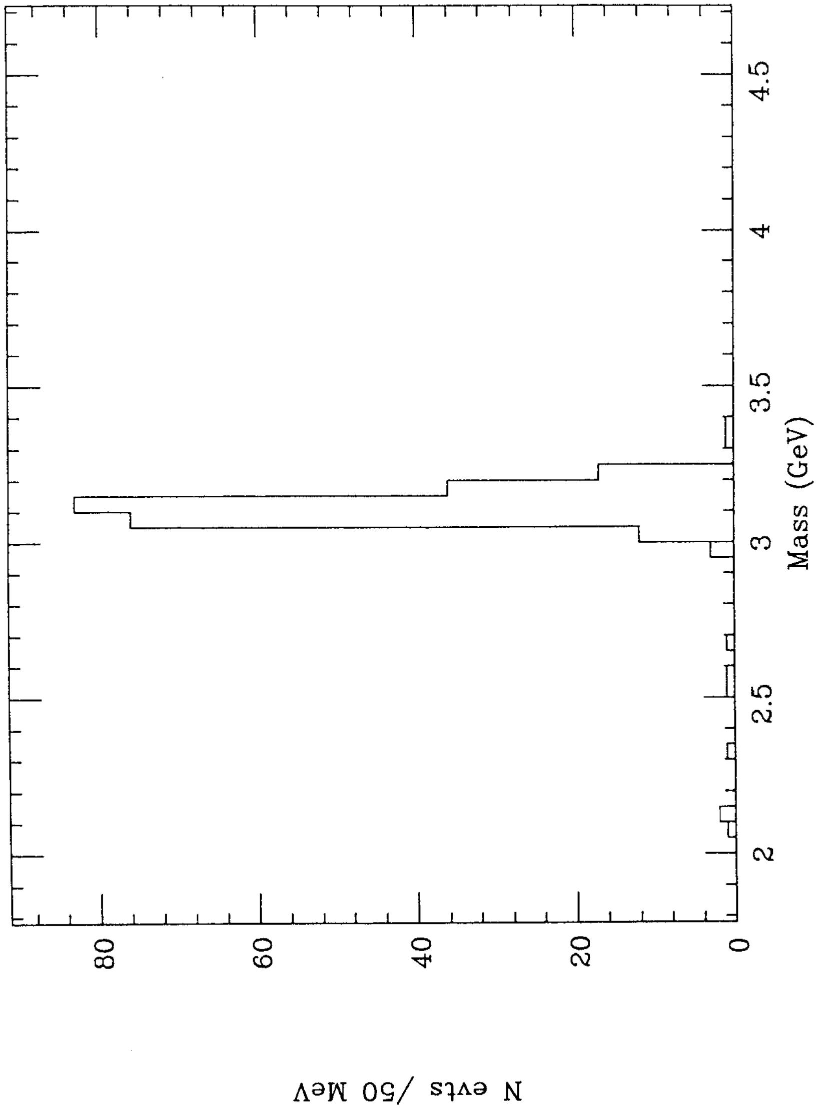

Fig.1 Mass $\mu^+\mu^-$

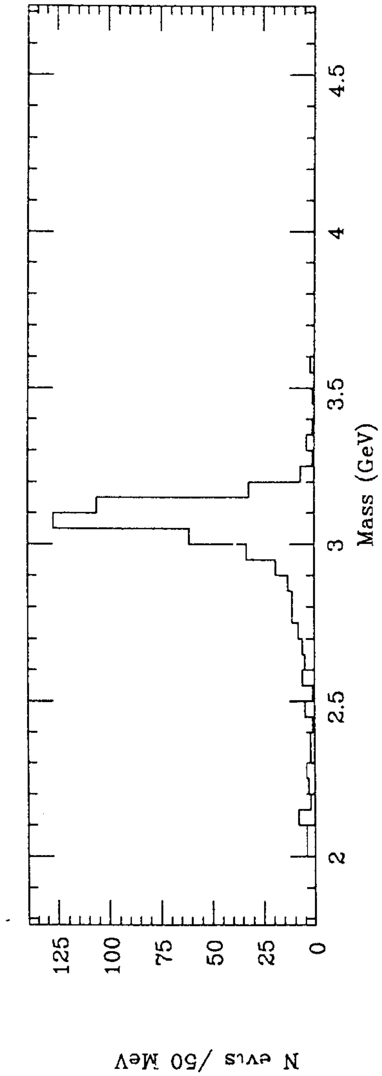

Fig. 2 Mass e^+e^-

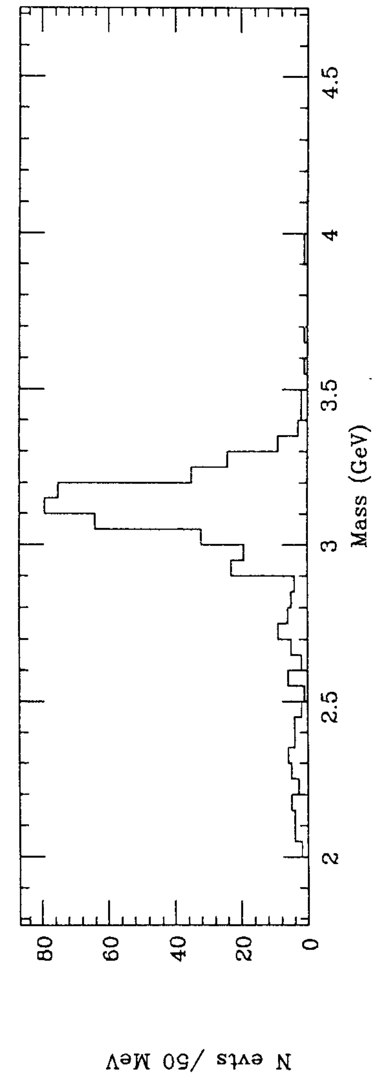

Fig. 3 Mass e^+e^- using L. Ar.

Fig.4 Mass $e^{\pm}{''}\gamma{''}$

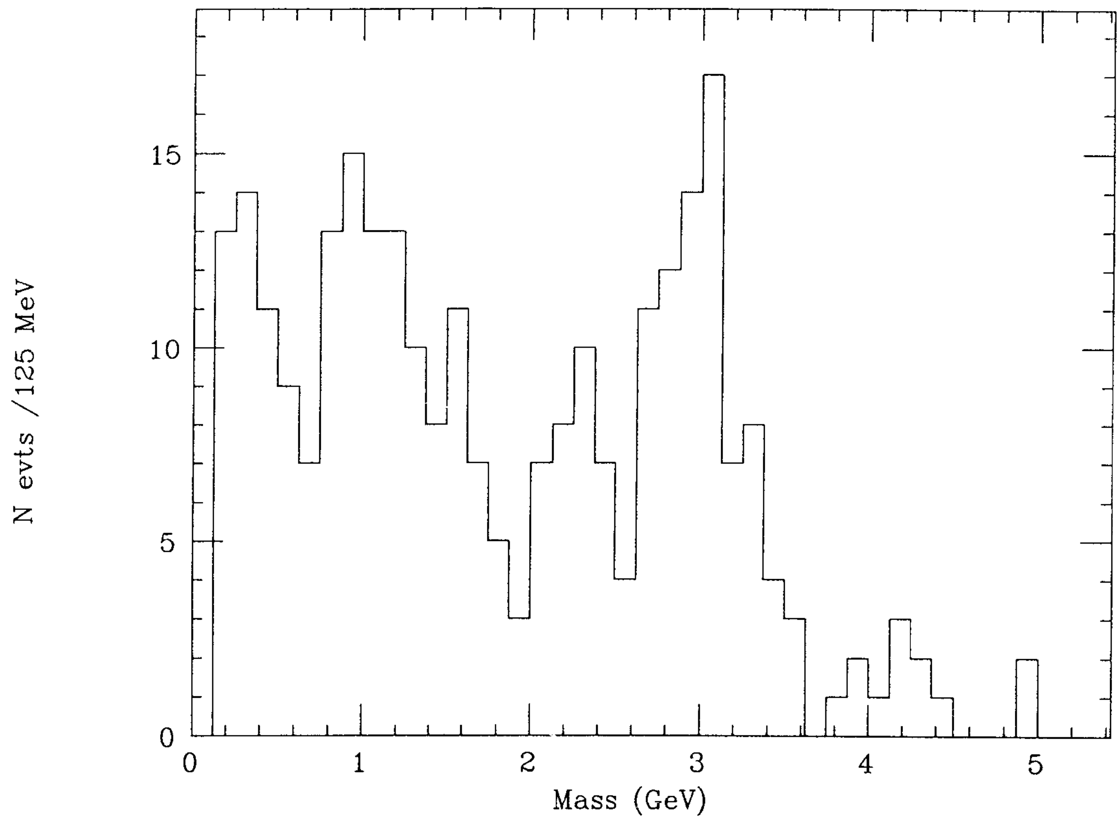

Fig. 5 Decay Length Data −MC

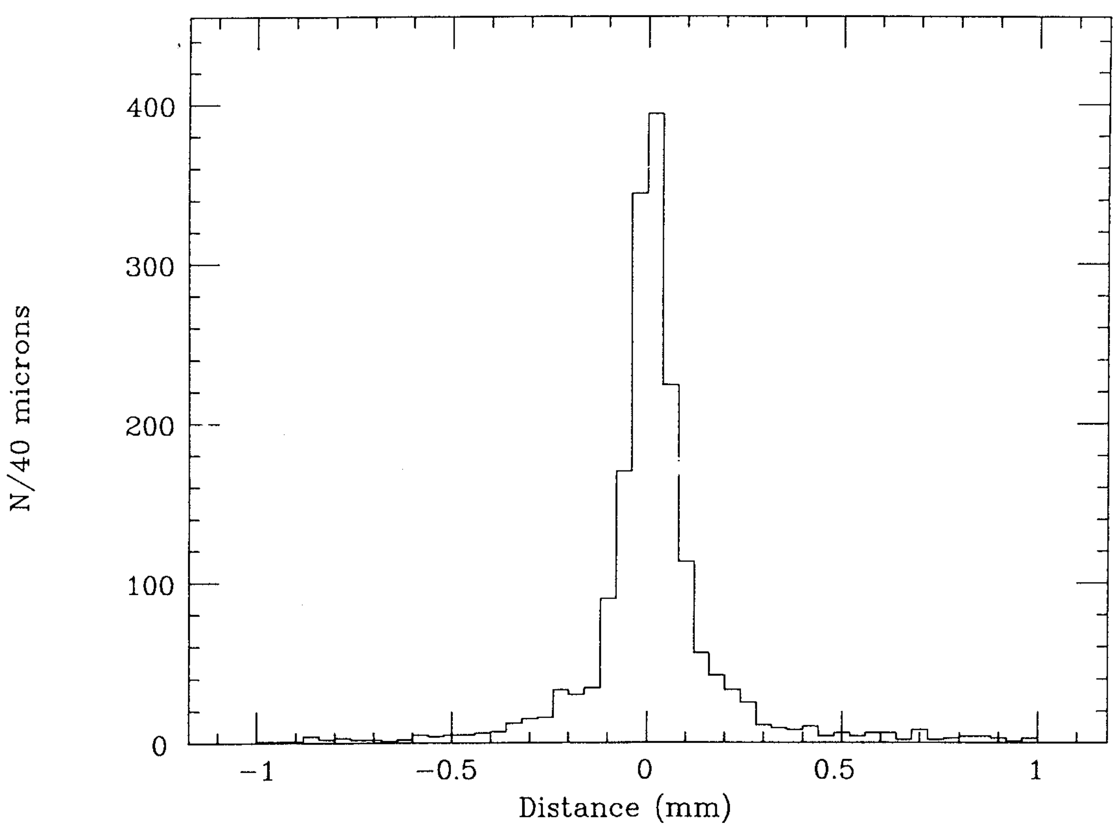

Fig. 6 Tracks not coming from the second. vertex

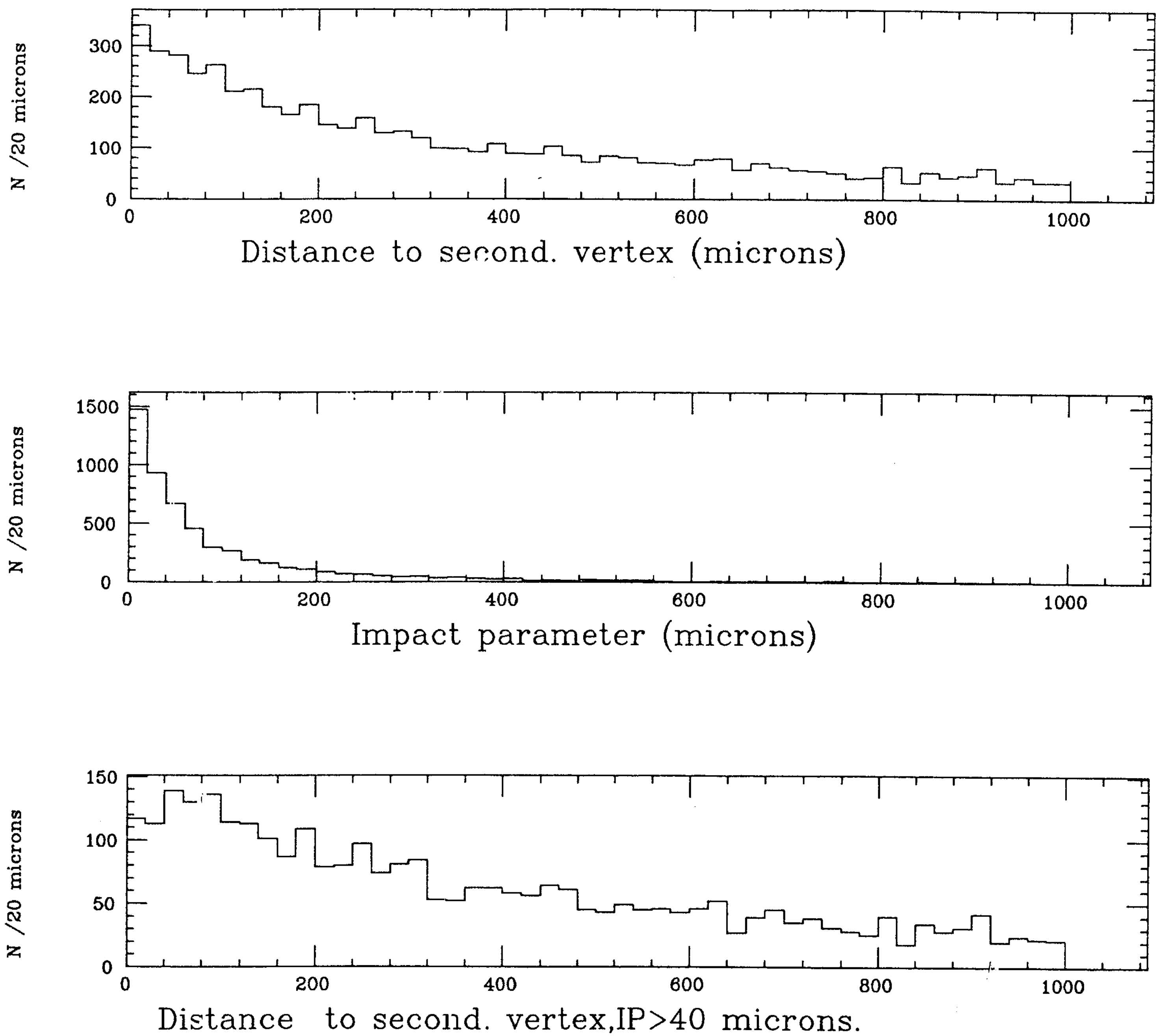

Fig. 7. Tracks coming from the second. vertex

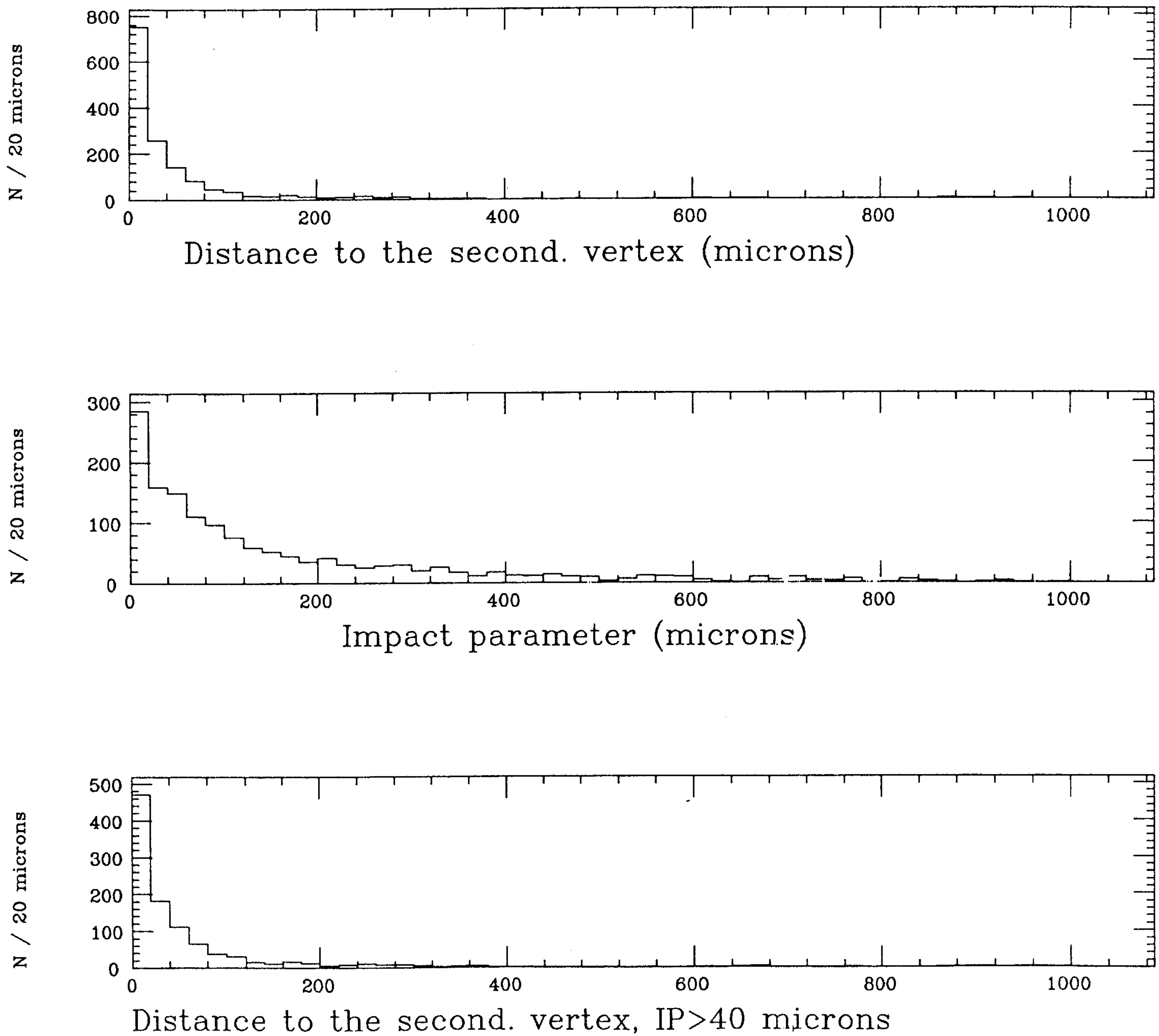

Mark II/SLC-Physics Working Group Note # 9–16

AUTHOR: Paul Weber

DATE: May 18, 1987

TITLE: Vertex Tagging of b Quarks and the $Z^0 \to$ b Fraction

---

$Z^0 \to b\bar{b}$ events are selected with a method that examines the impact parameter significances of charged tracks in an event. Using this efficient selection technique, and good Monte Carlo simulations, one can model the branching fraction of $Z^0 \to$ b quarks. The effectiveness of this method has been examined with Monte Carlo data that include the new drift chamber vertex detector simulation package.

1. Vertex Tagging Method

The vertex tagging method for selecting $Z^0 \to b\bar{b}$ events was first developed by Ken Hayes.[1] Its effectiveness derives from the large multiplicities and long decay lengths of B-hadrons. Good impact parameter resolution is essential to the success of this approach. This will be provided by the high-resolution vertex drift chamber (VDC) now under construction for initial SLC running of the MARKII.[2] It will be enhanced in later MARKII SLC running by the silicon strip vertex detector. The Monte Carlo simulations used in this study involve only the vertex drift chamber with the central drift chamber (CDC). Although the silicon strip simulation is complete, the aim here is to study the potential available from the initial running configuration at the SLC with the VDC as the sole vertex detector for the MARKII.

B-hadrons usually decay to charmed particles. The average multiplicity of a B-hadron decay is 5-6, while the D-decays give 2-3 charged particles. B-events are then distinguished from elementary charm events by a two-vertex structure with larger multiplicity. Further, the D-mesons from B decays will have smaller momenta than D-mesons from elementary charm formation. The net effect is that there will more tracks from b-events with impact parameters significantly different from zero, than from c-events. The tagging method requires that a sufficient number of charged tracks have impact parameter significances above a certain lower limit. The impact parameter significance is the quotient of the unsigned impact parameter of a track by the impact parameter resolution obtained from the covariance matrix of the fit. In this way, tracks are weighted by their momentum, because this resolution deteriorates from multiple scattering at the lower momenta. Figure 1 shows the distribution of momenta of B-hadron decay tracks from the Monte Carlo. Almost half these tracks are below 2 GeV/c. Figure 2 plots the impact

parameter resolution of the MARKII with the vertex drift chamber as a function of momentum, showing that it is just at this level where multiple scattering begins to dominate the impact parameter resolution. A rough fit of the data to the theoretically predicted form of the variation with momentum,

$$\sigma(p) = \sqrt{\left(\frac{A}{p}\right)^2 + B^2}$$

gives $A \sim 110\mu$m-GeV/c and $B \sim 25\ \mu$m. These values of A and B are only approximate – the material between the VDC and the interaction point has not yet been finalized, and this will have the greatest effect on resolution deterioration due to multiple scattering.

Before applying the vertex tagging cuts, events cuts are imposed to reduce backgrounds and to select events more favorable for the tagging algorithm. First, there are cuts applied by the four-vector manipulation package, VECSUB, which requires that all charged tracks satisfy

$$|z_{min} - z_{ip}| < 60 \text{ mm},$$
$$r_{min} < 4 \text{ cm},$$
$$p_t > 100 \text{ MeV/c},$$
$$p_{max} < E_{beam} + 3\sigma,$$

and also does dE/dx corrections for each particle, assuming pion mass. Then, further track cuts are imposed:

$$|cos\theta| < 0.9$$
$$p > 250 \text{ MeV/c}$$

after which the selected tracks are used in the event cuts:

1. $\geq$ 10 good charged tracks
2. sphericity axis satisfying $|cos\theta_{sph}| < 0.8$

The sphericity calculation is done using the charged tracks alone. In these high-multiplicity events there is negligible difference between sphericity calculations using charged-only vs. charged+neutral tracks. There is also negligible difference between use of sphericity vs. thrust in analyzing the events.

These event cuts reduce the size of a typical 5-flavor multihadron sample about 25-30 %. In a general data sample, they are strict enough to eliminate almost all known leptonic events and two-photon events.[3] However, these cuts bias the fraction of $Z^0 \to b\bar{b}$ events by about 1-2 % relative to the uncut multihadron sample, an effect which must be well understood in the branching fraction measurement described later.

Vertex tagging examines the passing events, divided into hemispheres by the sphericity axis. Each hemisphere is taken as defining a jet, and impact parameter significances of all charged tracks in the hemisphere are evaluated. The hemisphere is 'tagged' if there are $\geq n$ tracks of significance $\geq scut$, which ALSO satisfy:

- no other track within 5 milliradians in ϕ
- impact parameter less than .002 meters
- invariant mass of all such tracks taken together $\geq$ 1.95 GeV/c^2

The first restriction is compatible with the track separation capablities of the vertex drift chamber. The second cut eliminates pair production in the beampipe walls and cuts down on kaon decays from elementary strange quark production. The third cut further reduces elementary charm production by cutting on a mass just above that of the D-meson. Finally, an event is tagged as $Z^0 \to b\bar{b}$ if either or both its hemispheres are tagged in this manner.

Many values of n and $scut$ have been studied, to find a combination giving high efficiency for $Z^0 \to b\bar{b}$ event selection and low background. Multihadron samples from Lund Monte Carlos were prepared for the studies, using both the shower/leading log and the 2nd-order matrix element calculations, and using both the Lund and the Peterson fragmentation functions for the charm and bottom quarks. Tables 1 and 2 illustrate the effectiveness of the $scut = 3$ in selecting B events from a 5-flavor multihadron sample, generated with the leading log calculation and Lund fragmentation. Table 1 counts the number of tagged *hemispheres* and Table 2 counts the number of tagged *events* from a 9500-event sample. These are given as a function of the number of tracks required for the tag. With $scut =$ 3, the $n = 3$ cut selects about 7 % of the events, but those selected are about 92 % b events.

The efficiency and background are defined using the quantities

$N \equiv$ number of events passing event selection cuts

$N_b \equiv$ number of b-events in this passing sample

$n \equiv$ number of tagged events

$n_b \equiv$ number of b events in tagged set

$n_{bg} \equiv$ number of non-b events in tagged set

by the relations

$$\epsilon_b = \frac{n_b}{N_b}$$
$$b = \frac{n_{bg}}{N}.$$

Efficiencies and backgrounds have been examined for the various combinations of $scut$ and number of tagged tracks required for the four sets of Monte Carlo data.

The initial results show large variation from one type of Monte Carlo to the next, and indicate the work that must be done on tuning their parameters. For the $scut$ = 3 cut with 3 tagged tracks required, the efficiencies from Monte Carlo data range from .30 to .40, while the background as defined above ranges from .004 to .009. This means that about 8-10 % of the events tagged from a 5-flavor multihadron sample are background.

The vertex tagging method and estimates of efficiency and background are sensitive to variation from the value of the lifetimes of B hadrons. For example, reduction of the Lund value $c\tau_b = 3.30$ to half that value shows a 20-30 % decrease in ϵ_b with the same background. The D lifetimes are better determined, but variations in them will also affect these quantities.

Impact parameter significances also depend on good knowledge of the position of interaction point. Uncertainty in this position effectively adds in quadrature to the impact parameter error for each track, in momentum-independent fashion. If this uncertainty reaches, say 20 μm then at high momenta this error is as large as the tracking error. Even so, since most of the tracks involved in the tag are lower momentum the effect is less dramatic – a 20 μm uncertainty in interaction point position shows a reduction of 10-15 % in both the efficiency and background.

2. $Z^0 \to b\bar{b}$ Branching Fraction

The branching ratio for $Z^0 \to b\bar{b}$ is just the fraction of b events in a mutihadron sample,

$$R_b = \frac{N_b}{N}$$

The analysis parallels that for measurement of the multihadronic R. A general working relation for R_b would be

$$R_b = \frac{\frac{1}{\epsilon_b}[n_{tagged} - n_{bg}]}{\frac{1}{\epsilon_{MH}}[n_{MHtagged} - n_{MHbg}]}$$

The R_b measurement includes efficiencies and error estimates from the multihadronic R measurement. If one can take these as well-known then there will result a well-determined number of multihadronic events in the normalized sample. This is the number N defined in the previous section. Using the same definitions as before,

$$R_b = \frac{1}{\epsilon_b}[p - b]$$

where

$$b \equiv \frac{n_{bg}}{N},$$

and where

$$p \equiv \frac{n_{tagged}}{N}$$

is the fraction of passing events which are tagged. p is the only number available from the data analysis – ϵ_b and b must be obtained from Monte Carlos. As indicated in the previous section, the Monte Carlos differ in the predictions of these quantities, and a good deal of the systematic error in the R_b calculation will be due to the model dependence of ϵ_b and b that remains when the Monte Carlos have been tuned as well as possible.

A good estimate of the statistical error is possible from the analyses. With the 9500-event Lund shower with Lund fragmentation Monte Carlo, this error is about 1 % for the *scut* = 3 cut with 3 or more tagged tracks required.

3. Inclusion of t, b' Quarks

The data used in this study were all 5-flavor multihadron samples. Inclusion of new heavy quarks presents new opportunities and challenges for the vertex tagging algorithm. If the flavor-changing neutral currents are indeed suppressed then b' events will have to be distinguished from those which involve B hadrons. The performance of the algorithm on b' events has not yet been studied.

On the other hand, top decays usually do involve B hadrons. In combination with some of the current top-finding algorithms, it may be possible to use the vertex tagging method to reduce backgrounds for top selection to very low levels. The salient features for top decay are discussed in Gail Hanson's working group note.[4] The vertex tagging cuts as listed above, with *scut* = 3 and 3 or more charged tracks are probably too severe for finding the B hadrons resulting from top decays. This is evidenced by the fact that only about 25 % of top events which are selected by a typical top-selection scheme will go on to be vertex-tagged with this present set of cuts. However, these severe cuts do serve to reduce backgrounds from new, heavy charged or neutral leptons to almost zero when preceeded by the top selection cuts. Refinements and relaxations of these cuts need to be tried.

4. Conclusions

Because of the high resolution vertex detectors that will be implemented for the MARKII at SLC, vertex tagging should be very effective in selecting b events. The *scut* = 3 cut with 3 tagged tracks required seems to give a good balance of high efficiency and low background, for which $\epsilon_b \sim$ .30-.40 and $b \sim$ .004-.009. Statistical error for a 10,000-event multihadron sample should be less than 1 %.

Efficiency and background estimates are still model-dependent, and much work needs to be done in understanding the Monte Carlos. By matching distributions pertinent to this analysis, such as momentum spectra of bottom and charmed hadron decay tracks, one can begin to 'tune' the several types of Monte Carlos. Eventually, systematic errors will be evaluated and at that point a measurement of the $Z^0 \rightarrow b\bar{b}$ branching fraction becomes possible with data samples of perhaps tens of thousands of Z^0 events. This is true provided effects of exotic particles (if any are present!) are understood.

Finally, investigations are ongoing for more sophisticated versions of the vertex-tagging technique. Possible enhancements may be found from using cluster analysis to do more refined separations of the tracks in an event before applying the impact parameter significance cuts. Separation of vertices is still quite difficult to achieve with the current resolution, but at some level this may also be a useful tool in refining the technique.

May 18, 1987

REFERENCES

1. K. Hayes, MARKII/SLC Note # 73
2. The new vertex detector will be a jet cell design, with each 10 jet cells having 38 offset-radial sense wires. The optimal point resolution will be 30 microns. Prototype results are discussed in: NIM A252 (1986) 350.
3. G. Feldman, memo included in these proceedings.
4. G. Hanson, MKII/SLC Working Group Note # 3-10.

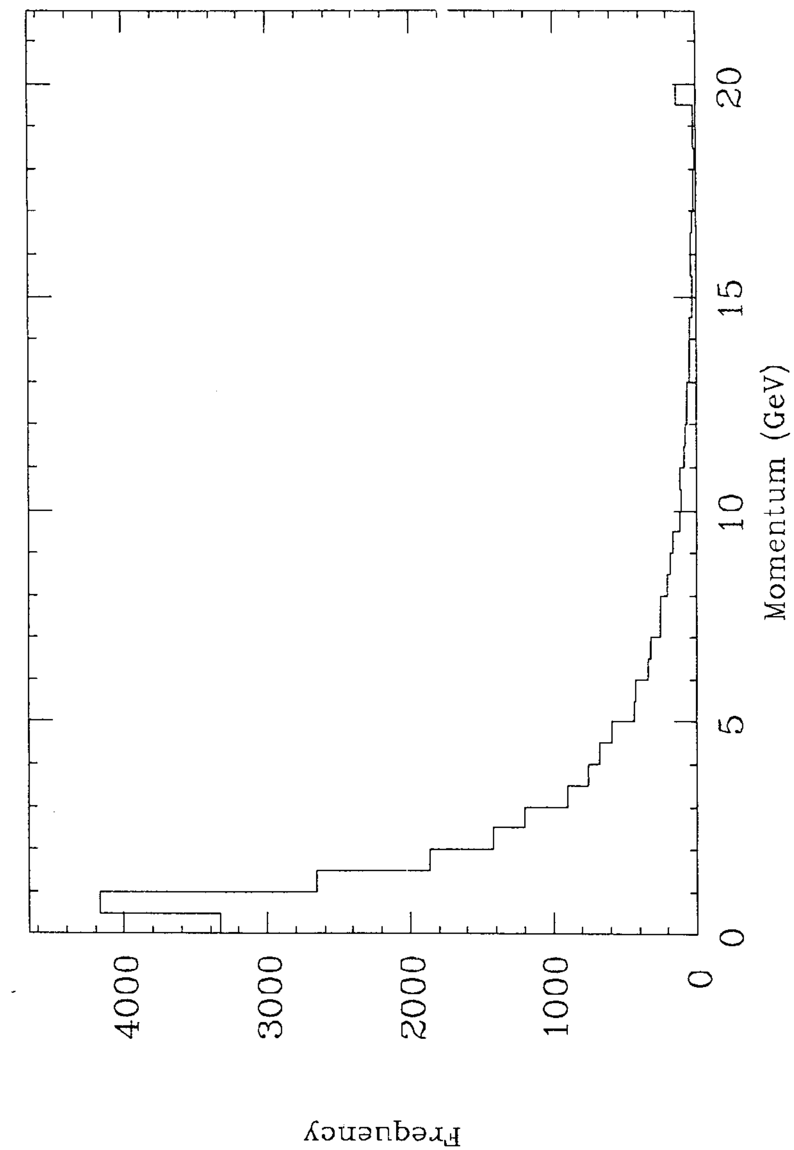

Fig. 1. Momentum Distribution of B Tracks

Fig. 2. IP Resolution vs. Momentum

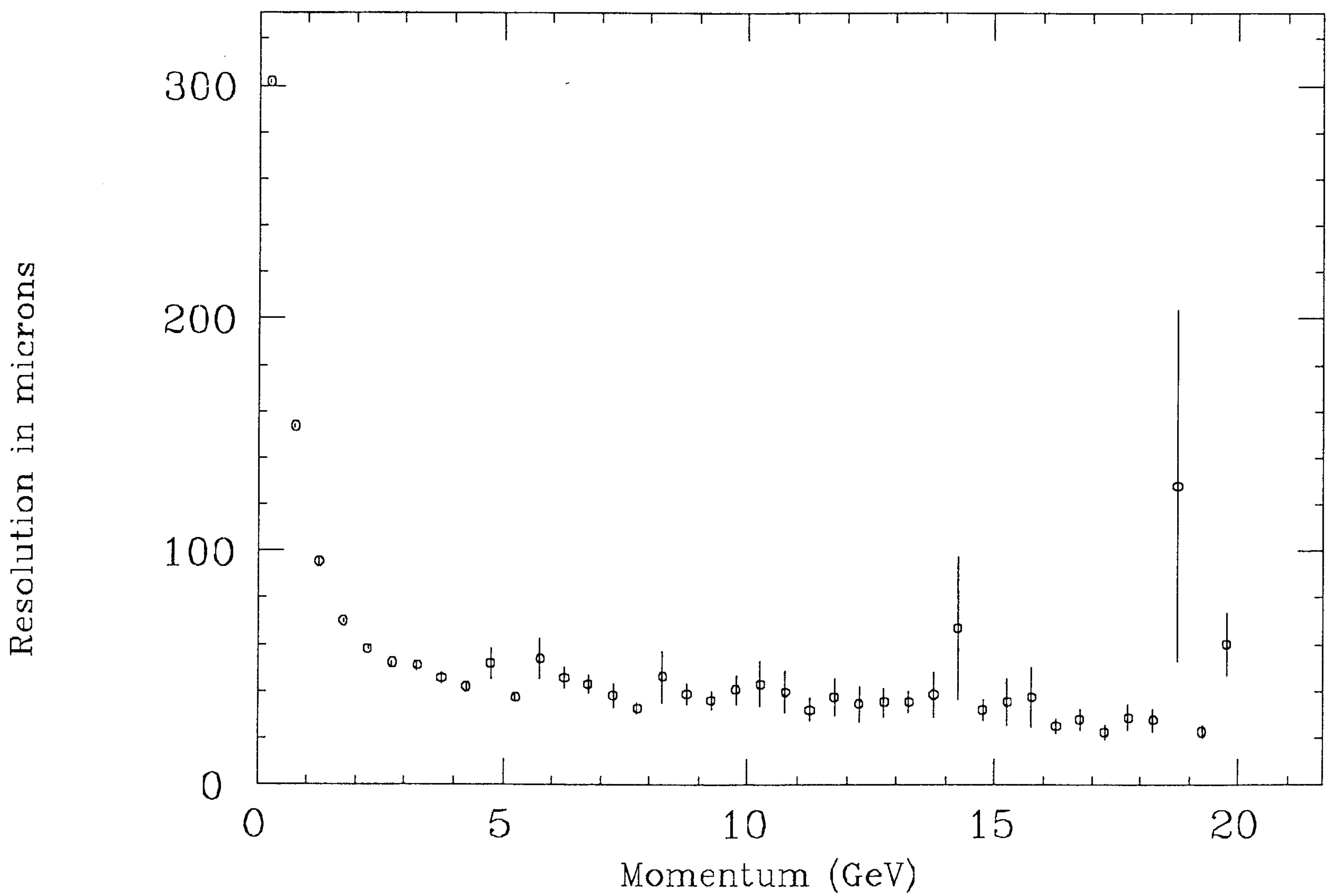

# tagged hemispheres vs. # tagged tracks							
	# tagged tracks required						
Flavor	2	3	4	5	6	7	8
U	5	3	1	0	0	0	0
D	4	1	0	0	0	0	0
S	16	10	2	0	0	0	0
C	45	28	8	0	0	0	0
B	640	556	355	191	68	31	7
BTAG/WAS	640	556	355	191	68	31	7
BTAG/NOT	70	42	11	0	0	0	0

Table 1. Hemisphere selections.

# tagged events vs. # tagged tracks							
	# tagged tracks required						
Flavor	2	3	4	5	6	7	8
U	5	3	1	0	0	0	0
D	4	1	0	0	0	0	0
S	16	10	2	0	0	0	0
C	44	27	8	0	0	0	0
B	580	497	307	161	54	22	5
BTAG/WAS	580	497	307	161	54	22	5
BTAG/NOT	69	41	11	0	0	0	0

Table 2. Event selections.

Mark II/SLC-Physics Working Group Note # 9–17

AUTHOR: W. T. Ford

TITLE: Measurement of the Bottom "Quark" Lifetime

DATE: April 28, 1987

The quark mixing matrix is constrained by the lifetime of the bottom quark, the off-diagonal elements involving the b quark being completely determined by the lifetime and the branching ratio between the decays $b \to u$ and $b \to c$. If the binding of the b quark into hadrons has no effect on its decay rate, the inclusive lifetime measurement discussed here reflects precisely the quark total decay rate. Our experience with charmed hadrons serves to warn that the situation may not be so simple, and we are eager to find techniques for determining the lifetimes of individual hadron states, particularly the mesons B^+, B_d^0 and B_s^0. The subject of this note, however, is a detailed evaluation of prospects for improving the inclusive measurement, as it has been performed at PEP and PETRA, based upon the impact parameter distribution of leptons from the b hadron semileptonic decays. This note supersedes intermediate reports[1,2] from the Asilomar and Granlibakken meetings.

The first two sections are based mainly upon studies with Monte Carlo generated quantities in which we explore the kinematics of bottom particle semileptonic decays to develop event selection criteria and measure sensitivity of the impact parameter to the lifetime and to the details of particle production. Detector effects are considered in section 3, data reduction in sections 4 and 5, and conclusions in section 6.

1. Event Selection and Sample Purity

As in previous experiments we look for electrons and muons among the final state particles in multihadron events. The reliability of the detector's electron and muon identification is the subject of other notes from this study group. Table 1, taken from Mark Nelson's Asilomar talk,[3] summarizes the relevant numbers for electrons. Compared with PEP-5 the electron identification hardware is considerably improved because of the new endcap calorimeters and dE/dx measurements in the central drift chamber. As a result we can expect to cover a larger fraction of phase space, in that the lower momentum limit for acceptable misidentification

TABLE 1. Misidentification probabilities for the combined calorimeter and dE/dx systems.

$p \backslash p_t$	0.0-0.5	0.5-1.0	1.0-1.5	1.5-2.0	> 2.0
1-3	.0002	.0000	.0000	.0000	.0000
3-5	.0023	.0003	.0002	.0002	.0002
5-7	.0078	.0010	.0007	.0007	.0007
7-9	.0121	.0022	.0013	.0013	.0014
9-11	.0137	.0025	.0017	.0015	.0016
11-13	.0126	.0020	.0020	.0019	.0022
13-15	.0129	.0023	.0022	.0034	.0021
15-17	.0112	.0026	.0021	.0021	.0026

background stays as at PEP, around $1 - 2$ GeV, while the signal electrons extend above 20 GeV (see Fig. 1).

The Monte Carlo program (LOWL) with the LUND61 event generator was run in a mode in which either pure $b\bar{b}$ or $c\bar{c}$ event samples were generated, each containing about 5000 events without detector simulation. The Lund fragmentation with either second-order matrix element (LUMA) or leading-log shower (LUSH) options were chosen for the event generation for the various studies presented here. The electronic branching ratio was forced to 1 for both b- and c-containing hadrons.

The relevant kinematic variables are the electron momentum p, and the transverse momentum $p_\perp$ measured with respect to the thrust axis. This axis and the thrust itself, T were computed from generated charged tracks via a call to LTHRU$. Events were kept if the thrust axis had $\cos\theta < 0.8$ and $T > 0.85$. These cuts were to insure that the thrust axis as computed from detected particles not be badly distorted by particles outside the acceptance, and that the parton axes remain reasonably collinear, with limited gluon radiation. Electrons were required to have $\cos\theta < 0.9$.

In Fig. 1 are shown the distributions in p and $p_\perp$ of both the parent hadron and the electron for bottom and charm hadrons, respectively, produced with the LUMA generator. As expected from fragmentation function measurements, b hadrons are harder than c hadrons, and the heavier b emits electrons with larger $p_\perp$ than c. The proper normalization of charm relative to bottomness has been applied to the p-$p_\perp$ correlation plots, Fig. 2. After removal of the electrons with $p < 1$ GeV we

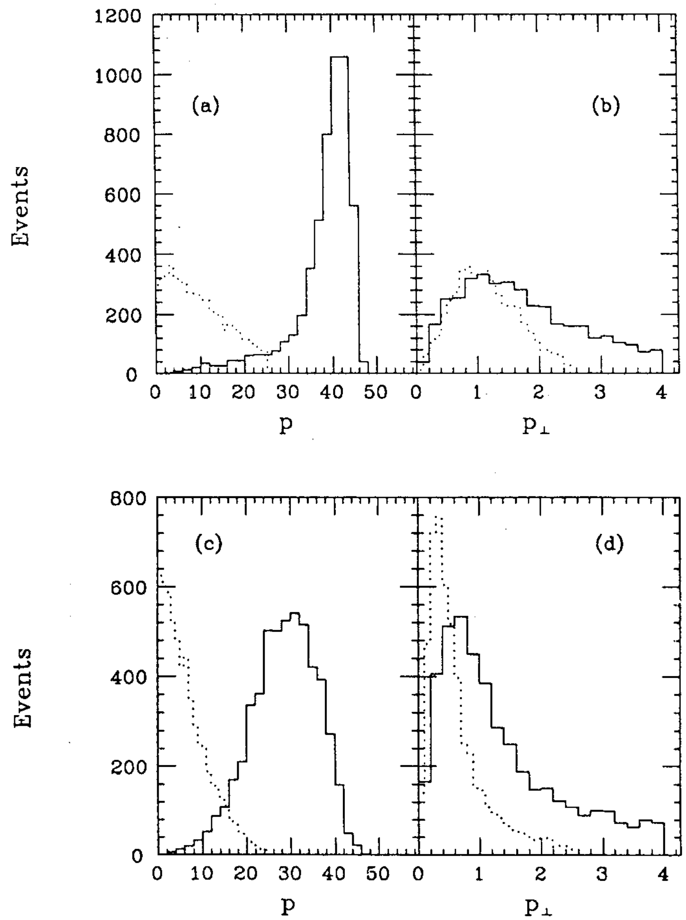

FIGURE 1. (a) Momentum distribution for electrons from b decay (dotted) and for the parent b hadron. The electron histogram is artificially cut off at 25 GeV. (b) $p_\perp$ distribution for electron (dotted) and parent b. (c, d) Corresponding distributions for charm.

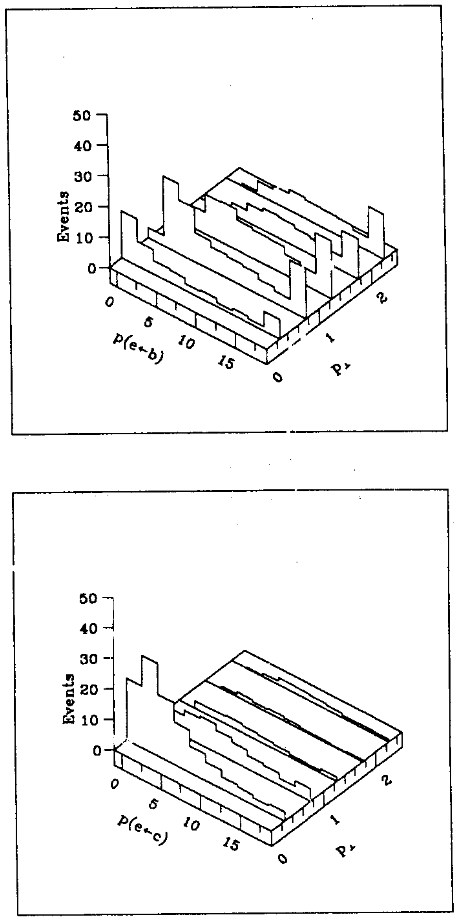

FIGURE 2. Distribution of events vs p and $p_\perp$ for generated $b \to e$ (above) and $c \to e$ (below). Overflows appear in the extreme bins.

see that bottom hadrons can be selected quite well with the requirement $p_\perp > 1$, as in the original PEP-5 measurement. Combining the information in Table 1 and Fig. 2 we find the following estimates for the b/c/background breakdown of the b-enriched sample:

$b \to e$	58%
$b \to c \to e$	15%
$c \to e$	6%
background	21%

2. Sensitivity

As a reminder of how the impact parameter method works, refer to Fig. 3 where we define some quantities relating parent hadron and decay lepton vectors and the thrust axis which is used to approximate the parent hadron direction of flight. The impact parameter, δ, is given by

$$\delta = \beta\gamma ct \sin\psi \sin\varsigma,$$

where ψ is the laboratory decay angle, ς is the polar angle of the impact parameter 3-vector, **b**, βc is the parent velocity, γ is the time dilation factor and t is the proper decay time. The angle ς appears because the tracking system measures the x, y-projection of **b**. δ is called positive if the lepton, assumed to decay to a forward angle, appears to come from a point downstream of the parent's production point.

Fig. 4a shows two distributions in δ for a b hadron that decayed exactly 1 ps after its production, for events within the acceptance defined above. The dotted curve describes decays for which the parent direction is known exactly; the absence (but one or two) of events with $\delta < 0$ indicates that backward decays are extremely rare. The distribution in δ reflects those of the angles ψ (see Fig. 3) and ς. The solid histogram in Fig. 4 is the result of approximating the parent direction by the thrust axis (computed from generated charged particles). The difference between the true and estimated flight direction sometimes results in the wrong sign for δ. This effect is much greater for charm decays, as shown in Fig. 4b.

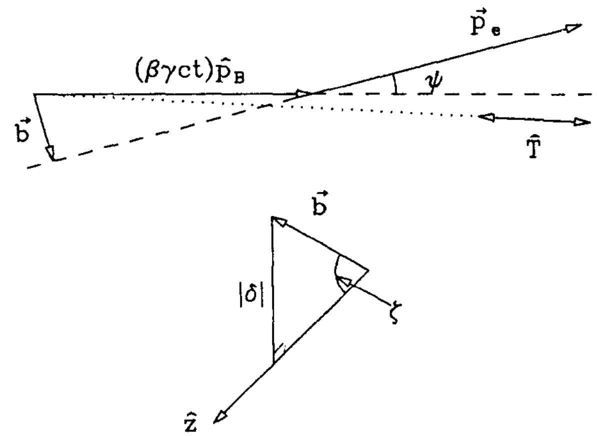

FIGURE 3. Vectors and angles pertinent to the decay process.

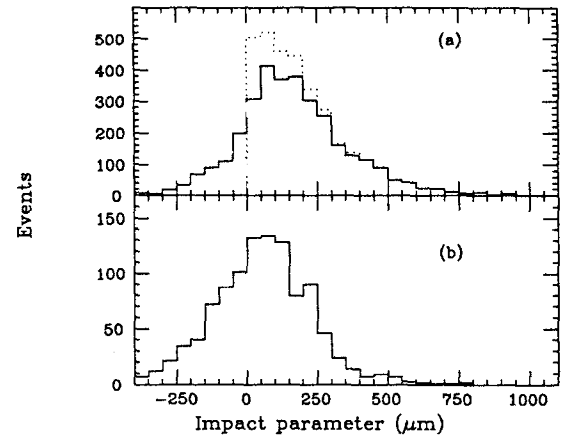

FIGURE 4. δ distributions for $t = 1$ ps. (a) b decays. The dotted histogram is obtained when the actual parent flight path is used for the extrapolation. The solid histogram corresponds to taking the thrust axis as the estimate of the parent direction. (b) c decays (thrust approximation).

2.1 AVERAGE IMPACT PARAMETER VS p, $p_\perp$

To get some feeling for the sensitivity of the events surviving the cuts, we

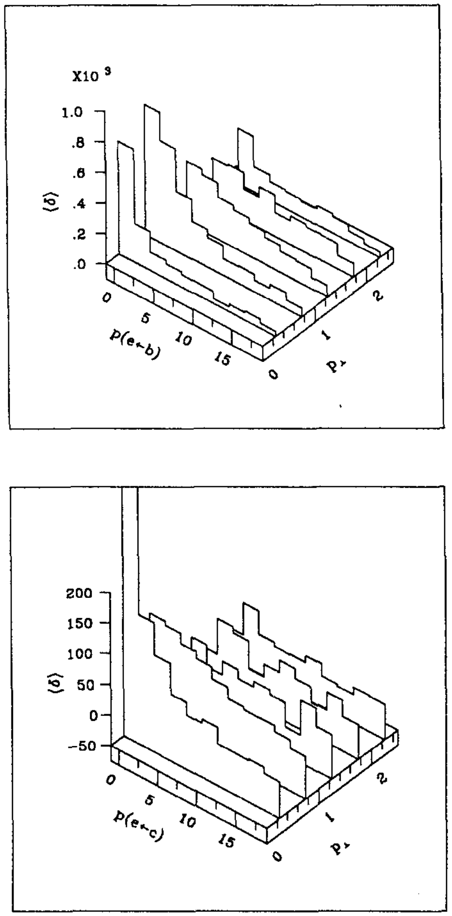

FIGURE 5. Average impact parameter vs p and $p_\perp$ for $b \to e$ (above), and $c \to e$ (below), measured with generated tracks.

examine in Fig. 5 the average value of δ, as a function of p and $p_\perp$. As was noted in the DELCO paper,[4] the very highest sensitivity occurs for leptons with very low momentum. On the other hand, the region below $p \simeq 1$ GeV contains relatively few signal events and high background, so it will be prudent to remove these, as noted above. The impact parameter for bottom hadrons averaged over the accepted region $p > 1$ GeV and $p_\perp > 1$ GeV is around 150 μm, while for the charm background it's much smaller, around 30 μm.

2.2 IMPACT PARAMETER DISTRIBUTION

We saw in Fig. 4 that lack of knowledge of the parent's flight direction flips some of the impact parameters to negative values. The impact parameter is also smeared by the distribution in the angles ψ and ς and the different $\beta\gamma$ values implied by the fragmentation function for the parent hadron (Actually the product $\gamma \sin\psi$ is approximately energy-independent at high energies—see below.) The histogram in Fig. 6 repeats from Fig. 4 the distribution of impact parameters resulting from the decay of a b hadron at 1 ps proper time. The width of this curve scales with t. The dashed curve is for an exponential distribution in t with 1 ps mean lifetime, τ, and the solid curve includes the effect of Gaussian measurement error with $\sigma = 25$ μm. We see that at this level the measurement error is not very important compared with the distribution being measured.

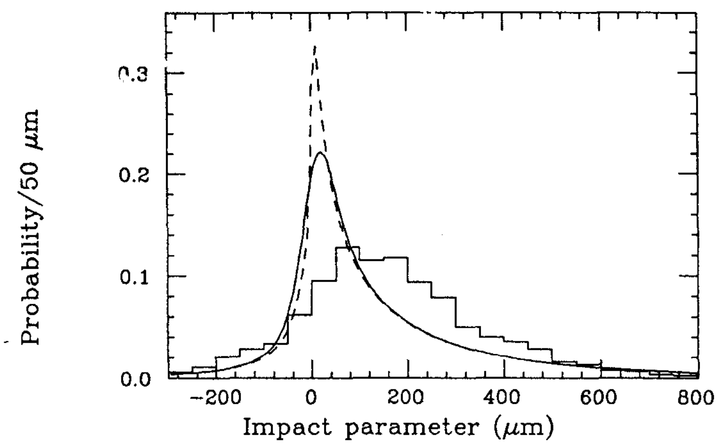

FIGURE 6. δ distributions for $t = 1$ ps (histogram); for exponential t-dependence, $\tau = 1$ ps (dashed curve); with 25 μm Gaussian resolution (solid curve).

The distribution in Fig. 7 corresponds to the dashed curve in Fig. 6, except that the assumed b lifetime is now the 1.1 ps currently assigned in LUND61. For comparison the shapes for $b \to c \to e$ cascades and direct charm decays are also given in Fig. 7.

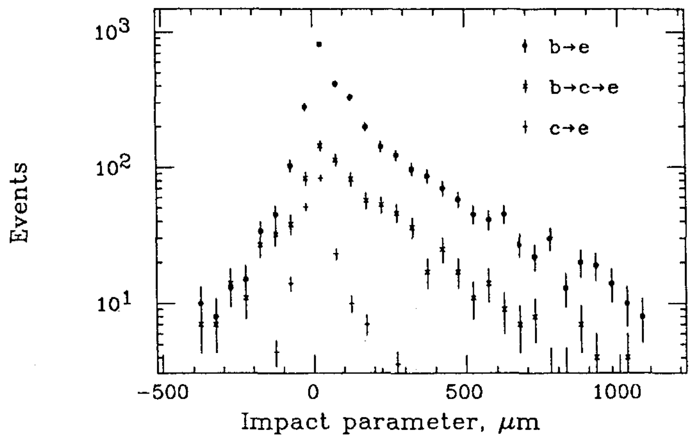

FIGURE 7. δ distribution for generated electron tracks, $\tau(b) = 1.1$ ps.

2.3 Dependence of $\langle\delta\rangle$ upon p_B, QCD and fragmentation

We asserted above that $\gamma \sin\psi$ is approximately energy-independent at high energies. The actual formula is

$$\delta = \beta\gamma ct \frac{\sin\psi^*}{\gamma(1+\beta\cos\psi^*)},$$

where ψ^* is the center-of-mass lepton decay angle and $\beta = p_B/E_B$ is the velocity of the B meson. The γ factors cancel, but some dependence upon β remains, principally because of the denominator which becomes small when $\cos\psi^*$ is near the value -1. Putting it another way, the (rare) decay in which the lepton is just forward of 90° in the lab has a positive impact parameter approximately equal to the decay path, which of course scales with γ.

The variation of $\langle\delta\rangle$ is studied in Fig. 8. The curves show $\langle\delta\rangle$ calculated with the known parent direction at the fixed momenta indicated by the data points.

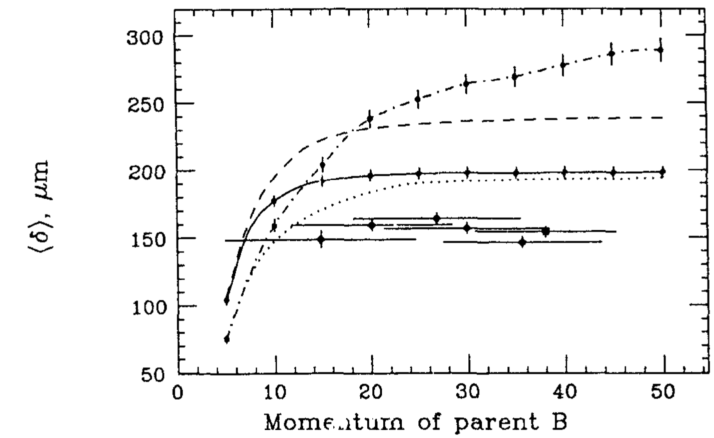

FIGURE 8. Mean lepton impact parameter vs B momentum. Dot-dashed curve: no lepton momentum or impact parameter cuts; dashed curve: $p > 1$ and $p_\perp > 1$; dotted curve: $-400\ \mu m < \delta < 1100\ \mu m$; solid curve: both cuts. Points with error bars: p_B spectrum and thrust axis from fragmentation. Open square: Lund symmetric fragmentation; diamonds: Peterson fragmentation, $\epsilon_b = 0.004, 0.04\ 0.1, 0.5, 0.8$.

From the dot-dashed curve we see the residual p_B-dependence, which is greatly reduced if we remove either the low $p, p_\perp$ tracks or the large $|\delta|$ tracks or both.

The points not connected by curves in Fig. 8 are obtained when the thrust axis estimate of the B direction is used to fix the sign of δ. The mean δ is smaller because of the smearing to negative values. The Peterson fragmentation function with various values of ϵ_b was used to scan the range of p_B values indicated. These points are consistent with a nearly flat curve, although the errors are too large to prove the constancy of $\langle\delta\rangle$ to the desired precision. What is clear from this study is that the p_B dependence is very small over the SLC energy range, and any sensitivity to QCD and fragmentation is caused by the smearing of the parent flight direction.

3. Detector Simulation

A sample of about 9,500 $Z^0 \rightarrow$ hadron events (Lund shower, no top quarks) has been processed to incorporate simulation of the full Mark II detector, including dE/dx in the main drift chamber and the 38-layer vertex drift chamber. The reconstructed track records on the tapes were produced by TRKFIT, a program which feeds the list of hits on each track, known from the Monte Carlo event generation, to the track fitter SARCS6. The tracks should therefore be fairly realistic in regard to resolution, assuming pattern recognition errors will not be important. Multiple Coulomb scattering is included. The silicon strip detector DAZMs were not included in the track fits.

Electron identification is based upon the information returned by the subroutine LAELEC, for the liquid argon system, and in TRKLST subtype 11 for the dE/dx. (The endcap calorimeters aren't used in the analysis because I haven't learned how to apply the information.) A measure of the electron probability from the dE/dx is shown in Fig. 9a for all detected charged tracks satisfying the requirement $p > 1$ and $p_\perp > 1$. The quantity plotted is the measured ionization excess over the expected ionization for a pion, divided by its uncertainty. In Fig. 9b the same quantity is plotted for those tracks satisfying the LA requirements for an electron (dotted histogram), and those further tagged as an electron in the produced-particle (MCMADE) block. We see that about 1% of non-electrons slip through the LA criteria (comparison of Fig. 9b with 9a), in agreement with the estimates in Ref. 3, and that with dE/dx tagging we get clean, efficient electron identification according to the Monte Carlo. Electron pairs from gamma ray conversions were rejected with the help of Pat Burchat's PRFIND routine.[5] Muons were required to register in all four layers of muon chambers.

About 65% of $b\bar{b}$ events satisfy the thrust and thrust axis polar angle cuts. Of these, about 13% are tagged by detected leptons. In the present sample, 290 leptons survive the selection.

The parentage of electrons and muons was identified from the Monte Carlo produced-particle lists. The distributions in δ for these are shown in Fig. 10, for decays to leptons of b, prompt c, cascade c and misidentified tracks. Here the thrust axis was computed from detected charged particles only. The misidentification background is rather tightly clustered near $\delta = 0$, while the prompt charm contribution is broader, but also consistent with zero mean. The bottom and cascade components are about 56% and 17%, respectively, of the total. About 15% come from direct charm and the remaining 12% are misidentification background.

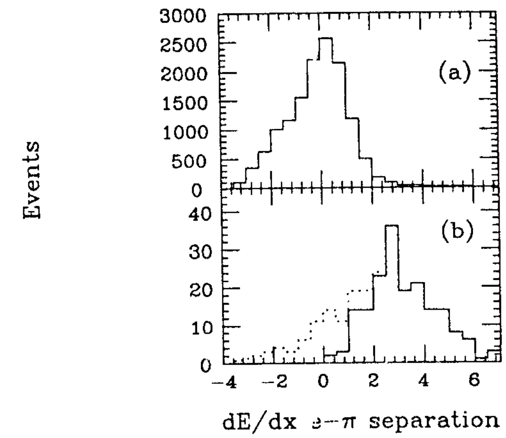

FIGURE 9. Distribution of $e - \pi$ separation measure from the dE/dx system for (a) all tracks having $p > 1$ and $p_\perp > 1$, and (b, dotted) those satisfying LA electron identification criteria. In (b), the solid histogram represents the actual electrons according to the produced particle information.

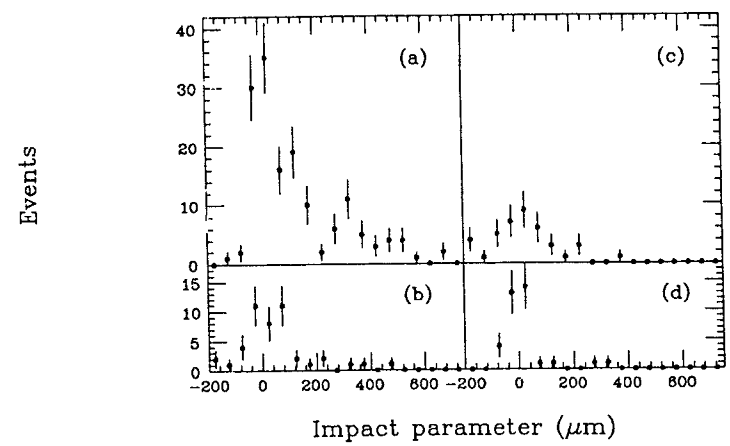

FIGURE 10. δ distribution of detected electron and muon tracks with $\tau(b) =$ 1.1 ps, for (a) $b \rightarrow l$, (b) $b \rightarrow c \rightarrow l$, (c) $c \rightarrow l$, (d) leptons from light quarks.

4. Likelihood Fit to the IP Distribution

A maximum-likelihood fit to the distribution of Fig. 10a can be used to determine the lifetime from the data. The true distribution of the events in t is the exponential

$$\frac{1}{\tau}\exp(-t/\tau).$$

The histogram in Fig. 6 gives the distribution in impact parameter for events at the fixed value $t = 1$ ps. It may be regarded as a Green's function, $G(\delta/t)$, where the indicated form of the (δ,t)-dependence reflects the fact that this distribution is a universal function that scales in the abscissa as t. If G is properly normalized, then the probability distribution (pdf) $q(\delta)$ is

$$d^2q(\delta) = G\Big(\frac{\delta}{t}\Big)d\Big(\frac{\delta}{t}\Big)\frac{1}{\tau}\exp(-t/\tau)dt.$$

Changing variables from (δ,t) to (δ,x), where $x \equiv \delta/t$, and integrating over x, we find

$$\frac{dq}{d\delta} = \int_0^{\delta\infty} G(x)\frac{1}{\tau x}\exp(-\delta/\tau x)dx.$$

The upper limit is $\pm\infty$ depending upon the sign of δ, since t is always positive but $x = \delta/t$. The Green's function G is available as a histogram, so the integral becomes a sum over the bins of G, and we integrate the coefficient of G_i over the ith bin. The integral of e^x/x can't be expressed in closed form, so we approximate the integral by the bin width times the central value:

$$\frac{dq}{d\delta} \simeq \sum_i G_i\frac{\Delta x}{\tau|x_i|}\exp(-\delta/\tau x_i),$$

where i runs over bins for which x_i has the same sign as δ.

When measurement error is to be accounted for, a further convolution with the resolution function, $R(\delta-\delta')$, is required. The new pdf is

$$\begin{aligned}\frac{dp}{d\delta} &= \int_{-\infty}^{\infty} d\delta' R(\delta-\delta')\int_0^{\delta'\infty} G(x)\frac{1}{\tau x}\exp(-\delta'/\tau x)dx\\ &= \sum_i G_i\frac{\Delta x}{\tau|x_i|}\int_{-\infty}^{\infty} R(\delta-\delta')\exp(-\delta'/\tau x_i)d\delta'.\end{aligned}$$

For a Gaussian resolution function,

$$R(\delta-\delta') = \frac{1}{\sqrt{2\pi}\sigma}\exp\Big[-\frac{1}{2}\frac{(\delta-\delta')^2}{\sigma^2}\Big],$$

we can perform the integral after completing the square in the argument of the exponential. The result is (see also, e.g., Larry Gladney's thesis,[6] section 4.2)

$$\frac{dp}{d\delta} = \sum_i \frac{G_i\Delta x}{2\tau|x_i|}\exp\Big[\frac{1}{2}\Big(\frac{\sigma}{\tau x_i}\Big)^2 - \frac{\delta}{\tau x_i}\Big]\Big[1-\frac{x_i}{|x_i|}\mathrm{erf}\Big(\frac{\sigma}{\sqrt{2}\tau x_i}-\frac{\delta}{\sqrt{2}\sigma}\Big)\Big].$$

Additional terms may be added to account for the background and cascade decays.

We should mention here that a bias that can creep into the result when this pdf is used arises from the tendency of low-momentum tracks to have both larger impact parameters and (because of multiple scattering) larger errors than average. The larger errors imply smaller weight for these events in the fit. This correlation between δ and σ biases the result toward a smaller value. One way out would be to correct the result from data with the bias measured with the Monte Carlo with detector simulation.

To fit unbinned data we maximize

$$\log\mathcal{L} = \sum_{n=1}^{N}\log\Big(\frac{dp}{d\delta}(\delta_n,\sigma_n)\Big),$$

where N is the number of events. Alternatively, we may reduce the data to a histogram of M bins, whence

$$\log\mathcal{L} = \log N! + \sum_{k=1}^{M}\big[n_k\log p_k - \log n_k!\big],$$

where n_k is the number of events in bin k and p_k is the pdf integrated over bin k. In this case the quantity

$$\chi^2 \equiv -2\log\mathcal{L}$$

should obey a χ^2 distribution with $M-2$ degrees of freedom.

5. Results for Monte Carlo Sample

The fitting procedure of the previous section was applied to the Monte Carlo sample with detector simulation, corresponding to the histograms of Fig. 10(a-d). The Green's function is from Fig. 6 (histogram). Contributions were included in the probability distribution function to account for misidentification background, treated as a pure resolution curve centered on zero, and for direct charm production and decay, treated as a Gaussian of width 130 μm and zero mean, as suggested by the distributions in Fig. 10d and c, respectively. The $b \to c$ part was taken to be the same as pure b.

The data and best-fit curve are shown in Fig. 11. For these 290 events, of which 212 are from b hadron decays, the lifetime comes out

$$\tau(b) = 1.13^{+0.17}_{-0.14} \text{ ps},$$

in good agreement with the input value of 1.1 ps.

It's interesting to compare the likelihood fit result with the result of taking simply the mean of the generated-track δ distribution of Fig. 7 compared with the generated lifetime to measure the sensitivity, and using this in conjunction with the mean from the detector-simulation data of Fig. 10. That result after correction for background is

$$\tau(b) = 1.19 \pm 0.15 \text{ ps}.$$

Evidently in the present situation the mean alone of the δ distribution contains essentially all of the information about $\tau(b)$.

To understand a little better the sensitivity of this measurement, consider the case where the proper time t is measured for each event with perfect resolution and no bias. The exponential distribution dictates that the fractional error for N events would be $1/\sqrt{N}$, or 0.07 for $N = 212$. The sensitivity of the impact parameter method is less by a factor of about 1.9 with our resolution and background. For perfect resolution and no background this factor would be about 1.5.

I've looked into the possibility of fitting the data as a function of the additional independent variable $\sin\varsigma$, which measures the projection of $\mathbf{b}$ onto the plane of the measurement of δ. The conclusion is that this gains us very little, because the distribution of events in $\sin\varsigma$ is (fortunately) peaked toward the value one anyway because of the Jacobian.

It should be remembered that the production point has been assumed here to be known for each event. The SLC beam may move around; the resulting uncertainty would add in quadrature to the 50-100 μm wide curves of Fig. 6.

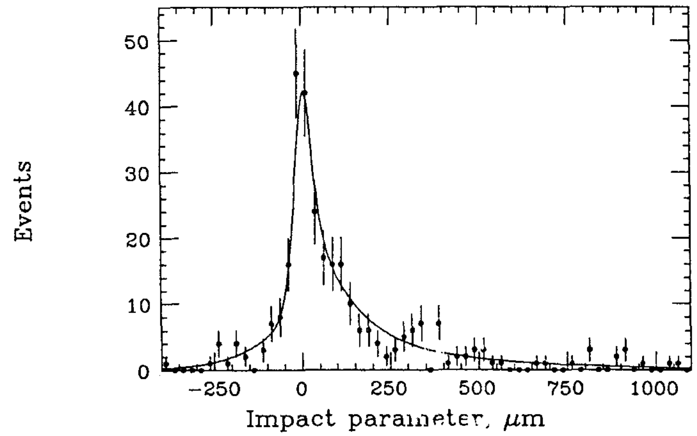

FIGURE 11. Best fit curve for the data points from Fig. 10.

6. Conclusions

The lepton impact parameter method for measuring the b-hadron average lifetime can be expected to yield a rather clean result with fractional statistical error for N events equal to about $2/\sqrt{N}$. Scaling from the Monte Carlo sample studied here, we expect about 160 signal events for 10,000 produced Z^0s (including those that decay to leptons), implying a statistical precision of about 16% for $\tau(b)$. This is about the level of the current experiments.

The track resolution of the vertex drift chamber, with or without the silicon strip detector, is not seriously limiting so far as this measurement is concerned. The dominant systematic uncertainties are in the purity fraction and the sensitivity of the Green's function to the fragmentation and gluon radiation, through the uncertainty in the parent hadron direction. Backgrounds are quite small, so that it should be possible to keep systematic errors less than 10%.

REFERENCES

1. W. T. Ford, Mark II/SLC-Physics Working Group Note #9-9 (1986).
2. W. T. Ford, Mark II/SLC-Physics Working Group Note #9-12, in *Proceedings of the Second Mark II Workshop on SLC Physics*, SLAC-Report-306, p. 389 (1986).
3. M. Nelson, Mark II/SLC-Physics Working Group Note #0-3 (1986).
4. D. E. Klem, *et al.*, *Phys. Rev. Letters* **53** (1984) 1873.
5. P. Burchat, Mark II/SLC-Physics Working Group Note #0-7 (1987).
6. L. D. Gladney, SLAC-279 (1985).

Mark II/SLC-Physics Working Group Note # 9–18

AUTHOR: David P. Coupal

DATE: June 16, 1987

TITLE: Inclusive Leptons and B^0-$\bar{B}^0$ Mixing at SLC

The Mark II detector is well suited for the study of leptons from the weak decays of heavy quarks. This note presents the Monte Carlo results of a study of inclusive lepton rates done in the b and c quark working group. These results are an extension of those of an earlier study by M. Nelson [1]. The single lepton rates, determined from Monte Carlo, will be used to predict the same sign dilepton rates from B^0-$\bar{B}^0$ mixing.

Earlier studies of inclusive leptons at SLC used Monte Carlo generated 4-vectors with approximations of the misidentification probabilities for electrons in the liquid argon calorimeter and drift chamber dE/dx and muons in the muon detector. This study used Monte Carlo generated raw data including simulated dE/dx data. Work on modelling lepton identification in the calorimeters and muon detector is still in progress—results from previous studies will be used here.

Monte Carlo Data Sample

These results are based on a study of approximately 9500 hadronic decays of the Z^0 generated using the LUND Monte Carlo with leading log parton showers (Λ_{LLA} = QCD scale = .5 GeV, Q_0 = invariant mass cutoff for shower evolution = 1.5 GeV). The sample contains $u\bar{u}$, $d\bar{d}$, $s\bar{s}$, $c\bar{c}$, and $b\bar{b}$ decays of the Z^0 and no top quark. The generated raw data is analyzed in the same way as real data excluding pattern recognition in the drift chamber, in which 100% efficiency is assumed.

Event Analysis

The lepton p_t was measured relative to the thrust axis, which was calculated using charged and neutral tracks. Charged tracks were required to satisfy the following cuts:

- $|cos\theta| < .9$
- $p > 100\ MeV/c$
- $r_{xy} < 1.6mm$
- $|z - z_V| < 60mm$

where θ is the angle of the track to the beam direction, r_{xy} is the distance of closest approach of the track to the vertex in the x-y plane, and $|z - z_V|$ is the distance in the z (beam) direction. Neutral tracks were included in the calculation if:

- $E > 150\ MeV$
- distance to nearest track > 30 cm

The angle between the thrust axis and the beam direction, θ_{THR}, was required to have $|cos\theta_{THR}| < .8$.

Electrons

Electrons were identified using the barrel and endcap calorimeters and the drift chamber dE/dx information. The dE/dx information is most useful for identifying electrons in the momentum range from $p = 250\ MeV/c$ to $p = 7\ GeV/c$, whereas the calorimeters work in a range $p > 2\ GeV/c$. In this study electrons are assumed to be identified with 100% efficiency, though in the calculation of misidentification probabilities discussed below an efficiency of 90% is assumed.

Backgrounds

The principal backgrounds to the electron signal are from hadron misidentification and from non-prompt sources such as γ-conversions and π^0 decay. There is also a small background of electrons from K and τ decay. Figure 1 shows the p_t distribution, cut on $p > 3\ GeV/c$, for prompt electrons from c and b quark decay, non-prompt sources, and all hadrons before any cuts to reduce background. From this figure it is obvious that the misidentification probability must be less than of order .5% to reduce this background.

Hadrons misidentified as electrons in the calorimeter arise primarily from overlap of photons and charged tracks. An estimate of the misidentification probability was made for the Mark II upgrade proposal[2] and shown in Table 1a) as a function of p and p_t. The numbers have been smoothed to take out statistical variations and the minimum value set to .010. The equivalent numbers for the dE/dx system were derived from a Monte Carlo simulation with 10% additional smearing to bring it in agreement with the current measured performance of the dE/dx system. The misidentification probabilities for the dE/dx system are shown in Table 1b). The combination of calorimeter and dE/dx are shown in Table 1c). The actual misidentification background is calculated by demanding that the dE/dx of hadrons be within the 90% CL limit of being an electron and then weighting the resulting yield in bins of p and p_t with the numbers of Table 1a).

The other major background is non-prompt electrons from γ- conversion and π^0 decay. This background can be reduced significantly by demanding that electron candidate tracks not have a small opening angle with another track which is consistent with being an electron. The technique has been used in a previous Mark II analysis[3] and is explained in detail in this reference and Ref. [4]. This study differs from that of Ref. [3] in that the demand that the second track be consistent being an electron is defined by the dE/dx system instead of the calorimeter. The efficiency of this cut as a function of momentum from Monte Carlo is shown in Figure 2.

Electron Results

Table 2 shows the yield of electrons in bins of p and p_t. Cutting on $p > 3\ GeV/c$, Figure 3 shows the p_t distribution for signal and background. Anticipating the application to B^0-$\bar{B}^0$ mixing one can define a "b-enriched" region by cutting on $p > 3.0\ GeV/c$ and $p_t > 1.0\ GeV/c$. In this region there are 161 electrons from primary bottom decay, 41 from primary charm, 31 from secondary charm, and 38 background events.

Muons

Muons are identified as those tracks with hits in all four planes of the muon detector. This study assumed a partially upgraded muon system, namely the "facades" described in Ref. [5], which provide additional muon detection down to $cos\theta < .85$. Again the muon identification was assumed to be 100% for those tracks which project into the instrumented detector.

Background

The muon background consists of muons from π and K decay and from hadron punchthrough. There is an additional small background from τ decay. Kink-finding in the drift chamber could be used to eliminate some of the background from π and K decay, but as will be shown below, this background is relatively small.

The hadron punchthrough probability was taken from a Monte Carlo study done for the Mark II muon upgrade proposal. The results were parameterized as a function of p and p_t as follows:

$$Prob(h \to \mu) = \begin{cases} .001 \times p(GeV/c) & p_t < 1\ GeV/c \\ .00075 \times p & 1 < p_t < 2\ GeV/c \\ .00055 \times p & p_t > 2\ GeV/c \end{cases}$$

Muon Results

Table 3 shows the yield of muon in bins of p and p_t. Cutting again on $p > 3\ GeV/c$, Figure 4 shows the p_t distribution for the different contributions. Defining a "b-enriched" region as in the electron case ($p > 3.0\ GeV/c$ and $p_t > 1.0\ GeV/c$) yields 99 muons from primary bottom decay, 29 from primary charm, 28 from secondary charm and 60 background events.

Application to B^0-$\bar{B}^0$ Mixing

Mixing in the B_d^0 (B_s^0) system can be described by the parameter r_d (r_s) defined by:

$$r_{d(s)} = \frac{\Gamma(B^0_{d(s)} \to \bar{B}^0_{d(s)} \to l^- X)}{\Gamma(B^0_{d(s)} \to l^+ X)}$$

which is the probability the bottom meson will decay into the wrong sign lepton. This decay together with a normal semileptonic decay of the other B will result in a like-sign dilepton. Like-sign dileptons can also occur from, for example, pairing a lepton from primary charm decay with a non-prompt background or a lepton from secondary charm decay. Thus mixing shows up as an excess of like-sign dileptons.

In this study, one does not differentiate between charged and neutral bottom mesons or bottom baryons. Define the parameter χ:

$$\chi = \frac{\Gamma(B \to l^- X)}{\Gamma(B \to l^\pm X)}$$

where B refers to any hadron containing the $\bar{b}$ quark. This parameter is related to $r_{d(s)}$ by

$$\chi = \frac{(BR)_d}{\langle BR \rangle} f_d \chi_d + \frac{(BR)_s}{\langle BR \rangle} f_s \chi_s$$

where $\chi_{d(s)} = \frac{r_{d(s)}}{1+r_{d(s)}}$ and $(BR)_{d(s)}$ is the semileptonic branching ratio for $B^0_{d(s)}$, $\langle BR \rangle = \sum f_i (BR)_i$ is the branching ratio for all bottom states, and f_i is the fraction of b quarks which fragment into B_i hadrons. For comparison with other measurements the branching ratios are all assumed equal and fragmentation fractions are assumed to be $f_d = .4$ and $f_s = .2$. This assumption also ignores bottom baryon production.

Using the single lepton rates in the b-enriched region one can predict the expected rate of dileptons. This calculation is explained in detail in the Appendix of Ref. [6]. The predicted number of events was calculated assuming 10^6 Z^0 's. Table 4 shows the expected number of dileptons assuming $\chi = 0$ (no mixing) and $\chi = .1$. Also shown in Table 4 is the yield of dileptons with the b-enriched region defined by $p > 5.\ GeV/c$ and $p_t > 1.5\ GeV/c$.

Assuming $\chi = .1$, the resulting constraints on r_d and r_s are shown in Figure 5. The alternative definition of the b-enriched region in Table 4 does not improve these limits. Previous measurements of B^0-$\bar{B}^0$ mixing[7-9] are shown in Figure 6. Thus if mixing is indeed present at a level indicated by the allowed region of Figure 6, then it should be easily visible with 10^6 Z^0 's at SLC.

Conclusions

This study still contains some limitations:

- The misidentification probability for hadrons in the calorimeter needs to be studied further. Ultimately the best estimate will come from studying real data.
- The muon misidentification from hadron punchthrough should be measured from the data.
- With increasing numbers of 3- and 4-jet events, the thrust axis becomes a poorer estimate of the original quark direction. One should explore using cluster algorithms.
- The presence of decays $Z^0 \to t\bar{t}$ would be additional background to the B^0-$\bar{B}^0$ mixing signal. The number of $t\bar{t}$ events is expected to be small, plus some of the same cuts used to isolate a top signal could be used to eliminate it in a search for mixing. For example cutting on thrust $> .85$ eliminates 65% of the top signal and only 13% of the non-top events.

It should be possible to obtain a relatively clean sample of prompt leptons from heavy quark decays with the Mark II detector at SLC. Misidentification probabilities of less than .3 % reduce the background to a manageable level. A clean sample of prompt leptons could be used to measure semileptonic branching ratios, fragmentation functions and, as presented here, B^0-$\bar{B}^0$ mixing.

REFERENCES

1. M. Nelson: Mark II/SLC Physics Working Group Note #0-3(1986)
2. Proposal for the Mark II at the SLC: SLAC-PUB-3561 or CALT-68-1015 (1983)
3. M. Nelson: Ph.D. Thesis, LBL-16724(1983)
4. P. Burchat: Mark II/SLC Physics Working Group Note #0-7(1987)
5. Proposal for a Forward Muon System for Mark II at SLC (unpublished)
6. T. Schaad: Ph.D. Thesis, Harvard (1985)
7. T. Schaad *et al.*,, *Phys. Lett.* **160B** (1985) 188
8. C. Albajar *et al.*,, *Phys. Lett.* **183B** (1987) 247
9. Argus Collaboration: DESY 87-029.

June 16, 1987

TABLES

1. Probabilities of a hadron being misidentified as an electron in bins of p and p_t for (a) the electromagnetic calorimeter, (b) the drift chamber dE/dx and (c) the combination of both systems.
2. Distribution of electron signal and background in bins of p and p_t.
3. Distribution of muon signal and background in bins of p and p_t.
4. Dilepton yield for $\chi = 0.$(no mixing) and $\chi = .1$, assuming 10^6 Z^0's.

FIGURES

1. p_t distribution for electrons from heavy quark decay, electrons from γ-conversion or π^0 decay, and all hadrons.
2. Efficiency for identifying electrons from γ-conversion and π^0 decay versus momentum, determined from Monte Carlo.
3. p_t distribution of electrons showing contributions from the different heavy quark decays and background.
4. p_t distribution of muons showing contributions from the different heavy quark decays and background.
5. 90% upper and lower limits on r_d vs r_s assuming $\chi = .1$ and 10^6 Z^0's.
6. Previous measurements of B^0-$\bar{B}^0$ mixing. The Mark II result is a 90% CL upper limit and the UA1 result is a 90% CL lower limit. The Argus measurement is sensitive only to the value of r_d so the result is presented as horizontal lines on the plot. The solid line is the actual measured value and the dashed lines show the one standard deviation errors.

$p\backslash p_t$	0.0-0.5	0.5-1.0	1.0-1.5	1.5-2.0	> 2.0
1-3	.060	.010	.010	.010	.010
3-5	.080	.015	.010	.010	.010
5-7	.100	.015	.010	.010	.010
7-9	.090	.020	.010	.010	.010
9-11	.080	.015	.010	.010	.010
11-13	.060	.010	.010	.010	.010
13-15	.050	.010	.010	.010	.010
15-17	.040	.010	.010	.010	.010

$p\backslash p_t$	0.0-0.5	0.5-1.0	1.0-1.5	1.5-2.0	> 2.0
1-3	$.003 \pm .001$	$.003 \pm .001$	$.003 \pm .001$	$.003 \pm .004$	.003
3-5	$.032 \pm .004$	$.028 \pm .005$	$.021 \pm .006$	$.017 \pm .008$	.02
5-7	$.088 \pm .011$	$.095 \pm .012$	$.090 \pm .017$	$.085 \pm .024$	.08
7-9	$.129 \pm .018$	$.128 \pm .018$	$.137 \pm .026$	$.121 \pm .035$	.12
9-11	$.195 \pm .029$	$.202 \pm .027$	$.169 \pm .037$	$.178 \pm .048$	.18
11-13	$.242 \pm .041$	$.214 \pm .034$	$.284 \pm .050$	$.210 \pm .066$	.24
13-15	$.216 \pm .050$	$.236 \pm .043$	$.190 \pm .055$	$.253 \pm .086$	.24
15-17	$.253 \pm .060$	$.255 \pm .060$	$.253 \pm .071$	$.265 \pm .095$	.25

$p\backslash p_t$	0.0-0.5	0.5-1.0	1.0-1.5	1.5-2.0	> 2.0
1-3	.0002	.0000	.0000	.0000	.0000
3-5	.0026	.0004	.0002	.0002	.0002
5-7	.0088	.0014	.0009	.0009	.0008
7-9	.0116	.0026	.0014	.0012	.0012
9-11	.0156	.0030	.0017	.0018	.0018
11-13	.0145	.0021	.0028	.0021	.0024
13-15	.0108	.0024	.0019	.0025	.0024
15-17	.0101	.0026	.0025	.0027	.0025

TABLE 1

KEY:
b primary
c primary (non-prompt)
c secondary (misidentification)

$p\backslash p_t$ (GeV/c)	0.0-0.5	0.5-1.0	1.0-1.5	1.5-2.0	2.0-2.5	> 2.5
1-3	10 39 (299) 64 (4.4)	30 13 (92) 39 (.5)	8 8 (28) 7 (.2)	3 3 (7) 4	2 (3) 	 2
3-5	4 16 (22) 24 (16.2)	15 10 (13) 26 (2.0)	8 6 (3) 5 (.4)	5 2 (2) 2 (.2)	1 (3) (.1)	6 4 (1) 1 (.2)
5-7	2 13 (6) 14 (24.3)	14 8 (2) 20 (3.5)	8 3 (4) 6 (1.0)	5 1 (1) 3 (.4)	4 1 (1) (.2)	2 4 3 (.6)
7-9	1 4 2 (15.7)	9 7 (2) 9 (3.5)	6 (1) 1 (.9)	5 (2) (.4)	7 1 (.2)	5 (.6)
9-11	 5 (2) 2 (11.3)	9 6 (1) 7 (2.5)	10 3 1 (.7)	5 (1) (.4)	1 1 (.2)	6 (1) 1 (.6)
11-13	3 1 3 (6.0)	3 3 2 (1.2)	5 5 2 (.9)	5 2 1 (.3)	2 (.2)	4 2 (.4)
13-15	2 1 (2.8)	4 1 (2) 2 (.9)	3 1 (1) 3 (.4)	6 (.2)	3 1 1 (.2)	5 1 (.5)
15-17	2 (2.0)	2 1 3 (.5)	7 (1) (.4)	4 1 (.2)	1 (.2)	5 (.3)
> 17	9 1 (1) 1 (4.5)	8 1 (2) (1.5)	9 2 (2) (1.2)	4 1 (.6)	4 (.4)	9 (1.0)

TABLE 2

KEY:
b primary
c primary (non-prompt)
c secondary (misidentification)

$p\backslash p_t$ (GeV/c)	0.0-0.5	0.5-1.0	1.0-1.5	1.5-2.0	2.0-2.5	> 2.5
1-3	3 8 (54) 17 (9.1)	11 5 (25) 6 (5.4)	2 6 (9) 5 (1.7)	3 1 (6) 1 (1.0)	 (1) 1 (.4)	 (.1)
3-5	 6 (13) 9 (13.0)	5 7 (6) 21 (9.5)	13 2 (5) 3 (2.8)	 2 (3) 1 (1.4)	2 1 (1) 2 (.7)	1 2 1 (1.0)
5-7	 5 (3) 3 (8.6)	4 [illegible] (3) 7 (7.5)	11 8 (1) 3 (2.3)	1 1 (1) 2 (1.2)	1 1 2 (.5)	3 (3) (1.1)
7-9	 6 (1) 4 (5.6)	8 3 (2) 2 (5.6)	7 6 (1) 2 (2.1)	3 2 (1.0)	 1 (.4)	1 3 (1.0)
9-11	 2 (1) 1 (3.8)	1 2 (1) [illegible] (4.3)	3 (2) 2 (1.5)	4 1 (1) (1.0)	 1 (.3)	3 (1) (.9)
11-13	1 (2.8)	4 1 1 (3.6)	8 2 (1) 2 (1.5)	2 (.6)	2 1 (1) (.2)	3 (.6)
13-15	3 (1) (2.1)	4 1 (1) 1 (2.8)	1 (2) 1 (1.0)	3 (1) (.5)	1 (.3)	1 1 (.7)
15-17	1 (1) (1.5)	1 (1.7)	1 (1.1)	3 (.5)	1 (.2)	3 (.5)
> 17	2 1 (1) (4.1)	3 1 (2) (6.0)	8 (2) (2.9)	4 1 (1.9)	 (.7)	5 (1.7)

TABLE 3

b-enriched region	Mixing parameter χ	ee	$e\mu$	$\mu\mu$
$p > 3.\ GeV/c$, $p_t > 1.\ GeV/c$	$\chi = 0.$ (no mixing)	104	69	173
	$\chi = .1$	130	77	202
$p > 5.\ GeV/c$, $p_t > 1.5\ GeV/c$	$\chi = 0.$ (no mixing)	20	12	34
	$\chi = .1$	31	14	42

TABLE 4

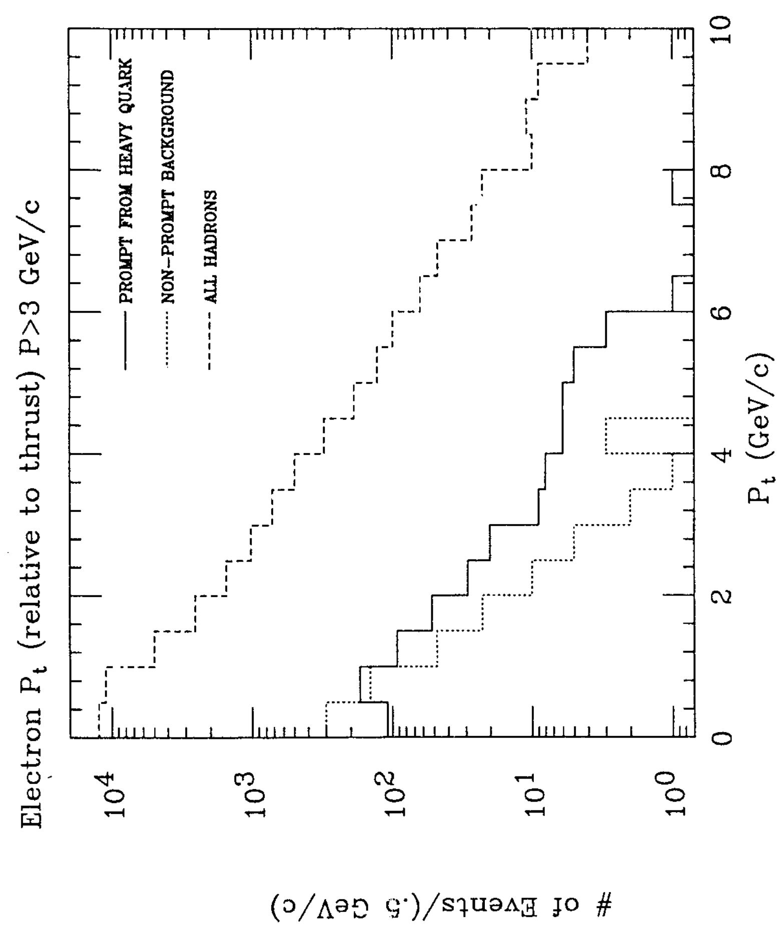

FIGURE 1

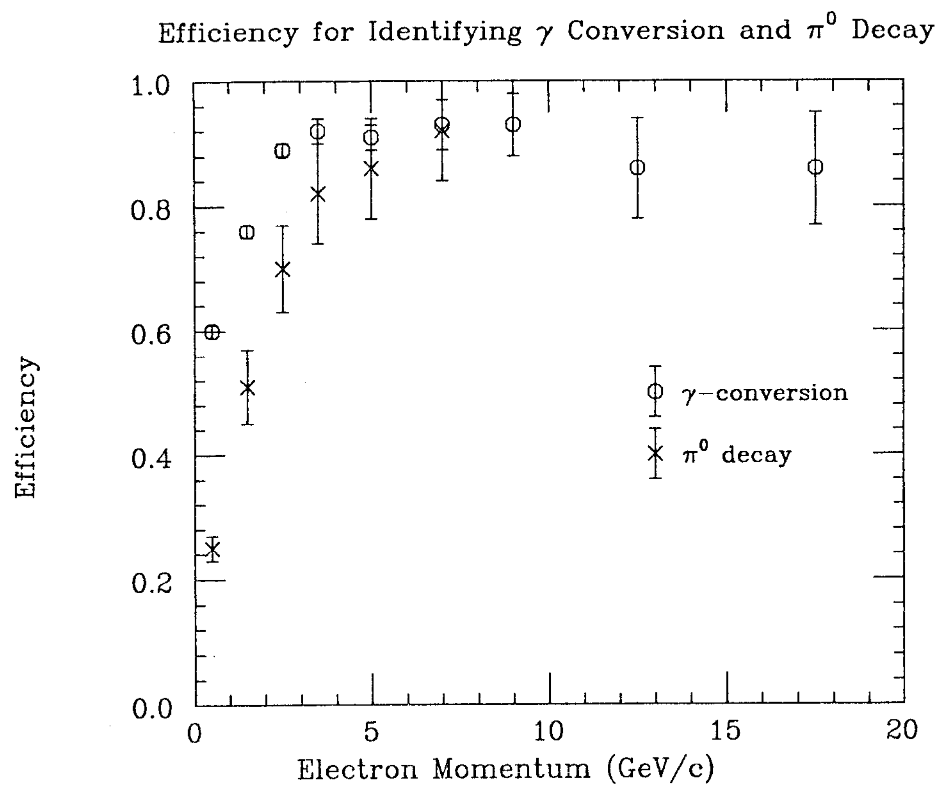

FIGURE 2

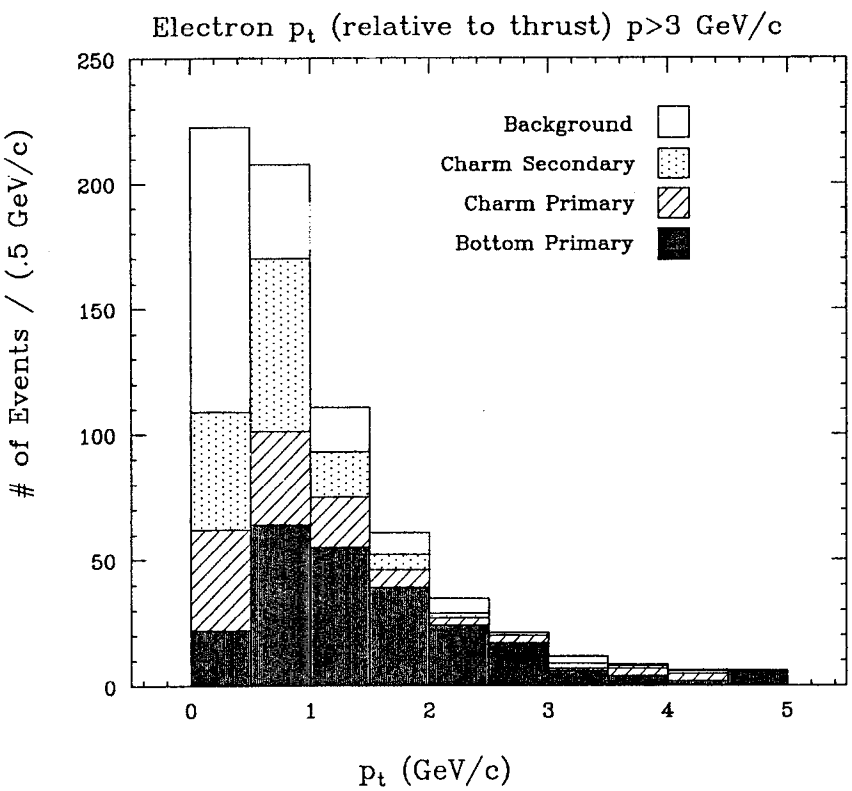

FIGURE 3

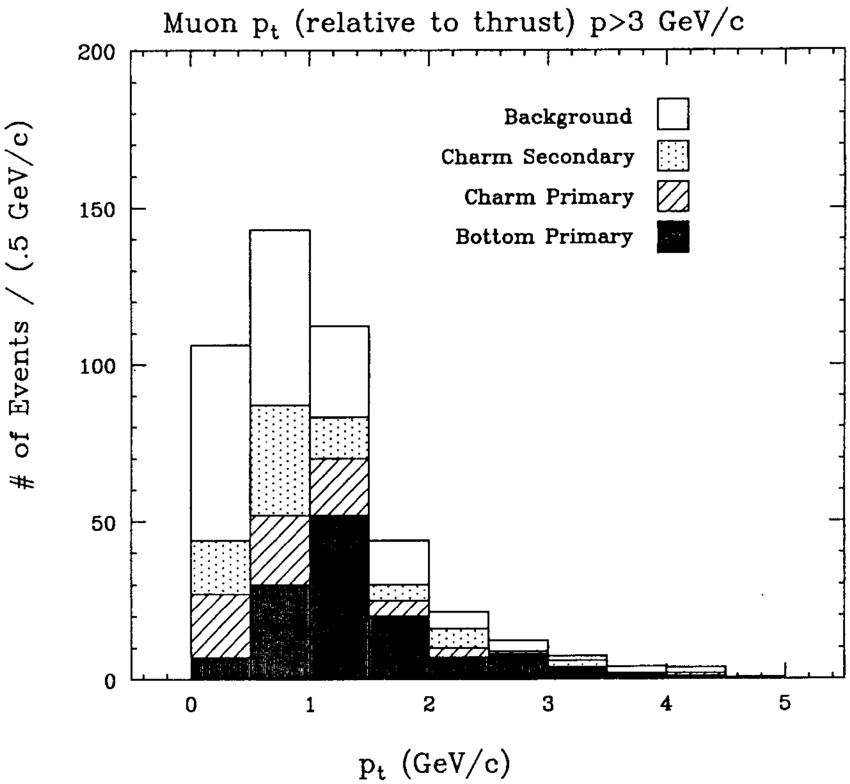

FIGURE 4

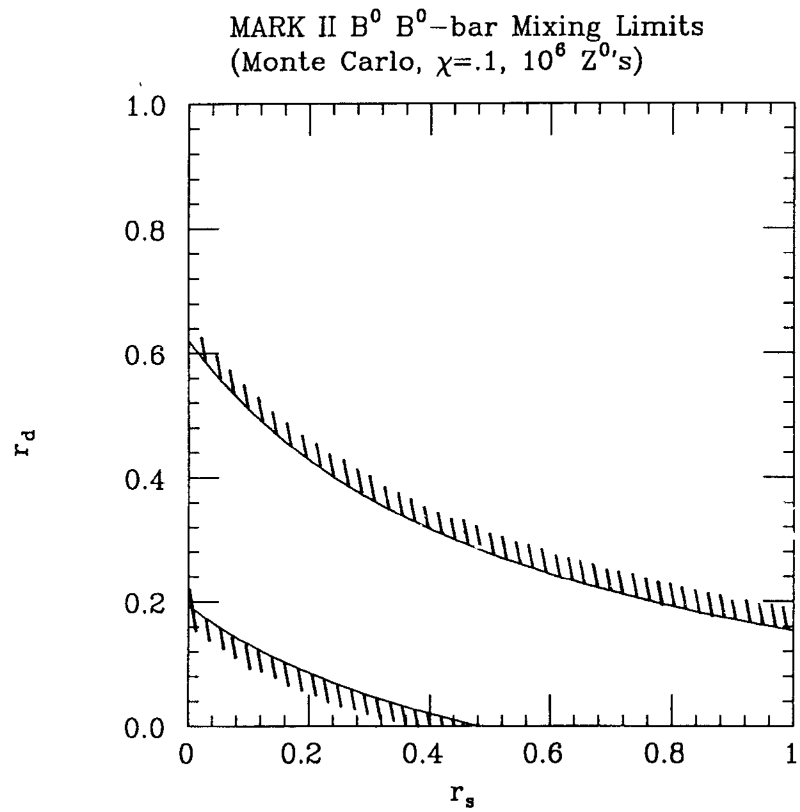

FIGURE 5

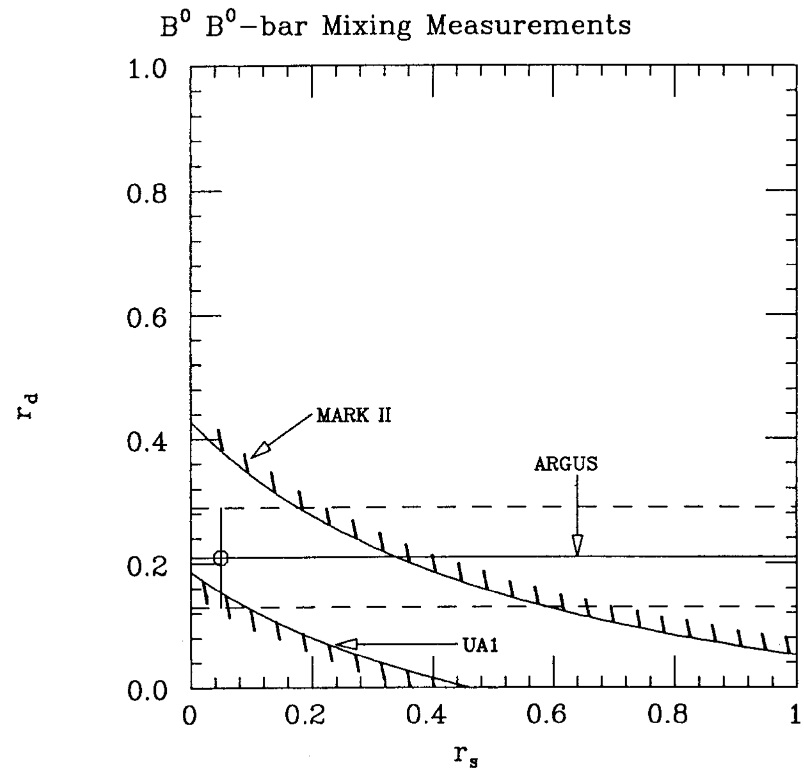

B^0 B^0–bar Mixing Measurements
1.0
0.8
0.6
0.4
0.2
0.0
r_d
MARK II
ARGUS
UA1
0
0.2
0.4
0.6
0.8
1
r_s

FIGURE 6

SLAC MEMORANDUM
Mark II/SLC-Physics Working Group Note # 9–19

AUTHOR: Ken Hayes

DATE: July 15, 1987

TITLE: b and c Quark Exclusive Decays With the Vertex Detector

1. Introduction

Two initial uses of the Mark II vertex detector at the SLC will be to tag b quark jets and to make lifetime measurements. The tagged b jets will be used to 1) measure the branching ratio for $Z \to b\bar{b}$, 2) search for the top quark using the $t \to b$ decay sequence, 3) study gluon jet production and fragmentation using $Z \to b\bar{b}g$ events where both b jets are tagged, and 4) study b quark fragmentation and decay using the tagged $Z \to b\bar{b}$ sample. Precision measurements of the b lifetime will be made, and if the top quark is found, an upper limit to its lifetime will be determined.

All of these physics topics can be studied making use of track impact parameter measurements only – no vertex reconstruction is required. But even a partial reconstruction of the event vertex topology provides additional information which may be helpful to an analysis. For example, one can test if the tracks which are inconsistent with originating in the primary vertex form a consistent secondary decay vertex, and the set of tracks which are consistent with both the primary and secondary vertices can be determined. How can this extra information be used? Can we use it to improve the b jet tagging efficiency or purity? Can b and c quark jets be separately identified with a reasonable efficiency? Can the primary quark charge be determined thereby allowing the forward backward charge asymmetry to be measured?

To help answer these questions, I have examined the reconstruction of some exclusive bottom and charm decays. This is one of the simplest vertex analysis

problems since only consistency with the hypothesized topology need be tested, and the invariant mass distribution provides a clean definition of efficiency and purity.

The remainder of this note is organized as follows: section 2 discusses some relevant exclusive b and c quark decays; section 3 evaluates the vertex detector resolution required to reconstruct the vertex topology of b and c decays and discusses the implications for use of the vertex chamber information; and section 4 illustrates the physics potential and some analysis techniques with a few examples: $B^0 \to \pi^+\pi^-$, $D^0 \to K^-\pi^+$, $D^+ \to K^-\pi^+\pi^+$, and use of the decay $B^0 \to D^+ + l^- + neutrals$ to measure the B^0 lifetime.

2. Some Relevant Exclusive b and c Decays

The large branching ratio for $Z \to b\bar{b}$ ($\approx 15\%$) and the excellent environment for vertex detection make Z^0 decays at the SLC a good place to study heavy quarks. Many physics topics can be explored by reconstructing exclusive heavy quark decays. These include the forward backward charge asymmetry for $Z \to q\bar{q}$ (A_{FB}), fragmentation, $B - \bar{B}$ mixing, particle spectroscopy, masses and lifetimes, KM matrix elements, and in the case of rare B decays, CP violation and tests of electroweak theory at the one loop level. Unfortunately, most of the relevant branching ratios are less than 10^{-3} and a large number of Z^0 decays are needed. For a decay mode with 10^{-3} branching ratio, 10 *produced* events require roughly 10^5 Z^0 decays. Therefore we will concentrate on those modes with the largest branching ratios.

Two simple exclusive modes with large branching fractions are $D^+ \to K^-\pi^+\pi^+$ and $D^0 \to K^-\pi^+$. The measured lifetimes[1] and branching ratios[2] for these decays are listed in Table 1. The expected production rate for these two exclusive modes is about 1200 decays per 10^5 Z^0 decays. About 30% of D^0 decays originate in the decay $D^{*+} \to D^0\pi^+$ which can be cleanly identified using the reconstructed $D^* - D$ mass difference.

Table 1

Mode	BR (%)	Lifetime (psec)
$D^+ \to K^-\pi^+\pi^+$	$4.2 \pm .4 \pm .4$	$0.43^{+.020}_{-.019}$
$D^0 \to K^-\pi^+$	$9.1 \pm 1.3 \pm .4$	$1.03^{+.052}_{-.044}$

Besides the obvious uses of measuring production rates, fragmentation properties and A_{FB}, the D^+ can be used to measure the B^0 lifetime. From the spectator diagrams shown in Figure 1 for B^0 and B^- decay, and from the fact that $D^{*+} \to (D^0, D^+)$, and $D^{*o} \to D^0$ but $D^{*o} \not\to D^+$, if these were the only diagrams contributing to B decay and if we ignore D^+ production at the W decay vertex, then D^+ are produced in B^0 decay but not in B^- decay. Thus, D^+ could be used to tag B^0 decay. Although the sum of B exclusive branching ratios measured by CLEO and ARGUS is only about 10%, we can use their measurements to test the prediction $B^- \not\to D^+$. From the results compiled in [1], the sum of measured B^- decay modes to D^{*+} or D^+ is $4.7 \pm 1.2\%$ while the sum of measured B^- decay modes to D^0 is $.38 \pm .18\%$; so this argument fails. Grinstein, Wise and Isgur have calculated, however, that in the case of semileptonic B decay, only the simplest hadronic states are produced. They calculate that[3]

$$\frac{\Gamma(B \to D, D^* l\nu)}{\Gamma(B \to Xl\nu)} = .90 \tag{2.1}$$

Therefore D^+ is a tag for B^0 in semileptonic B decay. The average charged particle multiplicity at the B vertex in semileptonic B decays $(1.3 \pm .4)$ is consistent with this conclusion.[4]

The production rate for events of the type $B^0 \to D^+ l^- \nu$ or $B^0 \to D^{*+} l^- \nu$, where $D^+ \to K^-\pi^+\pi^+$, $D^{*+} \to D^+(\pi^0\ or\ \gamma)$, and $l = e\ or\ \mu$, should be about 140 per 10^5 Z^0 decays. We will see in the next section that these events can be cleanly selected with the aid of the vertex detector. However, since the total detection efficiency (including event selection, lepton identification, and vertex detector cuts) is only about 10%, 10^6 Z^0 decays will be needed for a reasonable measurement of the B^0 lifetime using this method.

Exclusive reconstruction of B decays requires a very large data sample. The measured modes with the largest branching ratio products are $B^- \to \pi^+\pi^- D^+$ $(D^+ \to K^-\pi^+\pi^+)$ and $B^0 \to D^0\pi^+\pi^-(D^0 \to K^-\pi^+\pi^-\pi^+)$ with product branching ratios of $\approx 10^{-3}$. Given the reconstruction inefficiency, about 10^6 Z^0 decays would be needed to reconstruct a useful sample of these decays.

A simple example of the use of exclusive B decays is to measure the KM matrix element V_{bu}. Reconstruction of $B^0 \to \pi^+\pi^-$ or $B^- \to \rho^0\pi^-$ would immediately determine $|V_{bu}|$. B. Stech and collaborators have calculated the branching ratio for $B^0 \to \pi^+\pi^-$ to be[5]

$$BR(B^0 \to \pi^+\pi^-) \approx 2.1 \cdot 10^{-3} |V_{bu}/V_{bc}|^2.$$

CLEO has determined a 90% C.L. upper limit on the branching ratio for this mode of $2 \cdot 10^{-4}$ which gives $|V_{bu}| < .02$, a limit that is only slightly worse than that derived from fitting the lepton momentum distribution.[1] Unfortunately, this also limits the production rate for this decay mode to be less than 2 events for 10^5 Z^0 decays.

A more accessible decay is $B \to \rho l\nu$. Stech has calculated that[5]

$$\frac{\Gamma(B \to \rho l\nu)}{\Gamma(B \to D, D^* l\nu)} = 1 \cdot |V_{bu}/V_{bc}|^2.$$

Using the GWI result (Eq. 2.1) we find

$$BR(B \to \rho l\nu) = .11 \cdot |V_{bu}/V_{bc}|^2$$

which is about 50 times larger than $BR(B \to \pi^+\pi^-)$. The current limit on $|V_{bu}/V_{bc}|$ puts an upper limit on the rate of $B^- \to \rho^0 l^- \nu \to \pi^+\pi^- l\nu$ of about 100 produced events per 10^5 Z^0 decays. If the actual rate was near this upper limit, it would be promising, although separating this signal from $b \to c$ backgrounds would require tight kinematic cuts to remove backgrounds from unseen K_L^o, and excellent particle identification capability would also help.

3. Impact Parameter Resolution: Requirements and Implications

The ability of a vertex detector to provide useful information about a decay vertex falls into one of 3 rather loosely defined categories depending on the relative magnitude of the average impact parameter $\bar{\delta}$ to the impact parameter error σ_δ. If $\bar{\delta} \lesssim \sigma_\delta$, then essentially no topology information is available, although statistical analysis of impact parameter distributions can be done to measure particle lifetimes. At the other extreme where the average track impact parameter is very much larger than the impact parameter error, say $\bar{\delta} \gtrsim 30 \cdot \sigma_\delta$, then the event vertex topology can be reconstructed and nearly all tracks can be assigned to a unique vertex. In between these two extremes exists a large region where the resolution is sufficient to detect the presence of secondary decay vertices with good efficiency, but insufficient to precisely determine the number of decay vertices and unambiguously assign tracks to them.

These three regions are illustrated for the case of b quark decays in Figure 2 which plots the impact parameter distribution to the primary vertex for tracks from the b decay vertex. Since the δ distribution is a convolution of an exponential decay distribution and a P_T distribution, it is very broad and the distribution in $\log(\delta)$ is convenient to plot. For the Mark II vertex chamber at PEP, the average track impact parameter error is about 200 μm and only abut 10% of b decay tracks are inconsistent with originating in the primary vertex; secondary decay vertices in only a small fraction of b decays are detectable. For the SLC upgrade vertex chamber, the average b decay track impact parameter error will be about 40 μm.[6] About 50% of b and cascade c decay tracks will have $\delta/\sigma_\delta > 3$, and the *presence* of secondary decay vertices can be detected with reasonable efficiency. But only when the impact parameter resolution gets to the micron level will high efficiency vertex reconstruction and track assignment be possible.

The required impact parameter resolution for full vertex topology reconstruction is illustrated in Figure 3. This figure plots the fraction of $Z \to q\bar{q}$ decays for which the minimum impact parameter of all charged tracks to all other non-parent vertices is larger than the value given by the abscissa. For example, the impact

parameter of all tracks to all other non-parent vertices is larger than 10 μm in about 15 % of $Z \to b\bar{b}$ decays. Thus, if one had apriori knowledge of the number and location of all secondary decay vertices, all tracks could be uniquely assigned to these vertices at the 3 sigma level in 15% of $Z \to b\bar{b}$ decays for a vertex detector with 3 μm resolution. The fact that the vertices are not known makes the reconstruction process even more difficult. Multiple Coulomb scattering will always limit the obtainable resolution for low momentum tracks and will make their assignment to unique vertices much less probable.

The vertex topology reconstruction efficiency for $Z \to c\bar{c}$ decays is also shown in Fig. 3 and is only slightly better than the $Z \to b\bar{b}$ case. However, the reconstruction efficiency for light quark Z^0 decays is excellent. Vertex detectors which measure impact parameters in both projections (e.g CCDs) do a substantially better job of vertex reconstruction as is also shown in Fig. 3. For $Z \to b\bar{b}$ decays, going from 2 to 3 dimensions is about equivalent to a factor of 3 improvement in the 2 dimensional impact parameter resolution. Determining the vertex topology for low multiplicity decays in 3 dimensions is much easier since in 2 dimensions, two tracks always form a vertex.

Since full vertex topology reconstruction for $Z \to b\bar{b}$ and $Z \to c\bar{c}$ decays is so difficult, consider the other extreme. The simplest use of vertex detector information is to require only a small number of tracks be inconsistent with the primary vertex. Fig. 4 shows the fraction of b decays for which $\geq N$ tracks (N =1,2 or 3) have an impact parameter to the primary vertex larger than the value given on the abscissa. Note that the impact parameter scale is about 30 times larger than for Fig. 3. About 70% of all b decays have at least one track whose impact parameter to the IP is greater than 200 μm. It is clear that *good efficiency for vertex topology cuts will be obtained if significant impact parameters ($\delta/\sigma_\delta > 3$) are required for only a few tracks.*

Since the impact parameter resolution is by itself insufficient to determine the decay vertex topology, other information can help sort things out. For example, psuedorapidity can help distinguish tracks from the primary vertex. For exclusive decays, the invariant mass or other kinematic variables of the decay products can be used to determine if tracks which are consistent with both the primary and secondary decay vertices should be included in the secondary vertex. Testing if the vertex topology is consistent with a desired topology can be done with much higher efficiency than determining a unique topology for the event. And of course the choice of analysis is important since some are much less demanding on the vertex detector resolution than others. The examples discussed in the next section have good efficiency for cuts based on vertex detector data. And since the average track momentum is large for these decays, the addition of the silicon strip detector should improve the performance significantly.

4. Some Analysis Examples

4.1 $B^0 \to \pi^+\pi^-$

The large B mass, long lifetime, simple secondary vertex topology and high particle momentum make the decay $B^0 \to \pi^+\pi^-$ the simplest possible heavy quark exclusive decay to study with the vertex detector. Although the production rate is dismal, the analysis is clean and simple and provides a good benchmark for comparison with other modes (e.g. $D^0 \to K^-\pi^+$).

Event selection cuts are applied to reject events which go out the ends of the detector (number charged tracks ≥ 7, thrust $> .8$, $|cos(\theta_{thrust})| < .8$). Using the thrust axis, the event is divided into hemispheres and all pairs of oppositely charged tracks in each hemisphere are tested for consistency with the $B^0 \to \pi^+\pi^-$ hypothesis. To reduce background from low $x_{\pi^+\pi^-}$ ($\equiv P_{\pi^+\pi^-}/E_{beam}$) or asymmetric combinations, the candidate must satisfy $x_{\pi^+\pi^-} > .45$ and $|cos(\theta^*)| < .80$ where θ^* is the decay angle in the center of mass relative to the B^0 candidate direction. The mass spectrum of surviving candidates is shown in Fig. 5a from a monte carlo sample of 10^4 hadronic Z^0 decays.

Vertex topology cuts are now applied. In the desired topology, the B^0 decay vertex should be significantly separated from the primary vertex, and the B^0 and

all other tracks in the hemisphere should be consistent with originating in the IP. Consistency with this topology is achieved by demanding

$$\delta_{\pi^+}/\sigma_{\delta_{\pi^+}} + \delta_{\pi^-}/\sigma_{\delta_{\pi^-}} > 6 \ ,$$

$$\delta_{B^0}/\sigma_{\delta_{B^0}} < 2 \ ,$$

and the signed impact parameter significance to the IP, $s_i \cdot \delta_i/\sigma_{\delta_i}$ ($s_i = \pm 1$), of all other tracks in the hemisphere is less than 2. The candidate B^0 direction is used to determine the sign of the impact parameter. The vertex decay length significance $\ell_B/\sigma_{\|}$ is related to the sum of track impact parameter significance:

$$\ell_B/\sigma_{\|} = .71 \cdot \sum_{i=1}^{2} \delta_i/\sigma_{\delta_i}.$$

Thus the cut on $\sum_{i=1}^{2} \delta_i/\sigma_{\delta_i}$ is equivalent to a cut on decay length significance of $\ell_B/\sigma_{\|} \gtrsim 4$. These vertex topology cuts are about 60% efficient for $B^0 \to \pi^+\pi^-$ decays but reduce the background over the full $\pi^+\pi^-$ mass interval by about a factor of 50.

Figure 5b shows the background mass distribution after vertex topology cuts have been applied. The mass resolution function is also shown ($\sigma = 150\ MeV/c^2$). Two dominant background sources to the desired vertex topology exist. The low mass events ($m_{\pi^+\pi^-} < 2\ GeV/c^2$) are due to $Z \to c\bar{c}$ decays, while in the high mass events, at least one candidate track originates in a primary b decay vertex. The latter background is greatly reduced by the requirement that the B^0 and all other tracks are consistent with originating in the IP. No background events are present in the signal region ($4.80 < m_{\pi\pi} < 5.70\ GeV/c^2$) but extrapolating this result to a 10^6 Z^0 sample is uncertain. Assuming the vertex cuts reduce the background in the signal region by two orders of magnitude, we might expect about 1 background event for such a sample.

The net acceptance is 31%. It is the product of the hadronic event selection efficiency (.77), tracking efficiency including track quality cuts (.82), $x_{\pi^+\pi^-}$ and $cos(\theta^*)$ cuts (.85), and the vertex topology cut efficiency. For a braching ratio of $2 \cdot 10^{-4}$, we would reconstruct about 7 $B^0 \to \pi^+\pi^-$ decays/ 10^6 Z^0 events. Note that the current CLEO limit is background limited.

4.2 $D^0 \to K^-\pi^+$

The decay $D^0 \to K^-\pi^+$ will be produced at the SLC about 1000 times more often than $B^0 \to \pi^+\pi^-$ assuming the branching ratio for the latter mode is near its current measured upper limit. Relative to $B^0 \to \pi^+\pi^-$, the detection efficiency for $D^0 \to K^-\pi^+$ will be lower and the backgrounds will be much higher. Several factors contribute to making detection of this mode (without exploiting the $D^* - D$ mass difference) a difficult task. The average track impact parameter is much smaller for $D^0 \to K^-\pi^+$ than from $B^0 \to \pi^+\pi^-$ ($\approx$ 85 vs $\approx$ 280 μm) mainly due to the lifetime difference. From Fig. 5 it is clear that combinatorial backgrounds are much larger in the D^0 mass region. Furthermore, since our particle identification capability is insufficient to distinguish pions and kaons in the momentum region of interest, the combinatorial background will be doubled. Finally, the vertex topology for jets containing D mesons from a b cascade decay is more complex than the topology in $Z \to c\bar{c}$ events, and this requires more restrictive and therefore less efficient cuts to limit the greatly increased backgrounds.

The task of selecting $D^0 \to K^-\pi^+$ in $Z \to c\bar{c}$ events is equivalent to the $B^0 \to \pi^+\pi^-$ analysis discussed above with one modification: each candidate combination enters the mass plot twice (once each assuming $K^-\pi^+$ and $K^+\pi^-$). The detector mass resolution assuming correct particle ID varies from 20 to 45 MeV/c^2 depending on the D^0 momentum, while the mass difference between the correct and reversed particle assignment depends on P_π/P_K and has a sigma of 250 MeV/c^2. We define the signal region to be $m_D \pm 100 MeV/c^2$. For the cuts described above, the net acceptance is 8%, and the signal-to-background ratio is about 1.

For $D^0 \to K^-\pi^+$ selection in $Z \to b\bar{b}$ events, the requirement that the D^0 and all other tracks in the jet be consistent with originating in the IP can no longer be applied. The background is greatly increased since many more tracks have significant impact parameters, and background combinations where one or both of the tracks originate in the b decay vertex often have an invariant mass as large as the D mass. One way to reduce this background is to require that the D^0 candidates be consistent with being the most downstream decay vertex. This is done by forming the vertex of the D^0 and each other track in the hemisphere with pseudorapidity > 1.5, and requiring the D^0 decay distance from each of these vertices to be larger than 1.2 mm. With these cuts the net acceptance is about 5%, and the signal-to-background ratio is about 1/2. Although the vertex detector information greatly improves the sample purity, exploiting the $D^* - D$ mass difference results in a higher purity sample.

4.3 $D^+ \to K^-\pi^+\pi^+$

The longer D^+ lifetime ($\tau(D^+)/\tau(D^0) = 2.40 \pm .16$)[1] and the fact that the particle charge determines its identification make the mode $D^+ \to K^-\pi^+\pi^+$ much easier to reconstruct than $D^0 \to K^-\pi^+$. The analysis proceedure is similiar to that for $D^0 \to K^-\pi^+$ given above and is described in detail in Reference 7. The resulting efficiency for $D^+ \to K^-\pi^+\pi^+$ selection in $Z \to c\bar{c}$ ($Z \to b\bar{b}$) decays is 15% (9%) for a signal-to-background ratio of about 4 (2). The vertex detector cuts are about 40% efficient and improve the signal-to-background ratio by about 200.

4.4 MEASUREMENT OF THE B^0 LIFETIME USING $B^0 \to D^+ + l^- + neutrals$

The fact that D^+ is a tag for B^0 in semileptonic B decay provides a method for measurement of the B^0 lifetime using the decay $B^0 \to D^+ + l^- + neutrals$. Requiring a detected lepton simplifies the vertex topology analysis and improves the D^+ purity since we can assume no other charged tracks originate in the B^0 decay vertex (an assumption which can be tested).

The analysis begins by selecting hadronic events and dividing them into hemispheres as described in the section on $B^0 \to \pi^+\pi^-$ above. Then each hemisphere is tested for a semileptonic B^0 decay candidate. The hemisphere is required to contain 1 identified lepton with momentum above 3 GeV/c. Candidate $D^+ \rightarrow K^-\pi^+\pi^+$ decays are selected with cuts on x_D, $cos(\theta_K^*)$, and cuts on the impact parameter significance and vertex fit probability of the D^+ decay tracks as described in [7]. The D charge must be opposite to the lepton charge, and all other tracks in the hemisphere (excluding the lepton) must be consistent with originating in the primary vertex ($s_i \cdot \delta_i/\sigma_{\delta_i} < 2$) where s_i is determined using the D^+ direction.

Either the lepton or the D^+ impact parameter (or both) can be used to measure the B^0 lifetime. The sign of the impact parameter is determined by using the lepton and D to reconstruct the B^0 decay vertex, and then signing the impact parameter with the sign of the measured B^0 decay length. Figure 6 shows the lepton impact parameter distribution for a monte carlo sample of 279 decays.

The efficiency of the vertex topology cuts including track quality cuts is 41%. The total acceptance is about 12% assuming 100% electron identification efficiency for electrons which enter the LA solid angle. Thus we could expect about 100 detected events of the type $B^0 \rightarrow D^+ + e^- + neutrals$ ($D^+ \rightarrow K^-\pi^+\pi^+$) and about the same number of (upgraded) muon events in a 10^6 Z^0 decay sample.

Three potential sources of background exist: background D^+ plus lepton, D^+ plus misidentified lepton, and background D^+ plus misidentified lepton. The first source is negligible. Backgrounds from the other two sources were estimated using a 10^4 Z^0 sample by setting the misidentification probability to be 100% for non-lepton tracks with momentum above 3 GeV/c. The latter two sources are about of equal importance and together contribute about $14 \cdot P$ background events per 10^6 Z^0 decays where P is the lepton misidentification probability in percent. Thus the sample should be fairly pure.

5. Conclusions

Physics topics as diverse as the forward backward charge asymmetry to CP violation can be studied with the aid of heavy quark exclusive decays at the Z^0. The Mark II with its vertex detector is sufficiently powerful to do a good job on many of these topics with reasonable acceptances and sample purities. Measurements of $|V_{bu}|$ using $B^0 \rightarrow \pi^+\pi^-$ and of the B^0 lifetime using the decay $B^0 \rightarrow D^+ + l^- + neutrals$ ($D^+ \rightarrow K^-\pi^+\pi^+$) have been illustrated in this paper. Unfortunately, given the small branching ratios for most exclusive decay modes, large numbers of Z^0 decays are needed.

From the standpoint of vertex detector performance, the Mark II vertex detector can fully reconstruct the vertex topology of nearly all strange particle decays, but in general can only tag the presence of secondary b and c quark decay vertices with good efficiency. High efficiency full vertex reconstruction of heavy quark decays requires an order of magnitude improvement in impact parameter resolution. Analyses which use vertex detector information to make vertex topology cuts for b and c quark decay will have good efficiency if significant impact parameters ($\delta/\sigma_\delta > 3$) are required for only a few tracks.

REFERENCES

1. M.G.D. Gilchriese, in *Proceedings of 1986 International Conference on High-Energy Physics*, ed. S. Loken (Berkeley, 1986).
2. J. Adler *et al.*, SLAC-PUB-4291, to be published.
3. B. Grinstein, M.B. Wise, and N. Isgur, *Phys.Rev.Lett.* **56** (1986) 298.
4. R. Giles *et al.*, *Phys.Rev.* **D30** (1984)
5. M. Bauer, B. Stech, and M. Wirbel, Z. Phys **C34** (1987) 103; B. Stech, HD-THEP-86-7, XXI Moriond meeting, *Perspectives in Electroweak Interactions and Unified Theories* (1986).
6. The impact parameter error distribution has a long tail from tracks which have low momenta or which are poorly measured. The average only includes the 95% of all tracks whose error is less than 150 μm.
7. Ken Hayes, Mark II/SLC-Physics Working Group Note 9-13, in *Proceedings of the Second Mark II Workshop on SLC Physics*, SLAC-Report-306 (1986).

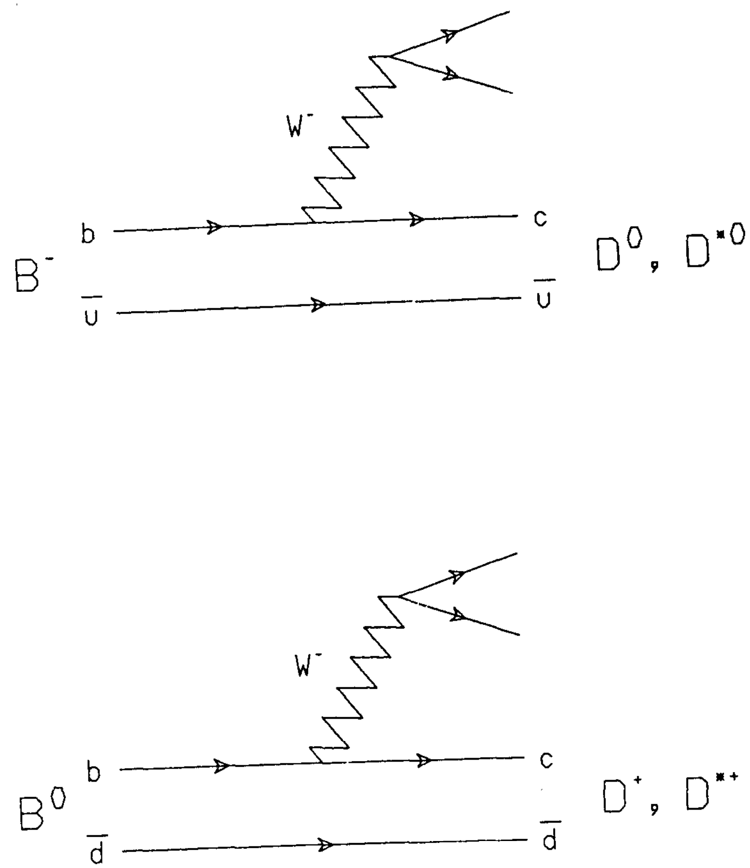

Figure 1. Spectator diagrams from B^0 and B^- decay.

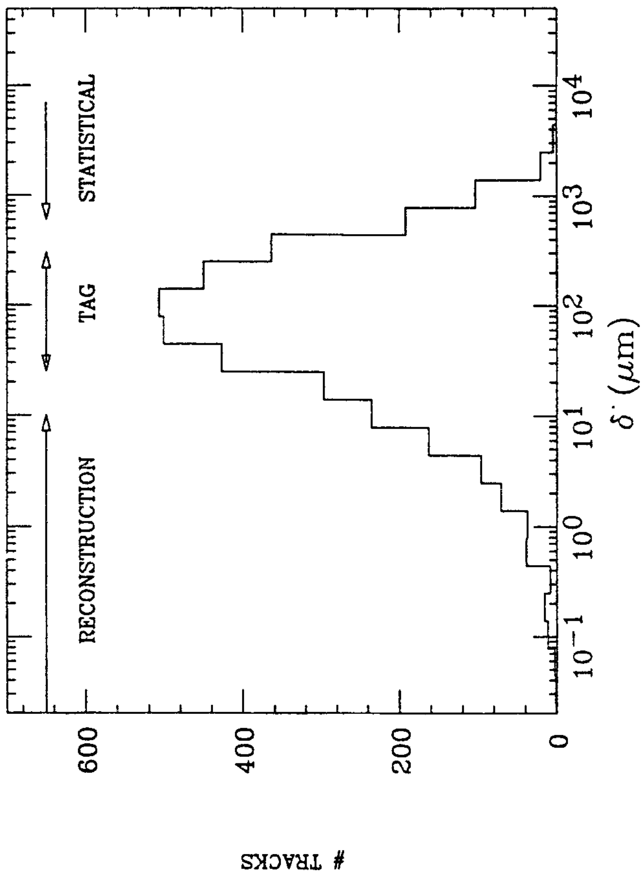

Figure 2. Impact parameter (δ) distribution to the primary vertex for tracks from the b decay vertex. The vertex reconstruction, vertex tagging, and statistical analysis regions (in $3 \cdot \sigma_\delta$) are indicated.

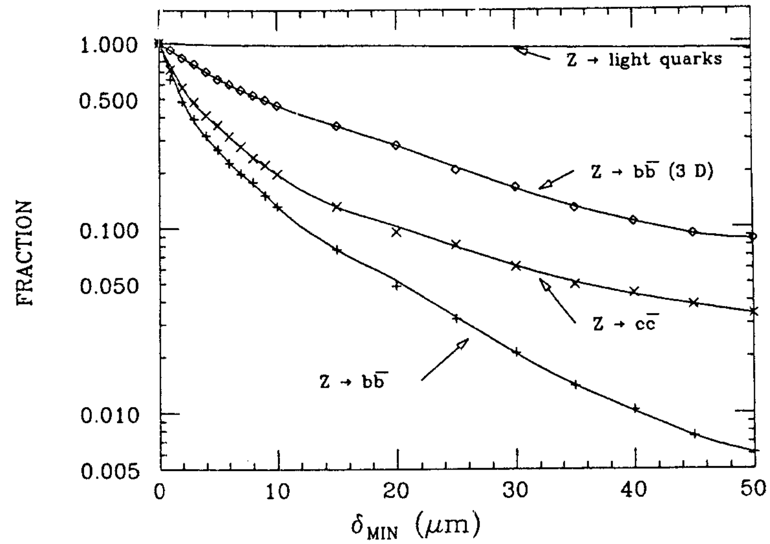

Figure 3. Fraction of $Z \to q\bar{q}$ decays for which the minimum projected impact parameter of all charged tracks to all other [illegible]n-parent vertices is larger than δ_{min}.

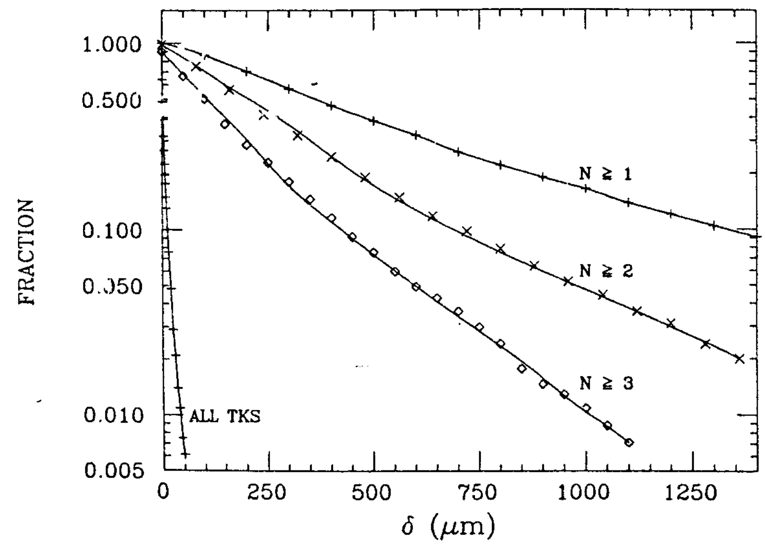

Figure 4. Fraction of b decays for which $\geq N$ charged tracks ($N = 1,2$ or 3) have an impact parameter to the primary vertex larger than δ. For comparison, the curve from Figure 3 for $Z \to b\bar{b}$ is also shown.

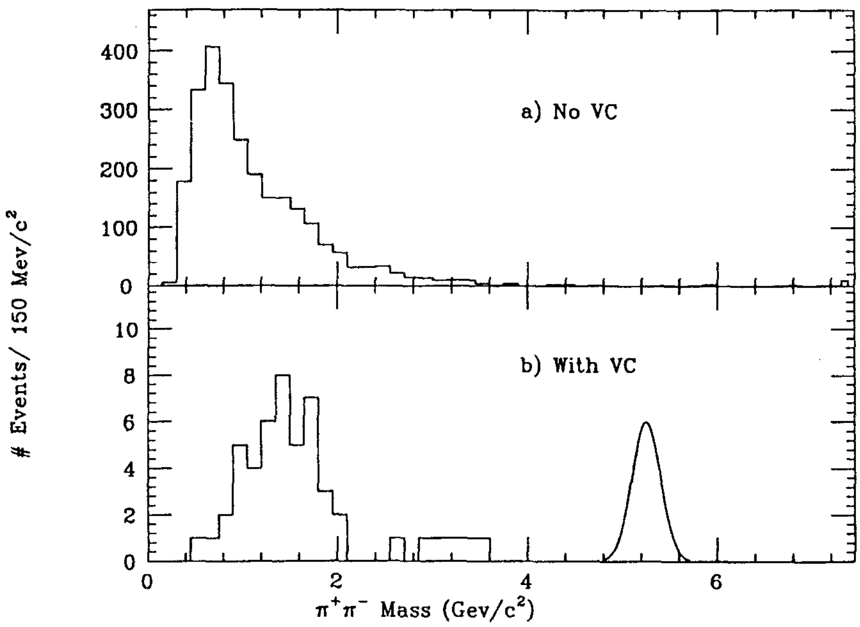

Figure 5. $\pi^+\pi^-$ mass distribution of background combinations in a 10^4 hadronic Z^0 decay sample a) without vertex detector cuts; b) with vertex detector cuts. The mass resolution function is also shown (with arbitrary normalization).

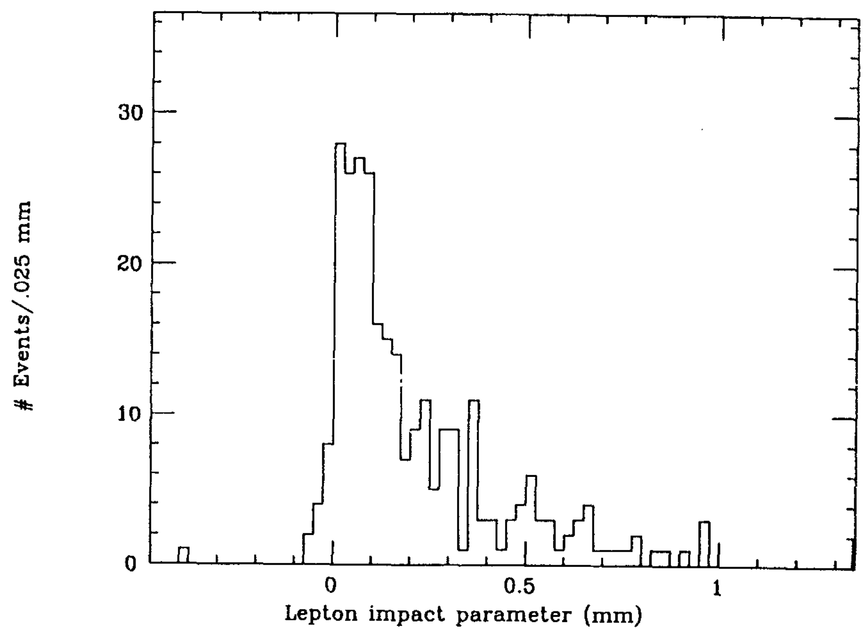

Figure 6. Signed lepton impact parameter for reconstructed $B^0 \to D^+ + l^- +$ *neutrals* decays.

Mark II/SLC-Physics Working Group Note # 10–2

AUTHOR: Dean Karlen
DATE: April 15, 1987
TITLE: Single γ background to neutrino counting from radiative Bhabha scattering

1. Introduction

Neutrino counting experiments attempt to measure the single γ cross section from the process,

$$e^+e^- \rightarrow \nu\bar{\nu}\gamma$$

to determine the number of light neutrino species. The major background to this process is from radiative Bhabha scattering,

$$e^+e^- \rightarrow e^+e^-\gamma$$

where both electrons escape detection at low angles. This background can be eliminated if the observed single photon is required to have sufficient transverse momentum so as to force an electron into the detector acceptance. Such a requirement significantly reduces the signal, especially when the center of mass energy is near M_{Z^0}. If the background from radiative Bhabha scattering is small and well understood, it would be possible to relax this requirement. In this talk, I will discuss calculations of this background to order α^3 and α^4, and compare results from a Monte Carlo event generator with data from the Mark II and ASP experiments.

2. Lowest order

To order α^3, radiative Bhabha scattering is described by the eight diagrams of fig. 1. For the configuration where only the photon is scattered at a large angle, the t channel diagrams are greatly enhanced by the pole for 0° scattering, whereas the s channel diagrams are suppressed due to the small solid angle involved. The correction from the weak sector can safely be ignored, even for $E_{\mathrm{cm}} \approx M_{Z^0}$.

a)

b)

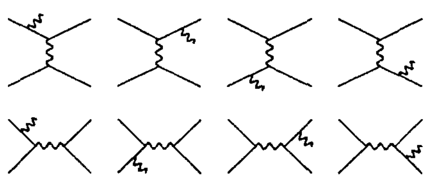

Figure 1. Order α^3 diagrams for radiative Bhabha scattering: a) t channel; b) s channel.

Although the diagrams of fig. 1 have been incorporated into the Berends and Kleiss Monte Carlo(1), the program is inadequate for the region of phase space considered here. The program requires electrons to scatter above a minimum angle and is inefficient for acollinear photon radiation. Also, the matrix element does not include some mass dependent terms that become important for small angle scattering. So it was necessary to produce a new Monte Carlo program(2) specifically designed for small angle radiative Bhabha scattering. The program, called TEEGG*, allows 0° scattering, is efficient for acollinear photon radiation, and includes the dominant mass terms.

3. Radiative correction to radiative Bhabha scattering

In order to describe radiative Bhabha scattering more accurately, it is necessary to include the contribution from order α^4 diagrams, such as those shown in fig. 2. An exact treatment would be extremely difficult, as there are more than 150 diagrams in this order. The dominant diagrams, however, can be calculated by using the Equivalent Photon Approximation(3) (EPA).

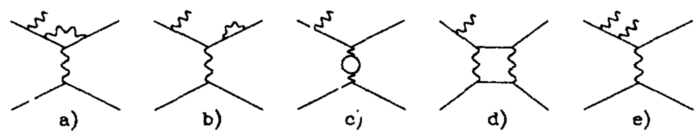

Figure 2. Some representative diagrams of the next order correction to radiative Bhabha scattering: a) Vertex correction; b) Electron self energy correction; c) Vacuum polarization; d) Box diagrams; e) Double radiative Bhabha scattering.

3.1 Equivalent Photon Approximation

The EPA provides a method of calculating a process that involves the exchange of an almost real photon, such as radiative Bhabha scattering when an electron scatters at a low angle. To illustrate the use of the EPA, I will show how it is applied to the order α^3 process. The results will then be compared with an exact calculation in order to judge the accuracy of the approximation.

The dominant event topology, for the single photon background, has one electron balancing the $p_\perp$ of the photon and the other electron near 0°. When the e^+ is

* TEEGG is named for t-channel dominated $ee\gamma(\gamma)$ final states

near $0°$, the two dominant diagrams are those shown in fig. 3. The EPA separates the process,

$$e^+(p_+)\; e^-(p_-) \rightarrow e^+(q_+)\; e^-(q_-)\; \gamma(k) \quad ,$$

into two components. The radiation of the almost real photon from the lower leg,

$$e^+(p_+) \rightarrow e^+(q_+)\; \gamma(\tilde{k}) \quad ,$$

is given by the equivalent photon spectrum, $d^3n_{e^+\to e^+\gamma}$. The scattering of this almost real photon by the incoming electron,

$$\gamma(\tilde{k})\; e^-(p_-) \rightarrow e^-(q_-)\; \gamma(k) \quad ,$$

is given by the ordinary Compton cross section, $d^2\sigma_{\gamma e^-\to\gamma e^-}$. Then the radiative Bhabha cross section is given by,

$$d^5\sigma_{e^+e^-\to e^+e^-\gamma} = d^3n_{e^+\to e^+\gamma}\, d^2\sigma_{\gamma e^-\to\gamma e^-} + d^3n_{e^-\to e^-\gamma}\, d^2\sigma_{\gamma e^+\to\gamma e^+} \quad .$$

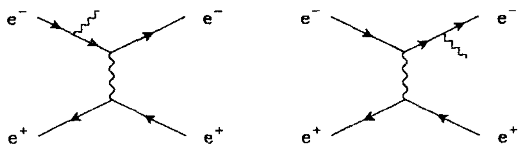

Figure 3. The two diagrams that dominate when the e^+ scatters at a small angle.

Treating the exchanged photon as real is a valid approximation if,

$$\tilde{k}^2 \ll (p_- + \tilde{k})^2 \quad .$$

That is, the 'invariant mass' of the exchanged photon must be much less than center of mass energy of the photon electron collision. In table 1, single photon cross sections calculated using the EPA are compared with that found using the matrix elements from the two diagrams of fig. 3 and from all eight diagrams of fig. 1. When one electron is allowed to scatter at $0°$ ($E_{\gamma\,\mathrm{min}} = 0.5$ and 1.0 GeV), the cross sections agree to about 3%. When the criteria force both electrons to scatter above $0°$ ($E_{\gamma\,\mathrm{min}} = 1.5$ GeV), the agreement is worse. The EPA method

Table 1. Single photon cross section calculations (in pb) to order α^3. $E_b = 47$ GeV, $\theta_{\gamma\,\mathrm{min}} = 30°$, $\theta_{e\,\mathrm{veto}} = 15$ mrad. EPA refers to the calculation based on the equivalent photon approximation; t channel is from the two diagrams of fig. 3; exact is from all eight diagrams of fig. 1. The same region of phase space was sampled for each of the matrix elements.

$E_{\gamma\,\mathrm{min}}$	0.5 GeV	1.0 GeV	1.5 GeV
EPA	33.29 ± 0.09	4.85 ± 0.02	0.120 ± 0.002
t channel	33.32 ± 0.09	4.87 ± 0.02	0.123 ± 0.002
exact	34.24 ± 0.09	5.06 ± 0.02	0.145 ± 0.003

agrees very well with the t channel matrix element. Hence, treating the exchanged photon as real is a very good approximation. The deviation of the EPA from the exact calculation is due to the s channel diagrams and the interference between the t and t' channels which are not included in the EPA calculation.

3.2 Order α^4 calculation

In the previous section the EPA was used with Compton scattering, to derive an approximate form for order α^3 radiative Bhabha scattering. By using the EPA with the known radiative corrections to Compton scattering, the dominant radiative correction to radiative Bhabha scattering, given by the diagrams shown in fig. 4, can be found. The diagrams not included are expected have little effect when at least one electron scatters at a small angle[(2)]. The contribution from the virtual and soft real photon emission diagrams is combined, as usual, to give a correction to the lowest order,

$$d^5\sigma^{\mathrm{vs}}_{e^+e^-\to e^+e^-\gamma} = d^5\sigma_{e^+e^-\to e^+e^-\gamma}\,(1+\delta)$$

where $d^5\sigma_{e^+e^-\to e^+e^-\gamma}$ is the exact order α^3 cross section for radiative Bhabha scattering, and δ is the correction for Compton scattering. The contribution from hard real photon emission is treated using the EPA once again,

$$d^8\sigma_{e^+e^-\to e^+e^-\gamma\gamma} = d^3n_{e^+\to e^+\gamma}\, d^5\sigma_{\gamma e^-\to e^-\gamma\gamma} \quad .$$

Reference 2 describes in more detail this calculation, and how it is included in the TEEGG Monte Carlo event generator.

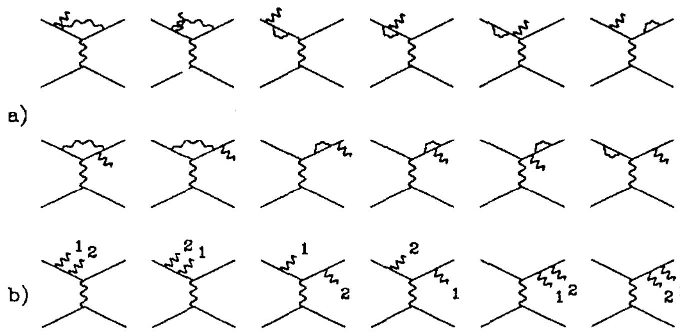

Figure 4. Diagrams included in the approximation of the radiative correction to radiative Bhabha scattering: a) Virtual correction diagrams; b) Double radiative Bhabha diagrams.

4. Comparison of TEEGG with data from PEP

4.1 MARK II DATA

Data accumulated by the Mark II detector at PEP cannot be used to measure the single photon cross sections, because the experiment did not trigger on that topology. A similar configuration, where both an electron and a photon scatter at large angles ($|\cos\theta| < .675$) with the other electron at a small angle, is used instead to compare with TEEGG. In order to constrain an electron to be at a small angle, the observed electron and photon are required to be coplanar with the beam axis within 80 mrad. Backgrounds from two particle final states, with a conversion or hard bremsstrahlung, are removed by requiring the observed particles to be acollinear by at least 20 mrad. The total energy observed in the data at large angles is shown in fig. 5a, along with the predictions from the Monte Carlo. There is a large contribution from order α^4 at low visible energies which are kinematically inaccessible by a three body final state. Another distribution sensitive to the order α^4, is the χ^2 fit to a three body hypothesis. By using the measured angles of the observed particles and assuming a three body final state, the energy of the particles can be determined. The χ^2 of the measured energies can then be calculated and the distribution is shown in fig. 5b. This distribution is however quite sensitive to the detector simulation. From this analysis, it is seen that order α^4 has a significant contribution to the large angle $e\gamma$ configuration and that the EPA method does well in approximating the correction.

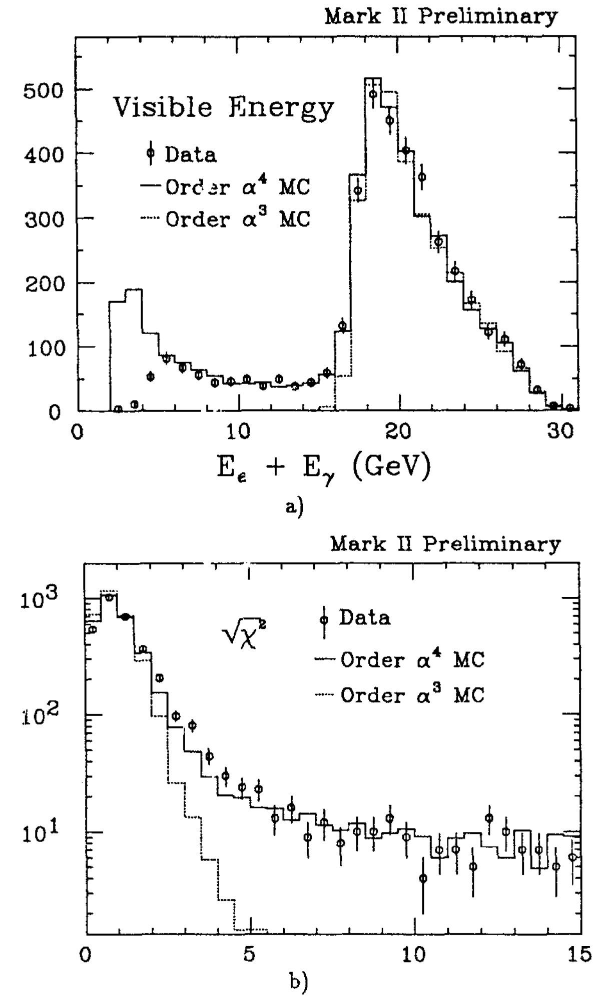

Figure 5. Comparison of $e\gamma$ data from the Mark II detector at PEP with the TEEGG Monte Carlo (after detector simulation and normalization to data): a) Visible energy of the $e\gamma$ pair. The discrepancy below 5 GeV is due to the first pass filter, CHUKIT, not included in the detector simulation; b) $\sqrt{\chi^2}$ for the constrained fit to a three body hypothesis.

4.2 ASP DATA

The ASP detector[4,5] was specially designed to detect anomalous single photon events at PEP and thus is very well suited to measure the radiative Bhabha single photon cross section. A very preliminary analysis of single particle configurations was carried out to check a surprising prediction* from the order α^4 calculation.

The important elements used in the analysis of single particle configurations are the central tracker (five layers of proportional tubes, used to distinguish charged from neutral tracks), the central calorimeter (five layers of lead glass bars), and the forward drift chambers and calorimeters.

For this analysis, a single central track (neutral or charged) with $p_\perp > 1$ GeV/c is required to be inside the lead glass acceptance ($30° < \theta < 150°$) and no other tracks are allowed to be above 150 mrad. In order to balance the central track $p_\perp$, at least one other particle must scatter above 35 mrad. Tracks between 21 and 150 mrad with $E > 4$ GeV are recorded as forward tracks. A data sample of 10 pb^{-1} is used in this analysis and the measured cross sections along with the order α^3 and α^4 Monte Carlo predictions are shown in table 2. Three topologies are considered; a charged or neutral central track with a single observed forward track, a neutral central track with a single observed forward track, and a charged or neutral central track with two observed forward tracks. In each case the data and Monte Carlo agree well. No attempt is made to include backgrounds from such sources as $e^+e^- \to \gamma\gamma\gamma$ and $e^+e^- \to e^+e^-e^+e^-$. Due to the preliminary nature of this analysis, systematic errors are not included.

Table 2. Comparison of single particle cross section measurements by ASP (preliminary) and predictions of the Monte Carlo. A central track has $p_\perp > 1$ GeV/c and is in the lead glass acceptance. A forward track has $E > 4$ GeV and is between 21 and 150 mrad from a beam axis.

	ASP	α^3	α^4
e or γ central, 1 forward	2.09 nb	2.10 nb	2.07 nb
γ central, 1 forward	0.19 nb	0.17 nb	0.17 nb
e or γ central, 2 forward	0.39 nb	0.40 nb	0.40 nb

* The Monte Carlo program had predicted a very large contribution to the single γ cross section from fourth order. This has since been found to be due to an error in the event generation procedure. I thank M. Martinez and R. Miquel for assistance in finding this problem.

Figures 6-8 show measured distributions of the single central–single forward track sample compared with the order α^3 and α^4 Monte Carlo predictions. In each case, the Monte Carlo results include the detector acceptance and simple energy smearing and are normalized to the measured integrated luminosity from low angle Bhabha scattering. Figure 6 shows the central track energy distribution as measured by the lead glass. The polar angle of the central track projected into the plane perpendicular to the lead glass array is shown in fig. 7 and in fig. 8 for the neutral central track only. This angle is measured with respect to the $+z$ or $-z$ axis according to the direction of the forward track. Figure 8 shows that the single photon is typically on the same side in z as the most scattered electron. The difference between fig. 7 and 8 can be understood by different topologies available to the single particle configurations, as shown in fig. 9.

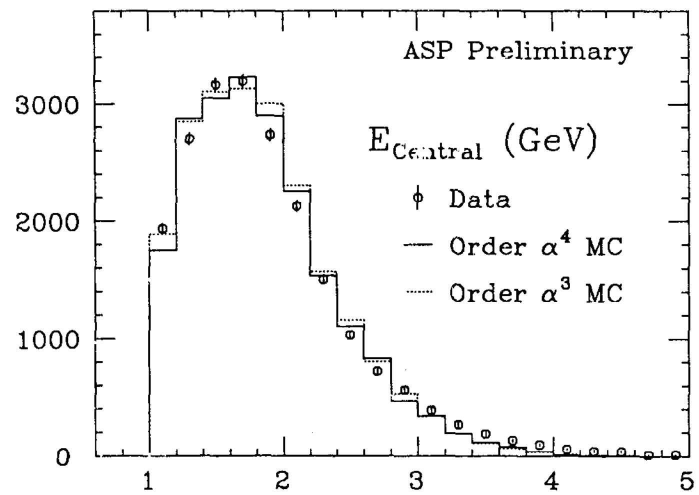

Figure 6. Neutral or charged central track energy distribution.

This preliminary analysis shows very good agreement with the Monte Carlo distributions. Unlike in the case of wide angle $e\gamma$ pairs studied with the Mark II data, the effect of order α^4 is very small for the single γ and the single e configurations.

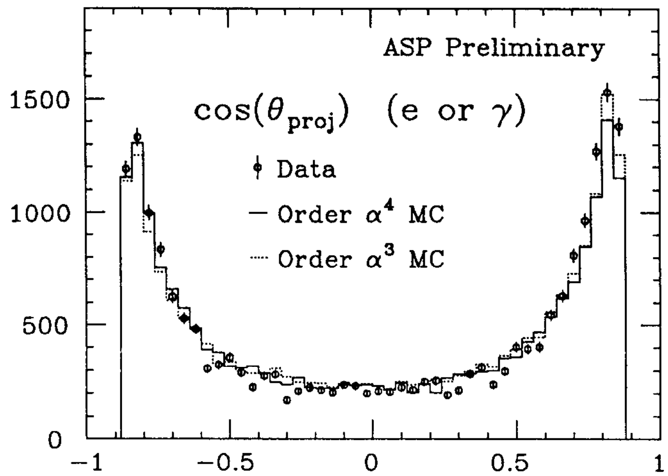

Figure 7. Cosine of the projected angle of the central neutral or charged track.

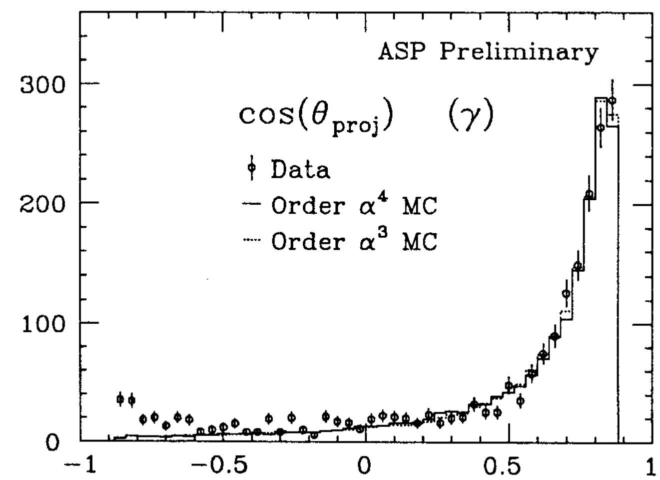

Figure 8. Cosine of the projected angle of the central neutral track.

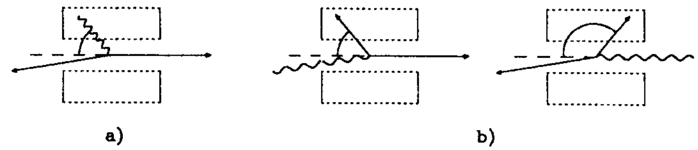

Figure 9. Dominant topologies for the single particle configurations: a) Single photon configuration; b) Single electron configuration.

5. Implications for neutrino counting at SLC

The Monte Carlo program, TEEGG, has been found to agree well with data from PEP. At SLC energies the program should work equally well, since there is little contribution from the weak sector. The order α^4 correction to the single photon configuration at $E_b = 47$ GeV is small, as indicated in table 3. Hence, the background from radiative Bhabha scattering seems sufficiently understood so as not to limit the sensitivity of the neutrino counting measurement at SLC.

Table 3. Comparison of single photon cross section calculations (in pb) to order α^3 and order α^4 for the experiment described in table 1.

$E_{\gamma\,min}$	0.5 GeV	1.0 GeV	1.5 GeV
Order α^3	34.24 ± 0.09	5.06 ± 0.02	0.145 ± 0.003
Order α^4	34.33 ± 0.10	4.77 ± 0.03	0.132 ± 0.003

I would like to thank the ASP collaboration and especially Tom Steele, for doing the analysis (with help from Gabor Bartha, Dave Burke, Chris Hawkins, and Natalie Roe) and for allowing me to present their preliminary results.

REFERENCES

1. F. A. Berends and R. Kleiss, Nucl. Phys. **B228** (1983) 537

2. D. Karlen, SLAC preprint SLAC-PUB-4121R (1987)

3. G. Bonneau and F. Martin, Nuovo Cim. **21A** (1974) 611;
   V. Gorgé, M. Locher and H. Rollnik, Nuovo Cim. **27** (1963) 928

4. The members of the ASP collaboration are:
   G. Bartha, D. L. Burke, P. Extermann, P. Garbincius, C. A. Hawkins, C. Hearty, R. J. Hollebeek, A. S. Johnson, M. J. Jonker, L. Keller, C. Matteuzzi, N. A. Roe, J. E. Rothberg, T. R. Steele, J. S. Whitaker, R. J. Wilson, and K. K. Young

5. The ASP detector is described in:
   G. Bartha, *et al.*, Phys. Rev. Lett. **56** (1986) 685

Mark II/SLC - Physics Working Group Note #10-3

Title: Report from the neutrino counting group.

Authors: G. Bonvicini, B. Barnett, D. Briggs, D. Burke, R. Cence, D. Fernandez, E. Gero, G. Gidal, P. Grosse Wiesmann, J. Haggerty, F. Harris, J. Hylen, B. Millikan and R. Thun.
Presented by G. Bonvicini

Date: June 14th, 1987.

The status of the work on measuring the number of neutrinos is reviewed. We discuss the importance of detecting and isolating single-photon events as a unique way of measuring the decay width of the Z to an undetectable final state. We describe in detail the necessary hardware and software requirements, and the efforts made by the MKII Collaboration to provide a hermetic detector with high trigger efficiency for single photons. The status of the theoretical work on radiative corrections is also discussed. Conclusions are presented with regard to luminosity and energy requirements for a definitive single-photon experiment.

1. Introduction

It is expected that the upcoming e^+e^- experiments in the energy region of the Z mass will allow detailed measurements of the particle content of nature below $M_Z/2$. Visible decays will be identified through a careful analysis of event topologies. The presence of invisible decays will be inferred from measurements of the total width of the Z, the width into invisible particles obtained from direct subtraction of the visible decay width, and of the $\mu\mu$ cross section at the peak. The most direct evidence for such invisible decays will be obtained from the detection of initial-state radiation in reactions with subsequent annihilation

into stable, neutral and weakly interacting particles [1,2]. These measurements should be able to establish a new constant of nature, the number of fermion families. Understanding the origin of this number poses a profound challenge to particle physicists. A definitive determination of the number of fermion species also represents an important input to cosmology.

In this paper we will review the state of the art for the neutrino counting experiment. Section 2 outlines the methods for establishing invisible decays mentioned above. Section 3 describes hardware and software requirements, and contains a summary of the MKII status as regards these requirements. Section 4 describes the expected backgrounds. Section 5 discusses the interpretation of the single-photon measurements with emphasis on radiative corrections. Conclusions and recommendations are given in Section 6.

2. On the methods to establish the number of families.

In this section we describe and compare the methods for counting the number of neutrino species. These are measurements of the total Z width, the measurement of the invisible width through direct subtraction of the measured visible widths, the $\mu\mu$ cross section at the Z peak, and the detection of radiative events of the type $\gamma\bar{\nu}\nu$.

Before discussing these measurements it is important to realize the interplay of the fundamental quantities α_{QED}, G_F, M_Z and $\sin^2\theta_W$ in calculating the expected effects. In the Standard Model, $\sin^2\theta_W$ can be derived from the three other quantities at the tree level; however, this relation could be modified by one-loop weak corrections[3]. It should be remembered in the following that use of $\sin^2\theta_W$ derived from the other quantities gives the result a dependence on the Standard Model, while the use of a measured value, as obtained, for example, from asymmetry measurements, automatically includes weak corrections and gives a model independent result.

We first discuss the direct measurement of the Z width. The width depends on phase space, weak coupling constants in the theory, radiative QED and QCD final-state corrections, and on particle content. Initial-state radiation has primarily the effect of reducing the available energy of the annihilation and can be accounted for, either via simulation or using analytic formulae[4]. The following formula holds at $\sqrt{s} = M_Z$ [1,2],

$$\Gamma_{tot} = \frac{M_Z^3 G_F}{24\sqrt{2}\pi} \sum \beta_i \cdot (N_c)_i \cdot (1 + (1 - 4q_i \sin^2 \theta_W)^2) \cdot (C_f)_i \tag{1}$$

where the sum is over all known pointlike fermions. The kinematic factor $\beta_i = \sqrt{1 - 4m_i^2/s}$ is close to one for the known fermions (.994 for the b quark, $> .999$ for the others), $(N_c)_i$ is the number of colors (three for quarks, one for leptons), and q_i is the electric charge of the fermion. The final-state correction $(C_f)_i$ depends on the phase space enlargement due to final-state radiation [5-6],

$$C_f = \left(1 + \frac{3\alpha_{QED}}{4\pi} q_i^2 + O(\alpha_{QED}^2)\right)\left(1 + (\frac{N_c - 1}{2})(\frac{\alpha_s}{\pi} + (\frac{\alpha_s}{\pi})^2 (1.98 - .115 N_f) + O(\alpha_s^3))\right) \tag{2}$$

N_f is the number of light flavors, and α_s corrections are in the modified minimal subtraction renormalization scheme [7].

The phase space change across the resonance makes the width change as

$$\Gamma(\sqrt{s}) = \frac{\sqrt{s}}{M_z}\Gamma(M_z). \tag{3}$$

An additional neutrino increases the expected width by about 6%. The width measurement is rather insensitive to systematic errors in luminosity and detection efficiency since these are expected to vary slowly across the resonance. However, the width determination improves only slowly with statistics. A few times 10^4 events are needed to reach the limit of the overall systematic error of 2%, which corresponds to about 0.3 neutrino generations. One important systematic error at the 1% level comes from uncertainties in α_s in Eq.(2).

The $\mu\mu$ cross section at the peak is related to the total width by

$$\sigma_{\mu\mu} = \frac{12\pi}{M_Z^2} \frac{\Gamma_{ee}\Gamma_{\mu\mu}}{\Gamma_{tot}^2} \tag{4}$$

where the e and μ widths are equal in the Standard Model and given in Eq. (1). The total width is therefore the only unknown in Eq.(4). The low $Z \to \mu\mu$ branching ratio requires about $3 \times 10^4 Z$ to bring the statistical errors below the systematic ones. This method can also achieve a precision on Γ_{tot} of around 2%.

In order to eliminate some of the assumptions contained in Eqs. (1) and (3) (for example, α_s uncertainties) it would be desirable to use the measured total width and to subtract from it the experimentally measured widths of all final states except neutrinos. The partial width is then

$$\Gamma_{\nu\nu} = \Gamma_{tot} - \Gamma_{visible}. \tag{5}$$

If Γ_{tot} is measured directly from the scan, the method has the disadvantage of subtracting two large numbers to get a small one. The two large numbers must be obtained with high precision. The errors propagate like

$$(\frac{\delta\Gamma_{\nu\nu}}{\Gamma_{\nu\nu}})^2 \approx 25 \cdot [(\frac{\delta\Gamma_{tot}}{\Gamma_{tot}})^2 + (\frac{\delta\Gamma_{visible}}{\Gamma_{visible}})^2]. \tag{6}$$

In this case, systematics are a limit to the measurement and both Γ_{tot} and $\Gamma_{visible}$ must be determined with a precision $\lesssim 2\%$. A recent analysis [8] shows that if both Γ_{tot} and $\Gamma_{visible}$ are measured at the peak the statistical error converges faster than in the previously described methods. A precision of about 0.3 neutrino families could be achievable with a data sample of 10^4 detected Z events.

A direct measurement of invisible decays can be made by counting events in which only a single photon, recoiling against undetectable particles, is observed [2]. The cross section for this kind of events is small after the kinematic cuts required to reduce the background [9] but the separation between 3 and 4 families is about 24% of the total cross section. Detailed measurements of the dependence of the cross section on energy (Fig.1), and the shape of the photon spectrum (Fig.2), can allow unambiguous interpretation of the results. The running strategy must take into account background rejection by vetoing particles at small angles. The choice of beam energy represents a compromise between event rates and the cleanliness of the photon signal. Ref. [9] concluded that the optimal strategy for an expected integrated luminosity of $\approx 3\text{pb}^{-1}$ and minimum vetoing angle $\theta_{min} = 15$mrad was dedicated running at about 4 GeV above the resonance. The limits on the phase space allowed for the photon were optimized as follows: $E_\gamma > 1$ GeV, $(p_T)_\gamma > .75$ GeV, and $\theta_\gamma > 20^o$.

Measurements at PEP and PETRA have yielded two good single-photon candidates[10] and give confidence in the feasibility of the experiment. We estimate that an optimized single-photon experiment with 5pb^{-1} can give a precision of ≈ 0.2 neutrino families.

3. Hardware and software requirements.

The experimental signature of a photon not accompanied by any other particle calls for highly hermetic, efficient and noise-free calorimetry. Machine backgrounds and low-q^2 QED processes are able to fake a single photon, and dictate small-angle coverage to veto efficiently against events where the photon transverse momentum is balanced by visible particles.

The MKII main calorimetry system is composed of a liquid argon calorimeter(LAC) at large angles ($\theta > 45^o$) and a proportional tube end cap calorimeter(ECC) in the forward region ($20^o < \theta < 45^o$). A small angle monitor (SAM), built with proportional tubes, has tracking and calorimetry between 50 and $\approx$ 180 mrad. These calorimeters are shown in the MKII cross sectional view of Fig.3.

The LAC is characterized by an energy resolution of $14\%/\sqrt{E}$ and by a strip geometry that allows some measurement of the shape of electromagnetic

showers. It is subdivided azimuthally into eight modules with a dead region of $\approx 2.5^o$ between the modules. A magnet coil is located in front of the LAC and has a thickness of 1.7 radiation lengths (X_0). Other material adds up to a few percent of X_0.

The ECC is characterized by an energy resolution of $20\%/\sqrt{E}$ and by good shower pattern recognition due to the smaller transverse dimensions of the tubes (the tubes are ganged together in increasingly bigger groups with increasing depth inside the ECC). It is hermetic in ϕ but the region $40^o < \theta < 45^o$ has a lower efficiency and worse energy resolution due to shower leakage in the ECC and LAC supports. The material in front of it consists of about $1X_0$ from the main drift chamber end plates and cables. The installation of the vertex drift chamber will add another radiation length at angles below 35^o. This material will be quite far in front of the ECC and may have a significant impact on the detected shower shape.

The quest for hermeticity and low-angle coverage has induced within the MKII Collaboration the design and construction of five small detectors (commonly named Micronesia) with the common theme of providing cheap shower counters in the solid angle regions not covered by the main calorimeters. As shown in Fig.4 hermeticity is achieved in the 15-250 mrad region with four of the Micronesia components and with the SAM.

The MINISAM luminosity monitor, located between 15 and 24 mrad, provides vetoing at the lowest possible angle. It has energy resolution $35\%/\sqrt{E}$, sharply defined angular acceptance and a rate an order of magnitude higher than the SAM.

Another shower detector is an active mask (25-50 mrad), originally designed to stop synchrotron radiation from entering the main detector. Optical fibers are buried within this mask and they detect and transport away Cherenkov light produced by electromagnetic showers. The response of this active mask for a 50 GeV electron has been studied with the EGS MC program and depends on the angle as shown in Fig.5.

Finally, the small cracks between MINISAM and the active mask, between the SAM and the ECC, and between the LAC modules have been filled with tungsten or lead and scintillator counters. These counters can veto background events and also provide information about energy leakage of the major detectors. Table 1 summarizes the information about the various Micronesia detectors.

A new trigger has been set up to allow for efficient detection of single-photon events, called SUPERTED. This trigger exploits the low repetition rate of the SLC, by digitizing the trigger signals from the LAC and ECC and using an SSP (Single Scan Processor) to process the digitized quantities. The SSP algorithms are able to localize showers in the calorimeter stacks instead of just summing over entire calorimeter modules as did the old TED trigger. This dramatically reduces backgrounds such as nearly horizontal cosmics rays and coherent noise inside a module. This trigger is expected to be fully efficient for photons with energies above $E_\gamma = 1$ GeV. Potential background trigger rates from cosmic rays and from electronic noise have been determined to be small. Other contributions as from RF noise and from other machine-related backgrounds will have to be measured when the MKII moves onto the beam line. The hardware has been installed, calibration and readout are being implemented, and a cosmic-ray test is planned for this spring. The energy threshold is expected to be as low as $\approx$250 MeV.

The software for analyzing single-photon events is not as advanced as the hardware, although the photon reconstruction algorithms, optimized long ago for low-energy photons at SPEAR can be used and need only to be reviewed for their suitability for high efficiency reconstruction of single photons. A well-defined and tuned program for event selection, carefully designed not to lose good events, will not be available until some experience is gained with the experimental environment and trigger rates of SLC. It is essential that any filtering of data at the PASS2 level be carefully examined to prevent loss of true single-photon

events.

Finally, we emphasize the role of an event generator in the understanding of such an experiment. As described in the next section, there are large changes in the cross section and significant deformations of the photon spectrum created by radiative corrections. Moreover, a second radiated photon may veto the event. Acceptance systematics involving conversion probabilities, reconstruction efficiencies, and energy resolution effects must be understood to minimize potential errors in the single-photon cross section measurements.

4. Backgrounds.

In this section we will not discuss machine backgrounds which will, in any case, be measured once the MKII is on the beam line, and focus instead on physics backgrounds. We just mention that given the repetition rate of SLC, neither cosmic rays nor beam-gas interactions are expected to contribute observable backgrounds. However, very little is yet known about stray beam particles and their ability to simulate a single-photon event.

In Ref. [2], QED backgrounds were first studied using the $ee\gamma$ and $\gamma\gamma\gamma$ MC programs of Refs. [11] and [12]. The 3-photon final state has no collinear singularity and in Ref. [12] the final state particles are generated over the full solid angle. It will be shown at the end of this section that the process has a small and predictable contribution to the single photon rate. The $ee\gamma$ MC program, on the contrary, had been designed to study fermion pairs, and avoids the collinear singularity by requiring both electrons outside a certain minimum scattering angle (Fig. 6a). Recent analytic[13] and MC program[14][15] calculations have shown that for kinematical configurations where one of the fermions has no p_T the rates are typically 10 times higher than those obtained using Ref. [11]. This can be explained as follows. The scattering happens between a quasi-real ($q^2 \approx 0$) photon coming from one of the beams and the opposite fermion(Fig. 6b), and results in a configuration with one fermion undeflected and the other balancing the p_T of the photon. An equivalent photon approximation (EPA) can be used [15] with results in very good agreement with more sophisticated methods. However, the MC program of Ref. [11] fails to properly extrapolate the total cross section, being sensitive only to those events in which both fermions share the p_T. This can be seen graphically in Fig. 7. Two different components are visible in the p_T spectrum of the photon, and including only the high p_T tail will cause a gross underestimation of the cross section.

This problem is now solved and well understood. The MC program of Ref. [15] has been designed to allow zero angle scattering, and reproduces PEP data quite well. The next order corrections ($ee\gamma\gamma$) are reliably estimated with the EPA method plus radiatively corrected Compton scattering[15], and have been shown to be small. We conclude that radiative Bhabha scattering as a source of background is understood and the necessary software for analysis is already available. The results of the analysis of Ref. [9] show that this background can be limited to $\lesssim$10% of the signal.

The abundant yield of $ee\gamma$ events with one undeflected electron requires that all these events be vetoed and that, at most, the small fraction of events with two fermions balancing the p_T be allowed into the data sample. This corresponds to the condition

$$(p_T)_\gamma > E_{beam}\theta_{min} \sim 750MeV, \tag{7}$$

already discussed in Ref. [9]. Such a requirement will also be useful for vetoing beam-gas events. This p_T limit corresponds roughly to the turn-on of full efficiency of the calorimetry chain (trigger and pattern recognition) and insures that the MKII apparatus configuration and software chain are well matched to one another and adequate for the single-photon measurement.

Low-q^2 events in which a soft, large-angle electron is balanced by a hard, low-angle photon (Fig. 6c) can be used as a QED control sample to measure inclusively the low-angle veto efficiency. In fact, the origin of single-electron

events is purely QED and the typical rate is one order of magnitude higher. Preliminary results are shown in Fig. 8. The angular distribution of the low angle electron(photon) is shown, with the following cuts: the electron on the opposite side escapes detection into the beam pipe, and the large-angle photon(electron) has $p_T > .75$ GeV, $E > 1$ GeV and $\theta > 20^o$. The ratio of the cross sections in the critical region $15 < \theta < 50$ mrad is 11.

Other physics contributions to the single-photon signal were studied through the many existing MKII MC program tapes at $\sqrt{s} \simeq M_Z$. A simulation of the small-angle systems has not been done; only the Drift Chamber, LAC and ECC were considered. The tapes were all generated with $E_{beam} = 47.1$ GeV. Table 2 shows the results obtained using somewhat arbitrary cuts. The $e^+e^- \to eeV^*V^*$ events (V^* is a vector hadronic state) come from a limited p_T phase space type two-photon Monte Carlo; the other processes are self-explanatory. The two-photon events were generated in specified ranges of W, the photon-photon center of mass energy, and the radiative events were generated in specified ranges of k, the photon momentum in beam energy units. The number of events left after each cut can be multiplied by the number in the "pb/event" column to get the background cross section. The analysis first looked for events with a photon having $E_\gamma > 1.0$ GeV in either the LAC or ECC. The event was rejected if the photon was less than 20° from the beam directions, or if there was a second photon in the event with $E_\gamma > 300$ MeV, or if there was a well defined Drift Chamber track with momentum > 300 MeV. A requirement that the transverse momentum of the photon be greater than 0.75 GeV/c, originally designed to reduce the radiative Bhabha background, also helps to reduce the background from two-photon events. The further requirement that the photon be more than 30° from the beam axis (perhaps forced on us anyway because of the position and significant thickness of the vertex chamber end plates) makes the two-photon background almost negligible. This is important, since systematic errors in the two-photon modeling would make a background subtraction unpleasant. The other processes listed will give small, but calculable, backgrounds. Monte Carlo simulation of the small-angle systems is necessary to see how much further these backgrounds can be reduced, especially those from radiative μ and τ pair production that are always accompanied by two or more charged tracks. Also, more events need to be generated for certain processes where current statistics are not very good.

5. Interpretation of the results and radiative corrections.

One of the interesting aspects of the neutrino counting experiment, and its unique feature, is that, should the invisible Z width be larger than expected, discrimination between different hypotheses will be feasible from a study of the photon spectrum and of the energy dependence of the cross section. A very large amount of literature exists for supersymmetric (SUSY) models and the interested reader should consult Refs.[16] and references therein. Depending on the model, different unobservable particles can be produced with different quantum numbers, energy threshold behavior, and coupling to the Z. For example, the approximate change of the width due to some possible new particles would be:

• Massive Dirac neutrinos	$1.5\% \cdot \beta(3+\beta^2)$;
• Massive Majorana neutrinos	$6.0\% \cdot \beta^3$;
• Scalar neutrinos	$3.0\% \cdot \beta^3$;
• Neutralinos	$0. - 10\%$;

where β is the same kinematic factor in Eq.(1), the velocity of the produced particles.

Minimal SUSY has been extensively searched for at PEP/PETRA[10]; two possible production diagrams are shown in Fig. 9. New particles other than standard neutrinos could increase the total width by amounts that correspond to a fraction of a neutrino number. If measurements show evidence for unexpected invisible particles beyond the standard three neutrinos, the correct interpretation will be an interesting challenge. For example, the diagram of Fig. 9a) has a non-resonant nature that is reflected in a very broad photon spectrum.

Independently of the particle content of nature, radiative corrections to the $\gamma\bar{\nu}\nu$ final state are an important, unavoidable subject. It is a well known fact that, whenever the cross section changes rapidly versus energy, QED higher order terms can be quite large, of the order of one neutrino generation close to the Z. Purely weak corrections have been discussed in Ref. [17], and Ref.[18] calculates the W-exchange diagrams of Fig.10 exactly; these corrections are at most a few percent, and will not be discussed here.

QED radiative corrections have been investigated recently by a number of authors. The diagrams corresponding to the Born term are shown in Fig.10 while the first-order corrections are shown in Fig.11. The W-exchange piece has been omitted in Fig.11 since the corresponding Born term is already very small. The QED radiative corrections have been calculated by Igarashi and Nakazawa [19] and Berends, Burgers and Van Der Neerven [20]. We show in Fig.12 the first order corrections to the energy spectrum of photons when running at 4 GeV above the resonance and $\theta_\gamma > 20^o$ but no p_T cut. They have the expected behavior of flattening the resonance reflection and shifting the spectrum to an average lower energy. The sign of the correction depends in a complicated way on the kinematic cuts on the photon. As pointed out in [19], the first order corrections are sufficiently accurate several widths above the Z, where the cross section is slowly varying. They are not sufficient in the rapidly varying region near the resonance where we are likely to run the experiment. However, inspection of Fig.12 gives a positive first-order correction of $\delta \approx 20\%$. The next order correction could be $.5\delta^2 \approx 2\%$ and would be fully sufficient to make the theoretical error negligible.

Another approach sums corrections to all orders, as described, for example, in Ref. [4]. We have used the suggestions contained in that paper to write a simple MC program based on the structure functions of Ref. [21]. Initial-state radiation, assumed purely collinear, is simulated on each initial leg to boost the

$\bar{\nu}\nu\gamma$ system in a moving frame with boost parameters

$$\beta = \frac{x_1 - x_2}{x_1 + x_2}, \qquad \gamma = \frac{x_1 + x_2}{2\sqrt{x_1 x_2}}, \tag{8}$$

where x_1, x_2 are the fractions of the beam energy lost by the e^+, e^- in soft initial-state radiation. The available energy is reduced accordingly, and this system is allowed to decay according to the Born term [1]. The results are shown in Fig.12. The all-orders correction reduces the size of the first-order one as qualitatively expected. The success of such an approach using structure functions depends on the fact that this process involves annihilation of essentially on-mass shell electrons; the leading logarithms are simulated correctly. Without pretention of being rigorous, we have used this MC program to extract the results described in the rest of this section. We first evaluate the corrections at $\sqrt{s}$ corresponding to an energy scan of the resonance, with the canonical cuts listed in Section 2, $E_\gamma > 1.$ GeV, $\theta_\gamma > 20^o$ and $(p_T)_\gamma > .75$ GeV. As shown in Fig.13, we find that the correction is large ($\approx$ 1 neutrino family) and negative everywhere in the energy range considered, because the redistribution of the center of mass energy from initial-state radiation is always towards a region of lower $(p_T)_\gamma$. The same MC program has been used to generate the energy spectra of Fig.14, with radiative corrections included and the cuts already mentioned.

To see what can be expected from measurements of single photon events during an energy scan, we have simulated what would happen with a 9-point, 200nb/point scan of the Z, that yields $\approx 3 - 4 \times 10^4 Z$. The results, shown in Fig. 15, gives a best fit of $N_\nu = 2.63 \pm .26$ excluding systematics. 99 events were generated in the scan, with 113 expected for three neutrino generations. With the data from the scan, the other above-mentioned ways of measuring the Z partial or total width are close to their systematic limits. The results of all measurements will provide important consistency checks on each other. It is worthwhile to comment on the sharp rise of the cross section just above M_Z. This can be a powerful handle during the analysis to understand the observed signal.

6. Conclusions and recommendations.

Among the various possibilities of measuring the number of fermion families at SLC, the detection of single photons stands out for being amenable to theoretical interpretation and for providing potentially the most precise measurement of the invisible decay width of the Z. Full success will require a dedicated run at an energy about 4 GeV above the peak of the Z with an integrated luminosity of $\int Ldt \gtrsim 3pb^{-1}$. A scan in the region between M_Z and $M_Z + \Gamma$ is anyway recommended, because the sharp increase of the cross section constitutes an experimentally important cross check of such a delicate experiment. At lower energies or luminosities, the single-photon measurement will still provide a powerful tool for understanding the particle content of nature when combined with measurements of the Z width.

MKII has achieved remarkable hermeticity and low-angle coverage with the implementation of several small detectors. The reconstruction program and triggering system appear well matched to the detector capabilities. However, much work has still to be done in software to be fully equipped for a careful analysis.

The physics backgrounds are understood and under control. The necessary software to analyze them already exists and has been used for this report as well as for a previous one[9]. In particular, the dominant radiative Bhabha background is well described by existing MC programs and forces a p_T cut on the detected photon. Radiative corrections to this process show no significant change in the total cross section.

The status of radiative corrections shows that first-order corrections are understood and sufficient for dedicated experiments away from the Z. More work is needed to either calculate second-order corrections or all-order corrections. Both ways should reach about 1% accuracy, sufficient for this experiment. It is already known that the corrections in our region of interest will be large and negative.

References

[1] E. Ma, J. Okada, PRL41:287,1978 and 41:1759,1978; K.J.F. Gaemers, R. Gastmans and F.M.Renard, PRD19:1605, 1979.

[2] G. Barbiellini, B. Richter and J. Siegrist, PL106B:414,1981.

[3] See for example B.W.Lynn, M.E.Peskin and R.G.Stuart, SLAC-PUB-3725.

[4] J. Alexander *et al.,* contribution to this conference, and references therein.

[5] F.A.Berends and R.P.Kleiss, NPB177:237,1981.

[6] M.Dine and J. Sapirstein, PRL 43:668,1979; W. Celmaster and R.J. Gonsalves, PRD21:3112,1980; K. G. Ketrychin *et al.*, PL 85B:277, 1979.

[7] W. A. Bardeen *et al.*, PRD 18:3998, 1978.

[8] G. Feldman, contribution to this conference.

[9] R.P.Thun, Granlibakken MKII Workshop, SLAC-REP-306.

[10] C. Hearty *et al.*, PRL 58:1711,1987; W.T.Ford *et al.*,, PRD33:3472,1986; H.J. Behrend *et al.*, PL 176B:247, 1986; W. Bartel *et al.*, PL 125B: 385, 1985.

[11] F.A. Berends and R.P. Kleiss, NPB 228:537,1983.

[12] F.A. Berends and R.P. Kleiss, NPB 186:22,1981.

[13] M. Caffo, R. Gatto and E. Remiddi, NPB 286: 293, 1987.

[14] C. Mana and M. Martinez, DESY 86-062.

[15] D. Karlen, SLAC-PUB-4121, submitted to Nuclear Physics B.

[16] K. Grassie and R.N.Pandita, PRD 30: 22, 1984; M.K. Gaillard *et al.*, PL 116B: 279, 1982; J.A. Grifols *et al.*, NPB 268: 151, 1986.

[17] M. Bohm and T. Sack, Print-87-0120 (Wurzburg).

[18] C. Romao, L. Bento and A. Barroso, IFM-2/87.

[19] M. Igarashi and N.Nakazawa, TKU-HEP-86/02.

[20] F.A. Berends, G.J.H. Burgers and W.L.Van Neerven, PL 177B:191,1986.

[21] O. Nicrosini and L. Trentadue, UPRF-86-132.

Figure captions.

[1] Single-photon Born cross section vs $\sqrt{s}$.

[2] Single-photon Born energy spectra for various $\sqrt{s}$.

[3] Cross section of the MKII experiment.

[4] Geometry of the MKII small-angle detectors. Only the active volumes are shown.

[5] Response of the active mask and surrounding detectors versus electron θ.

[6] a) event with the photon p_T balanced by 2e; b) same as a), 1e only; c) same as b), but the photon is forward and the e at large angle.

[7] p_T-spectrum of the photon, for $ee\gamma$ final state, and both e below θ =15 mrad.

[8] θ distribution for the low-angle electron(photon) balancing the p_T of the large angle photon(electron). The other electron in the event escapes detection below 15 mrad.

[9] a) SUSY photino production; b) SUSY Higgsino production.

[10] Lowest-order Feynman diagrams for $\bar{\nu}\nu\gamma$ final state.

[11] First-order Feynman diagrams for $\bar{\nu}\nu\gamma$ final state.

[12] Dashed line: Born term. Solid line:QED first-order correction to the photon energy spectrum. Points: all-order correction. x_γ is the photon energy in beam energy units.

[13] Energy dependence of the cross section, when a p_T cut is applied; radiative corrections are summed to all orders as in Fig. 12.

[14] All-order photon corrected spectra for 3 different energies. A p_T cut is applied.

[15] A simulated single-photon yield from a Z energy scan. Three generations were assumed in the simulation.

Table 1

All about Micronesia

Detector	People	θ coverage	ϕ coverage	Type	Readout
MiniSAM	B.Barnett B.Harral J.Hylen J.Matthews D.Stoker	15 - 25 mrad	2π	Tungsten Scintill.	Wavelength Shifter + PMT
Mask Plug	G.Gidal	24 - 27 mrad	2π	Tungsten Scintill.	Opt. fib. + PMT
Active Mask	D. Burke D. Fernandez	25 - 50 mrad	2π	Tungsten Opt. fib.	Opt. fib. + PMT
Ring counter	D. Fujino P. Voruganti	154-275mrad	2π	Tungsten Scintill.	Opt. fib. + PMT
Hole tagger	J. Dorfan J. Nash R. Van Kooten	$45^o - 135^o$	8×5^o	Lead Scintill.	PMT

Table 2

Number of events from Monte Carlos of various processes giving background to $\bar{\nu}\nu\gamma$.

PROCESS $e^+e^- \rightarrow$	W_{min} (GeV)	W_{max} (GeV)	events generated	events $E_\gamma > 1GeV$	& $\theta_\gamma > 20°$ & 0 tracks	& $P_\gamma^t >$ 0.75 GeV/c	& $\theta_\gamma > 30°$	pb/event
$eeee$	0.6	94.2	658	70	6	1	0	30.85
	3.	94.2	575	224	12	8	0	1.03
	10.	94.2	442	158	8	8	1	0.05
$ee\mu\mu$	0.	2.5	2418	6	3	0	0	21.17
	2.5	11.	1191	4	1	0	0	0.81
	11.	94.2	796	18	0	0	0	0.04
$ee\tau\tau$	0.	14.	1869	452	10	5	1	0.08
	14.	94.2	761	377	7	3	1	0.02
$eeu\bar{u}$	0.	5.	1726	52	3	0	0	2.32
	5.	15.	947	301	1	1	0	0.12
	15.	94.2	593	385	0	0	0	0.01
$eed\bar{d}$	0.	94.2	1590	71	5	2	1	0.16
$ees\bar{s}$	0.	6.	1701	77	9	2	1	0.06
	6.	94.2	470	171	1	0	0	0.01
$eec\bar{c}$	0.	13.	1116	191	4	2	1	0.12
	13.	94.2	310	191	0	0	0	0.03
eeV^*V^*	0.5	1.	3972	14	6	0	0	1.69
	1.	10.	2706	98	9	0	0	3.01
	10.	40.	1453	213	2	0	0	0.83
	40.	94.2	1195	265	0	0	0	0.10
	$(X_k)_{min}$	$(X_k)_{max}$						
$\mu\mu\gamma$	0.	0.011	2847	2	0	0	0	0.21
	0.011	0.1	2749	654	32	27	17	0.13
	0.1	1.	2532	1532	46	45	17	0.06
$\tau\tau\gamma$	0.	0.011	1984	1063	2	2	0	0.37
	0.011	0.1	2042	1282	23	23	20	0.14
	0.1	1.	1974	1782	31	30	20	0.04
$\gamma\gamma\gamma$			4454	652	147	141	96	0.09

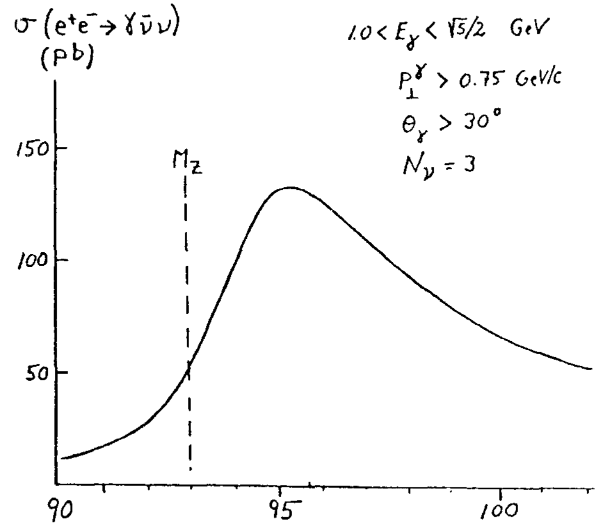

Fig. 1

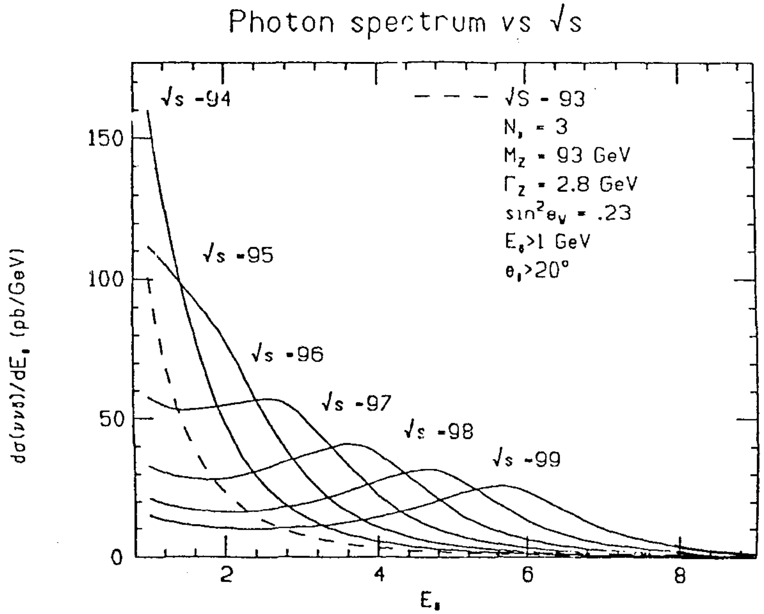

Fig. 2

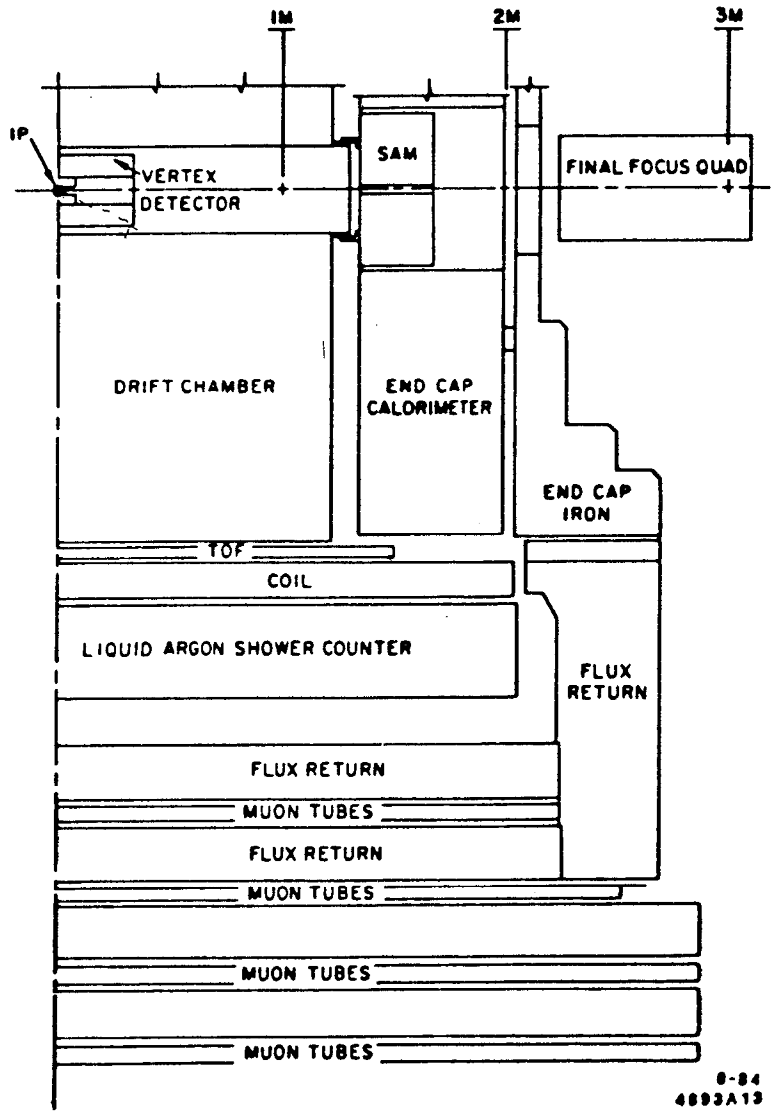

1M
2M
3M
IP
VERTEX
DETECTOR
SAM
FINAL FOCUS QUAD
DRIFT CHAMBER
END CAP
CALORIMETER
END CAP
IRON
TOF
COIL
LIQUID ARGON SHOWER COUNTER
FLUX
RETURN
FLUX RETURN
MUON TUBES
FLUX RETURN
MUON TUBES
MUON TUBES
MUON TUBES
8-84
4893A13

Fig. 3

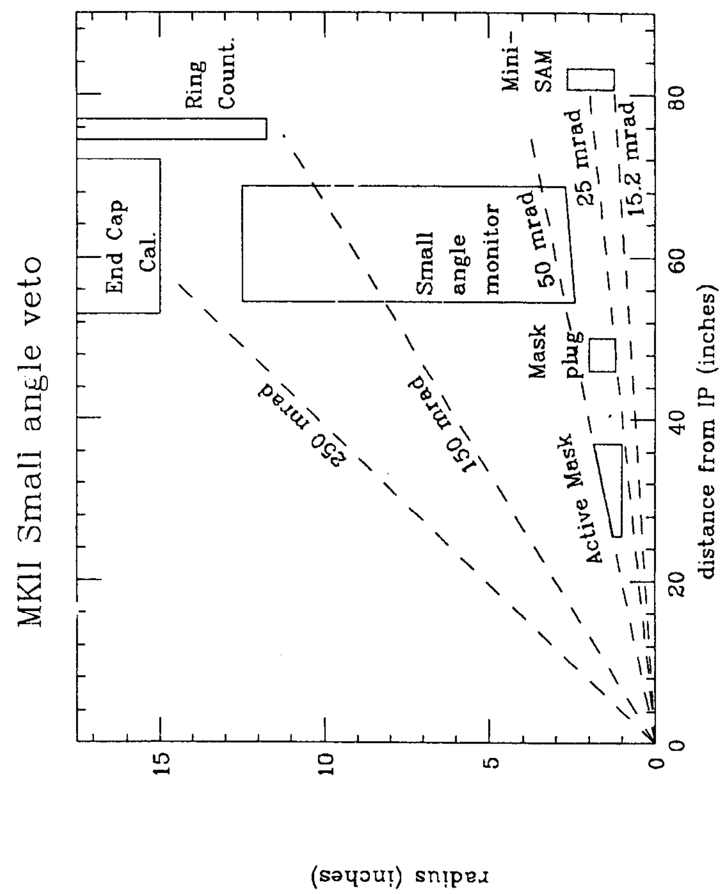

MKII Small angle veto
Ring
Count.
Mini-
SAM
End Cap
Cal.
Small
angle
monitor
Mask
plug
Active Mask
250 mrad
150 mrad
50 mrad
25 mrad
15.2 mrad
radius (inches)
distance from IP (inches)

Fig. 4

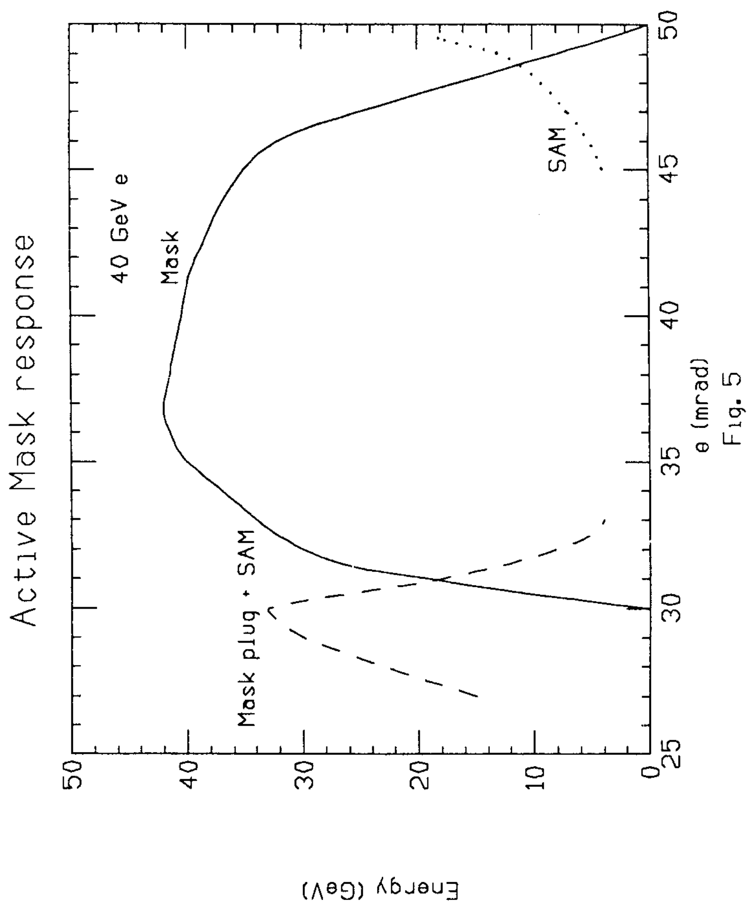

Fig. 5

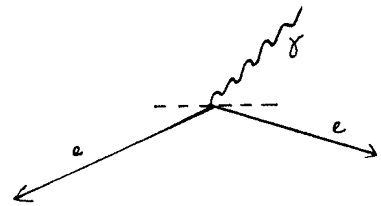

Fig. 6a)

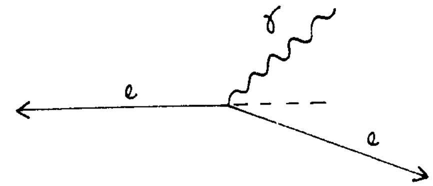

Fig. 6b)

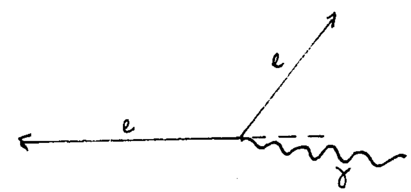

Fig. 6c)

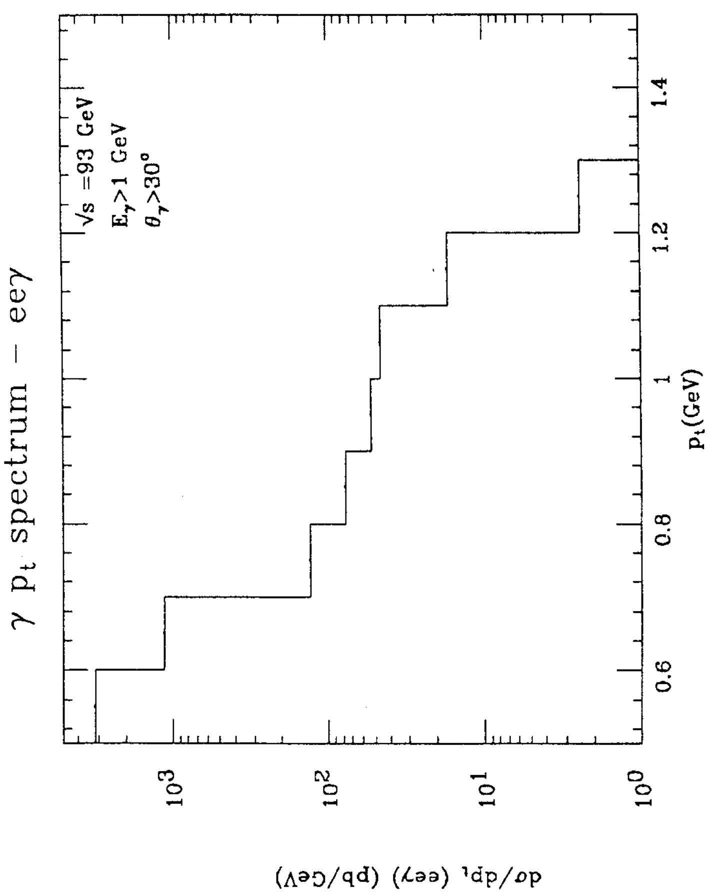

γ p_t spectrum - eeγ
√s =93 GeV
E_γ>1 GeV
θ_γ>30°
0.6
0.8
1
1.2
1.4
p_t(GeV)
10^3
10^2
10^1
10^0
dσ/dp_t (eeγ) (pb/GeV)

Fig. 7

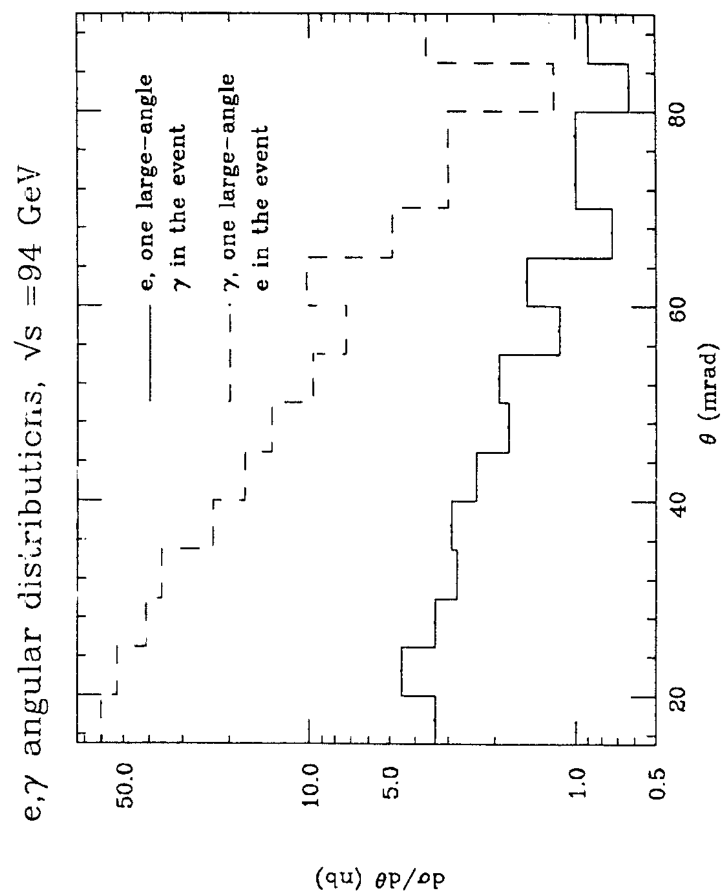

e,γ angular distributions, √s =94 GeV
e, one large-angle
γ in the event
γ, one large-angle
e in the event
20
40
60
80
θ (mrad)
50.0
10.0
5.0
1.0
0.5
dσ/dθ (nb)

Fig. 8

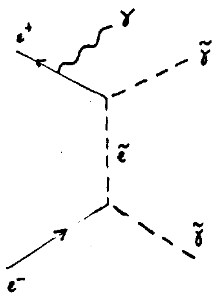

Fig. 9a)

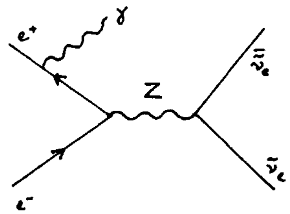

Fig. 9b)

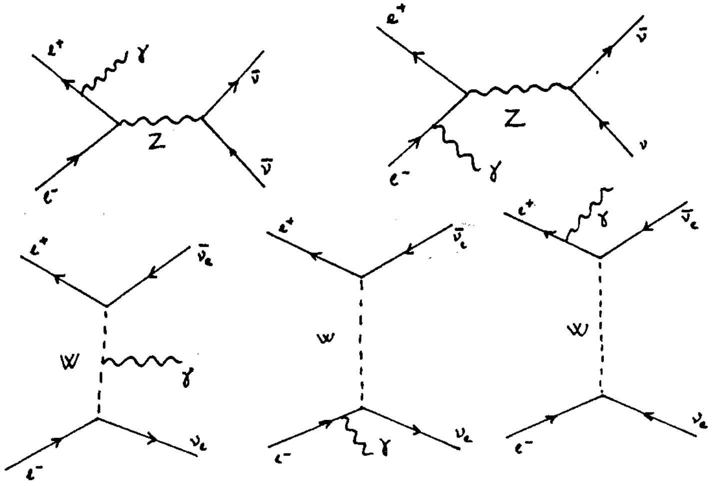

Fig. 10

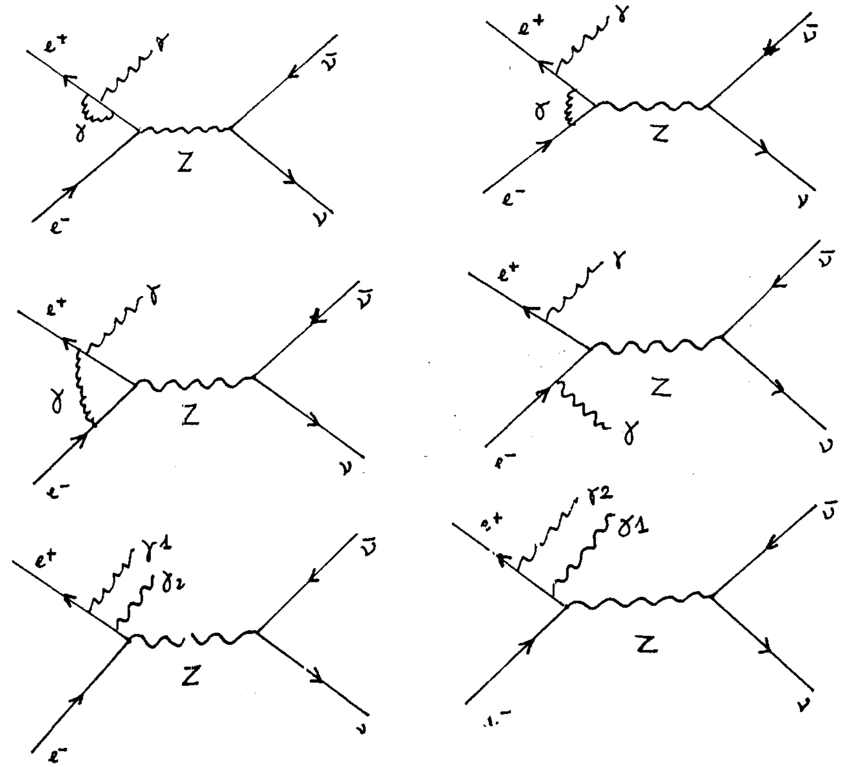

+ CROSSED

Fig. 11

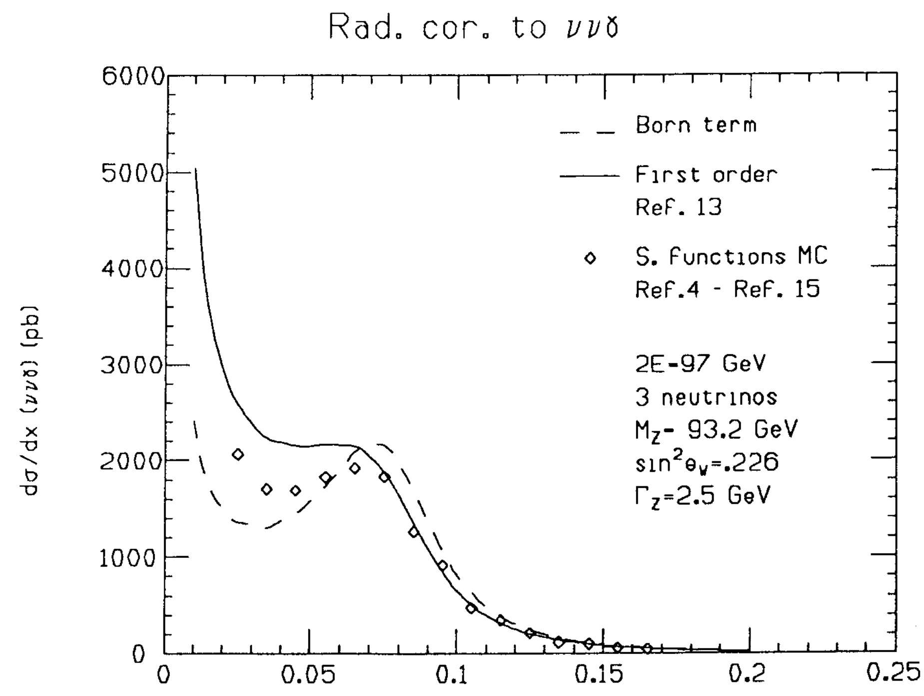
Rad. cor. to ννγ
dσ/dx (ννγ) (pb)
6000
5000
4000
3000
2000
1000
0
0
0.05
0.1
0.15
0.2
0.25
x
Born term
First order
Ref. 13
S. functions MC
Ref.4 - Ref. 15
2E-97 GeV
3 neutrinos
MZ- 93.2 GeV
sin2θW=.226
ΓZ=2.5 GeV

Fig. 12

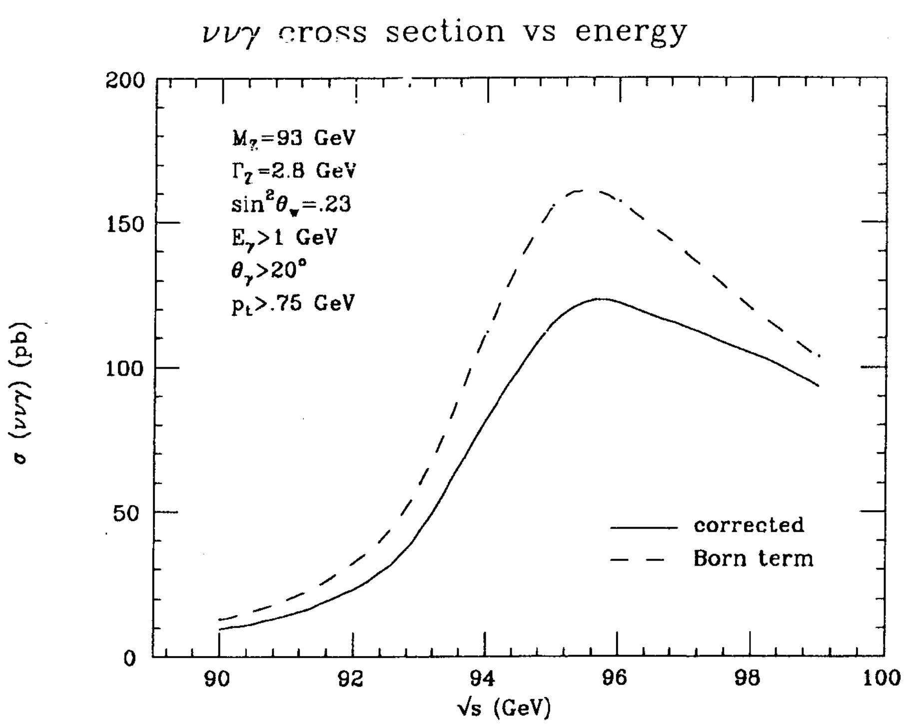
ννγ cross section vs energy
σ (ννγ) (pb)
200
150
100
50
0
90
92
94
96
98
100
√s (GeV)
MZ=93 GeV
ΓZ=2.8 GeV
sin2θW=.23
Eγ>1 GeV
θγ>20°
pt>.75 GeV
corrected
Born term

Fig. 13

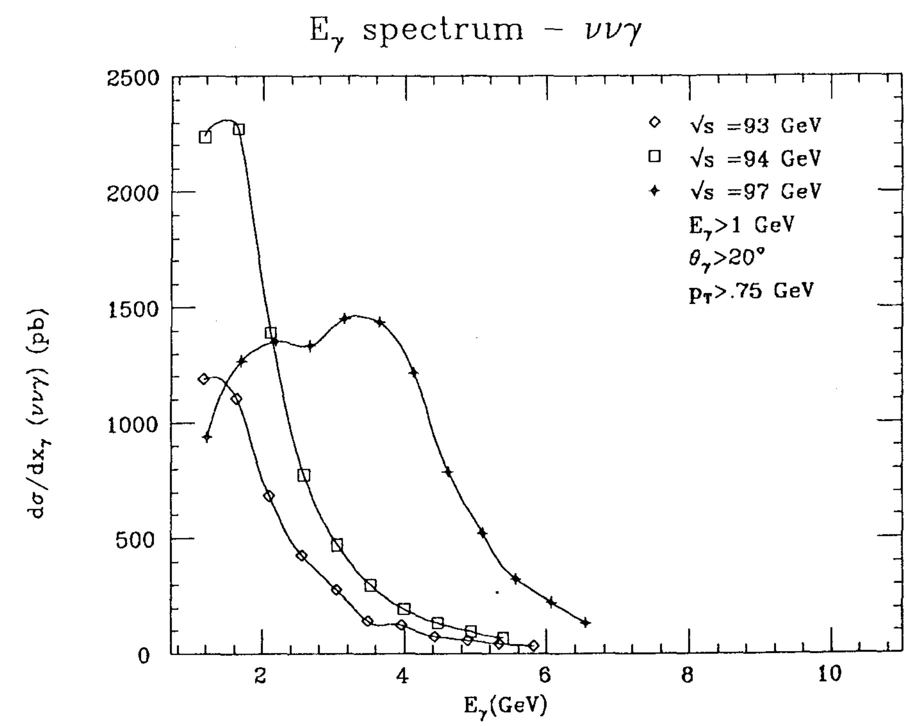

E$_\gamma$ spectrum - $\nu\nu\gamma$
2500
2000
1500
1000
500
0
$d\sigma/dx_\gamma$ ($\nu\nu\gamma$) (pb)
$\sqrt{s}$ =93 GeV
$\sqrt{s}$ =94 GeV
$\sqrt{s}$ =97 GeV
E_γ>1 GeV
θ_γ>20°
p_T>.75 GeV
2
4
6
8
10
E_γ(GeV)

Fig. 14

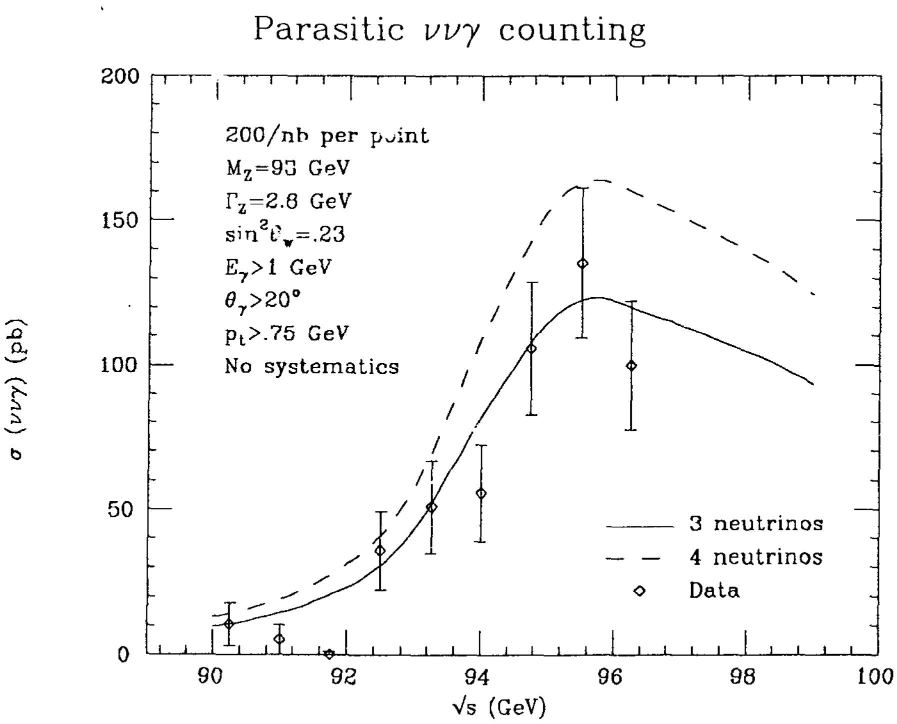

Parasitic $\nu\nu\gamma$ counting
200
150
100
50
0
σ ($\nu\nu\gamma$) (pb)
200/nb per point
M_Z=93 GeV
Γ_Z=2.8 GeV
$\sin^2\theta_w$=.23
E_γ>1 GeV
θ_γ>20°
p_t>.75 GeV
No systematics
3 neutrinos
4 neutrinos
Data
90
92
94
96
98
100
$\sqrt{s}$ (GeV)

Fig. 15

Mark II SLC Physics Working Group Notes Page 1

Working Group No. 0 – General 07/27/87

Number	Date	Author(s)	Title
0- 1	09/17/85	G. Feldman	CERN Lecture Notes on SLC Physics
0- 2	03/28/86		Transparencies from MarkII SLC-Physics Workshop, Asilomar, Mar. 16-19, 1986
0- 3	09/12/86	M. Nelson	Lepton p and p_t Distribution at SLC
0- 4	09/25/86		Transparencies from MarkII SLC-Physics Workshop, Granlibakken, Sept. 14-17, 1986
0- 5	11/17/86	G. Barbiellini H. Sadrozinski	Search for Flavour Changing-Neutral Current at the Z^0
0- 6	11/18/86	T. Glanzman	Granlibakken Report on the SSP Trigger
0- 7	03/26/87	P. Burchat	PRFIND, an e^+ e^- pair-finding routine
0- 8	03/05/87		Transparencies from MarkII SLC-Physics Workshop, Pajaro Dunes, 2/25/87-2/28/87
0- 9	04/09/87	Chris Hawkes	Status Report on Lepton Identification
0-10	02/25/87	G. Goldhaber	Review of $p\bar{p}$ Collider Physics Relevant to the Mark II
0-11	06/29/87	G. Feldman	Pajaro Dunes Workshop Summary

Mark II SLC Physics Working Group Notes Page 2

Working Group No. 1 – Z Direct Mass and Width 07/27/87

Number	Date	Author(s)	Title
1- 1	01/20/86	G. Feldman	Optimum Energy Scanning Strategy
1- 2	05/27/86	M. Levi	Low Energy Comparison of the Berends, Kleiss, and Jadach Program MMG1
1- 3	09/08/86	T. Rankin	Physics from Z^0 Measurements: Mass, Width, and Total Cross Section
1- 4	09/22/86	Dallas Kennedy B. Lynn	The Renormalization of Electroweak Interactions and the BREMMUS Monte Carlo Simulator
1- 5	10/08/86	J. Alexander G. Bonvicini P. Drell R. Frey B. Milliken	A Study of QED Radiative Corrections at the Z
1- 6	11/20/86	S. T. Jadach B.F.L. Ward	Renormalization Group Improved Yennie-Frautschi-Suura Theory and Monte Carlo Event Generators
1- 7	10/16/86	M. Levi	Status Report on the Mark II Energy Measurement System
1- 8	12/05/86	D. Bannon J. Kent	Stat. Errors from Extraction-line Spectrometer Data Sampling
1- 9	06/06/87	P. Rankin	Z^0 Measurements; The Theory and The Practice
1-10	04/09/87	G. Wormser	Beam Energy Measurements for the First 3 Months of SLC Operation
1-11	04/15/87	D. Kennedy	The BREM5 Electroweak Monte Carlo
1-12	07/16/87	J. Alexander et al,	Radiative Corrections to the Z^0 Resonance

Number	Date	Author(s)	Title
2- 1	09/16/85	B. Williams	The Momentum Spectrum of Leptons, the Helicity of $b\&\bar{b}$ Quarks, and the Forward-Backward $b\bar{b}$ Production Asymmetry
2- 2	12/04/85	B. Williams	The Observation of Λ Polarization
2- 3	01/28/86	J. Matthews	Improvement in Mark II Electron Identification Using dE/dx
2- 4	09/11/85	J. Matthews	Minutes of Sept. 10, 1985 Group 2 Meeting
2- 5	10/08/85	J. Matthews	Minutes of Oct. 8, 1985 Group 2 Meeting
2- 6	11/25/85	J. Matthews	Minutes of Nov. 5, 1985 Group 2 Meeting
2- 7	12/07/85	J. Matthews	Minutes of Dec. 5, 1985 Group 2 Meeting
2- 8	01/20/86	J. Matthews	Minutes of Jan. 9, 1986 Group 2 Meeting
2- 9	02/15/86	J. Matthews	Minutes of Feb. 6, 1986 Group 2 Meeting
2-10	06/02/86	J. Matthews	Minutes of May 7, 1986 Group 2 Meeting
2-11	06/20/86	J. Matthews	Minutes of Jun. 18, 1986 Group 2 Meeting
2-12	07/14/86	J. Matthews	Minutes of Jul. 11, 1986 Group 2 Meeting
2-13	08/11/86	J. Matthews	Comparison of $e^+ e^- \to e^+ e^-$ (gamma) Monte Carlos
2-14	08/15/86	J. Matthews	Minutes of Aug. 15, 1986 Group 2 Meeting
2-15	10/09/86	R. Van Kooton	Documentation for KORALZ-A new Monte Carlo generator for the process $e^+ e^- \to Z \to \gamma^+\gamma^-(\gamma)$
2-16	10/07/86	P. Buchat	Status of Monte Carlos for τ Pair Production at SLC
2-17	10/03/86	J. Matthews	Report on Electroweak Parameters
2-18	10/27/86	S. Wagner Jim Smith S. White	Forward-Backward Asymmetry for b and c Quarks
2-19	11/17/86	K. Moffeit	Status Report on the Polarization Facility at the SLC
2-20	11/15/86	J. Matthews	Minutes of the November 14, 1986 Group 2 Meeting
2-21	11/25/86	C. Heusch	The Search for New Interactions Via Lepton Flavor Violation at or Beyond the Z^0 Pole
2-22	04/10/87	J. Matthews	Mark II/SLC Luminosity Measurements
2-23	06/07/87	G. Feldman	Measurement of the Total Hadronic Cross Section

Number	Date	Author(s)	Title
2-24	06/07/87	G. Feldman	On the Possibility of Measuring the Number of Neutrino Species to a Precision of $\frac{1}{2}$ Species with Only 2000 Z Events
2-25	07/15/87	D. Cords et al.	Tau Physics at the Z^0

Number	Date	Author(s)	Title
3- 1	10/24/85	Mark Nelson Gail Hanson	Open Top Meeting (Oct. 18): Minutes Transparencies & Addenda
3- 2	11/19/85	Gail Hanson	Minutes of Open Top Subgroup Meeting, November 15, 1985
3- 3	01/02/86	Mark Nelson Gail Hanson	Minutes of Open Top Subgroup Meeting December 5, 1985
3- 4	01/17/86	Gail Hanson Mark Nelson	Minutes of Open Top Subgroup Meeting, January 9, 1986
3- 5	05/05/86	Gail Hanson Mark Nelson	Minutes of Open Top Subgroup Meeting, May 1, 1986
3- 6	06/12/86	Mark Nelson Gail Hanson	Minutes of Open Top Subgroup Meeting, June 12, 1986
3- 7	07/16/86	Gail Hanson	Minutes of Open Top Subgroup Meeting, July 14, 1986
3- 8	08/22/86	Mark Nelson Gail Hanson	Minutes of Open Top Subgroup Meeting, Aug. 21, 1986
3- 9	10/16/86	K. O'Shaughnessy	Monte Carlo Models for Top Production
3-10	10/20/86	G. Hanson	Finding Open Top
3-11	10/22/86	T. Barklow	Supersymmetric Particle Searches
3-12	10/15/86	M. Perl	Small Visible Energy Events and Close Mass Lepton Pairs
3-13	11/17/86	D. Fujino	Finding the Hadronic Decay Mode of Top
3-14	11/18/86	G. Hanson	Minutes of Open Top Subgroup Meeting, October 23, 1986
3-15	12/08/86	D. Stoker	Decay Modes and Branching Fractions of 'Close Mass' Lepton Pairs
3-16	12/16/86	G. Hanson	Minutes of Open Top Subgroup Meeting, December 4, 1986
3-17	01/26/87	G. Hanson	Minutes of Open Top Subgroup Meeting, January 8, 1987
3-18	04/13/87	G. Hanson	Searches for the Top Quark
3-19	04/15/87	K. K. Gan	Heavy Charged Lepton Search
3-20	04/30/87	S. Komamiya	Searches for Higgs Pairs
3-21	07/25/87	T. Barklow	Searches for Supersymmetric Particles
3-22	06/24/87	G. Hanson	Minutes of Open Top Subgroup Meeting, June 4, 1987

Number	Date	Author(s)	Title
3-23	07/01/87	M. Perl	Small Multiplicity Events in $e^+ + e^- \to Z^0$ and Unconventional Phenomena
3-24	07/08/87	G. Hanson	Minutes of the July 2, 1987, Meeting of Open Top Subgroup

Working Group # 4 – Toponium Search 07/27/87

Number	Date	Author(s)	Title
4-1	11/19/85	Frank Porter	Toponium Event Rates
4- 2	10/30/85	Frank Porter	Toponium Physics with a Small Data Sample
4- 3	/85	H. Sadrozinski F. Gilman	Semi-Leptonic SQD Decays of Toponium and the Determination of the K-M Matri Element V_{bt}.
4- 4	05/18/87	H. Sadrozinski	Higgs Search with the Toponium Decay $\Theta \rightarrow \gamma H^0$
4- 5	02/28/87	B. Ward	Single Quark Decays in Toponium
4- 6	05/18/87	H. Sadrozinski	View from the Top(onium)

Working Group # 5 – (Long-lived) New Neutral Particles 07/27/87

Number	Date	Author(s)	Title
5- 1	10/10/86	Alan Weinstein	Reconstructing Heavy Long-Lived Neutral Leptons
5- 2	04/09/87	Spencer Klein	Detection and Identification of (Long Lived) Neutral Particles

Working Group # 6–New Stable or Long-lived Charged Particles 07/27/87

Number	Date	Author(s)	Title
6- 1	10/ /86	T. Banks, J. Bartelt A. Boyarski M. Karliner C. Peck E. Soderstrom R. Stroynowski	New Stable Charged Particles
6- 2	05/13/87	J. Bartelt	Prospects for A Magnetic Monopole Search With the Mark II at SLC

Working Group # 7 – – Single Higgs Search 07/27/87

Number	Date	Author(s)	Title
7-1	09/09/85	Andreas Schwarz	A compilation of useful formulas
7-2	09/24/86	Darien Wood	Sumary of work on $Z^0 \to$ Higgs $\nu\bar{\nu}$
7-3	05/12/86	Andreas Schwarz	Higgs production at the SLC
7-4	10/22/86	Andreas Schwarz	Higgs boson production at the Z^0 and the possibilities of vertex detectors
7-5	/ /86	W. Innes	Summary of Work on $Z^0 \to$ Higgs $f\bar{f}$
7-6	/ /86	A. Weir	Summary of Work on QCD Backgrounds to $Z^0 \to H^0\, l\bar{l}$

Working Group # 8 - - QCD 07/27/87

Number	Date	Author(s)	Title
8- 1	09/18/85	A. Petersen	Summary QCD Working Group Meeting - Sept. 11.
8- 2	10/22/86	A. Petersen	Comparison of Multihadronic Event Generators
8- 3	06/10/87	A. Petersen	QCD at the Z^0

Working Group # 9 - - c and b Quark Studies 07/27/87

Number	Date	Author(s)	Title
9- 1	10/18/85	Steve Wagner	Minutes and Transparencies from October 10 Meeting
9- 2	11/01/85	Steve Wagner	Minutes and Transparencies from October 24 Meeting
9- 3	11/21/85	Steve Wagner	Minutes of the 11/14/85 Meeting and Call for Subtask Signup
9- 4	12/22/85	Steve Wagner	Minutes of the 12/5/85 Meeting
9- 5	01/10/86	Steve Wagner	Minutes of the 1/9/86 Meeting
9- 6	01/10/86	A. Schwarz	How to generate a trackbank from Monte Carlo data including the vertex drift chamber
9- 7	05/15/86	Steve Wagner	Minutes of the 5/1/86 Meeting
9- 8	05/21/86	Alan Breakstone	Exclusive b&c Quark States Subgroup Report
9- 9	06/06/86	W. T. Ford	Measurement of bottom hadron lifetime via lepton impact parameter
9-10	08/07/86	W. T. Ford	Minutes of 8/5/86 Meeting
9-11	09/05/86	B. Ward	Exotics Subgroup Report
9-12	09/30/86	W. T. Ford	Granlibakken Meeting: b & c quark summary
9-13	11/10/86	Ken Hayes	A Study of $D^+ \to K^-\pi^+\pi^+$ Selection Using the Vertex Drift Chamber
9-14	10/15/86	D. Burke	Beam Position Measurements at the SLC IP
9-15	04/27/87	G. Wormser	ψ Tagging and B Spectroscopy
9-16	05/18/87	P. Weber	Vertex Tagging of b Quarks and the $Z^0 \to b$ Fraction
9-17	04/28/87	W. T. Ford	Measurement of the Bottom "Quark" Lifetime
9-18	06/16/87	D. Coupal	Inclusive Leptons and $B^0 - \bar{B}^0$ Mixing at SLC
9-19	07/15/87	K. Hayes	b and c Quark Exclusive Decays with the Vertex Detector
9-20	06/09/87	W. Ford	Collaboration with the Open Top Group

Number	Date	Author(s)	Title
10- 1	11/06/86	R. Thun & Nutrino-Counting Study Grp.	Counting Neutrinos at SLC
10- 2	04/15/87	Dean Karlen	Single γ Background to Neutrino Counting from radiative Bhabha Scattering
10- 3	06/14/87	G. Bonvicini et al.	Report from the Neutrino Counting Group